

University of Illinois at Urbana-Champaign

The logo for the Air Conditioning and Refrigeration Center (ACRC) features the letters 'ACRC' in a large, bold, white, italicized sans-serif font with a black outline. The letters are set against a horizontal background bar that is red on the left and blue on the right.

Air Conditioning and Refrigeration Center A National Science Foundation/University Cooperative Research Center

## **Flow-Induced Noise in Heat Exchangers**

E. Rodarte and N. R. Miller

ACRC CR-42

October 2001

*For additional information:*

Air Conditioning and Refrigeration Center  
University of Illinois  
Mechanical & Industrial Engineering Dept.  
1206 West Green Street  
Urbana, IL 61801

(217) 333-3115

*The Air Conditioning and Refrigeration Center was founded in 1988 with a grant from the estate of Richard W. Kritzer, the founder of Peerless of America Inc. A State of Illinois Technology Challenge Grant helped build the laboratory facilities. The ACRC receives continuing support from the Richard W. Kritzer Endowment and the National Science Foundation. The following organizations have also become sponsors of the Center.*

Alcan Aluminum Corporation  
Amana Refrigeration, Inc.  
Arçelik A. S.  
Brazeway, Inc.  
Carrier Corporation  
Copeland Corporation  
Dacor  
Daikin Industries, Ltd.  
Delphi Harrison Thermal Systems  
General Motors Corporation  
Hill PHOENIX  
Honeywell, Inc.  
Hydro Aluminum Adrian, Inc.  
Ingersoll-Rand Company  
Invensys Climate Controls  
Kelon Electrical Holdings Co., Ltd.  
Lennox International, Inc.  
LG Electronics, Inc.  
Modine Manufacturing Co.  
Parker Hannifin Corporation  
Peerless of America, Inc.  
Samsung Electronics Co., Ltd.  
Tecumseh Products Company  
The Trane Company  
Valeo, Inc.  
Visteon Automotive Systems  
Wolverine Tube, Inc.  
York International, Inc.

*For additional information:*

*Air Conditioning & Refrigeration Center  
Mechanical & Industrial Engineering Dept.  
University of Illinois  
1206 West Green Street  
Urbana, IL 61801*

*217 333 3115*

## Abstract

Flow-induced tonal noise and acoustic resonance problems are found in a variety of applications that range from nuclear power plant heat exchangers to automobile air conditioning evaporators. Flow-induced noise in heat exchangers is a very complex phenomenon. The complexities are caused by several factors that affect the noise generation and attenuation mechanisms of sound sources inside ducts, and by fluid-acoustic-structural coupling effects. To predict the noise from bluff bodies inside a duct, one needs to account for the sound source's strength and directionality, the damping and sound attenuation mechanisms inside the duct, and the effects produced by the coupling between the acoustic field and the vortex generation process. Flow-induced tonal noise generated in plate heat exchangers has unusual features that have not been previously explored.

Measurements of the flow-induced noise produced by plate heat exchangers, arrays of cylinders, cylinders in tandem, side by side cylinders, single cylinders of constant diameter and "hourglass" shaped cylinders inside a rectangular duct have been made. The acoustic field in parts of the duct in which traveling hydrodynamic pressure fluctuations produced by vortex shedding do not contaminate the results was investigated by measuring sound pressure levels. Many of the results are believed to be unique. The measurements were then used to infer noise source strength and system damping using an acoustic model. The acoustic model was based on the inhomogeneous convected Helmholtz equation with a point dipole source term, volumetric damping and damping at the duct walls. The acoustic model was able to closely match the measured sound pressure field and the phase relationships between measurement points for sound generated by flow over short aspect ratio single cylinders inside a duct. The acoustic model based technique was also applied to investigate some of the flow-induced noise behavior and trends of side by side cylinders, cylinders in tandem and a staggered cylinder array with many cylinders.

# Table of Contents

	Page
<b>Abstract</b> .....	<b>iii</b>
<b>List of Figures</b> .....	<b>x</b>
<b>List of Tables</b> .....	<b>xxxiii</b>
<b>Nomenclature</b> .....	<b>xxxiv</b>
<b>Chapter 1: Introduction</b> .....	<b>1</b>
<b>1.1 Description of flow-induced acoustic resonance phenomena in heat exchangers</b> .....	<b>1</b>
<b>1.2 Plate heat exchanger acoustic resonance</b> .....	<b>2</b>
<b>1.3 State of the art before this project</b> .....	<b>3</b>
<b>1.4 Motivation</b> .....	<b>5</b>
<b>1.5 Goal of this project</b> .....	<b>6</b>
<b>Chapter 2: Literature Review</b> .....	<b>7</b>
<b>2.1 Introduction</b> .....	<b>7</b>
<b>2.2 Flow excitation mechanisms</b> .....	<b>7</b>
2.2.1 Staggered arrays .....	11
2.2.2 In-line arrays .....	13
<b>2.3 Design guidelines and damping parameters</b> .....	<b>16</b>
<b>2.4 Acoustic resonance strength estimation</b> .....	<b>21</b>
<b>2.5 Conditions that affect an acoustic resonance in tube array heat exchangers</b> .....	<b>23</b>
2.5.1 Effect of tube array on the speed of sound .....	23
2.5.2 Effects of number of rows .....	23
2.5.3 The effect of tube pattern on sound pressure level .....	23
2.5.4 Effect of turbulence .....	24
2.5.5 Effect of tube roughness/fouling .....	24
2.5.6 Effect of Reynolds number .....	24
2.5.7 Effect of Mach number and pressure drop .....	24
<b>2.6 Factors that affect flow-induced noise generation produced by circular cylinders</b> .....	<b>25</b>
2.6.1 Effect of aspect ratio .....	26
2.6.2 Horseshoe vortex effect on Strouhal vortex shedding .....	30
2.6.3 Turbulence effects .....	31

2.6.4 Surface roughness effects .....	31
2.6.5 Wall blockage and boundary proximity effects .....	32
<b>Chapter 3: Modeling Flow-Induced Noise of Circular Cylinders Subject to Cross Flow Inside a Rectangular Duct .....</b>	<b>35</b>
<b>3.1 Introduction .....</b>	<b>35</b>
<b>3.2 Dipole sound from cylinders in a free field.....</b>	<b>35</b>
<b>3.3 Aeroacoustic theory for the prediction of the sound from a small aspect ratio circular cylinder subject to cross flow in unbounded space .....</b>	<b>37</b>
<b>3.4 Proposed Model .....</b>	<b>42</b>
3.4.1 Advantages and disadvantages of proposed model.....	42
<b>3.5 Dipole sound inside rectangular ducts .....</b>	<b>44</b>
3.5.1 Modeling assumptions.....	45
3.5.2 Derivation of inhomogeneous convected wave equation with a dipole source term .....	46
3.5.3 Description of wall boundary conditions.....	49
3.5.4 Solution of the inhomogeneous convected Helmholtz equation with a dipole source term inside an infinite rectangular duct with rigid walls .....	51
3.5.5 Point dipole inside an infinite rectangular duct with absorbing walls and uniform flow.....	57
3.5.6 Point dipole inside an infinite rectangular duct with volumetric damping, rigid walls and uniform flow.....	60
3.5.7 Point dipole inside an infinite rectangular duct with volumetric damping, absorbing walls and uniform flow.....	60
3.5.8 Cutoff or resonant frequencies in a rectangular waveguide with flow .....	60
<b>3.6 Mathematical model convergence.....</b>	<b>61</b>
3.6.1 Introduction.....	61
3.6.2 Analytical model error estimation.....	62
3.6.3 Numerical experiments on model solution convergence .....	64
3.6.4 Comparison to a finite element solution from the literature .....	67
<b>Chapter 4: Experimental Apparatus, Test Specimens and Data Analysis .....</b>	<b>68</b>
<b>4.1 Introduction.....</b>	<b>68</b>
<b>4.2 Description of R134a refrigerant (1,1,1,2 tetrafluoroethane) experimental apparatus .....</b>	<b>68</b>
<b>4.3 Description of nitrogen experimental apparatus .....</b>	<b>70</b>
<b>4.4 Compressed air experimental apparatus .....</b>	<b>71</b>
4.4.1 Introduction.....	71
4.4.2 Description of compressed air experimental apparatus.....	72

4.4.3 Anechoic terminations used in the wind tunnel.....	75
4.4.4 Flow velocity inside the wind tunnel.....	76
<b>4.5 Description of plate heat exchanger test samples .....</b>	<b>81</b>
4.5.1 Introduction.....	81
4.5.2 Dynamic pressure measurements .....	81
4.5.3 Acceleration measurements .....	82
<b>4.6 Description of stereolithography prototypes and the test section .....</b>	<b>85</b>
4.6.1 Introduction.....	85
4.6.2 Stereolithography prototypes and test section.....	85
<b>4.7 Description of single cylinder and cylinder pair tests.....</b>	<b>87</b>
4.7.1 Introduction.....	87
4.7.2 Single cylinder tests.....	87
4.7.3 Test on pairs of cylinders .....	95
<b>4.8 Instrumentation and sensor calibration .....</b>	<b>97</b>
4.8.1 Introduction.....	97
4.8.2 Data acquisition system.....	97
4.8.3 Venturi flow meter calibration .....	98
4.8.4 Static pressure transducer calibration.....	100
4.8.5 Microphone specifications and amplitude calibration.....	102
4.8.6 Microphone pair phase calibration (¼” microphones).....	105
4.8.7 Dynamic pressure transducer pairs phase calibration (0.1” sensors).....	107
4.8.8 Effect of microphone size in measurement uncertainties .....	111
4.8.9 Effect of surface irregularities .....	113
<b>4.9 Data Reduction.....</b>	<b>113</b>
4.9.1 Introduction.....	113
4.9.2 Uncertainty analysis .....	114
<b>4.10 Hydrodynamic pressure fluctuations in 38.1 x 2.5 mm rectangular duct with flow .....</b>	<b>117</b>
<b>4.11 Acoustic vs. hydrodynamic pressure fluctuations.....</b>	<b>120</b>
<b>Chapter 5: Experimental Results .....</b>	<b>123</b>
<b>5.1 Introduction.....</b>	<b>123</b>
<b>5.2 Plate heat exchanger tests.....</b>	<b>123</b>
5.2.1 Acceleration tests .....	123
5.2.2 Dynamic pressure tests .....	131

<b>5.3 Stereolithography cylinder array tests</b> .....	<b>133</b>
5.3.1 Normal triangular arrays.....	133
5.3.2 In-line square arrays.....	138
5.3.3 Staggered arrays.....	142
<b>5.4 Results of tests of single circular cylinders inside a duct</b> .....	<b>146</b>
5.4.1 Cylinders of constant diameter.....	146
5.4.2 Hourglass shaped cylinders.....	163
<b>5.5 Tests on pairs of cylinders inside a duct</b> .....	<b>166</b>
5.5.1 Side-by-side cylinders.....	167
5.5.2 Cylinders in tandem.....	171
<b>Chapter 6: Acoustic Model Based Inferences Using Experimental Results</b> .....	<b>177</b>
6.1 Introduction.....	177
6.2 Dipole source strength from cylinders in cross-flows.....	177
6.3 Methodology used in the application of the acoustic model.....	178
6.5 Single cylinder experimental and modeling results.....	180
6.6 Hourglass single cylinder experimental and modeling results.....	190
6.7 Single cylinder with acoustic foam at y-walls experimental and modeling results.....	192
6.8 Tandem cylinders experimental and modeling results.....	194
6.9 Side-by-side cylinders experimental and modeling results.....	203
6.10 Cylinder array model and comparison with experimental results.....	204
6.11 Convection effects on first transverse acoustic resonance frequency.....	211
<b>Chapter 7: Numerical Experiments</b> .....	<b>213</b>
7.1 Introduction.....	213
7.2 Effect of volumetric damping on acoustic field.....	213
7.3 Effect of walls acoustic impedance on acoustic field.....	219
7.4 Effect of density, flow velocity, fluctuating lift coefficient, and cylinder dimensions (Parameters that influence dipole source strength).....	224
7.5 Effect of nondimensional volumetric damping and finite y-wall specific acoustic impedance on the first transverse acoustic resonance frequency of a duct with flow.....	225
<b>Chapter 8: Summary and Suggestions for Future Work</b> .....	<b>227</b>
8.1 Summary of results.....	227
8.2 Summary of results for single cylinders.....	227
8.2.1 Constant diameter cylinders.....	227

8.2.2 “Hourglass” shaped cylinders .....	228
<b>8.3 Summary of results for multiple cylinders .....</b>	<b>228</b>
8.3.1 Side-by-side cylinders .....	228
8.3.2 Tandem cylinders .....	228
8.3.3 Cylinder arrays .....	229
8.3.4 Plate heat exchangers .....	229
<b>8.4 Design recommendations to avoid flow-induced tonal noise in plate evaporators .....</b>	<b>229</b>
<b>8.5 Contributions of present study .....</b>	<b>230</b>
<b>8.6 Recommendations for future work .....</b>	<b>231</b>
<b>Appendix A: Acoustic Impedance and Reflections Coefficients of Different Duct Terminations .....</b>	<b>233</b>
A.1 Introduction .....	233
A.2 Formulation and limitations .....	233
A.3 Technique validation .....	235
A.4 Evaluation of different acoustic terminations .....	237
<b>Appendix B: Flow Velocity Mapping Inside 2.5 x 38.1 mm Test Section .....</b>	<b>242</b>
B.1 Introduction .....	242
B.2 Description of measurements .....	242
B.3 Flow velocity using a Pitot tube .....	242
B.4 Velocity profile estimation using the logarithmic overlap law .....	243
B.5 Description of included material .....	244
Flow velocity data reduction program for EES (engineering equation solver) Ver 6.026. ....	249
<b>Appendix C: Plate Sample Acceleration Measurement Test Results .....</b>	<b>251</b>
<b>Appendix D: Plate Sample Dynamic Pressure Test Results .....</b>	<b>257</b>
<b>Appendix E: In-line Square Arrays Test Results .....</b>	<b>269</b>
<b>Appendix F: Staggered Arrays Test Results .....</b>	<b>277</b>
<b>Appendix G: Single Cylinders Test Results .....</b>	<b>327</b>
<b>Appendix H: Pairs of Cylinders Test Results .....</b>	<b>357</b>
<b>Appendix I: Matlab Programs to Solve Modeling and Optimization Equations .....</b>	<b>381</b>
I.1 Main optimization program to find complex wall impedance coefficients .....	381
I.2 Objective function used by complex wall impedance coefficients main program .....	381



I.3 Function that solves for the complex acoustic pressure ratio for microphone pairs.....	382
I.4 Main optimization program to find complex volumetric damping coefficients.....	383
I.5 Objective function used by complex volumetric damping coefficients main program.....	384
I.6 Main optimization program to find fluctuating lift coefficient when values of acoustic damping are known or assumed.....	384
I.7 Objective function used by fluctuating lift coefficients main program.....	385
I.8 Function that solves for the acoustic pressures at each microphone position.....	385
I.9 Main optimization program to find fluctuating lift coefficients and Non-dimensional volumetric damping simultaneously.....	388
I.10 Objective function used by fluctuating lift coefficient and volumetric damping main program .....	388
I.11 Main program to find acoustic pressures produced by staggered cylinder array with $T/D=L/D=3.0$ .....	389
I.12 Function to determine acoustic pressure of each source at desired location used by main program shown in section I.11 .....	390
<b>Appendix J: Contour Plots of Acoustic Field .....</b>	<b>392</b>
<b>Bibliography .....</b>	<b>400</b>

## List of Figures

	Page
Figure 1.1 Schematic diagram of the acoustic resonance phenomenon in heat exchangers.....	1
Figure 1.2 Photograph of typical plate heat exchangers used in automobile applications.....	4
Figure 1.3 Photographs of three different single stamped plates used to make evaporators showing their internal structure design.....	4
Figure 2.1. Standard tube array geometries with relevant nomenclature. [Weaver 1993]. ....	8
Figure 2.2. In-line tube array inside a rectangular duct showing some definitions to be used in this document. Array with 7 columns and 14 rows.....	8
Figure 2.3 Tube array with nomenclature used in equation (2.1).....	9
Figure 2.4. Schematic of flow instabilities present for closely packed and intermediately spaced in-line tube arrays.....	15
Figure 2.5 Schematic showing description of resonant chamber in in-line arrays as described by Grotz and Arnold.....	17
Figure 2.6 Typical disturbances encountered by a single cylinder perpendicular to uniform flow: a) turbulence, b) surface roughness, c) wall blockage, d) wall proximity, e) aspect ration, f) free end, g) transverse oscillations, and h) streamwise oscillations. [Zdravkovich 1997].....	25
Figure 2.7 Fluctuating lift as a function of end plate separation. a) $Re = 1.6 \times 10^4$ , b) $Re = 4.3 \times 10^4$ . From Szepessy and Bearman 1992.....	27
Figure 2.8 Fluctuating lift as a function of end plate separation for different values of Reynolds number. Plotted with data taken from Szepessy and Bearman 1992.....	28
Figure 2.9 Fluctuating lift as a function of Reynolds number for aspect ratios of 1 and 6.7. From Szepessy and Bearman.....	29
Figure 2.10 Cross-correlation of pressure and velocity measurements along the cylinder span. Curves (a) for $L_{cyl}/D = 1.7$ (b) for $L_{cyl}/D = 6.7$ . From Szepessy and Bearman. Z represents here cylinder length and D cylinder diameter. ....	29
Figure 2.11 Stansby recommended circular cylinder endplate design to eliminate three-dimensional effects in tests with circular cylinders.....	30
Figure 2.12 Effect of surface roughness on circular cylinders. From Alemdaroglu et al. ....	33
Figure 2.13 Surface roughness effects on Strouhal number from circular cylinders. From Achenbach and Heinecke.....	33
Figure 2.14 Blockage effects on Strouhal number from circular cylinders. From Richter and Naudascher. B and D defined in Figure 2.6. ....	34
Figure 2.15 Blockage effects on fluctuating lift coefficient from circular cylinders. From Richter and Naudascher. B and D defined in Figure 2.6. ....	34
Figure 3.1 Coordinate systems used in modeling equations. With damping at the walls (center of the duct) and with rigid walls (duct corner). ....	51
Figure 3.2 Analytic series solution convergence assuming a point dipole produced by 6.35 mm cylinder at center of 2.5 x 38.1 mm duct. Calculations performed at microphone position 1a (see Figure 4.22). ....	64

Figure 3.3 Analytic series solution convergence assuming a point dipole produced by 6.35 mm cylinder at center of 2.5 x 38.1 mm duct. Calculations performed at microphone position 2a (see Figure 4.22).	65
Figure 3.4 Acoustic field predicted by model (SPL dB). Source strength estimations made assuming 6.35 mm cylinder at center of 2.5 x 38.1 mm duct. Solutions obtained at the wall. Graph made by interpolation of results obtained at a 16 x 16 matrix of equally spaced points in the plane of interest.	66
Figure 3.5 Square root of number of terms needed to obtain solutions presented in Figure 3.4.	66
Figure 3.6 Comparison between analytic solution from Model and Eversman and Steck finite element and analytic solution. Unit source at $X/L_c=Y/L_c=0.5$ (center of domain), $k_{L_c}=8.06$ , $M=0.3$ , $Y/L_c=0$ (at domain boundary) for different values of $X/L_c$ . X in flow direction, Y in width direction. (2 dimensional formulation)	67
Figure 4.1 Schematic of R134a refrigerant experimental setup.	69
Figure 4.2 Pressure-enthalpy diagram of refrigerant as it travels through the refrigerant test setup.	70
Figure 4.3 Schematic of nitrogen experimental setup.	71
Figure 4.4 Compressed air experimental apparatus.	73
Figure 4.5 Photograph of one of the two compressed air experimental test sections.	75
Figure 4.6 Schematic showing flow velocity measurement positions (black dots) in wind tunnel test section. Height (z direction) and width (y direction). Height scale twice width scale.	78
Figure 4.7 Contour plot showing velocity profile measured using compressed air at a Reynolds number (based on half the duct height and average velocity) of 7280. Height scale twice width scale. Contours in m/s.	78
Figure 4.8 Velocity profile comparison of measurements taken inside our test section and results from the literature. Solid triangles and squares overlap.	79
Figure 4.9 Comparison of velocity profile measurements with theoretical predictions using the logarithmic overlap law. Measurements at center of channel and along the channel height (z axis). Solid triangles and squares overlap.	80
Figure 4.10 Comparison of velocity profile measurements at center of channel and along the channel width (y direction).	80
Figure 4.11 Cross-sectional view of a plate heat exchanger used in automobile applications showing “hourglass” shaped cylinders. Cross section made at header location. Ruler graduations at side in millimeters.	83
Figure 4.12 Plate heat exchanger test sample showing the positions where the dynamic pressure transducers were mounted.	83
Figure 4.13 Schematic of two types of plate heat exchanger test samples showing the naming convention used for dynamic pressure (top) and acceleration measurements (bottom). The numbers on the bottom diagrams represent positions where accelerometers were mounted. The positions numbered S1-S5 represent side mounted locations.	84
Figure 4.14 Solid model of a typical prototype made using stereolithography.	85
Figure 4.15 Photograph of a finished stereolithography prototype being mounted for testing.	86
Figure 4.16 Photograph of top aluminum cover plate used to test the stereolithography prototypes.	86
Figure 4.17 Cross-sectional view of compressed air wind tunnel test section at cylinder position. The single cylinder samples were slid into position and aligned.	88

Figure 4.18 Photograph of aluminum constant diameter cylinder samples (ruler graduation in mm).....	88
Figure 4.19 Photograph of stereolithography constant diameter cylinder samples (ruler graduation in mm). ....	89
Figure 4.20 Photograph of hourglass shaped cylinders of different diameters (ruler graduation in mm).....	89
Figure 4.21 Drawings showing how the “hourglass” shaped cylinders were made. Dimensions in millimeters.....	90
Figure 4.22 Top view of test section showing 6.35 mm cylinder (dark circle) and microphone positions with the nomenclature used. Microphones Q6, Q7, d1, and d2 are mounted on a movable slide. Drawing to scale.....	92
Figure 4.23 Top view of test section showing dimension from microphone positions to test cylinder. Dimension in millimeters. Microphones Q6, Q7, d1, and d2 are mounted on a movable slide. Drawing to scale.....	93
Figure 4.24 Surface profile measurements on aluminum cylinder with no machining (as is). ....	94
Figure 4.25 Surface profile measurements on aluminum cylinder after machining. ....	94
Figure 4.26 Surface profile measurements on stereolithography cylinder. ....	95
Figure 4.27 Top view of test section for pairs of cylinders tests. Dimension in millimeters. The movable slide shown in Figure 4.23 was replaced for side by side cylinder tests. Drawing to scale. ....	96
Figure 4.28 Flow measurement errors for Coriolis mass flow meter. ....	98
Figure 4.29 Mass flow measurements comparison between Coriolis and Venturi mass flow meters.....	100
Figures 4.30 Calibration data and curve fits for the four pressure transducers.....	102
Figure 4.31 Pistonphone microphone amplitude calibrator. This instrument produces a constant sound pressure level of 114dB at 250 Hz. ....	104
Figure 4.32 Power spectrum of acoustic pressure measured with 0.1” (2.54 mm) microphone using the pistonphone calibrator. ....	105
Figure 4.33 Sound intensity calibrator. This instrument needs a source signal to operate. It produces an identical acoustic pressure signal at the two microphones.....	106
Figure 4.34 Results of ¼” microphone pair phase calibration.....	107
Figure 4.35 Experimental setup used to verify phase behavior of 0.1” dynamic pressure transducer pairs.....	108
Figure 4.36 Typical results of 0.1” microphone pairs phase calibration.....	110
Figure 4.37 Top view of relative positions between the cylinder and the hypothetical microphones where error estimation due to acoustic pressure gradient was performed. Diagram to scale. ....	112
Figure 4.38 Sound pressure level (SPL) determined at the center of position 3 in Figure 4.37 (middle line). Top and bottom lines delimit the maximum possible error associated with moving the microphone center to the edges of the 4 mm diaphragm in the y direction. $C_L' = 0.5$ , $\rho = 1.33 \text{ kg/m}^3$ , $c_o = 345 \text{ m/s}$ . ....	113
Figure 4.39 Dynamic wall pressure power spectral density as a function of flow velocity inside rectangular duct of 38.1 x 2.5 mm. Measurement position is at microphone Q6 (See Figure 4.22). ....	118
Figure 4.40 Dynamic pressure level at wall in empty duct as a function of flow velocity at 6 different microphone locations. Empty symbol overall (0-10 kHz), solid symbol tonal maximum. ....	118
Figure 4.41 Nondimensional power spectral density of dynamic pressure measurements shown in Figure 4.39.....	119
Figure 4.42 Representative coherence measured between microphone positions 1a and 5a at 99.6 m/s (dashed lines) and 10.8 m/s (solid line) and between microphone positions Q6-Q1 at 56.6 m/s (small dotted line). ....	122

Figure 4.43 Comparison of the overall RMS dynamic pressure fluctuations measured at different positions inside our experimental test section as a function of Reynolds number. Dark triangles from Corcos measurements in pipe flow (Figure 1 in his paper).....	122
Figure 5.1 Acceleration power spectra taken from plate evaporator A using R134a refrigerant. Accelerometer positions on plate sample shown in Figure 4.13.....	126
Figure 5.2 Acceleration spectra obtained at position 7 in plate A using nitrogen.....	128
Figure 5.3 Acceleration spectra obtained at position 23 in plate sample F using nitrogen.....	129
Figure 5.4 Frequency-velocity and amplitude-velocity plots made using dynamic pressure measurement of plate F taken with nitrogen. (see Appendix D).....	132
Figure 5.5 Compilation of Strouhal numbers for normal triangular arrays. Data from Oengören and Ziada 1998. ...	135
Figure 5.6 Density estimations from pressure measurements in normal triangular array with P/D ratio of 2.6. ....	135
Figure 5.7 Waterfall plot of dynamic pressure spectra (relative dB scale) taken after 2 <sup>nd</sup> row in normal triangular array with P/D = 2.6, 5 columns and 19 rows. Velocity at right estimated from mass flow and density at point of measurement.....	136
Figure 5.8 Waterfall plot of dynamic pressure spectra (relative dB scale) taken after 12 <sup>th</sup> row in normal triangular array with P/D = 2.6, 5 columns and 19 rows. Velocity at right estimated from mass flow and density at point of measurement.....	136
Figure 5.9 Frequency and amplitude plots of the dominant peak in the spectrum measured by dynamic pressure transducers placed at the center of a normal triangular array with P/D ratio of 2.6. Array with 19 rows and 5 columns inside a 2 x 37.5 mm duct. Velocity calculated using density at each row and minimum cross sectional area in array. ....	137
Figure 5.10 Strouhal number vs. Reynolds number for in-line square array with P/D = 2.0. Strouhal numbers from measurements at resonance except for the first two points at lower Reynolds number. ....	140
Figure 5.11 Strouhal number vs. Reynolds number for in-line square array with P/D = 1.5. Strouhal numbers from measurements at resonance except for the first two points at lower Reynolds number. ....	140
Figure 5.12 Strouhal numbers for square in-line arrays (from Weaver et al. 1987). ....	141
Figure 5.13 Comparison of measured resonant frequencies with estimations of resonant frequencies made assuming solidity ( $\sigma$ ) and flow effects (Ma), flow effects only (Ma) and no effects. In-line square array with P/D = 1.5. ....	141
Figure 5.14 Comparison of measured resonant frequencies with estimations of resonant frequencies made assuming solidity ( $\sigma$ ) and flow effects (Ma), flow effects only (Ma) and no effects. In-line square array with P/D = 2.0. ....	142
Figure 5.15 Frequency of dominant peak in spectra vs. mass flow for staggered array with T/D = 3.0 and L/D = 0.9. Lines of natural frequencies (fn1, fn2) estimated assuming effects of solidity ( $\sigma$ ) and Mach number (Ma).....	145
Figure 5.16 Frequency of dominant peak in spectra vs. empty duct flow velocity for staggered array with T/D = 3.0 and L/D = 0.9. Lines of natural frequencies (fn1, fn2) estimated assuming effects of solidity ( $\sigma$ ) and Mach number (Ma).....	145
Figure 5.17 Comparison of Strouhal numbers for arrays with T/D = 3.0 and different L/D ratios with results from Chen 1968 and Fitz-Hugh. ....	146

Figure 5.18 Waterfall plot of spectra measured at microphone position 2a. Single 6.35 mm cylinder diameter. Acoustic resonance estimated with flow velocity at resonance condition (fn1 with flow).....	148
Figure 5.19 Waterfall plot of spectra measured at microphone position 6a. 6.35 mm cylinder diameter. Acoustic resonance estimated with flow velocity at resonance condition (fn1 with flow).....	148
Figure 5.20 Plot of the frequencies of the dominant peak in the spectra as a function of flow velocities for different diameter cylinder. ....	150
Figure 5.21 Experimentally determined sound pressure levels at different microphone positions produced by a single 6.35 mm diameter cylinder inside a duct. Figure 4.22 and 4.23 show measurement positions. Acoustic resonance estimated with flow velocity at resonance condition (fn1 with flow) . ....	150
Figure 5.22 Experimentally determined transfer function phase angle between microphone pairs at dominant frequency in the spectra. Cylinder diameter = 6.35 mm. ....	151
Figure 5.23 Repeatability of sound pressure level measurements at microphone position 2a. Cylinder diameter = 6.35 mm . ....	152
Figure 5.24 Repeatability of phase measurements at vortex shedding frequency for microphone pair 2a -6a. Cylinder diameter = 6.35 mm. Microphone at position 2a used as reference. ....	152
Figure 5.25 Comparison of sound pressure levels (SPL) vs. frequency at microphone position 2a for different cylinder diameters (see Figure 4.22). ....	154
Figure 5.26 Comparison of sound pressure levels (SPL) vs. flow velocity at microphone position 2a for different cylinder diameters (see Figure 4.22). ....	154
Figure 5.27 Comparison of phase angle at frequency of dominant peak in spectra between microphones at positions 2a and 6a for different cylinder diameters.....	155
Figure 5.28 Sound pressure level vs. frequency of dominant peak in spectra at microphone position d1 for different cylinder diameters. ....	155
Figure 5.29 Sound pressure level vs. frequency of dominant peak in spectra at symmetric positions upstream (3a) and downstream (d1) of the test cylinder. Test performed with 6.35 mm diameter cylinder. ....	156
Figure 5.30 Strouhal vs. Reynolds number plot for different cylinder diameters. Reynolds and Strouhal numbers calculated using average flow velocity in the duct.....	157
Figure 5.31 Strouhal vs. Reynolds number plot for different cylinder diameters. Reynolds and Strouhal numbers calculated using average flow velocity in the duct. Detail view of Figure 5.30. ....	158
Figure 5.32 Repeatability of Strouhal number measurements.....	159
Figure 5.33 Comparison of sound pressure levels at microphone position 1a when different types of acoustic damping materials are applied to duct side walls. Cylinder diameter = 6.35mm. Acoustic resonance estimated with flow velocity at resonance condition (fn1 with flow). ....	161
Figure 5.34 Comparison of sound pressure levels at microphone position d1 when different types of acoustic damping materials are applied to duct side walls. Cylinder diameter = 6.35 mm. Acoustic resonance estimated with flow velocity at resonance condition (fn1 with flow). ....	162
Figure 5.35 Transfer function phase angle at frequency of dominant peak in spectra between microphone pair at positions 2a-1a. Acoustic resonance estimated with flow velocity at resonance condition (fn1 with flow). ....	162

Figure 5.36 Transfer function phase angle at frequency of dominant peak in spectra between microphone pair at positions 2a-4a. Acoustic resonance estimated with flow velocity at resonance condition ( $f_{n1}$ with flow).	163
Figure 5.37 Sound pressure levels at position 1a vs. frequency at dominant peak in spectra for cylinders with 0.5 mm curvature profile. Diameter at center of “hourglass” shaped cylinder (minimum diameter).	165
Figure 5.38 Comparison of Strouhal vs. Reynolds numbers calculated from measurements in “hourglass” cylinders. Diameter at center of “hourglass” shaped cylinder (minimum diameter).	165
Figure 5.39 Side-by-side and tandem cylinder arrangements showing flow regimes for spacing used in our tests. (from Zdravkovich 1987)	166
Figure 5.40 Comparison of Strouhal vs. Reynolds numbers for side-by-side tests. Strouhal number estimated using frequency of dominant peak in spectra at microphone position d3.	169
Figure 5.41 Sound pressure levels vs. average flow velocity at microphone position 2a.	170
Figure 5.42 Comparison of sound pressure levels vs. average flow velocity of 6.35mm side-by-side cylinders and 6.35 mm single cylinder. Measurement position 2a.	170
Figure 5.43 Comparison of sound pressure levels vs. frequency of 6.35 mm side-by-side cylinders and 6.35 mm single cylinder. Measurement position 2a. ( $f_{n1}$ and $f_{n2}$ with flow) acoustic resonances estimated with flow velocity at resonance condition.	171
Figure 5.44 Comparison of frequency of dominant peak in spectra vs. average flow velocity in the duct.	173
Figure 5.45 Comparison of Strouhal vs. Reynolds numbers from experiments on cylinders in tandem.	174
Figure 5.46 Comparison of phase angle vs. frequency of dominant peak in spectra for cylinders in tandem tests. Microphone pair 2a-4a. 3.5 mm single cylinder results also plotted for comparison.	174
Figure 5.48 Comparisons of sound pressure level vs. frequency and sound pressure level vs. velocity of single cylinder results with results from the cylinders in tandem tests. Microphone position 2a. Acoustic resonance estimated with flow velocity at resonance condition ( $f_{n1}$ with flow).	175
Figure 5.49 Comparisons of sound pressure level vs. frequency and sound pressure level vs. velocity of single cylinder results with results from the cylinders in tandem tests. Microphone position 2a. Acoustic resonance estimated with flow velocity at resonance condition ( $f_{n1}$ with flow).	176
Figure 6.1 Fluctuating lift coefficients obtained using acoustic field measurements of single cylinders in a duct.	181
Figure 6.2 Fluctuating lift coefficients from the literature obtained with nominally smooth flows.	182
Figure 6.3 Fluctuating lift coefficients from the literature obtained with turbulent flows. Turbulent intensities reported shown to the right of the names in percentages.	184
Figure 6.4 Comparison of fluctuating lift coefficients obtained using different experimental data sets.	185
Figure 6.5 Fluctuating lift coefficients obtained in conjunction with damping coefficients.	187
Figure 6.6 Non-dimensional volumetric damping coefficients obtained with results from Figure 6.5.	187
Figure 6.7 Wall damping coefficients obtained with results from Figure 6.5.	187
Figure 6.8 Comparison of experimental and model sound pressure levels as a function of tone frequency at different microphone positions. Cylinder diameter = 6.35 mm.	188
Figure 6.9 Comparison of experimental and modeling results of phase angle between microphone pairs as a function of tone frequency. Cylinder diameter = 6.35 mm.	189

Figure 6.10 Fluctuating lift coefficients obtained using the model and measurements of the acoustic field produced by an hourglass shaped cylinder inside a duct. ....	190
Figure 6.11 Comparison of experimental and model sound pressure levels as a function of tone frequency at different microphone positions. Hourglass cylinder 3.8 mm cylinder diameter and 1 mm base curvature. ....	191
Figure 6.12 Wall damping coefficients obtained for 2.5 mm acoustic foam on duct walls. ....	192
Figure 6.13 Comparison of experimental and model sound pressure levels as a function of tone frequency at different microphone positions. Using a 6.35 mm cylinder in duct with 2.5 mm acoustic foam on duct walls. ....	193
Figure 6.14 Fluctuating lift coefficients of cylinders in tandem and single cylinder. ....	197
Figure 6.15 Comparison of fluctuating lift coefficients found for the downstream cylinder using the model for the 6.35 mm and 4 mm diameter cylinders in tandem. ....	197
Figure 6.16 Comparison of measured and model sound pressure levels estimated for 6.35 mm diameter cylinders in tandem arrangement. ....	198
Figure 6.17 Comparison of measured and model sound pressure levels estimated for 4 mm diameter cylinders in tandem arrangement. ....	199
Figure 6.18 Sound pressure levels for 6.35 mm diameter cylinders in tandem arrangement. Experimental and model results at position 1a. Model results calculated assuming $C_L' = 0.5$ for both cylinders. ....	200
Figure 6.19 Sound pressure levels for 6.35 mm diameter cylinders in tandem arrangement. Experimental and model results at position 2a. Model results calculated assuming $C_L'$ from Figure 6.14 for each cylinder. ....	201
Figure 6.20 Sound pressure levels (dB) of cylinders in tandem arrangement obtained from the model. Small circles represent measurement positions. Large circles represent cylinders. The 6.35 mm diameter cylinders with $C_L'$ from Figure 6.14. Top 3562 Hz, middle 4187 Hz, bottom 5800 Hz. ....	202
Figure 6.21 Side-by-side cylinders modeling and experimental results comparisons. $C_L'$ assumed equal to single cylinder (shown in Figure 6.14). Measurements and calculations at microphone position 1a. Cylinder diameters = 6.35 mm. ....	206
Figure 6.22 Sound pressure levels field produced by two identical dipoles sources out of phase (top) and by only one of the dipole source present (bottom). Frequency 3725Hz. Small circles represent measurement positions. Large circles represent cylinders. Dipole source strength using 6.35 mm diameter cylinders data. ....	207
Figure 6.23 Comparison of sound pressure levels calculated using our model assuming two different fluctuating lift coefficients and noise sources to be in phase against results from measurements upstream of cylinder array. Staggered array with $T/D = L/D = 3.0$ ....	208
Figure 6.24 Similar to Figure 6.23 but plotted against frequency and for a reduced number of data points. ....	208
Figure 6.25 Fluctuating lift coefficients needed to adjust model results to be equal to measured results. Without velocity/density corrections. ....	210
Figure 6.26 Fluctuating lift coefficients needed to adjust model results to be equal to measured results. With velocity/density corrections. ....	211
Figure 6.27 Comparison of measurements and predictions of acoustic resonance frequency accounting for convection effects. ....	212



Figure 7.1 Sound pressure levels at different microphone positions as a function of frequency for different values of real nondimensional volumetric damping coefficient.....	215
Figure 7.2 Sound pressure levels at different microphone positions as a function of frequency for different values of imaginary nondimensional volumetric damping coefficient.....	216
Figure 7.3 Phase angle between different microphone pairs as a function of frequency for different values of real nondimensional volumetric damping coefficient.....	217
Figure 7.4 Phase angle between different microphone pairs as a function of frequency for different values of imaginary nondimensional volumetric damping coefficient.....	218
Figure 7.5 Sound pressure levels at different microphone positions as a function of frequency for different values of real y-walls specific acoustic impedance. ....	220
Figure 7.6 Sound pressure levels at different microphone positions as a function of frequency for different values of imaginary y-walls specific acoustic impedance. ....	221
Figure 7.7 Phase angle between different microphone pairs as a function of frequency for different values of real y-walls specific acoustic impedance.....	222
Figure 7.8 Phase angle between different microphone pairs as a function of frequency for different values of imaginary y-walls specific acoustic impedance. ....	223
Figure 7.9 Effect of changes in the variables that affect the dipole source strength on sound pressure levels. ....	225
Figure 7.10 Effect of changes in non-dimensional volumetric damping on first transverse acoustic resonance frequency of duct.....	226
Figure 7.11 Effect of changes in y-walls specific acoustic impedance on first transverse acoustic resonance frequency of duct.....	226
Figure A.1 Schematic of experimental apparatus needed to determine acoustic impedance and reflections coefficients using ASTM standard E1050-90.....	233
Figure A.2 Schematic of impedance tube arrangement used to measure acoustic impedance and reflection coefficients from different possible acoustic terminations.....	235
Figure A.3 Reflection coefficient of rectangular wind tunnel termination open to the atmosphere. ....	237
Figure A.4 Schematic of acoustic foam termination with foam at center of duct. Drawing to scale. Dimensions in mm. ....	239
Figure A.5 Reflection coefficient measured for acoustic termination shown in Figure A.4.....	239
Figure A.6 Schematic of acoustic foam termination with foam at sides of duct. Drawing to scale. Dimensions in mm. ....	240
Figure A.7 Reflection coefficient measured for acoustic termination shown in Figure A.6.....	240
Figure A.8 Schematic of acoustic foam termination with foam at sides of duct. Drawing to scale. Dimensions in mm. ....	241
Figure A.9 Reflection coefficient measured for acoustic termination shown in Figure A.8.....	241
Figure B.1 Contour plot showing velocity profile measured using compressed air at a Reynolds number (based on half the duct height and average velocity) of 2125. Height scale twice width scale. Contours in m/s.....	247
Figure B.2 Contour plot showing velocity profile measured using compressed air at a Reynolds number (based on half the duct height and average velocity) of 3170. Height scale twice width scale. Contours in m/s.....	247

Figure B.3 Contour plot showing velocity profile measured using compressed air at a Reynolds number (based on half the duct height and average velocity) of 4415. Height scale twice width scale. Contours in m/s.....	248
Figure B.4 Contour plot showing velocity profile measured using compressed air at a Reynolds number (based on half the duct height and average velocity) of 5860. Height scale twice width scale. Contours in m/s.....	248
Figure C.1 Photograph of plate A showing details of internal structure. The flow enters one side and exits the other side. The two passages are not connected. For our testing only one passage was used.....	251
Figure C.2 Frequencies at peaks in acceleration spectra for nitrogen and R134a tests. Differences in the frequencies caused by variations in speed of sound for the two fluids. Plate B identical to plate A except that a wire (baffle) was introduced in the center of the plates.....	251
Figure C.3 Photograph of plate C showing details of internal structure. ....	252
Figure C.4 Frequencies at peaks in acceleration spectra for nitrogen and R134a tests. Plate C.....	252
Figure C.5 Photograph of plate D showing details of internal structure. ....	253
Figure C.6 Frequencies at peaks in acceleration spectra for nitrogen and R134a tests. Plate D. ....	253
Figure C.7 Photograph of plate E showing details of internal structure. ....	254
Figure C.8 Frequencies at peaks in acceleration spectra for nitrogen and R134a tests. Plate E. ....	254
Figure C.9 Photograph of plate F showing details of internal structure.....	255
Figure C.10 Frequencies at peaks in acceleration spectra for nitrogen and R134a tests. Plate F. ....	255
Figure C.11 Photograph of plate G showing details of internal structure.....	256
Figure C.12 Frequencies at peaks in acceleration spectra for nitrogen and R134a tests. The spectra exhibit closely spaced peaks indicated as “frequency bands” in figure above. Plate G. ....	256
Figure D.1 Photograph of plate A2 showing details of internal structure. ....	257
Figure D.2 Frequency-velocity and amplitude-velocity plots made from values of peaks in dynamic pressure spectra obtained using nitrogen for plates A and A2.....	257
Figure D.3 Photograph of plate C2 showing details of internal structure.....	258
Figure D.4 Frequency-velocity and amplitude-velocity plots made from values of peaks in dynamic pressure spectra obtained using nitrogen for plates C and C2. ....	258
Figure D.5 Photograph of plate F2 showing details of internal structure. ....	259
Figure D.6 Frequency-velocity and amplitude-velocity plots made from values of peaks in dynamic pressure spectra obtained using nitrogen for plates F and F2. ....	259
Figure D.7 Dynamic pressure spectrum of plate sample A taken at inlet position. Inlet velocity and maximum pressure are plotted on the left.....	260
Figure D.8 Dynamic pressure spectrum of plate sample A2 taken at inlet and mid positions (left and right plots respectively). Inlet velocity and maximum pressure are plotted on the left. ....	261
Figure D.9 Dynamic pressure spectrum of plate sample C taken at inlet and mid positions (left and right plots respectively). Inlet velocity and maximum pressure are plotted on the left. ....	262
Figure D.10 Dynamic pressure spectrum of plate sample C2 taken at inlet and mid positions (left and right plots respectively). Inlet velocity and maximum pressure are plotted on the left. ....	263
Figure D.11 Dynamic pressure spectrum of plate sample F taken at mid position (right plots continue from end of left plots). Outlet velocity and maximum pressure are plotted on the left. ....	264

Figure D.12 Dynamic pressure spectrum of plate sample F2 taken at inlet and mid positions (left and right plots respectively). Inlet velocity and maximum pressure are plotted on the left. ....	265
Figure D.13 Dynamic pressure spectrum of plate sample A2 taken using R134a refrigerant. Inlet and mid positions (left and right plots respectively). Inlet velocity and maximum pressure are plotted on the left.....	266
Figure D.14 Dynamic pressure spectrum of plate sample F2 taken using R134a refrigerant. Mid and outlet positions (left and right plots respectively). Outlet velocity and maximum pressure are plotted on the left.....	267
Figure D.15 Dynamic pressure spectrum of plate sample F taken using R134a refrigerant. Inlet and mid positions (left and right plots respectively). Outlet velocity and maximum pressure are plotted on the left.....	268
Figure E.1 Schematic of in-line square array tested with $P/D = T/D = L/D = 2.0$ . Black dots represent microphone positions. Gray dots represent positions where static pressure measurements were made. Hatched dots are plugged microphone locations. Dimensions in mm. Drawing to scale. ....	269
Figure E.2 Sound pressure level of dominant peak in spectra. Microphone positions shown in Figure E.1. Inline array with $T/D = L/D = 2.0$ . ....	269
Figure E.3 Transfer function phase between microphone pairs shown at frequency of dominant peak in spectra of upstream microphone. Microphone positions shown in Figure E.1. Inline array with $T/D = L/D = 2.0$ . ....	270
Figure E.4 Coherence between microphone pairs at frequency of dominant peak in spectra of upstream microphone. Phase measurements presented in Figure E.3 prone to error if coherence not close to one. Inline array with $T/D = L/D = 2.0$ . ....	270
E.5 Plot of frequency of dominant peak in spectra vs. mass flow. Inline array with $T/D = L/D = 2.0$ . fn1, fn2... acoustic natural frequencies with solidity effect.....	271
E.6 Plot of frequency of dominant peak in spectra vs. flow velocity. Velocity estimated using density at measurement location and empty duct cross sectional area. Inline array with $T/D = L/D = 2.0$ . fn1, fn2... acoustic natural frequencies with solidity effect.....	271
Figure E.7 Representative spectra taken at upstream position, after 9 row and after 19 row (left, center and right respectively). Spectra in same line taken at identical mass flow conditions. Velocity estimated using density at measurement location and empty duct cross sectional area. Sound pressure level shown at left calculated for dominant peak in spectra. Inline array with $T/D = L/D = 2.0$ . ....	272
Figure E.8 Schematic of in-line square array tested with $P/D = T/D = L/D = 1.5$ . Black dots represent microphone positions. Gray dots represent positions where static pressure measurements were made. Hatched dots are plugged microphone locations. Dimensions in mm. Drawing to scale. ....	273
Figure E.9 Sound pressure level of dominant peak in spectra. Microphone positions shown in Figure E.8. Inline array with $T/D = L/D = 1.5$ . ....	273
Figure E.10 Transfer function phase between microphone pairs shown at frequency of dominant peak in spectra of upstream microphone. Microphone positions shown in Figure E.8. Inline array with $T/D = L/D = 1.5$ . ....	274
Figure E.11 Coherence between microphone pairs shown at frequency of dominant peak in spectra of upstream microphone. Phase measurements presented in Figure E.10 prone to error if coherence not close to one. Inline array with $T/D = L/D = 1.5$ . ....	274
E.12 Plot of frequency of dominant peak in spectra vs. mass flow. Inline array with $T/D = L/D = 1.5$ . fn1, fn2... acoustic natural frequencies with solidity effect.....	275

E.13 Plot of frequency of dominant peak in spectra vs. flow velocity. Velocity estimated using density at measurement location and empty duct cross sectional area. Inline array with $T/D = L/D = 1.5$ . $fn_1$ , $fn_2$ ... acoustic natural frequencies with solidity effect.....	275
Figure E.14 Representative spectra taken at upstream position, after 9 <sup>th</sup> row and after 19 <sup>th</sup> row (left, center and right respectively). Spectra in same line taken at identical mass flow conditions. Velocity estimated using density at measurement location and empty duct cross sectional area. Sound pressure level shown at left calculated for dominant peak in spectra. Inline array with $T/D = L/D = 1.5$ . ....	276
Figure F.1 Schematic of staggered array tested with $T/D = 3.0$ and $L/D = 3.0$ . Black dots represent microphone positions. Gray dots represent positions where static pressure measurements were made. Hatched dots are plugged microphone locations. Dimensions in mm. Drawing to scale. ....	277
Figure F.2 Sound pressure level of dominant peak in spectra. Microphone positions shown in Figure F.1. Staggered array with $T/D = 3.0$ and $L/D = 3.0$ . ....	277
Figure F.3 Transfer function phase between microphone pairs shown at frequency of dominant peak in spectra of upstream microphone. Microphone positions shown in Figure F.1. Staggered array with $T/D = 3.0$ and $L/D = 3.0$ . ....	278
Figure F.4 Coherence between microphone pairs at frequency of dominant peak in spectra of upstream microphone. Phase measurements presented in Figure F.3 prone to error if coherence not close to one. Staggered array with $T/D = 3.0$ and $L/D = 3.0$ . ....	278
F.5 Plot of frequency of dominant peak in spectra vs. mass flow. Staggered array with $T/D = 3.0$ and $L/D = 3.0$ . $fn_1$ , $fn_2$ ... acoustic natural frequencies with solidity effect.....	279
F.6 Plot of frequency of dominant peak in spectra vs. flow velocity. Velocity estimated using density at measurement location and empty duct cross-sectional area. Staggered array with $T/D = 3.0$ and $L/D = 3.0$ . $fn_1$ , $fn_2$ ... acoustic natural frequencies with solidity effect.....	279
Figure F.7 Strouhal numbers determined at different positions throughout the array using dominant peak in spectra. Velocity estimated using density at measurement location and full duct cross-sectional area. Staggered array with $T/D = 3.0$ and $L/D = 3.0$ . ....	280
Figure F.8 Zoom in of Figure F.7 showing Strouhal numbers behavior when frequencies of dominant peak in spectra below second transverse acoustic natural frequency of duct. Staggered array with $T/D = 3.0$ and $L/D = 3.0$ . ....	280
Figure F.9 Representative spectra taken at upstream position, after 8 <sup>th</sup> row and after 21 <sup>st</sup> row (left, center and right respectively). Spectra in same line taken at identical mass flow conditions. Velocity estimated using density at measurement location and empty duct cross-sectional area. Sound pressure level shown at left calculated for dominant peak in spectra. Staggered array with $T/D = 3.0$ and $L/D = 3.0$ .....	281
Figure F.10 Schematic of staggered array tested with $T/D = 3.0$ and $L/D = 2.5$ . Black dots represent microphone positions. Gray dots represent positions where static pressure measurements were made. Hatched dots are plugged microphone locations. Dimensions in mm. Drawing to scale. ....	282
Figure F.11 Sound pressure level of dominant peak in spectra. Microphone positions shown in Figure F.10. Staggered array with $T/D = 3.0$ and $L/D = 2.5$ . ....	282

Figure F.12 Transfer function phase between microphone pairs shown at frequency of dominant peak in spectra of upstream microphone. Microphone positions shown in Figure F.10. Staggered array with T/D = 3.0 and L/D =2.5. ....	283
Figure F.13 Coherence between microphone pairs at frequency of dominant peak in spectra of upstream microphone. Phase measurements presented in Figure F.12 prone to error if coherence not close to one. Staggered array with T/D = 3.0 and L/D =2.5. ....	283
Figure F.14 Plot of frequency of dominant peak in spectra vs. mass flow. Staggered array with T/D = 3.0 and L/D =2.5. fn1, fn2...acoustic natural frequencies with solidity effect. ....	284
Figure F.15 Plot of frequency of dominant peak in spectra vs. flow velocity. Velocity estimated using density at measurement location and empty duct cross-sectional area. Staggered array with T/D = 3.0 and L/D =2.5. fn1, fn2...acoustic natural frequencies with solidity effect. ....	284
Figure F.16 Strouhal numbers determined at different positions throughout the array using dominant peak in spectra. Velocity estimated using density at measurement location and full duct cross-sectional area. Staggered array with T/D = 3.0 and L/D =2.5. ....	285
Figure F.17 Representative spectra taken at upstream position, after 9 <sup>th</sup> row and after 25 <sup>th</sup> row (left, center and right respectively). Spectra in same line taken at identical mass flow conditions. Velocity estimated using density at measurement location and empty duct cross-sectional area. Sound pressure level shown at left calculated for dominant peak in spectra. Staggered array with T/D = 3.0 and L/D =2.5.....	286
Figure F.18 Schematic of staggered array tested with T/D = 3.0 and L/D = 2.0. Black dots represent microphone positions. Gray dots represent positions where static pressure measurements were made. Hatched dots are plugged microphone locations. Dimensions in mm. Drawing to scale. ....	287
Figure F.19 Sound pressure level of dominant peak in spectra. Microphone positions shown in Figure F.18. Staggered array with T/D = 3.0 and L/D =2.0. ....	287
Figure F.20 Transfer function phase between microphone pairs shown at frequency of dominant peak in spectra of upstream microphone. Microphone positions shown in Figure F.18. Staggered array with T/D = 3.0 and L/D =2.0. ....	288
Figure F.21 Coherence between microphone pairs at frequency of dominant peak in spectra of upstream microphone. Phase measurements presented in Figure F.20 prone to error if coherence not close to one. Staggered array with T/D = 3.0 and L/D =2.0. ....	288
Figure F.22 Plot of frequency of dominant peak in spectra vs. mass flow. Staggered array with T/D = 3.0 and L/D =2.0. fn1, fn2...acoustic natural frequencies with solidity effect. ....	289
Figure F.23 Plot of frequency of dominant peak in spectra vs. flow velocity. Velocity estimated using density at measurement location and empty duct cross-sectional area. Staggered array with T/D = 3.0 and L/D =2.0. fn1, fn2...acoustic natural frequencies with solidity effect. ....	289
Figure F.24 Strouhal numbers determined at different positions throughout the array using dominant peak in spectra. Velocity estimated using density at measurement location and full duct cross-sectional area. Staggered array with T/D = 3.0 and L/D =2.0. ....	290
Figure F.25 Representative spectra taken at upstream position, after 11 <sup>th</sup> row and after 32 <sup>nd</sup> row (left, center, and right, respectively). Spectra in same line taken at identical mass flow conditions. Velocity estimated	

using density at measurement location and empty duct cross-sectional area. Sound pressure level shown at left calculated for dominant peak in spectra. Staggered array with $T/D = 3.0$ and $L/D = 2.0$ .	291
Figure F.26 Schematic of staggered array tested with $T/D = 3.0$ and $L/D = 1.8$ . Black dots represent microphone positions. Gray dots represent positions where static pressure measurements were made. Hatched dots are plugged microphone locations. Dimensions in mm. Drawing to scale.	292
Figure F.27 Sound pressure level of dominant peak in spectra. Microphone positions shown in Figure F.26. Staggered array with $T/D = 3.0$ and $L/D = 1.8$ .	292
Figure F.28 Transfer function phase between microphone pairs shown at frequency of dominant peak in spectra of upstream microphone. Microphone positions shown in Figure F.26. Staggered array with $T/D = 3.0$ and $L/D = 1.8$ .	293
Figure F.29 Coherence between microphone pairs at frequency of dominant peak in spectra of upstream microphone. Phase measurements presented in Figure F.28 prone to error if coherence not close to one. Staggered array with $T/D = 3.0$ and $L/D = 1.8$ .	293
Figure F.30 Plot of frequency of dominant peak in spectra vs. mass flow. Staggered array with $T/D = 3.0$ and $L/D = 1.8$ . $fn_1, fn_2$ ...acoustic natural frequencies with solidity effect.	294
Figure F.31 Plot of frequency of dominant peak in spectra vs. flow velocity. Velocity estimated using density at measurement location and empty duct cross-sectional area. Staggered array with $T/D = 3.0$ and $L/D = 1.8$ . $fn_1, fn_2$ ...acoustic natural frequencies with solidity effect.	294
Figure F.32 Strouhal numbers determined at different positions throughout the array using dominant peak in spectra. Velocity estimated using density at measurement location and full duct cross-sectional area. Staggered array with $T/D = 3.0$ and $L/D = 1.8$ .	295
Figure F.33 Representative spectra taken at upstream position, after 25 <sup>th</sup> row and after 35 <sup>th</sup> row (left, center and right respectively). Spectra in same line taken at identical mass flow conditions. Velocity estimated using density at measurement location and empty duct cross-sectional area. Sound pressure level shown at left calculated for dominant peak in spectra. Staggered array with $T/D = 3.0$ and $L/D = 1.8$ .	296
Figure F.34 Schematic of staggered array tested with $T/D = 3.0$ and $L/D = 1.6$ . Black dots represent microphone positions. Gray dots represent positions where static pressure measurements were made. Hatched dots are plugged microphone locations. Dimensions in mm. Drawing to scale.	297
Figure F.35 Sound pressure level of dominant peak in spectra. Microphone positions shown in Figure F.34. Staggered array with $T/D = 3.0$ and $L/D = 1.6$ .	297
Figure F.36 Transfer function phase between microphone pairs shown at frequency of dominant peak in spectra of upstream microphone. Microphone positions shown in Figure F.34. Staggered array with $T/D = 3.0$ and $L/D = 1.6$ .	298
Figure F.37 Coherence between microphone pairs at frequency of dominant peak in spectra of upstream microphone. Phase measurements presented in Figure F.36 prone to error if coherence not close to one. Staggered array with $T/D = 3.0$ and $L/D = 1.6$ .	298
Figure F.38 Plot of frequency of dominant peak in spectra vs. mass flow. Staggered array with $T/D = 3.0$ and $L/D = 1.6$ . $fn_1, fn_2$ ...acoustic natural frequencies with solidity effect.	299

F.39 Plot of frequency of dominant peak in spectra vs. flow velocity. Velocity estimated using density at measurement location and empty duct cross-sectional area. Staggered array with $T/D = 3.0$ and $L/D = 1.6$ . fn1, fn2...acoustic natural frequencies with solidity effect.....	299
Figure F.40 Strouhal numbers determined at different positions throughout the array using dominant peak in spectra. Velocity estimated using density at measurement location and full duct cross-sectional area. Staggered array with $T/D = 3.0$ and $L/D = 1.6$ . .....	300
Figure F.41 Representative spectra taken at upstream position, after 18 <sup>th</sup> row and after 39 <sup>th</sup> row (left, center and right respectively). Spectra in same line taken at identical mass flow conditions. Velocity estimated using density at measurement location and empty duct cross-sectional area. Sound pressure level shown at left calculated for dominant peak in spectra. Staggered array with $T/D = 3.0$ and $L/D = 1.6$ .....	301
Figure F.42 Schematic of staggered array tested with $T/D = 3.0$ and $L/D = 1.4$ . Black dots represent microphone positions. Gray dots represent positions where static pressure measurements were made. Hatched dots are plugged microphone locations. Dimensions in mm. Drawing to scale. ....	302
Figure F.43 Sound pressure level of dominant peak in spectra. Microphone positions shown in Figure F.42. Staggered array with $T/D = 3.0$ and $L/D = 1.4$ . .....	302
Figure F.44 Transfer function phase between microphone pairs shown at frequency of dominant peak in spectra of upstream microphone. Microphone positions shown in Figure F.42. Staggered array with $T/D = 3.0$ and $L/D = 1.4$ . .....	303
Figure F.45 Coherence between microphone pairs at frequency of dominant peak in spectra of upstream microphone. Phase measurements presented in Figure F.44 prone to error if coherence not close to one. Staggered array with $T/D = 3.0$ and $L/D = 1.4$ . .....	303
Figure F.46 Plot of frequency of dominant peak in spectra vs. mass flow. Staggered array with $T/D = 3.0$ and $L/D = 1.4$ . fn1, fn2...acoustic natural frequencies with solidity effect. ....	304
Figure F.47 Plot of frequency of dominant peak in spectra vs. flow velocity. Velocity estimated using density at measurement location and empty duct cross-sectional area. Staggered array with $T/D = 3.0$ and $L/D = 1.4$ . fn1, fn2...acoustic natural frequencies with solidity effect. ....	304
Figure F.48 Strouhal numbers determined at different positions throughout the array using dominant peak in spectra. Velocity estimated using density at measurement location and full duct cross-sectional area. Staggered array with $T/D = 3.0$ and $L/D = 1.4$ . .....	305
Figure F.49 Representative spectra taken at upstream position, after 16 <sup>th</sup> row and after 45 <sup>th</sup> row (left, center and right respectively). Spectra in same line taken at identical mass flow conditions. Velocity estimated using density at measurement location and empty duct cross-sectional area. Sound pressure level shown at left calculated for dominant peak in spectra. Staggered array with $T/D = 3.0$ and $L/D = 1.4$ .....	306
Figure F.50 Schematic of staggered array tested with $T/D = 3.0$ and $L/D = 1.2$ . Black dots represent microphone positions. Gray dots represent positions where static pressure measurements were made. Hatched dots are plugged microphone locations. Dimensions in mm. Drawing to scale. ....	307
Figure F.51 Sound pressure level of dominant peak in spectra. Microphone positions shown in Figure F.50. Staggered array with $T/D = 3.0$ and $L/D = 1.2$ . .....	307

Figure F.52 Transfer function phase between microphone pairs shown at frequency of dominant peak in spectra of upstream microphone. Microphone positions shown in Figure F.50. Staggered array with T/D = 3.0 and L/D =1.2. ....	308
Figure F.53 Coherence between microphone pairs at frequency of dominant peak in spectra of upstream microphone. Phase measurements presented in Figure F.52 prone to error if coherence not close to one. Staggered array with T/D = 3.0 and L/D =1.2. ....	308
Figure F.54 Plot of frequency of dominant peak in spectra vs. mass flow. Staggered array with T/D = 3.0 and L/D =1.2. fn1, fn2...acoustic natural frequencies with solidity effect. ....	309
Figure F.55 Plot of frequency of dominant peak in spectra vs. flow velocity. Velocity estimated using density at measurement location and empty duct cross-sectional area. Staggered array with T/D = 3.0 and L/D =1.2. fn1, fn2...acoustic natural frequencies with solidity effect. ....	309
Figure F.56 Strouhal numbers determined at different positions throughout the array using dominant peak in spectra. Velocity estimated using density at measurement location and full duct cross-sectional area. Staggered array with T/D = 3.0 and L/D =1.2. ....	310
Figure F.57 Representative spectra taken at upstream position, after 24 <sup>th</sup> row and after 53 <sup>rd</sup> row (left, center and right respectively). Spectra in same line taken at identical mass flow conditions. Velocity estimated using density at measurement location and empty duct cross-sectional area. Sound pressure level shown at left calculated for dominant peak in spectra. Staggered array with T/D = 3.0 and L/D =1.2.....	311
Figure F.58 Schematic of staggered array tested with T/D = 3.0 and L/D = 1.1. Black dots represent microphone positions. Gray dots represent positions where static pressure measurements were made. Hatched dots are plugged microphone locations. Dimensions in mm. Drawing to scale. ....	312
Figure F.59 Sound pressure level of dominant peak in spectra. Microphone positions shown in Figure F.58. Staggered array with T/D = 3.0 and L/D =1.1. ....	312
Figure F.60 Transfer function phase between microphone pairs shown at frequency of dominant peak in spectra of upstream microphone. Microphone positions shown in Figure F.58. Staggered array with T/D = 3.0 and L/D =1.1. ....	313
Figure F.61 Coherence between microphone pairs at frequency of dominant peak in spectra of upstream microphone. Phase measurements presented in Figure F.60 prone to error if coherence not close to one. Staggered array with T/D = 3.0 and L/D =1.1. ....	313
Figure F.62 Plot of frequency of dominant peak in spectra vs. mass flow. Staggered array with T/D = 3.0 and L/D =1.1. fn1, fn2...acoustic natural frequencies with solidity effect. ....	314
Figure F.63 Plot of frequency of dominant peak in spectra vs. flow velocity. Velocity estimated using density at measurement location and empty duct cross-sectional area. Staggered array with T/D = 3.0 and L/D =1.1. fn1, fn2...acoustic natural frequencies with solidity effect. ....	314
Figure F.64 Strouhal numbers determined at different positions throughout the array using dominant peak in spectra. Velocity estimated using density at measurement location and full duct cross-sectional area. Staggered array with T/D = 3.0 and L/D =1.1. ....	315
Figure F.65 Representative spectra taken at upstream position, after 19 <sup>th</sup> row and after 57 <sup>th</sup> row (left, center and right respectively). Spectra in same line taken at identical mass flow conditions. Velocity estimated using	



density at measurement location and empty duct cross-sectional area. Sound pressure level shown at left calculated for dominant peak in spectra. Staggered array with $T/D = 3.0$ and $L/D = 1.1$ .....	316
Figure F.66 Schematic of staggered array tested with $T/D = 3.0$ and $L/D = 1.0$ . Black dots represent microphone positions. Gray dots represent positions where static pressure measurements were made. Hatched dots are plugged microphone locations. Dimensions in mm. Drawing to scale. ....	317
Figure F.67 Sound pressure level of dominant peak in spectra. Microphone positions shown in Figure F.66. Staggered array with $T/D = 3.0$ and $L/D = 1.0$ . ....	317
Figure F.68 Transfer function phase between microphone pairs shown at frequency of dominant peak in spectra of upstream microphone. Microphone positions shown in Figure F.66. Staggered array with $T/D = 3.0$ and $L/D = 1.0$ . ....	318
Figure F.69 Coherence between microphone pairs at frequency of dominant peak in spectra of upstream microphone. Phase measurements presented in Figure F.68 prone to error if coherence not close to one. Staggered array with $T/D = 3.0$ and $L/D = 1.0$ . ....	318
Figure F.70 Plot of frequency of dominant peak in spectra vs. mass flow. Staggered array with $T/D = 3.0$ and $L/D = 1.0$ . $fn_1, fn_2$ ...acoustic natural frequencies with solidity effect. ....	319
Figure F.71 Plot of frequency of dominant peak in spectra vs. flow velocity. Velocity estimated using density at measurement location and empty duct cross-sectional area. Staggered array with $T/D = 3.0$ and $L/D = 1.0$ . $fn_1, fn_2$ ...acoustic natural frequencies with solidity effect. ....	319
Figure F.72 Strouhal numbers determined at different positions throughout the array using dominant peak in spectra. Velocity estimated using density at measurement location and full duct cross-sectional area. Staggered array with $T/D = 3.0$ and $L/D = 1.0$ . ....	320
Figure F.73 Representative spectra taken at upstream position, after 21 <sup>st</sup> row and after 63 <sup>rd</sup> row (left, center and right respectively). Spectra in same line taken at identical mass flow conditions. Velocity estimated using density at measurement location and empty duct cross-sectional area. Sound pressure level shown at left calculated for dominant peak in spectra. Staggered array with $T/D = 3.0$ and $L/D = 1.0$ .....	321
Figure F.74 Schematic of staggered array tested with $T/D = 3.0$ and $L/D = 0.9$ . Black dots represent microphone positions. Gray dots represent positions where static pressure measurements were made. Hatched dots are plugged microphone locations. Dimensions in mm. Drawing to scale. ....	322
Figure F.75 Sound pressure level of dominant peak in spectra. Microphone positions shown in Figure F.74. Staggered array with $T/D = 3.0$ and $L/D = 0.9$ . ....	322
Figure F.76 Transfer function phase between microphone pairs shown at frequency of dominant peak in spectra of upstream microphone. Microphone positions shown in Figure F.74. Staggered array with $T/D = 3.0$ and $L/D = 0.9$ . ....	323
Figure F.77 Coherence between microphone pairs at frequency of dominant peak in spectra of upstream microphone. Phase measurements presented in Figure F.76 prone to error if coherence not close to one. Staggered array with $T/D = 3.0$ and $L/D = 0.9$ . ....	323
Figure F.78 Plot of frequency of dominant peak in spectra vs. mass flow. Staggered array with $T/D = 3.0$ and $L/D = 0.9$ . $fn_1, fn_2$ ...acoustic natural frequencies with solidity effect. ....	324

Figure F.79 Plot of frequency of dominant peak in spectra vs. flow velocity. Velocity estimated using density at measurement location and empty duct cross sectional area. Staggered array with $T/D = 3.0$ and $L/D = 0.9$ . $fn_1, fn_2 \dots$ acoustic natural frequencies with solidity effect. ....	324
Figure F.80 Strouhal numbers determined at different positions throughout the array using dominant peak in spectra. Velocity estimated using density at measurement location and full duct cross sectional area. Staggered array with $T/D = 3.0$ and $L/D = 0.9$ . ....	325
Figure F.81 Representative spectra taken at upstream position, after 31 <sup>st</sup> row and after 69 <sup>th</sup> row (left, center and right respectively). Spectra in same line taken at identical mass flow conditions. Velocity estimated using density at measurement location and empty duct cross sectional area. Sound pressure level shown at left calculated for dominant peak in spectra. Staggered array with $T/D = 3.0$ and $L/D = 0.9$ . ....	326
Figure G.1 Sound pressure level of dominant peak in spectra as a function of frequency. Microphones and cylinder positions shown in Figure 4.22. ( $fn_1$ with flow) acoustic resonance estimated with flow velocity at resonance condition. ....	327
Figure G.2 Sound pressure level as a function of average flow velocity. ....	327
Figure G.3 Transfer function phase angle at frequency of dominant peak in spectra between microphone pairs shown. ....	328
Figure G.4 Coherence at frequency of dominant peak in spectra between microphone pairs shown. Phase angle shown in figure above prone to error if coherence not close to one. ....	328
Figure G.5 Sound pressure level of dominant peak in spectra as a function of frequency. Microphones and cylinder positions shown in Figure 4.22. ( $fn_1$ with flow) acoustic resonance estimated with flow velocity at resonance condition. ....	329
Figure G.6 Sound pressure level as a function of average flow velocity. ....	329
Figure G.7 Transfer function phase angle at frequency of dominant peak in spectra between microphone pairs shown. ....	330
Figure G.8 Coherence at frequency of dominant peak in spectra between microphone pairs shown. Phase angle shown in figure above prone to error if coherence not close to one. ....	330
Figure G.9 Sound pressure level of dominant peak in spectra as a function of frequency. Microphones and cylinder positions shown in Figure 4.22. ( $fn_1$ with flow) acoustic resonance estimated with flow velocity at resonance condition. ....	331
Figure G.10 Sound pressure level as a function of average flow velocity. ....	331
Figure G.11 Transfer function phase angle at frequency of dominant peak in spectra between microphone pairs shown. ....	332
Figure G.12 Coherence at frequency of dominant peak in spectra between microphone pairs shown. Phase angle shown in figure above prone to error if coherence not close to one. ....	332
Figure G.13 Sound pressure level of dominant peak in spectra as a function of frequency. Microphones and cylinder positions shown in Figure 4.22. ( $fn_1$ with flow) acoustic resonance estimated with flow velocity at resonance condition. ....	333
Figure G.14 Sound pressure level as a function of average flow velocity. ....	333
Figure G.15 Transfer function phase angle at frequency of dominant peak in spectra between microphone pairs shown. ....	334

Figure G.16 Coherence at frequency of dominant peak in spectra between microphone pairs shown. Phase angle shown in figure above prone to error if coherence not close to one.....	334
Figure G.17 Sound pressure level of dominant peak in spectra as a function of frequency. Microphones and cylinder positions shown in Figure 4.22. (fn1 with flow) acoustic resonance estimated with flow velocity at resonance condition.....	335
Figure G.18 Sound pressure level as a function of average flow velocity.....	335
Figure G.19 Transfer function phase angle at frequency of dominant peak in spectra between microphone pairs shown.....	336
Figure G.20 Coherence at frequency of dominant peak in spectra between microphone pairs shown. Phase angle shown in figure above prone to error if coherence not close to one.....	336
Figure G.21 Sound pressure level of dominant peak in spectra as a function of frequency. Microphones and cylinder positions shown in Figure 4.22.(fn1 with flow) acoustic resonance estimated with flow velocity at resonance condition.....	337
Figure G.22 Sound pressure level as a function of average flow velocity.....	337
Figure G.23 Transfer function phase angle at frequency of dominant peak in spectra between microphone pairs shown.....	338
Figure G.24 Coherence at frequency of dominant peak in spectra between microphone pairs shown. Phase angle shown in figure above prone to error if coherence not close to one.....	338
Figure G.25 Sound pressure level of dominant peak in spectra as a function of frequency. Microphones and cylinder positions shown in Figure 4.22. (fn1 with flow) acoustic resonance estimated with flow velocity at resonance condition.....	339
Figure G.26 Sound pressure level as a function of average flow velocity.....	339
Figure G.27 Transfer function phase angle at frequency of dominant peak in spectra between microphone pairs shown.....	340
Figure G.28 Coherence at frequency of dominant peak in spectra between microphone pairs shown. Phase angle shown in figure above prone to error if coherence not close to one.....	340
Figure G.29 Sound pressure level of dominant peak in spectra as a function of frequency. Microphones and cylinder positions shown in Figure 4.22. (fn1 with flow) acoustic resonance estimated with flow velocity at resonance condition.....	341
Figure G.30 Sound pressure level as a function of average flow velocity.....	341
Figure G.31 Transfer function phase angle at frequency of dominant peak in spectra between microphone pairs shown.....	342
Figure G.32 Coherence at frequency of dominant peak in spectra between microphone pairs shown. Phase angle shown in figure above prone to error if coherence not close to one.....	342
Figure G.33 Sound pressure level of dominant peak in spectra as a function of frequency. Microphones and cylinder positions shown in Figure 4.22. (fn1 with flow) acoustic resonance estimated with flow velocity at resonance condition.....	343
Figure G.34 Sound pressure level as a function of average flow velocity.....	343
Figure G.35 Transfer function phase angle at frequency of dominant peak in spectra between microphone pairs shown.....	344

Figure G.36 Coherence at frequency of dominant peak in spectra between microphone pairs shown. Phase angle shown in figure above prone to error if coherence not close to one.....	344
Figure G.37 Sound pressure level of dominant peak in spectra as a function of frequency. Microphones and cylinder positions shown in Figure 4.22. (fn1 with flow) acoustic resonance estimated with flow velocity at resonance condition.....	345
Figure G.38 Sound pressure level as a function of average flow velocity.....	345
Figure G.39 Transfer function phase angle at frequency of dominant peak in spectra between microphone pairs shown.....	346
Figure G.40 Coherence at frequency of dominant peak in spectra between microphone pairs shown. Phase angle shown in figure above prone to error if coherence not close to one.....	346
Figure G.41 Comparison of sound pressure levels produced by cylinders of different shape against results from regular cylinders (see Figure 4.21). Measurements at microphone position 1a. (fn1 with flow) acoustic resonance estimated with flow velocity at resonance condition.....	347
Figure G.42 Comparison of sound pressure levels produced by cylinders of different shape against results from regular cylinders (see Figure 4.21). Measurements at microphone position d1. (fn1 with flow) acoustic resonance estimated with flow velocity at resonance condition.....	347
Figure G.43 Comparison of Strouhal vs. Reynolds number for cylinders of different shape against results from regular cylinders.....	348
Figure G.44 Comparison of transfer function phase angle between microphone pair 2a -4a for cylinders of different shape against results from regular cylinders.....	348
Figure G.45 Comparison of sound pressure levels produced by cylinders of different shape against results from regular cylinders (see Figure 4.21). Measurements at microphone position 1a. (fn1 with flow) acoustic resonance estimated with flow velocity at resonance condition.....	349
Figure G.46 Comparison of sound pressure levels produced by cylinders of different shape against results from regular cylinders (see Figure 4.21). Measurements at microphone position d1. (fn1 with flow) acoustic resonance estimated with flow velocity at resonance condition.....	349
Figure G.47 Comparison of Strouhal vs. Reynolds number for cylinders of different shape against results from regular cylinders.....	350
Figure G.48 Comparison of transfer function phase angle between microphone pair 2a -4a for cylinders of different shape against results from regular cylinders.....	350
Figure G.49 Comparison of sound pressure levels produced by cylinders of different shape against results from regular cylinders (see Figure 4.21). Measurements at microphone position 1a. (fn1 with flow) acoustic resonance estimated with flow velocity at resonance condition.....	351
Figure G.50 Comparison of sound pressure levels produced by cylinders of different shape against results from regular cylinders (see Figure 4.21). Measurements at microphone position d1. (fn1 with flow) acoustic resonance estimated with flow velocity at resonance condition.....	351
Figure G.51 Comparison of Strouhal vs. Reynolds number for cylinders of different shape against results from regular cylinders.....	352
Figure G.52 Comparison of transfer function phase angle between microphone pair 2a -4a for cylinders of different shape against results from regular cylinders.....	352

Figure G.53 Comparison of sound pressure levels produced by cylinders of different shape against results from regular cylinders (see Figure 4.21). Measurements at microphone position 1a. (fn1 with flow) acoustic resonance estimated with flow velocity at resonance condition.....	353
Figure G.54 Comparison of sound pressure levels produced by cylinders of different shape against results from regular cylinders (see Figure 4.21). Measurements at microphone position d1. (fn1 with flow) acoustic resonance estimated with flow velocity at resonance condition.....	353
Figure G.55 Comparison of Strouhal vs. Reynolds number for cylinders of different shape against results from regular cylinders.....	354
Figure G.56 Comparison of transfer function phase angle between microphone pair 2a-4a for cylinders of different shape against results from regular cylinders.....	354
Figure G.57 Comparison of sound pressure levels produced by cylinders of different shape against results from regular cylinders (see Figure 4.21). Measurements at microphone position 1a. (fn1 with flow) acoustic resonance estimated with flow velocity at resonance condition.....	355
Figure G.58 Comparison of sound pressure levels produced by cylinders of different shape against results from regular cylinders (see Figure 4.21). Measurements at microphone position d1. (fn1 with flow) acoustic resonance estimated with flow velocity at resonance condition.....	355
Figure G.59 Comparison of Strouhal vs. Reynolds number for cylinders of different shape against results from regular cylinders.....	356
Figure G.60 Comparison of transfer function phase angle between microphone pair 2a-4a for cylinders of different shape against results from regular cylinders.....	356
Figure H.1 Sound pressure level at dominant peak in spectra vs. average flow velocity. Microphones and cylinders positions shown in Figures 4.22 and 4.27. ....	357
Figure H.2 Comparison of single cylinder and side-by-side cylinders Strouhal numbers as a function of Reynolds number. Strouhal number for side-by-side cylinders estimated using measurements at position d3. ....	357
Figure H.3 Frequency of dominant peak in spectra at position d3 vs. average flow velocity. 6.35 mm side-by-side cylinders.....	358
Figure H.4 Representative spectra taken at microphone positions 1a, 6a and d3 (left, center and right respectively). 6.35 mm side-by-side cylinders. ....	359
Figure H.5 Sound pressure level at dominant peak in spectra vs. average flow velocity. Microphones and cylinders positions shown in Figures 4.22 and 4.27. ....	360
Figure H.6 Comparison of single cylinder and side-by-side cylinders Strouhal numbers as a function of Reynolds number. Strouhal number for side-by-side cylinders estimated using measurements at position d3. ....	360
Figure H.7 Frequency of dominant peak in spectra at position d3 vs. average flow velocity. 5.0 mm side-by-side cylinders.....	361
Figure H.8 Representative spectra taken at microphone positions 1a, 6a and d3 (left, center and right respectively). 5.0 mm side-by-side cylinders.....	362
Figure H.9 Sound pressure level at dominant peak in spectra vs. average flow velocity. Microphones and cylinders positions shown in Figures 4.22 and 4.27. ....	363

Figure H.10 Comparison of single cylinder and side-by-side cylinders Strouhal numbers as a function of Reynolds number. Strouhal number for side-by-side cylinders estimated using measurements at position d3. ....	363
Figure H.11 Frequency of dominant peak in spectra at position d3 vs. average flow velocity. 4.0 mm side-by-side cylinders.....	364
Figure H.12 Representative spectra taken at microphone positions 1a, 6a and d3 (left, center and right respectively). 4.0 mm side-by-side cylinders.....	365
Figure H.13 Sound pressure level at dominant peak in spectra vs. average flow velocity. Microphones and cylinders positions shown in Figures 4.22 and 4.27. ....	366
Figure H.14 Comparison of single cylinder and side-by-side cylinders Strouhal numbers as a function of Reynolds number. Strouhal number for side-by-side cylinders estimated using measurements at position d3. ....	366
Figure H.15 Frequency of dominant peak in spectra at position d3 vs. average flow velocity. 3.0 mm side-by-side cylinders.....	367
Figure H.16 Representative spectra taken at microphone positions 1a, 6a and d3 (left, center and right respectively). 3.0 mm side-by-side cylinders.....	368
Figure H.17 Sound pressure level at dominant peak in spectra vs. frequency. Microphones and cylinders positions shown in Figures 4.22 and 4.27. ....	369
Figure H.18 Sound pressure level at dominant peak in spectra vs. average flow velocity. Microphones and cylinders positions shown in Figures 4.22 and 4.27. ....	369
Figure H.19 Transfer function phase angle at frequency of dominant peak in spectra between microphone pairs shown.....	370
Figure H.20 Coherence at frequency of dominant peak in spectra between microphone pairs shown. Phase angle shown in figure above prone to error if coherence not close to one.....	370
Figure H.21 Representative spectra taken at microphone positions 1a, 6a and d3 (left, center and right respectively). 6.35 mm tandem cylinders.....	371
Figure H.22 Sound pressure level at dominant peak in spectra vs. frequency. Microphones and cylinders positions shown in Figures 4.22 and 4.27. ....	372
Figure H.23 Sound pressure level at dominant peak in spectra vs. average flow velocity. Microphones and cylinders positions shown in Figures 4.22 and 4.27. ....	372
Figure H.24 Transfer function phase angle at frequency of dominant peak in spectra between microphone pairs shown.....	373
Figure H.25 Coherence at frequency of dominant peak in spectra between microphone pairs shown. Phase angle shown in figure above prone to error if coherence not close to one.....	373
Figure H.26 Representative spectra taken at microphone positions 1a, 6a and d3 (left, center and right respectively). 5.0 mm tandem cylinders. ....	374
Figure H.27 Sound pressure level at dominant peak in spectra vs. frequency. Microphones and cylinders positions shown in Figures 4.22 and 4.27. ....	375
Figure H.28 Sound pressure level at dominant peak in spectra vs. average flow velocity. Microphones and cylinders positions shown in Figures 4.22 and 4.27. ....	375

Figure H.29 Transfer function phase angle at frequency of dominant peak in spectra between microphone pairs shown.....	376
Figure H.30 Coherence at frequency of dominant peak in spectra between microphone pairs shown. Phase angle shown in figure above prone to error if coherence not close to one.....	376
Figure H.31 Representative spectra taken at microphone positions 1a, 6a and d3 (left, center and right respectively). 4.0 mm tandem cylinders. ....	377
Figure H.32 Sound pressure level at dominant peak in spectra vs. frequency. Microphones and cylinders positions shown in Figures 4.22 and 4.27. ....	378
Figure H.33 Sound pressure level at dominant peak in spectra vs. average flow velocity. Microphones and cylinders positions shown in Figures 4.22 and 4.27. ....	378
Figure H.34 Transfer function phase angle at frequency of dominant peak in spectra between microphone pairs shown.....	379
Figure H.35 Coherence at frequency of dominant peak in spectra between microphone pairs shown. Phase angle shown in figure above prone to error if coherence not close to one.....	379
Figure H.36 Representative spectra taken at microphone positions 1a, 6a and d3 (left, center and right respectively). 3.0 mm tandem cylinders. ....	380
Figure J.1 Sound pressure level field (dB) at 4000Hz produced by single 6.35mm cylinder at center of duct (large black circle) for different real nondimensional volumetric damping ( $Q_{nd}$ ) values. Small circles represent microphone positions in our experimental setup. From top to bottom: No damping, $Q_{nd} = 3, 5$ and 10. ....	392
Figure J.2 Sound pressure level field (dB) at 5000Hz produced by single 6.35mm cylinder at center of duct (large black circle) for different real nondimensional volumetric damping ( $Q_{nd}$ ) values. Small circles represent microphone positions in our experimental setup. From top to bottom: No damping, $Q_{nd} = 3, 5$ and 10. ....	393
Figure J.3 Sound pressure level field (dB) at 4000Hz produced by single 6.35mm cylinder at center of duct (large black circle) for different imaginary nondimensional volumetric damping ( $Q_{nd}$ ) values. Small circles represent microphone positions in our experimental setup. From top to bottom: No damping, $Q_{nd} = 3i, 5i$ and $10i$ . ....	394
Figure J.4 Sound pressure level field (dB) at 5000Hz produced by single 6.35mm cylinder at center of duct (large black circle) for different imaginary nondimensional volumetric damping ( $Q_{nd}$ ) values. Small circles represent microphone positions in our experimental setup. From top to bottom: No damping, $Q_{nd} = 3i, 5i$ and $10i$ . ....	395
Figure J.5 Sound pressure level field (dB) at 4000Hz produced by single 6.35mm cylinder at center of duct (large black circle) for different real y-walls specific acoustic impedances ( $z_y$ ). Small circles represent microphone positions in our experimental setup. From top to bottom: No damping, $z_y = 5, 2$ and $0.5$ . ....	396
Figure J.7 Sound pressure level field (dB) at 4000Hz produced by single 6.35mm cylinder at center of duct (large black circle) for different imaginary y-walls specific acoustic impedances ( $z_y$ ). Small circles represent microphone positions in our experimental setup. From top to bottom: No damping, $z_y = 5i, 2i$ and $0.5i$ . ....	398

Figure J.8 Sound pressure level field (dB) at 5000Hz produced by single 6.35mm cylinder at center of duct (large black circle) for different imaginary y-walls specific acoustic impedances ( $z_y$ ). Small circles represent microphone positions in our experimental setup. From top to bottom: No damping,  $z_y = 5i$ ,  $2i$  and  $0.5i$ . ..... 399



## List of Tables

	<b>Page</b>
Table 4.1 Surface Roughness RMS values (Measured along cylinder axis).....	91
Table 4.2 Uncertainties of Measured Quantities .....	115
Table 4.3 Maximum Errors Associated with Derived Variables .....	116
Table 5.1 Comparison of acoustic resonance frequency ratios to speed of sound ratios for plate heat exchanger samples tested with accelerometers.....	128
Table 5.2 Estimated and experimentally determined acoustic resonances in plate heat exchangers.....	130
Table B.1 Local flow velocities in m/s measured inside test section for nominal Reynolds number of 2125. ....	245
Table B.2 Local flow velocities in m/s measured inside test section for nominal Reynolds number of 3170. ....	245
Table B.3 Local flow velocities in m/s measured inside test section for nominal Reynolds number of 4415. ....	245
Table B.4 Local flow velocities in m/s measured inside test section for nominal Reynolds number of 5860. ....	245
Table B.5 Local flow velocities in m/s measured inside test section for nominal Reynolds number of 7280. ....	246
Table B.6 Flow conditions at the test section during flow velocity profile measurements.....	246
Table B.7 Flow velocities in m/s measured at center of test section using nitrogen.....	246
Table D.1. R134a Refrigerant test conditions plate A2 tests.....	266
Table D.2. R134a Refrigerant test conditions plate F2 tests.....	267
Table D.3. R134a Refrigerant test conditions plate F tests.....	268

## Nomenclature

### Roman and script letters

a	= Distance between tube rows in an in-line arrays (Chapter 2), Rectangular piston height (Appendix A)
A	= Duct cross sectional area
$A_c$	= Cross-sectional area seen by the flow (for a cylinder = $D \cdot L_{cyl}$ )
$A_t$	= Venturi flow meter cross sectional area at the throat equation (4.1)
B	= Channel width (normal to flow direction and tube axis) same as W
b	= Rectangular piston width
c, $c_o$	= Speed of sound
$c_{eff}$	= Effective speed of sound (Speed of sound inside a tube array bundle)
$C_k$	= Venturi flow meter correction coefficient equation (4.1)
$C_L'$	= Coefficient of fluctuating lift, $F_L' / (0.5\rho U_{up}^2 A_c)$
$C_p$	= Specific heat of the gas at constant pressure
$C_v$	= Specific heat of the gas at constant volume
d	= Tube external diameter
D	= Circular cylinder/ tube external diameter
$D_t$	= Venturi diameter at throat equations (4.2)
$D_i$	= Venturi diameter at inlet equations (4.2)
$D_h$	= Hydraulic diameter, four times the area divided by the perimeter
f	= Frequency (Hz)
$f_a$	= Acoustic natural frequency
$f_i$	= Acoustic natural frequency of mode i (Equation 2.9)
$f_l$	= Lower frequency limit (Appendix A)
fn	= Acoustic natural frequency, the numbers after the “n” refer to the first, second, etc. acoustic natural frequency
$f_s$	= Excitation frequency estimated using Strouhal numbers
$f_u$	= Upper frequency limit (Appendix A)
$F_L'$	= Fluctuating lift force
$\vec{F}^*$	= Body force per unit of mass at point $\vec{x}_s^*$ (section 3.5.2)
$F_y$	= Component of body force per unit of mass at point $\vec{x}_s^*$ in the y direction
$f_{tb}$	= Turbulent buffeting dominant frequency {eqs. (1) and (17)}
g	= Diagonal gap present in staggered arrays (Figure 2.3), acceleration of gravity
$G_i$	= Ziada S., Oengören A., Bühlmann E.T., 1989b, resonance parameter for in-line arrays
$G_s$	= Ziada S., Oengören A., Bühlmann E.T., 1989b, resonance parameter for staggered arrays
h	= Microphone positions (equation (6.4))
H	= Duct height
$H_{12}$	= Corrected transfer function between microphones 1 and 2 (Appendix A)
$H_{meas}$	= Measured transfer function between microphones 1 and 2 in original configuration (Appendix A)
$H_o$	= Measured transfer function between microphones 1 and 2 in original configuration (Appendix A)
$H_s$	= Measured transfer function between microphones 1 and 2 in switched configuration (Appendix A)
i	= Acoustic mode number, square root of -1.
$\hat{i}$	= Unit vector in x direction

$\hat{j}$	=	Unit vector in y direction
$J_0$	=	Bessel function of order 0 (Appendix A)
$\hat{k}$	=	Unit vector in z direction
$k$	=	Wavenumber
$k_{x_{mn}}$	=	Wavenumber of the (m, n) mode in the x direction
$k_{y_m}$	=	Wavenumber of the m mode in the y direction
$k_{z_n}$	=	Wavenumber of the n mode in the z direction
$k_{Lc}$	=	Non-dimensional wavenumber
$K_{Pitot}$	=	Pitot tube correction factor
$K_s$	=	Cylinder surface roughness
$G_{Pitot}$	=	Pitot tube compressibility factor
$l$	=	Distance between test sample and closest microphone (Appendix A), length scale associate to the turbulence (Chapter 2)
$L$	=	Distance between tube rows (Figures 1.1 and 2.1), cylinder length (equations 3.27 and 6.1), spacing between cylinders in tandem
$L_c$	=	Characteristic length
$L_{cyl}$	=	Cylinder length
$\dot{m}$	=	Mass flow rate
$m_p$	=	Piston mass equation (4.3)
$M, Ma, M_a$	=	Mach number
$M_0$	=	Struve function of order zero (Appendix A)
$n$	=	Multiple of tandem cylinders distance separation (equation 5.6)
$\vec{n}$	=	Unit vector in normal direction
$N$	=	Number of tube rows in an array, number of measurement positions (equation (6.4))
$P$	=	Pitch, dimension between cylinders center in normal triangular and square arrays
$P_{ave}$	=	Average acoustic pressure detected in finite size diaphragm
$P_{exp_h}$	=	Measured acoustic pressure obtained at microphone position h
$P_i$	=	Static pressure at Venturi flow meter inlet port equations (4.2)
$P_{model_h}$	=	Estimated acoustic pressure obtained with the model at microphone position h
$P_t$	=	Static pressure at Venturi flow meter throat port equations (4.2)
$p', p$	=	Acoustic pressure
$p^*$	=	Dimensional acoustic pressure (section 3.5.2)
$P_{rms,max}$	=	Maximum acoustic pressure (root mean square)
$P_s$	=	Gas pressure in acoustic resonance chamber (equation 2.15)
$P_o$	=	Fluid static pressure
$P_T$	=	Fluid stagnation pressure
$Q$	=	Volumetric damping constant
$Q_{m,n}$	=	Auxiliary function
$R$	=	Radius or characteristic dimension in our case it should be equal to duct width, reflection coefficient (Appendix A)
$Re$	=	Reynolds number, $U D/\nu$
$Re_{up}$	=	Reynolds number, $U_{up}D/\nu$

$Re_{cr}$	=	Critical Reynolds number, $V_{cr} D/\nu$
$S(x,y,f)$	=	Spatial response of transducer as a function of position and frequency
$St$	=	Strouhal number, $fD/U$
$s$	=	(T-D) or flow lane width in in-line arrays, Shear wave or Stokes number, Microphone spacing (Appendix A).
$T$	=	Distance between tube columns (Figures 1.1 and 2.1), spacing between side-by-side cylinders
$T_i$	=	Turbulence intensity
$T_s$	=	Turbulent scale
$T_{vs}$	=	Vortex shedding period (equation 5.6)
$\vec{u}$	=	Acoustic particle velocity
$u$	=	Flow velocity
$u^*$	=	Friction velocity, $(\tau_w/\rho_o)^{0.5}$
$U$	=	Flow velocity
$U_{ave}$	=	Average velocity
$U_{max}$	=	Maximum velocity
$U_{up}$	=	Upstream Velocity
$U_1$	=	Velocity between tubes
$V$	=	Flow velocity
$V_{ave}$	=	Average flow velocity
$V_{cr}$	=	Critical gap velocity { $V_{cr} = V_g$ at frequency coincidence }
$V_i$	=	Flow velocity when acoustic mode $i$ is present
$V_g$	=	Gap velocity
$V_u$	=	Upstream flow velocity
$\vec{V}^*$	=	Dimensional acoustic velocity (section 3.5.2)
$V_o^*$	=	Dimensional uniform flow velocity in the $x$ direction (section 3.5.2)
$W$	=	Width of channel. Distance between walls that support the resonance.
$X_L$	=	(L/D) ratio of distance between tube centers normal to flow direction to tube outside diameter
$X_o$	=	$X_L$ for in-line arrays or $X_o = 2 X_L$ for staggered arrays
$X_p$	=	(P/D) ratio of distance between cylinder centers in normal triangular and square arrays to cylinder diameter
$X_T$	=	(T/D) ratio of distance between tube centers parallel to flow direction to tube outside diameter
$\vec{x}_s^*$	=	Dimensional dipole source location (section 3.5.2)
$x, y, z$	=	Cartesian coordinates variables, $x$ in flow direction, $y$ perpendicular to flow and cylinder axis, $z$ aligned with cylinder axis
$Y_c$	=	Compressibility factor (equations (4.2))
$Z$	=	Acoustic impedance
$z$	=	Specific acoustic impedance, cylinder length.

### **Greek letters**

$\alpha$	=	Wall impedance coefficient
$\alpha_{damp}$	=	Volumetric and wall damping variables (equation (6.4))
$\beta$	=	Specific acoustic admittance, Venturi flow meter diameter ratio equation (4.2)
$B$	=	Logarithmic overlap law constant
$\gamma$	=	Ratio of specific heats $C_p/C_v$

$\Gamma$	=	Grotz and Arnold damping parameter
$\delta$	=	Modified Chen Y.N. (1968) damping parameter (equation 2.14), Dirac delta function
$\partial P$	=	Differential pressure between Venturi flow meter inlet and throat ports equation (4.1)
$\Delta p$	=	Pressure drop (equations (2.11), (2.12) and (2.13))
$\Delta p_{\text{drop}}$	=	Pressure drop (equations (2.22))
$\Delta^*$	=	Fitzpatrick and Donaldson (1984) damping parameter
$\varepsilon$	=	Surface roughness
$\xi$	=	Specific acoustic conductance
$\eta_{1,2}$	=	Auxiliary variables that represent arbitrary functions (equation 3.72)
$\theta$	=	Specific acoustic resistance
$\theta_{\text{MI}}$	=	Function defined in Appendix A
$\Theta$	=	Auxiliary variable (equation 3.68)
$\kappa$	=	Logarithmic overlap law constant
$\kappa_{pq}$	=	Acoustic wavenumber associated with the (p,q)th mode (equation 4.4)
$\lambda$	=	Thermal conductivity of the gas
$\mu$	=	Viscosity, friction factor (equation 2.11)
$\nu$	=	Kinematic viscosity
$\rho$	=	Density perturbation or acoustic density
$\rho_i$	=	Density at Venturi flow meter inlet equation (4.1)
$\rho_o$	=	Static or steady density
$\rho_o^*$	=	Dimensional static density (section 3.5.2)
$\rho^*$	=	Dimensional acoustic density (section 3.5.2)
$\sigma$	=	Solidity ratio i.e. volume fraction occupied by tubes (Equation 2.9, 2.23), square root of Prandtl number, specific acoustic susceptance
$\tau_w$	=	Shear stress at the wall
$\phi$	=	Dimensional power spectral density
$\chi$	=	Specific acoustic reactance
$\chi_{\text{MI}}$	=	Function defined in Appendix A
$\psi$	=	Auxiliary variable (equation 3.125)
$\Psi$	=	Chen Y.N. (1968) damping parameter
$\omega$	=	Radial frequency
$\zeta$	=	Damping term in y and z direction eigenvalues equations

### **Subscripts**

ave	=	Average
adj	=	Adjusted
aux	=	Auxiliary
co	=	Cutoff frequency
cr	=	Critical
l,m,n	=	Modal indices in the x, y and z directions
meas	=	Measured
nd	=	Non-dimensional
o	=	Steady or static component, original configuration (Appendix A)
w	=	Property evaluate at the wall
s	=	Static component (static pressure), switched configuration (Appendix A)

T = Stagnation component (i.e., stagnation pressure)  
t = Total quantity (static and acoustic component)  
x, y, z = Related to the x, y, or z coordinate variables

### **Superscripts**

' = Spatial derivative, sinusoidally fluctuating component  
• = Time derivative  
→ = Vector quantity  
^ = Unit vector  
\* = Dimensional quantity

### **Abbreviations**

cm = Centimeters  
g = Gage pressure in psig and kPa g or grams as in g/s (grams per second)  
m = Meters  
mm = Millimeters  
s = Seconds  
SPL = Sound pressure level (dB)  
Vol. = Volume

# Chapter 1: Introduction

## 1.1 Description of flow-induced acoustic resonance phenomena in heat exchangers

Flow-induced noise in heat exchangers and in particular acoustic resonance is a phenomenon that has been a problem for a long time. Reports about this condition begin in the mid-fifties [Baird, Grotz and Arnold, Putnam]. Acoustic resonance problems in heat exchangers can be present in a variety of applications, including chemical process exchangers, air heaters, power-generation boilers, marine boilers, conventional power plants, nuclear power plants, and heat-recovery heat exchangers. Other equipment in which acoustic resonance problems caused by the flow of gases over bluff bodies inside a chamber occur include turbojet engine compressors, turning vanes of wind tunnels, plates in a wind tunnel, and the combustion chambers of rocket engines [Blevins 1994].

The flow-induced noise is caused when gases flow transversely to both an array of bluff bodies typically circular cylinders and a container cavity (see Figure 1.1). The noise emitted is usually dominated by a tonal component that increases in frequency as the flow velocity increases. For this reason the frequency of the flow noise produced by arrays of cylinders is characterized by a Strouhal number in direct analogy to the single cylinder case. If this tonal noise component increases in frequency such that it coincides with a transverse acoustic natural frequency of the containing duct, a noticeable acoustic resonance condition is possible if acoustic damping is small (see Figure 1.1). There are cases, however, where the noise emitted by certain types of cylinder arrays is significant at any frequency/flow velocity and can even be larger at nonresonance conditions than at resonance conditions [Blevins and Bressler 1987b, Oengören and Ziada 1998].

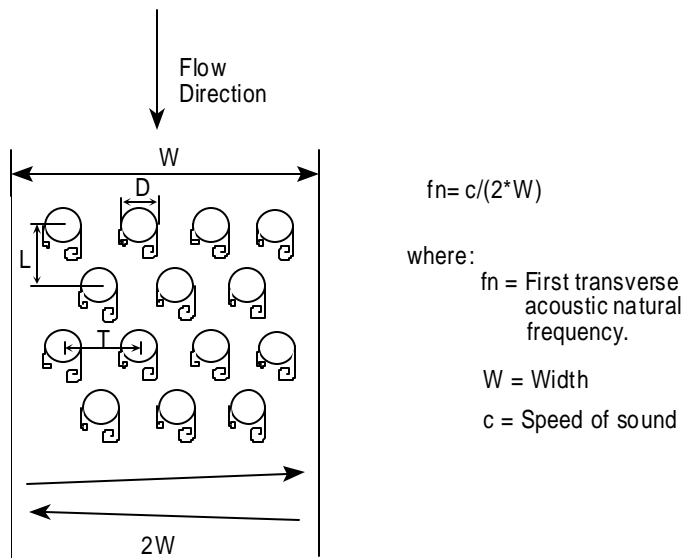


Figure 1.1 Schematic diagram of the acoustic resonance phenomenon in heat exchangers.

Figure 1.1 depicts some of the relevant variables related to acoustic resonance in heat exchangers. The arrows marked  $2W$  indicate where the resonance is established. Acoustic resonance has been observed for several different tube array configurations inside cavities of different shapes. The most common heat exchanger

configurations containing tube arrays are rectangular and cylindrical ducts. Figure 1.1 shows a staggered array inside a rectangular duct.

Flow-induced noise in heat exchangers is a very complex phenomenon. The complexities are caused by several factors that affect the noise generation and attenuation mechanisms of this type of sound source inside ducts, and by fluid-acoustic-structural coupling effects. To predict the flow-induced noise from bluff bodies inside a duct, it is necessary to know the type of aeroacoustic source created by the flow and its strength and directionality. Additionally, acoustic damping and sound attenuation mechanisms inside the duct must be considered. In certain cases the sound can also influence the vortex generation process [Blevins 1985, Ffowcs-Williams and Zhao, Parker and Welsh 1982, 1983, Peterka and Richardson]. This fluid-acoustic coupling effect must also be considered.

## **1.2 Plate heat exchanger acoustic resonance**

The problem of acoustic resonance in plate-type heat exchangers used as evaporators in the air conditioning systems of automobiles came to our attention when industry sponsors approached the Air Conditioning and Refrigeration Center with a "whistling" problem. Originally the source of this "whistling" sound was unknown. It was believed that the sound could be generated by the flow of refrigerant over a particular cavity like the ones formed by the plate inlet ports and header. Also, it was believed that the sound could be produced in the bellows or ribs formed in the header itself (Figure 1.2 shows some typical plate heat exchangers used as evaporators in automobile applications). The state of the refrigerant when the "whistling" noise was present was not known, but gaseous refrigerant was suspected. This proved to be correct after tests were performed in our laboratory. The tests performed originally used a R134a refrigerant experimental setup (described in Chapter 4) in which the R134a refrigerant conditions could be controlled accurately. Those tests showed that the resonance was established only when gaseous R134a flowed through the plate evaporator section.

Plate heat exchangers as shown in Figure 1.2 are formed by stacking a number of stamped plates together and placing fins between them. Figure 1.3 shows some typical stamped single plates used to make this kind of heat exchanger. The refrigerant flow passages are formed by stacking these plates one facing another. Fins are brazed on the exterior of this channel. Refrigerant flows through the cavity formed between these plates while air flows through the fins outside of these plates. Dimensions of the duct where the refrigerant flows are very small, of the order of 2 x 40 mm with lengths of around 300 mm. The full evaporator consists of many of these sections. When these sections are joined by brazing, the two stamped protrusions in contact at their tops fuse to form an "hourglass" shaped cylinder. Plate heat exchangers of the design shown in Figure 1.3 therefore consist of arrays of cylinders that have a nonconstant cylinder diameter along the cylinder axis.

The acoustic resonance present in plate heat exchangers was linked to the acoustic resonance phenomena reported in the literature when the tests confirmed that the resonance was established transversely to the refrigerant gas flow along the width of the duct (see Figure 1.1). Acoustic resonance in very large heat exchangers has been shown to be of the same nature as the acoustic resonance present in plate heat exchangers used in automobile applications [Rodarte et al. 1998a,b]. There are many similarities and differences between plate heat exchangers and shell and tube array type heat exchangers. These similarities and differences can be exploited to understand more generally the acoustic resonance phenomenon produced by the sound of arrays of bluff bodies in cross flow inside a



chamber. The size of plate heat exchangers and the use of techniques like stereolithography help to test a wide range of heat exchanger configurations quickly and cheaply. This can lead to a more complete understanding of the resonance phenomena and to better design guidelines for all types of heat exchangers.

There are a significant number of references related to the problem of acoustic resonance in tube array heat exchangers [see references]. To our knowledge only the work done by us at the University of Illinois [Hrnjak et al., Miller et al., and Rodarte et al. 1998a,b] is related to the acoustic resonance problem in plate type heat exchanger geometries.

In plate evaporators, many types of nontubular bluff bodies can be present. This is due to the different role that the flow obstructions play in plate heat exchangers. In tube array exchangers the role of the tube is to transfer heat from one fluid to other. The role of the flow obstructions that cause the acoustic resonance in plate heat exchangers is to serve as supports and flow distributors. This difference gives greater flexibility in the design of a plate supporting structure that minimizes the flow-induced noise.

### **1.3 State of the art before this project**

The flow-induced noise and acoustic resonance phenomenon in plate heat exchangers is a problem that is new to this type of heat exchanger. Plate heat exchangers were traditionally used for liquid-liquid operation, conditions under which noise problems are not a concern. The advantages of plate heat exchangers are related to the very large capacities relative to their size. Size reduction translates into cost and space savings in comparison to traditional fin and tube heat exchangers. This is of special importance to the automotive industry. Additionally, plate heat exchangers permit reductions in air conditioning system refrigerant charge and improvement in overall performance. When this technology was adapted as evaporators in automotive applications, the traditional liquid-liquid operation changed to two-phase refrigerant - air operation. However, during certain operating conditions the refrigerant flows as a gas, causing acoustic resonance and flow-induced noise problems. Flow-induced noise and acoustic resonance studies of plate-type heat exchanger geometries are not available in the literature.

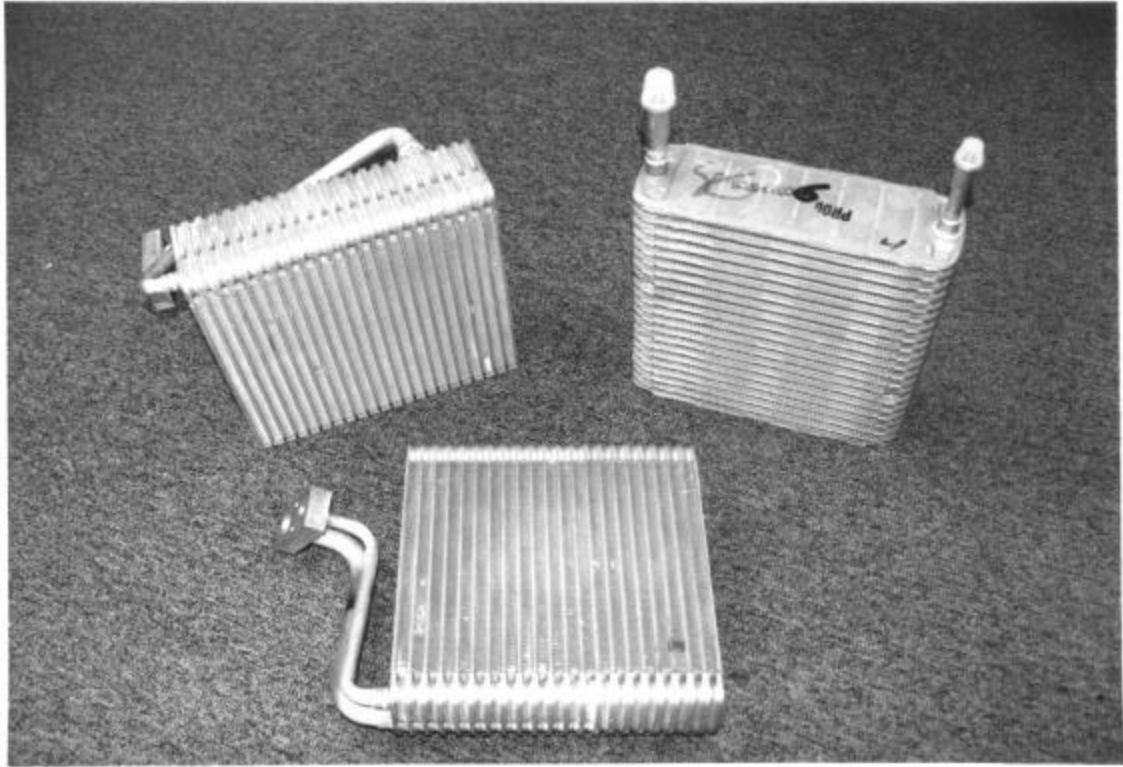


Figure 1.2 Photograph of typical plate heat exchangers used in automobile applications.

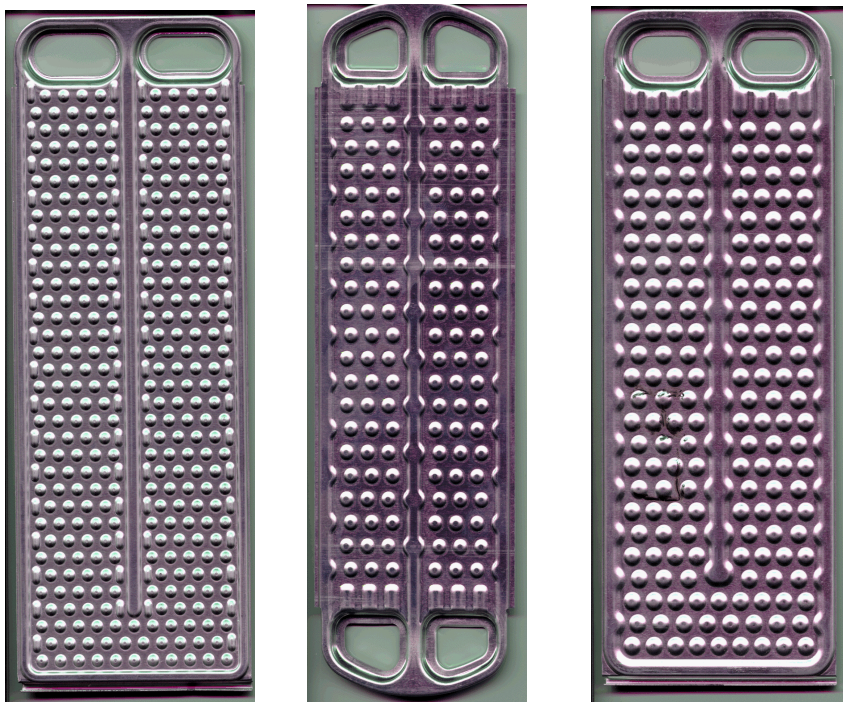


Figure 1.3 Photographs of three different single stamped plates used to make evaporators showing their internal structure design.

Studies of acoustic resonance in heat exchangers have produced a wealth of knowledge. The research focused in four general areas that will be described in detail in the next chapter: 1) flow excitation mechanisms, 2) damping factors, 3) sound pressure level predictions, and 4) factors that affect the acoustic resonance phenomena. The majority of this work has been experimental. This research has produced 1) Strouhal number maps for the different cylinder array configurations at acoustic resonance and nonresonant conditions, 2) empirical damping factors that try to predict if an acoustic resonance will develop, 3) empirical relations to determine sound pressure level for different array configurations, and 4) general understanding of the phenomenon. There are, however, different issues that have not been addressed. There are no empirical or fundamentally based models that address the different relevant parameters responsible for the noise generation and attenuation of bluff bodies inside ducts. The current empirical damping models do not work in many situations and are only applicable when there is a coincidence condition, that is, when the noise frequency produced by the array matches an acoustic natural frequency of the duct. Additionally, these models in general do not account for the effects of cavity size, number of cylinders in the array, and other relevant parameters that affect the noise produced in the duct. Damping models such as the ones available today do not give information on the sound pressure levels produced at resonance and nonresonance conditions. An empirical model to determine sound pressure level for single cylinders and cylinder arrays has been proposed by Blevins and Bressler 1993. This model is valid only at resonance condition, lacks generality, and does not account for the effects of the duct walls or acoustic damping.

In order to understand the flow-induced noise from cylinder arrays inside a duct, the acoustic field produced by a single cylinder in a duct should be studied. There appears to be no available reports of investigations of the acoustic field produced by a single cylinder in cross-flow inside a duct. The aeroacoustics of a cylinder in cross flow in unbounded space has been studied previously [Etkin et al., Grosche, Keefe 1961, 1962, Leehey and Hanson, Phillips]. The available theory links the relevant variables that affect noise generation by the cylinder in cross flow and agrees relatively well with experiments. This information has not been incorporated in a fundamentally based model that takes into account the effects of the walls on reflection and damping. Single cylinder experiments can be used to validate such an acoustic model.

There appears to be no systematic investigation that reports the results of studies on the acoustic field produced by two cylinders side-by-side or in tandem. Measurements performed for these configurations are valuable first steps necessary to understand noise generation and interaction characteristics of multiple cylinders in a duct.

A model that can determine the acoustic field produced by a single or multiple cylinders in cross flow is not available. Such a model could be used to explore how the acoustic field changes with changes in different parameters and thus provide the tools needed for designers to rationally design plate heat exchangers that produce less flow-induced noise.

#### **1.4 Motivation**

Flow-induced noise in plate heat exchangers is a current problem in the automotive industry. The costs associated with a problem evaporator are immense since these heat exchangers are installed in millions of vehicles. These costs include the replacement of problem heat exchangers, the addition of excess oil to the refrigerant to mitigate the problem and to the public perception that this noisy vehicle is not of good quality.

The cost of stamping dies is significant. Therefore, make and try methods are not a good option. The development of an experimental technique that produces comparable results to those in real stamped plates using simple prototypes made using stereolithography techniques is an improvement over conventional methods.

The understanding of flow-induced noise produced by bluff bodies inside a duct could guide a designer in the right direction to avoid or minimize problems. An acoustic model that could predict the trends and could differentiate between potential designs would be valuable.

The general problem of flow-induced noise of bluff bodies inside a duct is a very complex phenomenon, many aspects of which need to be studied further.

### **1.5 Goal of this project**

The main goal of this project is to gain a better understanding of the flow-induced noise and acoustic resonance phenomena caused by small aspect ratio cylinders in cross flow inside a rectangular duct.

To further this goal, the results of experiments will be used to test an acoustic model based on the inhomogeneous convected Helmholtz equation. The flow-induced noise generated by cylinders will be treated as point acoustic dipoles with source strength linked to the flow-induced fluctuating forces produced on the cylinders in cross flow. The model considers different wall boundary conditions and volumetric damping. This model could be used to predict sound pressure levels at different positions inside the duct at resonant and nonresonant conditions and will take into account the most important variables related to flow-induced noise generation inside ducts.

Acoustic measurements of the flow-induced noise produced by short aspect ratio cylinders in side-by-side and tandem arrangement inside a duct will also be pursued as a first step to understand the noise emitted from multiple cylinders in a duct.

Another goal of this project is to determine if heat exchangers and cylinder arrays of the dimensions used in plate heat exchangers behave in a way similar to large tube array heat exchangers for which literature is available.

## Chapter 2: Literature Review

### 2.1 Introduction

There have been investigations of the acoustic resonance phenomena in heat exchangers since the mid-fifties [Baird, Grotz and Arnold, Putnam]. The majority of the research has been experimental and focused on large tube array type heat exchangers. The work can be grouped in four areas:

1. Investigations focused on explaining, measuring or visualizing the flow excitation mechanisms. The output of this research has been a better understanding of the flow excitation mechanisms present for the different array configurations. Other products of this research include Strouhal number maps or correlations to determine the characteristic dominant peak in the frequency spectrum that will be generated by an array of some specified configuration.
2. Investigations presenting design guidelines or damping criteria. Design guidelines are necessary since there are cases in which the coincidence of the flow excitation and acoustic natural frequency will not produce a clearly noticeably acoustic resonance.
3. Prediction of the magnitude of the sound pressure amplitude once an acoustic resonance is established. Currently there is no damping criterion that is completely accurate in its prediction. This fact prompted Blevins and Bressler 1993 to propose a sound pressure level estimator instead.
4. Research related to factors that affect the acoustic resonant phenomena in one way or another. These factors can include the effect of the tube bundle in reducing the effective speed of sound in the gas, the effect of the flow characteristics such as turbulent intensity, the effect of tube roughness, end conditions, tube length, chamber walls, and number of tube rows.

This literature review has the objective of presenting an overview of the most important research done in this area. It will be divided into these four areas.

### 2.2 Flow excitation mechanisms

Before starting the discussion of flow excitation mechanism, it is necessary to define the basic geometries considered and nomenclature to be used. Figure 2.1 shows diagrams of the standard tube array layout with its naming convention. Figure 2.2 shows an in-line array with some definitions that will be used in this work. These definitions are not universally accepted. Work in this area must be examined carefully to avoid confusion due to nomenclature.

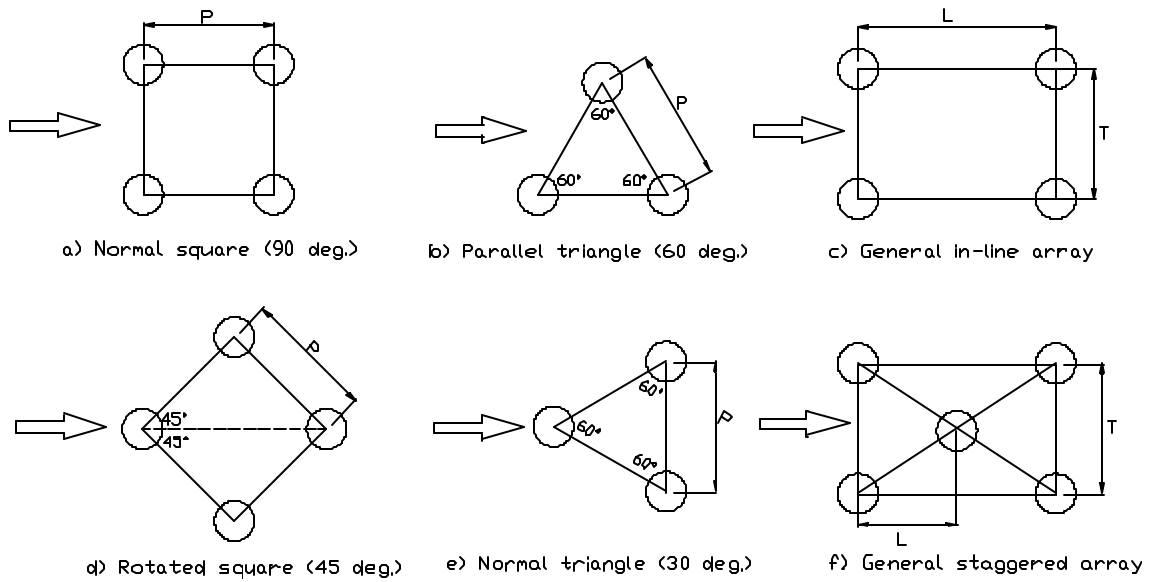


Figure 2.1. Standard tube array geometries with relevant nomenclature. [Weaver 1993].

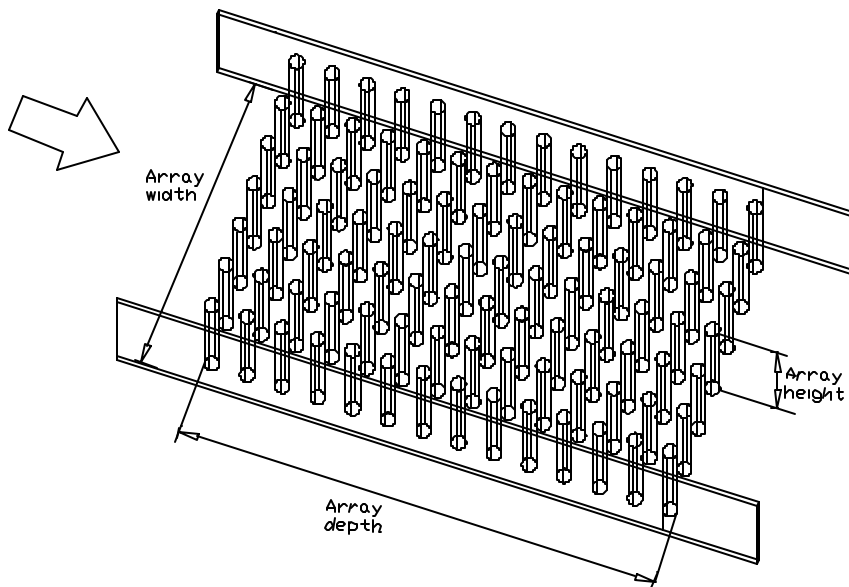


Figure 2.2. In-line tube array inside a rectangular duct showing some definitions to be used in this document. Array with 7 columns and 14 rows.

Flow phenomena in tube arrays is very complex. The complexity is related to flow separation and flow interactions between cylinders. In light of this, it is understandable that several theories have been created to explain the observed phenomena. What follows is a historic presentation of the most relevant advances in the field.

From the mid-fifties until 1965, vortex shedding was believed to be the cause of acoustic resonance. This belief was based largely on speculation by extrapolating what was known about the vortex streets formed by single cylinders in cross flows to tube arrays formed by many cylinders.

In 1965 Owen developed his turbulent buffeting model and presented an equation to determine the frequency of the turbulent buffeting excitation. This paper marks the beginning of a debate about the nature of the flow excitation mechanisms present for tube array bundles.

In his paper, Owen argues the impossibility of propagation of coherent "vortex-shedding like" structures from the first rows of tubes to deep within the tube bank. The argument is based on his personal opinion and argues that because of the cumulative randomness introduced by the shedding irregularities along the length of tubes and the "labyrinth-like, high Reynolds number flow present", there is no possibility for periodicities to be present deep in the tube bank. He proposes a turbulent buffeting type of excitation that is dependent on the flow velocity between tubes, the geometric characteristics of the tube bank, and a drag coefficient for the tubes. He establishes a dominant frequency for this turbulent excitation by combining expressions for energy conversion from the pressure drop terms to turbulence terms and by relating this to the predominant frequency of excitation, which should be related to  $f_{tb} = U/l$ , where  $U$  is the flow velocity and  $l$  is the length scale associated with the turbulence. From the results of his analysis, an equation that relates the functional relationship between the peak in the turbulent spectra and the geometric and flow variables is presented. This relationship is shown in equation (2.1).

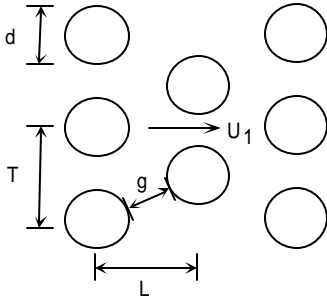
$$f_{tb} = \left( \frac{U_1 d}{LT} \right) \left( 3.05 \left( 1 - \frac{d}{T} \right)^2 + 0.28 \right) \quad (2.1)$$


Figure 2.3 Tube array with nomenclature used in equation (2.1).

He also establishes a Strouhal-like number ( $f L/U$ ), where  $L$  replaces  $d$ , for heat exchangers. This dimensionless grouping is  $0.5 \pm 10\%$  for  $0.6 > d/T > 0.2$ . He does not discriminate between staggered or in-line heat exchangers.

The turbulent buffeting theory has to explain why the broad spectrum of the turbulent eddies do not excite acoustical or mechanical resonances over a wide range of flow velocities. Owen presents data for the turbulent energy spectrum, which indicates that the size of the dominant eddies are of order  $L$ . For most heat exchangers,  $L$  and  $T$  are very similar, and  $L$  and  $T$  are of order  $d$  (usually  $L < 3d$ ). He argues that eddies which are a little larger than the tube diameter are the eddies which impart the most energy to the tubes (or fluid surrounding them). The effect of smaller eddies will be small since their local contributions will average out. Larger eddies, since their size is much greater than the tube diameter and "since the force on the tube is likely to be correlated over a span length of  $d$  in order of magnitude" will not contribute significantly.

Other authors like Y.N. Chen did not ascribe to Owens' arguments supporting turbulent buffeting. In his 1968 paper, Chen theorizes how vortex shedding can develop deep inside tube arrays. Chen tries to explain the mechanisms that affect the vortex shedding from cylinder to cylinder in a tube bank. He argues that one vortex generated upstream can affect the generation of vortices downstream when the vortices get near downstream tubes (for in-line type arrays) and tries to explain with this argument the importance of the tube spacing  $L$ . The importance of  $T$  depends in the relative magnitudes of the gap velocity (between rows) and the spacing between vortices shed from a cylinder (approx.  $D$ ). If  $T/D$  is greater than 2 or 3, then the effect of different columns of tubes on each other will be small. A more recent work by Zdravkovich 1987, describes the complexities involved in the interactions between cylinders and how the spacing between them play a crucial role in the flow phenomena. Chen described and illustrated only the types of interactions that he believed happen for in-line and staggered arrays. He presented figures showing different possible vortex shedding patterns. Strouhal number maps for general in-line and general staggered arrays are also shown, but these maps are based in relatively few data points.

Another frequently cited work is that of Fitz-Hugh. In his paper Fitz-Hugh presents Strouhal number maps for in-line and staggered arrays. The maps were made by compiling the work of several researchers and arranging them in graphs that used  $L/D$  and  $T/D$  as its abscissa and ordinate, respectively. The graphs were made for both general in-line and general staggered configurations. He then established regions in  $T/D$  and  $L/D$  space for which a given Strouhal number could be assumed. These graphs have found extensive use in industry [Eisinger and Eisinger et al.]. However, there are some discrepancies in certain sections of these graphs. For example, for in-line arrays with ratios  $L/D = 1.7$  the prediction for  $T/D = 1.5$  is  $S = 0.52$  but changing the  $T/D$  to only 1.7 changes the Strouhal number prediction by 50% to  $S = 0.26$ . A similar situation is present in the staggered tube array map where regions below and above  $T/D = 1.4$  and  $L/D = 1.2$  show Strouhal number variations from 0.7 to 0.35! Fitz-Hugh explained the above by noting that other researchers have found cases where two or more peaks in the spectra at different frequencies developed for some heat exchangers.

Paidoussis stated that Owen's Strouhal number predictions based on a turbulent buffeting theory differs from those of Chen's predictions based on the vortex shedding hypothesis as much as they differ from the maps established by Fitz-Hugh, which conceded that the excitation mechanism was not understood. Paidoussis concludes that both theories are probably trying to describe the same phenomenon. Weaver and Fitzpatrick state that Owen's and Chen's predictions for Strouhal number agree reasonably well since they use the same data. However, standardized methods to determine the excitation frequency for a given heat exchanger design call for the determination of this frequency using the turbulent buffeting equation developed by Owen and a Strouhal number for that array from another source; Chen's and Fitz-Hugh's maps being the more well-known sources [Holtz]. So and Savkar showed that the distinction between vortex shedding and turbulent buffeting was not clear once the turbulent intensities in the flow reached a certain level. According to them, for a 10% turbulent intensity level the vortex shedding "peak" was no longer identifiable and a drastic reduction in the lift coefficient was also observed. These facts could explain the differences in the resonance amplitude level results obtained in the field and the laboratory in which tests are run under more controlled conditions.



The belief that there was but one mechanism present, explained using different theories, was probably the representative thinking in the early 1980s [Weaver 1993]. During that decade, further research was performed to reconcile some of the apparent deviations from expected behavior. One of the main deviations observed was related to the behavior of in-line heat exchangers. Heat exchangers with an in-line tube array configuration apparently did not follow the classical excitation mechanism. For this type of heat exchanger, the measured flow periodicities at off-resonant conditions did not couple with the acoustic natural mode of the containing cavity. In what follows the current state of understanding of the flow instability mechanisms for in-line and staggered configurations will be presented.

### 2.2.1 Staggered arrays

For staggered arrays "there is a vast amount of evidence that shows that a discrete periodicity exists in the early tube rows and that the frequency of this periodicity increases linearly with flow velocity" [Weaver 1993]. These findings are addressed below in a more detailed way.

Abd-Rabbo and Weaver showed for the first time with flow visualization techniques a clear alternate vortex shedding in a closely packed staggered array. For very low flow velocities, vortex shedding begins at cylinders in the third row and then the vortex shedding process moves upstream when the Reynolds number is increased. The Reynolds number and flow velocity were, however, very low and not representative of real heat exchangers. The Strouhal number determined at these conditions was higher than those reported elsewhere. At higher velocities discrete periodic vortex shedding with Strouhal numbers in agreement with other reports were found. They found that this periodic vortex shedding in addition to broadband turbulence excitation is present at least in the early tube rows of heat exchanger tube arrays.

Ziada et al. 1989a report results of tests performed on a staggered array in an air tunnel. They showed the occurrence of different Strouhal numbers. They found three different Strouhal numbers for an array with  $T/D = 1.6$  and  $L/D = 1.85$ :  $S_1 = 0.55$ ,  $S_2 = 0.32$  and  $S_3 = 0.11$ .  $S_1$  and  $S_3$  are the strongest after the first row and then subside rapidly in the downstream direction.  $S_3$ , however, can be detected behind the first row, but it is hardly detectable in the second row. Neither  $S_1$  nor  $S_3$  could be detected after the fourth row.  $S_2$ , according to Ziada et al. 1989a seems to be caused by turbulent buffeting since "a) it is broadband in nature, b) it gains strength within the first few rows, c) it is persistent through the whole depth array, d) It is well predicted by Owen hypothesis." They determined that flow periodicities detected at off-resonance conditions for this staggered array are the cause of the acoustical resonance when the flow velocity increases. They compared the different Strouhal numbers and determined that the empirical formula of Žukauskas and Katinas predicts the Strouhal number to be 0.56, which agreed rather well with  $S_1$ , which is ultimately the flow instability responsible for the acoustic resonance. Ziada et al. 1989a presented three variations of the same heat exchanger by changing the duct dimensions and thus changing the acoustic natural frequencies. They showed that the Reynolds number or the resonant frequency is important in determining if a given acoustical resonance will materialize or not. Due to these facts, Ziada et al. 1989a recommend that the Reynolds number be included in the design guidelines. As mentioned above, the Strouhal number determined from the Owen hypothesis agrees rather well with the second Strouhal number ( $S_2 = 0.32$ ). This, however, proved to be irrelevant since the flow instability associated with  $S_1$  was responsible for the acoustic resonance. Using Owen's equation to

determine Strouhal number and ultimately critical velocity for this type of closely packed staggered array produced a nonconservative design. Ziada et al. 1989a suggest caution when using the Owen hypothesis to predict flow instability Strouhal numbers. They conclude that for staggered arrays, the flow periodicities responsible for the acoustic resonance are all present just after the first row. There may be more than one Strouhal number present. The flow instability responsible for the acoustic resonance is present in the first few rows of tubes. This agrees with Eisinger's comments, as reported by Weaver 1993, relating how he was able to eliminate an acoustic resonance from a heat exchanger in service by the insertion of baffles only a few rows into the staggered array.

Polak and Weaver reported the results from investigations into the flow periodicities caused by staggered-triangular tube arrays. They used hot wire measurements in addition to flow visualization to determine the different types of behavior for this type of tube arrangement during off-resonance conditions. By being far from a resonance, the influence of the acoustic-induced interactions with the vortex shedding from the tubes are eliminated. They found that depending on the  $P/D$  ratio of the tube array there are three different types of behavior. They show results for 9 different tube arrays with  $P/D$  ratios from 1.14 to 2.67. They determined that for tube arrays with the smallest  $P/D$  ratio ( $P/D = 1.14$ ) no distinctive peak in the frequency spectrum could be detected. For  $P/D < 2$  there is a distinctive peak in the frequency spectrum from the hot wire measurements that can be detected in the second and third tube row but not in the fourth (they used only tube arrays with four rows of tubes). Coherence and phase measurements between pairs of hot wires in the gap between tubes placed in the second and third rows indicated that vortex shedding from the first row of tubes causes this peak in the hot wire spectrum. Flow visualization confirmed these results. Hot wire spectra taken in the gap between tubes in the fourth row does not show any flow periodicity. For tube arrays having a  $P/D > 2$ , there are two distinctive peaks in the spectra. The higher frequency component is caused by vortex shedding from the first tube row, and the lower frequency component is caused by the second tube row. This appears to happen because the larger tube spacing permits the flow to reach the second tube row more directly and with less interference effects from the fluid disturbances generated by the first row. The lower-frequency peak in the spectra was never as intense or periodic as that generated by the first row, and only occurred at high Reynolds numbers. From these results Polak and Weaver concluded that the constant Strouhal phenomena is caused by the first few rows of tubes. The different Strouhal number generated by the second row for arrays with  $P/D \geq 2$  is due to differences in the local fluid velocities and the wake width, both of which play a central role in the vortex shedding process. They also showed that their results are in close agreement with the results of other researchers and present an experimental correlation by Žukauskas and Katinas, shown in equation (2.2), which correlates the experimental data well:

$$S = 0.2 + \exp\left(-\frac{(P/D)^{1.8}}{2.3}\right) \quad (2.2)$$

Price et al. performed flow visualization studies in parallel triangular and rotated square arrays with pitch to diameter ratios  $P/D = 1.375$  and  $P/D = 1.5$ , respectively. For the rotated square array, they found that at very low Reynolds numbers, symmetric vortices are formed behind all cylinders in the array. At higher Reynolds numbers, an

oscillation in the dividing line of the symmetric vortex pair starts to develop. This happens for Reynolds numbers in the range 130 - 215. This marks the beginning of alternate vortex shedding from the cylinders. The vortex shedding when hitting cylinders downstream increase the vorticity shed from the downstream cylinder. Part of the vorticity generated is transported through the clear diagonal paths present, thus mixing with the flow from different channels. The Strouhal number found at higher Reynolds numbers seem to be in reasonable agreement with results found elsewhere. For the parallel triangular array, no vortex shedding was observed behind cylinders in any row. Only attached eddies of recirculating flow formed behind the cylinders. Curiously, when a flexible cylinder was mounted in the middle of the array, this cylinder started to oscillate. The cause of oscillation was believed to be fluid-elastic instability. Once this tube started to oscillate, it triggered the formation of vortical structures, particularly in the cylinders upstream of the flexible tube. The vortices were shed from the wake region and then were swept downstream through the channels.

Ziada 1998 presented results and recommendations for the design of normal triangular arrays and parallel triangular arrays. For normal triangular arrays, he points out that the normal vorticity excitation and acoustic resonance have the same Strouhal number, and therefore, a single Strouhal number chart can be used for both tube vibration and acoustic resonance designs. For parallel triangular arrays, even when they can be considered as a kind of staggered arrangement; they can also be visualized as an in-line array in which alternate tube columns are placed a distance of  $L/2$  out of alignment (see Figure 2.1). This type of array behaves more or less like an in-line array. For this type of array Ziada 1998 therefore recommends the use of two different Strouhal number charts to avoid overly conservative designs. This highlights the need for more research related to parallel triangular arrays as Weaver 1993 points out.

### 2.2.2 In-line arrays

Fitzpatrick and Donaldson 1977 indicated that both the vortex shedding and turbulent buffeting theories available at the time were inadequate to predict the behavior of the flow phenomena in in-line tube arrays. The results of their research did not identify a particular mechanism but pointed to the possibility that acoustic resonance could be the result of vortex shedding, turbulent buffeting, broadband turbulence, or a combination of the three.

Chen 1984 noted that since the flow for in-line arrays passes directly in the gaps between tubes, the shedding of vortices is controlled by the jet in the flow lane. This jet is disrupted by the presence of the downstream tubes. This is why the main parameters that affect the flow phenomena for this type of arrays should be linked to the flow lane width ( $s$ ) and the tube spacing in the longitudinal direction  $L$ .

Weaver and Abd-Rabbo found the appearance of symmetric vortex formation in the wakes of tubes in their flow visualization study. Resonant tube vibrations were excited by this flow periodicity. It is important to point out that tube vibration resonance and acoustic resonance are generally not correlated. This is why different Strouhal number charts should be employed depending on the phenomena of interest [Ziada 1998].

A very detailed investigation for in-line arrays with geometries covering the full range of tube spacings was performed in a series of papers by Ziada and Oengören, Ziada et al. and Oengören and Ziada. What follows is a synthesis of the most important findings of their work. The findings represent the current state of understanding of the flow phenomena relevant to acoustic resonance for in-line arrays.

Ziada et al. 1989a performed tests on staggered and in-line heat exchangers in an air tunnel and in a water tunnel for the in-line heat exchanger. For the in-line case, three Strouhal numbers were detected behind the first tube row:  $S1 = 0.92$ ,  $S2 = 0.64$  and  $S3 = 0.46$ . Initially, they were able to detect only  $S1$  and  $S3$  in the air tests, but after testing in the water channel and detecting  $S2$ , they went back to the air test and were able to identify  $S2$ , but only by using a small number of samples during averaging and for only some flow rates.  $S2$  was found to be the one responsible for the acoustic resonance present in the air tunnel tests. With the in-line array configuration that they used ( $L/D = 1.35$ ,  $T/D = 1.6$ ) they were able to excite the third acoustic mode. No flow periodicity was able to excite the first two modes, and the third mode was excited by the very faint periodicity represented by  $S2$ . They present a detailed flow visualization study to try to explain the flow phenomena. This study presents a clearer picture of the phenomena. The flow periodicity present for this closely packed in-line array was a symmetric jet instability that could be seen in both the flow lanes and behind the tubes. This symmetric jet instability was responsible for the first Strouhal number measured ( $S1$ ). Only one or two rows of tubes had vortices. The positions of these rows depended on the Reynolds number and moved upstream with an increase in the Reynolds number until they reached the first row. This symmetric mode of vortex formation occasionally shifted to an unstable antisymmetric one, but only for short periods of time before returning to the more stable symmetric mode. Since both the anti-symmetric vortex formation mode and the flow periodicity measured as  $S2$  appeared occasionally, this was believed to be sufficient proof to state that this antisymmetric flow periodicity was the one occurring at  $S2$ . For this closely packed in-line array, the flow periodicities present at off-resonance conditions are caused by a symmetric jet that impinges on downstream tubes, but the vortices formed in this way due to their symmetry cannot excite transverse acoustic modes. For in-line arrays Ziada et al. argue that the antisymmetric jet instability that is suppressed at off-resonance conditions due to the presence of tubes can be triggered by the particle velocity of the transverse acoustic mode when frequency coincidence occurs. Once this happens, a feedback mechanism is established such that this antisymmetric jet instability couples with the transverse acoustic resonance. During flow visualization in the closely packed in-line array, it is determined that although the vortices seen are small and may not be very energetic, they still represent a discrete flow periodicity that is capable of exciting resonances. These results contradict what Owen said about the impossibility of vortex formation in highly packed arrays.

Strouhal numbers obtained for the in-line tube array and correlations or maps from the literature were compared. In the case of in-line arrays the empirical relationship by Fitzpatrick 1986 was the one that predicted more accurately the Strouhal number of the actual resonance. They also showed values of Strouhal numbers from the maps of Chen 1968 and Fitz-Hugh, but the values obtained from them predicted a Strouhal number that showed no relevance ( $S3$ ) and an even lower Strouhal number, respectively.

In the paper by Ziada and Öngören 1992 a detailed investigation of the flow phenomena inside an in-line tube array with intermediate tube spacings is presented. The results obtained for the intermediate tube spacing corroborate results obtained for more closely packed in-line arrays [Ziada et al. 1989a]. There are some major differences, however, between closely packed arrays (with  $L/D < 1.7$ ) and arrays with intermediate spacings ( $1.7 < L/D < 2.7$ ). For the closely packed array, the vorticity shedding generated by the symmetric jets occurs at the first rows only and the flow becomes fully turbulent downstream. For the intermediate spacing arrays, the vorticity

shedding produced by the jet is stronger and can be seen throughout the whole array. The other major difference found was that the closely packed arrays presented symmetric vortex formation in the jet from the tube lanes as well as symmetric vortex formation as seen from the tube wake. The vortex formed in the wake of the cylinders was more exactly formed in the shear layer right next to the tube and are very weak. Thus, the vortices did not interfere much with the flow in the wake of the cylinder. Since they did not interfere significantly in the wake of the cylinder, symmetric vortex formations could be seen in the cylinder wake and at the same time in the jet lane. For this to occur, vortex formation in adjacent lanes has to be in phase since the vortices formed in the wake of the cylinder depend on adjacent jet lanes. For the tube arrays with intermediate spacing, however, the symmetric vortices formed in the jet lane were significantly stronger and thus affected the flow in the wake of the cylinders. In this case the vortices formed in any given jet were out of phase with the one formed on adjacent jet lanes. This produced antisymmetric vortex formation in the wakes similar to that present for single cylinders in cross flow, but of a completely different nature, since such a vortex is caused by the jet instabilities in the flow lanes. Figure 2.4 shows a rough schematic of the different flow instability mechanisms for closely packed and intermediate in-line tube arrays.

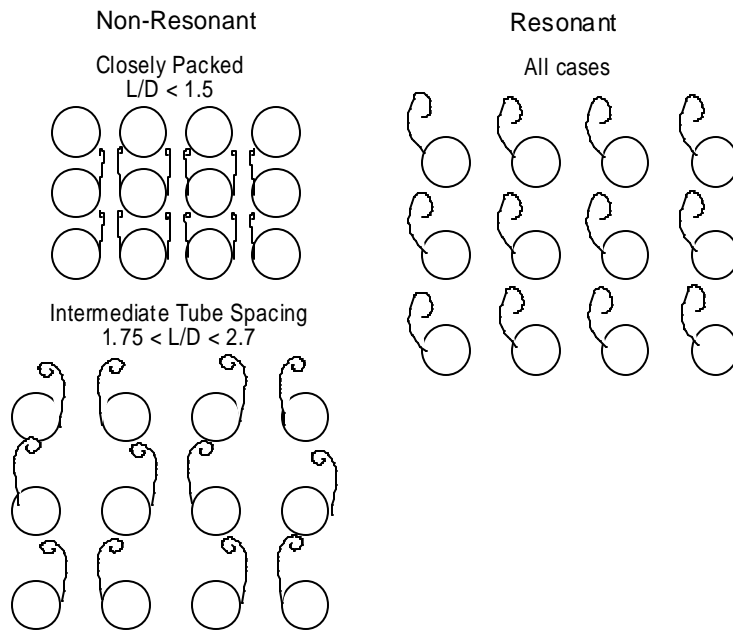


Figure 2.4. Schematic of flow instabilities present for closely packed and intermediately spaced in-line tube arrays.

Oengören and Ziada 1992 presented results of resonance tests of in-line arrays. They showed very clearly, using flow visualization techniques, the flow structure of the vortex formation during resonant conditions. This vortex formation was very different from what was found at off-resonant conditions and described above. During resonance, instead of the characteristic symmetric jet instability, a shear-layer instability was observed. The vortex formation was synchronized throughout the array with the tubes shedding vortices in phase. An additional proof that another excitation mechanism was present is that the Strouhal number determined at off-resonant conditions does not predict the onset of resonance. The authors then attempted to explain the shift from the symmetric jet instability present at off-resonant conditions and the shear layer instability not detectable at off-resonance conditions but

responsible for the observed resonance. They argue that the shear layer instability is triggered and synchronized by the acoustic particle velocity. Therefore, the occurrence of resonance depends on the flow-duct acoustics. They establish two prerequisites for the initiation of a resonant state: 1) "The frequency of the shear layer instability must be close to the resonant frequency", and 2) "The response of the acoustic mode to random turbulent excitation must be capable of exciting, and organizing, the shear layer instability." This shows the importance that turbulence level and acoustical damping have in the initiation of the shear layer mode. Once the shear layer is excited, a feedback mechanism between the shear layer oscillation and the acoustic response develops. This produces the characteristic lock-in effect seen in the frequency-velocity diagrams.

Ziada and Öngören 1993 present detailed results of work performed on an in-line array with large tube spacings ( $L/D = 3.25$  and  $T/D = 3.75$ ) to understand the flow instabilities for this geometry. The first test performed in air showed that in this case the flow instability detected at off-resonant conditions was responsible for the acoustic resonance! These results differ from the results for intermediate and closely packed arrays described above. When water tests were made, it was found that the turbulence level played a key role in the flow instability phenomena. Two different types of instabilities were found: "global jet mode" and a "local wake mode," each having their own characteristic Strouhal number and not occurring simultaneously. For low turbulence levels upstream of the tube array, a symmetric jet instability similar to the one found for the intermediate spaced array was seen. For higher turbulence levels, a local wake instability mode was present. In this mode, alternate vortex was shed from the wake of the cylinders of the first few rows, and this was independent from cylinder to cylinder. After the fifth row, a narrow band turbulent excitation at a different frequency was present. The local wake instability mode is the cause of the acoustic resonances once there is a frequency coincidence condition. When this happens, all the vortices in the wakes become synchronized with the particle velocity of the resonant mode. For bundles with intermediate spacing the turbulence level did not seem to affect the jet instability mode. Turbulence level, then, introduces a new variable in the determination of the appropriate Strouhal number. If a Strouhal number is determined for in-line arrays with large tube spacings under nonresonant conditions, there will be uncertainty as to which instability mode is present at the time of the measurement, and thus, acoustic resonance predictions might fail. On the other hand, if an acoustic Strouhal number is determined at resonance, then, if this Strouhal number is used in the prediction of tube vibration for which symmetric vortex formation is relevant, it might produce erroneous results.

### **2.3 Design guidelines and damping parameters.**

Design guidelines have been presented in a number of references [Blevins and Bressler 1993, Eisinger, Eisinger et al., Fitzpatrick 1986, and Ziada et al. 1989b] and also have been standardized [Holtz]. Design guidelines consist of basically three steps:

1. Determination of acoustic natural frequencies of the duct where the tube array will be placed. The majority of the ducts are either rectangular or cylindrical.
2. Determination of flow excitation produced by the tube array used.
3. Comparison of the excitation frequency predicted at the design conditions for the given heat exchangers with the acoustic natural frequency of the containing duct. If they are within 20% of each other, acoustic resonance might develop.

In roughly 30% to 40% of practically important cases where an acoustic resonance due to a coincidence condition is predicted, the acoustic resonance does not materialize [Blevins 1994]. The level of acoustic damping for any given acoustic mode of a given heat exchanger will determine if an acoustic resonance will materialize or not. To this effect, several researchers [Chen 1968, Eisinger, Eisinger et al., Fitzpatrick and Donaldson 1984, Grotz and Arnold, and Ziada et al. 1989b] have proposed a number of damping criteria that try to predict if an acoustic resonance of any given mode will be excited when a coincidence condition is established for that mode. A description of the different damping parameters and design guidelines follows.

Grotz and Arnold are the authors of one of the earliest investigations of acoustic resonance in heat exchanger tube bundles. They concentrated their efforts on in-line heat exchangers and reported data for twenty different configurations. Their data consists mainly of Strouhal numbers for these arrays under resonant conditions. Their data has been used extensively by other authors [Chen 1968, Fitz-Hugh, and Owen] in the creation of Strouhal maps and correlations. They introduced a damping parameter based on geometry only. This parameter defined by equation (2.3) represents the ratio of the width of the resonant chamber transverse to the flow and to the tube axis and the space between rows of tubes (Figure 2.5). They predict acoustic resonance if  $\Gamma < 62$  or 80. The variable  $i$  represent the acoustic mode that is being checked.

$$\Gamma = \frac{W}{a} = \frac{W}{(X_L - 1)Di} < 62 \text{ or } 80 \quad (2.3)$$

Grotz and Arnold argue that the damping parameter should be related to the dimensions of the resonating chamber (the shaded area in Figure 2.5). In this way, the effect of the tubes, which act as constricting boundaries, can be considered. Tube bundles, they say, are usually square, so the size of the chamber is an indication of "the number of tubes which are present to impede the air particle motions which lead to the establishment of the standing wave".

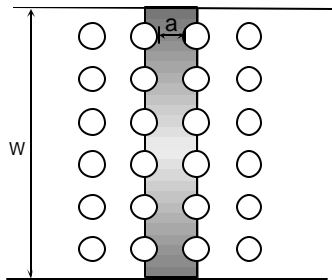


Figure 2.5 Schematic showing description of resonant chamber in in-line arrays as described by Grotz and Arnold.

Chen 1968, in addition to presenting his very well-known Strouhal number maps, also presents a damping parameter. This parameter is used to determine if an acoustic resonance condition could be excited or not. The damping parameter is

$$y = \left( \frac{\text{Re}}{St} \right) \left( \frac{L-d}{L} \right)^2 \left( \frac{d}{T} \right) > 600 \text{ or } 2000 \quad (2.4)$$

The value of 600 applies to laboratory condition and 2000 to industrial or field conditions. The variable L should be replaced by 2L for staggered arrays in equation (2.4). He does not mention the assumptions made in the determination of this damping parameter. It is assumed that it is an empirically fitted relationship.

Fitzpatrick and Donaldson 1984 introduce a damping parameter that is a modified version of the Chen 1968 and Grotz and Arnold damping parameters. This new damping parameter includes the effects of scaling (i.e., the effect of the size of the tubes and the channel width). This damping parameter is a slightly modified version of the parameter presented by Fitzpatrick 1985. Fitzpatrick and Donaldson argue that for a given array (with fixed L/D and T/D ratios) the damping should be the same for a given channel size independent of the tube size (D) as long as the L/D and T/D remain constant. The damping parameter established by them is presented in equation (2.5):

$$\Delta^* = \frac{\text{Re}^{1/2}}{M St} \left( \frac{1}{2(X_L - 1)} \right) \left( \frac{1}{X_T} \right) \quad (2.5)$$

Resonance is predicted for

$$8200 \left( \frac{D}{L} \right) - 3000 < \Delta^* < 8200 \left( \frac{D}{L} \right) - 700$$

This damping criterion was developed for in-line arrays.

A similar conclusion was reached by Ziada et al. 1989b who experimented with different channel widths for a fixed L/D and T/D ratio heat exchangers and found that sometimes the first acoustic mode was not excited into resonance. They concluded that any design criterion should include the effects of the Reynolds number.

Fitzpatrick 1986 reiterates the validity of his damping parameter for in-line tube arrays (equation (2.5)). In addition, he complements the design procedure with the introduction of a correlation for the prediction of acoustic Strouhal numbers (Strouhal numbers determined under conditions of acoustic resonance). The correlation is presented in equation (2.6):

$$St = 0.08 + 0.11(2X_T - X_L) \quad (2.6)$$

Fitzpatrick 1986 established a design guide proposal that required the determination of a critical velocity with the use of equation (2.6). If this velocity was lower than that needed for the heat exchanger duty then calculation of the damping parameter presented in equation (2.5) was required. If a resonance was predicted by the damping parameter, then modification of the dimensions of the resonating cavity with the introduction of baffles was needed. The placement of the baffles should be such that resonance is no longer predicted by the damping parameter or a coincidence condition is no longer achieved.

Ziada et al. 1989b established a damping criteria and then compared it to other design criteria by Chen 1968, Fitzpatrick and Donaldson 1984, and Blevins and Bressler 1987a. The damping criterion was established by a parametric study. The objective of this criterion is to separate resonant and non-resonant cases. To determine if an array will resonate, one needs to determine the values of the parameters described in equations (2.7) for in-line arrays or (2.8) for staggered arrays and then look them up in a map. The maps present  $G_i$  as a function of  $(L/D)^2$  for in-line arrays and  $G_s$  as a function of  $h$  for staggered arrays. The value of  $h$  is determined from the smaller of (T-



D)/2 or the diagonal gap in the array (see Figure 2.3). In these maps, a line is drawn between resonant and non-resonant cases, such that depending where a particular arrays lies it could be established if a resonant condition can be expected or not.

$$G_i = \sqrt{\text{Re}_{cr}} X_T \left( \frac{v}{c_o d} \right) \quad (2.7)$$

$$G_s = \sqrt{\text{Re}_{cr}} \left[ \frac{\sqrt{X_T(X_T - 1)}}{(X_T - 1)} \right] \left( \frac{v}{c_o d} \right) \quad (2.8)$$

Eisinger et al. evaluated a large number of in-line and staggered heat exchanger arrays. They present a very complete set of tables with resonant and nonresonant data for all heat exchangers used in developing the acoustic resonance prediction model. The main point of this paper is the introduction of criteria to establish if an acoustic resonance condition will develop for a particular mode in any given heat exchanger. The criteria are based on an input energy parameter defined as  $(M\Delta p)_i$ . They established a set of rules, which separate the resonant from the nonresonant cases.

The procedure to determine if an acoustic resonance will develop based on their method has the following steps:

1. Determine the value of  $(M\Delta p)_i$  for the heat exchanger. In order to do this, it is necessary to first determine the flow velocity at the coincidence condition. This can be done using equations (2.9) and (2.10) for each of the  $i$  modes that will be evaluated (Eisinger et al. recommend evaluation up to the 4<sup>th</sup> mode).

$$f_i = \frac{c_o i}{2 W \sqrt{1+s}} \quad (2.9)$$

$$V_i = \frac{f_i D}{St} \quad (2.10)$$

With the flow velocity, the Mach number can be readily determined. It is necessary to obtain a Strouhal number ( $St$ ) for the tube array in question. They recommend using Fitz-Hugh's Strouhal number maps. To determine the pressure drop through the array, they recommend using equation (2.11)

$$\Delta p = \frac{1}{2} V_i^2 r (4 m N) \quad (2.11)$$

In equation (2.11), the value of  $\mu$  used by the authors is 0.07. Blevins and Bressler 1993 report values of  $\mu$  between 0.02 and 0.12 for arrays that they tested.  $N$  represents the number of tube rows.

2. Estimate the value of the parameters  $(M\Delta p)_{p,i}$ , and  $(M\Delta p)_{v,i}$ , from equations (2.12-2.14).  $\delta$  is a modified form of Chen's 1968 damping parameter.

$$(M \Delta p)_{p,i} = (0.07)10^{0.4375 i} \quad (2.12)$$

$$(M \Delta p)_{v,j} = (0.07) d V_i \quad (2.13)$$

$$d = \frac{St X_T}{\left(1 - \frac{1}{X_L}\right)^2} \quad (2.14)$$

3. Compare the value of the parameter  $(M \Delta p)_i$  from step 1 to  $(M \Delta p)_{p,i}$ , and  $(M \Delta p)_{v,i}$  of step 2. if it is greater than both of them then an acoustic resonance is predicted for this mode. Otherwise no acoustic resonance is predicted. Repeat steps 1 through 3 for each of the first 4 acoustic modes. The input energy parameter  $(M \Delta p)_i$  represents the energy lost by the fluid as it passes through the heat exchanger. To develop, an acoustic resonance needs to have the excitation energy necessary to overcome the system damping. Analyzing the first criterion used in the prediction methodology, namely  $(M \Delta p)_{p,i}$ , Eisinger et al. based their method in the natural separation of the resonant and non-resonant cases when plotted as a function of acoustic mode number. This criterion should not be considered a "damping" criterion. More appropriately, this criterion could be considered an "instability/excitation strength" criteria. Since all the data used to evaluate this criterion was obtained using flue gases at 800 °C its applicability to other gases and conditions is questionable.

For the second criterion, the input energy parameter  $(M \Delta p)_i$  is compared to the modified Chen 1968 damping parameter (equation (2.14)) times the fluid velocity for the mode in question. In this case a comparison between the "instability/excitation strength" versus system damping is made. It is believed that this criterion performs a more suitable comparison. The drawback here is that Chen's damping parameter is given without mentioning the fundamentals behind its derivation. It is believed that this is an empirical correlation.

In the 8<sup>th</sup> Edition of the Tubular Heat Exchanger Manufacturers Association (TEMA) Standards, a design guide is given for the avoidance of acoustic and tube vibration resonance [Holtz]. To avoid acoustic resonance, the design guide recommends:

1. Determination of the acoustic natural frequencies:

$$f_a = \frac{i}{2W} \left( \frac{P_s g}{r_o} \right)^{1/2} \left( \frac{1}{\left(1 + \frac{0.5}{X_L X_T}\right)} \right)^{1/2} \quad (2.15)$$

Equation (2.15) is just another form of equation (2.9).

2. Determination of excitation Frequency:

Vortex shedding:

$$f_{St} = \frac{St V}{D} \quad (2.16)$$

Turbulent buffeting:

$$f_{tb} = \frac{V}{D X_T X_L} \left[ 3.05 \left(1 - \frac{1}{X_T}\right)^2 + 0.28 \right] \quad (2.17)$$

### 3. Prediction of acoustic resonance:

Acoustic resonance predicted if any of the following conditions are met:

Condition A:

$$\begin{aligned} 0.8 f_s < f_a < 1.2 f_s \\ 0.8 f_{tb} < f_a < 1.2 f_{tb} \end{aligned} \quad (2.18)$$

Condition B:

$$V > 2 f_a D (X_L - 0.5) \quad (2.19)$$

Condition C:

$$V > \frac{f_a D}{St} \quad \text{and} \quad \frac{Re}{St X_T} \left( 1 - \frac{1}{X_o} \right)^2 > 2000 \quad (2.20)$$

In equation (2.20),  $X_o = X_L$  for in-line arrays or  $X_o = 2 X_L$  for staggered arrays.

The standard is very conservative. The procedure calls for the determination of excitation frequency by means of the Owen turbulent buffeting correlation and also by the use of an appropriate Strouhal number. With respect to the conditions for which a given resonance is predicted, the parameters used are a combination of design criteria from several sources. Condition A follows from the observation that the acoustic resonance can shift the vortex shedding frequency up or down [Blevins 1993]. The values of 20% up or down were recommended by Barrington and Rogers and Penterson. Blevins and Bressler 1987a,b found values somewhat higher than these. Condition C predicts a resonance if the flow velocity of the heat exchanger is greater than the velocity needed to have a coincidence condition and if the Chen 1968 damping parameter is satisfied. However, if this velocity is greater than the critical velocity, condition A is satisfied. Therefore, condition C is redundant since condition A is more restrictive.

## 2.4 Acoustic resonance strength estimation

Acoustic resonance prediction from methods by Grotz and Arnold, Chen 1968, Fitzpatrick and Donaldson 1984, and Ziada et al. 1989b were compared to experimental results by Blevins and Bressler 1993. All the predictions fail for some of the cases presented. The inability of the different damping criteria to establish without error if a given acoustic resonance will materialize or not prompted Blevins and Bressler 1993 to develop a method to predict the magnitude of the acoustic pressure fluctuations that will be present once a coincidence condition occurs. Blevins in the design guidelines presented in his book [Blevins 1994] follows similar steps as those presented before, that is, determination of acoustic natural frequencies and flow excitation frequencies. If there is coincidence, however, instead of trying to determine from damping parameters if the resonance will materialize or not, he recommends estimating the magnitude of the resonance instead. The research to support this concept is

presented in Blevins and Bressler 1993. There, they present acoustic resonance results for tests with single cylinders, a single row of tubes and for full arrays of tubes.

For single cylinder tests Blevins and Bressler 1993 show the development of the vortex shedding from the single cylinders and how this vortex shedding couples with duct acoustics to produce a clear resonance. The resonance followed the classical excitation mechanism; that is, the resonance appears once the coincidence condition is established. The characteristic lock in phenomena can also be seen in the frequency-velocity diagrams. A theoretical expression based on Lighthill's theory for aeroacoustic sound generated by vortex-shedding from a cylinder was modified to predict the resonant noise using the results of single cylinder tests. This expression (2.21) is a function of the Mach number, diameter of cylinder, width of chamber and the pressure drop.

$$P_{\text{rms,max}} = \left( 12.5 r_o \frac{U^2}{2} \right) \left( \frac{U}{c_o} \right) \left( \frac{D}{B} \right) \quad (2.21)$$

A modified version of equation (2.21) obtained by establishing the relationship between pressure drop produced by the cylinder drag, and then noting that the drag coefficient is approximately 1 for typical values of the Reynolds number is shown below (2.22). This equation can be used for arrays of tubes.

$$P_{\text{rms,max}} = 12.5 \left( \frac{U}{c_o} \right) \Delta p_{\text{drop}} \quad (2.22)$$

The range of conditions for which these equations are expected to be the most accurate are:

$$\begin{aligned} 0.02 < M < 0.5 \\ 5 < \Delta p_{\text{drop}} < 50 \text{ (in H}_2\text{O)} \\ \text{and } 2000 < \text{Re} < 300000 \end{aligned}$$

Work by Ziada et al. 1989a shows how the acoustic resonance develops as a function of Reynolds number. The Reynolds number seems to be very important in establishing the strength of the resonance, and, if a resonance is not established, the maximum sound pressure level at the condition of frequency coincidence. This they believe is due to "the higher level of fluctuating energy associated with the flow periodicity at higher Reynolds number." The higher the Reynolds number at the coincidence condition, the clearer the resonance and the higher the resonant acoustic pressure. According to Blevins and Bressler 1993, however, the Reynolds number is a secondary parameter when compared to the influence of the Mach number and pressure drop. The results of Ziada et al. 1984, Ziada et al. 1989a and Fitzpatrick and Donaldson 1977 were compared by Blevins and Bressler 1993 to the results obtained using equation (2.22). Results from equation (2.22) follow closely the results obtained by Ziada et al. 1989a except for cases where the resonance was marginal. For marginal resonance cases the authors warn that equation (2.22) should only be used if the data is carefully scaled.

The strength of the acoustic resonance is very important since this will determine the relative magnitude of the noise generated by a given heat exchanger. In the case of plate evaporators used in automobiles estimation of how noisy a plate evaporator is could be more important than determining if a resonance will develop or not.

## 2.5 Conditions that affect an acoustic resonance in tube array heat exchangers

There are a number of factors that can affect an acoustic resonance. All of these factors must be related to the variables that play a role in the development of the resonance. As the research progressed in this field, several researchers started to test these effects. The purpose of this section is to present the results of these investigations.

### 2.5.1 Effect of tube array on the speed of sound.

The effect of the tubes on the speed of sound has been shown to be significant [Blevins 1986, Parker 1978]. The tube array reduces the speed of sound. This reduction was found to be dependent on the solidity ratio  $\sigma$  (volume occupied by tubes divided by volume of the duct). Parker 1978 determined the effective speed of sound to be in the range:

$$1 < \frac{c_{\text{eff}}}{c_o} < \frac{1}{\sqrt{1+s}} \quad (2.23)$$

Ziada et al. 1989a demonstrated that the effective speed of sound actually lies in this range and also showed the strong dependence of this effective speed of sound as a function of tube array depth to height ratio.

Tests performed for two different plate heat exchangers (one with an in-line type configuration and another one with a staggered type configuration) with different depth to height ratios apparently showed mixed behavior [Rodarte et al. 1998a]. One seemed to follow more closely predictions using the effective speed of sound while the other was better predicted when using the regular speed of sound estimate for the gas.

### 2.5.2 Effects of number of rows

Blevins and Bressler 1993 showed the effect that increasing the number of rows has on the pressure drop and on the magnitude of the acoustic pressure level. They tested an in-line array with  $L/D = T/D = 2$  with 15, 8, 4, 2 and 1 tube rows. They noticed that "as the number of rows increased, the onset of resonance commences earlier and the intensity of the resonance increases." The single row of tubes did not produce an audible tone at the first acoustic mode.

Fitzpatrick and Donaldson 1977, 1980 tested several arrays and reported results as a function of number of rows. They found most of the differences in the critical Reynolds number and acoustic Strouhal numbers for any given array were more pronounced for arrays with less than 10 rows. Arrays with more than 10 rows showed a more stable behavior. For these arrays, the critical Reynolds number and acoustic Strouhal number was approximately constant.

The number of rows is also directly related to the depth of an array (see Figure 2.2). As mentioned above, Ziada et al. 1989a have found that the speed of sound of a gas in an array is a function of the ratio of array depth to height.

### 2.5.3 The effect of tube pattern on sound pressure level

Blevins and Bressler 1993 performed a comparison between arrays of a given configuration but with different dimensions to determine if some particular array dimensions for each specific configuration are more likely to produce higher acoustic sound pressure levels. The different array configurations for which they performed tests include in-line square, in-line rectangular, and normal triangular arrays. They then developed maps of maximum sound pressure level for general in-line and staggered arrays. It is known that the magnitude of the resonance

strength is a function of other parameters like depth of an array, number of rows, pressure drop, etc., all of which are related and which affect the magnitude of the resonance as well as other factors like lock-in range etc. Acoustic damping is also believed to be a function of tube number and arrangement [Grotz and Arnold]. The sound pressure level maps are therefore only indicative of the development of resonances for the arrays tested by the authors.

#### 2.5.4 Effect of turbulence

Fitzpatrick and Donaldson 1977 mention the importance that broadband turbulence could have and suggest that any theory that addresses the acoustic resonance phenomena should include this effect.

Blevins and Bressler 1993 discuss the effect of turbulence in the flow upstream of the tube arrays. They found no noticeable differences when there is a turbulence screen upstream from the tube array than when the flow is smooth.

Ziada and Oengören 1993 determined that turbulence level plays a very important role in the flow instability mechanism present for in-line tube arrays with large tube spacings as discussed previously.

#### 2.5.5 Effect of tube roughness/fouling

Blevins and Bressler 1987 discuss tube surface roughness effects. Tube surface roughness increases the strength of the resonance and reduces the velocity at which resonance starts. The increase in the SPL at resonance is related to the increase in pressure drop for the arrays with rough tubes.

Apparently later Blevins 1994 found contradictory results for tube surface roughness. He found that "the buildup of dirt and soot in a tube bank has been associated with the reduction of resonant sound" [Blevins 1994]. The roughening of the tubes with sandpaper had no effect on a loud and persistent resonance [Blevins 1994]. Apparently Blevins believed that the buildup of dirt and soot increased the roughness of the tubes. It is our belief that the buildup of dirt and soot is more pronounced in the wakes of the cylinders, changing their shape to a more airfoil-like form. Tests of a stereolithography prototype of an array of airfoils presented by Rodarte et al. 1998b show that for this particular array there was no characteristic peak in the acoustic pressure spectra, and an acoustic resonance was never established.

#### 2.5.6 Effect of Reynolds number

The Reynolds number has an effect on the Strouhal number of single cylinders and banks of cylinders [Price et al.]. However the effect of the Reynolds number is not very pronounced and for a large Reynolds number range the Strouhal number can be considered constant.

Ziada et al. 1989a noticed that a tube array in which the Reynolds number was doubled by reducing the height of the duct walls produced a first mode acoustic resonance that was not excited for the same array before the reduction of wall height. Based on this, they recommend the use of the Reynolds number in any design criterion. They also noticed that for the arrays they tested the higher the critical Reynolds number, the higher the response and the clearer the resonance.

#### 2.5.7 Effect of Mach number and pressure drop

Blevins and Bressler 1993 show the importance of the Mach number in predicting the magnitude of the acoustic sound pressure. They develop a semiempirical relationship that relates the acoustic sound pressure to the Mach number times the pressure drop for resonant conditions.

The Mach number has also been used by Eisinger and Eisinger et al. as described in detail in section 2.3. They used the Mach number as an indicator of the energy of the fluid flowing through the heat exchanger. When the Mach number is multiplied by the pressure drop through the array, the result is a direct indicator of the energy that has been lost by the fluid when it passed through the array. This energy could be related to the energy of the flow periodicity/instability that triggers an acoustic resonance.

## 2.6 Factors that affect flow-induced noise generation produced by circular cylinders

Up to this point the literature review was focused on the work done for cylinder array heat exchangers. The modeling scheme that will be used in this work is based on the concept of a dipole sound source produced by the fluctuating forces generated by the flow of gases over a cylinder. In this section emphasis will be placed on understanding the factors that affect these fluctuating forces.

A single cylinder inside a rectangular duct is the most basic of structures that are relevant for the study of acoustic resonance produced by bluff bodies inside a rectangular cavity. Bluff bodies produce oscillating forces and pressures in directions normal and perpendicular to the flow. These flow oscillations have characteristic frequencies, which are related to the shedding of vortices in their wakes. The flow oscillations that are transverse to both the fluid flow and the axis of the cylinder are characterized by the fluctuating lift. Typically the fluctuating lift is much larger than the fluctuating drag (approx. 1 order of magnitude). These pressure pulsations, at the right conditions, can excite the acoustic natural frequencies of the cavity. There are several flow and geometric parameters that can affect the Strouhal number, vortex correlation length, and flow-induced forces and thus the flow-induced noise generation from circular cylinders. In this section the effects of these factors will be described.

The disturbances that have an effect on the flow phenomena around a single cylinder that is perpendicular to a uniform flow are shown in Figure 2.6.

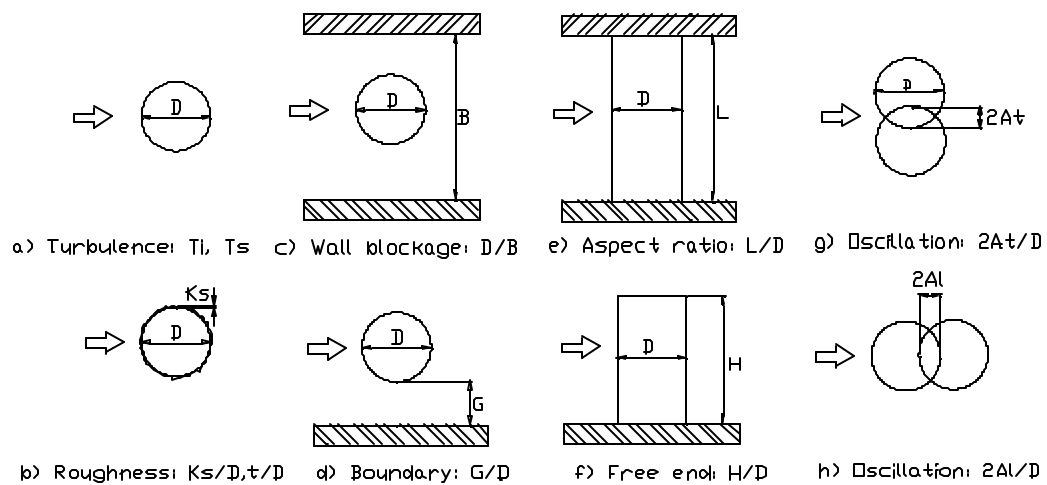


Figure 2.6 Typical disturbances encountered by a single cylinder perpendicular to uniform flow: a) turbulence, b) surface roughness, c) wall blockage, d) wall proximity, e) aspect ration, f) free end, g) transverse oscillations, and h) streamwise oscillations. [Zdravkovich 1997]

In the case of a single rigid cylinder in a rectangular duct the relevant disturbances are aspect ratio, wall blockage, cylinder roughness, flow turbulence, and proximity of cylinder to wall.

The flow behavior is very dependent on the Reynolds number. For a single cylinder there are three characteristic ranges of Reynolds number associated with particular types of flow behavior. Each of these ranges is further subdivided to specify more closely particular flow behavior. The following is a description of the ranges as presented by Zdravkovich 1997:

Range 1: Laminar flow, Laminar L,  $0 < Re_{up} < (180-200)$

L1: Nonseparating flow;  $0 < Re_{up} < 4$  to 5

L2: Steady separation or closed near-wake regime;  $4$  to  $5 < Re_{up} < 30$  to 48

L3: Periodic Laminar regime;  $30$  to  $48 < Re_{up} < 180$  to 200

Range 2: Subcritical flow, Transition-in-shear-layers TrSL,  $(350-400) < Re_{up} < (100-200k)$

TrSL1: Development of transition waves;  $(350-400) < Re_{up} < (1k-2k)$

TrSL2: Formation of transition eddies;  $(1k-2k) < Re_{up} < (20k-40k)$

TrSL3: Burst to turbulence;  $(20k-40k) < Re_{up} < (100k-200k)$

Range 3: Critical flow, Transition-in-boundary-layers TrBL,  $(100k-200k) < Re_{up} < (unknown)$

TrBL0: Precritical regime;  $(100k-200k) < Re_{up} < (300k-340k)$

TrBL1: One-bubble regime;  $(300k-3340k) < Re_{up} < (380k-400k)$

TrBL2: Two-bubble regime;  $(380k-400k) < Re_{up} < (0.5M-1M)$

TrBL3: Supercritical regime;  $(0.5M-1M) < Re_{up} < (3.4M-6M)$

TrBL4: Postcritical regime;  $(3.4M-6M) < Re_{up} < (unknown)$

The values of Reynolds numbers that we see in our tests are all in the subcritical flow regime more specifically in the TrSL2 and TrSL3 Reynolds number ranges.

### 2.6.1 Effect of aspect ratio

The most relevant references found about the effects of aspect ratio on vortex shedding from a cylinder are by Szepessy 1993 and Szepessy and Bearman 1992. In Szepessy and Bearman's tests were performed on single cylinders to which end plates were attached. The range of aspect ratios ( $L/D$ ) that they investigated was from 0.25 to 12, where  $L$  is the length of the cylinder between end plates and  $D$  is the cylinder diameter. They performed tests in the Reynolds number range from  $8k < Re_{up} < 140k$ . They found a very strong dependence of the fluctuating lift coefficient ( $C_L'$ ) on aspect ratio with values of  $C_L'$  at an aspect ratio of 1 almost twice those at large aspect ratios for a range of Reynolds numbers. The fluctuating lift coefficient also varied with Reynolds number for any given aspect ratio especially for aspect ratios of order 1.

Figure 2.7 has been taken directly from Szepessy and Bearman 1992. Figure 2.7 shows how the fluctuating lift changes significantly with aspect ratio and Reynolds number. The fluctuating lift is directly related to the vortex shedding strength. Figure 2.7 shows how the fluctuating lift increases as the end plate separation decreases (i.e., as the aspect ratio diminishes) especially for the higher Reynolds number trace until an aspect ratio of about 1. For smaller aspect ratios there is a decrease in the fluctuating lift coefficient that occurs at the two Reynolds numbers.



The authors attribute this decrease to the "probable significant interference from the boundary layers between the plates".

Figure 2.8 is a graph made with data taken from Szepessy and Bearman. Figure 2.8 shows the more pronounced variations in fluctuating lift present for different values of Reynolds number especially at aspect ratios around 1. The traces with dark symbols appear to follow a similar behavior. They are characterized by Reynolds number in the range of 40k-70k. At the low value of Reynolds number or at the near critical Reynolds number values the behavior changes and there is a sharp decrease in the fluctuating lift around aspect ratios of 1. Apparently there is a transition between 120k and 130k where a very large decrease in the lift coefficient for an L/D=1 was found.

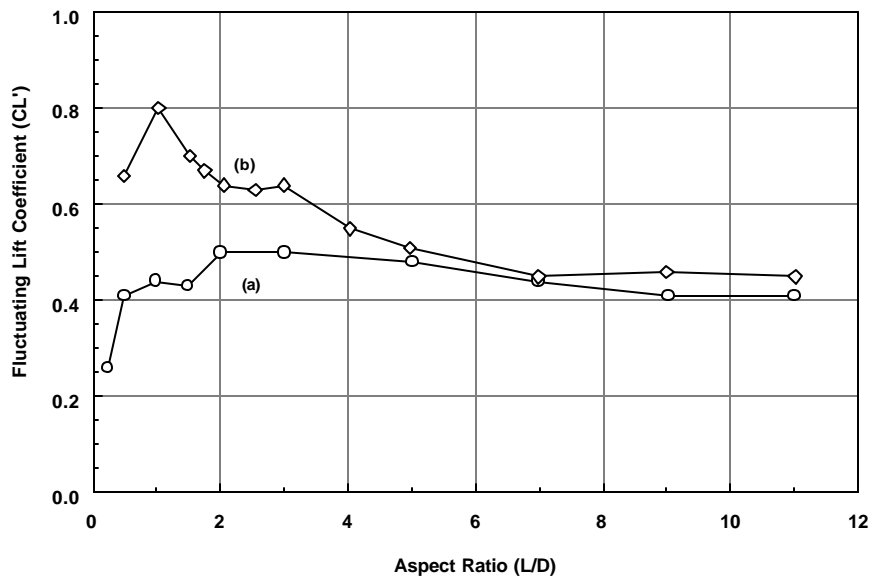


Figure 2.7 Fluctuating lift as a function of end plate separation. a)  $Re = 1.6 \times 10^4$  , b)  $Re = 4.3 \times 10^4$  . From Szepessy and Bearman 1992.

In Figure 2.9 the widely different fluctuating lift behaviors as a function of Reynolds number are shown for two aspect ratios representative of large and small aspect ratios behavior. For large aspect ratios the fluctuating lift is not as strong a function of the Reynolds number as for the small aspect ratios and only increases slightly as the Reynolds number increases. On the other hand, considerable variation in the fluctuating lift as a function of Reynolds number can be seen for an aspect ratio of 1.

With respect to shedding frequency Szepessy and Bearman 1992 report that there is a small shift in the shedding frequency for small aspect ratio cylinders compared to the shedding frequencies of large aspect ratio cylinders at values of Reynolds numbers where there is a significant variation in the fluctuating lift coefficient. For  $L/D = 1$  at  $Re_{up} = 45k$ , the Strouhal number is 0.17 versus 0.19 for a cylinder with  $L/D = 6.7$ . Also, it was noted that the spectral density peak was higher for the  $L/D = 1$  cylinder at the shedding frequency. The variation in fluctuating lift coefficient for these two cases are 0.75 and 0.5, respectively. For a Reynolds number of 13k the fluctuating lift coefficients are 0.41 and 0.42 for the large and small aspect ratio cylinders, respectively. In this case the Strouhal

number is 0.2 and is the same for the two cylinders. These results show a dependence between vortex strength and shedding frequency.

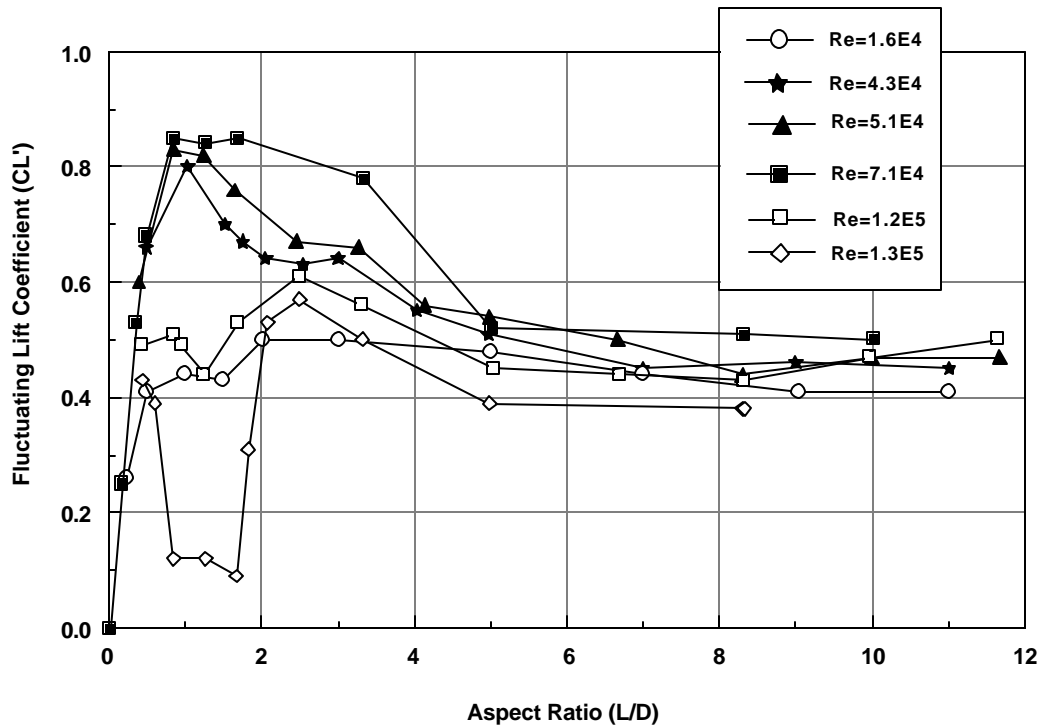


Figure 2.8 Fluctuating lift as a function of end plate separation for different values of Reynolds number. Plotted with data taken from Szepeszy and Bearman 1992.

Szepeszy and Bearman 1992 included results of the spanwise correlation of the vortex shedding for two cylinders with aspect ratios of 1.7 and 6.7. This part of the study was performed to investigate if the vortex shedding enhancement at low aspect ratios was due to a more two-dimensional flow for smaller aspect ratio cylinders. They investigated spanwise correlation by taking measurements between the pressure at the surface of the cylinder  $90^\circ$  from the forward stagnation point and a hot wire probe positioned at a distance of  $D/3$  on top of the cylinder. The pressure port was located at the midspan of the cylinder, while the hot wire probe was moved along the span. Figure 2.10 shows results of the cross-correlation between these two signals. It is shown that there is a better correlation for the smaller aspect ratio cylinder in the Reynolds number range where there is a larger fluctuating lift coefficient. The authors conclude that this is proof that the stronger vortex shedding also has enhanced spanwise correlation.

According to Kubo et al., end plates serve to maintain a two dimensional flow in the wake structure of two dimensional bluff bodies.

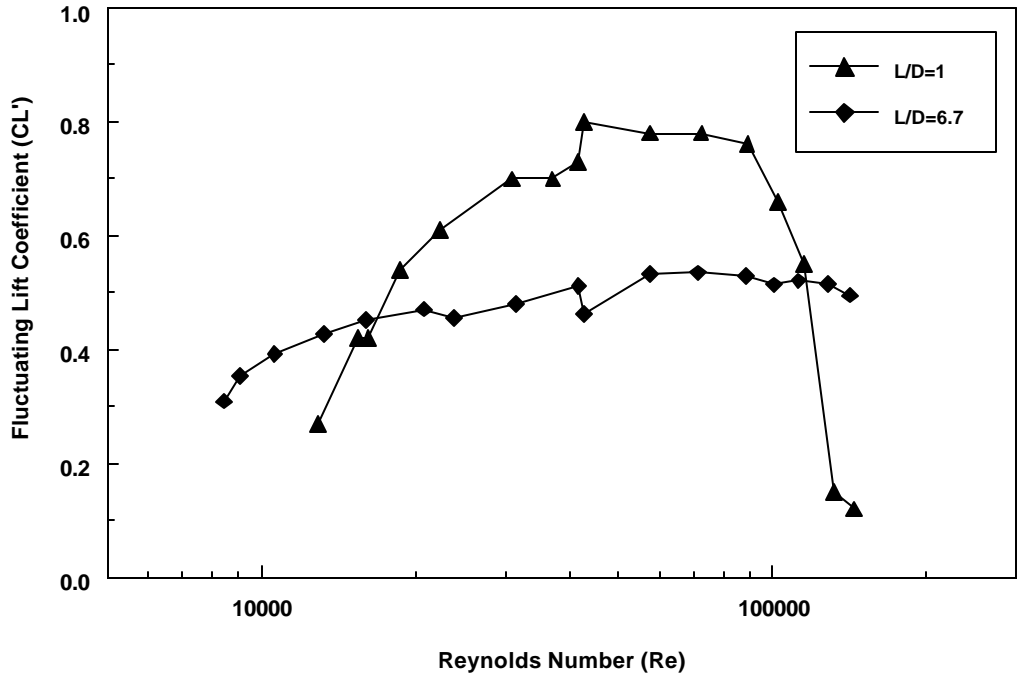


Figure 2.9 Fluctuating lift as a function of Reynolds number for aspect ratios of 1 and 6.7. From Szepessy and Bearman.

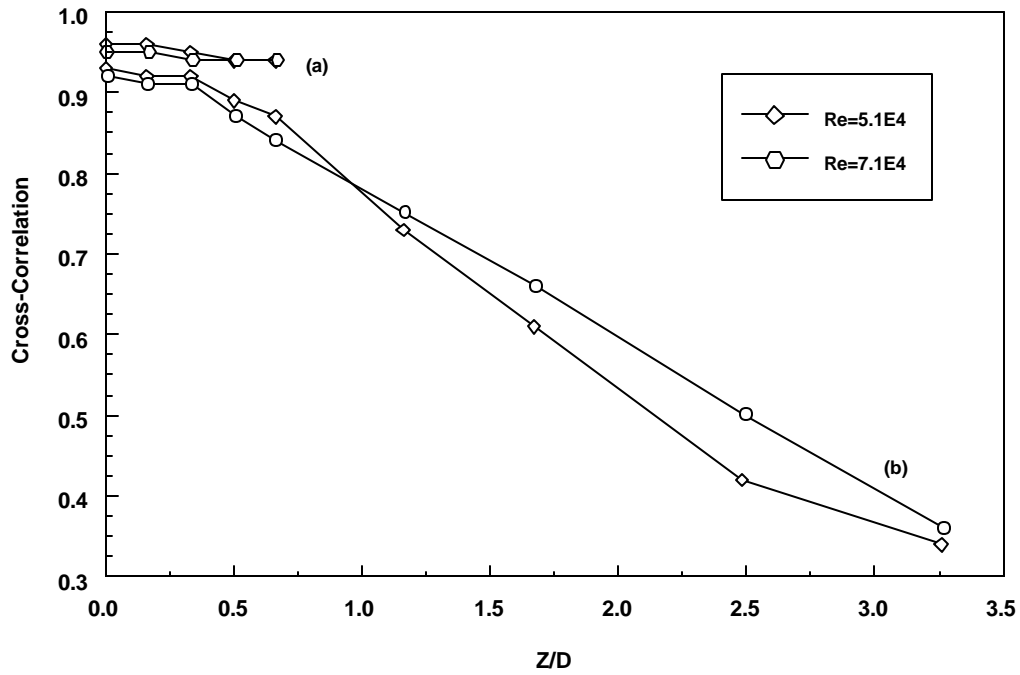


Figure 2.10 Cross-correlation of pressure and velocity measurements along the cylinder span. Curves (a) for  $L_{cyl}/D = 1.7$  (b) for  $L_{cyl}/D = 6.7$ . From Szepessy and Bearman.  $Z$  represents here cylinder length and  $D$  cylinder diameter.

Cox et al. cite some references that report the three-dimensionality of the circular cylinder wake and the spanwise correlation of vortex shedding which according to them occurs for  $L < 10D$ . Norberg mentions that the axial correlation is smaller than about 5 diameters for Reynolds number greater than 10k. Szepessy 1993 determined that the spanwise correlation length for a circular cylinder at the Reynolds number range of the order of about 10k is between 3 to 5 diameters. This is in sharp contrast to the spanwise correlation length of laminar shedding at  $Re_{up} < 160$  which is several hundred diameters long.

Stansby performed tests for the optimization of end plates attached to cylinders. He tested cylinders with aspect ratios of 16 and 8. Base pressure coefficients were measured. It was determined that with endplates that were 7D wide and 8D long in which the cylinder was placed as shown in Figure 2.11 a more two-dimensional flow was obtained than without the use of endplates. Also, the base pressure coefficient was reduced which, causes the drag to increase. These facts show that the test results obtained without endplates are not representative of two-dimensional flow.

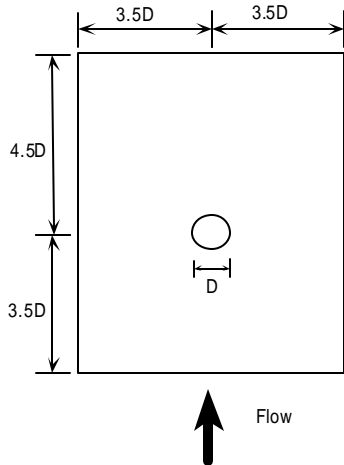


Figure 2.11 Stansby recommended circular cylinder endplate design to eliminate three-dimensional effects in tests with circular cylinders.

### 2.6.2 Horseshoe vortex effect on Strouhal vortex shedding

The introduction of endplates at the ends of the cylinder produces vortices attached to the base of the cylinder that are called horseshoe vortices. This type of vortex is called “horseshoe” because it forms starting from the forward stagnation point and goes around the cylinder until it separates from the cylinder in its wake without joining at the back, thus forming in the shape of a horseshoe. Szepessy 1993 reported results of tests aimed at determining the effect of aspect ratio and Reynolds numbers on the horseshoe vortices and its influence on the Strouhal vortices. He concluded with his investigation that the horseshoe vortex develops independently from the Strouhal vortex and depends only on aspect ratio for  $L/D < 1$ .

The effects of the horseshoe vortex on the Strouhal vortex is the really relevant and hard question. Szepessy 1993 addresses this problem by determining the strength of the horseshoe vortex and Strouhal vortex assuming potential flow and determining that the vortices are circular. He determined the ration of vortex circulation of the horseshoe vortex to the Strouhal vortex to be between 0.1 and 0.2. This implies that the horseshoe vortex has enough strength to affect the Strouhal vortex. However, he points out that since the axes of the Strouhal and

horseshoe vortices are perpendicular, the interaction between them should be weaker. Base pressure distribution tests for aspect ratios larger than 2 using different types of endplate designs with and without fully developed horseshoe vortices indicate that there is a very weak influence of the horseshoe vortex on the Strouhal vortex shedding at least for  $L/D > 2$ .

### 2.6.3 Turbulence effects

Turbulence has an effect on the flow behavior of cylinders. Most of the research performed on cylinders has been conducted in wind tunnels with very low turbulence levels. However, in real-world applications, turbulence can be significant, and therefore, turbulence effects should be considered.

Turbulence is characterized by two parameters: turbulence intensity ( $T_i$ ) and turbulence scale ( $T_s$ ). Turbulence intensity is defined as the ratio of the root mean square fluctuating velocity component in the streamwise direction to the average velocity in the same direction. Turbulence scale tries to give an average measure of the ever changing eddy sizes [Zdravkovich 1997].

The different flow behavior present on circular cylinders as a function of Reynolds numbers as tabulated in section 2.6 is influenced by turbulence. The initiation of the transitions between flow regimes is very sensitive to pressure gradients. While a negative pressure gradient delays transition a positive one promotes it at lower Reynolds numbers. Turbulence imposes both types of gradients and therefore has a significant effect on the transition between regimes.

For our particular case we are most interested in the TrSL2 and TrSL3 regimes (see section 2.6 for definition of flow regimes). It should be noted that turbulence effects are strongest in this regimes [Zdravkovich, 1990]. The effect of turbulence is to accelerate the transition between regimes by lowering the Reynolds number at which each regimes' characteristic phenomena develop [Blackburn and Melbourne]. For example, if the turbulence intensity is greater than 10%, the TrSL3 regime moves to  $10k < Re_{up} < 100k$ .

Turbulence also reduces the vortex formation length and spanwise correlation, and this causes a decrease in drag. The Strouhal number, on the other hand, remains almost constant since the wake width is not changed [Zdravkovich, 1990].

### 2.6.4 Surface roughness effects

Surface roughness is characterized by at least two parameters:  $K_s/D$  the relative size of roughness and its texture [Zdravkovich 1997]. Surface roughness has an insignificant effect in the laminar flow regimes for  $Re_{up} < 300$ . This is due to the thickness of the boundary layers that mask any surface imperfection of the cylinder. However, in the subcritical flow regimes surface roughness effects start to become noticeable. Surface roughness is not as influential in disturbing the flow as turbulence. This is because turbulence affects the boundary and free-shear layers directly while surface roughness affects only the boundary layer directly and the free-shear layer indirectly by the effects of the boundary layer. The most influential regime for surface roughness effects is in the TrBL states (see section 2.6) where surface roughness creates local turbulence and lowers the Reynolds number into the precritical regime. This effect reduces drag and is used to reduce drag on golf balls by dimpling their surface.

Figure 2.12 taken from Alemdaroglu et al. shows how an increase in the relative surface roughness lowers the transition to the critical regime.

Surface roughness also has an effect on the Strouhal number of vortex shedding from cylinders. Achenback and Heinecke measured the Strouhal number produced by cylinders of different relative surface roughness. Their work showed that increasing the surface roughness helps maintain a more stable behavior in the Strouhal number as it passed through the critical regime. Figure 2.13 shows their results.

#### 2.6.5 Wall blockage and boundary proximity effects

The walls of wind and water tunnels restrict the flow sideways and impose an additional pressure gradient [Zdravkovich 1997]. If the wall blockage is large, the transition in both the boundary and free shear layers may be affected.

The vicinity of a wall to the cylinders produces a kind of asymmetric blockage that may become a governing parameter for small  $G/D$  ratios (see Figure 2.6) [Zdravkovich 1997].

Richter and Naudascher studied the effect of blockage on different parameters of importance related to flow around circular cylinders, including Strouhal number and fluctuating lift coefficient. They tested a cylinder with aspect ratio of 8.6 and relative surface roughness of 0.0008 (which could be considered smooth). The tests were performed in a wind tunnel with a reported turbulence intensity of 0.5%.

Figure 2.14 shows the behavior of the Strouhal number found by these researchers around the critical Reynolds number regime. The Strouhal number according to their results increases with an increase in the blockage ratio both in the subcritical and transcritical regimes.

Figure 2.15 shows the behavior of the fluctuating lift coefficient as a function of Reynolds number for different blockage ratios. Richter and Naudascher report that the fluctuating lift increases slightly with Reynolds number until an abrupt transition that marks the transition to the transcritical regime. Blockage values greater than approximately  $1/6$  have a very significant influence in the magnitude of the fluctuating lift coefficient as can be seen in Figure 2.15.

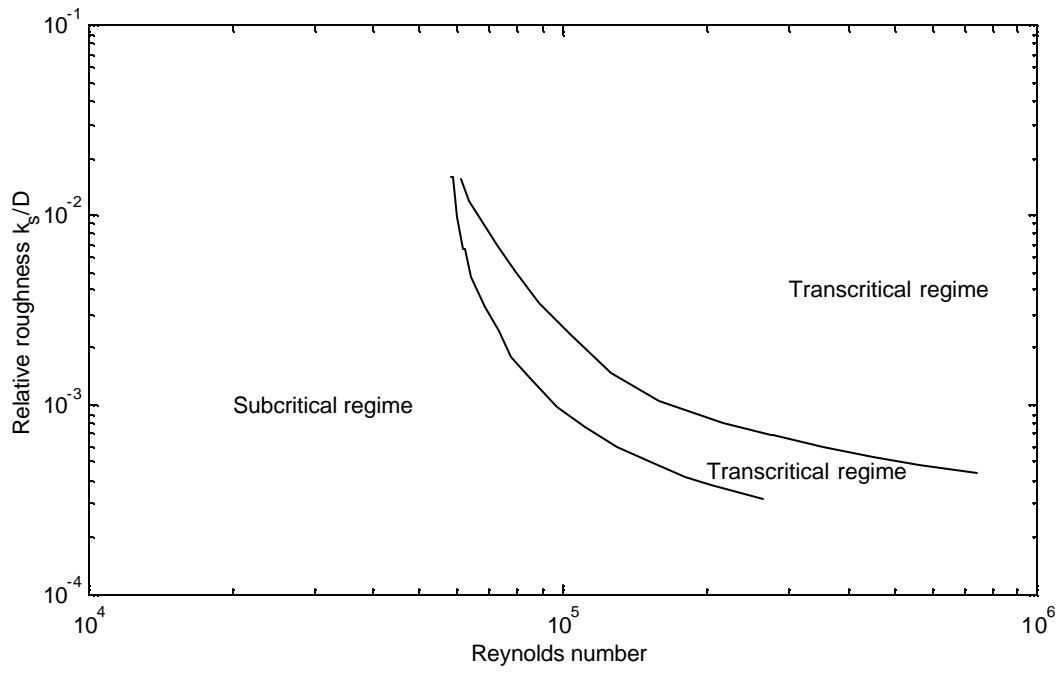


Figure 2.12 Effect of surface roughness on circular cylinders. From Alemdaroglu et al.

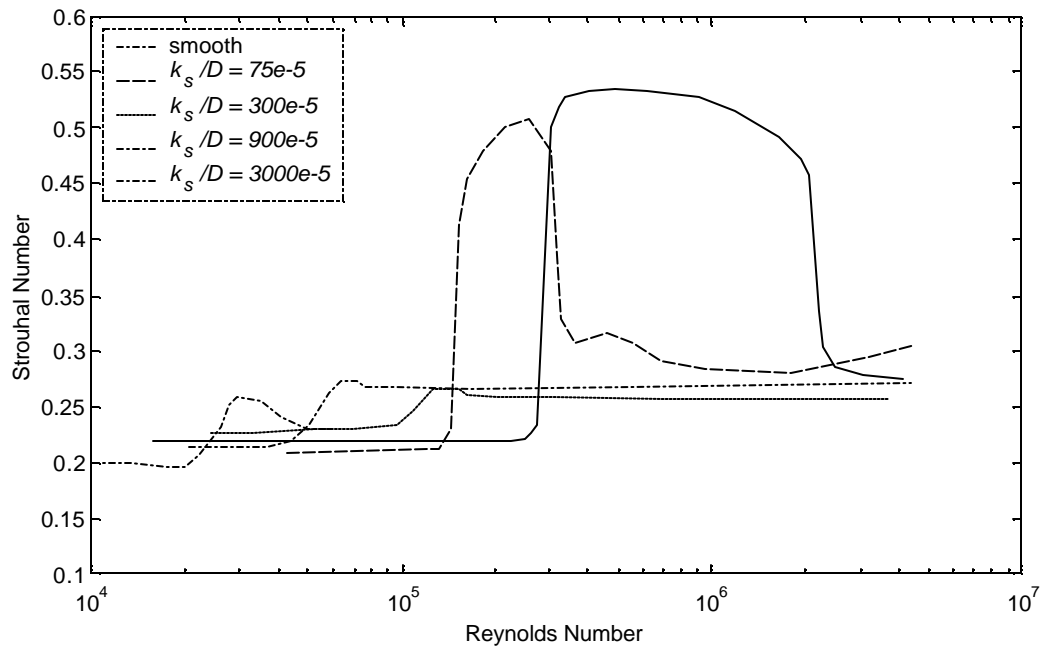


Figure 2.13 Surface roughness effects on Strouhal number from circular cylinders. From Achenbach and Heinecke.

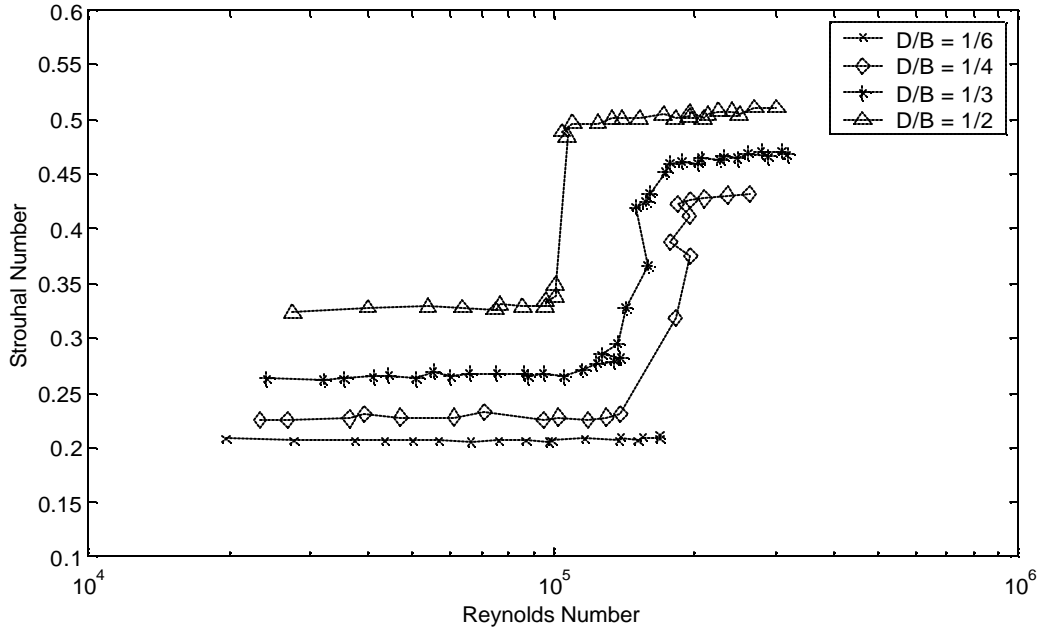


Figure 2.14 Blockage effects on Strouhal number from circular cylinders. From Richter and Naudascher. B and D defined in Figure 2.6.

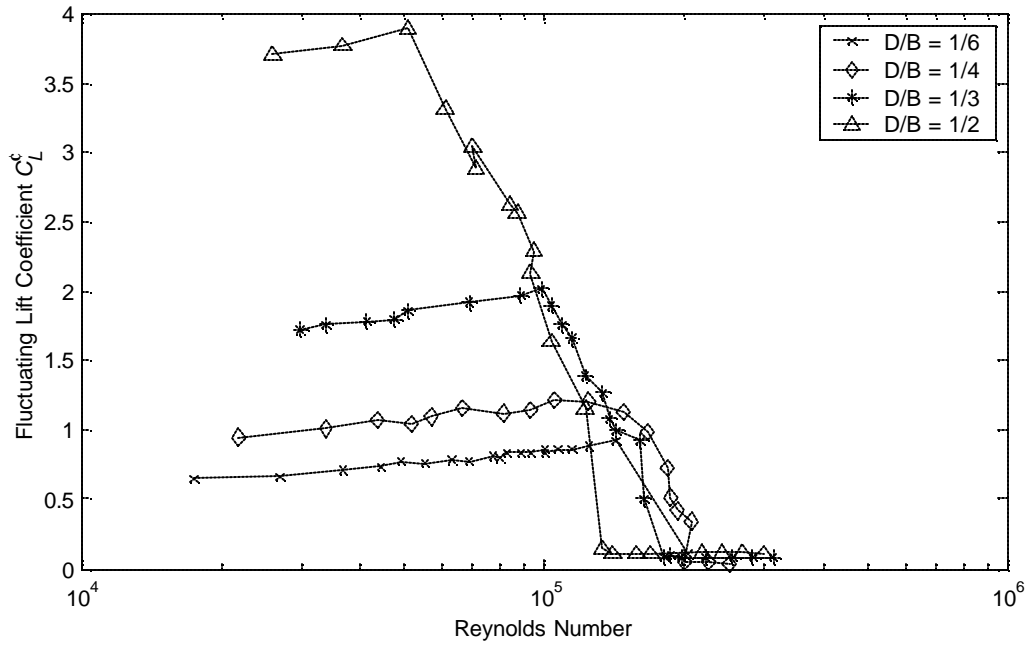


Figure 2.15 Blockage effects on fluctuating lift coefficient from circular cylinders. From Richter and Naudascher. B and D defined in Figure 2.6.



## **Chapter 3: Modeling Flow-Induced Noise of Circular Cylinders Subject to Cross Flow Inside a Rectangular Duct**

### **3.1 Introduction**

The formulation of a model of the tonal noise produced by a cylinder in cross flow both in free field and inside a rectangular cavity will be presented in this Chapter. This tonal component of the noise is associated with the vortex shedding process. Vortex shedding produces fluctuating forces on a cylinder in both the drag and lift directions. Of these forces the dominant force is the one in the lift direction which is approximately an order of magnitude larger than the force in the drag direction in the sub-critical Reynolds number range. These fluctuating forces on a rigid cylinder create the pressure fluctuations that produce the flow-induced sound.

### **3.2 Dipole sound from cylinders in a free field**

The free field noise characteristics of cylinders subject to cross-flows have been studied by many researchers [Blake 1986, Etkin et al. 1957, Gerrard 1955, Grosche 1985, Holle 1938, Keefe 1961, 1962, Koopman 1969, Leehey and Hanson 1971, Phillips 1956, Rayleigh 1915, Richardson 1923,1958, Stowell and Deming 1965,1936, and Strouhal 1878]. The work reported was empirical until the landmark papers by Lighthill in the fifties that established the foundations of aeroacoustics, or more generally, noise generation by fluid flow. Lighthill's papers were concerned with the sound field generated by the unsteady fluid motion of an unbounded fluid. Curle extended Lighthill's work by considering the noise produced by the flow when solid boundaries were present. He showed that when solid boundaries are present, Lighthill's solution should include other terms associated with the noise produced by the effect of the surfaces. Ffowcs-Williams and Hawkings later generalized Lighthill's and Curle's results by including convective effects and surfaces in arbitrary motion. These results, especially those of Curle, were extended by Phillips, who reduced Curle's expression to account only for the noise generated by the fluctuating fluid forces produced by the cylinder. Fluctuating fluid forces create dipole sound sources. This fact was demonstrated experimentally using cylinders by Stowell and Deming, and Gerrard 1955. Stowell and Deming, and Gerrard 1955 measured the characteristic directionality produced by acoustic dipoles from cylinders. Dipole sources of sound are more effective sound radiators than quadrupole sources of sound at lower Mach numbers [see for example Blake]. This means that sound emissions from cylinders can be estimated at lower Mach numbers by measuring only the fluctuating forces. This fundamental theory has been shown to predict the noise from cylinders relatively well ( $\pm 3$  dB). Noise from cylinders therefore can be modeled as an acoustic dipole with source strength dependent on the flow-induced forces imparted on the cylinder.

The periodic vortex shedding that occurs for a very large range of flow conditions causes these fluctuating forces. Fluctuating forces on cylinders have been extensively measured for single cylinders. However, there is significant scatter in the data. Fluctuating forces on cylinders are affected by aspect ratio, surface roughness, flow turbulence, wall blockage, cylinder movement or vibration, boundary proximity, and tube termination [Achenbach 1971, Achenbach and Heinecke 1981, Bishop and Hassan 1963a,b, Bruun and Davis 1975, Blackburn 1994, Blackburn and Melbourne 1996, Buresti 1981, Chen 1987, Duarte Ribeiro 1992, Gerrard 1961, Keefe 1961, 1962, Norberg and Sunden 1987, Schewe 1983, So and Savkar 1981, Szepessy 1994, Szepessy and Bearman 1992, and

Zdravkovich 1990, 1997]. In addition to these parameters, the vortex shedding will not be in phase along the tube axis if the aspect ratio is large. For cylinders inside a tube array the experimental data is very limited. Fluctuating forces produced on single cylinders inside tube arrays have been measured by Chen 1972b, Chen 1987, Oengören and Ziada 1998, and Savkar 1984.

When a source of sound is placed inside a duct, the duct walls reflect and absorb the acoustic waves that hit its surface. For this reason, the acoustic field of a sound source inside a duct is very different from that in unbounded space. The acoustic field inside the duct is composed of the acoustic free field plus the acoustic field created by the reflections. Sound reflections vary according to the duct wall's impedance. For very rigid walls, where the specific acoustic impedance can be considered very large, visco-thermal effects dominate the damping at the walls [Morse and Ingard]. For arrays of cylinders the sound scattering as well as the visco-thermal dissipation at the tube surfaces also play important roles [Howe].

Modeling the noise from cylinders in cross-flow is a very difficult task even for a single cylinder in a free field where the effects of the duct on the acoustic field and fluid mechanics are not present. Recently Cox et al. 1997, 1998 explored the ability of existing techniques to predict the tonal noise produced by cylinders over a wide range of Reynolds numbers. They used a Reynolds-averaged Navier-Stokes computational fluid mechanics technique to estimate the unsteady flow field. These results were then used with an acoustic solver based on the Ffowcs-Williams and Hawkings equations. They show that the two-dimensional formulation was not able to predict Strouhal number, drag, and the fluctuating lift coefficient accurately for Reynolds number larger than 200. Preliminary results for a single three-dimensional case with a Reynolds number of 1000 showed improvements in the estimations. These results, when used with the acoustic solver caused significant errors in both the tone frequency and amplitude.

Vortex shedding is affected by sound [Blevins 1985, Ffowcs-Williams and Zhao, Peterka and Richardson]. The sound can be externally introduced or can be the result of the reflections of the sound produced by the cylinder in the duct. Fluid-acoustic coupling effects can significantly change the sound generation and attenuation characteristics of bluff bodies inside a duct as demonstrated by Stoneman et al.

If the cylinder is not rigid, two different complications arise. First, cylinder vibration affects the vortex shedding process [Bishop and Hassan 1963b, Leehey and Hanson]. Second, an additional contribution due to the sound from moving surfaces needs to be considered. For more than one cylinder and cylinder arrays, the vortex shedding from upstream cylinders hitting cylinders downstream can also influence the vortex shedding process [Morse and Ingard].

Measurements of sound pressure levels produced by single cylinders and cylinder arrays inside a rectangular duct have been reported by many researchers [Barrington, Baylac et al., Blevins and Bressler 1987a, 1993, Chen 1968, Eisenger et al. 1996, Nemoto and Yamada 1992, Oengören and Ziada 1992, Xia 1986, Ziada and Oengören 1992, 1993]. However, the work focused on measurements taken only at resonance conditions and made no attempt to measure or model the acoustic field or to account for the effects of the duct walls.

### 3.3 Aeroacoustic theory for the prediction of the sound from a small aspect ratio circular cylinder subject to cross flow in unbounded space

Lighthill's groundbreaking work in 1952 established the foundations of aeroacoustics. His approach is unique in the sense that he considers that a region of the flow generates the sound that propagates in the adjacent fluid. Lighthill's inhomogeneous wave equation is derived from the continuity and momentum conservation equations. Lighthill's original work neglected the effect of rigid surfaces on the flow. Curle and later Ffwoos-Williams and Hawings generalized Lighthill's work to include surfaces effects. These theoretical developments were used for the first time by Phillips and apparently simultaneously by Etkin et al. to treat the noise from cylinders in cross flow.

In this section starting from the derivation of the Lighthill equation and using Curle's solution and Phillips' source separation technique the relations that permit the calculation of the noise produced by fully correlated vortex shedding from rigid cylinders in cross flows will be developed.

Starting with the conservation equations:

Continuity equation:

$$\frac{\partial \mathbf{r}}{\partial t} + \frac{\partial(\mathbf{r} v_j)}{\partial x_j} = 0 \quad (3.1)$$

Momentum Equation:

$$\mathbf{r} \left( \frac{\partial v_i}{\partial t} + v_j \frac{\partial v_i}{\partial x_j} \right) = -\frac{\partial p}{\partial x_i} + \frac{\partial e_{ij}}{\partial x_j} \quad (3.2)$$

Where:

$$e_{ij} = \mathbf{m} \left( \frac{\partial v_i}{\partial t} + \frac{\partial v_j}{\partial x_i} - \frac{2}{3} \delta_{ij} \frac{\partial v_k}{\partial x_k} \right) \quad (3.3)$$

In (3.2) the term  $e_{ij}$  is the viscous stress tensor. Equation (3.1) and (3.2) can be combined by multiplying (3.1) by  $v_i$ , adding the result to (3.2). This is expressed as

$$v_i \frac{\partial \mathbf{r}}{\partial t} + \mathbf{r} \frac{\partial v_i}{\partial t} + v_i \frac{\partial(\mathbf{r} v_j)}{\partial x_j} + \mathbf{r} v_j \frac{\partial v_i}{\partial x_j} = -\frac{\partial p}{\partial x_i} + \frac{\partial e_{ij}}{\partial x_j} \quad (3.4)$$

and combining derivatives

$$\frac{\partial(\mathbf{r} v_i)}{\partial t} + \frac{\partial(\mathbf{r} v_j v_i)}{\partial x_j} = -\frac{\partial p}{\partial x_i} + \frac{\partial e_{ij}}{\partial x_j} \quad (3.5)$$

Equation (3.5) can be rearranged as

$$\frac{\partial(\mathbf{r} v_i)}{\partial t} = - \frac{\partial(\mathbf{r} v_j v_i + \partial_{ij} p - \mathbf{e}_{ij})}{\partial x_j} \quad (3.6)$$

If we add and subtract the term  $c_o^2 \frac{\partial \rho}{\partial x_i}$ , equation (3.6) becomes

$$\frac{\partial(\mathbf{r} v_i)}{\partial t} + c_o^2 \frac{\partial \mathbf{r}}{\partial x_i} = - \frac{\partial T_{ij}}{\partial x_j} \quad (3.7)$$

where

$$T_{ij} = \mathbf{r} v_j v_i + \partial_{ij} \left\{ (\rho - \rho_o) - c_o^2 (\mathbf{r} - \mathbf{r}_o) \right\} - \mathbf{e}_{ij} \quad (3.8)$$

$T_{ij}$  is known as the Lighthill turbulence stress tensor. The terms  $\rho - \rho_o$  and  $\mathbf{r} - \mathbf{r}_o$  are introduced in (3.8) to represent the acoustic pressure and density. Differentiation of equation (3.1) with respect to time and subtraction of equation (3.7) after taking the divergence lead us to the nonhomogenous wave equation known as Lighthill's equation:

$$\frac{\partial^2 \mathbf{r}}{\partial t^2} + \frac{\partial^2(\mathbf{r} v_j)}{\partial t \partial x_j} - \nabla \frac{\partial(\mathbf{r} v_i)}{\partial t} - \nabla \cdot c_o^2 \frac{\partial \mathbf{r}}{\partial x_i} = \nabla \cdot \frac{\partial T_{ij}}{\partial x_j} \quad (3.9)$$

And simplifying (3.9) leads to Lighthill's equation.

$$\frac{\partial^2 \mathbf{r}}{\partial t^2} - c_o^2 \nabla^2 \mathbf{r} = \frac{\partial^2 T_{ij}}{\partial x_i \partial x_j} \quad (3.10)$$

Another derivation of equation (3.10) for the case where viscosity is neglected and where isentropic conditions are assumed follows. In this case the continuity and momentum equations are modified to:

Continuity equation:

$$\frac{\partial \mathbf{r}}{\partial t} + \mathbf{r}_o \nabla \cdot \mathbf{v} = 0 \quad (3.11)$$

Momentum equation:

$$\mathbf{r}_o \frac{\partial \mathbf{v}}{\partial t} + \nabla p + \frac{\partial}{\partial x_j} (\mathbf{r}_o v_i v_j) = 0 \quad (3.12)$$

In addition to these equations, the relationships between acoustic pressure and acoustic density is obtained by a Taylor series expansion of the pressure relation  $p = p(\rho, s)$  for an isentropic process [Pierce]:

$$p = \left( \frac{\partial p}{\partial \mathbf{r}} \right)_{s=s_o} \mathbf{r} + \frac{1}{2} \left( \frac{\partial^2 p}{\partial \mathbf{r}^2} \right)_{s=s_o} \mathbf{r}^2 + \dots \quad (3.13)$$

If this series is limited to linear terms, then

$$\mathbf{p} = \left( \frac{\partial \mathbf{p}}{\partial \mathbf{r}} \right)_{\mathbf{s}=\mathbf{s}_o} \mathbf{r} \quad (3.14)$$

where:

$$\left( \frac{\partial \mathbf{p}}{\partial \mathbf{r}} \right)_{\mathbf{s}=\mathbf{s}_o} = \mathbf{c}_o^2$$

By taking the time derivative of (3.11) and noting that  $\nabla \cdot (\rho_o \partial \mathbf{v} / \partial t) = \rho_o \partial (\nabla \cdot \mathbf{v}) / \partial t$

$$\frac{\partial^2 \mathbf{r}}{\partial t^2} + \nabla \cdot \left( \mathbf{r}_o \frac{\partial \mathbf{v}}{\partial t} \right) = 0 \quad (3.15)$$

from (3.12)

$$\mathbf{r}_o \frac{\partial \mathbf{v}}{\partial t} = -\nabla \mathbf{p} - \frac{\partial}{\partial x_j} (\mathbf{r}_o v_i v_j) \quad (3.16)$$

and substitution of (3.16) into (3.15):

$$\frac{\partial^2 \mathbf{r}}{\partial t^2} + \nabla \cdot \left( -\nabla \mathbf{p} - \frac{\partial}{\partial x_j} (\mathbf{r}_o v_i v_j) \right) = 0 \quad (3.17)$$

Equation (3.17) can be rearranged to (3.18) upon converting acoustic pressure to acoustic density using (3.14):

$$\frac{\partial^2 \mathbf{r}}{\partial t^2} - \mathbf{c}_o^2 \nabla^2 \mathbf{r} = \frac{\partial^2 \mathbf{T}_{ij}}{\partial x_i \partial x_j} \quad (3.18)$$

where

$$\mathbf{T}_{ij} = \mathbf{r}_o v_i v_j$$

$\mathbf{T}_{ij}$  is called the Lighthill stress tensor. The particular case presented here covers conditions for constant entropy throughout the fluid and neglects the effects of viscosity.

Equation (3.18) is the nonhomogenous wave equation. The term on the right is the source term. The solution for this equation is expressed in (3.19). This solution has been taken from Curle's paper, who himself took it from Stratton.

$$\mathbf{r} = \frac{1}{4\mathbf{p} \mathbf{c}_o^2} \int_V \frac{\partial^2 \mathbf{T}_{ij}}{\partial y_i \partial y_j} \frac{dy}{|\mathbf{x} - \mathbf{y}|} + \frac{1}{4\mathbf{p}} \int_S \left\{ \frac{1}{r} \frac{\partial \mathbf{r}}{\partial n} + \frac{1}{r^2} \frac{\partial r}{\partial n} \mathbf{r} + \frac{1}{\mathbf{c}_o r} \frac{\partial r}{\partial n} \frac{\partial \mathbf{r}}{\partial t} \right\} d\mathbf{S}(\mathbf{y}) \quad (3.19)$$

In the absence of surfaces, only the first term in equation (3.19) is important. This represents the noise due to turbulence in the flow. This solution was presented by Lighthill 1952 and is equivalent to a quadrupole source of

sound. Solid surfaces in contact with flowing fluids support fluctuating forces. This type of interaction can be represented by dipole sound sources which in many cases especially at low Mach numbers dominate. Another form of (3.19) presented by Curle is shown in (3.20).

$$\mathbf{r} = \frac{1}{4\rho c_o^2} \frac{\partial^2}{\partial x_i \partial x_j} \int_V \frac{T_{ij}\left(y, t - \frac{r}{c_o}\right) dy}{r} - \frac{1}{4\rho c_o^2} \frac{\partial}{\partial x_i} \int_S \frac{P_i\left(y, t - \frac{r}{c_o}\right)}{r} dS(y) \quad (3.20)$$

There are three different sound contributors that equation (3.20) should take into account. The first contributor is due to the unsteadiness in the fluid and was shown by Lighthill to be equivalent to quadrupole sound sources distributed through the fluid. The other two contributions come from the interaction of the flow with solid boundaries. The first one is due to the fluctuating stresses' action on the boundary. In the case of a bluff body, this represents the fluctuating forces created such as fluctuating components of the lift and drag. The final contribution is that due to the movement of the solid boundary. Phillips modified Curle's equation (3.20) so that these three contributions could be considered independently. The modified version of the solution of equation (3.18) as presented by Phillips is shown in equation (3.21).

$$\mathbf{r} = \frac{1}{4\rho c_o^2} \frac{\partial^2}{\partial x_i \partial x_j} \int_V \frac{1}{r} T_{ij}(y) dV(y) + \frac{1}{4\rho c_o^2} \frac{\partial}{\partial x_i} \int_S \frac{1}{r} (\mathbf{r}_o v_i v_j + p_{ij}) dS(y) - \frac{1}{4\rho c_o^2} \int_S \frac{\partial(\mathbf{r} v_i)}{\partial t} dS(y) \quad (3.21)$$

This equation when applied to the neighborhood of a closed solid surface is approximated by

$$\mathbf{r} \approx \frac{1}{4\rho c_o^4} \frac{x_i x_j}{|x|^3} \int_V \frac{\partial^2}{\partial t^2} T_{ij} dV(y) + \frac{1}{4\rho c_o^3} \frac{x_i}{|x|^2} \int_S \frac{\partial}{\partial t} (\mathbf{r}_o v_i v_j + p_{ij}) dS(y) - \frac{1}{4\rho c_o^2} \frac{\mathbf{r}_o}{|x|} \int_S \frac{\partial(v_i)}{\partial t} dS(y) \quad (3.22)$$

The terms on the right-hand of equation (3.22) can be interpreted physically as follows [Curle 1968]:

1. The term  $T_{ij}$  represent Lighthill's stress tensor which produces quadrupole sources.
2. The term  $\rho_o v_i v_j$ , which is zero for rigid solids, is of dipole type. This term represents the momentum imparted to the nearby fluid by a normal moving boundary.
3.  $P_{ij}$  represents the fluctuating pressure that when integrated around the solid is equivalent to a fluctuating force. This term is therefore of a dipole nature.
4. The term  $\rho_o \partial v_i / \partial t$  represent the monopole sources. This term is also zero when there is no boundary movement. This term represent displacement of fluid by the boundary movement.

Further simplifications to (3.22) are made when assuming a fixed solid boundary. If this is the case, equation (3.22) reduces to

$$\mathbf{r} \approx \frac{1}{4\rho c^4} \frac{x_i x_j}{|x|^3} \int_V \frac{\partial^2}{\partial t^2} T_{ij} dV(y) + \frac{1}{4\rho c^3} \frac{x_i}{|x|^2} \frac{\partial}{\partial t} \int_S p_{ij} dS(y) \quad (3.23)$$

In equation (3.23) the first term represents the noise produced by the flow in the absence of solid surfaces. This term is important for high flow velocities. The noise produced by the solid rigid surface reduces to:

$$\mathbf{r} \approx -\frac{1}{4\rho c_0^3} \frac{x_i}{|\mathbf{x}|^2} \frac{\partial F_i}{\partial t} \quad (3.24)$$

where:

$$F_i = -\int_S p_{ij} dS(y)$$

Equation (3.24) is the equation of relevance for the production of sound by the fluctuating components of the forces generated by the flow on a circular cylinder. This equation will now be applied to obtain a general solution for the noise generated by a cylinder at the vortex shedding frequency.

First an expression for the fluctuating force  $F_i$  for a circular cylinder must be determined. This is obtained from the definition of the fluctuating coefficient of lift

$$C_L = \frac{F_L}{\frac{1}{2} \rho U^2 D L} \quad (3.25)$$

or

$$|F_L| = \frac{C_L \rho U^2 D L}{2} \quad (3.26)$$

Equation (3.26) represents the magnitude of the fluctuating force. The sinusoidal variation of this force is represented by equation (3.27).

$$F_L = \frac{C_L \rho U^2 D L}{2} e^{i(\omega t - \phi(z,t))} \quad (3.27)$$

In equation (3.27),  $\phi(z,t)$  represents the phase angle that must be considered when the cylinder aspect ratio is large enough that the vortex shedding is not in phase along the length of the cylinder. For aspect ratios smaller than 3-5 in the Reynolds number range of interest (see section 2.6) the vortex shedding is in phase and  $\phi(z,t) = 0$ . Substitution of equation (3.27) into equation (3.24):

$$\mathbf{r} \approx -\frac{1}{4\rho c_0^3} \frac{x_i}{|\mathbf{x}|^2} \frac{\partial}{\partial t} \frac{C_L \rho U^2 D L}{2} e^{i\omega t} = -\frac{i x_i C_L \rho U^2 D L \omega}{8\rho c_0^3 |\mathbf{x}|^2} \quad (3.28)$$

The mean square acoustic density is equivalent to the square of equation (3.28). This equation can be further simplified by the introduction of the Strouhal number definition  $S = fD/U$  or  $S = \omega \cdot D / (2 \cdot \pi \cdot U)$  and noting that  $|\mathbf{x}| = r$ , and  $x_i = r \cos(\theta)$ .

$$r^2 \approx \frac{\cos^2(q) C_L^2 r_o^2 U^6 L^2 S_t^2}{16 c_o^6 r^2} \quad (3.29)$$

Other useful expressions can be obtained by converting (3.29) to acoustic pressure or intensity. The relations between acoustic pressure, density and intensity are

$$p = c_o^2 r, \quad I = \frac{p^2}{r_o c_o} \quad (3.30)$$

So, (3.29) can also be expressed as

$$p^2 \approx \frac{\cos^2(q) C_L^2 r_o^2 U^6 L^2 S_t^2}{16 c_o^2 r^2} \quad (3.31)$$

Equation (3.31) can also be expressed as a function of the fluctuating force magnitude (equation (3.26)) as

$$p^2 \approx \frac{|F_L|^2 f^2 \cos^2(q)}{4 c_o^2 r^2} \quad (3.32)$$

and

$$I \approx \frac{\cos^2(q) C_L^2 r_o U^6 L^2 S_t^2}{16 c_o^3 r^2} \quad (3.33)$$

Equation (3.32) shows the dependence of the sound generated by the cylinder in cross flow to the flow-induced fluctuating forces in the transverse direction. The dipole directionality of this sound source is introduced by the cosine factor.

### 3.4 Proposed Model

The previous sections described the work and developments made to establish the fundamental relations to estimate the sound produced by single cylinders in unbounded space. This work was based on using the dominant fluctuating lift dipole source produced by the cylinder in cross flow. The model proposed and evaluated in this study is based on using a point dipole source term to represent the noise produced by cylinders in cross flow. This source term will be introduced in the convected Helmholtz equation with appropriate boundary conditions to find expressions to determine the now bounded acoustic field. Although it is well known that the sound produced by cylinders in cross-flow can be modeled as a dipole sound source and the theory needed to model acoustic sources inside ducts or cavities is available, to our knowledge, this is the first time that an investigation of the correlation between measured sound pressure levels in a duct excited by one or more cylinders in cross flow and an acoustic model driven by dipole sources has been made.

#### 3.4.1 Advantages and disadvantages of proposed model

The acoustic model permits the separation of the complex fluid mechanics phenomena present as long as the fluid mechanics effects responsible for the generation of sound from cylinders can be measured, assumed, or



estimated. This “separation” of the fluid region responsible for the noise sources from the region, with no source and only acoustic propagation present, constitute the essence of the acoustic analogy approach first established by Lighthill in 1952 [Farassat].

This modeling approach accounts for the source strength and directionality, the effects of the walls in damping and reflections, and can be used to determine the full acoustic field. The dipole source strength is determined from the fluctuating flow-induced forces produced between the cylinder and the flow. These forces are a function of the flow parameters and the fluctuating lift coefficient, a coefficient that is typically determined by experiments. The dipole frequency can be determined from the Strouhal number, flow velocity, and diameter of the cylinder. Boundary conditions in the duct walls permit the introduction of damping through use of the acoustic wall impedance. In addition, a volumetric damping term was introduced in the convected wave equation as Cumpsty and Whitehead did in their study on resonances excited in a duct by plates in cross flow. In this work the analytical series solution was obtained.

The approach developed herein has the following advantages:

- A. The model accounts for source strength and system dynamics.
- B. The model can be used to solve for the acoustic field produced by a cylinder in cross-flow inside a duct. To model multiple cylinders, each individual solution is added throughout the domain to determine the final acoustic field.
- C. The model takes into account duct dimensions. Acoustic natural frequencies are dependent on duct dimensions. When a source frequency is close to an acoustic resonance the acoustic field is amplified.
- D. The model takes into account flow velocity. Flow velocity changes the speed at which a wave travels. This fact modifies the acoustic natural frequencies as well as wave propagation in the flow direction.
- E. The model can be used to solve for the acoustic pressure at one location in the duct without having to solve for the full acoustic field.
- F. The model is in a form that can incorporate acoustic damping.
- G. Numerical techniques could be used to solve for more complex geometries [Eversman and Steck 1984, Baumeister and Kreider 1996, and Mosher 1986a,b].
- H. It is often necessary to determine the maximum sound pressure level that occurs for a particular heat exchanger and condition of operation. The model could be used to estimate this upper limit and its location once the appropriate information is known. The model accounts for many factors and their interactions and thus could provide the basis to predict heat exchanger tonal noise problems.

However, there are also some disadvantages:

- A. The model assumes the knowledge of several parameters in advance of its application. It assumes that the fluctuating flow-induced forces, frequencies, and phases of the sources are known. This means knowledge of the fluctuating lift coefficient, vortex correlation length (for long cylinders), and the fluid mechanics that creates the fluctuating forces in cylinders in general. While fluctuating lift coefficients have been measured extensively for single cylinders in a wide range of conditions, there is

- a significant scatter in the data. For cylinders inside arrays, fewer measurements are available and only for limited conditions.
- B. The model does not account for flow-acoustic-structural interactions. Vortex shedding can be affected by the internal acoustics of the cavity or by cylinder vibrations. In our case of short rigid cylinders, only the fluid–acoustic interactions are believed to be important.
  - C. Once multiple sources are present, even if they generate tonal noise at the same frequency, the phases of each source relative to the others must be assumed. There is experimental proof that at resonance the cylinders inside an array shed vortices in phase [Ziada and Oengören 1992 and Oengören and Ziada 1992]. This condition could be used to determine the critical case using the model.
  - D. The model assumes a uniform velocity profile inside the channel. Flow velocity affects the acoustics of the channel. To account for its effects typically a uniform velocity profile is assumed [Eversman and Steck 1984, Eversman and Baumeister 1984, and Mosher 1986a,b]. This approximation predicts relatively well the shift of the transverse natural frequency of the duct as shown in Chapter 5.
  - E. The model does not account for broadband noise generated by turbulence.
  - F. The model in its current form can account for two forms of damping: 1) linear damping at the walls expressed as complex acoustic impedances, and 2) volumetric damping. However, it is not known if actual damping mechanisms can be represented in these ways. Additionally, damping at the walls in our analytic series solution assumes that the specific acoustic impedance is the same for opposing walls.
  - G. The model assumes that the cylinder/cylinders that produce the dipole sources do not affect the sound field. This assumption is expected to be more limiting for cylinder arrays.
  - H. In general all the restrictions of linear acoustics apply. That is, small acoustic pressures and densities in comparison to the mean values and ideal gas behavior.

It is believed that the proposed acoustic model can be used as a tool to further the understanding of the noise generated by flow over single or multiple cylinders inside a duct. This work presents the results of its evaluation.

In the next sections the derivation of the proposed acoustic model equations and solutions are presented.

### **3.5 Dipole sound inside rectangular ducts**

The sound produced by an acoustic source inside a duct or cavity creates a more complicated acoustic field than that created when the source emits in an unbounded region of constant acoustic impedance. The acoustic field created in the absence of reflecting walls produces what is known as an acoustic free-field. When a source of sound is placed inside a duct, the duct walls reflect and absorb the acoustic waves that hit its surface. For this reason, the acoustic field of a sound source inside a duct is very different from that in unbounded space. The acoustic field inside a duct depends on many factors such as 1) the source frequency, 2) source radiation pattern, 3) source position, 4) source strength, 5) walls acoustic impedance, and 6) size and shape of enclosure. All of these factors should be considered in a model to correctly estimate the acoustic field.

In this section a fundamentally based model to determine the acoustic field produced by a dipole inside a duct will be developed.

### 3.5.1 Modeling assumptions

To model the sound produced by a point dipole inside a duct with flow the inhomogeneous convected acoustic wave equation with a point dipole term should be used. This equation is derived from the mass and momentum conservation equations and the ideal gas equation of state once the following simplifying assumptions have been introduced.

- A. The fluid is a perfect gas.
- B. The fluid is inviscid.
- C. The fluid is non-heat conducting.
- D. The fluid is isotropic and homogeneous.
- E. No external body forces act on the fluid.
- F. The acoustic field is irrotational.
- G. Acoustic perturbations are small.
- H. An inertial coordinate systems is used.
- I. A uniform velocity profile is assumed.
- J. Constant velocity at any cross section of the duct is assumed.
- K. Known source strength, directionality and position is assumed.
- L. The cylinder does not disturb the acoustic field.

### 3.5.2 Derivation of inhomogeneous convected wave equation with a dipole source term

The conservation equations to which the above simplifying assumptions have been introduced are

$$\frac{D\mathbf{r}_t}{Dt^*} + \mathbf{r}_t \nabla \cdot \vec{V}_t = 0$$

$$\frac{D\vec{V}_t}{Dt^*} = F^*(t) d \left( \vec{x}^* - \vec{x}_s \right) - \frac{1}{\mathbf{r}_t} \nabla p_t \quad (3.34)$$

$$p_t = p_t(\mathbf{r}_t, s_o)$$

where

$$\frac{D}{Dt^*} = \left[ \frac{\partial}{\partial t^*} + \vec{V}_t \cdot \nabla \right] \quad \Rightarrow \text{for scalars} \quad (3.35)$$

$$\frac{D\vec{V}_t}{Dt^*} = \left[ \frac{\partial \vec{V}_t}{\partial t^*} + \nabla \frac{\vec{V}_t \cdot \vec{V}_t}{2} - \vec{V}_t \times (\nabla \times \vec{V}_t) \right] \quad \Rightarrow \text{for the velocity vector}$$

There are three main basic models of noise sources: monopoles, dipoles, and quadrupoles. Monopoles can be visualized as a pulsating sphere that has a surface that moves back and forth in a sinusoidal fashion. If the sphere radius is small a monopole acts like a pulsating mass source. For this reason, a monopole can be introduced in the conservation of mass equation. A dipole is defined as two monopoles separated a small distance that have the same strength and that oscillate 180 degrees out of phase with each other. This out of phase oscillation produces effectively a net fluctuating force. For this reason processes that create fluctuating forces in fluids such as vortex shedding from cylinders can be modeled as acoustic dipoles. The way to introduce an acoustic dipole is therefore through the momentum equations as shown in the middle equation presented in (3.34). A quadrupole consists of two dipoles separated a small distance and oscillating 180 degrees out of phase. There are lateral and longitudinal quadrupoles depending on how the two dipoles are oriented. The dominant sound produced by cylinders in cross flow can more closely be modeled as an acoustic dipole [Blake]. For this reason only dipole sources will be considered.

Acoustic disturbances can usually be regarded as small amplitude perturbations on top of an ambient state [Pierce]. The acoustic conservation equations are obtained when the acoustic perturbations are separated from the steady or ambient components. To separate the acoustic perturbations, the equations describing the steady and acoustic components are introduced in the conservation equations. These equations are

$$\begin{aligned} p_t &= p_o^* + p^* \\ \mathbf{r}_t &= \mathbf{r}_o^* + \mathbf{r}^* \\ \vec{V}_t &= \vec{V}_o^* + \vec{V}^* = (\vec{V}_o^*, 0, 0) + \vec{V}^* \end{aligned} \quad (3.36)$$

Where the \* represent dimensional quantities. The o represent steady component and the  $\rightarrow$  represents a vector quantity (see nomenclature). Introducing equation (3.36) to the conservation equations:

$$\frac{D(\mathbf{r}_o^* + \mathbf{r}^*)}{Dt^*} + (\mathbf{r}_o^* + \mathbf{r}^*) \nabla \cdot \left( \vec{V}_o^* + \vec{V}^* \right) = 0 \quad (3.37)$$

$$\frac{D \left( \vec{V}_o^* + \vec{V}^* \right)}{Dt^*} = \vec{F}^*(t) \mathbf{d} \left( \vec{x}^* - \vec{x}_s^* \right) - \frac{1}{(\mathbf{r}_o^* + \mathbf{r}^*)} \nabla (\rho_o^* + \rho^*)$$

Additionally, the relationship between the acoustic pressure and density can be obtained as shown by equations (3.13) and (3.14).

Using the linear or acoustic approximation in which second and higher order terms are neglected, the acoustic conservation equations in terms of dimensional variables take the form:

$$\frac{1}{\mathbf{r}_o^*} \frac{D\mathbf{r}^*}{Dt^*} + \nabla \cdot \vec{V}^* = 0$$

$$\frac{D\vec{V}^*}{Dt^*} = \vec{F}^*(t) \mathbf{d} \left( \vec{x}^* - \vec{x}_s^* \right) - \frac{1}{\mathbf{r}_o^*} \nabla \rho^* \quad (3.38)$$

$$\rho^* = c_o^2 \mathbf{r}^*$$

And for uniform flow in the x direction

$$\frac{1}{\mathbf{r}_o^*} \left[ \frac{\partial \mathbf{r}^*}{\partial t^*} + V_o^* \frac{\partial \mathbf{r}^*}{\partial x^*} \right] + \nabla \cdot \vec{V}^* = 0$$

$$\frac{\partial \vec{V}^*}{\partial t^*} + V_o^* \frac{\partial \vec{V}^*}{\partial x^*} = \vec{F}^*(t) \mathbf{d} \left( \vec{x}^* - \vec{x}_s^* \right) - \frac{1}{\mathbf{r}_o^*} \nabla \rho^* \quad (3.39)$$

$$\rho^* = c_o^2 \mathbf{r}^*$$

In equation (3.39)  $p^*$ ,  $\rho^*$ , and  $\vec{V}^*$  represent the dimensional acoustic pressure, acoustic density, and acoustic velocity and  $V_o^*$ ,  $\rho_o^*$ ,  $c_o$ , and  $\vec{F}^*$  are the dimensional uniform flow velocity in the x direction, fluid density, fluid speed of sound, and body force per unit of mass at point  $\vec{x}_s^*$ .

To obtain the convected wave equation from equations (3.39), first the operator presented in equations (3.35) is applied to the continuity equation. The momentum and equation of state are then substituted in the resulting equation. The convected wave equation is:

$$\nabla^2 p^* - \frac{1}{c_o^2} \frac{D^2 p^*}{Dt^{*2}} = r_o^* \nabla \cdot \left[ \vec{F}^*(t) \mathbf{d} \left( \vec{x}^* - \vec{x}_s^* \right) \right] \quad \text{or} \quad (3.40)$$

$$c_o^{*2} \nabla^2 p^* - \frac{\partial^2 p^*}{\partial t^{*2}} - 2V_o^* \frac{\partial^2 p^*}{\partial x^* \partial t^*} - V_o^{*2} \frac{\partial^2 p^*}{\partial x^{*2}} = c_o^{*2} r_o^* \nabla \cdot \left[ \vec{F}^*(t) \mathbf{d} \left( \vec{x}^* - \vec{x}_s^* \right) \right]$$

The dimensional inhomogeneous convected wave equation presented in (3.40) does not include damping terms. There are different possible damping mechanisms available that can modify the acoustic field produced by sources inside ducts. Acoustic damping can also be due to imperfect reflection when the duct walls have finite acoustic impedance. Acoustic damping due to boundary conditions will be treated later. Independently of the acoustic damping produced by the walls, there are other damping mechanisms. Some of these mechanisms are caused by flow phenomena such as turbulence and convection. Other are produced by thermo-viscous processes. For cylinder arrays damping could be the result of sound scattering or thermo-viscous processes at the cylinder walls [Howe]. The inclusion of a volumetric damping term in the inhomogeneous convected wave equation could be used to account for some of these damping processes. "If damping is small, the addition of a linear damping term gives a good approximation to the response of the actual system" [Cumpsty and Whitehead]. The addition of a damping term modifies equation (3.40) to

$$c_o^{*2} \nabla^2 p^* - \frac{\partial^2 p^*}{\partial t^{*2}} - Q \frac{\partial p^*}{\partial t^*} - 2V_o^* \frac{\partial^2 p^*}{\partial x^* \partial t^*} - V_o^{*2} \frac{\partial^2 p^*}{\partial x^{*2}} = c_o^{*2} r_o^* \nabla \cdot \left[ \vec{F}^*(t) \mathbf{d} \left( \vec{x}^* - \vec{x}_s^* \right) \right] \quad (3.41)$$

where Q represents the constant volumetric damping in the acoustic medium.

To nondimensionalize equation (3.41), the following list of relationships will be introduced:

$$\begin{aligned} p^* &= r_o c_o^2 p & r^* &= r_o r & \vec{V}^* &= c_o \vec{V} & V_o^* &= c_o M \\ t^* &= t \left( \frac{L_c}{c_o} \right) & \vec{F}^* &= \vec{F} \left( \frac{c_o^2}{L_c} \right) & & & & \\ x^* &= L_c x & y^* &= L_c y & z^* &= L_c z & & \end{aligned} \quad (3.42)$$

Introducing equations (3.42) to equation (3.41) transforms it to

$$\nabla^2 p - \frac{\partial^2 p}{\partial t^2} - Q \frac{L_c}{c_o} \frac{\partial p}{\partial t} - 2M \frac{\partial^2 p}{\partial x \partial t} - M^2 \frac{\partial^2 p}{\partial x^2} = \nabla \cdot \left[ \vec{F}(t) \mathbf{d} \left( \vec{x} - \vec{x}_s \right) \right]$$

And if we introduce  $Q_{nd} = QL_c / c_o$ , then

$$\nabla^2 p - \frac{\partial^2 p}{\partial t^2} - Q_{nd} \frac{\partial p}{\partial t} - 2M \frac{\partial^2 p}{\partial x \partial t} - M^2 \frac{\partial^2 p}{\partial x^2} = \nabla \cdot \left[ \vec{F}(t) \mathbf{d} \left( \vec{x} - \vec{x}_s \right) \right] \quad (3.43)$$

For harmonically varying variables with a time dependence of the form  $\exp(-i\omega t^*) = \exp(-i\omega L_c t / c_o) = \exp(-i k_{Lc} t)$ , equation (3.43) changes to the inhomogeneous convected Helmholtz equation with volumetric damping (equation (3.44)). The solution of this equation after the appropriate boundary conditions are introduced expresses the acoustic field produced by a dipole sound source of source strength  $\vec{F}$  at radial frequency  $(k_{Lc} c_o) / L_c$  in the bounded domain. Where  $k_{Lc} = \omega L_c / c_o$ , is the nondimensional wavenumber or Helmholtz number, and  $L_c$  is a characteristic reference length.

$$\nabla^2 p - M^2 \frac{\partial^2 p}{\partial x^2} + 2i k_{Lc} M \frac{\partial p}{\partial x} + (k_{Lc}^2 + i Q_{nd} k_{Lc}) p = \nabla \cdot \left[ \vec{F} \mathbf{d} \left( \vec{x} - \vec{x}_s \right) \right] \quad (3.44)$$

This decomposition into the different frequencies simplifies the solution and its appropriate for our case of a dominant single dipole source emitting at a given frequency. The solution when more than one acoustic source are present in the domain of influence can be obtained by the superposition of all the individual acoustic fields. If the sources are emitting at different frequencies, the solutions are obtained in the same way, but now each point in the domain will have a spectrum containing components at the various source frequencies.

### 3.5.3 Description of wall boundary conditions

Wall boundary conditions can very significantly modify the acoustic field produced by sound sources inside an enclosure. The specific acoustic impedance characterizes wall acoustic behavior. Some thermo-viscous dissipation processes occurring at the walls can be modeled by modifying the actual wall-specific acoustic impedance especially when the walls could be considered to be rigid [Morse and Ingard]. Acoustic damping at the walls is a very important factor to determine if a noticeable acoustic resonance can develop. However, no attempt has been made to include its effects in current damping models that try to predict acoustic resonance conditions for heat exchangers.

There are cases when it might be desirable to find a solution assuming rigid walls. For this reason, rigid wall as well as absorbing wall boundary conditions will be described here.

Typical boundary conditions for rigid walls are 1) the particle velocity is zero, or 2) the derivative of the acoustic pressure normal to the wall is zero. The latter form of boundary conditions will be used here and are shown next.

$$\begin{aligned}\frac{\partial p}{\partial y} = 0 & \quad \text{at } y = 0, \frac{W}{L_c} \\ \frac{\partial p}{\partial z} = 0 & \quad \text{at } z = 0, \frac{H}{L_c}\end{aligned}\tag{3.45}$$

For imperfect reflection at the walls the boundary conditions change to

$$\begin{aligned}\frac{\partial p}{\partial y} \pm \mathbf{a}_y p = 0 & \quad \text{at } y = \pm \frac{W}{2L_c} \\ \frac{\partial p}{\partial z} \pm \mathbf{a}_z p = 0 & \quad \text{at } z = \pm \frac{H}{2L_c}\end{aligned}\tag{3.46}$$

When using boundary conditions (3.45), it is more appropriate to solve the problem using a coordinate system with its origin on a duct corner. For absorbing walls, it is more convenient to solve the problem using a coordinate system with origin at the center of the duct. This is why boundary conditions are specified differently in equations (3.45) and (3.46). It is assumed in equations (3.46) that wall acoustic impedance is independent of position.

### 3.5.3.1 Wall Impedance definitions

The ratio between the pressure and normal acoustic velocity at a point in a surface is called acoustic impedance. This impedance may depend on the frequency of the wave, and it can be complex. A complex impedance indicates that the normal acoustic velocity and acoustic pressure are not in phase.

The following relationships related to the acoustic impedance  $Z$  are commonly used in the literature [see Morse and Ingard, for example]:

$$\begin{aligned}Z = \frac{p}{\vec{u} \cdot \vec{n}} & \quad z = \frac{Z}{r c_0} = \mathbf{q} - i\mathbf{c} \\ \mathbf{b} = \frac{1}{z} = \mathbf{x} - i\mathbf{s} & \quad \mathbf{x} = \frac{\mathbf{q}}{\mathbf{q}^2 + \mathbf{c}^2} & \quad \mathbf{s} = \frac{-\mathbf{c}}{\mathbf{q}^2 + \mathbf{c}^2}\end{aligned}\tag{3.47}$$

$$\mathbf{a} = -ik \mathbf{b}$$

In equations (3.47)  $Z$  and  $z$  represent the acoustic impedance and specific acoustic impedance respectively while  $\theta$  and  $\chi$  are the specific acoustic resistance and reactance in the same order. The terms  $\beta$ ,  $\xi$ , and  $\sigma$  are the specific acoustic admittance, conductance and susceptance respectively. While the terms  $\alpha$ ,  $k$  and  $i$  represent the wall impedance coefficient, the wavenumber, and the square root of  $-1$ .

The acoustic impedance can also be a function of position. In this work, the dependence of acoustic impedance on position will be neglected.



### 3.5.4 Solution of the inhomogeneous convected Helmholtz equation with a dipole source term inside an infinite rectangular duct with rigid walls

To solve for this problem, the inhomogeneous convected wave equation (3.44) without the volumetric damping term would be solved using boundary conditions specified by equations (3.45). The first step in the solution procedure is to obtain the solution of the homogeneous problem. The solution of the homogeneous problem gives us the required equations to obtain the characteristic values or eigenvalues. Each discrete mode eigenvalue satisfies the specified boundary conditions for that mode in question only. The eigenfunctions in this case have been directly specified since they are well known for rectangular sections (cosine functions).

The next step in the solution process is to decompose the source term so that the dipole orientation is expressed correctly. For the coordinate system chosen, this means a dipole orientation in the y direction (see Figure 3.1). The last step consists of solving the inhomogeneous problem with this source term.

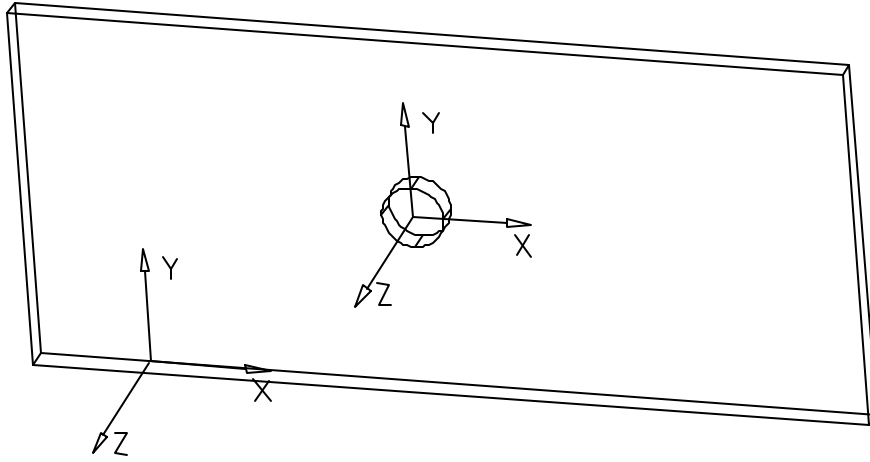


Figure 3.1 Coordinate systems used in modeling equations. With damping at the walls (center of the duct) and with rigid walls (duct corner).

#### 3.5.4.1 Solution to the homogeneous problem

The propagation only part of the convected Helmholtz equation, with no sources present and without volumetric damping is described by equation (3.48):

$$\nabla^2 p - M^2 \frac{\partial^2 p}{\partial x^2} + 2ik_{L_c} M \frac{\partial p}{\partial x} + k_{L_c}^2 p = 0 \quad (3.48)$$

The solutions to the homogeneous problem are of the form shown in equation (3.49) [Morse and Ingard]:

$$\begin{aligned} p^+ &= \sum_{n=0}^{\infty} \sum_{m=0}^{\infty} p_{mn}^+ \cos(k_{y_m} y) \cos(k_{z_n} z) e^{ik_{x_{mn}}^+ (x-x_s)} & x > x_s \\ p^- &= \sum_{n=0}^{\infty} \sum_{m=0}^{\infty} p_{mn}^- \cos(k_{y_m} y) \cos(k_{z_n} z) e^{-ik_{x_{mn}}^- (x-x_s)} & x < x_s \end{aligned} \quad (3.49)$$

Substitution of (3.49) into (3.38) yields

$$\left(ik_{x_{mn}}^{\pm}\right)^2 p^{\pm} - k_{y_m}^2 p^{\pm} - k_{z_n}^2 p^{\pm} - M^2 \left(ik_{x_{mn}}^{\pm}\right)^2 p^{\pm} \pm 2ik_{L_c} M \left(ik_{x_{mn}}^{\pm}\right) p^{\pm} + k_{L_c}^2 p^{\pm} = 0$$

or

$$(1 - M^2) k_{x_{mn}}^{\pm 2} + k_{y_m}^2 + k_{z_n}^2 \pm 2k_{L_c} M k_{x_{mn}}^{\pm} = k_{L_c}^2 \quad (3.50)$$

From (3.50), the eigenvalues of the m,n mode in the x direction are determined to be:

$$k_{x_{mn,1,2}}^{\pm} = \frac{-k_{L_c} M \pm \sqrt{k_{L_c}^2 - (1 - M^2)(k_{y_m}^2 + k_{z_n}^2)}}{(1 - M^2)} \quad (3.51)$$

$$k_{x_{mn,1,2}}^{\pm} = \frac{k_{L_c} M \pm \sqrt{k_{L_c}^2 - (1 - M^2)(k_{y_m}^2 + k_{z_n}^2)}}{(1 - M^2)}$$

Substitution of the boundary conditions (3.45) leads to solutions for the eigenvalues in the y and z directions as shown below:

$$\left. \frac{\partial p}{\partial y} \right|_{0, W/L_c} = \sum_{n=0}^{\infty} \sum_{m=0}^{\infty} -k_{y_m} p_{mn}^{\pm} \sin\left(k_{y_m} \frac{W}{L_c}\right) \cos(k_{z_n} z) e^{\pm ik_{x_{mn}}^{\pm}(x-x_s)} = 0 \quad (3.52)$$

The above expression is true if

$$\sum_{m=0}^{\infty} \sin\left(k_{y_m} \frac{W}{L_c}\right) = 0 \quad (3.53)$$

so that the eigenvalues are:

$$k_{y_m} = \frac{m\pi L_c}{W} \quad (3.54)$$

Similarly, in the z direction:

$$k_{z_n} = \frac{n\pi L_c}{H} \quad (3.55)$$

### 3.5.4.2 Decomposition of the dipole source term

Dipoles, unlike monopoles, produce sound in a preferential direction. Thus, in addition to dipole position, dipole orientation is necessary to completely specify this type of acoustic source. The sound from cylinders in cross-flow consists of two types of dipoles. These dipoles are associated with the lift and drag components of the fluctuating forces generated by the vortex shedding process. The lift dipole is approximately an order of magnitude larger than the drag dipole. The lift dipole is oriented transversely to the rectangular duct walls, and is in the majority of cases the direction that supports the acoustic resonance inside heat exchangers [Eisinger and Sullivan]. For these reasons the lift dipole dominates the acoustic field generated by the cylinders in cross-flow inside a duct.

The source term present in equation (3.44) expresses dipole sources in all axis directions. In our coordinate system, the lift dipole is oriented in the y-axis direction and is of primary importance. The source term for a dipole so oriented can be obtained from the general dipole source term of equation (3.44) as shown below.

The source term in equation (3.44) can be expressed as

$$\nabla \cdot \left[ \vec{F} \mathbf{d} \left( \vec{x} - \vec{x}_s \right) \right] = -\vec{F} \cdot \nabla \mathbf{d} \left( \vec{x} - \vec{x}_s \right) \quad (3.56)$$

The right hand side of equation (3.56) can be decomposed as

$$-\vec{F} \cdot \nabla \mathbf{d} \left( \vec{x} - \vec{x}_s \right) = - \left( F_x \hat{i} + F_y \hat{j} + F_z \hat{k} \right) \cdot \left( \frac{\partial \mathbf{d} \left( \vec{x} - \vec{x}_s \right)}{\partial x} \hat{i} + \frac{\partial \mathbf{d} \left( \vec{x} - \vec{x}_s \right)}{\partial y} \hat{j} + \frac{\partial \mathbf{d} \left( \vec{x} - \vec{x}_s \right)}{\partial z} \hat{k} \right) \quad (3.57)$$

If only the force in the y direction is present, then (3.57) simplifies to

$$-\vec{F} \cdot \nabla \mathbf{d} \left( \vec{x} - \vec{x}_s \right) = -F_y \frac{\partial \mathbf{d} \left( \vec{x} - \vec{x}_s \right)}{\partial y} = -F_y \mathbf{d} \left( x - x_s \right) \mathbf{d}' \left( y - y_s \right) \mathbf{d} \left( z - z_s \right) \quad (3.58)$$

### 3.5.4.3 Solution to the inhomogeneous problem

Equation (3.44), assuming a dipole term in the y direction and no volumetric damping, becomes

$$\nabla^2 \mathbf{p} - M^2 \frac{\partial^2 \mathbf{p}}{\partial x^2} + 2ik_{L_c} M \frac{\partial \mathbf{p}}{\partial x} + k_{L_c}^2 \mathbf{p} = -F_y \mathbf{d} \left( x - x_s \right) \mathbf{d}' \left( y - y_s \right) \mathbf{d} \left( z - z_s \right) \quad (3.59)$$

The solution of this equation is of the form

$$\begin{aligned} \mathbf{p}^+ &= \sum_{n=0}^{\infty} \sum_{m=0}^{\infty} \mathbf{Q}_{mn}^+ (x) \cos(k_{y_m} y) \cos(k_{z_n} z) & x > x_s \\ \mathbf{p}^- &= \sum_{n=0}^{\infty} \sum_{m=0}^{\infty} \mathbf{Q}_{mn}^- (x) \cos(k_{y_m} y) \cos(k_{z_n} z) & x < x_s \end{aligned} \quad (3.60)$$

Substituting (3.60) into (3.59),

$$\begin{aligned} & \left\{ \sum_{n=0}^{\infty} \sum_{m=0}^{\infty} \cos(k_{y_m} y) \cos(k_{z_n} z) \right\} * \\ & \left\{ \frac{\partial^2 \mathbf{Q}_{mn}^{\pm} (x)}{\partial x^2} - k_{y_m}^2 \mathbf{Q}_{mn}^{\pm} (x) - k_{z_n}^2 \mathbf{Q}_{mn}^{\pm} (x) - M^2 \frac{\partial^2 \mathbf{Q}_{mn}^{\pm} (x)}{\partial x^2} + 2ik_{L_c} M \frac{\partial \mathbf{Q}_{mn}^{\pm} (x)}{\partial x} + k_{L_c}^2 \mathbf{Q}_{mn}^{\pm} (x) \right\} \\ & = -F_y \mathbf{d} \left( x - x_s \right) \mathbf{d}' \left( y - y_s \right) \mathbf{d} \left( z - z_s \right) \end{aligned} \quad (3.61)$$

Multiplying (3.61) by

$$\sum_{n=0}^{\infty} \sum_{m=0}^{\infty} \cos(k_{y_m} y) \cos(k_{z_n} z) \quad (3.62)$$

and integrating from  $y=0, W/L_c$  and  $z=0, H/L_c$ ,

$$\begin{aligned}
& \int_0^{H/L_c} \int_0^{W/L_c} \left\{ \sum_{n=0}^{\infty} \sum_{m=0}^{\infty} \cos^2(k_{y_m} y) \cos^2(k_{z_n} z) \right\} * \\
& \left\{ (1-M^2) \frac{\partial^2 Q_{mn}^{\pm}(x)}{\partial x^2} + 2ik_{L_c} M \frac{\partial Q_{mn}^{\pm}(x)}{\partial x} + (k_{L_c}^2 - k_{y_m}^2 - k_{z_n}^2) Q_{mn}^{\pm}(x) \right\} dydz \quad (3.62) \\
& = \int_0^{H/L_c} \int_0^{W/L_c} \left\{ \sum_{n=0}^{\infty} \sum_{m=0}^{\infty} \cos(k_{y_m} y) \cos(k_{z_n} z) \right\} \left\{ -F_y d(x-x_s) d'(y-y_s) d(z-z_s) \right\} dydz
\end{aligned}$$

Useful integral formulas:

$$\int_0^{W/L_c} \cos^2(k_{y_m} y) dy = \left[ \frac{y}{2} + \frac{\sin(2k_{y_m} y)}{4k_{y_m}} \right]_0^{W/L_c} \quad (3.63)$$

For  $m=0$ , the integrand becomes 1; thus, when evaluating for the limits of integration and introducing the values of  $k_{y_m}$

$$A_{y_m} = \int_0^{W/L_c} \cos^2(k_{y_m} y) dy = \begin{cases} \frac{W}{L_c} & \text{for } m=0 \\ \frac{W}{2L_c} & \text{for } m>0 \end{cases} \quad (3.64)$$

Similarly, in  $z$ :

$$A_{z_n} = \int_0^{H/L_c} \cos^2(k_{z_n} z) dz = \begin{cases} \frac{H}{L_c} & \text{for } n=0 \\ \frac{H}{2L_c} & \text{for } n>0 \end{cases} \quad (3.65)$$

In addition to (3.63), the following properties of the delta function are needed:

$$\begin{aligned}
& \int f(x) d(x-x_s) dx = f(x_s) \\
& \int f(x) d'(x-x_s) dx = \left. \frac{df}{dx} \right|_{x_s} = f'(x_s) \quad (3.66)
\end{aligned}$$

Using equations (3.64), (3.65) and the properties of the delta function, equation (3.62) can be simplified to

$$\begin{aligned}
& (1-M^2) \frac{\partial^2 Q_{mn}^{\pm}(x)}{\partial x^2} + 2ik_{L_c} M \frac{\partial Q_{mn}^{\pm}(x)}{\partial x} + (k_{L_c}^2 - k_{y_m}^2 - k_{z_n}^2) Q_{mn}^{\pm}(x) \\
& = \frac{-k_{y_m} \sin(k_{y_m} y_s) \cos(k_{z_n} z_s) \left\{ -F_y d(x-x_s) \right\}}{A_{y_m} A_{z_n}} \quad (3.67)
\end{aligned}$$

Equation (3.67) is a linear second-order nonhomogeneous equation that will be solved below using the method of variation of parameters.

The first step in this procedure is finding a solution to the homogenous linear differential equation. To do this the characteristic equation (3.68) needs to be solved:

$$(1-M^2)\Theta^2 + 2ik_{L_c}M\Theta + (k_{L_c}^2 - k_{y_m}^2 - k_{z_n}^2) = 0 \quad (3.68)$$

The solution to the homogeneous problem is of the form

$$Q = Q_1 + Q_2 = B_1 e^{\Theta^+ x} + B_2 e^{\Theta^- x} \quad (3.69)$$

Solving for the values of  $\alpha$  using the quadratic formula and using equations (3.51),

$$\Theta^\pm = i \left( \frac{-k_{L_c} M \pm \sqrt{k_{L_c}^2 - (1-M^2)(k_{y_m}^2 + k_{z_n}^2)}}{(1-M^2)} \right) = ik_{x_{mn,1,2}}^+ \quad (3.70)$$

the homogeneous solution to the problem becomes

$$Q = B_1 e^{ik_{x_{mn,1}}^+ x} + B_2 e^{ik_{x_{mn,2}}^+ x} \quad (3.71)$$

where the  $k_{x_{mn,1}}^+$  and  $k_{x_{mn,2}}^+$  represent the + and – parts, respectively, of the axial eigenvalues shown in equation (3.51).

To find solutions to the nonhomogeneous problem, the constants  $B_1$  and  $B_2$  are replaced by arbitrary functions, say,  $\eta_1$  and  $\eta_2$ , that should satisfy the nonhomogeneity. To solve for the two unknown functions, two independent equations are needed. The first equation is obtained when equation (3.71) is substituted into equation (3.67). The second equation is obtained such that second derivatives of the functions  $\eta_1$  and  $\eta_2$  are avoided [see Wylie and Barrett, page 82]. The set of equations needed to solve for  $\eta_1$  and  $\eta_2$  are:

$$\begin{aligned} h_1' e^{ik_{x_{mn,1}}^+ x} + h_2' e^{ik_{x_{mn,2}}^+ x} &= 0 \\ ik_{x_{mn,1}}^+ h_1' e^{ik_{x_{mn,1}}^+ x} + ik_{x_{mn,2}}^+ h_2' e^{ik_{x_{mn,2}}^+ x} &= \frac{k_{y_m} \sin(k_{y_m} y_s) \cos(k_{y_m} z_s) \{F_y d(x - x_s)\}}{A_{y_m} A_{z_n} (1-M^2)} \end{aligned} \quad (3.72)$$

Equations (3.72) can be solved using Cramer's rule. This approach requires the determination of the Wronskian:

$$Wr = \begin{vmatrix} e^{ik_{x_{mn,1}}^+ x} & e^{ik_{x_{mn,2}}^+ x} \\ ik_{x_{mn,1}}^+ e^{ik_{x_{mn,1}}^+ x} & ik_{x_{mn,2}}^+ e^{ik_{x_{mn,2}}^+ x} \end{vmatrix} = -i \left( k_{x_{mn,1}}^+ - k_{x_{mn,2}}^+ \right) e^{ix \left( k_{x_{mn,1}}^+ + k_{x_{mn,2}}^+ \right)} \quad (3.73)$$

and solving for  $\eta_1$  and  $\eta_2$

$$h_1 = \int \frac{\left| \frac{k_{y_m} \sin(k_{y_m} y_s) \cos(k_{z_n} z_s) \{F_y d(x - x_s)\}}{A_{y_m} A_{z_n} (1 - M^2)} \frac{e^{i k_{x_{mn},2}^+ x}}{i k_{x_{mn},2}^+ e^{i k_{x_{mn},1}^+ x}} \right|}{-i \left( k_{x_{mn},1}^+ - k_{x_{mn},2}^+ \right) e^{i x (k_{x_{mn},1}^+ + k_{x_{mn},2}^+)}} dx =$$

$$h_1 = \frac{k_{y_m} \sin(k_{y_m} y_s) \cos(k_{z_n} z_s) \{F_y\}}{-i A_{y_m} A_{z_n} (1 - M^2) (k_{x_{mn},1}^+ - k_{x_{mn},2}^+)} \int d(x - x_s) e^{-i k_{x_{mn},1}^+ x} \quad (3.74)$$

and evaluating the integral

$$h_1 = \frac{k_{y_m} \sin(k_{y_m} y_s) \cos(k_{z_n} z_s) \{F_y\}}{-i A_{y_m} A_{z_n} (1 - M^2) (k_{x_{mn},1}^+ - k_{x_{mn},2}^+)} e^{-i k_{x_{mn},1}^+ x_s} \quad (3.75)$$

Similarly, for  $\eta_2$ :

$$h_2 = \int \frac{\left| \frac{e^{i k_{x_{mn},1}^+ x}}{i k_{x_{mn},1}^+ e^{i k_{x_{mn},1}^+ x}} \frac{k_{y_m} \sin(k_{y_m} y_s) \cos(k_{z_n} z_s) \{F_y d(x - x_s)\}}{A_{y_m} A_{z_n} (1 - M^2)} \right|}{-i \left( k_{x_{mn},1}^+ - k_{x_{mn},2}^+ \right) e^{i x (k_{x_{mn},1}^+ + k_{x_{mn},2}^+)}} dx$$

And evaluating the integral,

$$h_2 = \frac{k_{y_m} \sin(k_{y_m} y_s) \cos(k_{z_n} z_s) \{F_y\}}{-i A_{y_m} A_{z_n} (1 - M^2) (k_{x_{mn},1}^+ - k_{x_{mn},2}^+)} e^{-i k_{x_{mn},2}^+ x_s} \quad (3.76)$$

Solutions for  $Q_{mn}$  are

$$Q_{mn}^\pm = h_1 e^{i k_{x_{mn},1}^+ x} + h_2 e^{i k_{x_{mn},2}^+ x} = \quad (3.77)$$

$$Q_{mn}^\pm = \frac{i (k_{y_m}) \sin(k_{y_m} y_s) \cos(k_{z_n} z_s) \{F_y\}}{A_{y_m} A_{z_n} (1 - M^2) (k_{x_{mn},1}^+ - k_{x_{mn},2}^+)} e^{i k_{x_{mn},1}^+ (x - x_s)} + \frac{i (k_{y_m}) \sin(k_{y_m} y_s) \cos(k_{z_n} z_s) \{F_y\}}{A_{y_m} A_{z_n} (1 - M^2) (k_{x_{mn},1}^+ - k_{x_{mn},2}^+)} e^{i k_{x_{mn},2}^+ (x - x_s)}$$

Finally, the solutions for the acoustic pressure inside a duct with a transverse dipole located at  $(x_s, y_s, z_s)$  are

$$p^+ = \sum_{n=0}^{\infty} \sum_{m=0}^{\infty} \frac{i F_y k_{y_m} \sin(k_{y_m} y_s) \cos(k_{z_n} z_s) \cos(k_{y_m} y) \cos(k_{z_n} z)}{A_{y_m} A_{z_n} (1 - M^2) (k_{x_{mn},1}^+ - k_{x_{mn},2}^+)} e^{i k_{x_{mn},1}^+ (x - x_s)} \quad x > x_s$$

$$p^- = \sum_{n=0}^{\infty} \sum_{m=0}^{\infty} \frac{i F_y k_{y_m} \sin(k_{y_m} y_s) \cos(k_{z_n} z_s) \cos(k_{y_m} y) \cos(k_{z_n} z)}{A_{y_m} A_{z_n} (1 - M^2) (k_{x_{mn},1}^+ - k_{x_{mn},2}^+)} e^{i k_{x_{mn},2}^+ (x - x_s)} \quad x < x_s \quad (3.78)$$

### 3.5.4.4 Solution for dipole oriented along the x-axis

If the dipole axis coincides with the flow direction (in our coordinate system, this means coincidence with the x-axis), then the solution procedure would be similar to the one shown above, except that the right-hand side term presented in equation (3.59) should be changed to its equivalent x-axis dipole source term shown below:

$$-F_x \mathbf{d}^t(x-x_s) \mathbf{d}(y-y_s) \mathbf{d}(z-z_s) \quad (3.79)$$

In this case, the integral shown in equation (3.75) is modified and the final solution for an x-axis dipole becomes

$$p^+ = \sum_{n=0}^{\infty} \sum_{m=0}^{\infty} \frac{k_{x_{mn,1}}^+ F_x \cos(k_{y_m} y_s) \cos(k_{z_n} z_s) \cos(k_{y_m} y) \cos(k_{z_n} z)}{A_{y_m} A_{z_n} (1-M^2) (k_{x_{mn,1}}^+ - k_{x_{mn,2}}^+)} e^{i k_{x_{mn,1}}^+ (x-x_s)} \quad x > x_s$$

$$p^- = \sum_{n=0}^{\infty} \sum_{m=0}^{\infty} \frac{k_{x_{mn,2}}^+ F_x \cos(k_{y_m} y_s) \cos(k_{z_n} z_s) \cos(k_{y_m} y) \cos(k_{z_n} z)}{A_{y_m} A_{z_n} (1-M^2) (k_{x_{mn,1}}^+ - k_{x_{mn,2}}^+)} e^{i k_{x_{mn,2}}^+ (x-x_s)} \quad x < x_s \quad (3.80)$$

### 3.5.5 Point dipole inside an infinite rectangular duct with absorbing walls and uniform flow

Heat exchanger wall materials and a combination of different physical phenomena present at the walls influence the interaction of acoustic waves with these surfaces. For these reasons, even when the heat exchanger walls could be considered acoustically rigid, a finite acoustic impedance needs to be used to model approximately the wall acoustic properties. In general, wall acoustic properties vary as a function of frequency. In the limiting case of fully absorbing walls at a particular frequency of interest, the walls produce the effect of free field conditions and cannot sustain an acoustic resonance. Free field conditions inside a room can only be approximated by anechoic rooms. Some of the physical phenomena that affect acoustic impedance of the walls include thermo-viscous sound attenuation processes [Morse and Ingard] and boundary layer effects [Moshier]. The finite acoustic impedance of the walls of heat exchangers have not been considered before as a possible cause of sound attenuation in these containers.

Absorbing wall boundary conditions presented in equations (3.46) will be introduced in this section to develop a nondimensional solution to equation (3.44) for an acoustic dipole perpendicular to the y axis inside an infinite rectangular duct that considers the effects of finite impedance on the duct walls.

The solution procedure is similar to the one presented in section 3.4.4 for rigid walls. The changes involve a change in the coordinate system which now is located in the center of the duct and the use of cosine and sine solutions as described below.

#### 3.5.5.1 Solution to the homogeneous problem

The solutions to this problem are of the form presented in equations (3.81) [Morse and Ingard].

$$p^+ = \sum_{n=0}^{\infty} \sum_{m=0}^{\infty} p_{mn}^+ \text{Cs}(k_{y_m} y) \text{Cs}(k_{z_n} z) e^{i k_{x_{mn}}^+ (x-x_s)} \quad x > x_s$$

$$p^- = \sum_{n=0}^{\infty} \sum_{m=0}^{\infty} p_{mn}^- \text{Cs}(k_{y_m} y) \text{Cs}(k_{z_n} z) e^{-i k_{x_{mn}}^- (x-x_s)} \quad x < x_s \quad (3.81)$$

where

$$Cs(k_n) = \begin{cases} \cos(k_n) & \text{for } n = 0, 2, 4, 6, \dots \\ \sin(k_n) & \text{for } n = 1, 3, 5, 7, \dots \end{cases} \quad (3.82)$$

The x-direction eigenvalues are obtained by substitution of equations (3.81) into equation (3.48). These eigenvalues are identical to those presented in equations (3.51).

Substitution of the boundary conditions (3.46) leads to solutions for the eigenvalues in the y and z directions as shown below:

$$\left. \frac{\partial p}{\partial y} \pm a_y p \right|_{\pm W/2L_c} = \sum_{m=0}^{\infty} \sum_{n=0}^{\infty} \left\{ \begin{array}{l} -k_{y_m} p_{mn}^{\pm} \sin\left(\pm \frac{k_{y_m} W}{2L_c}\right) \cos(k_{z_n} z) \\ \pm a_y p_{mn}^{\pm} \cos\left(\pm \frac{k_{y_m} W}{2L_c}\right) \cos(k_{z_n} z) \end{array} \right\} = 0 \quad \text{For } m = 0, 2, 4, \dots$$

$$\left. \frac{\partial p}{\partial y} \pm a_y p \right|_{\pm W/2L_c} = \sum_{m=0}^{\infty} \sum_{n=0}^{\infty} \left\{ \begin{array}{l} -k_{y_m} p_{mn}^{\pm} \cos\left(\pm \frac{k_{y_m} W}{2L_c}\right) \sin(k_{z_n} z) \\ \pm a_y p_{mn}^{\pm} \sin\left(\pm \frac{k_{y_m} W}{2L_c}\right) \sin(k_{z_n} z) \end{array} \right\} = 0 \quad \text{For } m = 1, 3, 5, \dots$$

The above expressions are true if

$$-k_{y_m} \sin\left(\pm \frac{k_{y_m} W}{2L_c}\right) \pm a_y \cos\left(\pm \frac{k_{y_m} W}{2L_c}\right) = 0 \quad \text{For } m = 0, 2, 4, \dots$$

$$-k_{y_m} \cos\left(\pm \frac{k_{y_m} W}{2L_c}\right) \pm a_y \sin\left(\pm \frac{k_{y_m} W}{2L_c}\right) = 0 \quad \text{For } m = 1, 3, 5, \dots$$

or

$$k_{y_m} \tan\left(\frac{k_{y_m} W}{2L_c}\right) = a_y \quad \text{For } m = 0, 2, 4, \dots$$

$$k_{y_m} \tan\left(\frac{k_{y_m} W}{2L_c} + \frac{\mathbf{p}}{2}\right) = a_y \quad \text{For } m = 1, 3, 5, \dots$$

The eigenvalues  $k_{y_m}$  are of the form

$$k_{y_m} = \frac{m \mathbf{p} L_c}{W} + z_{y_m} \quad (3.86)$$

If the walls could be considered close to being hard, (i.e., when the wall absorption coefficients are small) substitution of (3.86) into (3.85) leads to [Morse and Ingard]



$$z_{y_m} = \sqrt{\frac{2a_y L_c}{W}} \quad m = 0 \quad (3.87)$$

$$z_{y_m} = \frac{2a_y}{p m} \quad m > 0$$

Similarly, for z we have:

$$k_{z_n} = \frac{n p L_c}{H} + z_{z_n} \quad (3.88)$$

and

$$z_{z_n} = \sqrt{\frac{2a_z L_c}{H}} \quad n = 0 \quad (3.89)$$

$$z_{z_n} = \frac{2a_z}{p n} \quad n > 0$$

### 3.5.5.2 Solution to the inhomogeneous problem

The introduction of absorbing walls boundary conditions modifies slightly the solution found for rigid walls in section 3.5.4.3. In this case, the solution obtained following the same steps presented in section 3.5.4.3 is

$$p^+ = \sum_{m=0}^{\infty} \sum_{n=0}^{\infty} \frac{-i F_y \text{Cs}'(k_{y_m} y) \Big|_{y_s} \text{Cs}(k_{z_n} z_s) \text{Cs}(k_{y_m} y) \text{Cs}(k_{z_n} z)}{A_{y_m} A_{z_n} (1-M^2) (k_{x_{mn,1}}^+ - k_{x_{mn,2}}^+)} e^{i k_{x_{mn,1}}^+ (x-x_s)} \quad x > x_s \quad (3.90)$$

$$p^- = \sum_{m=0}^{\infty} \sum_{n=0}^{\infty} \frac{-i F_y \text{Cs}'(k_{y_m} y) \Big|_{y_s} \text{Cs}(k_{z_n} z_s) \text{Cs}(k_{y_m} y) \text{Cs}(k_{z_n} z)}{A_{y_m} A_{z_n} (1-M^2) (k_{x_{mn,1}}^+ - k_{x_{mn,2}}^+)} e^{i k_{x_{mn,2}}^+ (x-x_s)} \quad x < x_s$$

where the constants  $A_{y_m}$  and  $A_{z_n}$  are now defined as

$$A_{y_m} = \int_{-W/2L_c}^{W/2L_c} \text{Cs}^2(k_{y_m} y) dy = \begin{cases} \frac{W}{L_c} & \text{for } m = 0 \\ \frac{W}{2L_c} + \frac{(-1)^m \sin\left(\frac{k_{y_m} W}{L_c}\right)}{2k_{y_m}} & \text{for } m > 0 \end{cases} \quad (3.91)$$

and

$$A_{z_n} = \int_{-H/2L_c}^{H/2L_c} \text{Cs}^2(k_{z_n} z) dz = \begin{cases} \frac{H}{L_c} & \text{for } n = 0 \\ \frac{H}{2L_c} + \frac{(-1)^n \sin\left(\frac{k_{z_n} H}{L_c}\right)}{2k_{z_n}} & \text{for } n > 0 \end{cases} \quad (3.92)$$

### 3.5.6 Point dipole inside an infinite rectangular duct with volumetric damping, rigid walls and uniform flow

The introduction of volumetric damping in the inhomogeneous convected wave equation provides another way to account for sound damping mechanisms. In this case the damping mechanisms would need to be isotropic and homogeneously distributed throughout the acoustic medium to be correctly modeled by this approximation. Volumetric damping is also expected to be a function of frequency.

The solution when volumetric damping and rigid walls are present changes from the one shown in section 3.4.4 by modifying the x-direction eigenvalues. The homogeneous form of equation (3.44) shown in equation (3.93) is needed to obtain these eigenvalues.

$$\nabla^2 p - M^2 \frac{\partial^2 p}{\partial x^2} + 2i k_{Lc} M \frac{\partial p}{\partial x} + (k_{Lc}^2 + i Q_{nd} k_{Lc}) p = 0 \quad (3.93)$$

Substituting equations (3.49) into equation (3.93) leads to the required relationships (3.94) to obtain new x-direction eigenvalues:

$$(1 - M^2) k_{x_{mn}}^{\pm 2} \pm 2k_{Lc} M k_{x_{mn}}^{\pm} + k_{y_m}^2 + k_{z_n}^2 - (k_{Lc}^2 + i Q_{nd} k_{Lc}) = 0 \quad (3.94)$$

From (3.94), the x-direction eigenvalues of the m,n mode are determined to be

$$k_{x_{mn}}^+ = \frac{-k_{Lc} M \pm \sqrt{k_{Lc}^2 - (1 - M^2)(k_{y_m}^2 + k_{z_n}^2 - i Q_{nd} k_{Lc})}}{(1 - M^2)} \quad (3.95)$$

$$k_{x_{mn}}^- = \frac{k_{Lc} M \pm \sqrt{k_{Lc}^2 - (1 - M^2)(k_{y_m}^2 + k_{z_n}^2 - i Q_{nd} k_{Lc})}}{(1 - M^2)}$$

From the above two equations only  $k_{x_{mn}}^+$  which is required in the inhomogeneous solution should be used.

The full solution for a y-direction dipole inside a duct with volumetric damping and rigid walls boundary conditions is identical to equation (3.78). The eigenvalues are obtained using equations (3.95), (3.54), and (3.55).

### 3.5.7 Point dipole inside an infinite rectangular duct with volumetric damping, absorbing walls and uniform flow

The solution for a y-axis point dipole inside an infinite rectangular duct with volumetric damping and absorbing walls can be assembled using the results developed in previous sections. The acoustic field in this case can also be described by equations (3.90) if the correct eigenvalues are used. The eigenvalues that account for the volumetric and wall damping, which should be used in this case, are found in equations (3.95) for x, (3.86) for y and (3.88) for z.

In equations (3.90) the  $k_{x_{mn,1}}^+$  and  $k_{x_{mn,2}}^+$  represent the + and - parts respectively of the axial eigenvalues shown in the top equation of the equations shown in (3.95). The constants  $A_{y_m}$  and  $A_{z_n}$  are defined in equations (3.91) and (3.92).

### 3.5.8 Cutoff or resonant frequencies in a rectangular waveguide with flow

A resonance frequency for each mode propagating inside the duct is determined when the denominator in equation (3.90) is zero. If this condition is encountered, the acoustic wave of that mode stops propagating along the

duct and a resonance condition is established. For this to happen, the argument of the radical in equation (3.95) should be zero. That is,

$$k_{L_c c_o}^2 - (1-M^2)(k_{y_m}^2 + k_{z_n}^2 - iQ_{nd} k_{L_c c_o}) = 0 \quad (3.96)$$

If volumetric damping is zero,

$$f_{co m,n} = \frac{k_{L_c c_o} c_o}{2p L_c} = \frac{c_o (1-M^2)^{1/2}}{2p L_c} (k_{y_m}^2 + k_{z_n}^2)^{1/2} \quad (3.97)$$

and if the walls are rigid,

$$f_{co m,n} = \frac{c_o (1-M^2)^{1/2}}{2p L_c} \left( \left( \frac{mp L_c}{W} \right)^2 + \left( \frac{np L_c}{H} \right)^2 \right)^{1/2} \quad (3.98)$$

The above equations show the influence of the Mach number in determining the cutoff frequencies of each mode. Its effect could be perceived as an effective reduction in the speed of sound. The speed of sound  $c_o$  used above is the speed of sound of the gas in a duct where no cylinder array is present. This is adequate for single cylinders, but the presence of cylinder arrays has been shown by Parker 1978 and Blevins 1986 to reduce the effective sound speed. To estimate the acoustic natural frequencies if a cylinder array is present inside the duct,  $c_o$  should be replaced by  $c_{eff}$  shown in equation (2.23).

If volumetric damping is not zero, then from equation (3.96),

$$k_{L_c c_o} = \frac{-(1-M^2)iQ_{nd} \pm \sqrt{-(1-M^2)^2 Q_{nd}^2 + 4(1-M^2)(k_{y_m}^2 + k_{z_n}^2)}}{2} \quad (3.99)$$

or

$$f_{co} = \frac{k_{L_c c_o} c_o}{2p L_c} = \frac{-c_o (1-M^2)iQ_{nd} \pm c_o \sqrt{4(1-M^2)(k_{y_m}^2 + k_{z_n}^2) - (1-M^2)^2 Q_{nd}^2}}{4p L_c} \quad (3.100)$$

and if the walls are rigid,

$$f_{co} = \frac{-c_o (1-M^2)iQ_{nd} \pm c_o \sqrt{4(1-M^2) \left( \left( \frac{mp L_c}{W} \right)^2 + \left( \frac{np L_c}{H} \right)^2 \right) - (1-M^2)^2 Q_{nd}^2}}{4p L_c} \quad (3.101)$$

### 3.6 Mathematical model convergence

#### 3.6.1 Introduction

The use of analytic series solution as developed in the previous sections has advantages and disadvantages. Three of the main disadvantages are the following:

1. This type of series in general might not converge.
2. The practical limits of using a finite number of terms might introduce errors.

3. Solutions for complex geometries cannot be obtained.

There are also benefits to the use of this type of solution. A very important one is that the solution can be found at any point independently, without having to solve for the complete acoustic field.

In this section, limits on the error introduced by the use of a finite number of terms will be presented, first by providing an expression that delimits these errors, and then by numerical experiments of the solution both as a function of space in the solution domain and as a function of frequency of the dipole source.

### 3.7.2 Analytical model error estimation

In this section, an expression that delimits the error associated with the use a finite number of terms in the series solution will be developed. To simplify the analysis, rigid walls and zero uniform flow velocity will be assumed. For these conditions the solution reduces to

$$p^{\pm} = \sum_{m=0}^{\infty} \sum_{n=0}^{\infty} \frac{-i F_y \text{Cs}'(k_{y_m} y) \Big|_{y_s} \text{Cs}(k_{z_n} z_s) \text{Cs}(k_{y_m} y) \text{Cs}(k_{z_n} z)}{A_{y_m} A_{z_n} (k_{X_{mn,1}}^+ - k_{X_{mn,2}}^+)} e^{i k_{X_{mn,1,2}}^+ (x-x_s)} \quad (3.115)$$

where

$$\begin{aligned} k_{X_{mn,1,2}}^+ &= \pm \sqrt{k_{L_c}^2 - (k_{y_m}^2 + k_{z_n}^2)} & k_{y_m} &= \frac{m \pi L_c}{W} & k_{z_n} &= \frac{n \pi L_c}{H} \\ A_{y_m} &= \frac{W}{2L_c} & A_{z_n} &= \frac{H}{2L_c} & k_{L_c} &= \frac{\omega L_c}{c_o} \end{aligned} \quad (3.116)$$

If we use  $m = M_{\text{terms}} - 1$  and  $n = N_{\text{terms}} - 1$  terms in the series, then the residual acoustic pressure would be

$$p_{\text{res}}^{\pm} = \sum_{m=M_{\text{terms}}}^{\infty} \sum_{n=N_{\text{terms}}}^{\infty} \frac{-i F_y \text{Cs}'(k_{y_m} y) \Big|_{y_s} \text{Cs}(k_{z_n} z_s) \text{Cs}(k_{y_m} y) \text{Cs}(k_{z_n} z)}{A_{y_m} A_{z_n} (k_{X_{mn,1}}^+ - k_{X_{mn,2}}^+)} e^{i k_{X_{mn,1,2}}^+ (x-x_s)} \quad (3.117)$$

Since the trigonometric functions are bounded by one, the limits of the acoustic pressure can be set as

$$\left| p_{\text{res}}^{\pm} \right| \leq \sum_{m=M_{\text{terms}}}^{\infty} \sum_{n=N_{\text{terms}}}^{\infty} \left| \frac{F_y k_{y_m}}{A_{y_m} A_{z_n} (k_{X_{mn,1}}^+ - k_{X_{mn,2}}^+)} e^{i k_{X_{mn,1,2}}^+ (x-x_s)} \right| \quad (3.118)$$

Substituting equations (3.116) into (3.118) results in

$$\left| p_{\text{res}}^{\pm} \right| \leq \sum_{m=M_{\text{terms}}}^{\infty} \sum_{n=N_{\text{terms}}}^{\infty} \left| \frac{2 L_c^2 F_y k_{y_m} e^{\pm \sqrt{k_{L_c}^2 - k_{y_m}^2 - k_{z_n}^2} (x-x_s)}}{W H \sqrt{k_{L_c}^2 - k_{y_m}^2 - k_{z_n}^2}} \right| \quad (3.119)$$

or

$$|p_{res}^{\pm}| \leq \sum_{m=M_{terms}}^{\infty} \sum_{n=N_{terms}}^{\infty} \left| \frac{2 p m L_c^3 F_y e^{\pm \sqrt{\frac{w^2 L_c^2}{c_o^2} - \frac{m^2 p^2 L_c^2}{W^2} - \frac{n^2 p^2 L_c^2}{H^2}} (x-x_s)}}{W^2 H \sqrt{\frac{w^2 L_c^2}{c_o^2} - \frac{m^2 p^2 L_c^2}{W^2} - \frac{n^2 p^2 L_c^2}{H^2}}} \right| \quad (3.120)$$

The series can be bounded by integrals as

$$|p_{res}^{\pm}| \leq \frac{2 L_c F_y}{p H} \int_{M_{terms}}^{\infty} \int_{N_{terms}}^{\infty} \left| \frac{\frac{m p^2 L_c^2}{W^2} e^{\pm \sqrt{\frac{w^2 L_c^2}{c_o^2} - \frac{m^2 p^2 L_c^2}{W^2} - \frac{n^2 p^2 L_c^2}{H^2}} (x-x_s)}}{\sqrt{\frac{w^2 L_c^2}{c_o^2} - \frac{m^2 p^2 L_c^2}{W^2} - \frac{n^2 p^2 L_c^2}{H^2}}} \right| dn dm \quad (3.121)$$

The above expression can be integrated directly for m. The resulting equation is

$$|p_{res}^{\pm}| \leq \frac{2 L_c F_y}{p H} \int_{N_{terms}}^{\infty} \left| \frac{e^{\pm \sqrt{\frac{w^2 L_c^2}{c_o^2} - \frac{m^2 p^2 L_c^2}{W^2} - \frac{n^2 p^2 L_c^2}{H^2}} |x-x_s|}}{|x-x_s|} \right|_{M_{terms}}^{\infty} dn \quad (3.122)$$

Equation (3.122) shows that for any value of m and n sufficiently large, the radical will be negative, and the exponential could then be decomposed into trigonometric functions of sine and cosine. By assuming this, equation (3.122) transforms to:

$$|p_{res}^{\pm}| \leq \frac{2 L_c F_y}{p H} \int_{N_{terms}}^{\infty} \left| \frac{\cos \left( \sqrt{\frac{w^2 L_c^2}{c_o^2} - \frac{m^2 p^2 L_c^2}{W^2} - \frac{n^2 p^2 L_c^2}{H^2}} |x-x_s| \right) + i \sin \left( \sqrt{\frac{w^2 L_c^2}{c_o^2} - \frac{m^2 p^2 L_c^2}{W^2} - \frac{n^2 p^2 L_c^2}{H^2}} |x-x_s| \right)}{|x-x_s|} \right|_{M_{terms}}^{\infty} dn \quad (3.123)$$

To integrate the expression above, the Taylor series of the cosine and sine functions presented next could be used:

$$\sin(x) = x - \frac{x^3}{3!} + \frac{x^5}{5!} - \frac{x^7}{7!} + \frac{x^9}{9!} - \dots \quad -\infty < x < \infty \quad (3.124)$$

$$\cos(x) = 1 - \frac{x^2}{2!} + \frac{x^4}{4!} - \frac{x^6}{6!} + \frac{x^8}{8!} - \dots \quad -\infty < x < \infty$$

Substituting these series into (3.123) transforms it to

$$|p_{res}^{\pm}| \leq \frac{2 L_c F_y}{p H} \int_{N_{terms}}^{\infty} \left| \frac{1 - \frac{x^2}{2!} + \frac{x^4}{4!} - \frac{x^6}{6!} + \frac{x^8}{8!} - \dots + i \left( x - \frac{x^3}{3!} + \frac{x^5}{5!} - \frac{x^7}{7!} + \frac{x^9}{9!} - \dots \right)}{|x-x_s|} \right|_{M_{terms}}^{\infty} dn \quad (3.125)$$

where

$$\kappa = \sqrt{\left| \frac{w^2 L_c^2}{c_o^2} - \frac{m^2 p^2 L_c^2}{W^2} - \frac{n^2 p^2 L_c^2}{H^2} \right|} |x - x_s|$$

The sine and cosine series converge very rapidly. This means that, regardless of the values of  $m$  and  $n$ , as long as  $m$  and/or  $n$  are large enough to produce a negative radical, the series will converge and would be delimited by equation (3.125).

### 3.6.3 Numerical experiments on model solution convergence

A more practical method to determine the convergence characteristics of our series solution is to perform some numerical experiments. The numerical experiments will determine the number of terms necessary to obtain convergence as a function of position and source frequency. In this section, the results of these experiments are presented.

Figure 3.2 shows results of numerical convergence experiments. The graphs show the sound pressure level calculated at microphone position 1a (see Figure 4.22) assuming no volumetric damping and zero specific acoustic admittance. The dipole source strength was estimated assuming that it is produced by a 6.35 mm cylinder at the center of a 2.5 x 38.1 mm duct. The flow velocity was estimated using a constant Strouhal number of 0.21. The fluid density was fixed at 1.3 kg/m<sup>3</sup> and the speed of sound was set constant at 345 m/s.

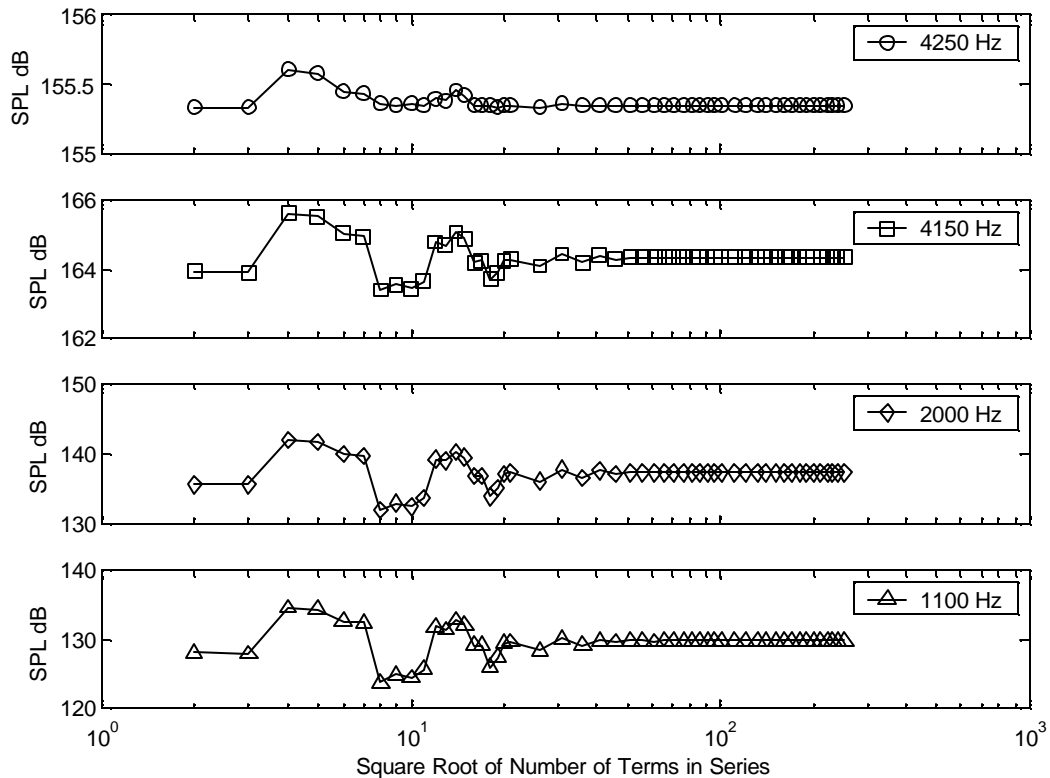


Figure 3.2 Analytic series solution convergence assuming a point dipole produced by 6.35 mm cylinder at center of 2.5 x 38.1 mm duct. Calculations performed at microphone position 1a (see Figure 4.22).

Figure 3.3 is similar to Figure 3.2 except that in this case the numerical convergence experiment was performed for microphone position 2a. For position 2a, which is further away from the dipole source, the number of terms drops significantly, as seen in Figures 3.2 and 3.3. Another feature of the solution is that there is less variation in the sound pressure level (SPL) results for position 2a than 1a. Both of these trends continue for positions further away from the dipole source. Acoustic pressure or phase angle could have been plotted in Figures 3.2 and 3.3 instead of sound pressure level with similar results.

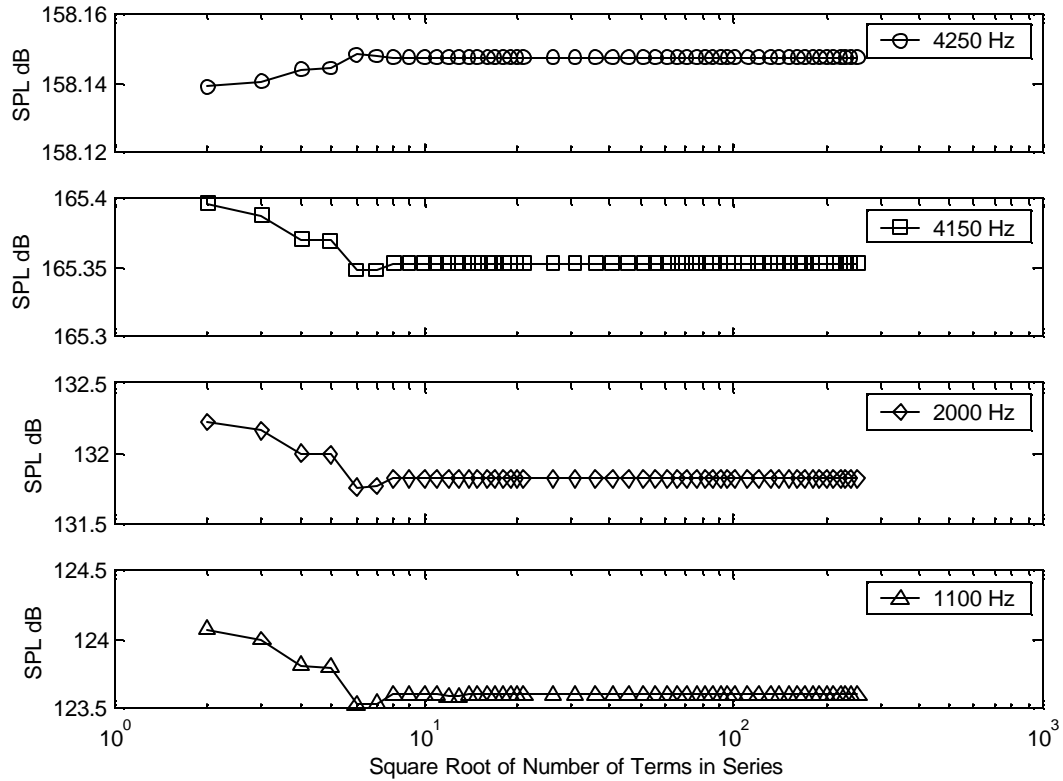


Figure 3.3 Analytic series solution convergence assuming a point dipole produced by 6.35 mm cylinder at center of 2.5 x 38.1 mm duct. Calculations performed at microphone position 2a (see Figure 4.22).

To avoid errors associated with using fewer terms than required to obtain convergence at the positions of interest and at the same time to reduce computation time by not using more terms than required, the programs used to solve the analytic series solutions initially assumed that a solution was reached when the sound pressure level estimated at a particular point did not change more than 0.01 dB from the solution with  $(N_{\text{term}})^2$  to the solution with  $(N_{\text{term}}+1)^2$  where  $N_{\text{term}}$  represents the number of terms in each of the two sums in the infinite duct solution. This technique is not perfect and is slower than simply choosing a fixed number of terms in the summation. After some experimentation, it was decided to fix the number of terms to  $30^2$  for positions close to the cylinder (position 1a in Figure 4.22) and  $10^2$  terms for other positions.

Figures 3.4 and 3.5 show contour plots of the sound pressure level and square root of number of terms required for convergence using the criteria defined above. The results were obtained assuming the same source strength and fluid properties as those used to obtain the results of Figure 3.2 and 3.3. The source frequency in this case is 4 kHz. The duct width is represented by  $L_c = 38.1$  mm.

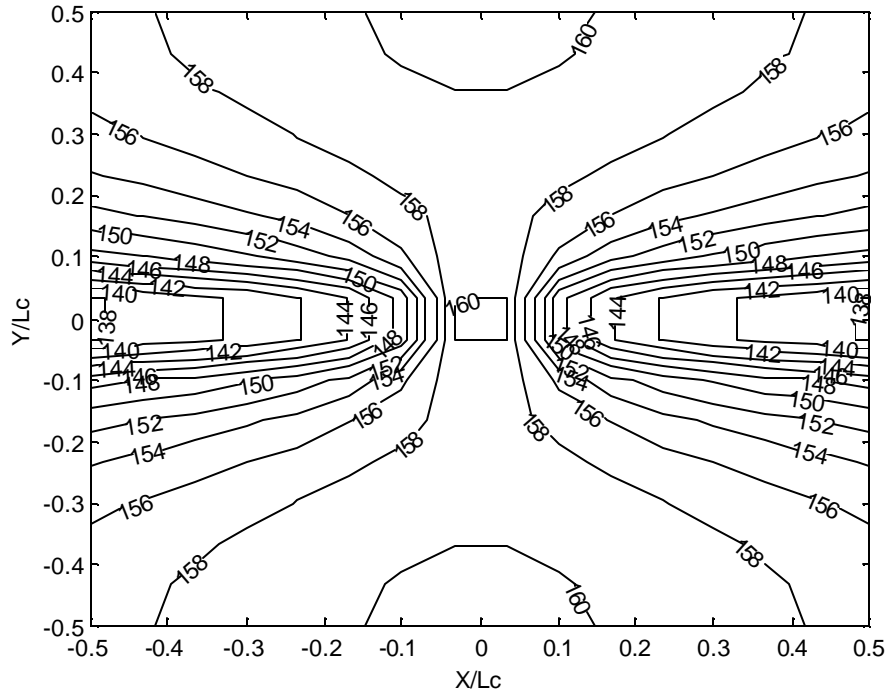


Figure 3.4 Acoustic field predicted by model (SPL dB). Source strength estimations made assuming 6.35 mm cylinder at center of 2.5 x 38.1 mm duct. Solutions obtained at the wall. Graph made by interpolation of results obtained at a 16 x 16 matrix of equally spaced points in the plane of interest.

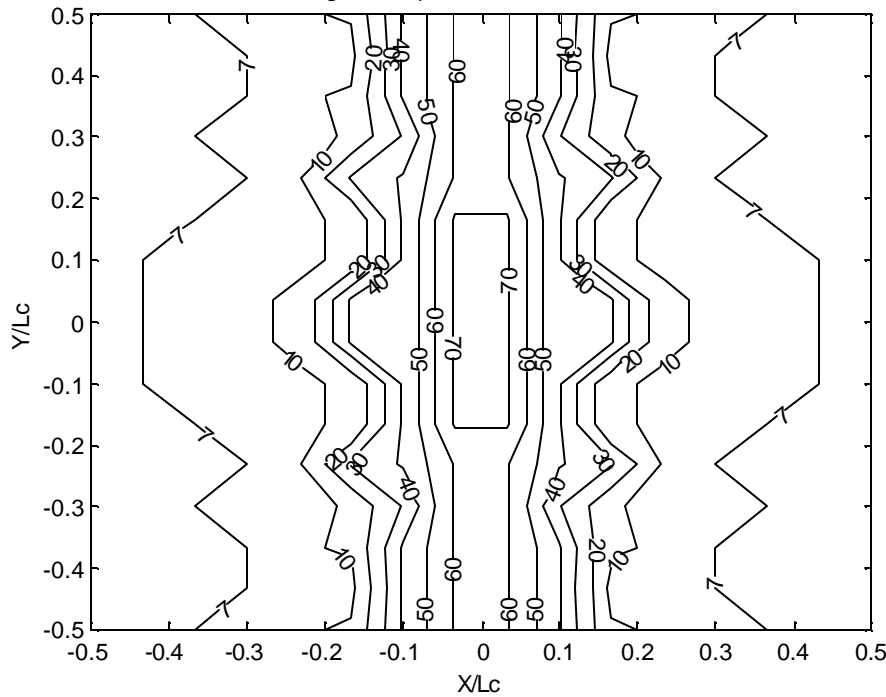


Figure 3.5 Square root of number of terms needed to obtain solutions presented in Figure 3.4.



### 3.6.4 Comparison to a finite element solution from the literature

Eversman and Steck developed a finite element formulation to obtain the acoustic field produced by acoustic singularities in one and two dimensions. In their paper, they compare the results of their numerical formulation to results of analytic series solutions. The results of their numerical procedure agree very well with the exact results of the series solution as presented in their work.

Figure 3.6 shows the results of comparing the solution of the model presented here for a unit dipole at the center of the two-dimensional duct after the required simplifications have been introduced to results presented by Eversman and Steck. Figure 3.6 shows the real and imaginary parts of the acoustic pressure at  $Y/L_c = 0$  for different values of  $X/L_c$ . In this particular solution,  $Y/L_c = 0$  represents a duct wall, not the center of the channel. As can be seen in the figure, the solutions are identical.

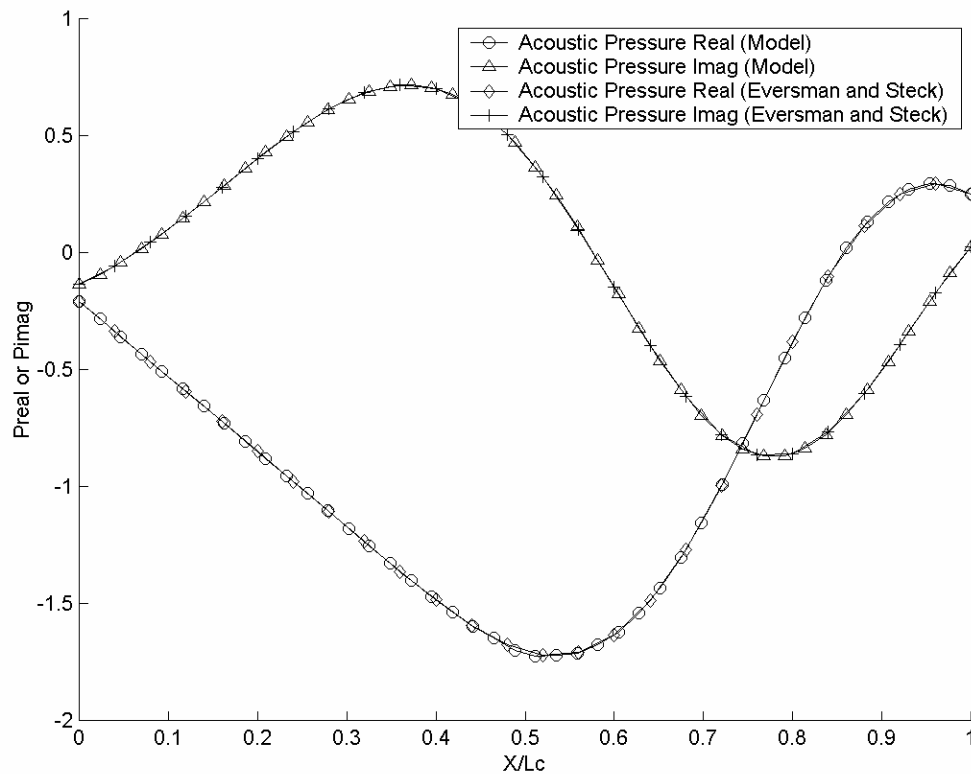


Figure 3.6 Comparison between analytic solution from Model and Eversman and Steck finite element and analytic solution. Unit source at  $X/L_c = Y/L_c = 0.5$  (center of domain),  $k_{L_c} = 8.06$ ,  $M = 0.3$ ,  $Y/L_c = 0$  (at domain boundary) for different values of  $X/L_c$ . X in flow direction, Y in width direction. (2 dimensional formulation)

## Chapter 4: Experimental Apparatus, Test Specimens and Data Analysis

### 4.1 Introduction

In this chapter, three different experimental setups that were used in this work will be presented.

Initially, it was not clear what caused the tonal noise produced by plate heat exchangers. There was speculation that the broadband noise produced by the thermal expansion valve could be exciting an acoustic or structural resonance that was responsible for the tonal noise [Rodarte et al. 1998a, 1999b]. Additionally, the reports of the tonal noise produced by this type of heat exchanger indicated that this phenomenon occurred only transiently in the field and only during extreme operating conditions. Therefore, initially the experimental setup was used to 1) reproduce the tonal noise 2) determine the cause of the tonal noise, and 3) study the phenomena. Later, the need to study different array configurations and to isolate the flow-induced noise characteristics produced by short aspect ratio cylinders in cross-flow inside a rectangular channel and to correlate these results with the proposed model made necessary the use of different experimental setups and fluids.

Additionally, in this chapter the test samples will be described, as well as the sensor calibration and data uncertainty analysis.

### 4.2 Description of R134a refrigerant (1,1,1,2 tetrafluoroethane) experimental apparatus

The main objective of the R134a test set up is to maintain the required state (pressure, temperature, and superheat or quality) at the inlet of the plate evaporator sample under test. The schematic of the experimental facility which consists of a continuous flow system designed initially for expansion valve studies around a diaphragm pump and a number of coaxial heaters and heat exchangers is shown in Figure 4.1.

A high head diaphragm pump instead of a compressor is used to move the refrigerant. A pump was used since it gives more freedom in choosing the refrigerant and the oil. During our tests, only pure R134a refrigerant (1,1,1,2 tetrafluoroethane) was used. The first array of heaters after the pump was used to vaporize the refrigerant in order to reduce pressure pulsations. The refrigerant was re-condensed in the subcooler before entering the Coriolis mass flow meter. A second array of heaters was then used for conditioning the refrigerant before entering the expansion device. The flow rate was controlled by the expansion device (typically an orifice tube), refrigerant bypass and heater settings.

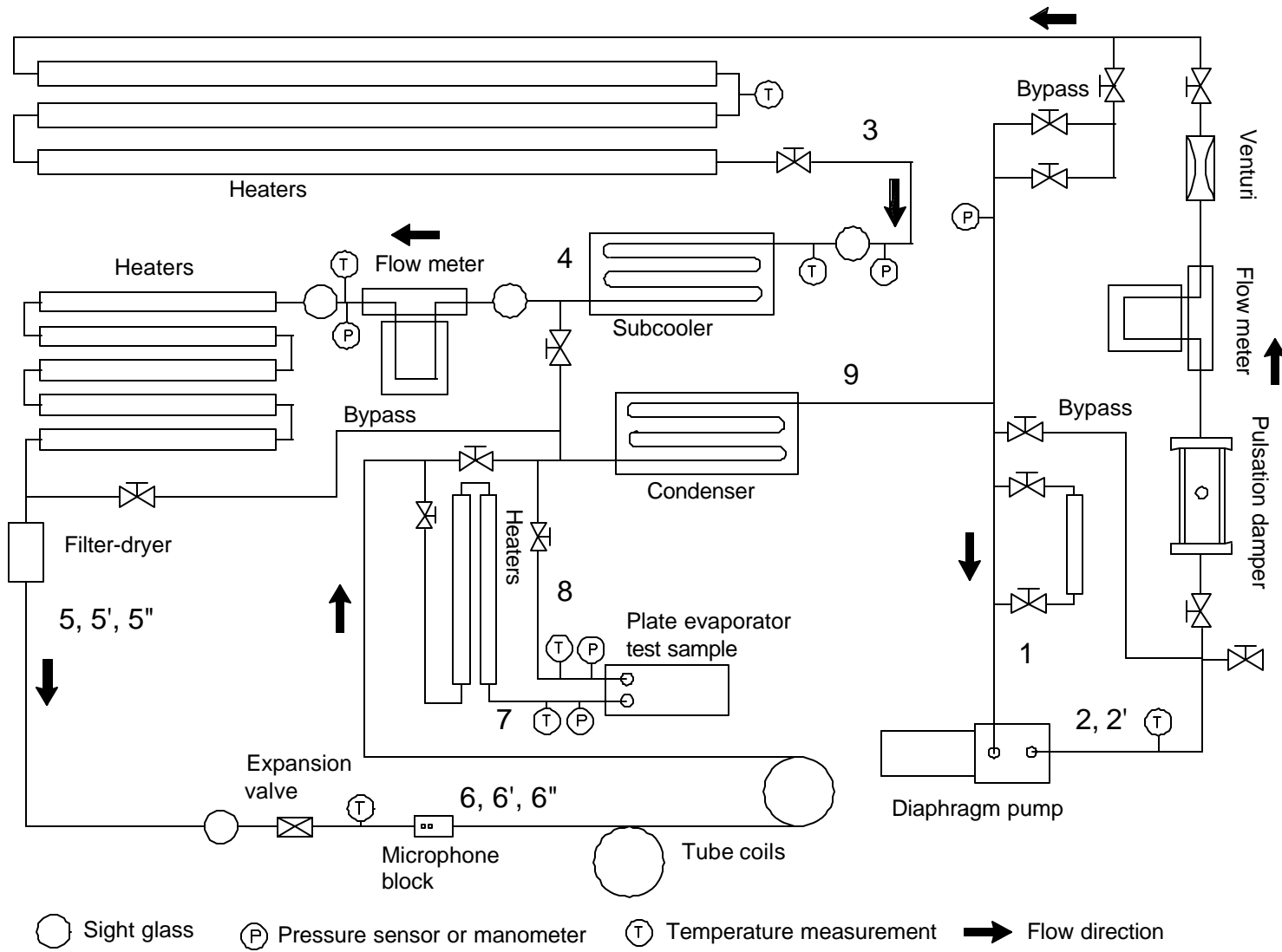


Figure 4.1 Schematic of R134a refrigerant experimental setup.

Figure 4.2 shows the pressure-enthalpy diagram of the refrigerant as it flows through the test section. The diaphragm pump moved subcooled liquid from state 1 to 2 (state 2' represents an ideal, isenthalpic, process). The first array of heater then heated and evaporated or partially evaporated the refrigerant to state 3. Point 3 could be superheated or in the two-phase region. This arrangement significantly reduced the pressure pulsations created by the diaphragm pump. Vapor was then condensed and sufficiently subcooled in the subcooler to ensure single phase liquid flow through the mass flow meter (state 4). The next array of heaters adjusted the refrigerant state prior to the expansion device. Depending on the condition after these heaters, the refrigerant could be subcooled, two-phase, or superheated (5'', 5', or 5, respectively). Similarly, after expansion, the refrigerant could be in the two-phase region (6'', 6') or more typically in the superheated region (6). Between state 6 and 7 there were two small heaters that could further superheat the refrigerant. The plate heat exchanger test section creates a significant pressure drop. At the same time, the refrigerant can be further superheated in the plate heat exchanger sample. The process in the plate heat exchanger test sample is shown with line 7 - 8. Between points 8 and 9 lies a condenser that brings the refrigerant back to the liquid state. Further subcooling is achieved in the pump subcooler which brings the refrigerant back to the state 1.

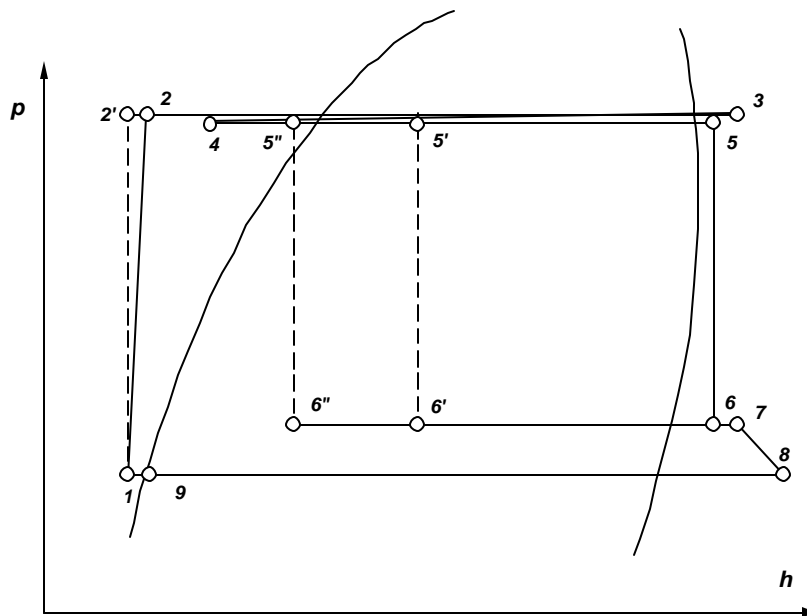


Figure 4.2 Pressure-enthalpy diagram of refrigerant as it travels through the refrigerant test setup.

### 4.3 Description of nitrogen experimental apparatus

Tests with refrigerant require significant time for sample preparation, and the experimental apparatus is difficult to operate. For these reasons, an alternative testing technique was necessary. A nitrogen blow-down facility proved to be a good approach to further study the flow-induced noise phenomena under a wider range of conditions. A schematic of the nitrogen blow-down experimental setup can be seen in Figure 4.3. The nitrogen experimental setup proved more flexible than the refrigerant setup because the test samples were not required to hold the significant pressures present when using refrigerant. This factor permitted the test of a wider range of

concepts since test samples could be made using a stereolithography technique available at the University. Additionally, this setup is much simpler than the R134a refrigerant setup principally because this is an open loop (i.e., nitrogen is released to the atmosphere). This loop is extremely simple to use and reaches a steady state condition in just a few seconds in comparison with the R134a facility which needs between 1-2 hours to reach steady state conditions.

In this experimental setup, nitrogen at very high pressures (up to 2500 psig) is expanded using a pressure regulator to control the flow rate. During expansion nitrogen temperature is brought back to ambient conditions by passing the nitrogen through a very large heat exchanger. This permits the use of a constant speed of sound for all the tests at any flow rate. In contrast, during refrigerant testing, the speed of sound varies considerably between tests due to the different refrigerant superheated conditions, and therefore, this parameter has to be considered for each test.

After the heat exchanger, two independent mass flow measurements were made using a Coriolis mass flow meter and a Venturi flow meter. This two-mass flow meter configuration was used only for a brief period of time to calibrate the Venturi flow meter. Temperature and pressure measurements upstream of the Venturi flow meter were taken to estimate fluid density necessary to determine the mass flow rate. During tests, there is typically a very significant pressure drop from the inlet to outlet of the plate heat exchanger samples. This condition creates gradients in fluid density and therefore flow velocity along the length of the plate. The severity of the gradients increases as the mass flow rate increases.

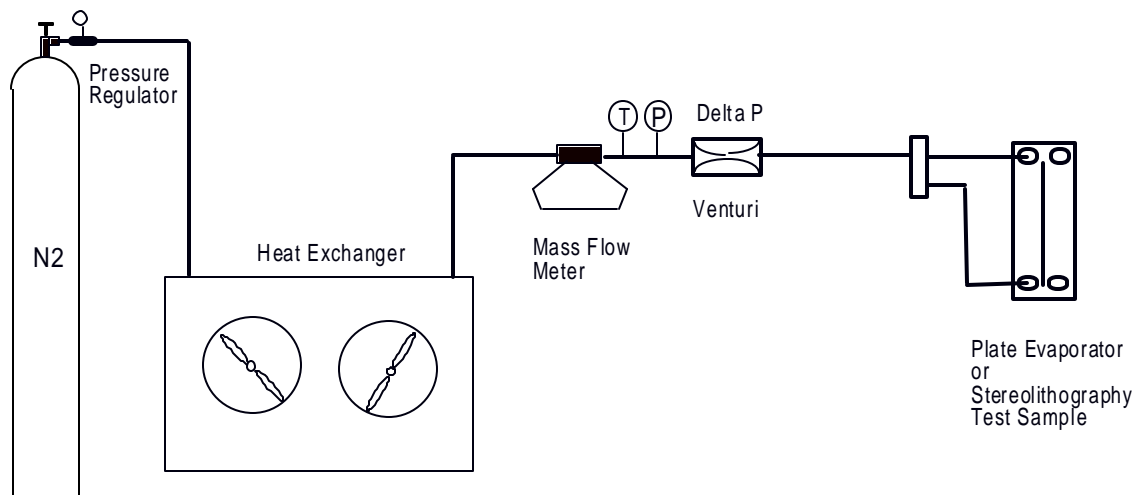


Figure 4.3 Schematic of nitrogen experimental setup.

#### 4.4 Compressed air experimental apparatus

##### 4.4.1 Introduction

The refrigerant and nitrogen experimental facilities were used initially to test plate heat exchanger and stereolithography samples. Due to the geometry of these samples, there was no need to condition the flow upstream of the test section since the conditions used were similar to the conditions of operation of these heat exchangers. Additionally, the very compact array of cylinders or flow obstructions in the plate heat exchanger

and stereolithography samples was expected to produce uniform flow through the arrays. In order to test our hypothesis that the sound from short aspect ratio cylinders can be modeled as a point dipoles inside a duct, it was necessary to make a new experimental apparatus in which the flow upstream of the cylinder or cylinder arrays was fully developed and uniform. Additionally, it was desirable that other noise sources inside the wind tunnel be eliminated or reduced. A further improvement of the experimental setup involved the use of compressed air instead of nitrogen. As noted above, nitrogen testing has some advantages over refrigerant testing. Compressed air, in addition to having the same advantages as nitrogen has, the additional advantage that it is directly produced in the Mechanical Engineering Laboratory building and the very large capacity of production and storage permits running our experiments at large flow rates for as long as required.

#### 4.4.2 Description of compressed air experimental apparatus

The compressed air experimental apparatus is similar to the nitrogen setup, except that when air is used there is no need to have a heat exchanger after the air is expanded (see Figure 4.4). The apparatus uses a Venturi flow meter. Pressure and temperature measurements are taken as shown in Figure 4.4.

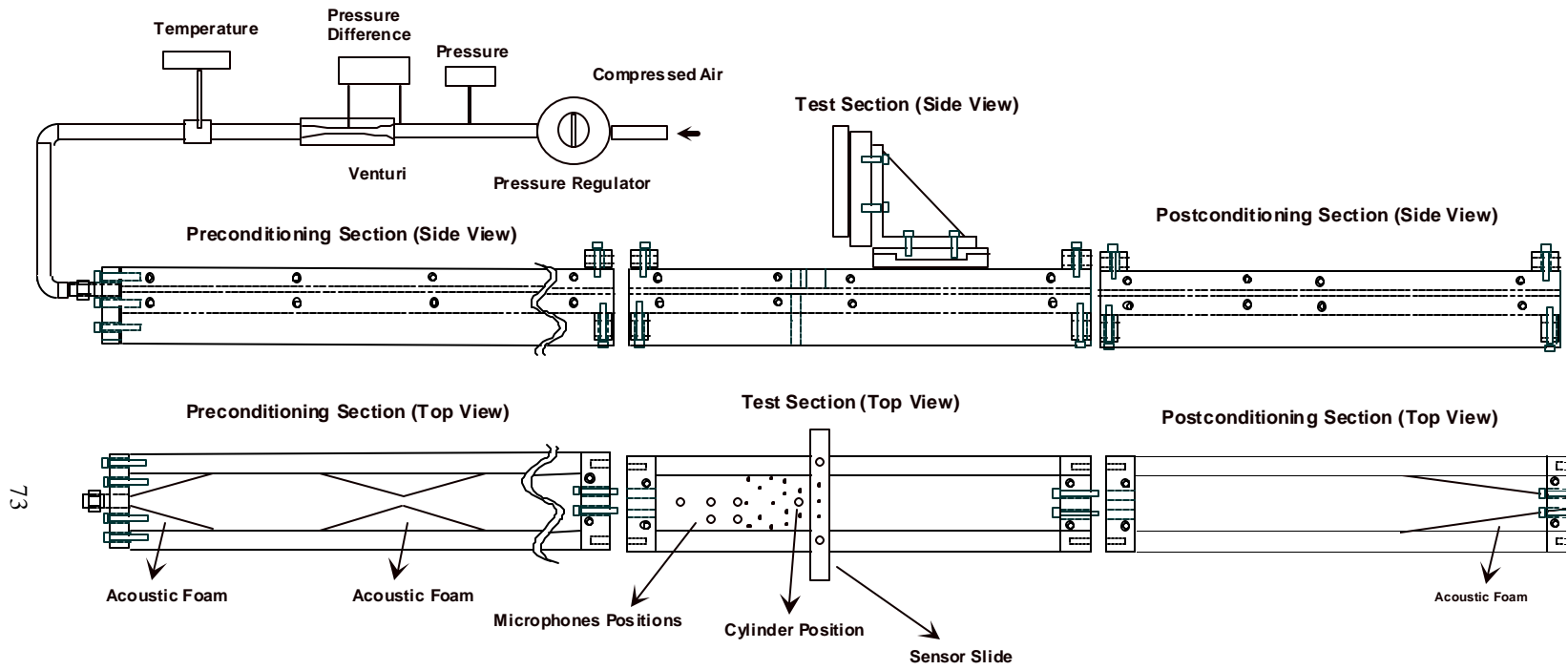


Figure 4.4 Compressed air experimental apparatus

After the flow meter, the air enters a series of rectangular duct sections of dimensions similar to a plate heat exchanger's refrigerant passages. These rectangular duct sections have a width of 38.1 mm (1.5 inches) and can have a height of 2.5, 5, 7.5, 10 or 15 mm. The first of these sections is the preconditioning section. This section measures 1.5 m in length. The length to height ratio of the preconditioning test section is 600 assuming a height of 2.5 mm. This length to height ratio is well above the recommended ratio of 100 suggested for achieving fully developed flow in the test section [Niederschulte]. The purpose of this section is to provide fully developed flow and to eliminate flow-generated noise from upstream disturbances. Following the preconditioning section, a test section can be mounted. Two different test sections have been constructed. One permits the following measurements: velocity profile across the test section with a miniature Pitot tube, acoustic field of single cylinders and cylinder pairs, acoustic impedance of different duct terminations or materials, and hotwire measurements. Figure 4.5 shows a photograph of this test section. The other test section has been designed to take acoustic pressure and static pressure measurements at different fixed positions along the channel of stereolithography prototypes. This test section will be described in section 4.6. Initially, an additional duct section called the postconditioning section was installed after the test section. The purpose of the postconditioning test section was to eliminate any possible sound reflections from the duct discontinuity where the air is discharged to the atmosphere. This section limited the flow velocity of the wind tunnel. For this reason, tests were made to measure the acoustic field at different microphone positions with and without the postconditioning section to determine the effects of sound reflections from the wind tunnel termination. No noticeable changes in the acoustic field were observed at the flow velocities tested. For this reason this section was not used.



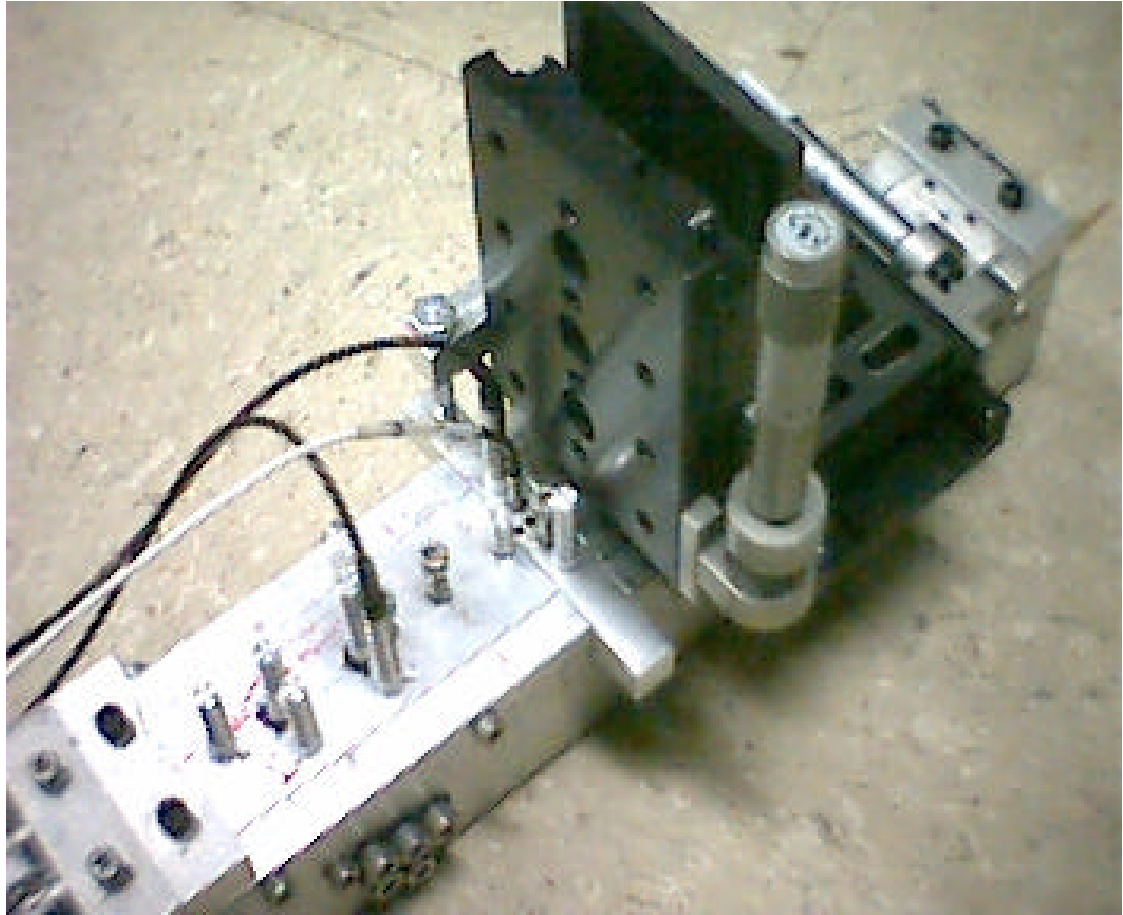


Figure 4.5 Photograph of one of the two compressed air experimental test sections.

#### 4.4.3 Anechoic terminations used in the wind tunnel

The preconditioning and postconditioning sections were designed to approximate infinite duct conditions. During real tests, there are two ways to establish infinite duct conditions: 1) use long duct sections [Rodarte et al. 1999b], or 2) introduce anechoic terminations. In our experimental apparatus, anechoic terminations could be introduced in the preconditioning and postconditioning test sections without the need of long sections. Long sections cannot be used downstream since they will limit significantly the flow velocities at the test section. Later, as mentioned above, it was found that the anechoic termination downstream of the test section also limited the flow velocity. The tests described above showed that the test section itself is long enough for the termination reflections to not be important, even at resonance conditions. This could be the result of the directivity of the dipole source term normal to the wind tunnel exit. On the other hand, the noise produced by the contraction where the air enters the rectangular section produces plane waves that can interact with the cylinders at the test section and could reflect from the wind tunnel termination. For this reason, anechoic terminations could still be needed to precondition the flow before the test section. Anechoic terminations upstream of the test section, even if not needed, would not affect measurements or limit the wind tunnel operation range. To select the anechoic terminations used in the preconditioning and postconditioning sections, testing of different possible acoustic foam terminations was performed using a modified version of the compressed air experimental

apparatus. To measure the specific acoustic impedance of these terminations, the technique of Chung and Blasser 1980a,b that has become an ASTM standard was used [ASTM standard E 1050-90]. An innovative approach was used to generate the required sound source. Instead of using a speaker, which for this geometry is impractical, the noise source employed was an orifice tube that is used as an expansion valve in automobile air conditioning applications. This type of noise source produces white noise at high sound pressure levels [Rodarte et al. 1999a,b], and its size proved ideal for this application. Very good results were obtained using acoustic foam wedges. The acoustic foam wedges were bonded to the side of the test section and did not touch at the center. The foam termination used consists of two wedges 12 cm long placed against the walls of the 2.5 x 38.1 mm rectangular duct. The wedges do not touch at the center of the duct to permit the flow of air more freely. For this reason, they are separated 1.5 cm at the center. Appendix A describes in detail the experimental apparatus as well as the equations necessary to estimate the acoustic properties of different terminations.

#### 4.4.4 Flow velocity inside the wind tunnel

The flow velocity distribution inside the test section is an important parameter in this investigation for several reasons. The frequency of vortex shedding from cylinders and bluff bodies in general is directly proportional to flow velocity. Cylinder Strouhal number estimations are typically made using uniform flow upstream of the test cylinders [see, for example, Keefe]. In our case the cylinders have very short aspect ratios, and they are immersed inside a very small wind tunnel. This means that the cylinders would be subject to a nonuniform velocity profile along their length, and the determination of the velocity profile is necessary to understand their flow-induced noise behavior. Flow velocity is also a dominant flow variable needed to predict the dipole sound emitted from cylinders as can be seen in equation (3.31).

Measurements of the flow velocity profile inside the 2.5 x 38.1 mm wind tunnel section were taken using a very small Pitot tube. The Pitot tube was made using 24 gauge Luer lock type syringe needles. Figure 4.6 shows the positions at which the flow velocity measurements were taken. The Pitot tube was calibrated by area-averaging the flow velocity readings and comparing this flow velocity with the average flow velocity estimated from mass flow measurements. The Pitot tube calibration constant determined from this procedure was found to be in agreement with typical Pitot tube calibration constants [Miller 1996].

Five different flow velocity profiles were measured using compressed air at Reynolds numbers (based on half the duct height and average velocity) of 2125, 3170, 4415, 5860, and 7280. Figure 4.7 shows the flow velocity profile for the largest Reynolds number (the rest can be found in Appendix B). Nitrogen was also used to measure the velocity profile at the center of the test section. Five different measurements were made at Reynolds numbers of 1540, 2660, 3915, 5240, and 6115. The results from the air and nitrogen tests do not deviate significantly from each other for any value of the Reynolds number. For this reason, only the results for three Reynolds numbers were plotted in Figures 4.8 and 4.9.

Figure 4.8 compares the results from three different sources that cover from the parabolic regime at a Reynolds number of 790 to the fully turbulent regimes for Reynolds numbers above approximately 1300. The Reynolds number used by Laufer 1950 and Hussain and Reynolds 1975 was based on the maximum velocity, while the one used by Patel and Head 1969 was based on the average velocity. The discrepancies in the definitions of Reynolds number could modify its value in the order of 20 percent. These variations are not

significant enough to change Figure 4.8 appreciably. The test section used by Laufer measured 152.4 x 12.7 cm. Hussein and Reynolds test section measured 114.3 x 6.35 cm and Patel and Head test section measured 30.48 x 0.635 cm. The test section aspect ratios are 12, 18, and 48 respectively. Our test section has an aspect ratio of 15.24.

Figure 4.9 compares some of our measured velocity profiles to velocity profiles determined using the logarithmic overlap law [White]. As can be seen, the logarithmic overlap law describes very well the turbulent flow velocity profile inside the test section.

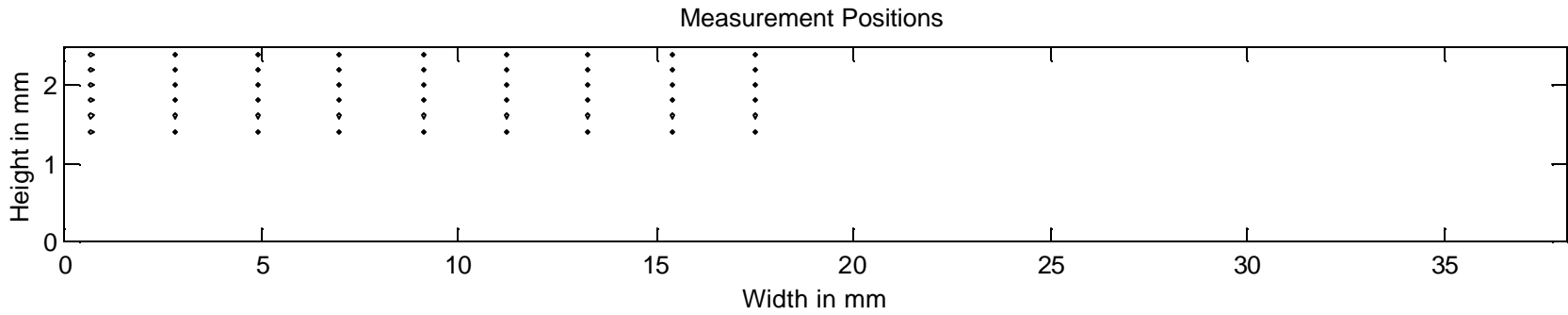


Figure 4.6 Schematic showing flow velocity measurement positions (black dots) in wind tunnel test section. Height (z direction) and width (y direction). Height scale twice width scale.

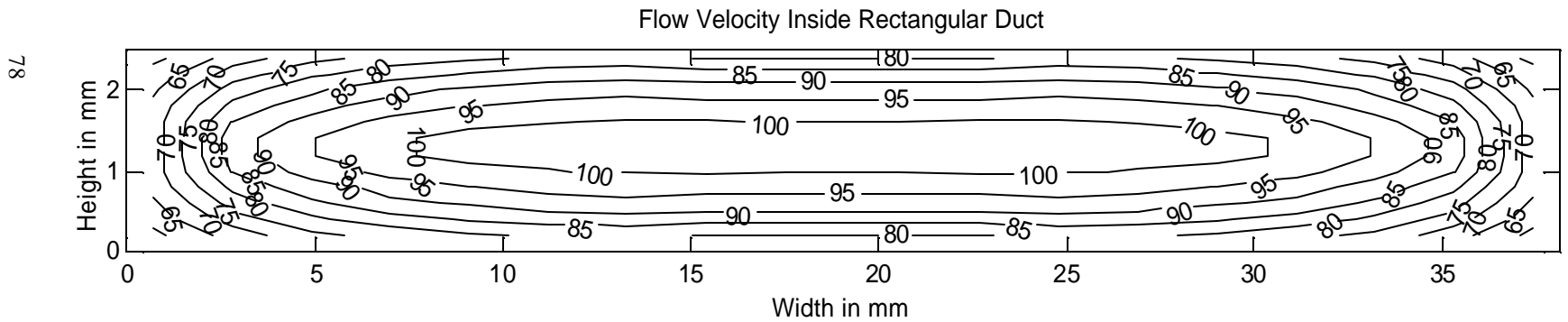


Figure 4.7 Contour plot showing velocity profile measured using compressed air at a Reynolds number (based on half the duct height and average velocity) of 7280. Height scale twice width scale. Contours in m/s.

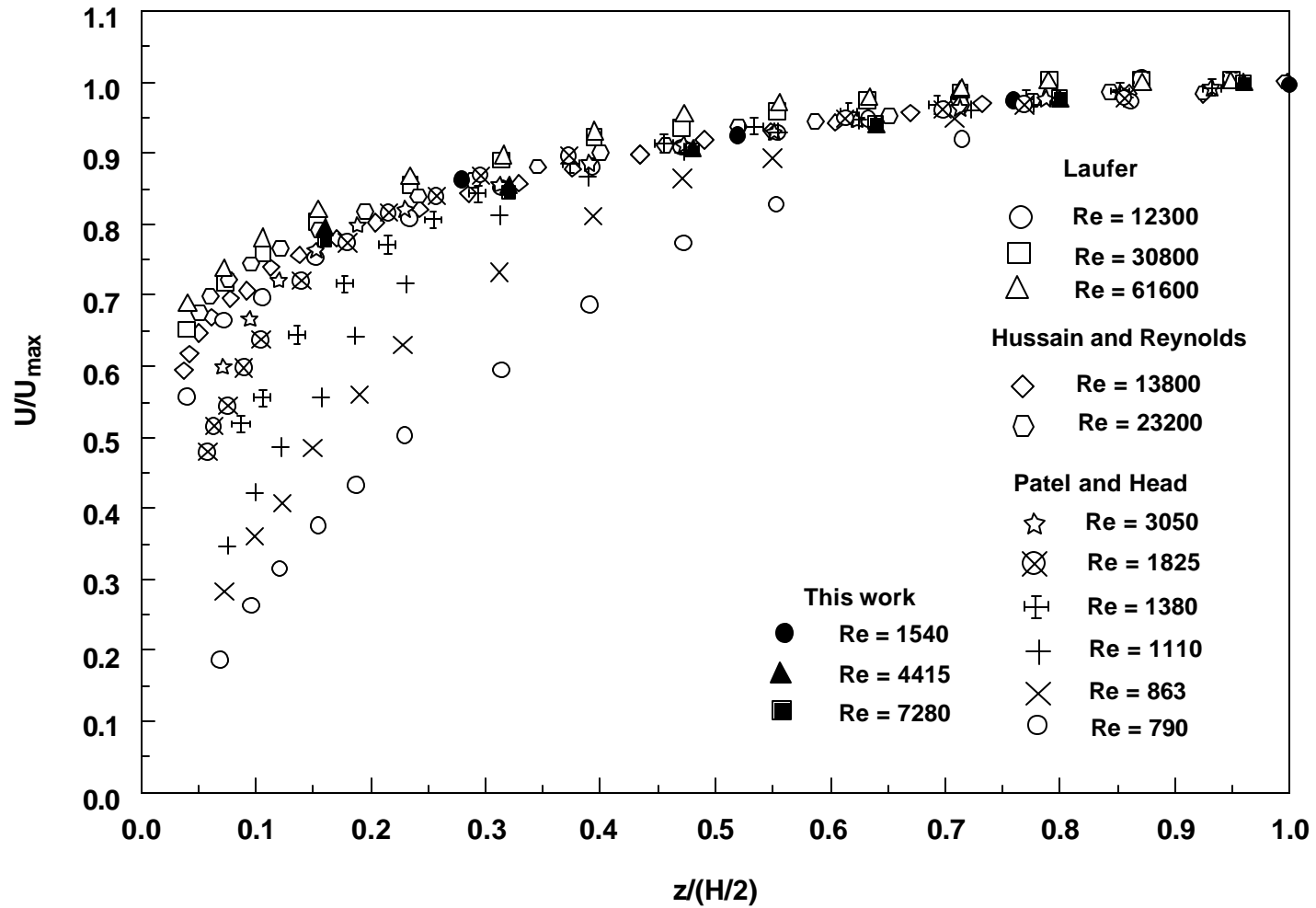


Figure 4.8 Velocity profile comparison of measurements taken inside our test section and results from the literature. Solid triangles and squares overlap.

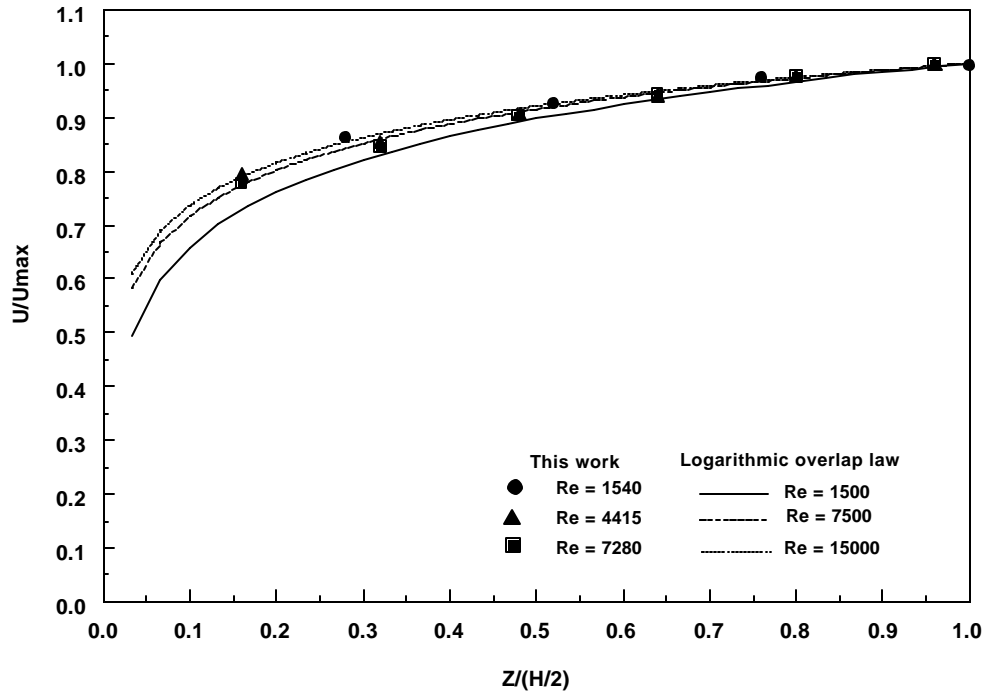


Figure 4.9 Comparison of velocity profile measurements with theoretical predictions using the logarithmic overlap law. Measurements at center of channel and along the channel height ( $z$  axis). Solid triangles and squares overlap.

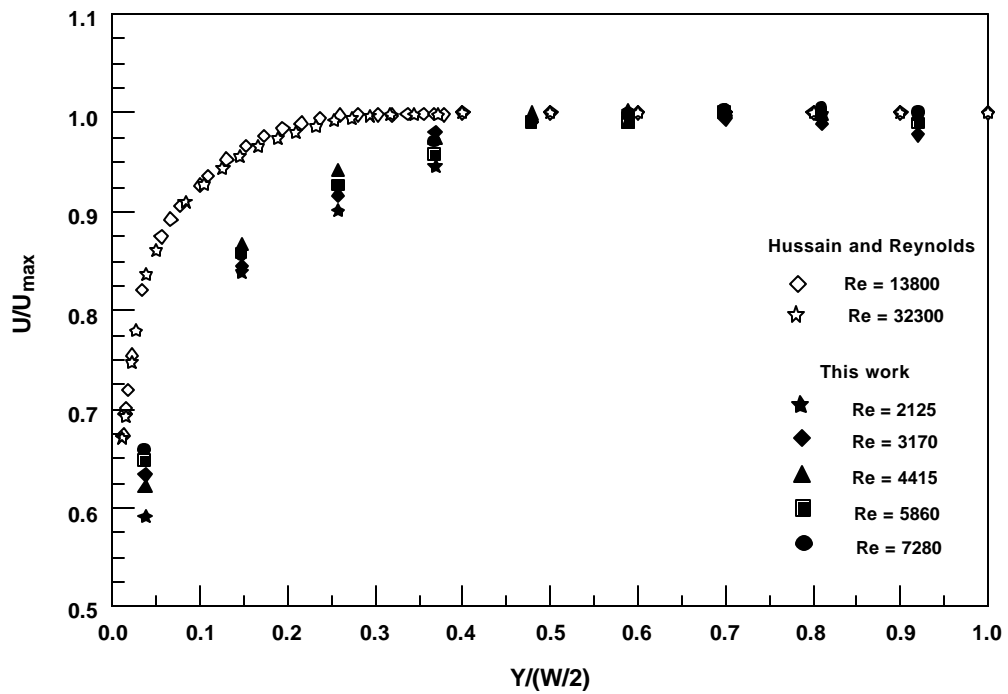


Figure 4.10 Comparison of velocity profile measurements at center of channel and along the channel width ( $y$  direction).

Figure 4.10 shows the velocity profile at the center of the duct in the width direction. Our results are compared to results presented by Hussain and Reynolds. Hussain and Reynolds measured the velocity profiles at three different values of Reynolds number. Figure 4.10 plots the velocity profiles for the lower and higher Reynolds numbers. As can be seen, there is no significant variation in the velocity profiles. No velocity profiles in the width direction at lower Reynolds numbers were found.

Appendix B complements the material presented here and presents in detail the procedure, data and plots of the velocity profiles measured in our test section.

## **4.5 Description of plate heat exchanger test samples**

### 4.5.1 Introduction

Originally, plate heat exchangers were designed for liquid-liquid operation. These heat exchangers exhibit excellent performance. Their compact size and reduced system charge were the driving forces that prompted the modification of this type of heat exchanger for automobile applications. When this type of heat exchanger is used in an air conditioning system, it is subjected to conditions that can cause the refrigerant to flow as a gas, especially during transient operation in a hot environment. Gaseous refrigerant flow can produce acoustic resonance in these heat exchangers.

Flow-induced resonance in plate heat exchangers was first investigated by placing accelerometers on the outside of the test samples. Later, when suitable sensors were found, direct measurements of the dynamic pressures inside the samples were made. A description of how test samples were made follows.

### 4.5.2 Dynamic pressure measurements

Plate heat exchangers as shown in Figure 1.2 (Chapter 1) are formed by stacking a number of stamped plates together and placing fins between them. The assembly is then brazed in a high temperature oven. Figure 1.3 shows some typical stamped single plates used to make this kind of heat exchangers. The refrigerant flow passages are formed by stacking these plates one facing another. The fins are brazed on the exterior of this channel. Refrigerant flows through the cavity formed between these plates while air flows through the fins outside of these plates. Dimensions of the duct where the refrigerant flows are very small, of the order of 2 x 40 mm with lengths of around 300 mm. The full evaporator consists of many of these sections. When these sections are joined, the two stamped protrusions in contact at their tops join to form an "hourglass" shaped cylinder. Plate heat exchangers of the design shown in Figure 1.3 therefore consist of arrays of cylinders that have a nonconstant cylinder diameter along the cylinder axis. The flow-acoustic behavior of this type of cylinder is discussed later. Figure 4.11 is a photograph of a cross section of a plate heat exchanger that shows the "hourglass" shaped bluff bodies as seen from the flow inlet header.

Since the plate heat exchangers consist of many sections, in order to isolate the problem and study it in more detail tests samples consisting of a single refrigerant passage were cut from a full heat exchanger. In order to attach the dynamic pressure transducers to measure the acoustic pressure in the refrigerant passage the fins brazed to the exterior of the channel were removed. Finally, aluminum blocks were epoxied at different positions in the heat exchanger such that previously drilled holes coincided with the dynamic pressure transducers mounted in the aluminum blocks. The holes drilled to the walls of the passage were of 2.5 mm

diameter. This diameter corresponds to the diameter of the dynamic pressure transducer head that was mounted flush to the wall of the heat exchanger. Figure 4.12 shows a photograph of a typical plate evaporator test sample.

This arrangement permitted the test sample to be tested under significant pressure. This is necessary in order to perform tests with R134a refrigerant. By performing tests using R134a refrigerant as well as nitrogen or air we could compare results obtained using very different fluids.

The fact that these heat exchangers are stamped allows for significantly greater flexibility in the design of the interior structure. The internal structure has multiple functions. It serves as an internal support that permits the heat exchanger to withstand high refrigerant pressures (above 2.75 MPa (400 psig)). It also helps to achieve good refrigerant distribution and good refrigerant side heat transfer.

Some of the more successful stamped plate designs, from a performance point of view, have a design like the ones shown in Figure 1.3 (Chapter 1). However, these designs are among the more problematic designs in terms of flow-induced noise especially during transient operation with gaseous refrigerant flow. Under "normal" operating conditions the refrigerant flows is two-phase. During two-phase operation flow-noise is greatly attenuated and is not normally a problem.

#### 4.5.3 Acceleration measurements

Initially the flow-induced noise problem was studied by placing accelerometers on the outside of test samples. The test samples used were identical to the ones used for dynamic pressure measurements, except that instead of aluminum blocks nuts were epoxied at different positions to mount the accelerometers. Figure 4.13 shows schematics of two different types of test samples. The numbers indicate the positions where the accelerometer measurements were made. Positions starting with the letter S indicate side locations. Measurements were made at these locations since they are the only accessible locations for the full plate heat exchangers.

Acceleration measurements are affected by different parameters such as rigidity of the structure at the accelerometer mounting location and sensor mass. Other problems associated with acceleration measurements include insensitivity and difficulties with studying the phenomena in detail. Additionally, surface vibration might be preferentially excited when acoustic and structural resonances coincide [See, for example, Rodarte et al. 1999a]. For these reasons acceleration measurements were only used until a technique for measuring the internal dynamic pressures was developed.



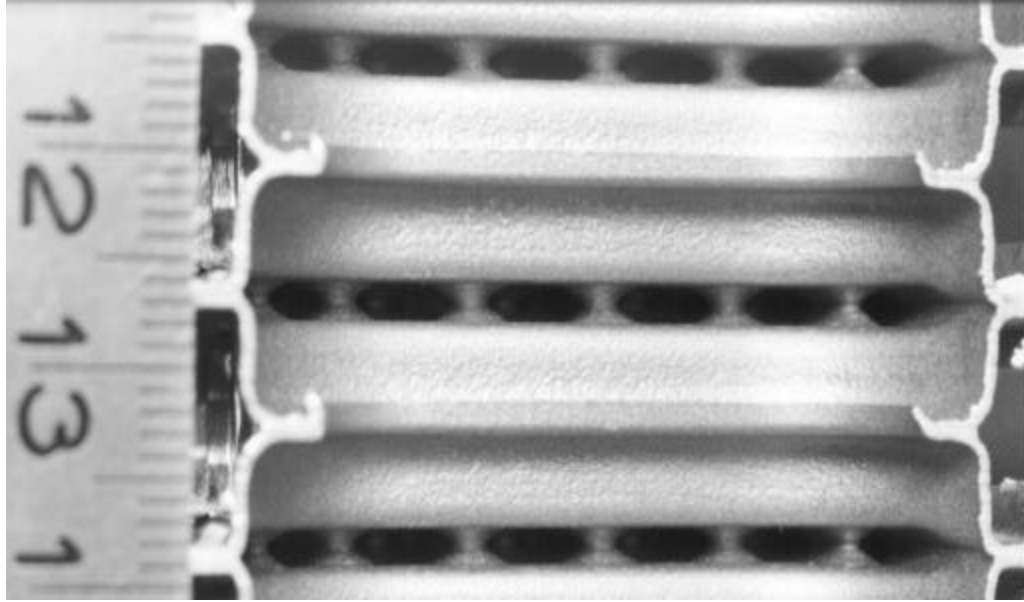


Figure 4.11 Cross-sectional view of a plate heat exchanger used in automobile applications showing “hourglass” shaped cylinders. Cross section made at header location. Ruler graduations at side in millimeters.

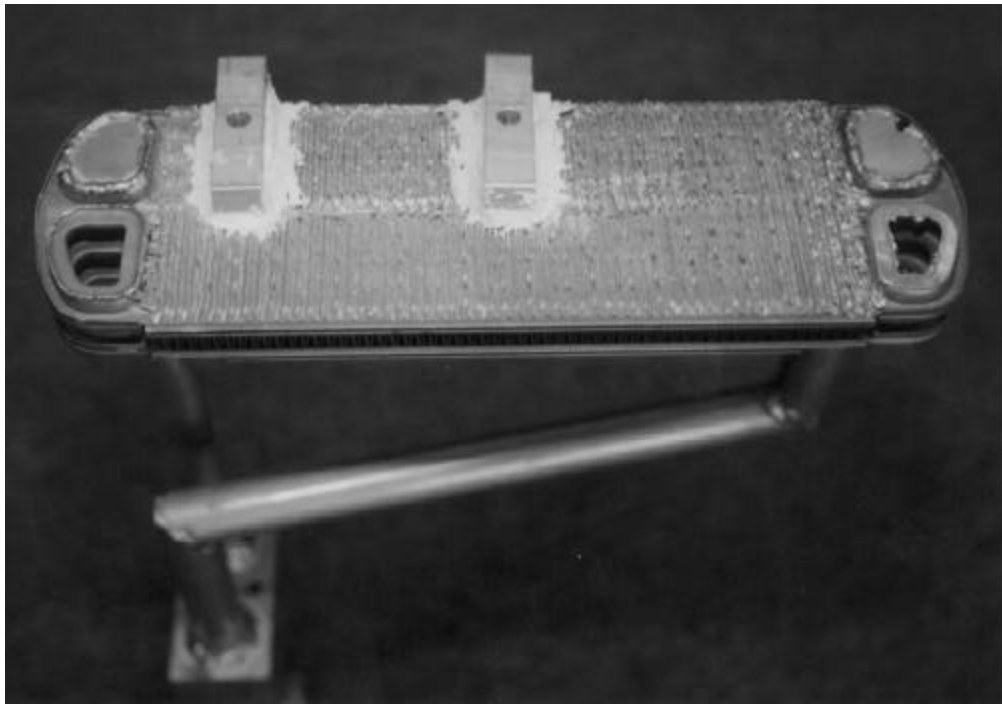


Figure 4.12 Plate heat exchanger test sample showing the positions where the dynamic pressure transducers were mounted.

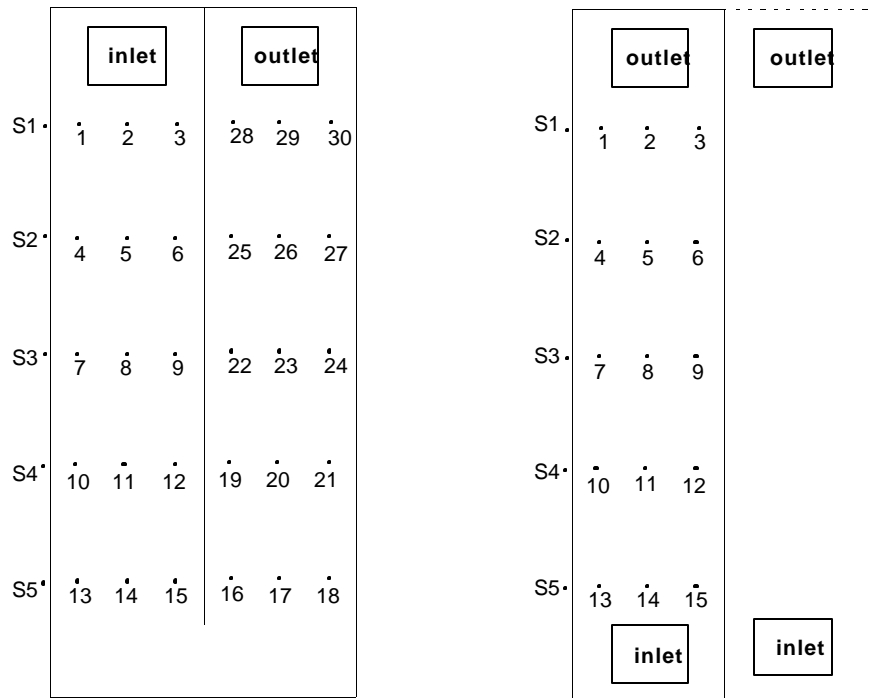
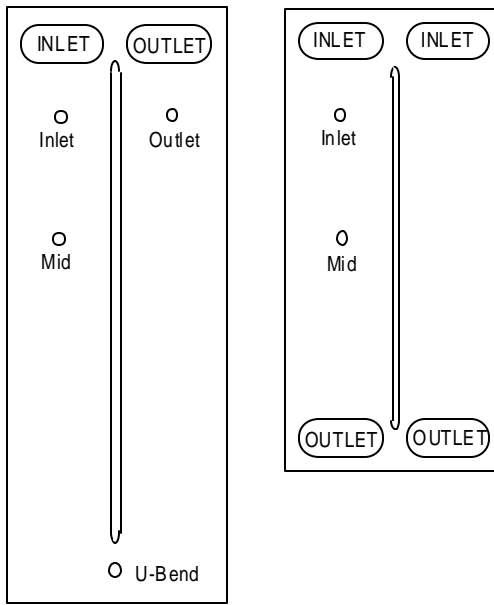


Figure 4.13 Schematic of two types of plate heat exchanger test samples showing the naming convention used for dynamic pressure (top) and acceleration measurements (bottom). The numbers on the bottom diagrams represent positions where accelerometers were mounted. The positions numbered S1-S5 represent side mounted locations.

## 4.6 Description of stereolithography prototypes and the test section

### 4.6.1 Introduction

The complex nature of the flow-induced noise phenomena requires extensive experimentation. Unfortunately, plate stamping is a very expensive process. For this reason it is desirable to find an alternative way to construct prototypes in a fast and inexpensive way. In this case, stereolithography rapid prototyping proved to be a valuable technique. The results of this technique compared favorably to results obtained in real plate heat exchangers [Rodarte et al. 1998b].

### 4.6.2 Stereolithography prototypes and test section

Stereolithography is a technique that creates a prototype layer by layer. The layers are made of a liquid photosensitive resin that solidifies when it is irradiated by a laser light source. Once the resin solidifies, it becomes extremely hard and rigid. Several plate prototypes have been made using this technique. Figure 4.14 shows a drawing of a typical solid model used to create a prototype for testing. Figure 4.15 shows a picture of a finished stereolithography prototype as is mounted on the testing plates.

To test this type of model, two specially designed aluminum covers are placed on the top and bottom of the prototype. The top cover (i.e., the one placed on the open portion of the prototype and in direct contact with the cylinder array) has several holes where dynamic and static pressure can be measured. Figure 4.16 shows a photograph of the top aluminum cover plate. Once the covers are in place, the assembly is aligned with a wind tunnel. A schematic of the wind tunnel can be seen in Figure 4.4. The stereolithography test section replaces the single cylinder test section. After passing through the test section, the fluid is discarded to the atmosphere. For this reason, stereolithography models used in our study have only been tested using nitrogen and air.

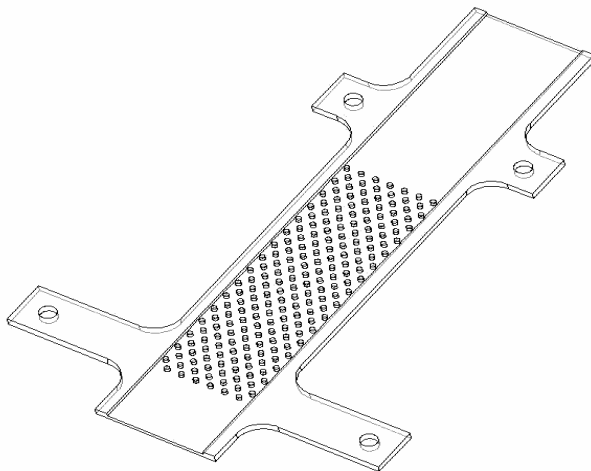


Figure 4.14 Solid model of a typical prototype made using stereolithography.

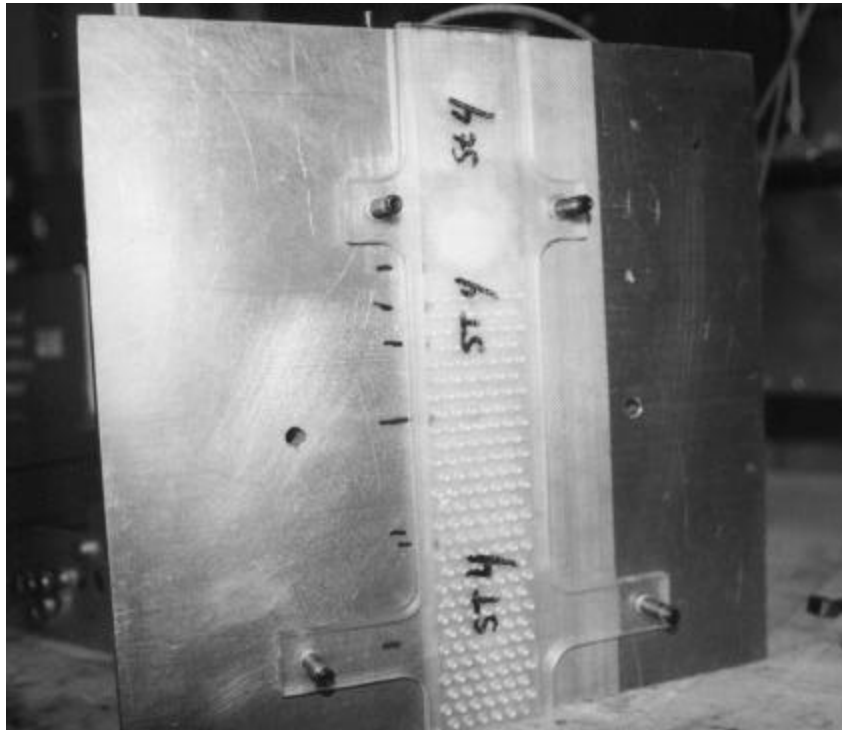


Figure 4.15 Photograph of a finished stereolithography prototype being mounted for testing.

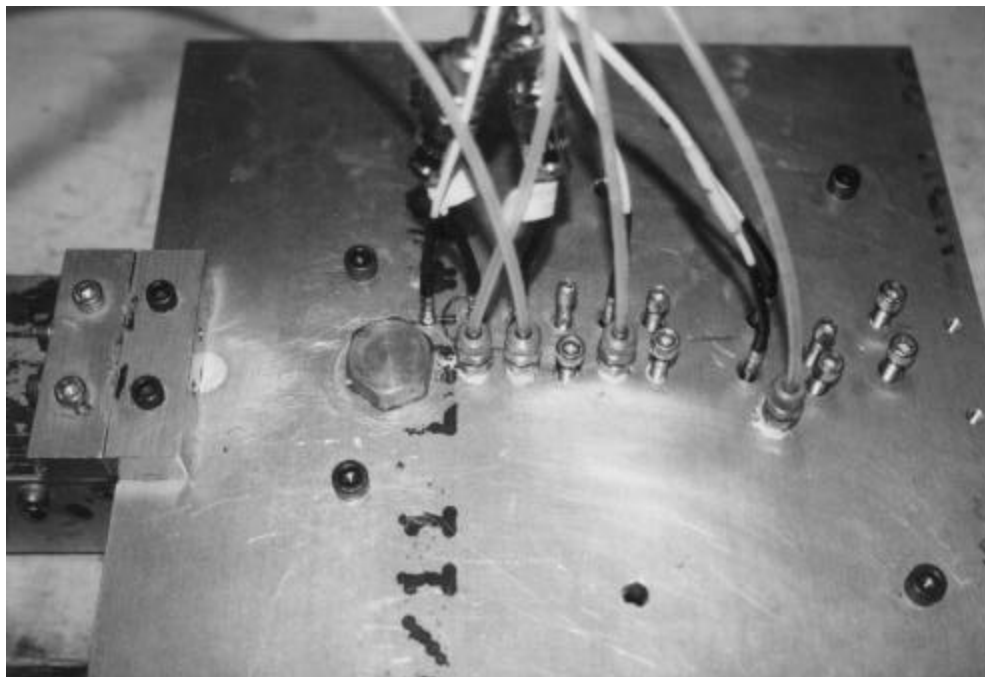


Figure 4.16 Photograph of top aluminum cover plate used to test the stereolithography prototypes.

## **4.7 Description of single cylinder and cylinder pair tests**

### 4.7.1 Introduction

Single cylinder testing is necessary since this is the simplest case of flow-induced acoustic resonance by a bluff body in a rectangular duct. For this reason, if the acoustic resonance phenomena in heat exchangers are to be understood, first the flow-induced noise behavior of single cylinders in a duct needs to be understood. The results of single cylinder testing are also essential to validate the theoretical model presented in Chapter 3.

The next logical step after single cylinder testing is to test pairs of cylinders. Testing pairs of cylinders will lead to an initial understanding of the flow-acoustic interactions of multiple cylinders inside a rectangular duct. The results of these tests can also be used to compare results obtained with the theoretical model for multiple cylinders.

### 4.7.2 Single cylinder tests

Single cylinder tests comprise experiments with two different types of cylinders. Cylinders of constant diameter and “hourglass” shaped cylinders (see Figure 4.17). Cylinders of constant diameter were made by cutting a ¼” aluminum rod in a lathe to the desired diameter. Single cylinders were also made using stereolithography. Stereolithography cylinders have a considerably rougher surface. The purpose of tests on these cylinders was to study the effects of surface roughness. If the surface roughness present in stereolithography cylinders does not change the flow-acoustic behavior of this type of cylinder the technique could more confidently be used. Figures 4.18, 4.19, and 4.20 show photographs of some of the constant diameter aluminum and stereolithography cylinder samples used and of some “hourglass” shaped cylinders, respectively.

“Hourglass” shaped cylinders were made with different circular cutters of 0.5, 0.75, and 1 mm radius. The procedure consisted in cutting straight in to the ¼” aluminum bar and then returning the cutter at an angle to produce the “hourglass” shape. Figure 4.21 illustrates this process.

Independently of the shape of the cylinders, single cylinder tests were performed using compressed air as the working fluid and the experimental apparatus described in section 4.4. The tests consisted of obtaining the power spectral density of dynamic pressure transducers mounted flush to the walls of the wind tunnel. The dynamic pressure transducers were mounted at several different positions to map the acoustic field. Additionally, the transfer function of different microphone pairs was obtained to gather phase information between them at the dominant peak in the power spectral density. Coherence measurements were also taken between microphone pairs to serve as an indicator of the goodness of the phase information. During the experiment, air temperature, Venturi flow meter differential pressure, Venturi flow meter inlet pressure, and pressure at the test section were recorded. This data was needed to determine mass flow rate, speed of sound and air density.

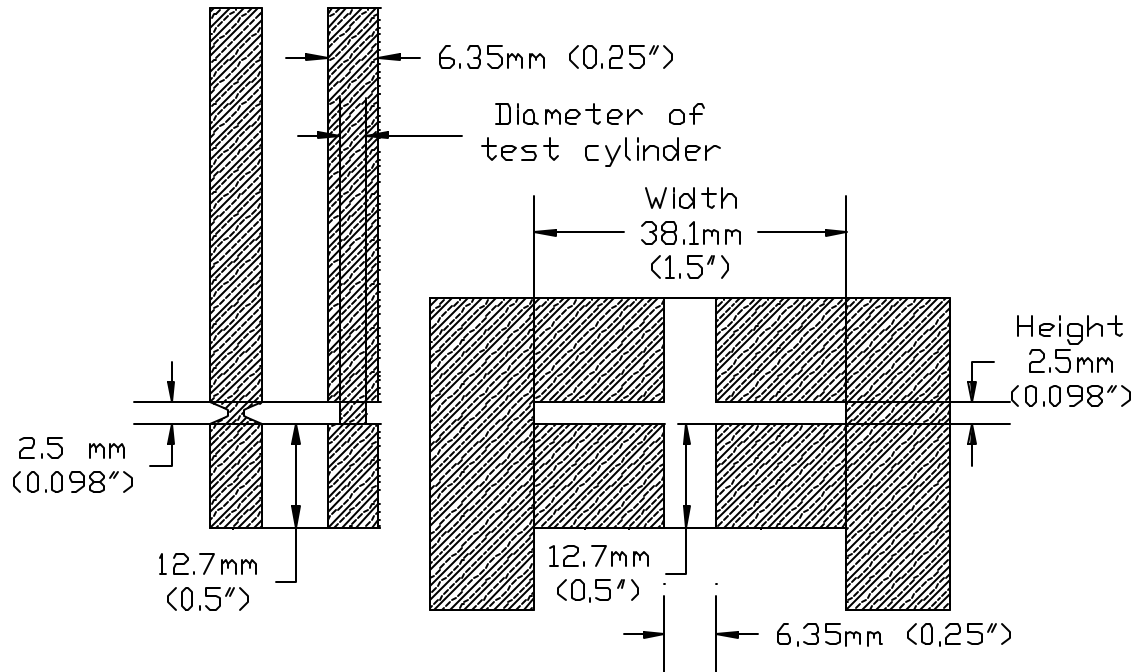


Figure 4.17 Cross-sectional view of compressed air wind tunnel test section at cylinder position. The single cylinder samples were slid into position and aligned.

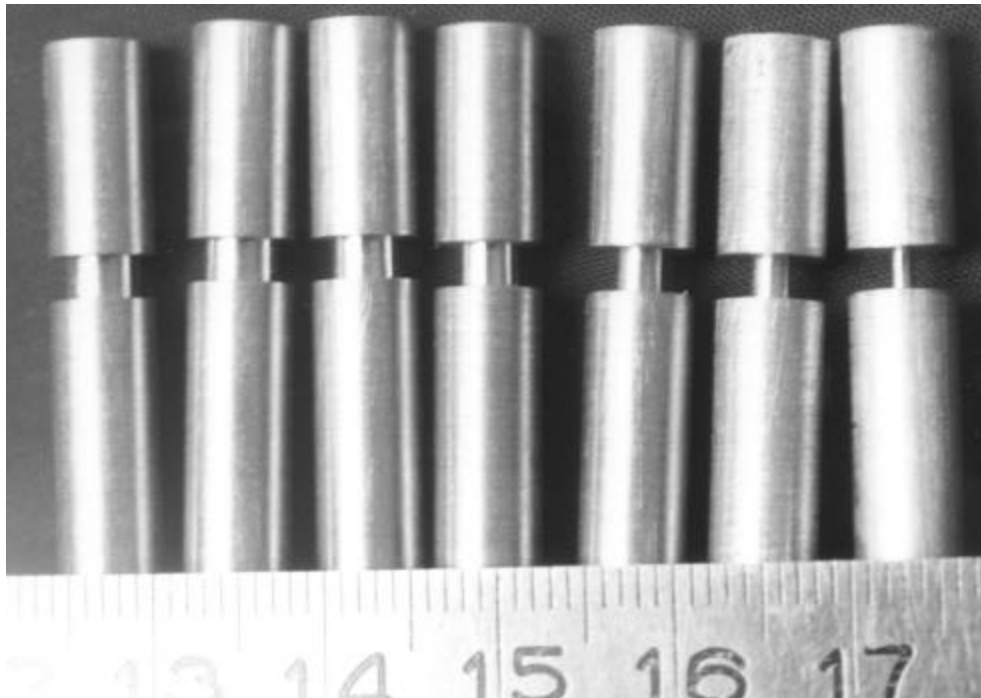


Figure 4.18 Photograph of aluminum constant diameter cylinder samples (ruler graduation in mm).

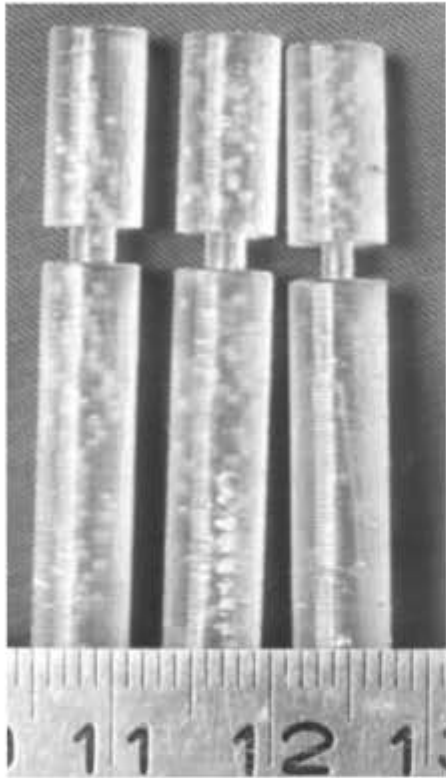


Figure 4.19 Photograph of stereolithography constant diameter cylinder samples (ruler graduation in mm).

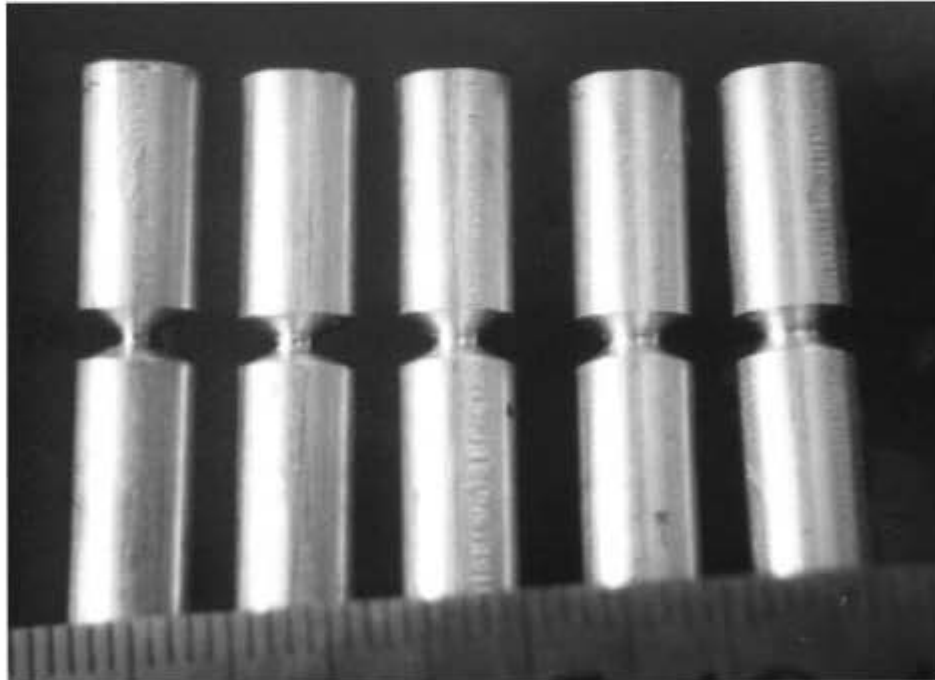


Figure 4.20 Photograph of hourglass shaped cylinders of different diameters (ruler graduation in mm).

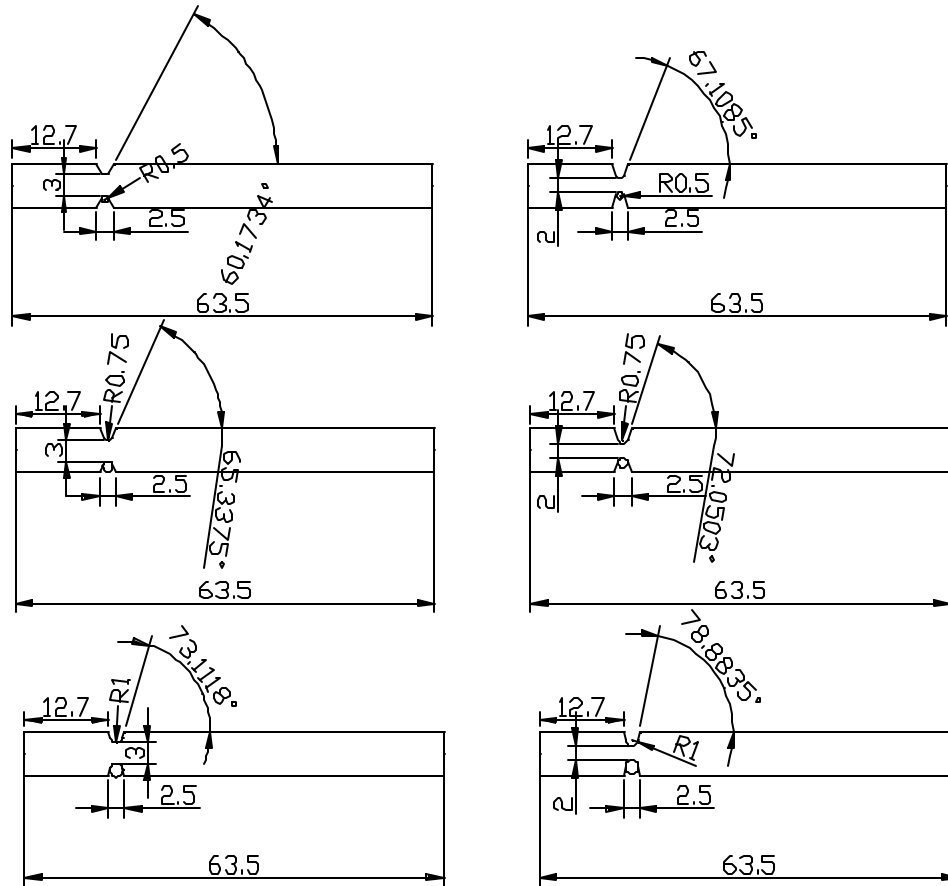


Figure 4.21 Drawings showing how the “hourglass” shaped cylinders were made. Dimensions in millimeters.

Figures 4.22 and 4.23 show the microphone position naming convention used and the location of these positions with respect to the center of the test cylinder respectively.

Two different types of microphones were used. PCB model 105B02 microphones were mostly used during single cylinder tests since their small size permitted a better acoustic field mapping (see section 4.8.5 for other reasons). These small microphones permitted their installation very close to each other and to the cylinder under test. TMS Gras  $\frac{1}{4}$ ” microphones could be installed at positions Q1-Q7. Positions Q1 – Q5 were mainly used when the test section was employed to determine the acoustic impedance and reflection coefficient of different duct terminations (see Appendix A). Microphone mounting positions d1-d2 and Q6-Q7 were on a movable slide. Once set into position the slide was sealed to eliminate air leaks.

As shown in Figures 4.22 and 4.23, there is a  $\frac{1}{4}$ ” (6.35 mm) hole in the test section where the different cylinders were inserted. Figure 4.17 shows the cross section of two single cylinders test samples and of the test section at the cylinder location. The test sample on the left is a nonconstant diameter test sample (“hourglass” cylinder) while the one on the right is a constant diameter test sample. These test cylinders are inserted at the center of the duct as shown in the figure. The samples are aligned by installing them flush to the bottom of the



wind tunnel. The maximum cylinder diameter was 6.35 mm (0.25”) for which the smallest aspect ratio (L/D) equal to 0.39 and the maximum blockage ratio (D/B) was equal to 0.167.

A small amount of silicone sealant was applied to the edges of the hole and test sample to eliminate any possible leaks that might develop at high flow velocities.

Surface roughness estimations were made for three different surfaces. The aluminum cylinder bar as it arrives (used for the 6.35 mm cylinder tests), the aluminum cylinder after machining (most of the cylinders), and finally of cylinders made using stereolithography.

Surface roughness measurements consist of taking the RMS (root mean square) of the surface profile of the different samples. The surface profile was measured using a Tencor Instruments alpha step-200 profilometer. Figures 4.24, 4.25, and 4.26 show the profiles of the “as is” aluminum bar, machined aluminum and a stereolithography sample. Figure 4.26 shows clearly the pattern of the layers of resin. Table 4.1 presents the measured RMS surface roughness values.

Table 4.1 Surface Roughness RMS values (Measured along cylinder axis)

Description	RMS Values
Aluminum cylinder (not machined, “as is”)	0.39 $\mu\text{m}$
Aluminum cylinder (after machining)	0.49 $\mu\text{m}$
Stereolithography Cylinders	10.83 $\mu\text{m}$

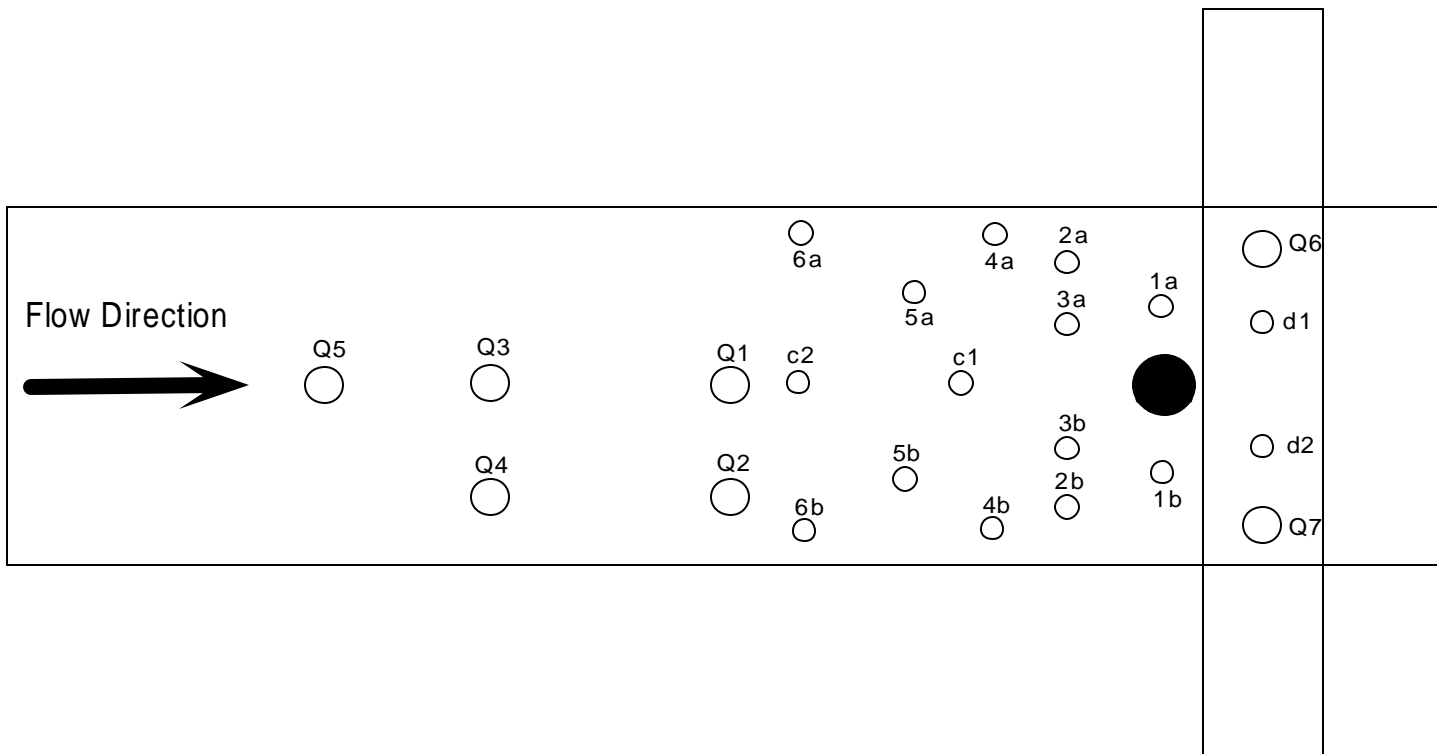


Figure 4.22 Top view of test section showing 6.35 mm cylinder (dark circle) and microphone positions with the nomenclature used. Microphones Q6, Q7, d1, and d2 are mounted on a movable slide. Drawing to scale.

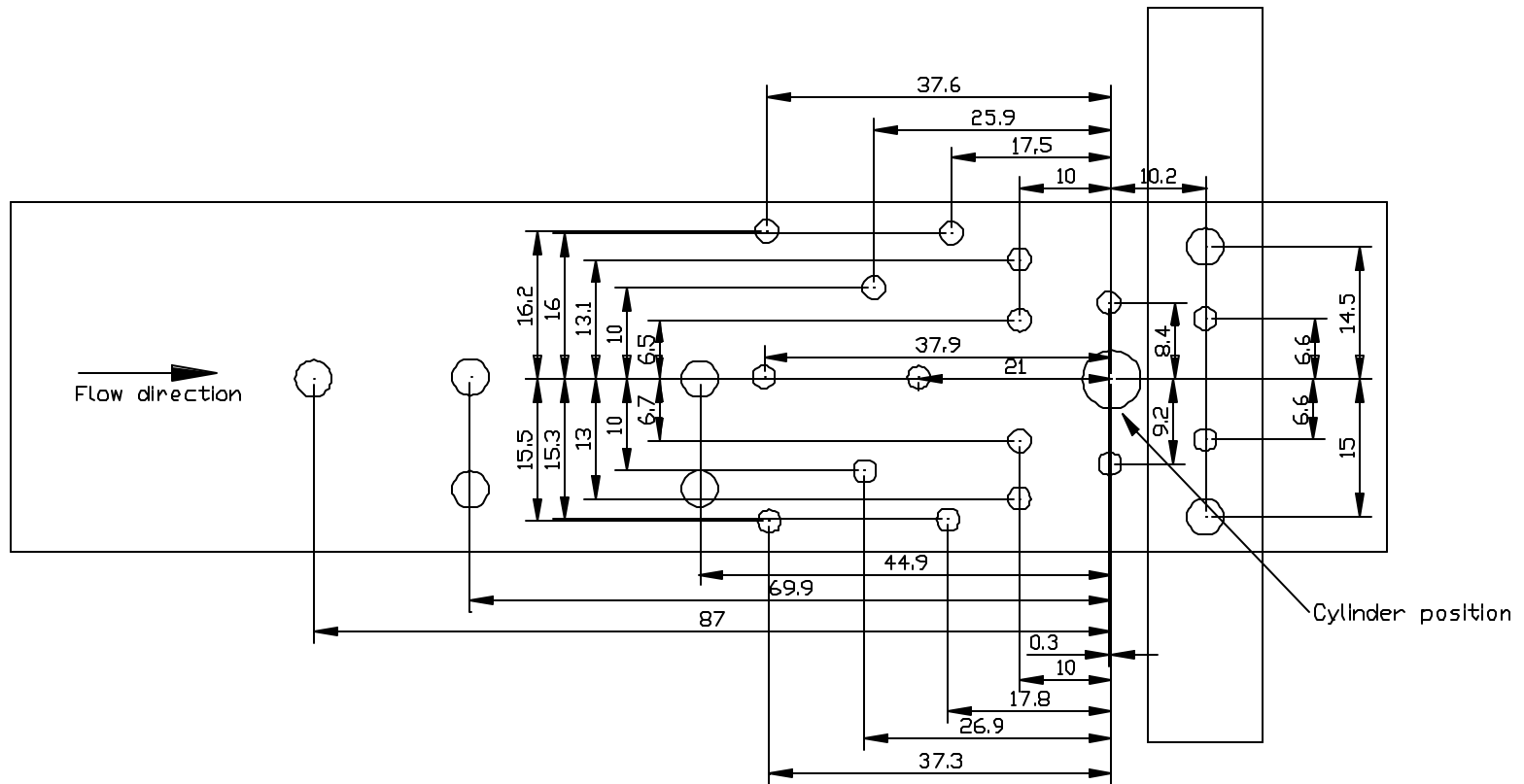


Figure 4.23 Top view of test section showing dimension from microphone positions to test cylinder. Dimension in millimeters. Microphones Q6, Q7, d1, and d2 are mounted on a movable slide. Drawing to scale.

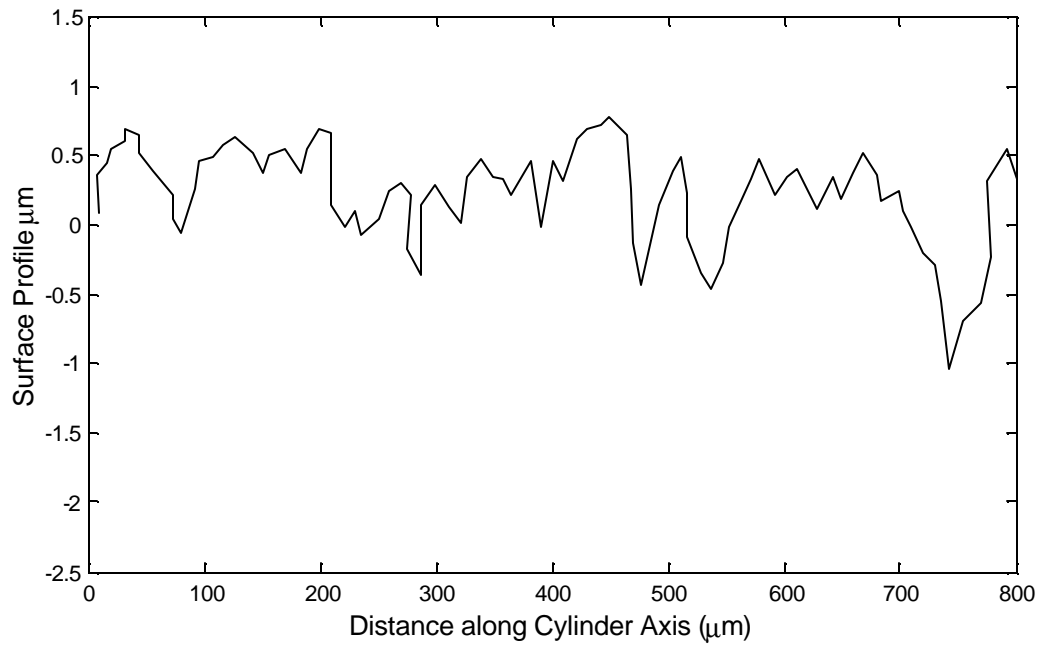


Figure 4.24 Surface profile measurements on aluminum cylinder with no machining (as is).

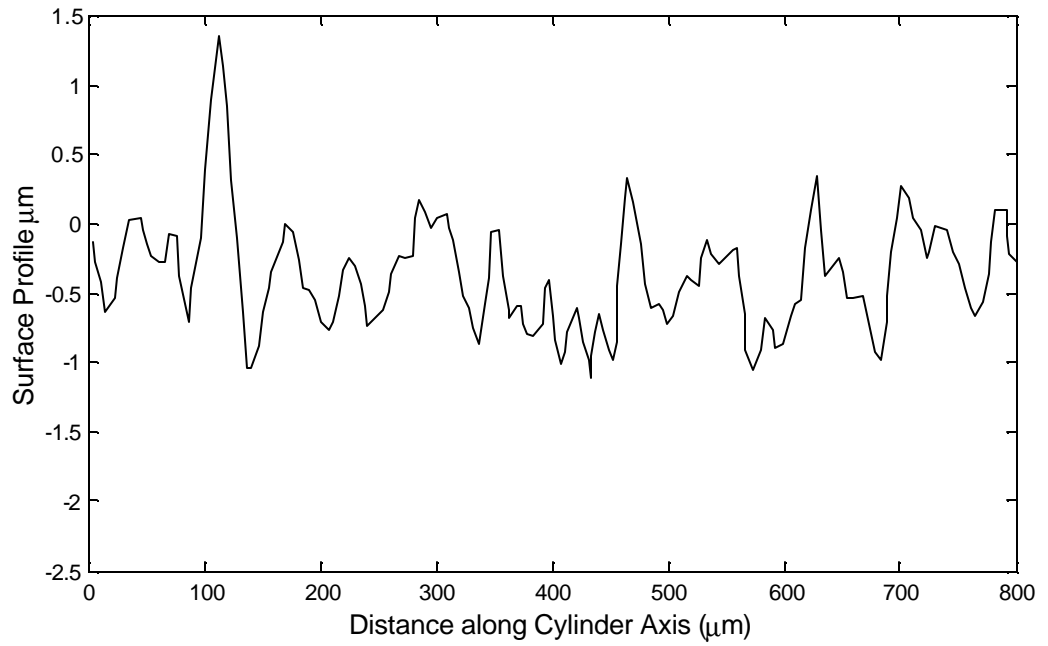


Figure 4.25 Surface profile measurements on aluminum cylinder after machining.

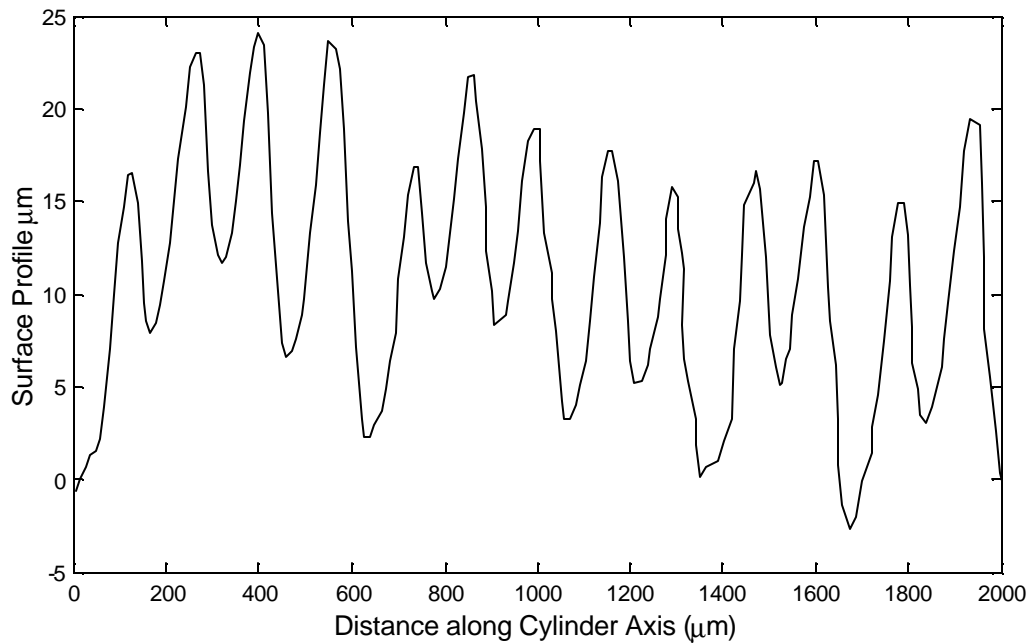


Figure 4.26 Surface profile measurements on stereolithography cylinder.

#### 4.7.3 Test on pairs of cylinders

The flow-induced noise of pairs of cylinders in a rectangular duct was experimentally and analytically studied. Pairs of cylinders in tandem and side by side were placed in the same test section as single cylinders. Needed modifications consisted in drilling holes at appropriate locations. Figure 4.27 shows the modified test section for pairs of cylinders tests.

First tandem cylinders were tested. To do this a 1/4" diameter hole was drilled downstream of the hole used for single cylinder tests as shown in Figure 4.27. Additionally, a dynamic pressure transducer mounting hole labeled d3 was made. With this hole spacing, L/D ratios of 3.28 through 6.93 can be obtained using cylinders of 6.35 and 3 mm, respectively. This range was chosen to explore the excessive fluctuating lift created in the downstream cylinder due to the combined effects of the upstream and downstream vortices as reported by Zdravkovich 1987 and Morse and Ingard.

Side-by-side tests were made by replacing the sensor slide with an aluminum bar that was then drilled at the locations shown in Figure 4.27. These holes did not exist for the tandem tests. The holes made for the tandem tests were plugged for the side by side tests. The T/D ratios obtained with this hole spacing are between 2 and 4.23 for cylinder diameters between 6.35 and 3 mm. This cylinder spacing was chosen for two reasons: 1) to position the cylinders in the center of the flow field away from channel edge gradients in the width direction (see appendix B and section 4.4.4), and 2) to explore the region  $2.7 < T/D < 4$  or 5 where the cylinders "nearwakes are equal in size, but the two vortex streets are coupled and 'mirror' each other along the gap axis" [Zdravkovich 1987]. This condition indicates the phasing of the cylinders fluctuating forces and could be used during modeling.

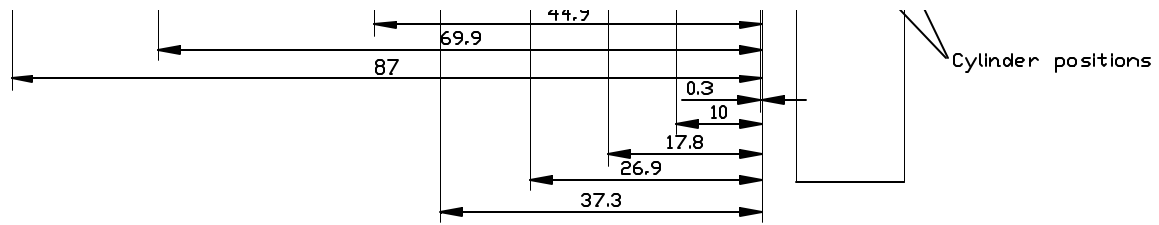


Figure 4.27 Top view of test section for pairs of cylinders tests. Dimension in millimeters. The movable slide shown in Figure 4.23 was replaced for side by side cylinder tests. Drawing to scale.

## 4.8 Instrumentation and sensor calibration

### 4.8.1 Introduction

In this section the instrumentation used and a description of how the compressed air experimental setup was automated is presented. Additionally, the most important sensor specifications, as well as sensor calibration procedures and curves are included.

### 4.8.2 Data acquisition system

The extensive and time-consuming tests motivated the automation of the compressed air experimental setup. An additional benefit of automating the data-gathering process is a more detailed study of the flow-acoustic behavior of cylinders in a duct since the flow rate can be controlled more accurately than previously.

The data acquisition system consists of a standard VXI B size mainframe and different boards for data acquisition, signal switching, and control. The system uses a 5½ digit multimeter, a multiplexer connected to the multimeter, and a multiplexer for signal switching between the different dynamic pressure sensors to the dynamic signal analyzer. Additionally, a digital to analog conversion board that sends a DC voltage signal to control the wind tunnel upstream pressure with an electro-pneumatic actuator was used. By controlling the air pressure upstream of the wind tunnel, the flow rates can be controlled in the test section. The multiplexer connected to the multimeter was used to measure voltages from the pressure transducers, and since it has thermocouple compensation was also used to measure fluid temperature directly from the single thermocouple used. A brief description of the data acquisition and control components is presented below.

Manufacturer:	Hewlett-Packard/Agilent Technologies
Model:	E1300A B size VXI mainframe chassis
	E1326B 5½ Digit Multimeter board
	E1347A Thermocouple compensated multiplexer board
	E1361A 4x4 Matrix switch board modified for 2x8 switching
	E1328A Digital to analog conversion board
Uncertainty:	0.020% + 50µV for the multimeter assuming an 8V range and measurements within 1 year of calibration and at the calibration temperature.

The only element that introduces uncertainty in the measurements from the above system is the multimeter. The multiplexer errors are due to thermal offset and are negligible. The insertion losses for the E1361A are listed at 0.1 dB for signal frequencies below 100 kHz. The analog-to-digital conversion board is used to programmatically send the voltage signal required by the electro-pneumatic transducer to establish the compressed air pressure upstream of the test section. The electro-pneumatic actuator used is made by Proportion Air Inc. and is a model number QB1TFEE100. This actuator converts a voltage between 0 and 10 VDC to a pressure between 0 and 100 psig. The transducer is used with a volume booster made by the same company to accommodate the required flow rates. The volume booster model number is PSR-6. The flow rate in the test section is not directly proportional to air pressure. For this reason, a curve fit was used to approximately set the

flow rate. There was no need to have high accuracy of the flow control system from voltage to pressure conversion since the flow rate is measured independently.

#### 4.8.3 Venturi flow meter calibration

A Venturi flow meter was used to measure flow rate in the nitrogen and compressed air test setups. The Venturi was calibrated using a Coriolis mass flow meter. This calibration method is the most accurate method available other than designing a flow meter calibration facility. The Venturi flow meter used was made by Gerand Engineering Co. and is a model ¾"-550. The Coriolis meter used in the calibration is made by Micro Motion Inc. and is a model Elite CMF050.

The Micro Motion sensor has an accuracy for gases of  $\pm 0.5\% \pm (\text{zero stability/flowrate} \times 100)\%$  of rate, where the zero stability is equal to  $0.163 \text{ kg/h} = 4.53 \times 10^{-2} \text{ g/s}$ . The above specification translates to an error measurement as shown in Figure 4.28.

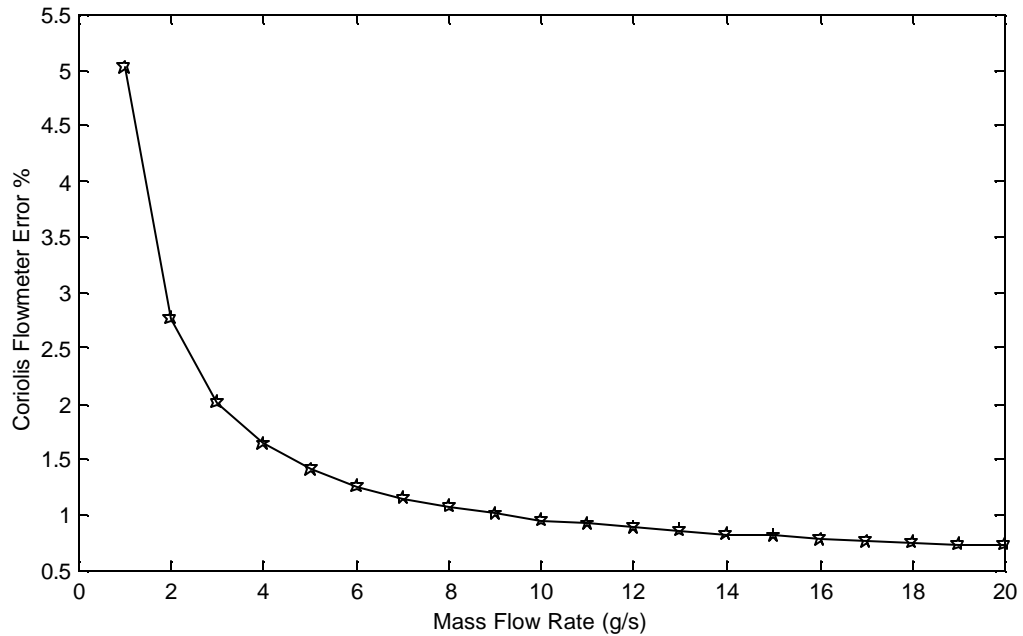


Figure 4.28 Flow measurement errors for Coriolis mass flow meter.

The mass flow measurement equations for a Venturi flow meter or any other differential-producing flow meter are identical. The equation used to determine mass flow is developed from the Bernoulli equation and then modified to include correction factors based on fluid compressibility, flow meter geometrical parameters or empirical evidence [Miller 1996].

The equation to determine mass flow using a Venturi flow meter is

$$\dot{m} = C_k Y_c A_t \sqrt{\frac{2 \partial P}{1 - b^4}} \quad (4.1)$$

where



$$b = \frac{D_t}{D_i}$$

$$Y_c = \frac{(1 - b^4) \left( \frac{g}{g-1} \right) \left( 1 - \left( \frac{P_t}{P_i} \right)^{\left( \frac{g-1}{g} \right)} \right) \left( \frac{P_t}{P_i} \right)^{\left( \frac{2}{g} \right)}}{\left( 1 - b^4 \left( \frac{P_t}{P_i} \right)^{\left( \frac{2}{g} \right)} \right) \left( 1 - \left( \frac{P_t}{P_i} \right) \right)} \quad (4.2)$$

In equation (4.1),  $C_k$ ,  $Y_c$ ,  $A_t$ ,  $\partial P$ , and  $\rho_i$  represent the Venturi correction factor, compressibility factor, area at the throat, pressure difference between inlet, and throat and density at inlet of Venturi, respectively. Mass flow through a Venturi is affected by several parameters, some of which include area thermal expansion, friction energy loss between inlet and throat, the velocity profile, and errors associated with area and pressure measurements. While equation (4.1) includes a compressibility factor shown in equations (4.2), other corrections are grouped in the experimentally determined Venturi correction factor  $C_k$ . The Venturi correction factor was obtained by substituting the mass flow measurement obtained with the Coriolis flow meter in equation (4.1) and then solving for this coefficient. After several of these measurements were made, the final correction coefficient used was obtained by averaging the coefficients obtain in each of the mass flow measurements. The Venturi correction coefficient obtained by this method is within the range of expected values [Miller 1996]. Once the averaged coefficient is used, the error in the mass flow measurements between the Coriolis and Venturi flow meters was within 1.3%. Figure 4.29 shows the mass flow calibration curve.

Based on the errors associated to the calibration of the Venturi flow meter and those of the Coriolis flow meter itself, it is estimated that the errors in mass flow measurement are at most of the order of 3% for all flow rates used in our experimental setup. These errors include the errors associated with the two pressure measurements needed to obtain the parameters in equation (4.1) (see next section). Since density is also needed in equation (4.1), density estimation errors are also included. Fluid properties determined in this work were obtained from the engineering equation solver software version 6.026.

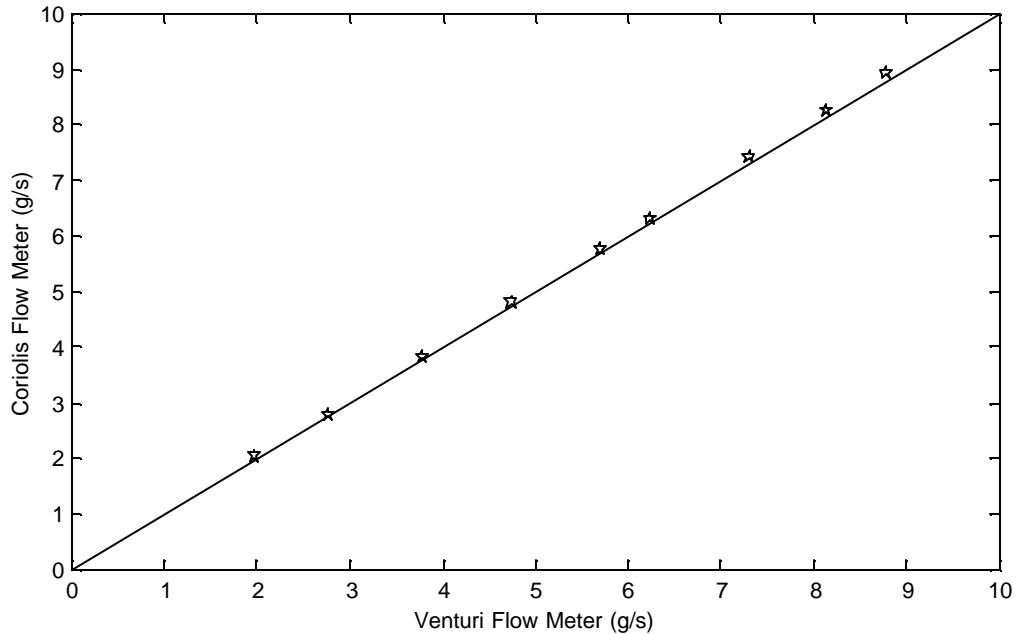


Figure 4.29 Mass flow measurements comparison between Coriolis and Venturi mass flow meters.

#### 4.8.4 Static pressure transducer calibration

Pressure transducers are used to measure the static pressure in the test section for the purpose of estimating the fluid density needed to obtain average flow velocity in the channel once mass flow is measured. Pressure transducers are also needed to measure mass flow as mentioned in the previous section. Two pressure measurements are needed to obtain flow rate. First a differential pressure is measured from the Venturi flow meter inlet and throat ports. Pressure difference as shown in equation (4.1) is needed to obtain mass flow in any differential producing flow meter. The other measurement is of static pressure at the Venturi inlet port. This measurement is again needed to estimate fluid density but now at the Venturi inlet port.

The pressure transducers used are the variable reluctance type and are made by Validyne Engineering Co. Four different pressure transducer are used. They need a carrier demodulator for transducer coil excitation and for converting the output signal to 0-10 VDC for measurement by the data acquisition systems.

Both the pressure transducer and carrier demodulator have some measurement uncertainties. The combined uncertainties are  $\pm 0.4\%$  of the full scale neglecting thermal effects. Thermal effects are neglected since the carrier demodulator is maintained at a constant temperature and also in a powered on state to eliminate electronics warm up errors. Some of the relevant pressure transducer specifications are shown below:

Manufacturer:	Validyne Engineering Co.
Pressure sensors	
Model:	DP15
Sensitivity:	Varies depending on diaphragm used
Uncertainty:	$\pm 0.25\%$ Full Scale (including effects of hysteresis, linearity and repeatability)
Carrier \demodulator	
Model:	CD280

Uncertainty:  $\pm 0.05\%$  linearity,  $\pm 0.1\%$  Stability  
Thermal effects: 0.005% per °F on zero, 0.001% per °F on span

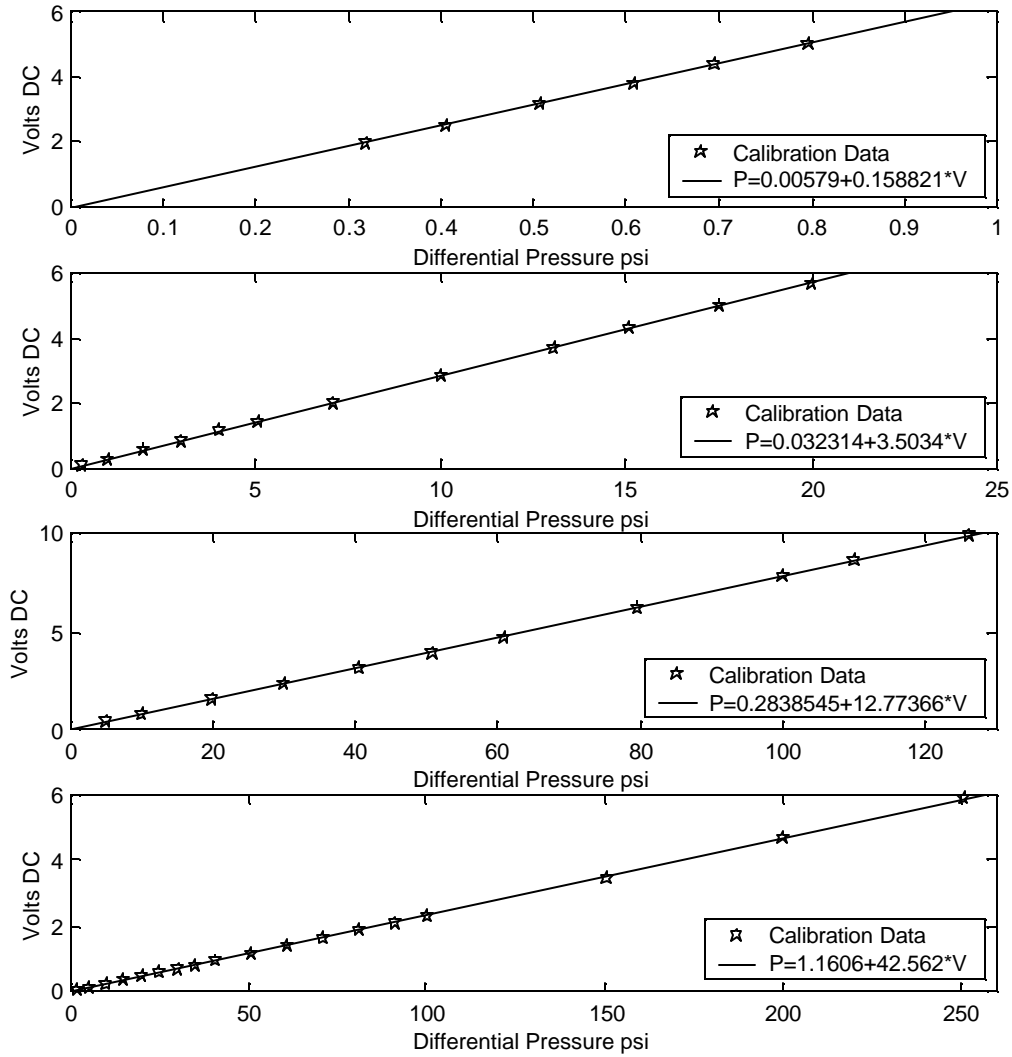
The pressure transducers were calibrated using a Bell and Howell dead weight tester model No. 6-201-0001. This calibration instrument is a primary pressure standard. The dead weight tester creates a known pressure by using a known weight on top of pistons of different area that slide in a very low friction cylinder. If the piston/weight combination is floating freely, the pressure inside the cylinder chamber can be defined by

$$P_o = \frac{m_p g}{A_p} \quad (4.3)$$

where  $P_o$  is the static pressure in the cylinder chamber, and  $m_p$ ,  $A_p$ , and  $g$  are the piston mass, area, and standard acceleration of gravity, respectively. In equation (4.3) the acceleration of gravity used should be that of the particular location where the measurement is made. Weston et al. presented an equation to correct for the variation in this “constant” as a function of location latitude. This equation predicts that the difference between the acceleration of gravity at Urbana and that of the standard acceleration of gravity to be less than 5 parts in 10,000. For this reason, this factor was neglected. Figure 4.30 shows the calibration data and curve fits for the four different pressure transducers.

Figure 4.30 shows the differential pressure on the x-axis. The pressure transducers are differential pressure transducers. All of them, except the one used with the Venturi flow meter, measure absolute or manometric pressure. To do this, one port of the pressure transducer was opened to the atmosphere and the atmospheric pressure was recorded separately.

During the course of this research, the pressure transducers were calibrated several times to confirm the calibration factors. This was done once it was noticed that there was some drift in the pressure measurements. After recalibrating the transducers, it was found that the slope of the calibration lines did not change. The drift in the readings was caused only by changes in the zero values, which, although minimal, have to be adjusted periodically. Another case in which pressure transducers were recalibrated was when the transducers were subjected intentionally or by mistake to overpressures. It was found that even when the transducer’s response to pressure was flat, (i.e., when the voltage did not increase with increases in pressure), the calibration remained valid once the pressure returned to normal values. The transducer response is flat once the metal diaphragm can no longer move when it reaches an inner wall. It is believed that this fact prevents the plastic deformation of the diaphragm and allows it to operate normally once the pressure is released.



Figures 4.30 Calibration data and curve fits for the four pressure transducers.

#### 4.8.5 Microphone specifications and amplitude calibration

Two different types of microphones were used during the course of this work. The first were very small and rugged dynamic pressure transducers 0.1" (2.54 mm) in diameter. This transducer can be used to measure very small dynamic signals on top of high static pressures and can be easily mounted in pressure vessels. These transducers proved to be a good choice during R134a refrigerant testing. The drawback of these transducers is that they are not very sensitive. The second type of transducers were 1/4" (6.35 mm) diameter microphones that are specially designed for sound intensity measurements. These transducers are very sensitive (on the order of 500 times more sensitive than the 0.1" (2.54 mm) transducers) and have excellent phase-matched characteristics, as will be seen in the next section. The drawbacks of these transducers are that they are significantly larger, do not support high static pressures, can be damaged by large dynamic pressures (of the order that we saw in some of our tests) and are in general significantly more fragile and expensive.

Some of the more relevant information of the two types of microphones used is presented below:

0.1" (2.54 mm) Dynamic Pressure Transducers

Manufacturer: PCB Piezotronics Inc.  
Model: 105B02  
Sensitivity: 40 mV/psi  
Resonant frequency: 250 kHz  
Maximum pressure: 250 psi  
Acceleration sensitivity: 0.003 psi/g  
Uncertainty in calibration:  $\pm 0.2$  mV/psi (from linearity < 1% FS)

1/4" (6.35 mm) Sound Intensity Microphone Pair

Manufacturer: The Modal Shop GRAS  
Model: TMS140BI  
Sensitivity: 4 mV/Pa  
Resonant frequency: 100 kHz  
Maximum pressure: 166 dB re to 20  $\mu$ Pa (3990 Pa)  
Acceleration sensitivity: 0.018 Pa/(m/s<sup>2</sup>)  
Uncertainty: 0.02 mV/Pa  
Frequency response (10 Hz-40 kHz):  $\pm 1$  dB

The PCB sensors need an ICP (integrated circuit piezoelectric) 4 mA constant current source. The ICP power source used with these sensors is battery operated. This power source was made by the same company and is model number 480C02. It was found that the battery-operated power source introduced less signal noise than another similar unit (model 482A05) that uses regular 115V AC power. For this reason, only the battery-operated unit was used in our tests.

The 1/4" microphones use preamplifier model number TMS126AA and a power supply model number TMS112AA made by the Modal Shop GRAS.

The manufacturer originally supplied microphone amplitude calibration for all sensors, however, the manufacturer calibration was verified in the laboratory using a pistonphone calibrator (see Figure 4.31). The pistonphone calibrator provides a known sound pressure level at a specified frequency. The specifications for the one used are the following:

Pistonphone Calibrator Specifications

Manufacturer: The Modal Shop GRAS  
Model: TMS 142AA  
Sound pressure level: 113.96 dB re to 20  $\mu$ Pa  
Nominal frequency: 250 Hz  
Uncertainty: < 0.09 dB



Figure 4.31 Pistonphone microphone amplitude calibrator. This instrument produces a constant sound pressure level of 114dB at 250 Hz.

If the pistonphone calibrator is used at a barometric pressure other than the standard atmosphere (101.3 kPa), then the sound pressure level should be corrected with a correction barometer.

The pistonphone calibrator is designed to calibrate ½” microphones. The ¼” microphones can also be calibrated using a special adaptor that comes standard with the pistonphone. To calibrate the 0.1” microphones using this instrument, a special adaptor was machined. A typical calibration power spectrum for the 0.1” microphones is shown in Figure 4.32. A similar spectrum is obtained using the much more sensitive ¼” microphones but with the noise level significantly reduced at frequencies other than 250 Hz.

The pistonphone calibration showed that the manufacturers’ calibration curves were very good for both types of microphones. For the ¼” microphones the errors in acoustic pressure at 250 Hz were of the order of  $\pm 5\%$ , which correspond to sound pressure level errors of the order of  $\pm 0.2$  dB. For the 0.1” microphones the errors in acoustic pressure at 250 Hz were of the order of  $\pm 12\%$ , which correspond to sound pressure level errors of the order of  $\pm 0.6$  dB.

In addition to calibrating amplitude, the pistonphone calibrator was also used to verify errors in frequency estimations. Different frequency spans were used in the dynamic signal analyzer to detect errors in frequency. The test results indicate that errors in frequency are negligible.

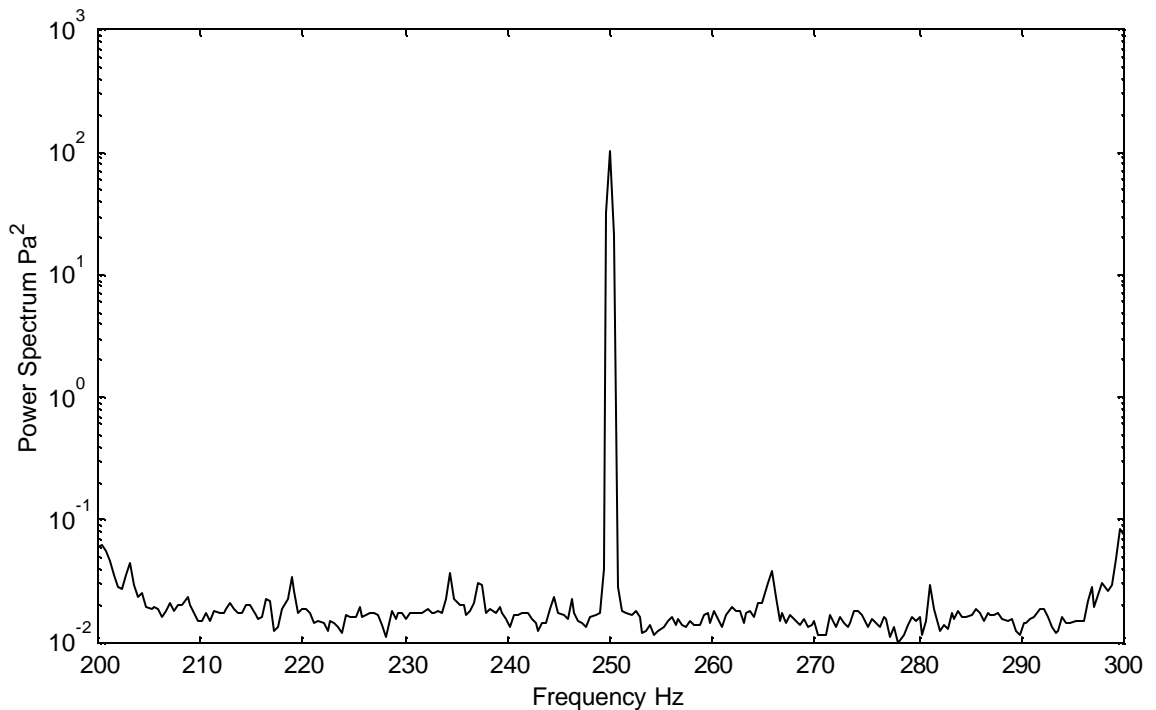


Figure 4.32 Power spectrum of acoustic pressure measured with 0.1" (2.54 mm) microphone using the pistonphone calibrator.

#### 4.8.6 Microphone pair phase calibration (¼" microphones)

Phase calibration for the ¼" microphones was performed using the sound intensity calibrator shown in Figure 4.33. This instrument is also made by The Modal Shop GRAS and is model number TMS151AB. The sound intensity calibrator can be used for phase and level calibration of ½" microphones. As with the pistonphone calibrator, this device comes with adaptors for the ¼" microphones. The sound pressure level of this instrument is significantly less than the pistonphone calibrator (approx. 20 dB less) but, since it uses an external signal source, can be used to calibrate a range of frequencies. Due to the sound pressure level limitations, the 0.1" dynamic pressure transducers could not be calibrated with this instrument. For the smaller sensors, an innovative technique was used and will be discussed in the next section.

The sound intensity calibrator supplies a well-defined sound pressure field simultaneously to the diaphragms of the two microphones inserted in the calibrator. The sound pressure level provided by the calibrator depends on the level of the signal received by the calibrator. The phase error associated with the calibrator is negligible.

The phase calibration procedure consisted of sending a white noise signal to the calibrator at 90% of its recommended maximum level (0.9 Vrms) using the HP 3562a dynamic signal analyzer source capabilities. Simultaneously, using the same analyzer, power spectral density, coherence, and frequency response

measurements for the microphone pair were taken. The analyzer had a frequency span of 10 kHz. It was AC coupled and used a Hanning window. The measurement was averaged 50 times.

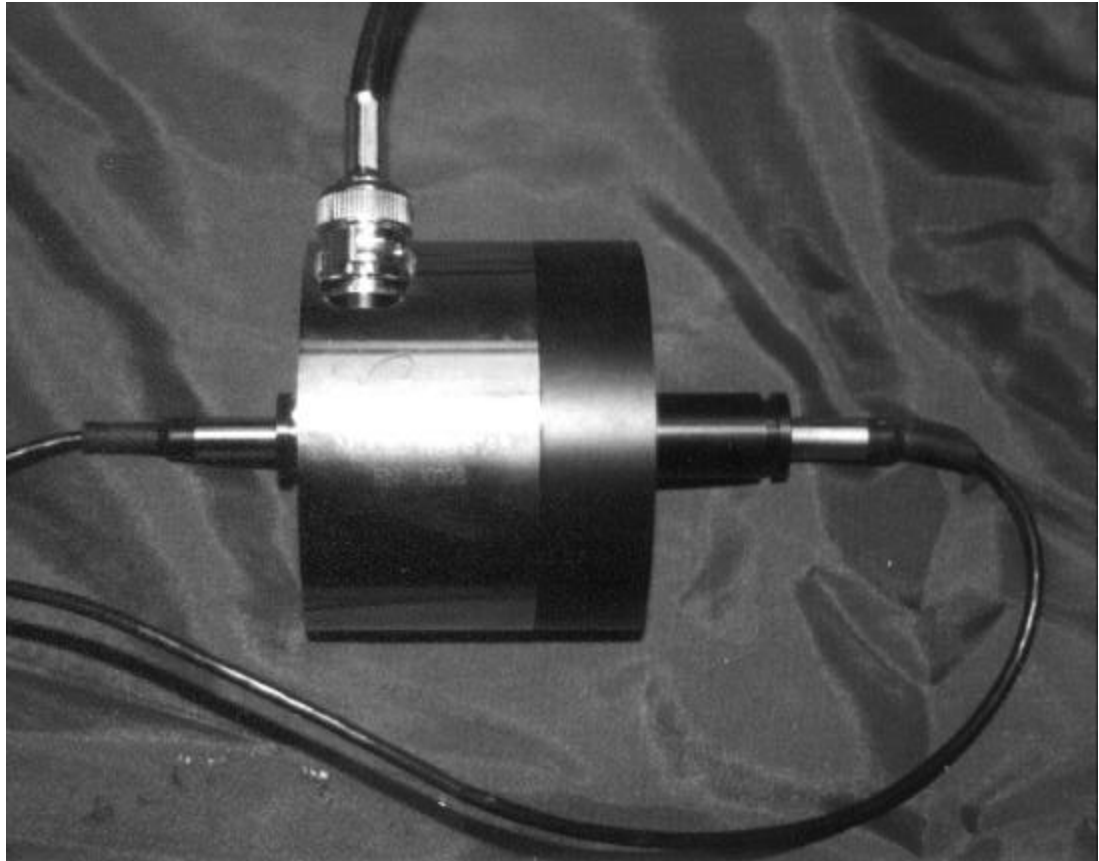


Figure 4.33 Sound intensity calibrator. This instrument needs a source signal to operate. It produces an identical acoustic pressure signal at the two microphones.

Figure 4.34 shows the results of this calibration. It can be seen that the power spectral density for each of the two microphones is identical, which is an additional proof of the correct microphone amplitude calibration. The coherence for the microphone pair as well as the frequency response magnitude, is excellent. The  $\pm 1$  degree lines, as well as the 0 degree lines, have been drawn in the frequency response phase plot as visual aids. As can be seen, the phase angle between the microphone pair is within less than 1 degree in the frequency range of interest.



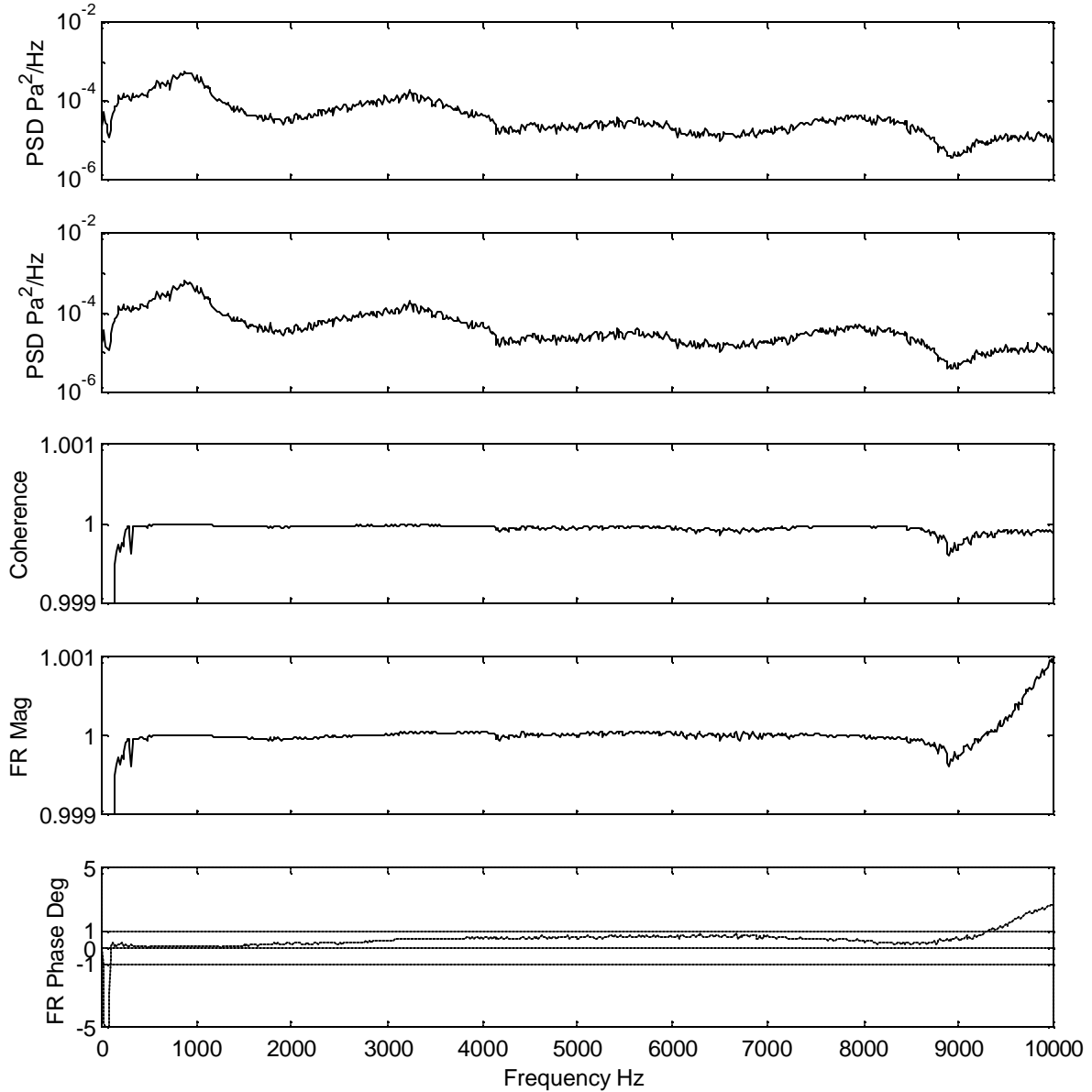


Figure 4.34 Results of 1/4" microphone pair phase calibration.

#### 4.8.7 Dynamic pressure transducer pairs phase calibration (0.1" sensors)

To verify the phase-matching characteristics of the small dynamic pressure transducer pairs, a different and innovative procedure had to be developed since these transducers are not sufficiently sensitive to be used with the sound intensity calibrator. The new procedure was identical to the one used in the previous section, but the acoustic signal was created by an orifice tube. Orifice tubes are used as thermal expansion devices in automobile applications. They are well-known sound generators and produce a white noise spectra in a wide frequency band when used under superheated refrigerant conditions or with gases [Rodarte et al. 1999b]. Orifice tubes are 1.5" (38.1 mm) long, and the one used has an internal diameter of 1.71 mm.

The orifice tube was installed inside a 0.5" (12.7 mm) nominal diameter copper pipe (10.8 mm internal diameter). The sensors were mounted to a bronze block with machined sensor-mounting holes. The sensor block was installed on the outside of the pipe, and carefully drilled holes were made to permit the microphones diaphragm to be mounted flush to the interior wall of the pipe (See Figure 4.35).

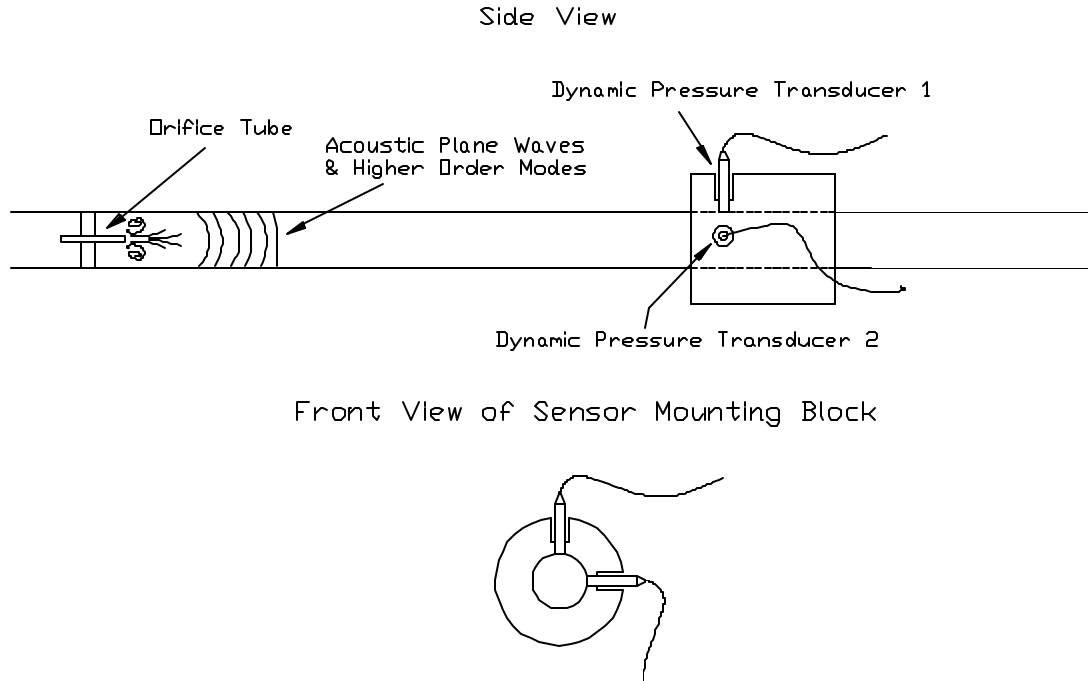


Figure 4.35 Experimental setup used to verify phase behavior of 0.1" dynamic pressure transducer pairs.

The experimental setup shown in Figure 4.35 can be used for phase calibration if plane waves are present. For plane waves propagating in the tube, the phase matching of sensors in the same diametral plane should be identical. The same is true for plane wave reflections from the tube exit. For this reason there is a limit imposed by the first acoustic cut-off frequency of the tube for phase calibration. Above the first acoustic cutoff frequency, higher-order modes propagate inside the tube, and phase characteristics with this sensor arrangement cannot be obtained. The cutoff frequencies of acoustic modes inside a cylindrical pipe can be determined with equation (4.4) [Norton].

$$f_{co} = \frac{\kappa_{pq} c_o (1 - M^2)^{1/2}}{2p} \quad (4.4)$$

In equation (4.4)  $\kappa_{pq}$  is the acoustic wavenumber associated with the  $(p,q)^{th}$  mode inside the cylindrical pipe. For the first higher-order mode (1,0),  $\kappa_{pq}$  is equal to  $1.8412/a_i$ , where  $a_i$  is the internal pipe radius. In this case, the first acoustic cutoff frequency using air at standard conditions is greater than 18 kHz; thus, the calibration procedure is valid in the frequency range of interest.

Figure 4.36 shows a typical result for a 0.1” transducer pair. The results show a less than perfect coherence and frequency response, especially in certain regions with dips in the power spectral density plots. Depending on the length of the experimental setup, the microphone pair will always coincide with nodes of the standing wave produced at certain frequencies. When this condition occurs, the acoustic pressures detected by the microphones will be very small. Such small signals can cause the observed reductions in power spectral density and coherence. These reductions imply limitations of this experimental setup. That is, for certain discrete frequencies the acoustic pressures at the microphone positions would be so small that this setup cannot be used to infer phase matching between microphones.

The reduction in acoustic pressures due to nodes cannot explain the large decrease in coherence present at approximately 3300 Hz. At this frequency, even though the measured power spectral densities are relatively large and significantly above the values at the dips in the spectra, the measured coherence and phase angle were not in line with results at other frequencies with similar power spectral density values. This discrepancy could be associated with local hydrodynamic pressure fluctuations that develop from any imperfection in the sensor mountings.

The problem of standing wave nodes can be solved by changing the position of the microphones in the tube or by changing the tube length. By performing the phase matching tests with the two setups, the limitations of each will be overcome. To reduce problems with local hydrodynamic pressure fluctuations, extreme care should be taken to eliminate any protrusion or cavity in the microphone mountings. The microphones should be perfectly flush to the interior of the tube wall. In this case, since there is no reason to expect the phase matching between microphones to not be a smooth function of frequency, it was not felt worthwhile to modify the setup.

The 0.1” (2.5 mm) microphone pairs phase matching tests results show that in the 0-10 kHz frequency range the phase matching had an RMS error level of the order of 10 degrees. It was noted that the phase errors were reduced when the coherence was close to one. For coherence values between 0.95 and 1, the RMS error in phase was around 5 degrees. For coherence values between 0.9995 and 1, the RMS error in phase was around 2.5 degrees.

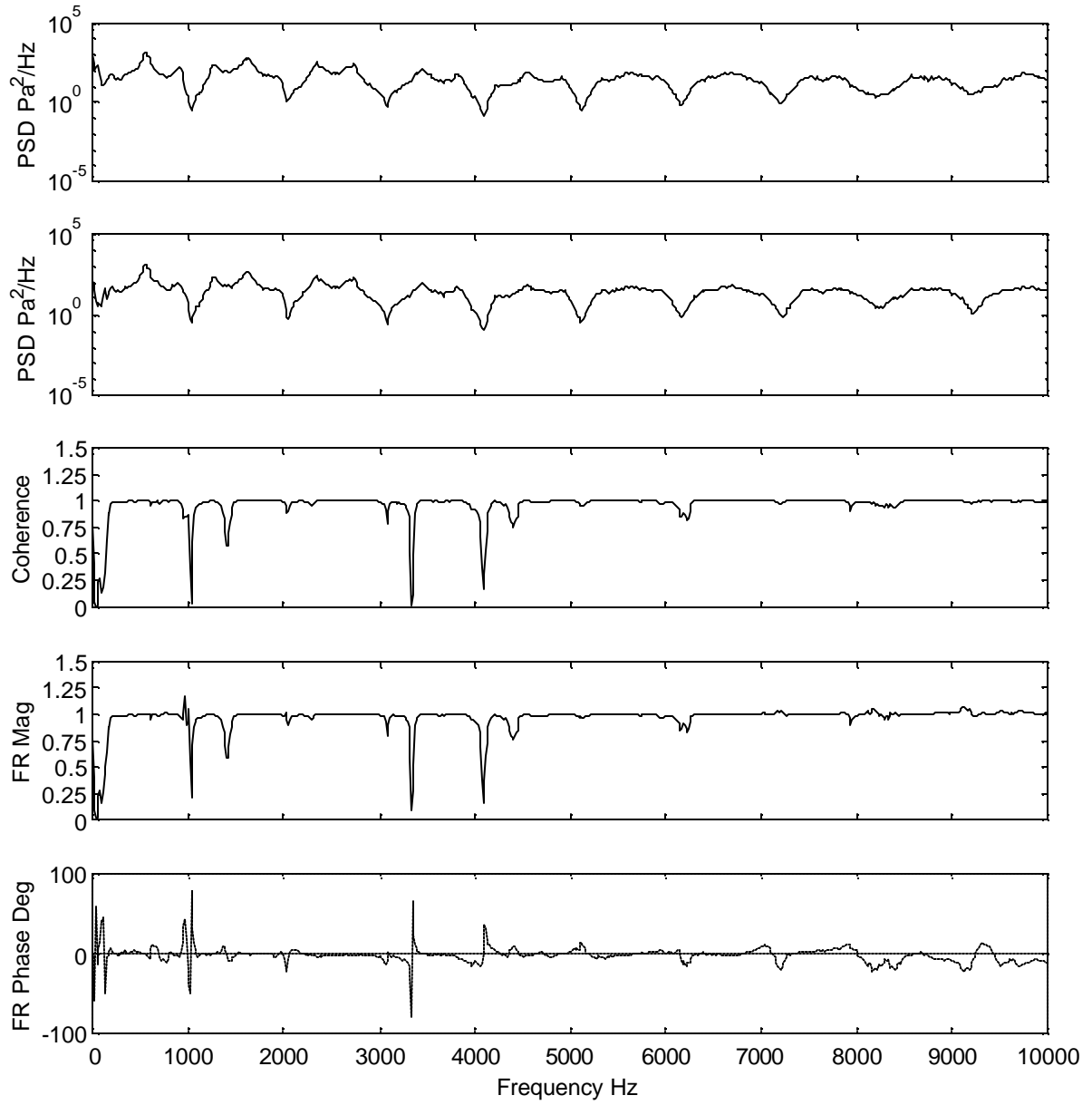


Figure 4.36 Typical results of 0.1" microphone pairs phase calibration.

#### 4.8.8 Effect of microphone size in measurement uncertainties

The physical size of a given transducer limits its ability to resolve adequately the measurements that it is intended to perform. In the case of a microphone, if the dynamic pressure field has scales that are smaller than the microphone diaphragm then this portion of the phenomena is not accurately captured by the transducer. The scales of the flow disturbances near a wall are inversely proportional to the frequencies that they produce in the dynamic pressure field [Bull 1968]. The transducer will average out these components of the dynamic pressure field. This concern is of special importance when measuring the broadband characteristics of dynamic wall pressure spectra.

For acoustic disturbances, microphone size is important when the wavelength of the acoustic pressure fluctuation is smaller than the microphone diaphragm, since under these conditions the same averaging effect described above will be present. In the case of a monochromatic acoustic disturbance such as the noise from cylinders in cross-flow, the average pressure on the sensor diaphragm could be estimated as

$$P_{ave} = \iint_s S(x,y,f) |P(x,y,f)| ds \quad (4.4)$$

where  $S(x,y,f)$  is the spatial response of the transducer as a function of position in the diaphragm and at the frequency of interest  $f$ .  $P_{ave}$  represents the average acoustic pressure detected by the diaphragm and  $P(x,y,f)$  is the local acoustic pressure at the diaphragm surface at the frequency  $f$ . Equation (4.4) assumes an instantaneous response of the microphone.

The parameters to solve equation (4.4) are difficult to determine. Even when the analytic solution presented in chapter 3 can be used to estimate the values of  $P(x,y,f)$ , the local response of the transducer is difficult to know.

An alternative approach to assess the importance of microphone size can be obtained by estimating values of the acoustic pressure using the formulations presented in chapter 3. By determining how much the acoustic pressure level varies at extreme positions within the diaphragm at different locations on the duct wall and as a function of frequency, a maximum error condition due to microphone true acoustic center variation can be established. If the acoustic pressures do not vary significantly across the diaphragm for any frequency of interest or microphone positions within the test section, then it can be assumed that errors introduced due to microphone true center position or to averaging will be negligible.

Figure 4.37 shows microphone positions relative to a single cylinder. The dark circle represent the 6.35 mm cylinder, while the shaded circles represent the 4 mm diaphragms of the nominal ¼” microphones. Acoustic pressures were estimated at the dark dots in the center and on the edges of the shaded circles as shown for frequencies in the range 1-7 kHz. The microphones were assumed to be flush to the wall. Using the differences between these calculated values, the maximum possible error between the positions on the microphone diaphragm was estimated. The maximum errors are in the  $y$  direction. To determine the maximum difference seen at any position in the diaphragm, the gradient of the acoustic pressure must be estimated at

extreme positions in this direction. This maximum varies as a function of frequency. However, the small differences associated with the changes in acoustic pressure in the x direction in comparison to the changes in the y direction indicate that there is only a small error associated with determining the maximum differences in the acoustic pressure by using the differences in the y direction directly.

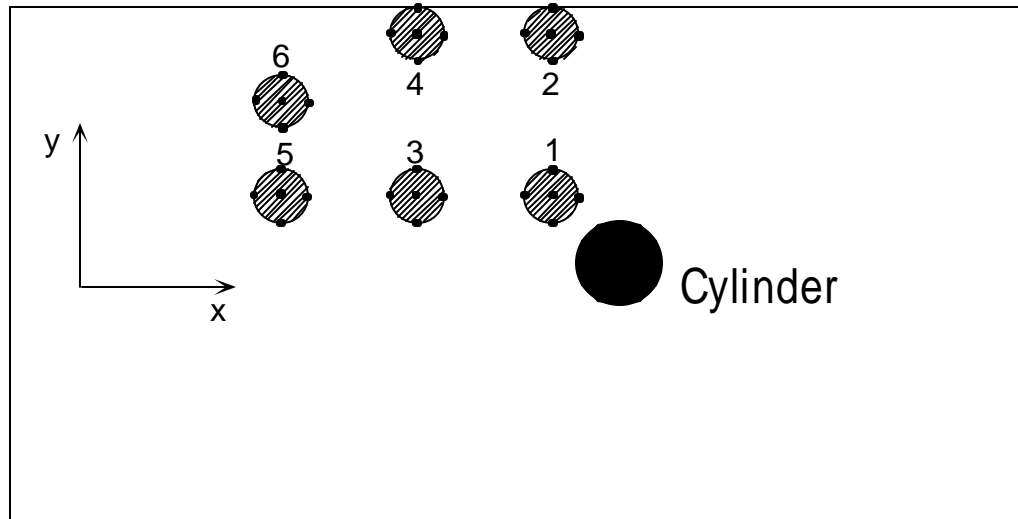


Figure 4.37 Top view of relative positions between the cylinder and the hypothetical microphones where error estimation due to acoustic pressure gradient was performed. Diagram to scale.

Figure 4.38 is a plot of the estimated acoustic pressure level at the center of microphone position 3 in Figure 4.37. This position showed the maximum deviations in the acoustic pressures calculated at the diaphragm face compared to other positions shown in Figure 4.37. The acoustic pressure was estimated assuming no volumetric damping and rigid walls, a 6.35 mm cylinder using a fluctuating lift coefficient of 0.5, and a constant density of  $1.33 \text{ kg/m}^3$ . The top and bottom lines represent the acoustic pressures levels estimated at the top and bottom positions within that diaphragm. The vertical lines show the positions where calculations were performed. This graph shows the maximum possible error associated with an eccentric microphone true center position.

From this analysis, it was found that in general the maximum possible error will be present when the microphone diaphragm is tangential to the channel center line where theoretically the acoustic pressure should be zero in the case of a single center dipole. The possible errors associated with microphone size as a function of position and frequency are strongly dependent on position and only weakly dependent on microphone frequency. This analysis showed that the maximum errors are of the order of  $\pm 4 \text{ dB}$  and are found for the microphones close to the channel centerline where the strongest acoustic pressure gradients are found. In our experimental apparatus, smaller microphones are more widely used (see Figure 4.22) and are at positions further away from the centerline (except the ones that are right on the centerline for dipole source identification). So the maximum possible errors due to microphone size, position, and frequency are smaller than those described here.

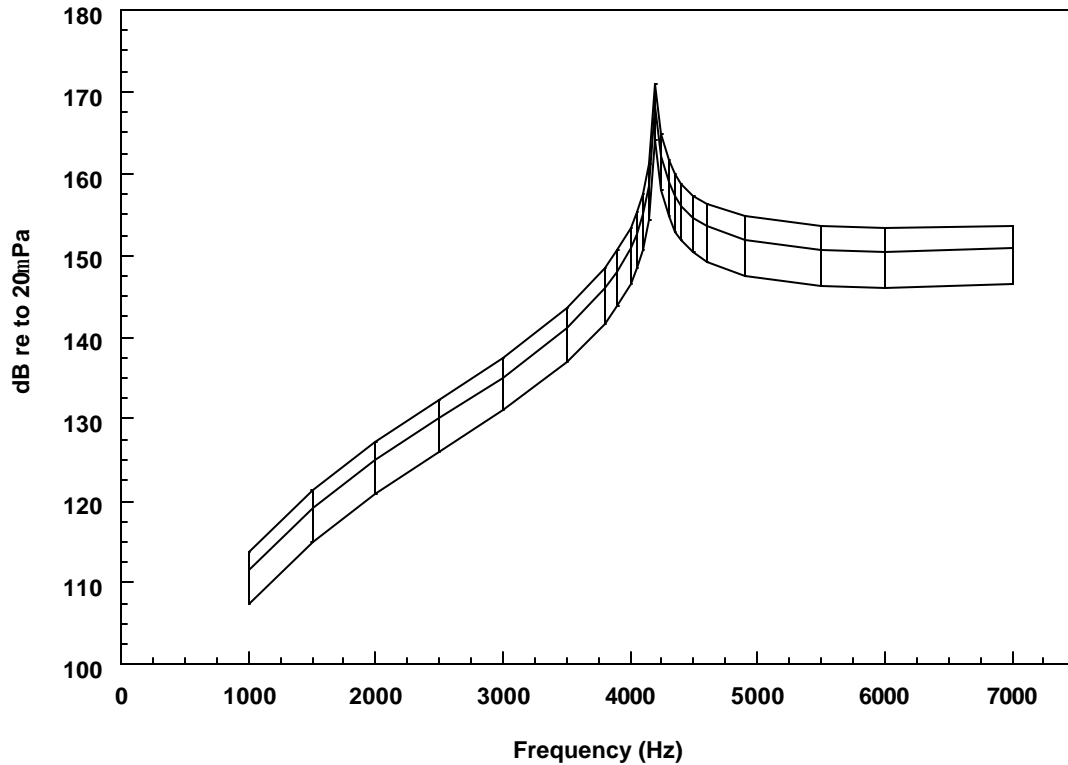


Figure 4.38 Sound pressure level (SPL) determined at the center of position 3 in Figure 4.37 (middle line). Top and bottom lines delimit the maximum possible error associated with moving the microphone center to the edges of the 4 mm diaphragm in the y direction.  $C_L' = 0.5$ ,  $\rho = 1.33 \text{ kg/m}^3$ ,  $c_o = 345 \text{ m/s}$ .

#### 4.8.9 Effect of surface irregularities

Another source of error in the measurements taken by the microphones and dynamic pressure transducers is associated with surface irregularities in the vicinity of the transducer mounting. If there are surface marks near the transducer or if the transducer is not perfectly flush to the wall, these irregularities can cause significant variations in the measured values of the dynamic pressure. These deviations from the measurements are caused when the sensor picks up the local disturbances in the flow. Bull 1968 emphasizes that results of Willmarth and Wooldridge show increases as high as 50% in the nondimensional overall dynamic pressures measured when small irregularities or machined marks were detected in the vicinity of a transducer. For this reason, great care was taken to mount the transducers as flush as possible.

### **4.9 Data Reduction**

#### 4.9.1 Introduction

As with any experimental work the results presented have limited accuracy due to measurement errors. Section 4.8 presented the calibration procedures and estimated errors of the fundamental quantities that are measured in our experimental apparatus. In this section an uncertainty analysis of the quantities used in this work that are calculated from the fundamental measurements will be presented.

#### 4.9.2 Uncertainty analysis

Uncertainty analysis is a standard procedure applied to experimental data to evaluate its precision. In most cases the accuracy of the data is essential to determine if a given hypothesis can be proved or disproved. The conclusions drawn from the results of experiments are intimately linked to the accuracy of the measured data and of the calculated variables. Most quantities of interest are not measured directly, but can be derived from directly measured variables such as pressure, temperature, and frequency. For this reason a procedure to establish how the uncertainties are propagated through the calculations is necessary.

The propagation of uncertainties for a function of several variables is described in equation (4.5) [Taylor]:

$$dq = \sqrt{\left(\frac{\partial q}{\partial x} dx\right)^2 + \dots + \left(\frac{\partial q}{\partial z} dz\right)^2} \quad (4.5)$$

The error  $\delta q$  in equation (4.5) is never larger than the ordinary sum

$$dq \leq \left|\frac{\partial q}{\partial x}\right| dx + \dots + \left|\frac{\partial q}{\partial z}\right| dz \quad (4.6)$$

Equation (4.5) can be used if the uncertainties in the measured variables  $x, \dots, z$  can be considered independent and random. They also need to present a Gaussian distribution, and all of the measured variables' uncertainties need to have the same odds. Usually the odds are expressed as a 95% confidence interval for the measurements. The 95% confidence interval tells us that the measured values are at most approximately 2 standard deviations from the mean.

In many cases it is difficult to accurately determine the confidence intervals. In our case, the errors specified in the calibrations presented in section 4.8 are the maximum estimated errors for that particular measurement since no statistical analysis to determine the confidence interval was conducted. The maximum errors used are significantly greater than the true expected errors for the majority of the measurements. For this reason, the uncertainty propagation analysis provides a maximum possible error associated with the calculated value and even when no confidence interval can be stated the real value is expected to fall in this extended range.

The uncertainty propagation calculations were performed using the software Engineering Equation Solver (EES) by Klein and Alvarado [see bibliography]. This software was used also for the data reduction and fluid properties estimations. The method for determining the uncertainty propagation used by the software is described in NIST Technical Note 1297 [Taylor and Kuyatt]. This method uses equation (4.5).

Table 4.2 presents the absolute and relative uncertainties of the measured variables used to estimate the calculated values. These values were used in the EES software.

The absolute uncertainties for the pressure measurements are based on manufacturer-specified relative uncertainties and the pressure sensor range that depends on the diaphragm installed.

As mentioned in section 4.8.5 the pistonphone calibration also provides a way to measure the accuracy of the frequency measurements for the cylinder vortex shedding generated tonal noise. Errors in frequency



measurements are negligible. However, noises produced by cylinders in cross-flows are not purely tonal but consist of a range of frequencies grouped closely together. For this reason, the absolute error in frequency measurements was chosen to be two discrete frequency increments in the spectra. The frequency increments for the dynamic signal analyzer used depend on the frequency span. In our case, most of the data was taken using a 10 kHz frequency span that, when divided by the eight hundred points of resolution gives 12.5 Hz per point.

The absolute error in cylinder diameter is estimated to be at most  $\pm 0.002$  inches (0.05 mm) for all cylinder diameters. Channel width errors are minimal since the width is set by the aluminum extrusion material used for its construction. The errors in channel width are assumed to be of the order of 0.1 mm. Errors in channel height are the most critical of all as can be seen in Table 4.3. These errors were measured to be at most +0.005 inches (+0.13 mm).

Note that the errors associated with the channel width and height are important when comparing our results to results from the literature. When comparing the results of Strouhal numbers between different samples tested in our experimental setup the height and width remain fixed for a number of samples and therefore this inaccuracy is eliminated. For this reason, the channel, once set into position, was used to test different samples before disassembling so that the trends would not be affected by this uncertainty.

Table 4.2 Uncertainties of Measured Quantities

<b>VARIABLE DESCRIPTION</b>	<b>UNITS</b>	<b>ABSOLUTE UNCERTAINTY</b>	<b>RELATIVE UNCERTAINTY (to full scale)</b>
Venturi Differential Pressure	inches of water	$\pm 0.05$	$\pm 0.25\%$
Venturi Absolute Pressure	psia	$\pm 0.8$	$\pm 0.25\%$
Test Section Absolute Pressure	psia	$\pm 0.1$	$\pm 0.25\%$
Test Section Temperature	$^{\circ}\text{C}$	$\pm 1$	N/a
Shedding Frequency	Hz	25	N/a
Cylinder Diameter	m	$\pm 0.00005$	Varies
Channel Width	m	$\pm 0.0001$	0.26%
Channel Height	m	$\pm 0.00013$	8%

Table 4.3 Maximum Errors Associated with Derived Variables

Variable	Units	Max Error due to Venturi Differential Pressure inaccuracy	Max Error due to Venturi Absolute Pressure inaccuracy	Max Error due to Test Section Absolute Pressure inaccuracy	Max Error due to Temp. inaccuracy	Max Error due to Shedding Frequency inaccuracy	Max Error due to Cylinder Diameter inaccuracy	Max Error due to Channel Width inaccuracy	Max Error due to Channel Height inaccuracy	Total
Average Flow Velocity	m/s	2.5%	2.3%	0.7%	0.2%	0	0	0.03%	5.2%	6.3%
Mass flow	g/s	2.5%	2.3%	0	0.2%	0	0	0	0	3.4%
Strouhal No.		2.5%	2.3%	0.7%	0.2%	2.3%	0.9%	0.3%	5.2%	7.3%
Reynolds No.		2.5%	2.3%	0	0.4%	0	0.9%	0.3%	5.2%	6.3%
Speed of Sound	m/s	0	0	0	0.2%	0	0	0	0	0.2%

#### **4.10 Hydrodynamic pressure fluctuations in 38.1 x 2.5 mm rectangular duct with flow**

Turbulent flow inside a rectangular duct will generate dynamic pressure fluctuations. These dynamic pressures are created by the interaction of the turbulence in the flow with the mean shear layer next to the walls [Bull]. In order to be able to measure the acoustic pressures of the flow-induced noise from cylinders, the acoustic pressures produced by the cylinder must be greater than the dynamic pressure fluctuations that the flow itself produces on the wind tunnel walls.

Dynamic pressure fluctuation measurements in our experimental test section were made at different microphone positions. The microphone positions referenced in this section can be seen in Figure 4.22. The measurements were made using two different types of transducers, 0.1" PCB105B02 dynamic pressure transducers, and ¼" Gunnar Rasmussen series phase matched microphones (see section 4.8). Power spectral density and coherence between pairs of transducers were taken with an HP3562A dynamic signal analyzer. The analyzer settings were: AC coupling, Hanning window, frequency span of 10 kHz, frequency bandwidth resolution of 12.5 Hz, and 50 averages. The measurements were taken using three different pairs of transducers at different positions. The measured pair were taken from positions 1a – 5a, d1-2a, Q6-Q1 (see Figure 4.22).

The measured dynamic pressure fluctuations can be contaminated by acoustic pressure fluctuations generated by noise-producing devices such as orifices, elbows, fans, or other devices that are used in wind tunnels. In our case, in which compressed air is used as the flow generator, flow-generated propagational dynamic pressure disturbances have two sources: 1) the pressure regulator that is used to control the flow rate, and 2) the inlet to the long rectangular duct at which there is a discontinuity in the flow path when the air passes from the round hose to the square duct (See Figure 4.4). To eliminate these sources of noise from the dynamic pressure measurements, acoustic foam was used to create an anechoic termination (see Appendix A).

Figure 4.39 shows the power spectral density taken at position Q6 as a function of flow velocity. Power spectral density plots made at different positions were similar to those presented here. Figure 4.40 compares the total and maximum tonal dynamic pressure levels of the measurements taken at the six different positions in the duct. The ¼" microphones are significantly more sensitive than the 0.1" dynamic pressure transducers. As can be seen in Figure 4.40, the measurements are more dispersed at lower flow velocities. Figure 4.40 indicates that even when there are significant differences in transducer sensitivities, the overall dynamic pressure levels agree relatively well even at very low flow velocities. Additionally, neither the overall dynamic pressure level nor the shape of the spectra showed variations as a function of measurement position. Figure 4.40 shows an increase of approximately 30 dB in the dynamic pressure levels in the flow velocities used in our experimental test section. This increase is linear with velocity in the decibel scale and shows a relatively small slope.

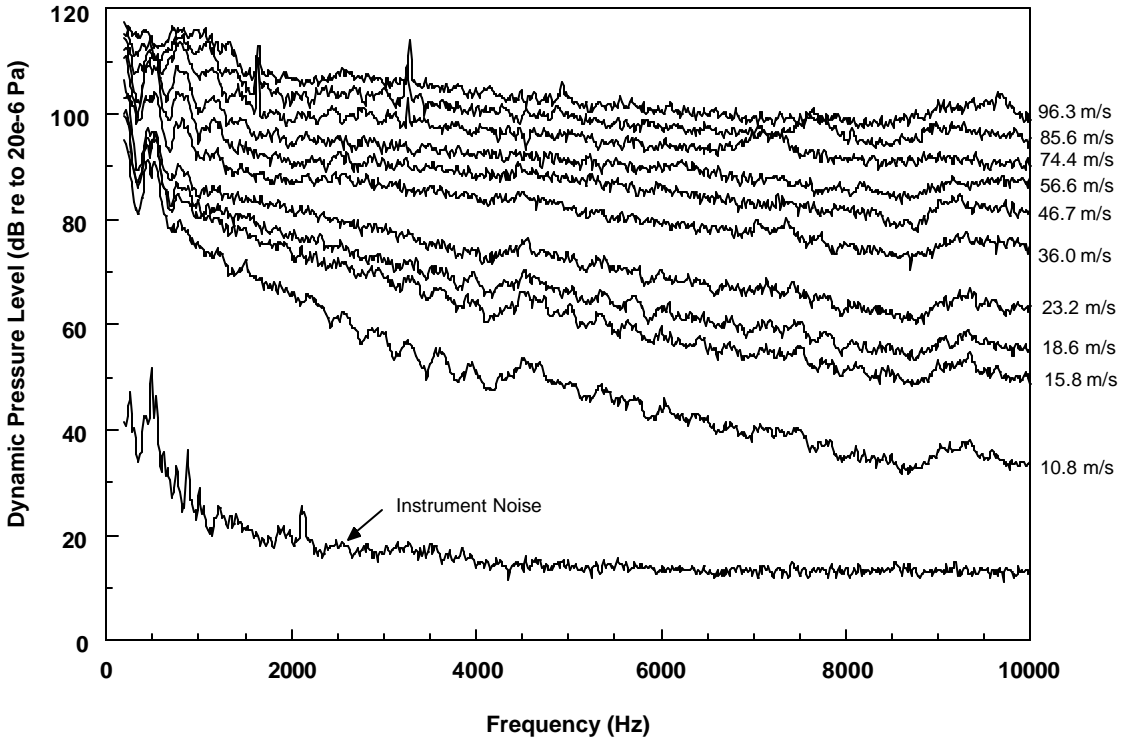


Figure 4.39 Dynamic wall pressure power spectral density as a function of flow velocity inside rectangular duct of 38.1 x 2.5 mm. Measurement position is at microphone Q6 (See Figure 4.22).

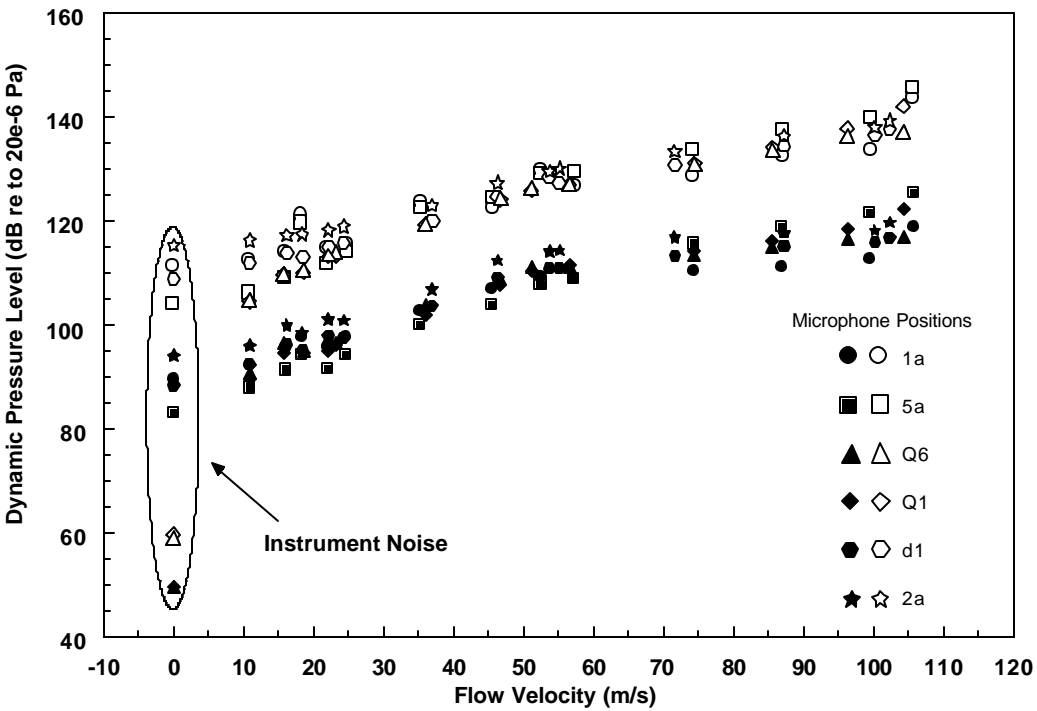


Figure 4.40 Dynamic pressure level at wall in empty duct as a function of flow velocity at 6 different microphone locations. Empty symbol overall (0-10 kHz), solid symbol tonal maximum.

Figure 4.40 separates the total overall dynamic pressure level (DPL) from the maximum tonal DPL. This is a more useful indicator of the noise floor level in our case in which tonal noise is the main interest. The maximum tonal noise usually occurred for lower frequencies, as seen in Figure 4.39. For this reason, the tonal noise presented will be an upper limit for measurements at higher frequencies.

An attempt at collapsing the data using the scaling variables used by Corcos for the wall-pressure fluctuations present in pipe flow is shown in Figure 4.41. The same parameters used by Corcos collapse the data relatively well for our case of a 38.1 x 2.5 mm rectangular duct. Figure 4.41 plots the same spectra presented in Figure 4.39 after nondimensionalization.

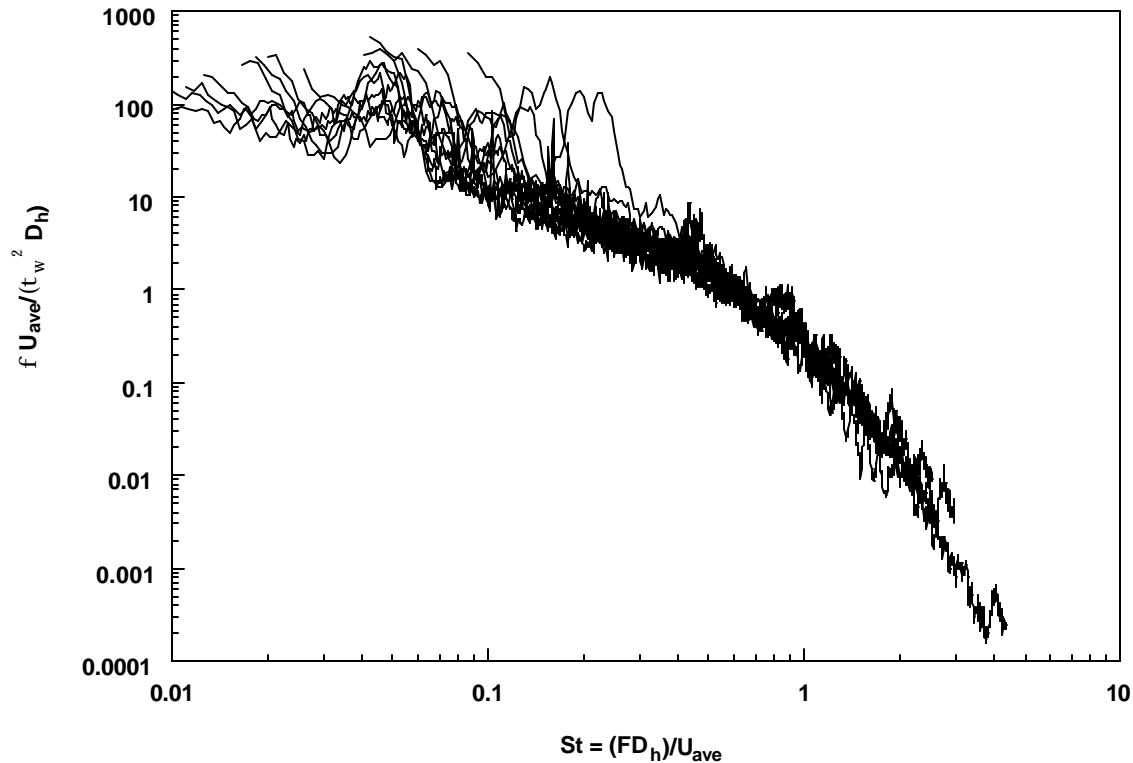


Figure 4.41 Nondimensional power spectral density of dynamic pressure measurements shown in Figure 4.39.

Dynamic pressure fluctuation measured at the wall of a duct with flow can be composed of several different components that create pressure disturbances and that cannot be separated directly. Possible pressure fluctuations can include 1) propagating acoustic plane waves, 2) propagating acoustic higher order modes, 3) acoustic standing waves, 4) other localized nonpropagating acoustic phenomena, 5) propagating hydrodynamic pulsations such as vortex shedding, 6) propagating hydrodynamic turbulent flow fields, and 7) nonpropagating localized hydrodynamic phenomena [Pedersen and Norton].

In our case, the introduction of acoustic foam at the inlet of the test section minimizes the possibility of propagating plane waves generated by the flow inlet (see Appendix A and Figure 4.4). This is especially true at the more easily damped higher frequency plane waves. Lower frequency plane waves are harder to attenuate, and complete elimination of them by the acoustic foam termination was not achieved. Another source of plane wave

generation is at the termination of the test section where there is a flow discontinuity. At this discontinuity, the flow itself or the internal duct pressure fluctuations might excite plane and higher order modes. Propagating higher modes are only present above their respective cutoff frequency. For our test section in air, and assuming no flow, the first three cutoff frequencies are harmonics of 4525 Hz. This means that for the frequencies on interest in our case (0-10 kHz) only the first two higher modes could be present. Higher modes that might be excited will be exponentially attenuated a few hydraulic diameters from their origin [Norton]. The measurements shown in Figures 4.39, 4.40, and 4.41 were made far from any possible acoustic source. One way to determine if there are propagating pressure disturbances is to determine the coherence of microphone pairs. If the coherence is close to one, then it can be assumed that the dynamic pressures contain a high component of propagating fluctuations. If the coherence is close to zero then it can be assumed that the pressure fluctuations are either due to localized hydrodynamic fluctuations or caused by nonpropagating localized acoustic fluctuations. Nonpropagating acoustic fluctuations can be caused close to an acoustic source where many modes might be excited. These higher modes cannot propagate and therefore are only important in the vicinity of the source. If no sources are present and the coherence is close to 0, then the measurements represent only hydrodynamic pressure fluctuations.

Figure 4.42 shows representative coherence of measurements taken at microphone positions 1a-5a at the highest and lower flow velocities and also from measurements taken at microphone positions Q6-Q1 at an intermediate flow velocity. The coherence between microphone pairs was similar except at frequencies below 1 kHz and above 9 kHz where significant values of coherence were seen at the different microphone positions. It is not clear what is the cause of the larger coherence below 1 kHz and above 9 kHz. Additionally, it is unknown what causes the increase in coherence at higher flow rates. It is speculated that for higher flow velocities a propagating turbulent flow field might increase the coherence values when convective effects transport these disturbances.

Boundary layer pressure fluctuations on flat plates have been studied extensively as reported by Bull 1968, 1996. The earliest theoretical work on pressure fluctuations on a boundary surface was done by Kraichnan in 1956 [Bull 1968]. Kraichnan and Lilley linked the root mean square (RMS) value of the wall pressure fluctuations to the mean shear stress at the wall  $\tau_w$ . Wall pressure fluctuation values reported by these researchers lie in the range  $2\tau_w < p' < 6\tau_w$  for a wide range of Reynolds numbers. Figure 4.43 compares the overall dynamic pressure levels nondimensionalized by the estimated wall shear stress. At lower values of Reynolds numbers, there is significant dispersion in the measurements, and some of the values do not fall in the estimated range. This is very likely the result of dynamic pressure transducer insensitivity. Microphones at positions Q1 and Q6 follow very closely the results by Corcos. Those two microphones are approximately two orders of magnitude more sensitive than the microphones at other positions. At higher values of Reynolds number the results fall right in the middle of the expected range and compare favorably with other measurements made inside pipes with flow. The dynamic pressures at higher Reynolds numbers are significantly higher than instrument noise even for the more insensitive transducers.

#### **4.11 Acoustic vs. hydrodynamic pressure fluctuations**

For single cylinders in cross-flow, flow separation and the creation of vortex shedding are responsible for the very near sinusoidal pressure oscillations on the cylinder's surface that create the cylinder fluctuating forces and

generate sound. The flow phenomena responsible for these effects is concentrated in a very narrow region in front and on the sides of the cylinder [Zdravkovich 1997] and also in a larger region downstream in the wake where the vortex shedding is convected downstream and latter diffuses into turbulence. Vortex shedding affects mainly the wake of the cylinder; for this reason, the acoustic near field is very close to the cylinder everywhere except in the cylinder wake where the hydrodynamic incompressible fluid dynamic pressures called “pseudosound” by Ribner are present. This confirms our experimental observations from measurements at symmetric positions upstream and downstream of the cylinder. For upstream measurements, the sound pressure levels correlate well with results of the model presented in chapter 3. For downstream measurements in symmetrical positions in the cylinder wake, the pressure oscillations are significantly higher in amplitude. Measurements downstream of the cylinder but at positions where wake effects are not present also show results that are predicted by the model. Acoustic attenuation over short distances is very small and may be neglected for the distance of our microphone spacing [see, for example, Rodarte et al. 2000]. If the downstream “pseudosound” dynamic pressure fluctuations were actually acoustic, the noted discrepancies in dynamic pressures measured upstream and downstream from the cylinder (presented in Chapter 5) could not be detected. These observations mean that for a cylinder array where the cylinder wakes are everywhere present, the dynamic pressure measurements would include acoustic and hydrodynamic effects. The only place where the true acoustic pressures can be measured is upstream of the array since here there are no hydrodynamic pressure oscillations. At those locations the combined effects of sources downstream can be measured and only here the experimentally determined dynamic pressures could be assumed to be purely acoustic assuming that the regular hydrodynamic pressure fluctuations produced by turbulent flow are significantly smaller than the acoustic perturbations.

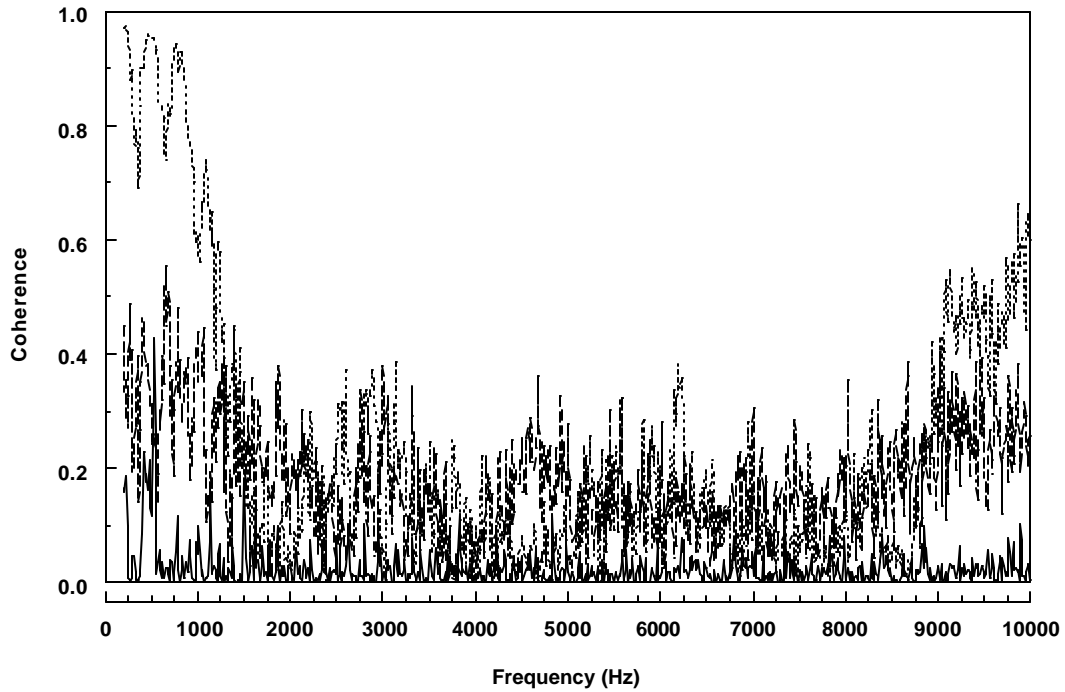


Figure 4.42 Representative coherence measured between microphone positions 1a and 5a at 99.6 m/s (dashed lines) and 10.8 m/s (solid line) and between microphone positions Q6-Q1 at 56.6 m/s (small dotted line).

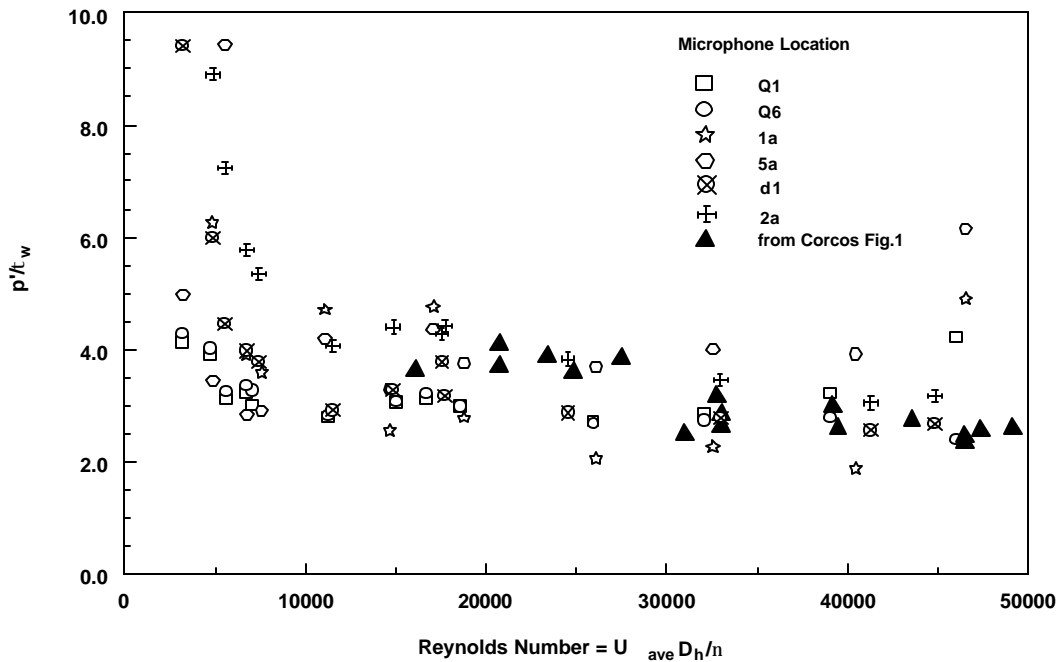


Figure 4.43 Comparison of the overall RMS dynamic pressure fluctuations measured at different positions inside our experimental test section as a function of Reynolds number. Dark triangles from Corcos measurements in pipe flow (Figure 1 in his paper).



## Chapter 5: Experimental Results

### 5.1 Introduction

In this chapter the results of different types of tests performed on plate heat exchanger samples, stereolithography cylinder arrays, single cylinders of constant and nonconstant diameter and pairs of cylinders will be presented.

This research started with the testing of plate heat exchanger samples using accelerometers. Later, dynamic pressure transducers were employed. The early work helped to establish that the noise problem in plate heat exchangers is similar to the well-known problem of acoustic resonance in large heat exchangers [Rodarte et al. 1998a].

Plate heat exchanger design and construction introduces complexities that are unique to this type of heat exchanger and make it difficult to generalize results. For this reason, stereolithography prototypes with “normal” cylinder arrays were made to study in more detail the flow-induced noise behavior of these short aspect ratio cylinders in a channel. The results of these tests helped establish some of the similarities and differences of the flow-induced noise phenomena between this type of heat exchanger and the large heat exchangers reported in the literature (see Chapter 2) [Rodarte and Miller 2000].

The simplest way to excite transverse acoustic resonances in a rectangular duct is using a single cylinder in cross-flow. For this reason it is of primary importance to understand the acoustics and flow-acoustic interactions for this case of acoustic resonance. Tests on single cylinders were used to validate the acoustic model based on fundamental concepts presented in Chapter 3.

Tests of nonconstant diameter “hourglass” shaped single cylinders were made to compare their flow-acoustic behavior to that of “normal” constant diameter cylinders. This type of cylinder is formed during the brazing process in some designs of plate heat exchangers (see Figure 4.11).

Single cylinders made using stereolithography were also tested. The purpose of these tests was to compare the behavior of significantly rougher cylinders to that of the smooth aluminum cylinders. This comparison is necessary to confirm the validity of using stereolithography for cylinder array testing.

Results of tests on pairs of cylinders in tandem and side-by-side arrangements are reported. These tests were made to begin to explore the acoustics and flow-acoustic interactions of multiple cylinders. The results of these tests are also used to test the mathematical model when more than one cylinder is present in the duct.

### 5.2 Plate heat exchanger tests

#### 5.2.1 Acceleration tests

Acceleration tests on plate heat exchanger samples were made on 6 different designs of plate heat exchangers. The tests were made using R134a and nitrogen as the working fluids. A description of the test procedure and accelerometer mounting locations is found in Section 4.5.3.

Acceleration tests on plate heat exchangers were made when the project began. At that time the source of the noise was not clear. It was not known if the noise was created by the heat exchanger itself or if it was created by the thermal expansion valve immediately upstream of the heat exchanger. Thermal expansion valves are known

noise producers, especially during transients when they often operate with superheated refrigerant [Rodarte et al. 1999b]. Thermal expansion valve noise is broadband in nature, but this fact alone could not exclude this noise source from creating tonal components. Broadband noise can transmit preferentially through the piping when internal acoustic modes and structural pipe modes coincide. When this happens, the particular valve-fluid-pipe arrangement used could become a narrow band pass filter that could explain tonal noise transmitting from a structure excited by broadband expansion valve noise [Rodarte et al. 1999a].

Different tests were conducted in the laboratory to identify the source of the noise in plate heat exchangers. To see if the valve noise was responsible for exciting the resonance seen in the plate evaporator, three tests were made. The first one involved an acoustic muffler placed between the expansion valve and the plate evaporator. The muffler significantly reduced the expansion valve noise that reached the heat exchanger. However, the resonance was not affected by the introduction of the muffler. The second test involved placing a speaker at the inlet tube to the heat exchanger and reproducing the broadband noise of the expansion valve without the flow effects. This test showed that no resonance was excited by this method. The final and perhaps the most conclusive test was performed in the R134a refrigerant experimental setup. The setup was operated to obtain two-phase refrigerant at the exit of the expansion valve, and then the refrigerant was evaporated in downstream heaters before reaching the plate heat exchanger test sample (see Figure 4.1). When two phase refrigerant exits the expansion valve the valve noise is reduced approximately an order of magnitude. The resonance present in the plate heat exchanger sample was unaffected. In other words, the conditions of the refrigerant exiting the thermal expansion valve have a very important effect in the noise generation from the valve but did not affect at all the resonance present in the plate sample.

The conclusion after these tests was that the expansion valve was not responsible for the resonance. However other types of flow-induced resonances different from the transverse acoustic resonance reported in large heat exchangers could be responsible. The results of the acceleration tests confirmed that the acoustic resonance phenomenon was similar to that of large heat exchangers since these results compared favorably with acoustic resonances established transversely in the plate evaporator samples.

The acoustic natural frequencies of the plate heat exchanger flow passage were determined using equation (3.98) after assuming several simplifications. First, the refrigerant flow passage is considered to be a rectangular volume. The actual passage deviates from this since there are protrusions in the walls of some plate evaporator designs. Another difference is that the walls are not perfectly flat on the sides. Simplifications include negligible flow velocity, no volumetric damping, and perfectly rigid walls. Finally, a correction for the speed of sound of the fluid will be used. This correction in the speed of sound has been used in previous studies and has been found to agree with experimental results made on large heat exchangers. The effective speed of sound depends on the solidity ratio  $\sigma$  and is defined as the lower limit of the inequality presented in equation (2.23).

The effective speed of sound of the fluid in the tube bundle is reduced by the presence of the tubes, which scatter the sound waves. If the array elements have dimensions that are a small fraction of the acoustic wavelength, the net result is a reduction in the speed of sound and an increase in dissipation [Blevins 1986]. The rationale behind

the concept of effective speed of sound is that the travel time for a sound pressure front is lengthened by the scattering due to the obstructions of the tubes.

Figure 5.1 shows acceleration spectra at different positions for plate evaporator sample A tested using R134a refrigerant. Photographs of the different plate evaporators showing their internal structure and naming convention used for the acceleration tests are presented in Appendix C. Plate evaporator A is the only plate with an in-line bluff body configuration. The bluff bodies formed are crosslike in shape. This shape is formed when two plates are placed face to face and then brazed. This design produced very strong resonance at virtually every condition as long as the fluid used was in the gaseous state. Plate heat exchangers C, F, and G have cylinder-array-like structures. These structures can be seen in Figure 4.11. Plate evaporators D and E have a very complicated three-dimensional structure after brazing. For this reason, it is difficult in this plate heat exchanger design to establish where the acoustic resonance is established and how this resonance is excited.

Refrigerant testing as mentioned in section 4.3 has some disadvantages, including a limited flow rate range. For these reasons testing of plate evaporators samples was also done using nitrogen. Nitrogen testing permits studying the acoustic resonance phenomena for a much wider range of flow velocities. Comparison of acceleration spectra for the two fluids shows similar frequency behavior once the speed of sound is considered. Table 5.1 compares the ratio of experimentally determined acoustic resonances obtained when the plate samples were tested with R134a and nitrogen to the ratios of speed of sound for these two fluids. The Mach number has an effect on the acoustic resonance of a rectangular duct with flow as mentioned above (see equation 3.98). When changing fluids, the Mach number effects are more important for the higher speed of sound fluid since for this fluid a greater flow rate is needed before a resonance condition can be established. The good agreement of the ratios presented in Table 5.1 show that the effect of the Mach number on the acoustic resonance in these cases is small. This is not the case in the acoustic resonances established with single cylinders, as will be discussed in section 5.4.

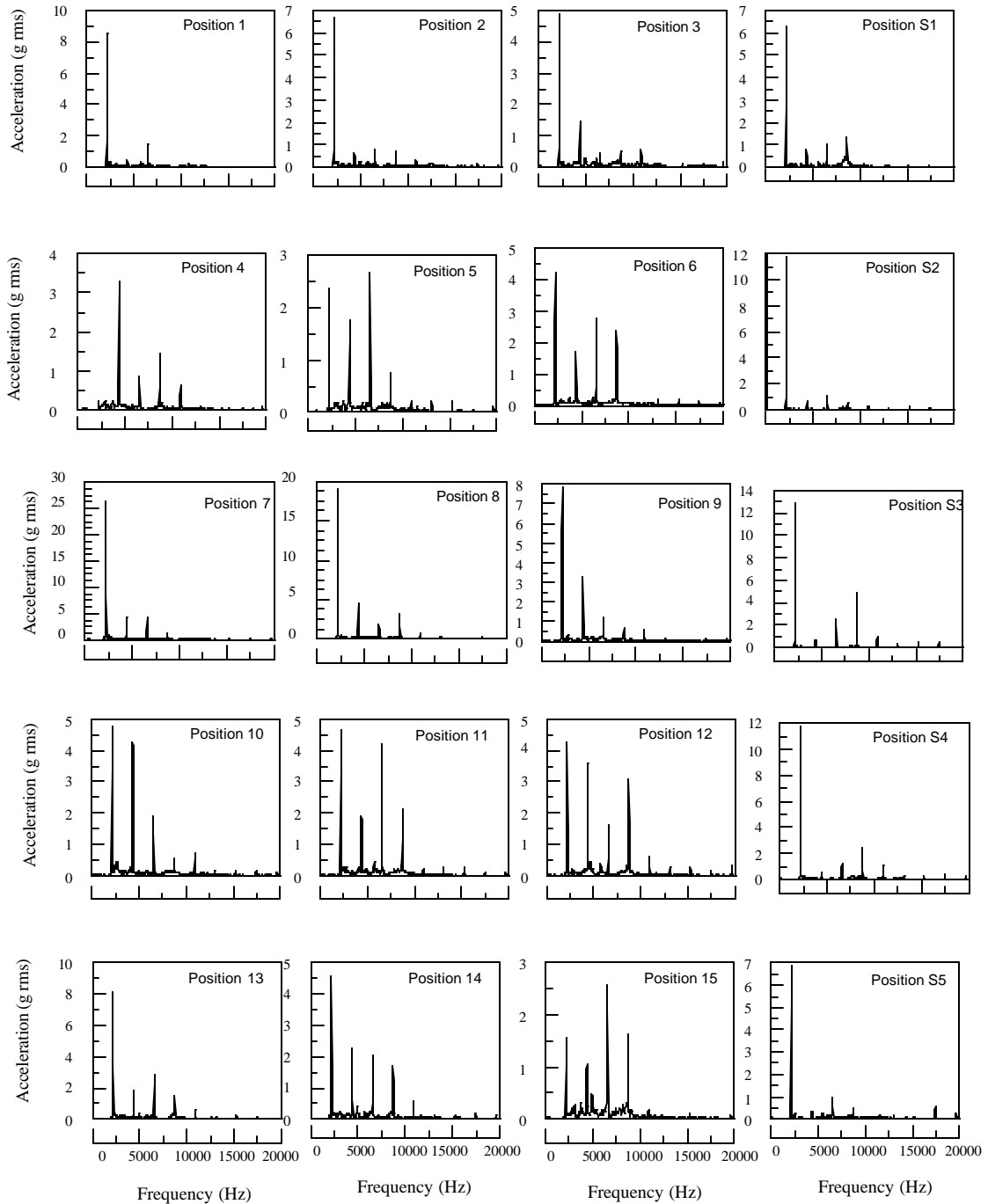


Figure 5.1 Acceleration power spectra taken from plate evaporator A using R134a refrigerant. Accelerometer positions on plate sample shown in Figure 4.13.

Appendix C shows frequency-velocity graphs. These plots show the frequency at which the peak of the acceleration spectra occurs for a given flow rate. The flow rates are estimated at the exit of the plate evaporator sample. In general the graphs for the plate samples A, C, F, and G have a lock in region and are similar to results found in the literature for large heat exchangers. Plate D and E do not follow the same trends probably due to their

complicated geometry. Figure C.12 for plate sample G shows a frequency band since for this heat exchanger the spectra was not clearly tonal but instead covered the whole band shown. These frequency bands are believed to be the result of resonances occurring at different frequencies due to the variations in transverse dimensions. These variations are caused by the “bumps” on the side walls of the plates.

Nitrogen tests were performed to study the acoustic resonance as it developed when increasing the flow velocity. Figure 5.2 shows the acceleration power spectra of the tests performed on plate sample A at position 7. The peaks in the acceleration spectrum does not show a linear frequency velocity dependence (Strouhal effect) and thus no Strouhal number at off resonance can be determined. In-line heat exchangers do not follow the classical excitation mechanism present for staggered arrays or single cylinders in a duct [Ziada and Oengören 1992, 1993]. This was believed to be one possible explanation but testing of plate F which has a staggered arrangement showed the same behavior (see Figure 5.3). Later tests using dynamic pressure transducers showed that the accelerometer was not sensitive enough to detect the Strouhal effect.

Table 5.2 summarizes results of the acceleration tests. It presents some possible channel dimension (widths) where an acoustic resonance might be sustained. The various widths are due to “bumps” on the side walls and to an increase in the channel width at the flow return section. The transverse acoustic resonance frequencies are then computed using these different dimensions as well as the solidity ratio for each heat exchanger. The ranges in the estimated frequencies are due to the variation in the speed of sound of R134a refrigerant depending on the amount of superheat.

Table 5.2 presents the experimentally determined acoustic resonant frequencies obtained with the two fluids. Comparison of the experimental and estimated natural frequencies points out where the resonance was established. The Strouhal number of the heat exchanger is also presented. The Strouhal number was calculated using the characteristic dimension  $D$ .

The full set of data for the acceleration tests can be found in the report by Hrnjak et al. 1997.

Table 5.1 Comparison of acoustic resonance frequency ratios to speed of sound ratios for plate heat exchanger samples tested with accelerometers.

Plate Name	R134a Freq. (Hz)	N <sub>2</sub> Freq. (Hz)	Freq. Ratio	R134a c (m/s)	N <sub>2</sub> c (m/s)	c ratio
A	2078-2220	4831-5053	2.18-2.43	148.4-156.7	350	2.23-2.36
C	1787-1957	4140-4676	2.11-2.61	146.5-165.0	350	2.12-2.39
D	3415-3740	7707-8513	2.06-2.49	142.9-165.2	350	2.12-2.45
E	1443-2391	3320-3768	1.38-2.61	146.5-161.0	350	2.17-2.39
F	1982-2016	4359-4393	2.16-2.21	148.6-159.0	350	2.20-2.35
G	1937-2593	4312-5125	1.66-2.65	154.6-163.0	350	2.15-2.26

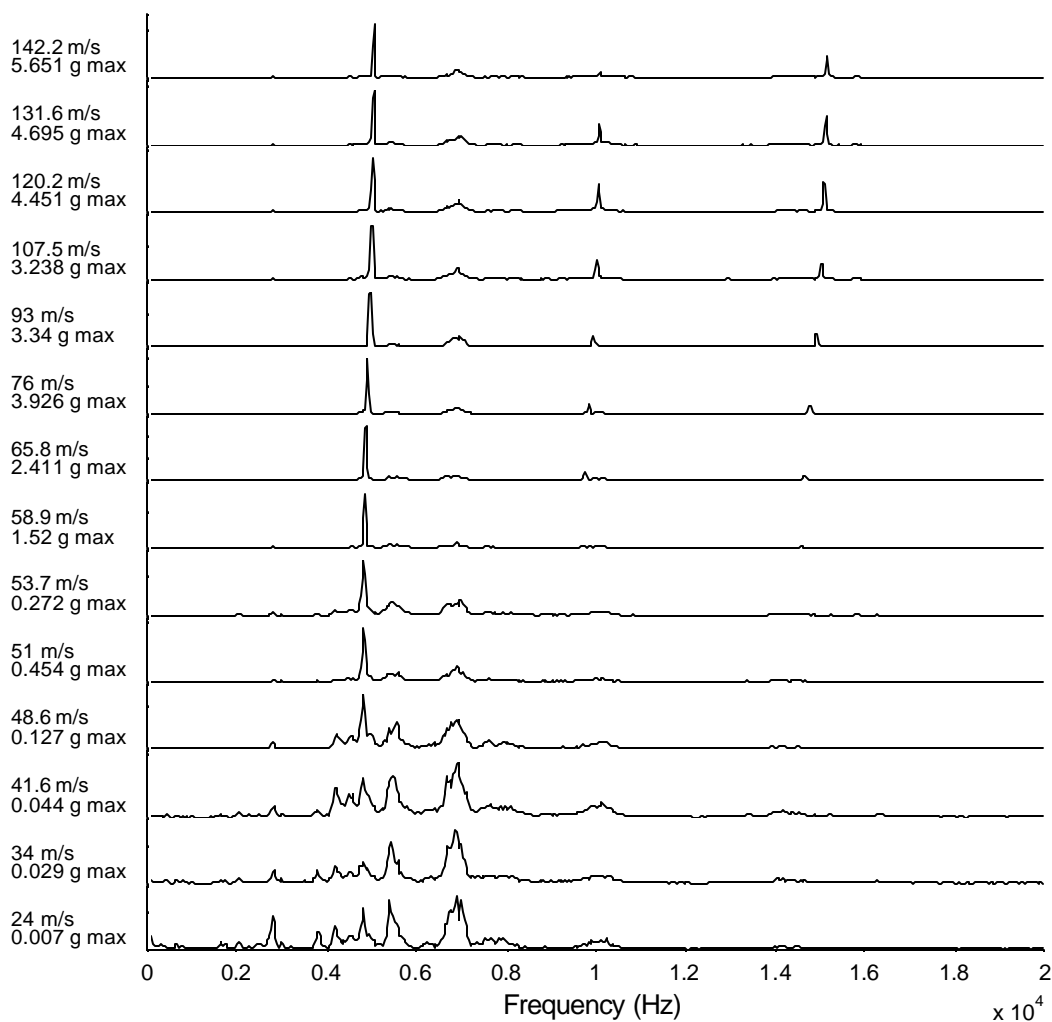


Figure 5.2 Acceleration spectra obtained at position 7 in plate A using nitrogen.

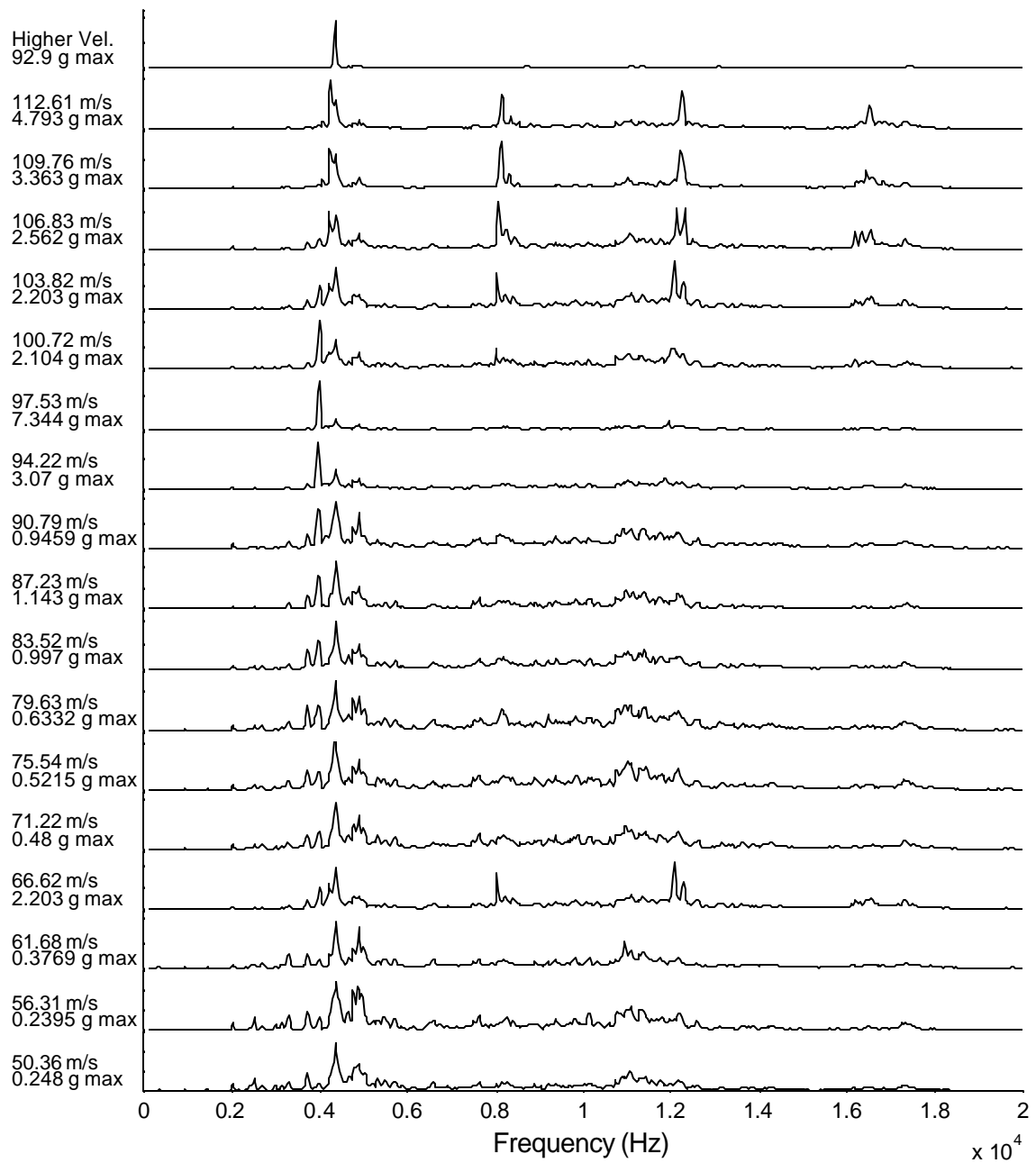


Figure 5.3 Acceleration spectra obtained at position 23 in plate sample F using nitrogen.

Table 5.2 Estimated and experimentally determined acoustic resonances in plate heat exchangers.

Plate Name	Duct widths W mm	Solidity ratio $\sigma$	Resonance Frequency (Estimated) R134a Hz	Resonance Frequency (Experimental) R134a Hz	Resonance Frequency (Estimated) N <sub>2</sub> Hz	Resonance Frequency (Experimental) N <sub>2</sub> Hz	D mm	Strouhal No.
A	31.4	0.356	1914-2256	2156	4786	4840-5060	5	0.503
C	37.5 29.5 80	0.404	1575-1857 2003-2360 738-870	1969	3938 5006 1846	4170-4640	3.5	0.134
D	31 65.5	0.25	2020-2380 956-1127	3770	5049 2390	7610-8300	3	0.178
E	35 37 74 79	0.18	1761-2075 1666-1963 833-982 780-919	1430	4402 4164 2082 1950	3310 7070-7320	4	0.463
F	38 29 79 71	0.29	1648-1942 2159-2544 793-934 882-1039	2000	4119 5397 1981 2205	3970-4375	4.5	0.392
G	37.5 33.5 79 75	0.25	1718-2025 1924-2267 816-961 859-1013	1935	4296 4809 2039 2148	4200-4800	4.5	0.499



### 5.2.2 Dynamic pressure tests

Dynamic pressure tests were performed on 6 different types of plate heat exchanger designs. Plate samples A, C, and F for which acceleration measurements were made (see section 5.2.1) and new variations of these plates designated as A2, C2, and F2, respectively, shown in Appendix D. Dynamic pressure tests were made using nitrogen and R134a refrigerant as the working fluids.

Appendix D shows the velocity-frequency and velocity-amplitude plots of the results obtained for the six different plate samples. Dynamic pressure spectrum taken using nitrogen and R134a refrigerant are also presented in Appendix D.

All of the plate samples tested except the plate sample A have an “hourglass” shaped circular cylinder arrangement with staggered or close to staggered configuration (see Appendix C and D photographs). For these structures in general flow periodicity frequency increases with flow velocity in the classical way. And all of the plate samples produced very loud acoustic emissions with gaseous flows. The acoustic emissions typically contain one or sometimes a few dominant frequencies. The noise significantly increased if the flow periodicity frequency coincided with the acoustic natural frequency of the duct.

Figure 5.4 show frequency-velocity and dynamic pressure–velocity diagrams for plate F when tested using nitrogen (similar diagrams for the other plate samples are presented in Appendix D). Empty circles show the frequency and amplitude in the region of flow velocities in which the frequency increases linearly with flow velocity (Strouhal effect). Empty squares show the same parameters after the onset of resonance. Finally, the full circles show the same parameters of a second peak in the power spectra that appeared before resonance at about the same frequency as the transverse natural frequency of the cavity. This resonance may have been excited by turbulence. Figure D.11 shows the spectra from which the data to make Figure 5.4 was taken.

The lines drawn in Figure 5.4 (top) show that there is a change of slope of the frequency versus velocity curve as soon as the second peak appears in the power spectrum. The projection of the slope of the frequency-velocity curve before the onset of the second peak coincides with the onset of a strong resonant peak. This supports the classical flow-induced acoustic resonance mechanism. It also indicates that measurements of Strouhal number should be performed far from resonance as discussed by Polak and Weaver.

From Figure 5.4, a resonance condition can be seen to develop at about 80 m/s. Figure C.10, made using accelerometer data on the other hand, seems to indicate that the resonance starts at 50 m/s. Comparison of Figure 5.4 and C.10 indicates that for our acceleration measurements what was believed to be a resonant condition was in fact a maximum in the power spectra at what was previously described as the second peak. Acceleration measurements seem to be more sensitive than was originally anticipated since even this weak peak in the spectrum could be detected. However since acceleration measurements are dependent on mounting position they should only be used to detect clearly resonant conditions or when a dynamic pressure sensor cannot be installed.

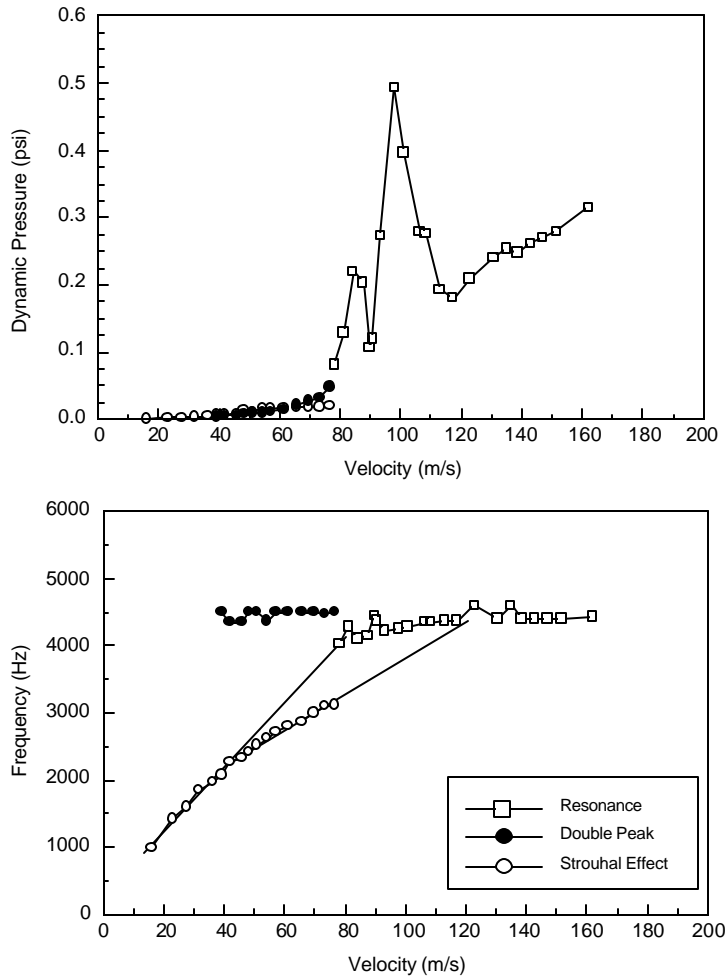


Figure 5.4 Frequency-velocity and amplitude-velocity plots made using dynamic pressure measurement of plate F taken with nitrogen. (see Appendix D).

Figure D.2 in Appendix D shows that plate A2 follows the classical linear frequency velocity relationship of the dominant peak in the spectrum that excites the acoustic resonance at the right frequency. The velocity plotted in Figure D.2 is the velocity at the inlet of the plate sample. The velocity at the exit can be significantly larger and can even reach choked conditions. Plate A2 reaches the first acoustic natural frequency with nitrogen when the flow at the exit is almost choked. For this reason, there is a very large increase in the dynamic pressure with no increase in flow velocity at the inlet. This happens since compressibility effects cause large increases in density while keeping the inlet flow velocity almost constant. Plate A which has an in-line type configuration with non-cylindrical bluff bodies does not follow the same linear frequency velocity behavior. However the same compressibility effects can be seen for this plate.

Figure D.4 shows that plates C and C2 also have pressure fluctuations that increase in frequency with flow rate. Plate C has a staggered configuration while plate C2 has a close to staggered configuration (see Figures C.3 and D.3). Plate C reaches acoustic resonance at a lower flow velocity. The amplitude velocity plots show the characteristic increase and decrease of the dynamic pressure measurements as it passes through the

resonance with increasing flow velocity (45-50 m/s). For this plate, the flow at the inlet is limited to around 55 m/s before the choking condition at the exit is reached. This flow is not enough to completely pass the resonance frequency, and a combined effect of resonance and an increase in density cause the large increase in dynamic pressure levels. This same phenomenon is seen for plate F in Figure D.6. For plate C2, the resonance and exit choking condition appear together and create the increase in the dynamic pressure seen in Figure D.4. A similar condition can also be seen for plate A2 in Figure D.2.

The significant increase in dynamic pressure at the high end of the inlet flow velocity shown in the amplitude plots in appendix D are caused by the increase in density of the working fluid. The flow velocity throughout the plate hardly changes, but the density increases considerably. The increase in density causes changes in Reynolds number and may explain why some researchers identified the importance of the Reynolds number [Ziada et al. 1989a] with the establishment of well-defined acoustic resonances. Ziada et al. 1989a created the increases in Reynolds number by increasing the flow velocity. Flow velocity and density are directly linked to the strength of the fluctuating lift forces on the cylinders that produce the sound. Additional results of tests on plate heat exchangers can be found in the report by Miller et al. 1998.

### 5.3 Stereolithography cylinder array tests

#### 5.3.1 Normal triangular arrays

Tests were performed on 5 normal triangular arrays (see Figure 2.1 for array description). Normal triangular arrays can be considered a subgroup of staggered arrays. This type of array is characterized by the pitch-to-diameter ratio ( $P/D$ ) where the pitch is defined as the distance between cylinder centers for any two adjacent cylinders. This is equivalent to a staggered array with  $T/D=P/D$  and  $L/D=(P/D)(\cos(\pi/6))$ . Tests were performed on 5 different normal triangular arrays with pitch to diameter ratios of 2.6, 2, 1.75, 1.6, and 1.45. The arrays consisted of 5 columns and 19 rows. The different pitch-to-diameter ratios were obtained by modifying the diameter while keeping the cylinder center positions fixed. The Strouhal numbers measured for the first three arrays closely follow the behavior of their larger counterparts as shown in Figure 5.5. Figure 5.5 data were obtained from the work by Oengören and Ziada 1998 (Figure 32 in their paper). The Strouhal numbers are, respectively, 0.27, 0.30, 0.315. These Strouhal numbers correspond to the lower frequency periodicity of the two periodicities that have been reported for this type of array. The higher Strouhal number could not be detected in our tests. The more densely packed arrays did not exhibit a linear frequency-velocity relationship nor any clear resonance, thus no Strouhal number could be determined.

Figure 5.7 and 5.8 present spectra taken from an array with pitch to diameter ratio of 2.6. Dynamic pressure transducers were installed at the center of the array after the 2<sup>nd</sup>, 4<sup>th</sup>, 12<sup>th</sup>, and 18<sup>th</sup> rows. Figures 5.7 and 5.8 show the spectra for the 2<sup>nd</sup> and 12<sup>th</sup> rows. In addition to dynamic pressures, the static pressure was also measured at each of these positions. Figure 5.6 shows density estimations from pressure measurements at each dynamic pressure sensor location. Temperature changes of the gas due to the near isothermal expansion were minimal and the temperature therefore remained close to ambient conditions throughout the sample under test. Using mass flow, cross sectional area, and density at each dynamic pressure sensor position, the flow velocity was estimated. Since there is a significant pressure drop, especially at higher flow rates, the flow velocity

changed considerably for any given mass flow rate at each measurement position. The velocities to the right of the spectra show the estimated velocity at the measurement point.

The spectra in Figure 5.7 show that there are two dominant peaks close to each other and to the first transverse acoustic mode for flow rates between around 40 to 50 m/s. This behavior is not seen in Figure 5.8. One of the two peaks seen in Figure 5.7 corresponds to the flow periodicity present at the second row of cylinders. This is clear since it follows a linear frequency velocity relationship. The second peak appears to be generated by flow periodicities present at positions inside the array, but further downstream where the flow velocities are larger. Similarly, at the higher flow rates, there are peaks between 6-7 kHz and 8-9 kHz in both figures. In Figure 5.7 at the higher flow rates, the peaks between 6 and 7 kHz are stronger and follow approximately a linear frequency velocity relationship. For this reason, it is believed that this periodicity is generated by the vortex shedding in the first rows of cylinders in the array. The higher-frequency peaks at around 8-9 kHz detected at the second row appear to be generated at positions inside the array but further downstream. For Figure 5.8 the inverse is true.

Figure 5.9 compiles the information presented in Figures 5.7 and 5.8 in addition to that obtained after the 4<sup>th</sup> and 18<sup>th</sup> rows. Since there are significant flow velocity variations throughout the array mass flow was used to plot the frequencies and power spectral density. Figure 5.9 (middle plot) clearly shows that at a given test condition (mass flow rate) flow periodicities at different frequencies are present in the array. These differences can be significant. At a mass flow rate of 4.55 g/s, for example, the frequency of the periodicities detected at the different positions in the array were 5775, 6125, 7400, and 7750 Hz! The frequency differences increase as the flow rate increases since larger flow rates cause larger velocity gradients in the array. When flow velocities instead of mass flow rates are used the data shows approximately a linear flow-velocity behavior. At low flow velocities, the data points approximately follow a single line indicating a constant Strouhal number throughout the array.

The increase in amplitude for the larger mass flows/flow velocities does not appear to be caused by proximity to a natural frequency but to increases in flow velocity and density alone. This can be seen in the region between 4 and 5 g/s where the power spectral density plots are significantly higher than when the frequency passed through the first transverse acoustic resonance of the duct at approximately 2.5 to 3 g/s.

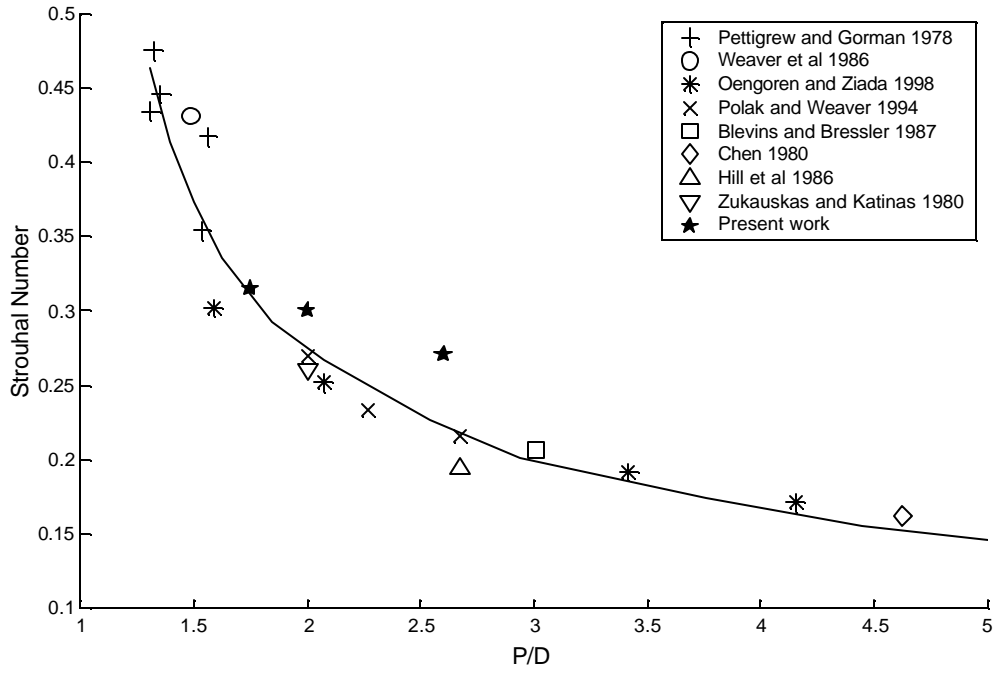


Figure 5.5 Compilation of Strouhal numbers for normal triangular arrays. Data from Oengören and Ziada 1998.

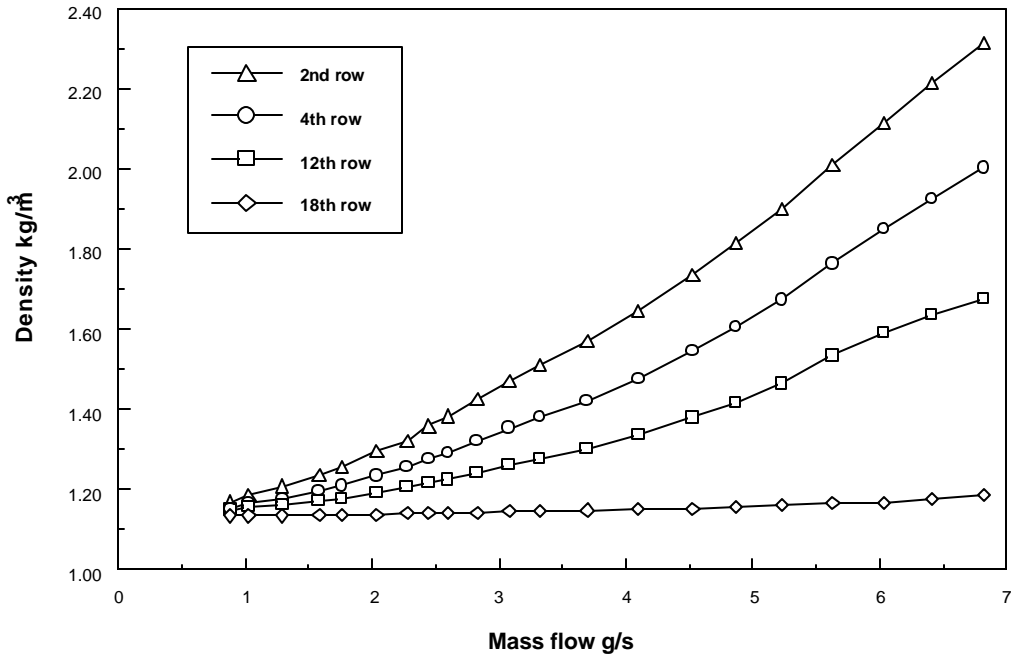


Figure 5.6 Density estimations from pressure measurements in normal triangular array with P/D ratio of 2.6.

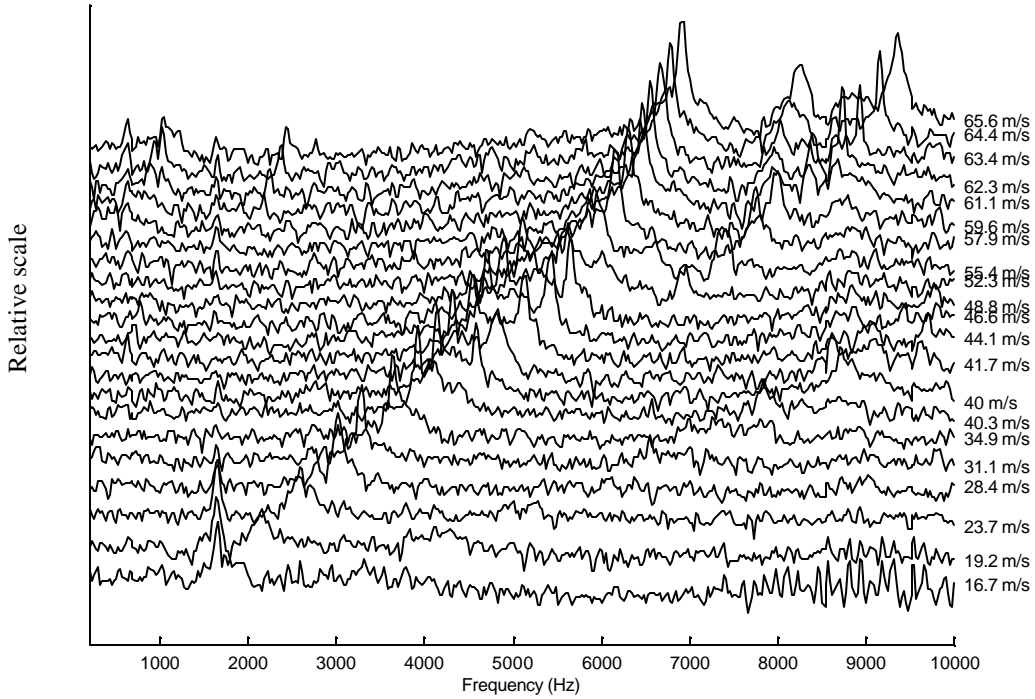


Figure 5.7 Waterfall plot of dynamic pressure spectra (relative dB scale) taken after 2<sup>nd</sup> row in normal triangular array with  $P/D = 2.6$ , 5 columns and 19 rows. Velocity at right estimated from mass flow and density at point of measurement.

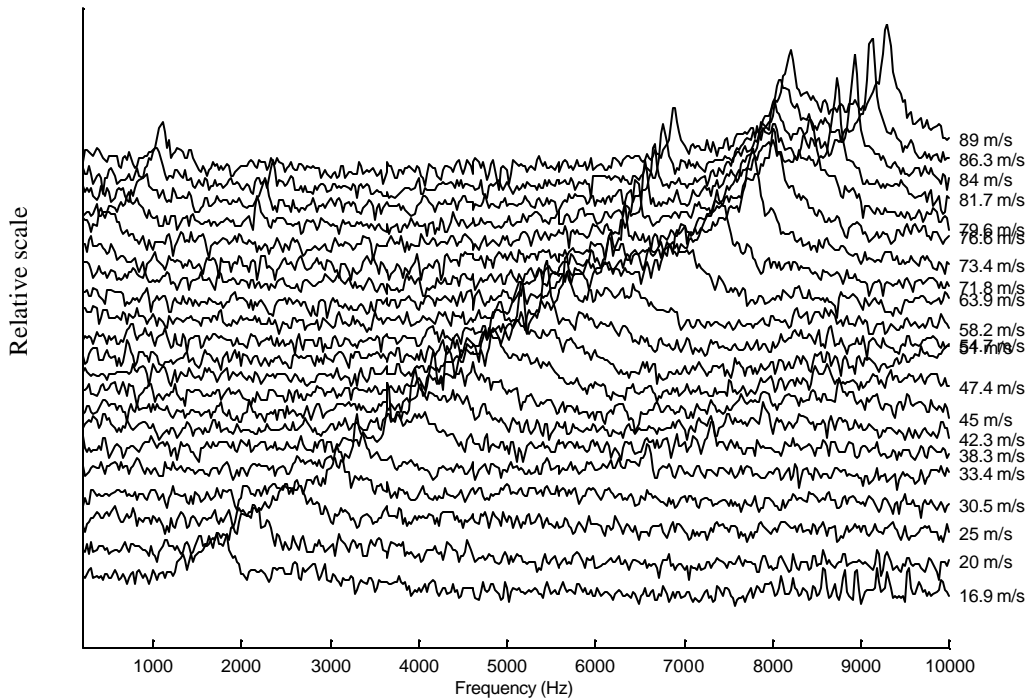


Figure 5.8 Waterfall plot of dynamic pressure spectra (relative dB scale) taken after 12<sup>th</sup> row in normal triangular array with  $P/D = 2.6$ , 5 columns and 19 rows. Velocity at right estimated from mass flow and density at point of measurement.

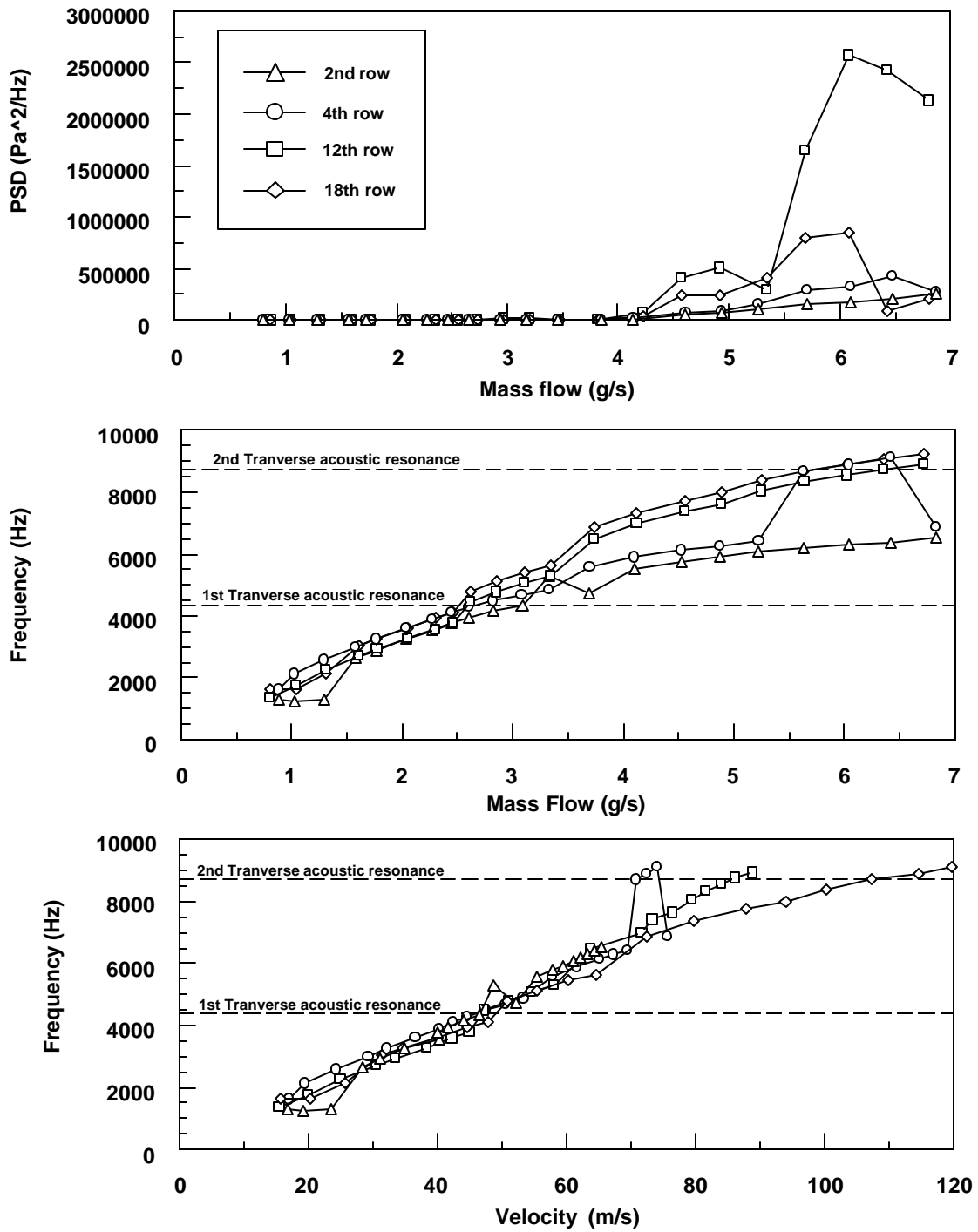


Figure 5.9 Frequency and amplitude plots of the dominant peak in the spectrum measured by dynamic pressure transducers placed at the center of a normal triangular array with P/D ratio of 2.6. Array with 19 rows and 5 columns inside a 2 x 37.5 mm duct. Velocity calculated using density at each row and minimum cross sectional area in array.

### 5.3.2 In-line square arrays

Two stereolithography in-line arrays were tested. The arrays have equal T/D and L/D ratios and thus can be also be classified as normal square arrays using only the pitch to diameter ratio (P/D) (see Figure 2.1 (a) and (c)). The P/D ratios for these arrays were 1.5 and 2.

Tests on the two arrays showed that once an acoustic resonance was excited the resonance remained for a very large range of flow velocities (see Figure E.6 and E.13 in Appendix E). Only after very large increases in flow velocity the frequency of the dominant peak in spectra shifts. The shift then appeared as a jump from the first mode to the second mode. This jump occurred earlier at the end of the array.

The Reynolds number remains constant throughout the array, even when the velocity increases since the ratio  $\rho_o V$  which is equal to the mass flow rate divided by the cross sectional area remains constant. Strouhal number on the other hand is not affected by changes in density. Velocity is one of its dominant variables. These facts have two implications. First, the Strouhal number determined at different locations throughout the array will not be the same for a given Reynolds number. The flow velocity changes throughout the array but the Reynolds number and frequency at resonance remain constant. Second, the Strouhal number will decrease with increases in Reynolds number. This happens since the frequency of the excited resonance is minimally affected by large increases in flow velocity, but the Strouhal number is reduced by flow velocity increases. Figures 5.10 and 5.11 show this behavior.

The shape of Figures 5.10 and 5.11 can be explained by the following relationship that can be derived from the Strouhal and Reynolds number definitions:

$$St = \frac{f D^2}{m} \frac{1}{Re} \quad (5.1)$$

The frequency at resonance does not change sharply with Reynolds number (see Figure 5.13 and 5.14). The main deviations are caused by the density increase with Reynolds number. These changes cause the plots to deviate from the perfect hyperbolic shape that would otherwise exist between Strouhal and Reynolds numbers.

Weaver et al. 1987 present two relations to obtain the Strouhal numbers for square in-line arrays. One was developed by Zukauskas and Katinas, and the other was developed by Weaver et al. 1987 using arguments from a paper by Owen. Owen predicted that the dominant peak in a bank of tubes would be equal to the interstitial gas velocity ( $V_t$ ) divided by twice the distance between successive rows as long as the ratio of diameter to lateral spacing lies between 0.2 to 0.6, or

$$f = \frac{V_g}{2L} \quad (5.2)$$

Weaver et al. 1987 obtained the Strouhal number as a function of pitch for a square in-line array by converting the gap velocity to upstream velocity using the following relationship:

$$V_u = \left( \frac{P-D}{P} \right) V_g = \left( 1 - \frac{1}{X_p} \right) V_g \quad (5.3)$$

and using the Strouhal number definition



$$\text{St} = \frac{f D}{V_u} = \frac{V_g D X_p}{2 L (X_p - 1) V_g} = \frac{1}{2(X_p - 1)} \quad (5.4)$$

The correlation by Zukauskas and Katinas after is has been converted for upstream flow is expressed in equation (5.5) below:

$$\text{St} = \left( 0.2 + \exp\left(\frac{-X_p^{1.83}}{0.88}\right) \right) \left( \frac{X_p}{X_p - 1} \right) \quad (5.5)$$

Figure 5.12 compares results of equations (5.4) and (5.5) to results of Strouhal number measurements from the literature. The Strouhal numbers obtained from Figures 5.10 and 5.11 are plotted as dark stars joined with a line to represent the range of Strouhal numbers found. The Strouhal numbers fall in the range found by other researchers. In particular the Strouhal numbers of the array with 1.5 pitch to diameter ratio seems to fill a gap in data from other work.

Figures 5.13 and 5.14 compare measured resonant frequencies to estimations of the transverse acoustic natural frequency of the duct calculated with solidity and flow effects, with flow effects only and with no effects. The results show that the resonances for the  $P/D = 1.5$  array closely follow the prediction obtained with solidity and flow effects. The  $P/D = 2.0$  array shows very different results even though the two arrays are very similar (see schematics in Appendix E). For the  $P/D=2$  array the solidity ratio does not seem to play a role.

Appendix E shows schematics of each array with microphone measurement locations, sound pressure level (SPL) graphs for each microphone location, phase between microphone pairs using the microphone position upstream of the array as the reference, coherence between microphone pairs and representative spectra for the two arrays.

SPL graphs show that at the end of the array the SPL is lower than at the initial row. This is believed to be caused by the higher density at the beginning of the array. The SPL at the center of the array (rows 9 and 14) is greater than at the end of the array. This condition was explained by Blevins 1986 as caused by the acoustic modes bound to the array.

Phase plots between microphone pairs show different behavior for the two arrays. Phase measurements are only valid for coherence values very close to one. For this reason coherence plots are included.

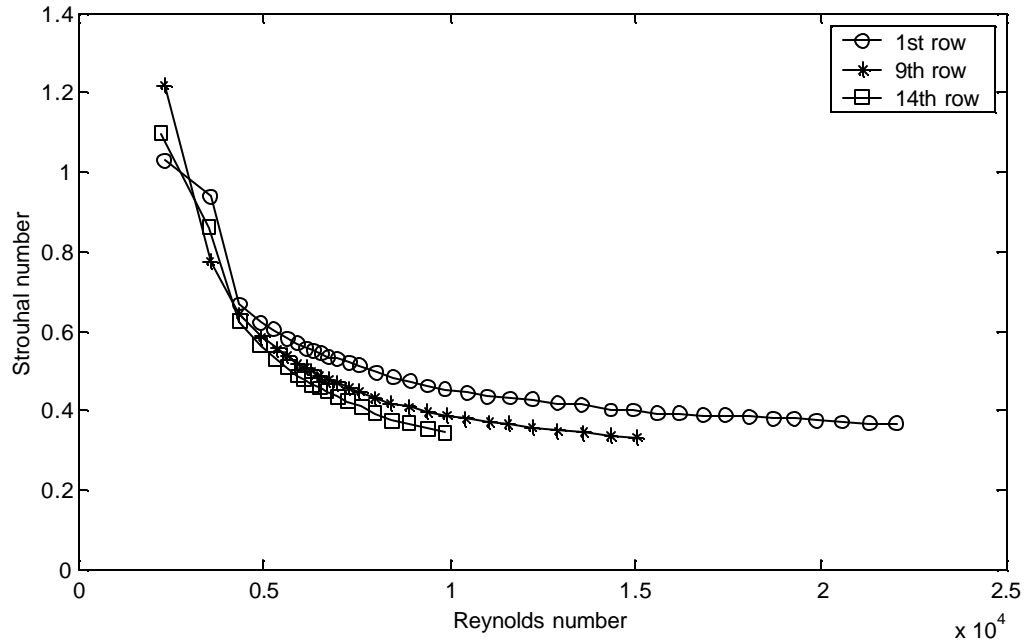


Figure 5.10 Strouhal number vs. Reynolds number for in-line square array with  $P/D = 2.0$ . Strouhal numbers from measurements at resonance except for the first two points at lower Reynolds number.

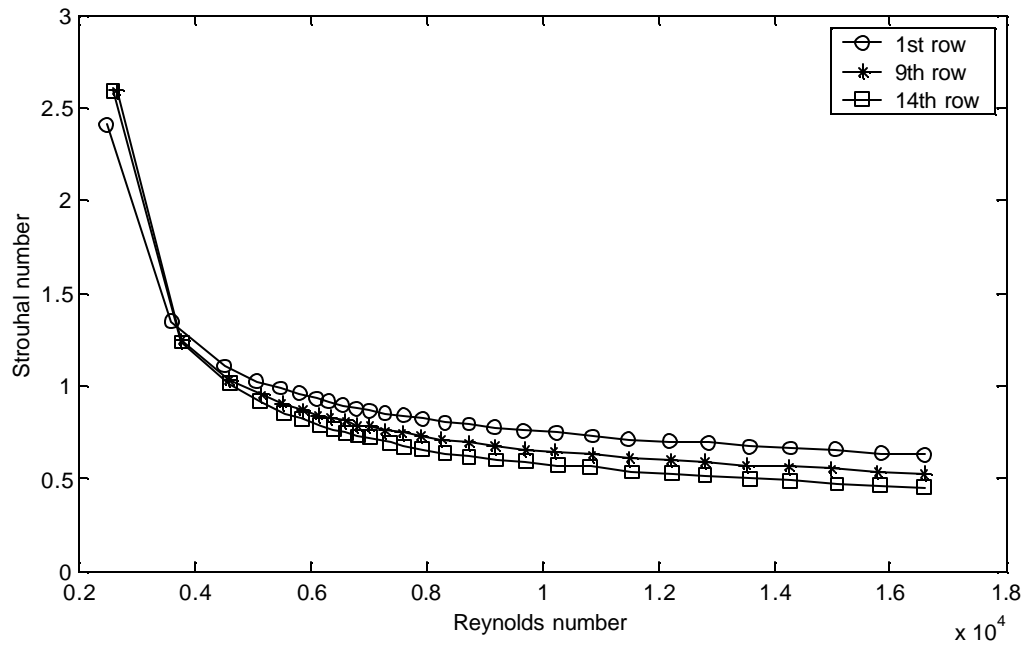


Figure 5.11 Strouhal number vs. Reynolds number for in-line square array with  $P/D = 1.5$ . Strouhal numbers from measurements at resonance except for the first two points at lower Reynolds number.

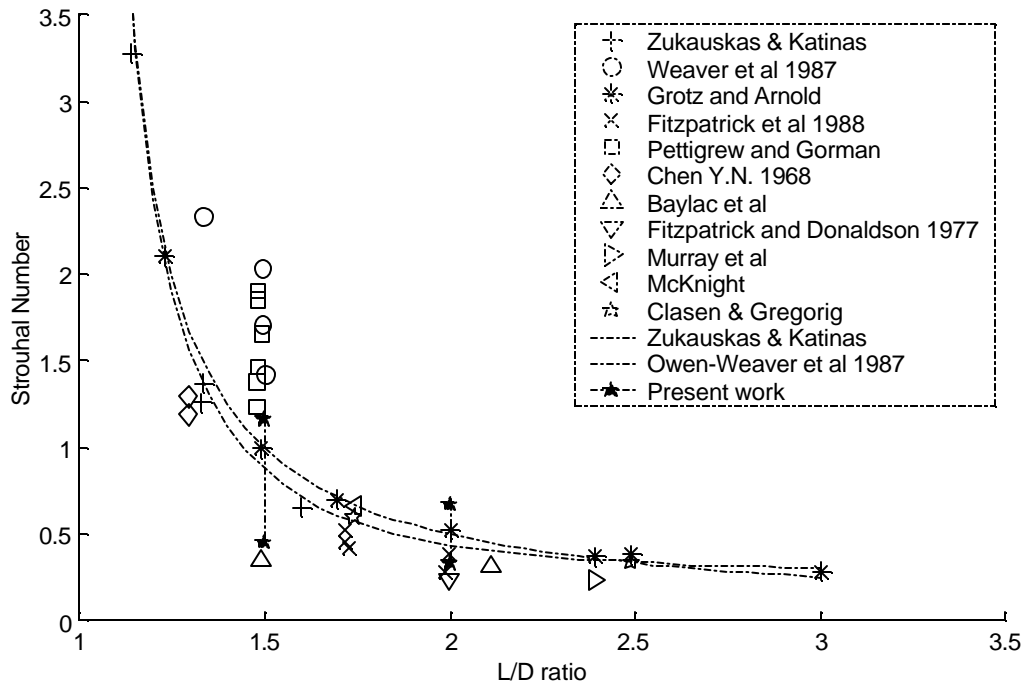


Figure 5.12 Strouhal numbers for square in-line arrays (from Weaver et al. 1987).

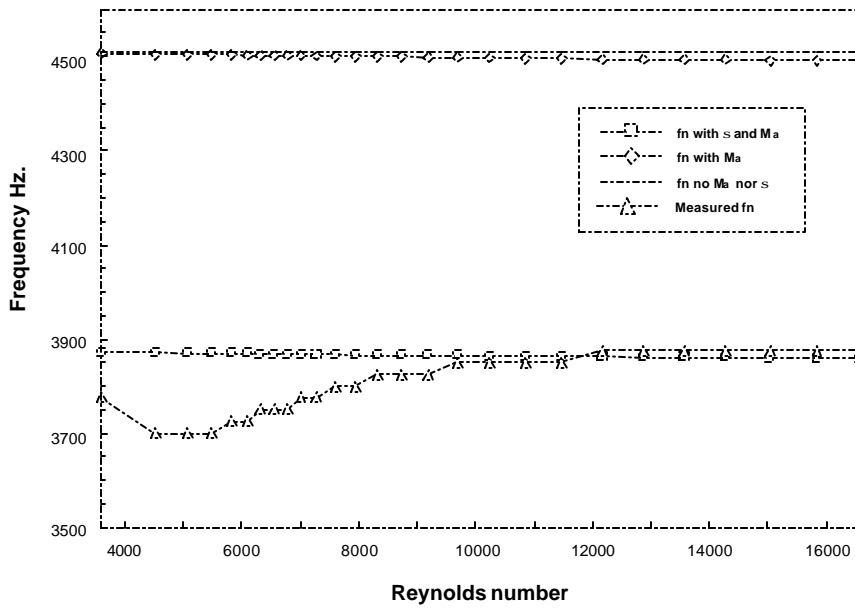


Figure 5.13 Comparison of measured resonant frequencies with estimations of resonant frequencies made assuming solidity ( $\sigma$ ) and flow effects ( $Ma$ ), flow effects only ( $Ma$ ) and no effects. In-line square array with  $P/D = 1.5$ .

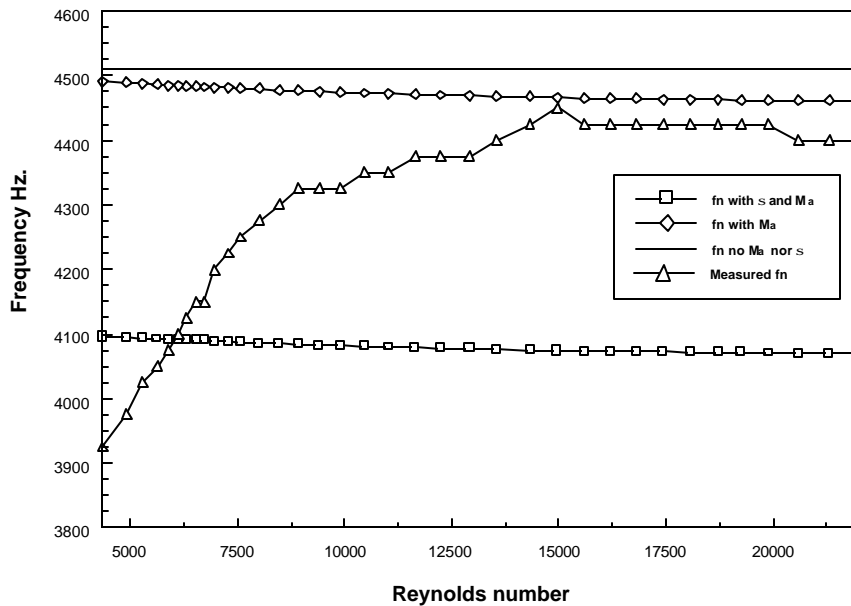


Figure 5.14 Comparison of measured resonant frequencies with estimations of resonant frequencies made assuming solidity ( $\sigma$ ) and flow effects (Ma), flow effects only (Ma) and no effects. In-line square array with  $P/D = 2.0$ .

### 5.3.3 Staggered arrays

Tests were performed on 10 different stereolithography staggered arrays. The arrays tested had the same  $T/D$  ratio of 3.0 and varying  $L/D$  ratios. The  $L/D$  ratios were 3.0, 2.5, 2.0, 1.8, 1.6, 1.4, 1.2, 1.1, 1.0, and 0.9. All of the 10 arrays had the same cylinder diameter of 1.905 mm. The arrays were inside a duct of 38.1 x 2.5 mm. All of the arrays had approximately the same length to cover the fixed microphone positions in the testing plate (see Figures 4.15 and 4.16). For this reason, the arrays had the same number of columns but different number of rows. Appendix F shows schematics of each of these arrays with dynamic pressure sensor positions. Appendix F also shows plots of the results obtained from the tests. The plots included are:

- M. SPL of dominant peak in spectra versus mass flow at all microphones locations.
- N. Phase and coherence measurements of different microphone pairs at dominant peak in spectra versus mass flow.
- O. Dominant frequency versus mass flow
- P. Dominant frequency versus flow velocity
- Q. Strouhal versus Reynolds numbers
- R. Some representative spectra at 3 sensor positions.

For all microphone pair measurements the microphone upstream of the arrays was always used as the reference.

In general, the results show that the sound pressure levels are larger at the center positions in the array. These results confirm the work of Blevins 1986, which measured the acoustic modes inside tube bundles. Sound pressure levels remain higher at center positions even when there is no resonance present. The combined sound produced by each cylinder inside the duct will be maximum at the center of the array from purely geometric

reasoning. It is believed that both of these effects, the tube array bound acoustic modes [Blevins 1986] and the superposition of the sound produced by the cylinders are responsible for this condition.

The first acoustic mode was always excited for all arrays and shows in general the characteristic rise in the sound pressure level. The sound pressure level dropped approximately 15 dB after the resonance frequency was passed. This only occurred for arrays in which there was a gradual increase in the flow-induced noise frequency. In cases where the noise frequency jumped from first to second or higher modes without intermediate steps, there was no decrease in the sound pressure level. At higher flow rates there was always a resonance present in the duct. In general, the sound pressure levels were higher at higher flow rates. This can be explained by the effect of the flow velocity on the dipole source strength from cylinders in cross-flow (see equation (3.31)).

Plots of phase between the microphone positions upstream of the array and the different microphone positions inside the array are also presented in Appendix F. The phase plotted was obtained from the transfer function measurements between the microphone pair at the frequency of the dominant peak in the power spectral density spectra of the upstream microphone. The upstream microphone was chosen as the reference since at this position hydrodynamic fluctuating pressures would be minimal. At this point, the fluctuating pressures would be those of the turbulent flow at the wall and not of the vortex shedding from the cylinders in the array (see section 4.11). Coherence plots of the same microphone pairs is included to validate phase measurements. Only when the coherence at the frequency of interest is very close to one phase measurements from the microphone pair can be considered to be accurate (see sections 4.8.6 and 4.8.7).

The frequency versus mass flow and frequency versus flow velocity plots are useful. They help identify if a given array locked at a resonance condition, if the array resonated at a predicted natural frequency of the duct, and how many modes were present at any given time. In these plots the estimated transverse acoustic resonances are also plotted as  $fn_1$ ,  $fn_2$  etc. The estimation of these resonance frequencies included solidity effects and neglected the effect of Mach number. Mach number effects are important only for very high velocities. For a flow velocity of 100 m/s, Mach number effects would reduce the resonance frequency 4.3% for air at atmospheric conditions. The velocity plotted was estimated using the density at the measuring point and the empty duct cross sectional area.

The frequency plots show that for most arrays and especially for higher acoustic modes the frequency of the main tonal noise “locked-in” at the acoustic resonance frequency (see for example Figures F.63, F.47). In a few cases and at low flow velocities, there was no “lock-in” of the dominant frequency after passing through an acoustic mode. This can be seen in Figure F.6. The “locking-in” phenomenon does not necessary imply a perfectly fixed frequency as a function of flow velocity, but more often a very shallow slope of the frequency-velocity line in comparison with the slope of the frequency-velocity curve below the first acoustic natural frequency.

Short aspect ratio cylinder arrays with many rows exhibit large pressure gradients down the duct, especially at high mass flow rates. This condition creates a range of flow velocities in the array for any given mass flow rate. Since flow velocity controls the frequency of the noise emitted by cylinders, the range of flow velocities present in the array causes tonal noise at different frequencies. This condition excites different

acoustic modes simultaneously, as can be seen in Figures F.46 and F.62. The excitation of different modes simultaneously is a condition not previously reported in the heat exchanger noise literature.

A very interesting phenomena appears to be occurring for the arrays with L/D of 0.9, 1.0, and 1.2. For these arrays, the tonal noise frequency has a “lock-in” behavior, but at frequencies far from the estimated resonance (see Figures F.54, F.70 and F.78). This could have three explanations. 1) The acoustic field is strong enough, even when no resonance is present, to disturb the vortex shedding process. 2) Mach number effects are important and should be estimated for the maximum velocity present in the array, that is, at the end of the array. 3) There are other parameters of importance for higher density arrays that might play a role in lowering the effective speed of sound of the fluid in the array.

Figures 5.15 and 5.16 are modified versions of Figures F.78 and F.79. In these figures different natural frequency lines are plotted. The natural frequencies were estimated using solidity ( $\sigma$ ) and Mach number (Ma) effects. The two different Mach numbers used were calculated assuming the velocity in the empty duct and the velocity in the free flow path in the array. The free flow path velocity is 2.85 times greater than the empty duct velocity.

Figure 5.15 and 5.16 show that the empty duct cross section area is not high enough to significantly modify the acoustic natural frequencies estimated using the solidity parameter alone. The flow velocity estimated using the fluid path in the array should be used to account for Mach number effects on speed of sound since this is where the convection effects are taking place.

At the higher flow rates it appears that the higher Mach numbers could lower the effective speed of sound to the point where the frequency of the resonance is observed. This however cannot explain the apparent resonance at lower flow velocities. Another factor that cannot be explained is why there appears to be a resonance at an intermediate frequency.

Strouhal number versus Reynolds number plots for the different arrays present very similar features. As mentioned in section 5.3.2, the Reynolds number is not affected by changes in density and velocity throughout the arrays since the ratio  $\dot{m} / A$  remains constant. The velocity increases deeper in the array for a given mass flow rate. Since the frequency of the dominant peaks in the spectra taken at different positions in the array is in many cases the same, the Strouhal number estimated at the end of the array is lower for a given Reynolds number than that estimated at the beginning.

As in the case of square in-line arrays, it can be seen that the Strouhal number decreases with Reynolds number (see Figure F.8 for example). In this case, the reduction in Strouhal number is not related to the near “locking in” phenomena present at the resonance conditions for in-line square arrays. In this case the frequencies, although increasing with flow velocity (see for example Figure F.6), are slightly nonlinear and produce Strouhal number decreases for increases in Reynolds number.

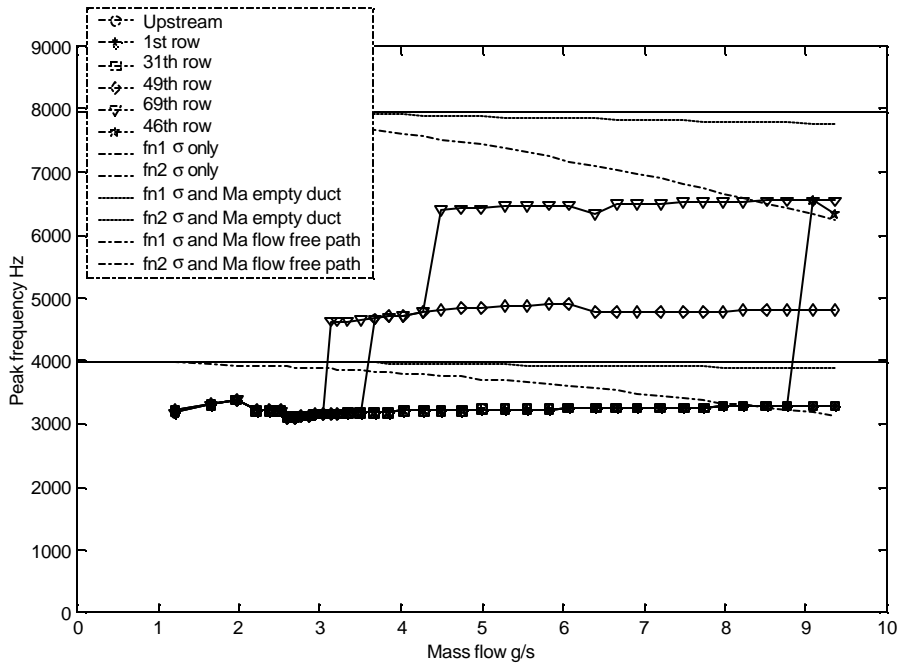


Figure 5.15 Frequency of dominant peak in spectra vs. mass flow for staggered array with  $T/D = 3.0$  and  $L/D = 0.9$ . Lines of natural frequencies ( $fn1$ ,  $fn2$ ) estimated assuming effects of solidity ( $\sigma$ ) and Mach number ( $Ma$ ).

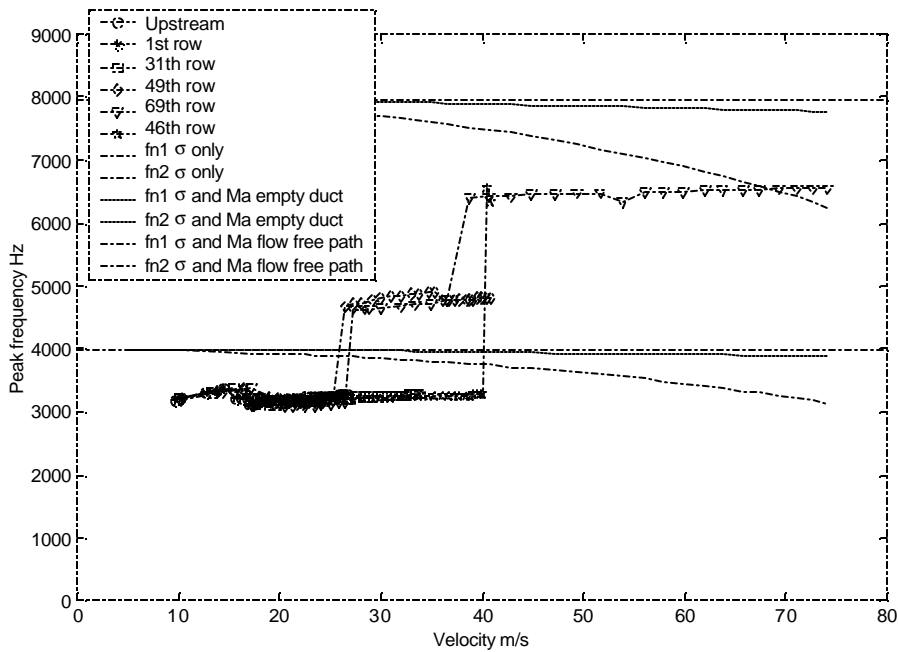


Figure 5.16 Frequency of dominant peak in spectra vs. empty duct flow velocity for staggered array with  $T/D = 3.0$  and  $L/D = 0.9$ . Lines of natural frequencies ( $fn1$ ,  $fn2$ ) estimated assuming effects of solidity ( $\sigma$ ) and Mach number ( $Ma$ ).

Figure 5.17 compiles the Strouhal numbers for the different arrays and compares them to Strouhal numbers obtained from maps of the well-known works by Fitz-Hugh and Chen 1968. The maps of Chen and Fitz-Hugh use the velocity at the minimum gap in the array so their Strouhal numbers were corrected for comparison purposes. Figure 5.17 shows that the Strouhal numbers compare favorably except for the arrays with the distinct frequency behavior discussed previously in this section. The two stars present at any given L/D ratio represent the limits of the range of Strouhal numbers found. The Strouhal numbers plotted were determined using results obtained at the 1<sup>st</sup> row.

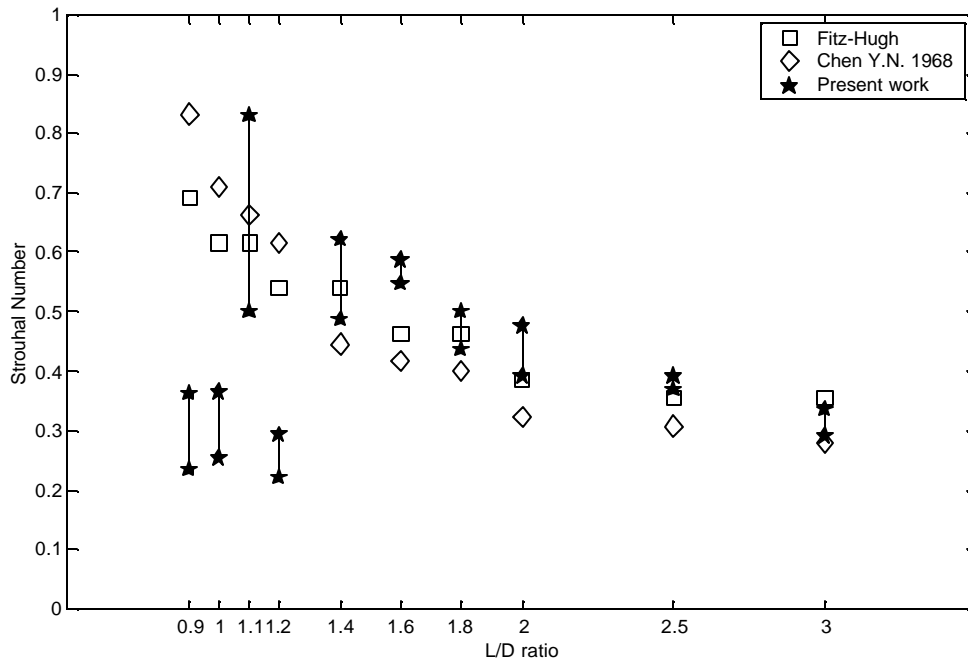


Figure 5.17 Comparison of Strouhal numbers for arrays with  $T/D = 3.0$  and different  $L/D$  ratios with results from Chen 1968 and Fitz-Hugh.

#### 5.4 Results of tests of single circular cylinders inside a duct

Single cylinders subject to cross-flow inside a duct provide the simplest case of flow-induced acoustic resonance in a duct. For this reason, a good understanding of the sound generation and attenuation mechanisms and phenomena present for this case is necessary to begin the understanding of the more complex flow-induced noise phenomena present in heat exchangers.

Single cylinder measurements were taken for cylinders of different constant diameter, as well as for cylinders in which the diameter varied along the cylinder axis. This second class of cylinders was tested since this is the type of profile that is present in many different plate heat exchangers.

##### 5.4.1 Cylinders of constant diameter

Single cylinder tests consist of measuring the SPL produced by the tested cylinder at different positions throughout the duct. The microphone positions naming convention and location are shown in Figures 4.22 and 4.23. In addition to sound pressure level the transfer function and coherence between microphone pairs was also measured.



Tests were performed for constant diameter cylinders made of aluminum and produced using stereolithography. Cylinders fabricated using stereolithography had diameters of 6.35, 3.0, 2.5, 2.0, and 1.5 mm. The aluminum cylinders had diameters of 6.35, 5.5, 5.0, 4.5, 4.0, 3.5, 3.0, 2.5, and 1.5 mm. No difference in behavior between the cylinders made using stereolithography and the machined aluminum cylinders was observed. The cylinders made using stereolithography are significantly rougher than machined aluminum cylinders (see section 4.7.2). This large difference in roughness apparently was not sufficient to alter their flow-induced noise behavior.

The 6.35 mm diameter aluminum cylinder was the first cylinder tested. Six 0.1" microphones were installed at any given time in the test section. These microphones were hooked in pairs to an HP 3562a dynamic signal analyzer. The microphones for these tests were installed at positions 1a, 2a, 4a, 5a, 6a and d1. Power spectral density at each position, as well as the transfer function and coherence of microphone pairs 2a-1a, 2a-4a, 2a-5a, 2a-6a, and 2a-d1, was measured. All the data taken with the dynamic signal analyzer had a frequency span of 10 kHz. The analyzer has 800 lines of measurement resolution. Each spectrum was averaged 50 times and the analyzer was self-calibrated before every measurement.

Figures 5.18 and 5.19 show representative sound pressure level spectra at two different locations. The values to the right of the spectra show the flow velocity present at the center of the test section when the measurement was taken. The values to the left of the graph are the measured sound pressure level. Sound pressure level was estimated by integrating the power spectral density around the dominant peak in the spectra. The integration included 50 Hz before and 50 Hz after the frequency of the dominant peak in the spectra.

Many of the spectra in Figures 5.18 and 5.19 show harmonic components of the dominant peak. This is especially true close to resonance. When the sound emitted by the cylinder is very close to the first transverse acoustic resonance, this resonance is excited, and two peaks can be seen, one at the acoustic resonance frequency and the other, usually the larger, at the vortex shedding frequency.

The flow velocity affects the acoustic resonance frequencies of a duct as expressed in the equations presented in section 3.5.8. The sound source excitation frequency, which is directly linked to the vortex shedding from the cylinder, is a function of the flow velocity and cylinder diameter. For this reason, the acoustic natural frequencies excited by the noise produced from different cylinders will vary since different cylinders produce noise that match the first transverse acoustic resonance frequency at different flow rates depending on their diameter. Figure 5.20 shows the experimentally determined frequency of the dominant peak in the spectra versus flow velocity for cylinders of different diameter. Figure 5.20 graphically shows what velocity is required for a cylinder of a given diameter to emit sound at a specific frequency. Since convection effects are nonlinear, the higher the acoustic natural frequency, the more important these effects become. A comparison between experimentally determined resonance frequencies and first transverse acoustic resonance frequencies determined using the theory presented in section 3.5.8 is shown in Chapter 6 (section 6.11). In this section, the differences between the acoustic resonances with and without convection effects will be shown where appropriate. The effect of convection on the acoustic natural frequency ( $f_{n1}$  with flow) was estimated using the velocity measured when the noise source coincided with the acoustic natural frequency.

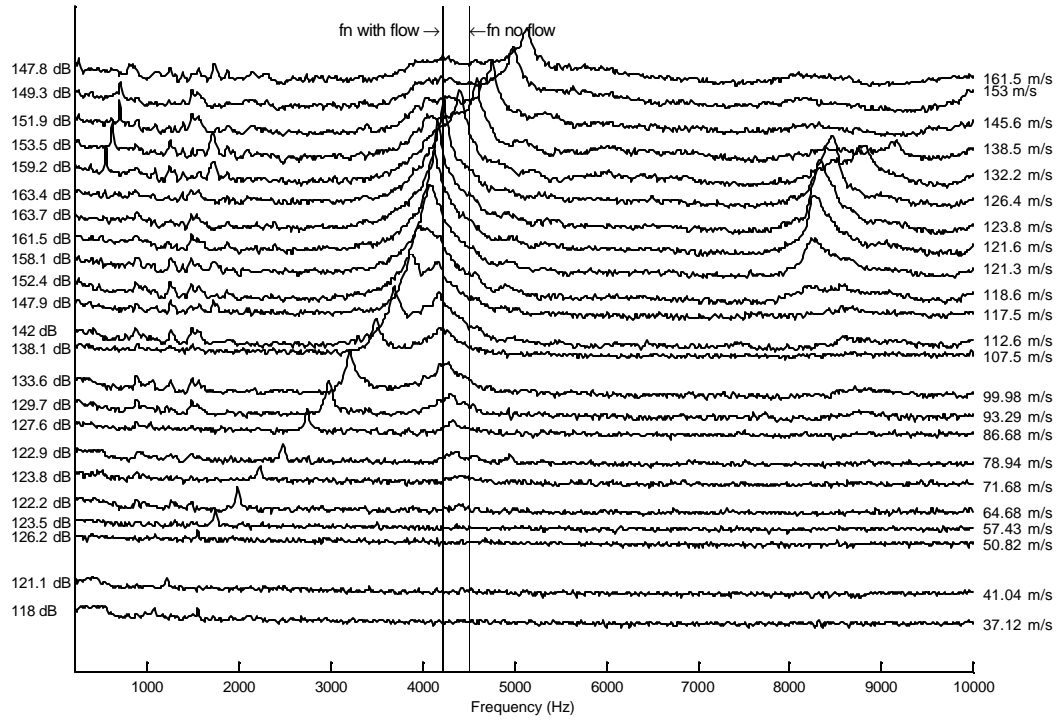


Figure 5.18 Waterfall plot of spectra measured at microphone position 2a. Single 6.35 mm cylinder diameter. Acoustic resonance estimated with flow velocity at resonance condition ( $f_{n1}$  with flow).

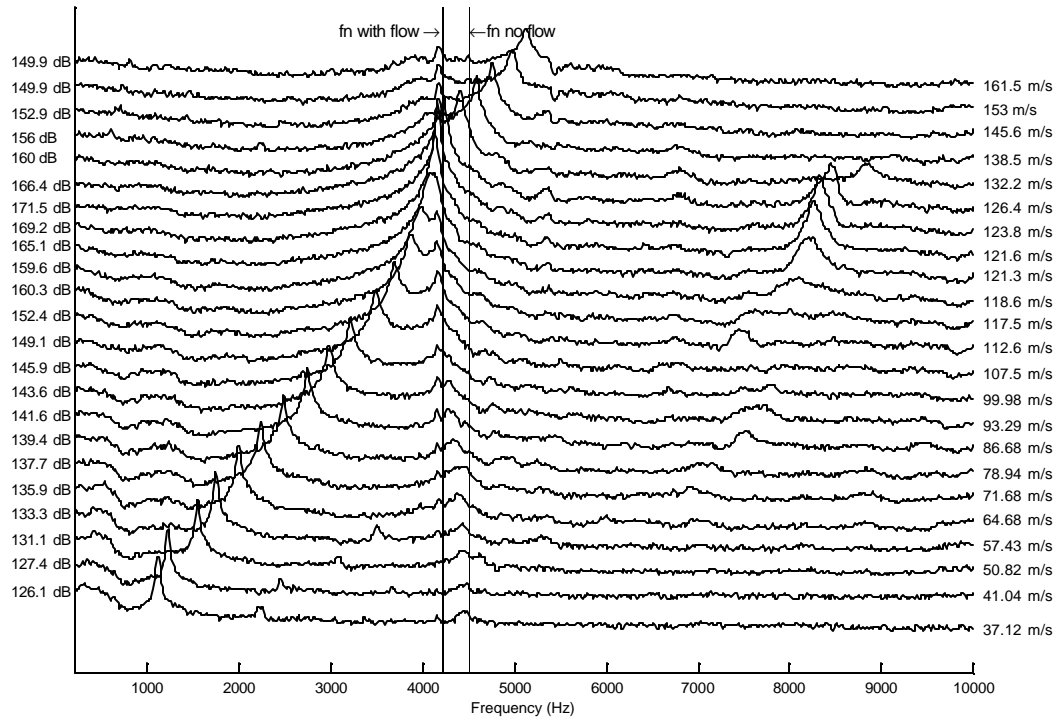


Figure 5.19 Waterfall plot of spectra measured at microphone position 6a. 6.35 mm cylinder diameter. Acoustic resonance estimated with flow velocity at resonance condition ( $f_{n1}$  with flow).

Figure 5.20 can be obtained using the spectra taken at any microphone position. The velocity used in the plot is the average velocity in the duct. This figure shows an almost perfectly linear relationship between these quantities. The linear relationship was not broken when coincidence between first transverse acoustic natural frequency and the sound source frequency was reached. Heat exchangers and single cylinders inside a duct have been reported to present the condition of vortex “lock in” when the vortex shedding frequency matches an acoustic natural frequency [see Ziada et al. 1989a and Blevins and Bressler 1987a,b, 1993, for example]. Under these conditions the frequency of vortex shedding remains nearly constant with increases in flow velocity until the velocity is high enough to get outside the “lock in” region where the normal linear frequency-velocity relationship is re-established or when a higher acoustic mode is excited. During single cylinder testing, no “lock in” region at resonance was observed as seen in Figure 5.20.

The main purpose of single cylinder tests was to validate the modeling approach developed in Chapter 3 and in general to understand from a fundamental perspective the flow-induced noise phenomena produced by bluff bodies in cross-flows inside a duct. The information required to validate the model is the acoustic pressure field and phase information between measuring points as well as fluid related properties such as density, speed of sound and flow velocity.

Figure 5.21 shows a typical result of the sound pressure level at the frequency of the dominant peak in spectra versus dominant peak frequency. Appendix G shows results of the tests for cylinders of different diameters. One of the characteristic features of the SPL versus frequency plots in our tests was that as expected the SPL is greater at sensor positions closest to the cylinder. Also noted, as expected, was a characteristic rise in the SPL close to the first transverse acoustic mode of the duct. As mentioned above convection effects are important for the flow velocities present in the duct. Figure 5.21 shows that the first resonance experienced is very close to the first transverse acoustic mode estimated with convection effects.

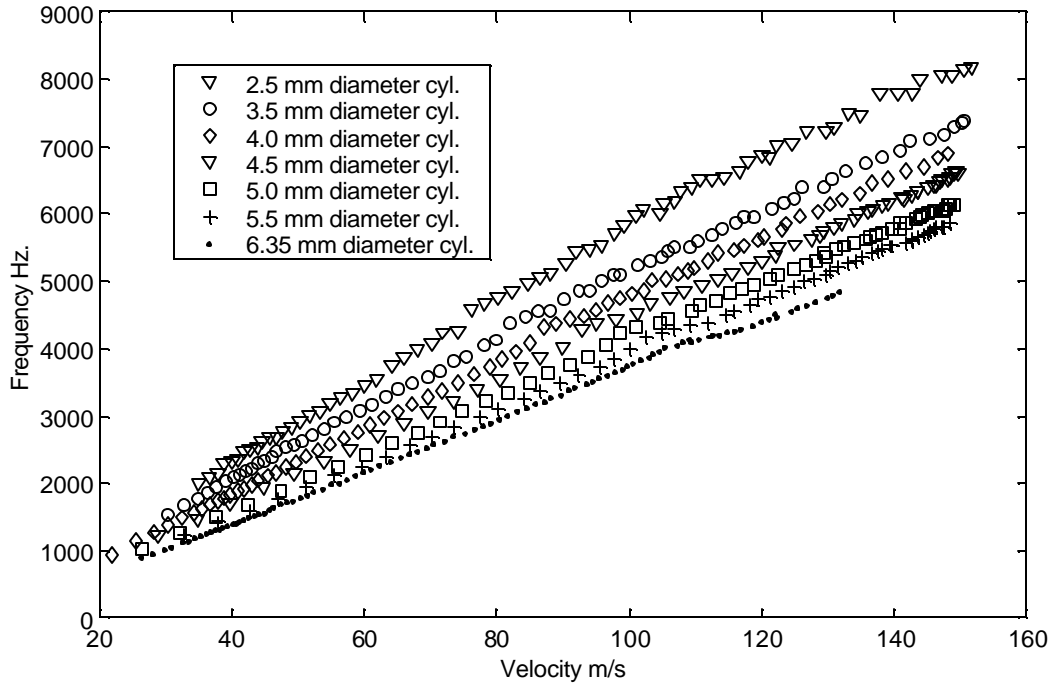


Figure 5.20 Plot of the frequencies of the dominant peak in the spectra as a function of flow velocities for different diameter cylinder.

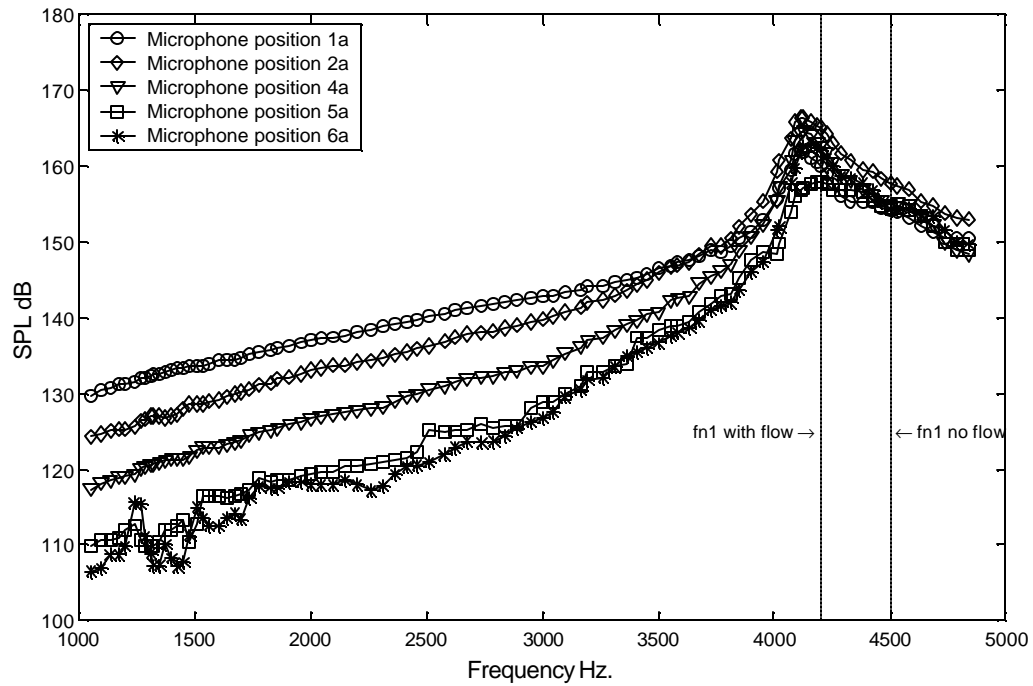


Figure 5.21 Experimentally determined sound pressure levels at different microphone positions produced by a single 6.35 mm diameter cylinder inside a duct. Figure 4.22 and 4.23 show measurement positions. Acoustic resonance estimated with flow velocity at resonance condition (fn1 with flow) .

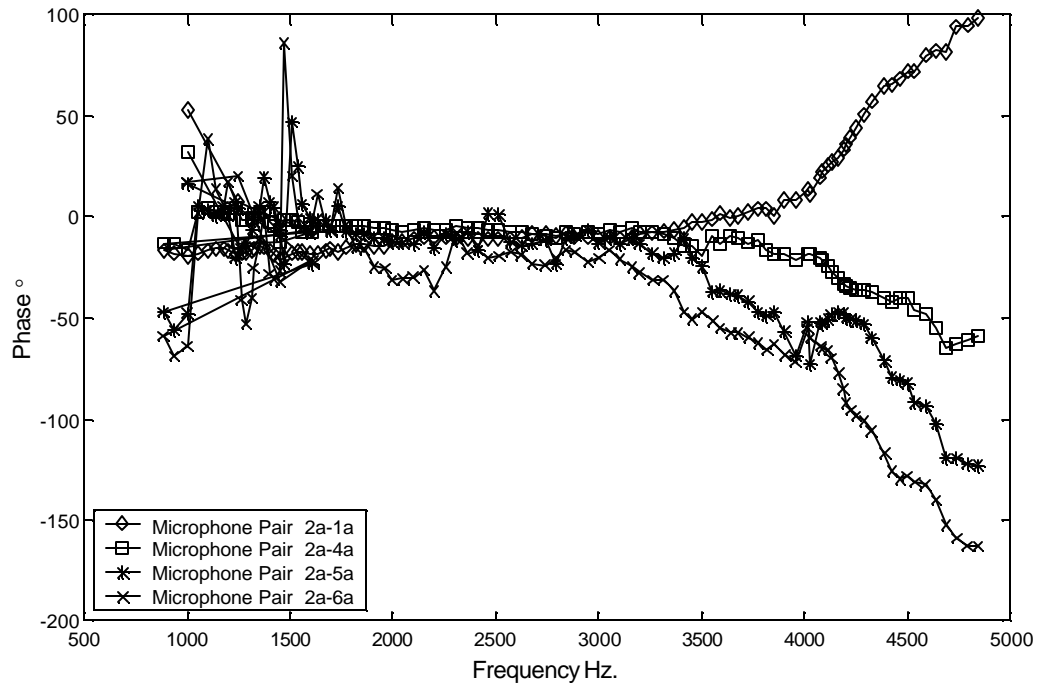


Figure 5.22 Experimentally determined transfer function phase angle between microphone pairs at dominant frequency in the spectra. Cylinder diameter = 6.35 mm.

Figure 5.22 presents the transfer function phase angle in degrees as a function of frequency of dominant peak in spectra. The phase angle was obtained between the microphone pair specified at the frequency of the dominant peak in the measured spectra. Phase between the microphone pairs remained very close to zero until a frequency of approximately 3 kHz where the phase angle of the different pairs started to separate. Pair 2a-1a is the only pair that has a positive slope. This is in contrast to the other three microphone pairs. Note the different orientation of pair 2a-1a in Figure 4.22. Since microphone 2a is always the reference microphone the change in slope is attributable to the change in orientation for this microphone pair.

Tests with the different cylinders in many cases were repeated to confirm results and check repeatability. Figures 5.23 and 5.24 are presented to show measurement repeatability. The figures are similar to Figures 5.21 and 5.22. The difference in these figures is that only the sound pressure level at one position and the phase angle between one microphone pair respectively are shown. The main discrepancies in the data presented in Figure 5.23 occur in the 2-3.5 kHz range. Some of the data presented in Figure 5.23 and 5.24 was obtained by adjusting the flow manually while most of the data was obtained after the test and control equipment was automated.

Figure 5.24 shows significant scatter in the data below 2 kHz. The reason for this is unknown. This scatter was greater for the 6.35 mm diameter cylinder. Similar plots made for other cylinder diameter presented in Appendix G show less scatter at lower frequencies.

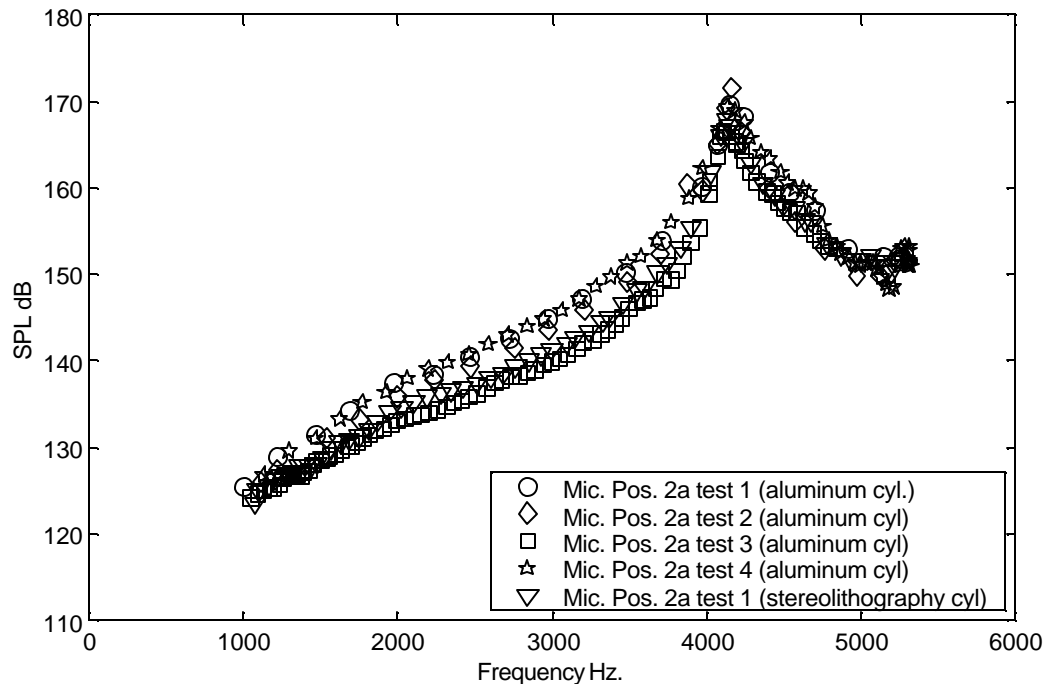


Figure 5.23 Repeatability of sound pressure level measurements at microphone position 2a. Cylinder diameter = 6.35 mm .

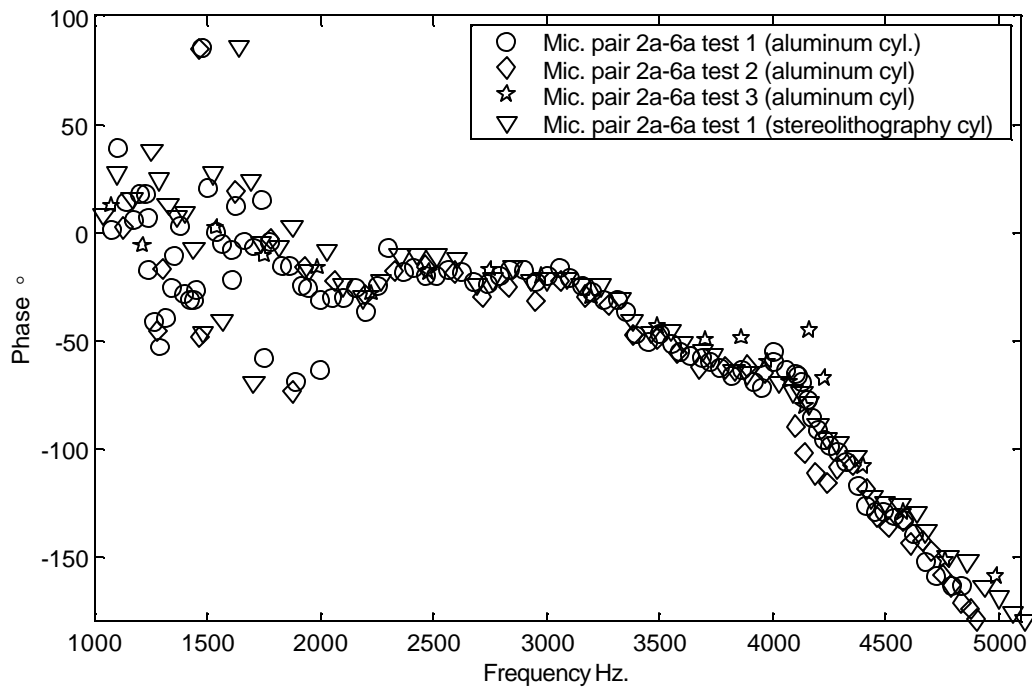


Figure 5.24 Repeatability of phase measurements at vortex shedding frequency for microphone pair 2a-6a. Cylinder diameter = 6.35 mm. Microphone at position 2a used as reference.

A comparison between the sound pressure levels measured at microphone position 2a for many cylinders is shown in Figures 5.25 and 5.26. Figure 5.26 shows the gradual increase in the frequency at the resonance point as the cylinder diameter gets smaller. As mentioned above, the smaller diameter cylinders reach the resonance at lower flow velocities, and therefore, the resonance is closer to the empty duct resonance. Figure 5.26 shows the velocity at which the resonance was reached.

Figure 5.25 shows that sound pressure level is higher at any given frequency for the larger diameter cylinders. This might not be a fair comparison since the flow conditions (mainly density and flow velocity) are different when each cylinder reaches the frequency of interest. Figure 5.26 compares the sound pressure levels versus flow velocity. When comparing sound pressure level against flow velocity, it is still observed that the larger diameter cylinders produce higher sound pressure level (with the notable exception between the 5.5 mm and 6.35 mm diameter cylinders which could be attributable to experimental variability). These observations agree with the dipole source model in which the dipole strength is linked to the fluctuating lift forces (see equation (3.26)).

Figure 5.27 compares the transfer function phase angle at the frequency of the dominant peak in spectra between microphones at positions 2a and 6a for cylinders of different diameters. The microphone at position 2a was always used as the reference. Unlike Figure 5.25, where at any given frequency there are significant variations in SPL as a function of cylinder diameter, Figure 5.27 shows no variations in phase at a given frequency as the diameter varied. The phase between the microphone pair is not dependent on noise source level but only in its frequency. This result is in agreement with the proposed model.

Due to the design of our experimental setup, there were limits on the maximum possible test velocity. Since cylinders of smaller diameter shed vortices at higher frequencies, the higher frequency results shown in Figure 5.27 were obtained with these cylinders.

Figure 5.28 presents the results of sound pressure levels versus frequency of the dominant peak in the spectra for measurements made at microphone positions d1 (see Figure 4.22). This position is the only position downstream of the cylinder where measurements were made. As shown, the behavior of the SPL versus frequency is very different from that presented in Figures 5.25 or 5.23. Figure 5.28 shows a very distinctive decline in the sound pressure level at the resonance frequency. This decline is believed to indicate a change in the vortex shedding pattern. Around the decline the sound pressure level measured at this position matches that of upstream positions. No other match occurs elsewhere (see Appendix G). A possible explanation for this is that during this time the propagating hydrodynamic disturbances created by the vortex downstream of the cylinder no longer pass on top of the sensor and therefore the sensor only sees the acoustic field.

Figure 5.29 presents the comparison between the symmetrical position 3a and d1. The differences in the SPL at the two positions is attributable to the hydrodynamic dynamic pressures of the vortex shedding. This type of test might be used to study propagating hydrodynamic disturbances.

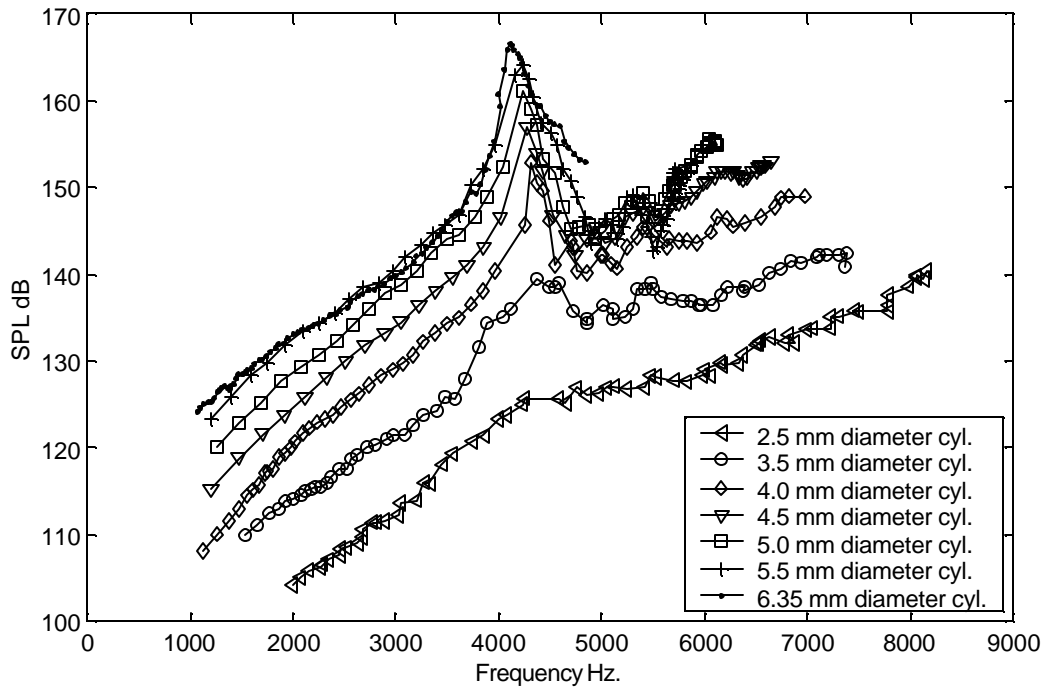


Figure 5.25 Comparison of sound pressure levels (SPL) vs. frequency at microphone position 2a for different cylinder diameters (see Figure 4.22).

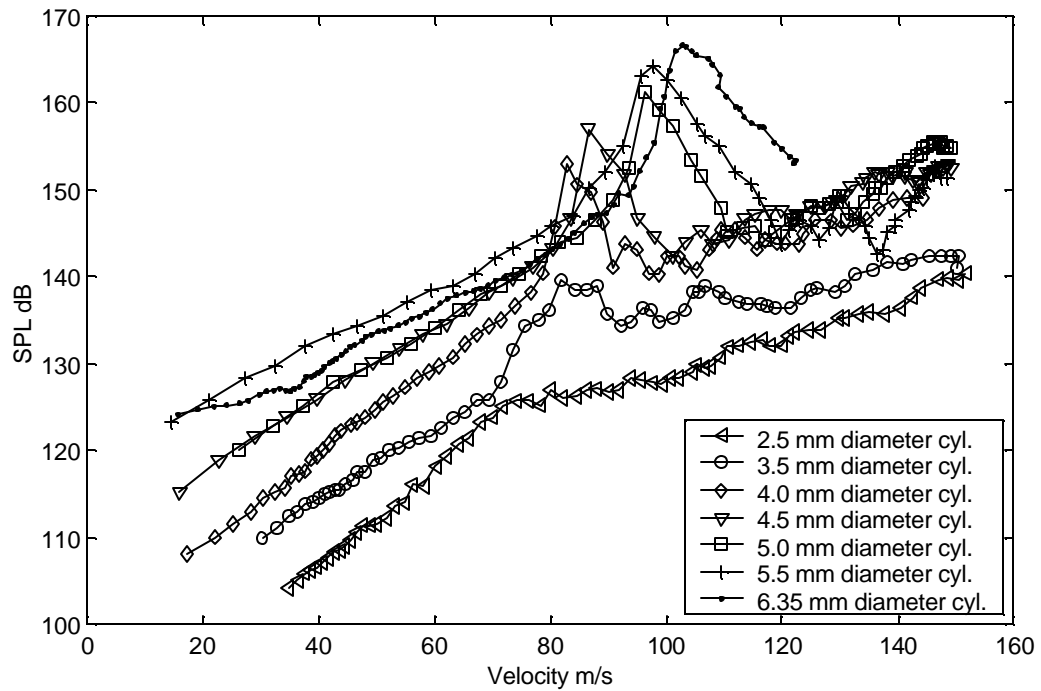


Figure 5.26 Comparison of sound pressure levels (SPL) vs. flow velocity at microphone position 2a for different cylinder diameters (see Figure 4.22).



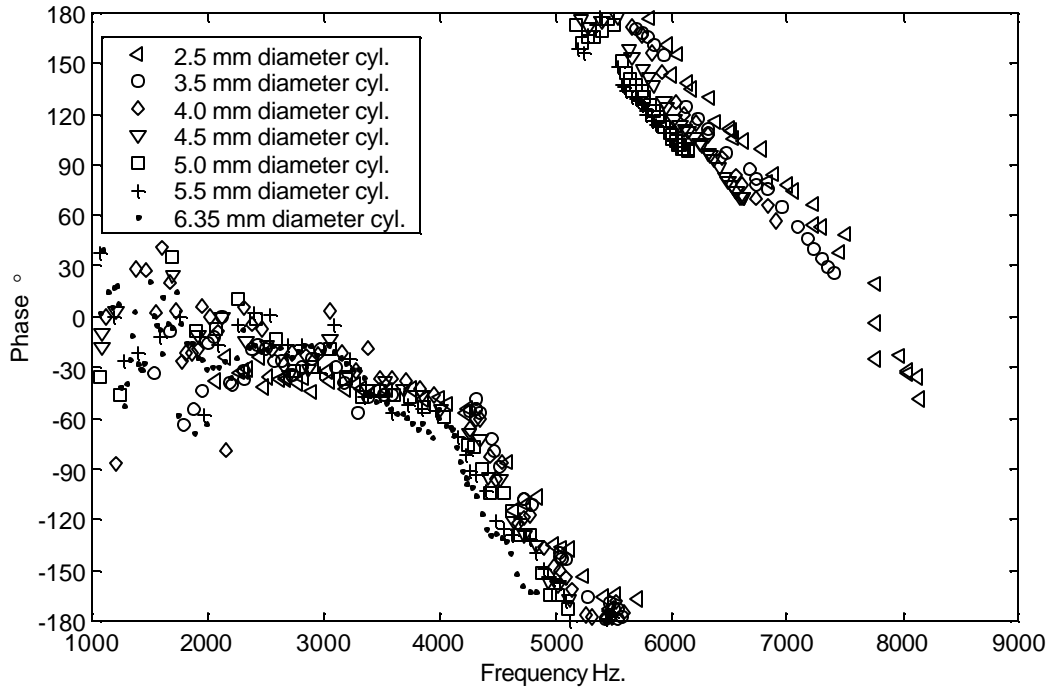


Figure 5.27 Comparison of phase angle at frequency of dominant peak in spectra between microphones at positions 2a and 6a for different cylinder diameters.

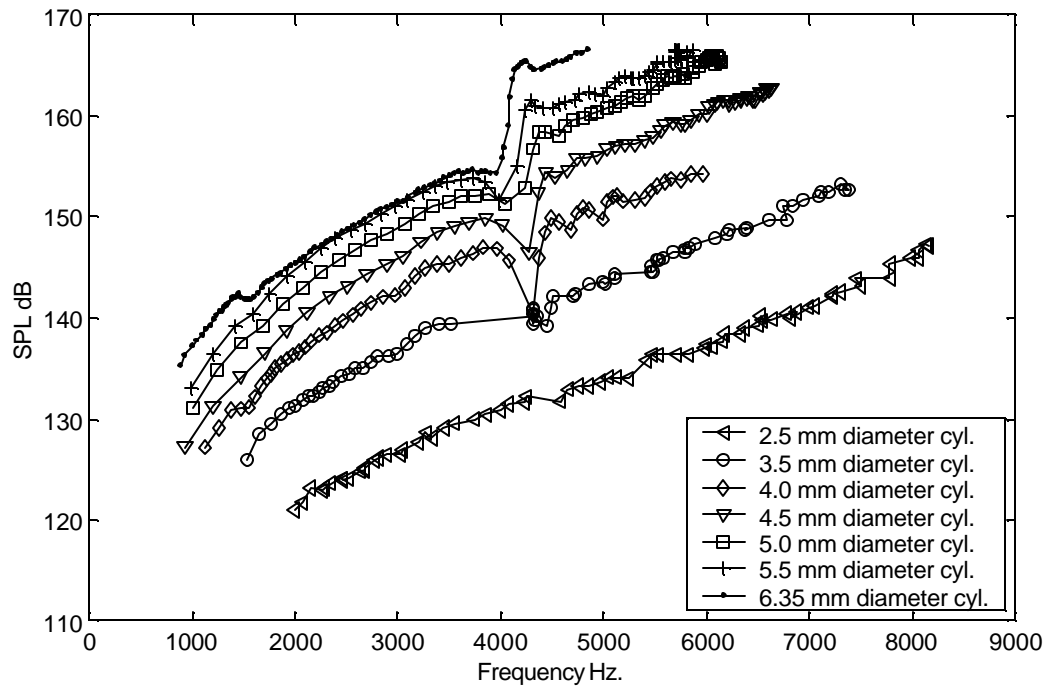


Figure 5.28 Sound pressure level vs. frequency of dominant peak in spectra at microphone position d1 for different cylinder diameters.

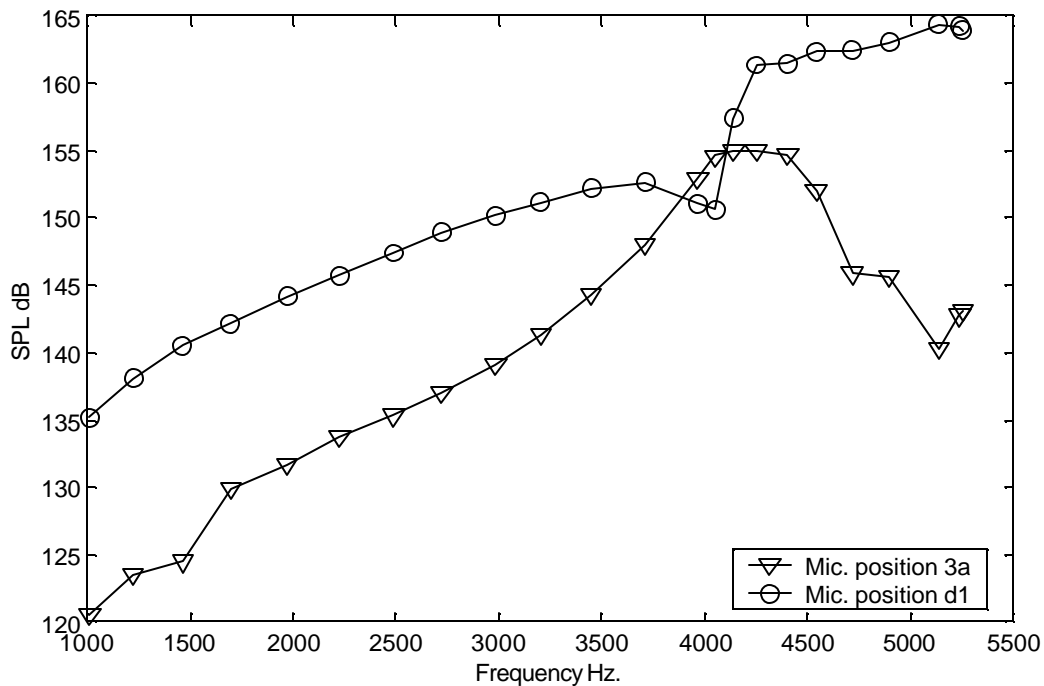


Figure 5.29 Sound pressure level vs. frequency of dominant peak in spectra at symmetric positions upstream (3a) and downstream (d1) of the test cylinder. Test performed with 6.35 mm diameter cylinder.

Strouhal numbers have been calculated from the results of our tests for all the cylinders tested and are shown versus Reynolds number in Figures 5.30, 5.31, and 5.32. Figure 5.30 compares our results to values reported by other researchers in a wide range of Reynolds numbers. Figure 5.31 is similar to Figure 5.30 but “zooms in” in the range of Reynolds numbers at which our measurements were made. Our data show a distinctive reduction in Strouhal numbers for the smaller diameter cylinders. This result could not be explained. Figure 5.31 shows results of different tests. Figure 5.31 confirmed the repeatability of these trends. It was also noted during the course of our tests that the smaller diameter cylinders have a wider spectra at the shedding frequency than the larger diameter cylinders. An exception to this case were the tests performed using a 1.5 mm diameter cylinder which again showed behavior similar to that of the 6.35 mm diameter cylinder. Possible causes for this condition were explored. Uncertainty in measurements and variation in testing conditions were considered but could not account for this phenomenon. In our test section cylinder replacement can be made while the experimental setup is running. Without changing flow conditions but exchanging a 3 mm cylinder by a 1.5 mm cylinder did not double the frequency of the measured spectrum. The results obtained coincided with results shown in Figures 5.30 and 5.31. This requires further study.

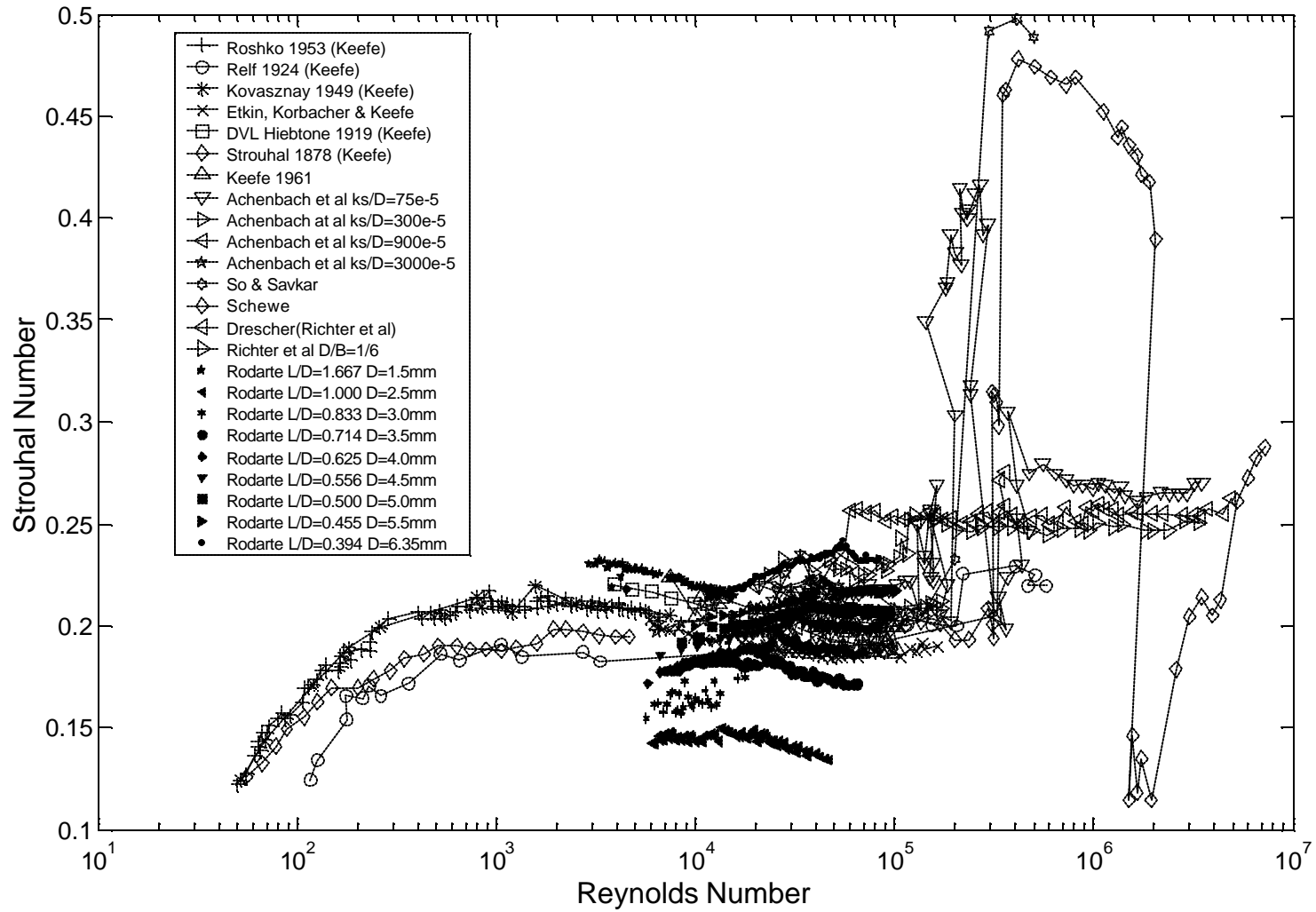


Figure 5.30 Strouhal vs. Reynolds number plot for different cylinder diameters. Reynolds and Strouhal numbers calculated using average flow velocity in the duct.

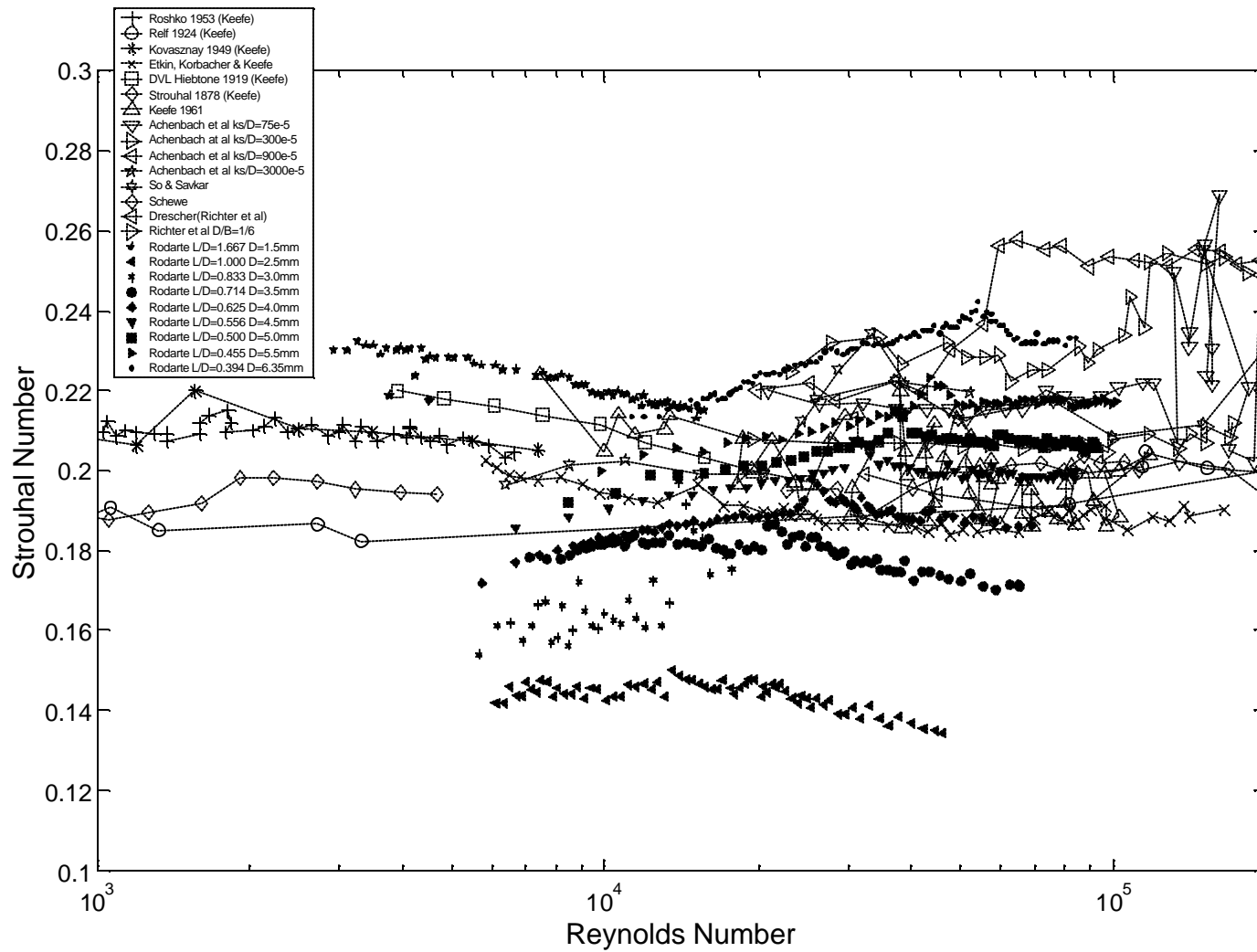


Figure 5.31 Strouhal vs. Reynolds number plot for different cylinder diameters. Reynolds and Strouhal numbers calculated using average flow velocity in the duct. Detail view of Figure 5.30.

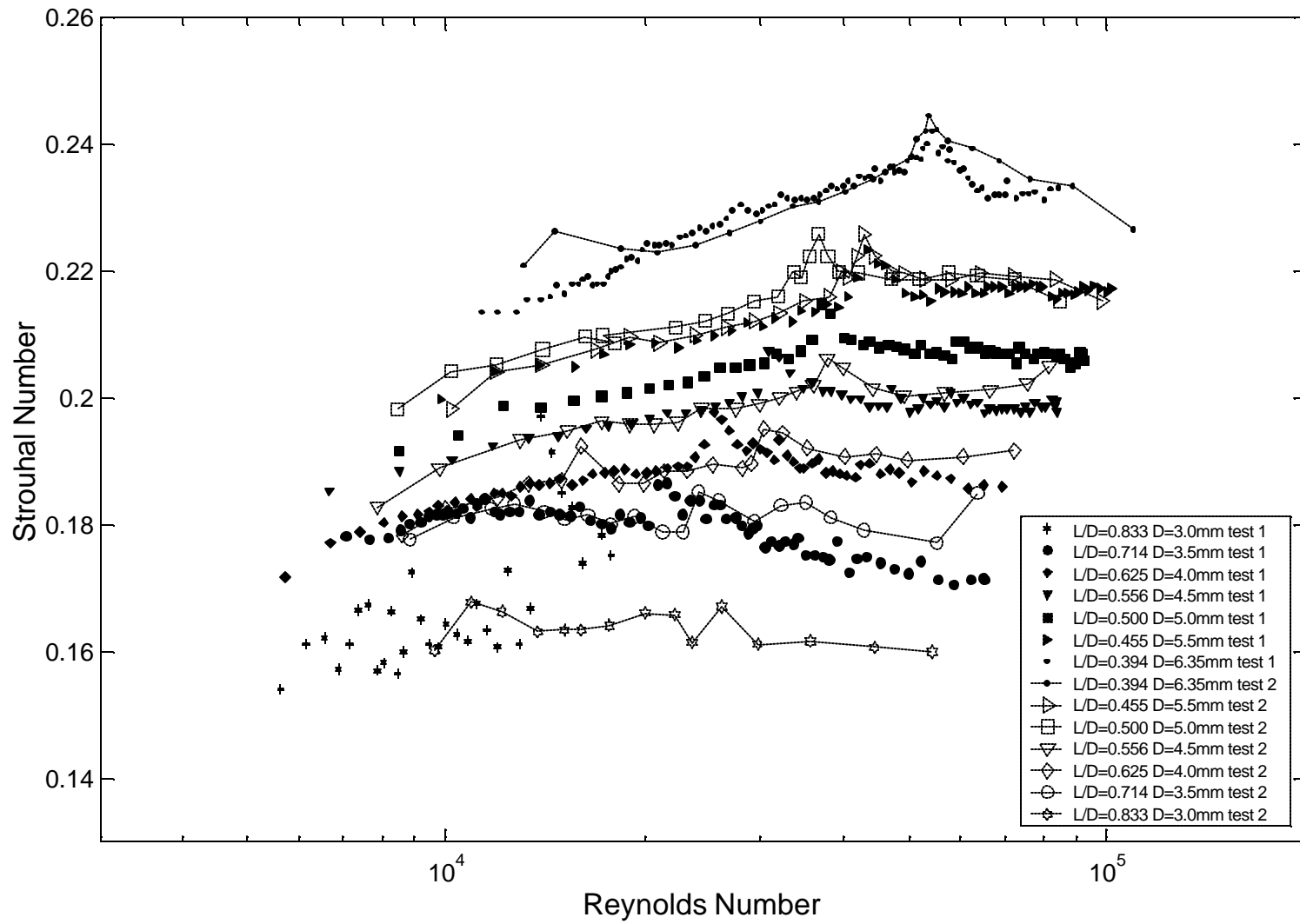


Figure 5.32 Repeatability of Strouhal number measurements.

#### 5.4.1.1 Tests with damping material on the side walls

Tests to explore changes in the acoustic field by modifying acoustic damping were made. The tests were similar to those reported in the previous section, but in this case, the duct was modified by attaching plastic foam to the walls that support the resonance. Two types of foam were used. One of the foams has open cells and permits the flow of gases. This foam is typically used in anechoic chambers. This foam is made by Sonex Illbruck under the name of WILLTEC(r). The material used in our test section was cut from an anechoic chamber foam wedge. The other foam material used has closed cells and it is sold in tape form. The open cell foam attached to the walls was 2.5 mm thick and was applied to the walls normal to the cylinder axis and the flow. The closed cell foam had a thickness of 1.5 mm.

Figure 5.33 compares the sound pressure levels measured at position 1a with and without the damping material. The behavior shown in Figure 5.33 is very similar at other microphone positions upstream from the cylinder. It can be seen that the acoustic resonance frequency of the duct with closed cell foam is increased. For the open cell foam, the increase is not observed. In this case, the resonance frequency appears to be very similar to the one supported by the bare walls once convection effects have been considered. The increase in the natural frequency noticed when using closed cell foam occurs since this material is impermeable to gases and thus can sustain a resonance. When the closed cell foam material is attached to the walls, there is a reduction of the distance between the walls supporting the acoustic resonance, and the natural frequency is raised accordingly. The auxiliary lines that show the first transverse acoustic natural frequency of the cavity with and without convection effects were calculated for the 6.35 mm diameter cylinder with no damping material present. Once damping material is present, the flow velocity at resonance changes since the cross-sectional area is reduced. This causes convection effects to vary slightly from case to case. The acoustic natural frequency calculated using the distance and velocities associated with the 1.5 mm foam tests agree relatively well with experimental results obtained for this case.

It is difficult to compare directly the sound pressure levels presented in Figure 5.33. The sound pressure level is affected by the strength of the sound source, which is related to the flow velocity and the density at resonance (see equation (3.26) and section 6.2). In this case, while the flow velocity can be expected to be the same for a given frequency, the introduced material increases the fluid density due to the increased flow friction. This effect, however, is enough to account for the difference seen in Figure 5.33. The sound pressure level is also dependent in how close the source frequency is to a resonance. This implies that at a given frequency below the first mode for the closed cell foam case, the sound pressure level could be lower since is farther away from the resonance and not necessarily because there is increased acoustic damping. The effect of damping should be more noticeable at resonance. Figure 5.33 shows that the acoustic cell foam reduced the SPL approximately 10 dB at resonance while only 2 dB at non-resonance conditions.

Figure 5.34 shows sound pressure levels at microphone position d1. More accurately than sound pressure level, it should be described as dynamic pressure level since these fluctuating pressures are affected by the propagating hydrodynamic disturbances produced by the passing vortices. Propagating hydrodynamic disturbances move with the flow at velocities close to those of the flow and for a limited distance. This should

not be confused with acoustic propagation. Figure 5.34 presents the characteristic behavior downstream of the cylinders. Compare with Figure 5.28.

The flow velocity necessary to produce noise of a certain frequency is very similar for cylinders of the same diameter. For this reason the propagating hydrodynamic disturbances created by the travelling vortex shedding should also be similar. At measurement position d1 the combined acoustic and hydrodynamic fields are superimposed and the combined effect is measured. Thus, the differences seen in Figure 5.34 could be explained by the reduction in the acoustic field. These reductions could have been caused by changes in source strength, closeness to a resonance and acoustic damping.

Figures 5.35 and 5.36 compare the measured phase angle between two different microphone pairs. In general it can be seen that the same trends are followed in the three cases. However for the closed foam cell the traces appear slightly shifted to the right. This effect could also be related to the higher acoustic natural frequency present for this case.

Appendix G presents complementary plots of the results presented in this section.

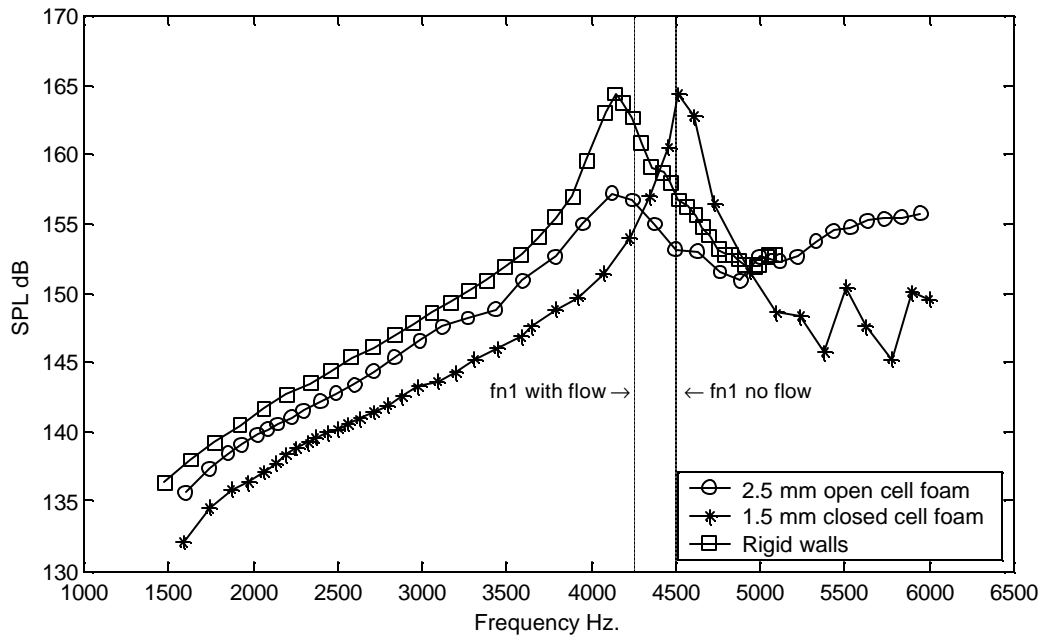


Figure 5.33 Comparison of sound pressure levels at microphone position 1a when different types of acoustic damping materials are applied to duct side walls. Cylinder diameter = 6.35mm. Acoustic resonance estimated with flow velocity at resonance condition (fn1 with flow).

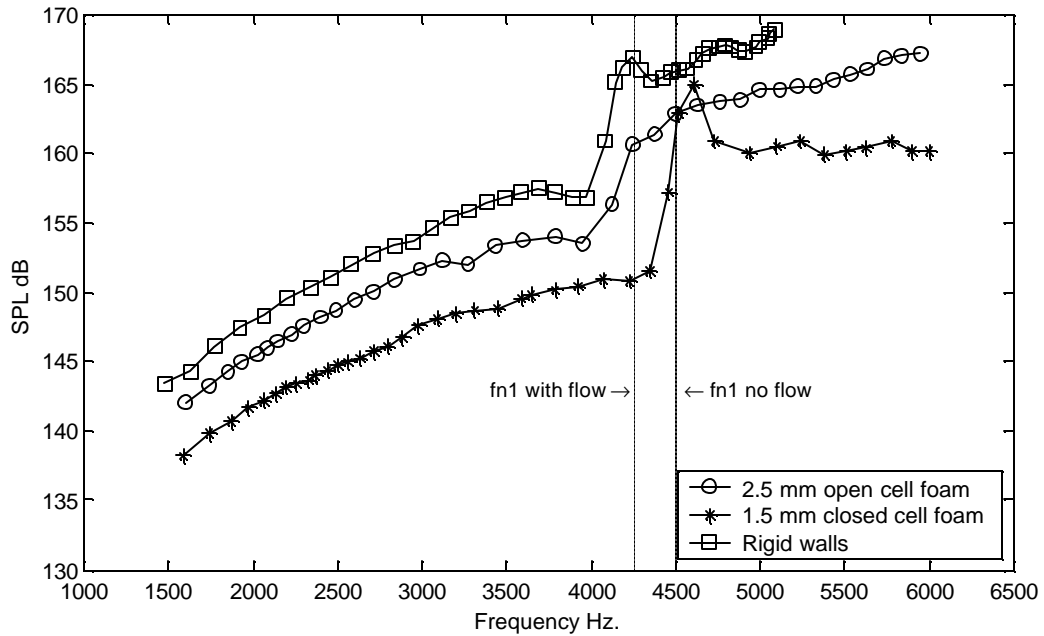


Figure 5.34 Comparison of sound pressure levels at microphone position d1 when different types of acoustic damping materials are applied to duct side walls. Cylinder diameter = 6.35 mm. Acoustic resonance estimated with flow velocity at resonance condition (fn1 with flow).

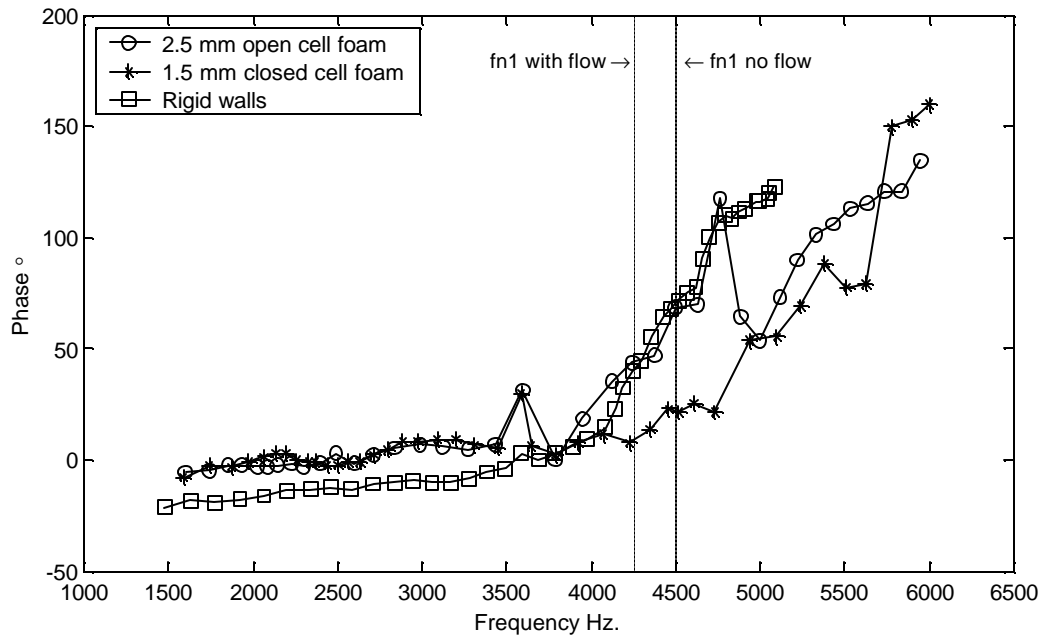


Figure 5.35 Transfer function phase angle at frequency of dominant peak in spectra between microphone pair at positions 2a-1a. Acoustic resonance estimated with flow velocity at resonance condition (fn1 with flow).



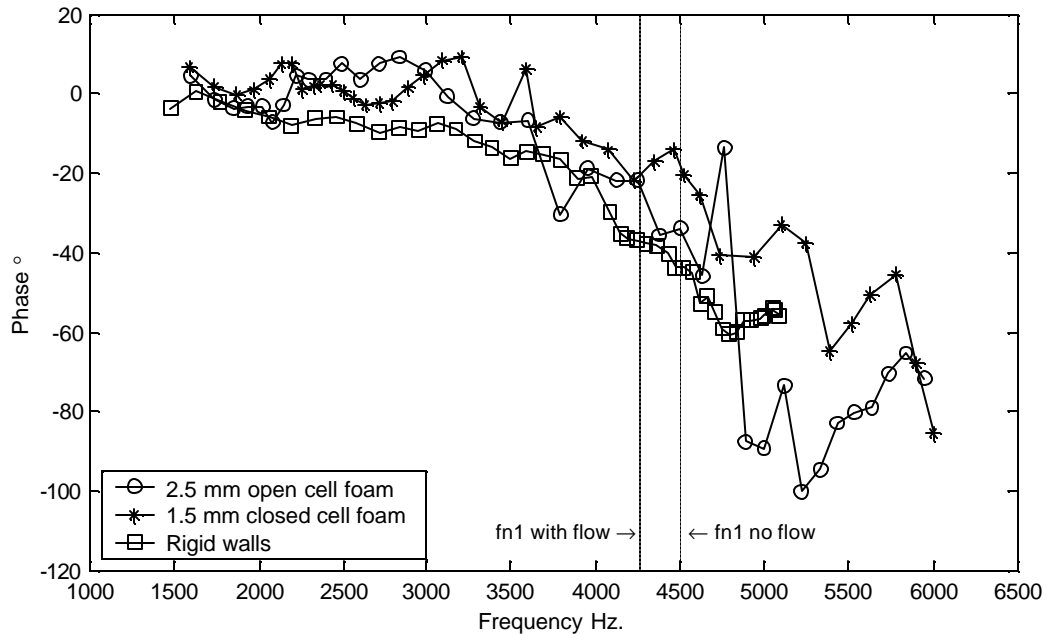


Figure 5.36 Transfer function phase angle at frequency of dominant peak in spectra between microphone pair at positions 2a-4a. Acoustic resonance estimated with flow velocity at resonance condition (fn1 with flow).

#### 5.4.2 Hourglass shaped cylinders

Cylinders of variable diameter along the cylinder axis were tested. The exact shape of the cylinders tested can be seen in Figures 4.20 and 4.21. This type of bluff body was tested to study its flow-acoustic behavior since similarly shaped cylinders can be found in some plate heat exchangers. Certain plate heat exchangers have a “dimple-like” stamped pattern (see Appendix C and D). The “dimples” are protuberances that are approximately shaped like hemispheres. When these plates are placed one against the other and brazed to form the heat exchanger, nonconstant diameter cylinders are formed (see Figure 4.11).

Tests on five different diameters were conducted. The diameter was measured at the center of the test cylinder. For each diameter there were 3 different variations of profile that corresponded to the changes in the radius of curvature of the cutting tool used to machine the cylinders. Figure 4.21 shows the details of how these profiles were made. Thus a total of 15 different diameter/profile combinations were tested. The tests made on these cylinders were identical to the constant diameter cylinder tests described in section 5.4.1.

Figure 5.37 shows sound pressure levels measured at microphone position 1a for cylinders made using a 0.5 mm radius cutter. The graphs present results similar to those found for constant diameter cylinders; that is, for a given frequency the sound pressure level increases with cylinder diameter. Although only the results of the 0.5 mm curvature profile are shown in Figure 5.37, the results were not very different from those obtained for the other different curvature profiles of the same diameter (see Appendix G).

Appendix G presents a few representative plots of the measurements made with nonconstant diameter cylinders (hourglass-shaped cylinders). The graphs included in the appendix for this kind of cylinder are

comparisons of sound pressure levels at positions 1a and d1 versus frequency for the hourglass shaped cylinders against results for constant diameter cylinders of similar diameter, comparison of Strouhal versus Reynolds numbers obtained for the hourglass and constant diameter cylinders, and comparisons of phase angle measurements between positions 2a-4a between the hourglass shaped and constant diameter cylinders.

The sound pressure level graphs presented in Appendix G show that the sound pressure levels produced by the hourglass shaped cylinders are larger than those produced by constant diameter cylinders of comparable minimum diameter.

Figure 5.38 shows results of Strouhal versus Reynolds numbers obtained from measurements made on the hourglass-shaped cylinders. The Strouhal numbers decrease with smaller diameter and thus show the same trends seen in constant diameter cylinders. There were no noticeable differences in Strouhal numbers obtained for the three largest diameters as a function of profiles. For the two smaller diameters, however, the Strouhal numbers were smaller for the profiles with the smaller radii. These differences are especially noticeable for the 2.35 mm diameter cylinders (see Figure G.55).

From these observations, several conclusions can be reached. Hourglass-shaped cylinders behave as larger diameter cylinders from a sound pressure level view point. There were no noticeable differences in SPL with respect to cylinder curvature for the curvatures shown. This indicates that even a small curvature at the bases of the cylinder might be sufficient to alter the flow-induced behavior of cylinders in this aspect ratio range. The Strouhal numbers estimated with the diameter at the center of the hourglass-shaped cylinder was very low. This is another indication that the cylinders behave as larger diameter cylinders. For a given flow velocity and vortex shedding frequency, if the diameter used in the calculations of the Strouhal number is smaller than the “real” cylinder diameter, then the Strouhal number estimate will be lower than it would be if the “real” diameter was used. Figure G.55 shows that the smaller Strouhal numbers are found for the smaller radius profile. This observation supports the hypothesis that the curvature at the cylinder base increases the “effective” diameter. The narrower the passage at the center of the hourglass shaped cylinder the larger the curvature effect and the larger the “effective” diameter. The “effective” diameter concept could not be used for both sound pressure level and frequency purposes since corresponding differences are not seen in all cases.

The mechanism for the increase in the effective diameter or the reduction of the vortex shedding frequency seems to be linked to the combined effect of the larger diameter and lower velocity close to the walls. This phenomenon requires further study. The reductions seen in the Strouhal numbers of constant diameter cylinders (see Figures 5.31 and 5.32) could possibly be explained by a similar flow effect that reduced the vortex shedding frequency or effectively increased the diameter of the cylinder tested for a given set of conditions.

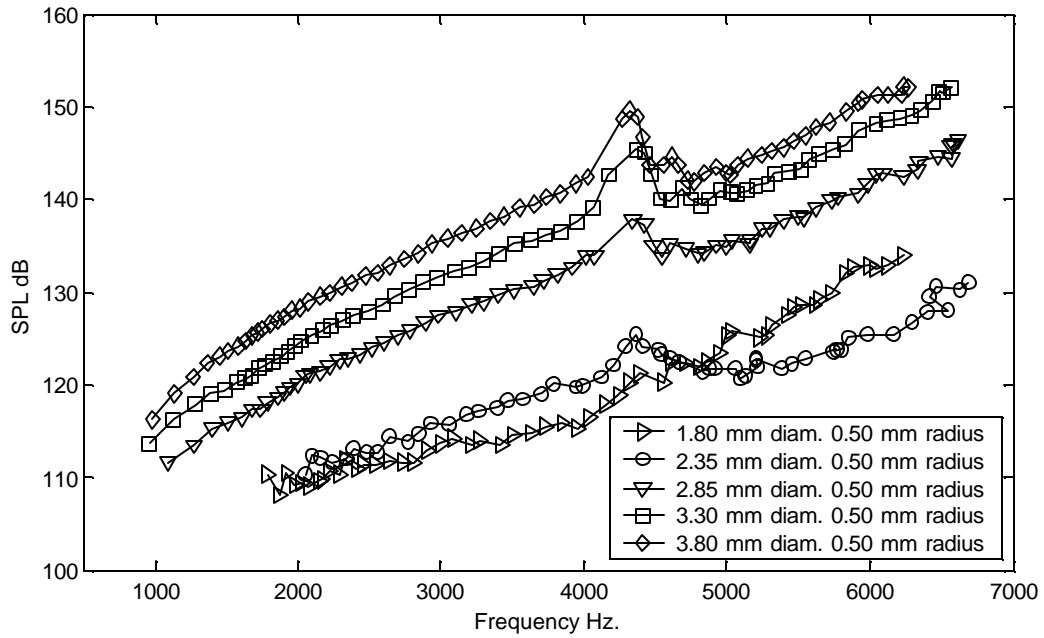


Figure 5.37 Sound pressure levels at position 1a vs. frequency at dominant peak in spectra for cylinders with 0.5 mm curvature profile. Diameter at center of “hourglass” shaped cylinder (minimum diameter).

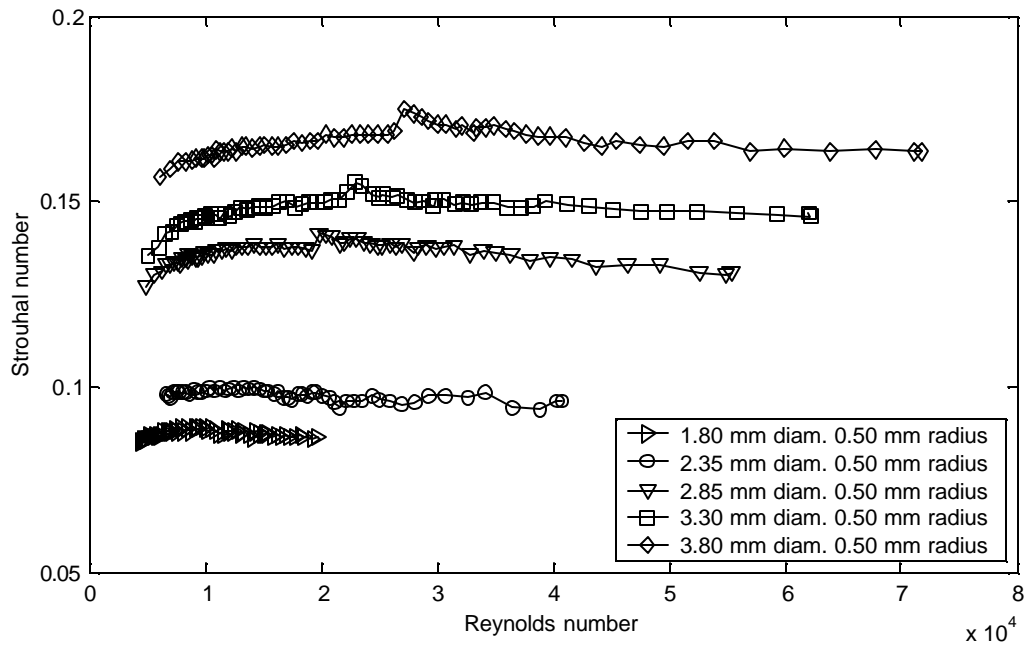


Figure 5.38 Comparison of Strouhal vs. Reynolds numbers calculated from measurements in “hourglass” cylinders. Diameter at center of “hourglass” shaped cylinder (minimum diameter).

## 5.5 Tests on pairs of cylinders inside a duct

Side-by-side and tandem cylinder configurations present very interesting cases to begin exploring the flow-induced noise of multiple cylinders in cross-flows. Depending in the cylinder spacing, the pairs of cylinders can behave either as a single bluff body if they are very close to each other or as single cylinders if they are sufficiently separated. For intermediate spacing they exhibit very interesting behavior.

One limitation of the modeling technique discussed in Chapter 3 for multiple cylinders is that it requires the phasing of the fluctuating lift forces produced by each cylinder with respect to all others to be known. Reports in the literature for side-by-side arrangements with spacing between  $T/D = 2.7$  to 4 or 5 and in the subcritical Reynolds number regime state that “both near wakes are equal in size but the two vortex streets are coupled and mirror each other along the gap axis” [Zdravkovich 1987]. Figure 5.39, extracted from Zdravkovich’s 1987 work, graphically shows this flow behavior. This observation indicates that the fluctuating lift forces are  $180^\circ$  out of phase with each other. Dipole sources separated by a small distance and  $180^\circ$  out of phase are equivalent to quadrupole noise sources (longitudinal quadrupole in this case). This type of source produces significantly lower acoustic emissions. Tests on side-by-side cylinders are aimed at experimentally verifying this observation and trying to analytically corroborate the results of the experiments with the acoustic model.

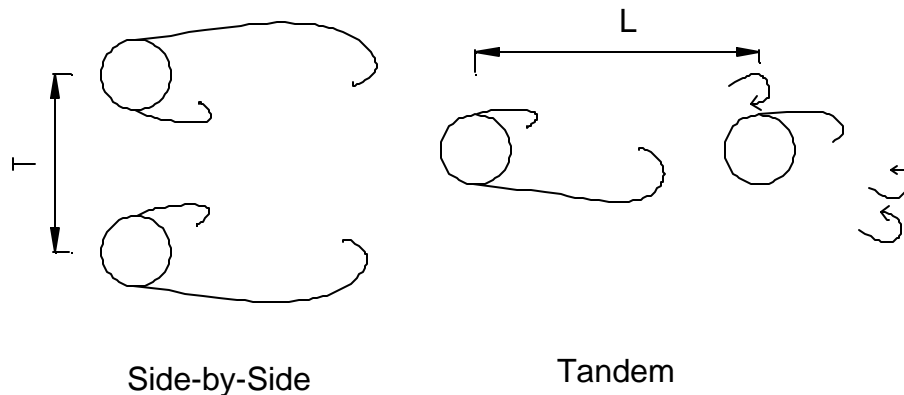


Figure 5.39 Side-by-side and tandem cylinder arrangements showing flow regimes for spacing used in our tests. (from Zdravkovich 1987)

Zdravkovich 1987 also reports that for cylinders in a tandem arrangement with  $L/D$  spacing greater than approximately 3.4 to 3.8, vortices are formed behind the upstream cylinder and in front of the downstream cylinder. When these vortices reach the downstream cylinders, they join the vortices produced by the downstream cylinder and form what he defines as binary vortices (see Figure 5.39). Arie et al. found that these binary vortices cause an excessive fluctuating lift in the downstream cylinder. The phase information between the fluctuating lift forces of the two cylinders is missing in this case and very likely will depend in the  $L/D$  spacing. If the upstream cylinder vortices reach the downstream cylinder at the same time that a new vortex is produced in the upstream cylinder it could be assumed that the fluctuating lift forces will be in phase. Morse and Ingard (page 757) demonstrated that this distance is equal to four diameters. They reached this conclusion assuming that the vortices travel at 80% the speed of the flow. Morse and Ingard discuss the flow-acoustic

coupling of cylinders in tandem. They believe that an acoustic disturbance or pulse produced by the upstream vortex hitting the downstream cylinder interacts with the upstream cylinder and can stimulate the formation of the vortex. This interaction they say is responsible for the increased sound or “resonance” seen for cylinders in tandem placed with this spacing. For this “resonance” the cylinders do not need to be inside a duct. It is believed that flow-acoustic coupling is not necessarily responsible for this condition as reported by Morse and Ingard. Based on our work, there are two factors that play a role and that could explain this phenomenon. 1) The increase in the sound emission for cylinders in tandem occurs for  $L/D = 4$  since at this spacing the fluctuating lift forces are in phase. For spacings that differ from  $L/D = 4$ , the phases of the noise sources interact and reduce the sound field. In this scenario the worst case would be for a spacing  $L/D = 2$  since at this distance the fluctuating lifts would be perfectly out of phase ( $180^\circ$  out of phase). This condition would create quadrupoles, but in this case the quadrupoles created would be lateral quadrupoles. 2) Fluid mechanics interactions alone at the downstream cylinder create larger fluctuating forces and thus increase the strength of the acoustic dipole. The increases of the fluctuating lift at the downstream cylinder in the tandem configuration are reported for  $L/D$  values greater than around 3.4 to 3.8 [Arie et al.]. If the spacing when the fluctuating lift forces in the downstream cylinder are larger coincide with the phase matching of the upstream and downstream dipole source, then both conditions for the increase in the acoustic field will be met. That is, the dipole source will be in phase and the dipole source strength will be larger. This could explain the increases seen in the sound field without the fluid-acoustic effects.

#### 5.5.1 Side-by-side cylinders

Side-by-side cylinders with diameter of 6.35, 5.0, 4.0, and 3.0 mm were tested. Figure 4.27 shows the dimensions of the test section and the positions of both the cylinders and microphones. Since the spacing in the test section between cylinders is fixed at 12.70 mm the  $T/D$  ratios for the four pairs of cylinders were 2, 2.54, 3.175, and 4.23, respectively. The results of the tests on side-by-side cylinders is presented in Appendix H.

Appendix H shows plots of sound pressure level versus average flow velocity, Strouhal versus Reynolds number, frequency versus average velocity, and representative spectra for each of the four configurations tested. Appendix H does not present plots of sound pressure level versus frequency since the frequency of the dominant peak in the spectra measured upstream of the side-by-side cylinders did not necessarily increase with flow velocity. Phase between microphone pairs is only meaningful at the frequency of the dominant peak in spectra at the microphone position 2a. Microphone 2a was always used as the reference for all phase measurements between the microphone pairs. The selection of microphone position 2a as the reference point was arbitrary. A plot of phase versus frequency of dominant peak in spectra for the side-by-side cylinders similar to the one presented for single cylinders tests would be difficult to interpret or use.

Plots of representative spectra for single cylinders were not necessary since single cylinders flow-noise have a very well-known behavior in which the frequency of the dominant peak in the spectra is linear with velocity (see Figure 5.20). Since side-by-side cylinders behaved very differently from single cylinders, representative spectra at three different microphone positions is presented in Appendix H.

Sound pressure level increases when close to an acoustic resonance. Since it was not possible to plot SPL versus frequency for side-by-side cylinders, plots of frequency versus velocity at microphone position d3

were made. This position was the only place where the spectra reasonably followed the linear frequency velocity relationship seen for single cylinders. Measurements at d3 also show that side-by-side cylinders shed vortices downstream as single cylinders producing the hydrodynamic disturbances picked up at this position, but their acoustic behavior is changed completely by the companion cylinder. The reason for this change in the acoustic behavior as described in section 5.5 is believed to be due to the canceling effect of having two closely spaced dipoles out of phase. The differences in SPL at the vortex shedding frequency measured for a single cylinder and side-by-side cylinders is a measure of this canceling effect.

Coherence measurements close to one at the peak frequency of the spectra in position 2a were observed. This frequency in most cases was different from the vortex shedding frequency picked up at position d3. This fact points out that other acoustic sources might be present. In some instances, the frequencies of the dominant peak were double what was measured at position d3. This made us think that now that the dominant fluctuating lift dipole was canceled, the much weaker fluctuating drag dipole was being observed. However for this to be true, the frequencies of the dominant peak in the spectra should have behaved in a linear fashion with respect to flow velocity, and this was not the case.

Figure 5.40 compares the Strouhal versus Reynolds numbers obtained from the side-by-side tests. No clear relationship or behavior can be seen such as that present in Figures 5.31 and 5.32. Comparisons of side-by-side cylinders' Strouhal versus Reynolds numbers with those from single cylinders are shown in Appendix H. Figure H.2 and H.6 show that at lower Reynolds numbers Strouhal numbers from side-by-side cylinders are smaller than those for single cylinders. For both cases at a Reynolds number of approximately 50,000, the Strouhal number curves intersect, and after that side-by-side cylinders show larger Strouhal numbers. For the 3 and 4 mm cases, the side-by-side Strouhal numbers at all Reynolds numbers measured are always larger than the single cylinders of the same diameter.

Figure 5.41 compares the SPL at microphone position 2a versus average flow velocity for the different side-by-side tests. At low flow velocities, the SPL for the 3 mm cylinder is greater than the rest of the side-by-side cylinders tested! Figure 5.26 is similar to Figure 5.41 but is made for single cylinders in a duct. In this figure it can be seen that as long as the SPL is measured far from the resonance, the larger the cylinder diameter the larger the SPL at a given flow velocity. A possible explanation for the different behavior observed is that the 3 mm cylinders are spaced far enough from each other that the formation of the longitudinal quadrupole is inhibited. This is supported by measurements of spectra at microphone positions upstream of the cylinders. For the 3 mm side-by-side cylinders tests, upstream and downstream measurements produced spectra showing similar behavior. This is the only case that this was observed for side-by-side cylinders tests.

Figures 5.42 and 5.43 compare the sound pressure levels of the 6.35 mm side-by-side cylinders with the 6.35 mm single cylinder case at microphone position 2a as a function of average flow velocity and frequency of dominant peak in spectra, respectively. In Figure 5.42, it is seen that the sound pressure levels are significantly higher at all points except at around 120 m/s. At this velocity the side-by-side cylinders appear to excite the second transverse acoustic mode of the duct. There is a jump from the first to the second mode when the frequency reaches the first mode, and only at this point is there an associated increase in SPL for the side-

by-side cylinders. This behavior was similar for the 5.0 mm side-by-side cylinders but not for the 4.0 and 3.0 mm cases.

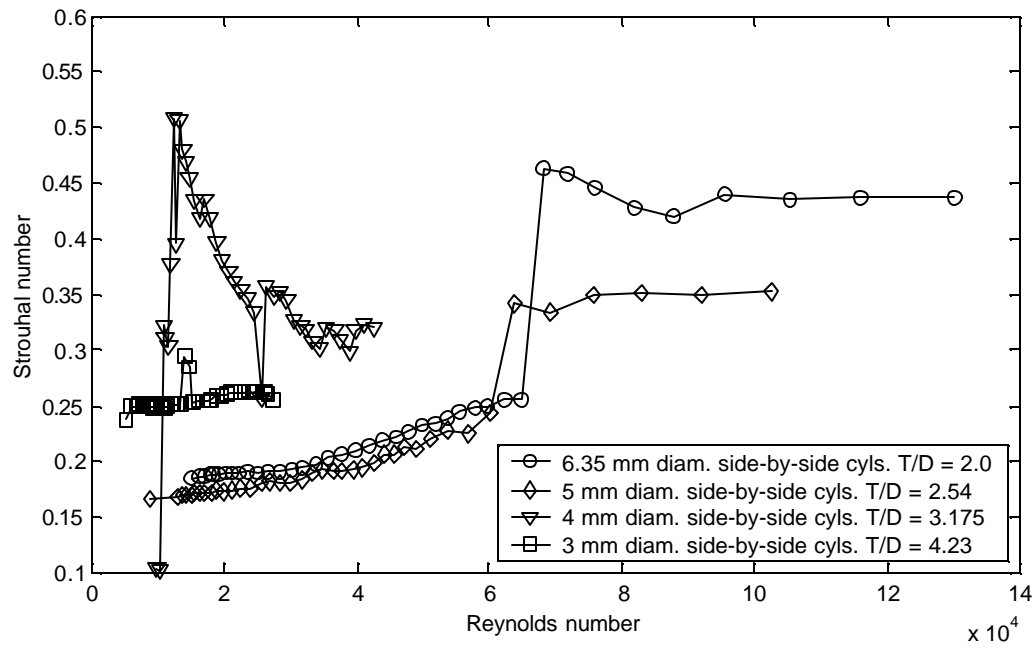


Figure 5.40 Comparison of Strouhal vs. Reynolds numbers for side-by-side tests. Strouhal number estimated using frequency of dominant peak in spectra at microphone position d3.

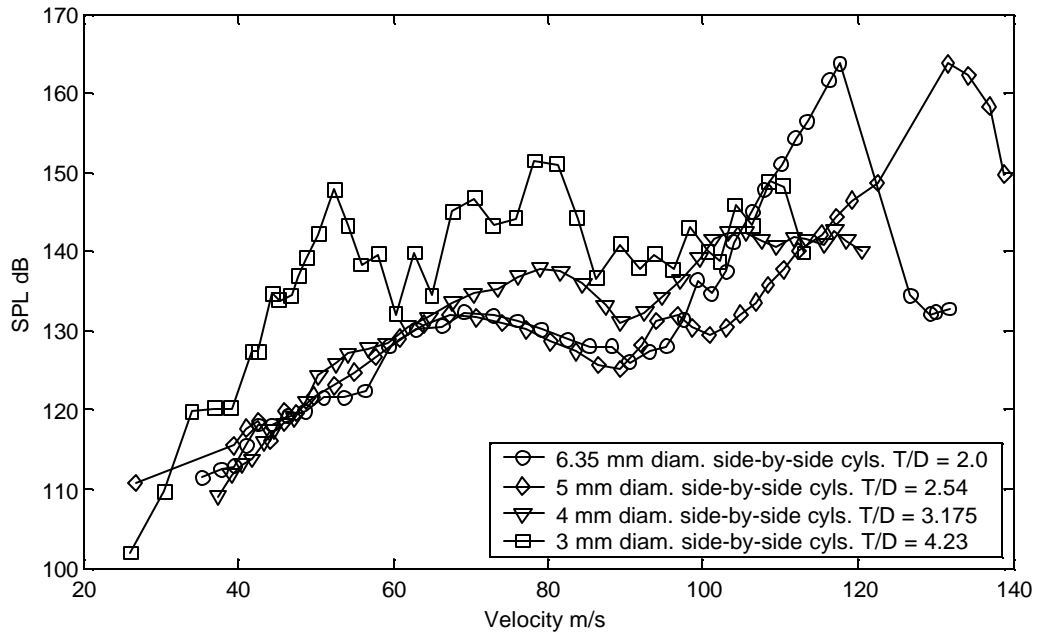


Figure 5.41 Sound pressure levels vs. average flow velocity at microphone position 2a.

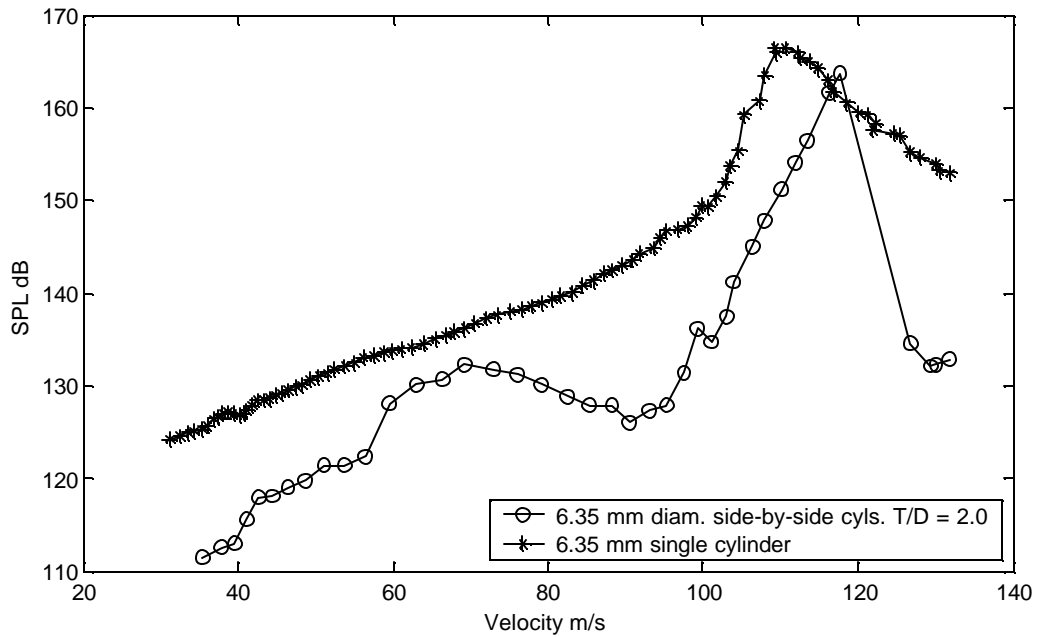


Figure 5.42 Comparison of sound pressure levels vs. average flow velocity of 6.35mm side-by-side cylinders and 6.35 mm single cylinder. Measurement position 2a.



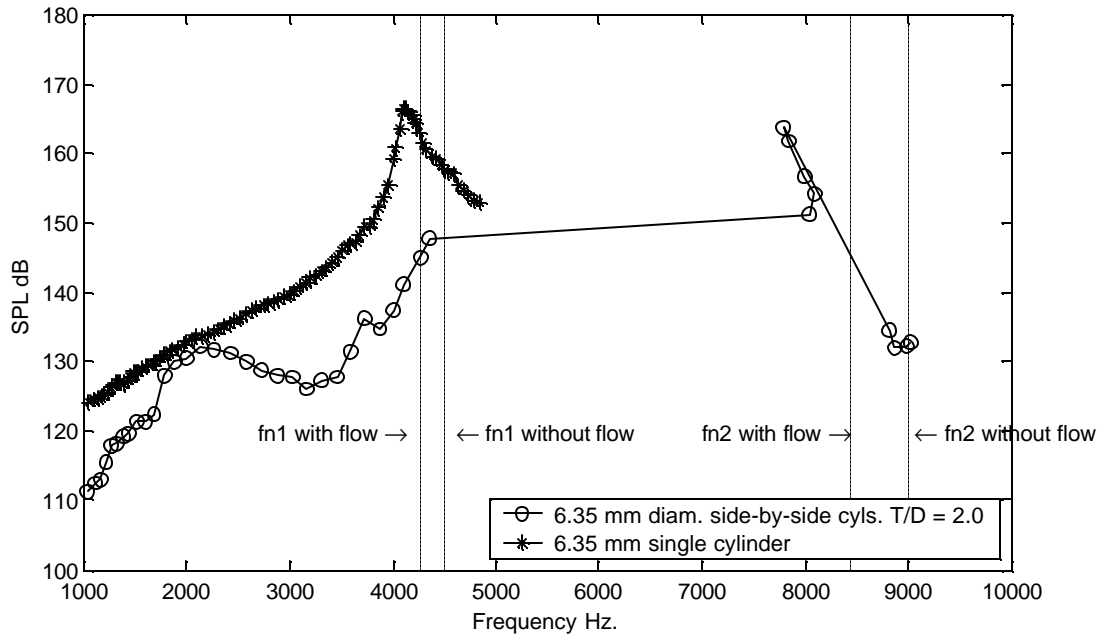


Figure 5.43 Comparison of sound pressure levels vs. frequency of 6.35 mm side-by-side cylinders and 6.35 mm single cylinder. Measurement position 2a. (fn1 and fn2 with flow) acoustic resonances estimated with flow velocity at resonance condition.

### 5.5.2 Cylinders in tandem

Tests on cylinders in a tandem arrangement were made for cylinders of 6.35, 5.0, 4.0 and 3.0 mm diameter. The same setup used for side-by-side tests was used. Tandem tests were made first, then side-by-side tests, so the tandem holes were plugged for the side-by-side tests. The test section dimensions can be seen in Figure 4.27. The spacing of the tandem holes was fixed. With this spacing and the different cylinder diameters, the L/D ratios of the tandem tests were fixed at 3.28, 4.16, 5.2, and 6.93.

For the tandem cylinders tests it was observed that in general this configuration behaved very similarly to single cylinders. For this reason in this case it was possible to plot the SPL versus frequency of the dominant peaks in the spectra in Appendix H. Additionally it was also possible to plot the phase and coherence versus frequency in the same way that it was done for single cylinders. Representative spectra measured at three microphone positions are also included in Appendix H.

Figure 5.44 shows the linear frequency velocity behavior seen for the tandem tests. This figure is similar to Figure 5.20. While in Figure 5.20 there is practically no disturbance in the linear behavior for frequencies in the range 4200-4500 where the first transverse acoustic mode lies, Figure 5.44 shows that there is a slight change in behavior at the resonance frequency for the larger diameter cylinders.

While the Strouhal numbers in the case of single cylinders were gradually decreasing as the cylinder diameter was being reduced (see Figure 5.31 and 5.32), for cylinders in tandem this was not the case. Strouhal versus Reynolds numbers of cylinders in tandem are shown in Figure 5.45. The Strouhal numbers for the 6.35

and 5.0 mm diameter cylinders show some peaks. These peaks are the results of the change in slope seen in Figure 5.44 at the resonance condition.

Figure 5.46 compares the measured transfer function phase angle at the frequency of the dominant peak in the spectra for the 2a -4a microphone pair. The microphone at position 2a was always used as the reference. In addition to the results for the cylinders in tandem tests, the results for the single 3.5 mm cylinder are shown for comparison. This cylinder was chosen since the smaller cylinders were tested at higher frequencies. Figure 5.46 show the same trends in the measured phase as the single cylinder cases.

A comparison of the sound pressure levels as a function of frequency for the four cases is shown in Figure 5.47. This figure is analogous to Figure 5.25. Figure 5.25 shows that the sound pressure levels for a given frequency are greater for the larger diameters. This is caused as mentioned in section 5.4.1 by the increase in the fluid velocity and density and thus dipole strength for the larger cylinders. Figure 5.47 shows similar behavior, but in this case there is no significant difference between the 3.0 and 4.0 mm diameter cylinders below the first acoustic resonance of the duct. Figures 5.48 and 5.49 compare the sound pressure levels versus frequency and versus velocity for the cylinders in tandem tests with single cylinders. In this figures it can be seen that the 6.35 and 3.0 mm diameter cylinders are the only cases in which the sound pressure level is noticeable larger than the single cylinder case.

Morse and Ingard as described in section 5.5 explained why they believe cylinders in tandem with a L/D spacing equal to 4 show increased noise levels than cylinders in tandem with other spacing. In their derivation to obtain this number they assumed the Strouhal number of the vortex shedding equal to 0.2 and that the vortex traveled with 80% the speed of the main flow. Following Morse and Ingard's analysis, for this "resonance" condition to occur, both the vortex shedding period and the time of travel of the vortex between cylinders should be equal. This can be expressed as:

$$T_{vs} = \frac{D}{V St} = \frac{L n}{0.8 V} \quad (5.6)$$

In equation (5.6)  $T_{vs}$ ,  $D$ ,  $V$ ,  $St$ ,  $L$ , and  $n$  represent the vortex shedding period, cylinder diameter, flow velocity, Strouhal number, tandem cylinders spacing, and multiples of the cylinders spacing respectively. As seen in Figure 5.45, the Strouhal numbers measured in our tests are slightly higher than 0.2. Substitution of Strouhal numbers of 0.25 instead of 0.2 in equation 5.6 change Morse and Ingard's value of the spacing L/D necessary for "resonance" from 4 to 3.2. Strouhal numbers close to 0.25 are seen for the 6.35 and 3.0 mm cylinders. These cylinders also happen to be located with spacing very close to 3.2 or a multiple of it.

These observations do not necessarily prove that flow-acoustic coupling can be responsible for the increases in sound pressure level seen for the 6.35 and 3.0 mm cylinders as Morse and Ingard believed. As mentioned in section 5.5, this can be just the results of having each cylinder dipole in phase. This explanation is also supported by the assumptions that leads to equation (5.6). For other cylinder spacing the two dipoles would very likely not be in phase and this could account for the behavior seen. These issues will be explored in the next chapter.

Figures 5.48 and 5.49 also show comparison plots of sound pressure levels versus flow velocity. In all cases, it is seen that the cylinders in tandem reach the resonance condition at lower velocities. This is explained by the higher Strouhal numbers observed for cylinders in tandem.

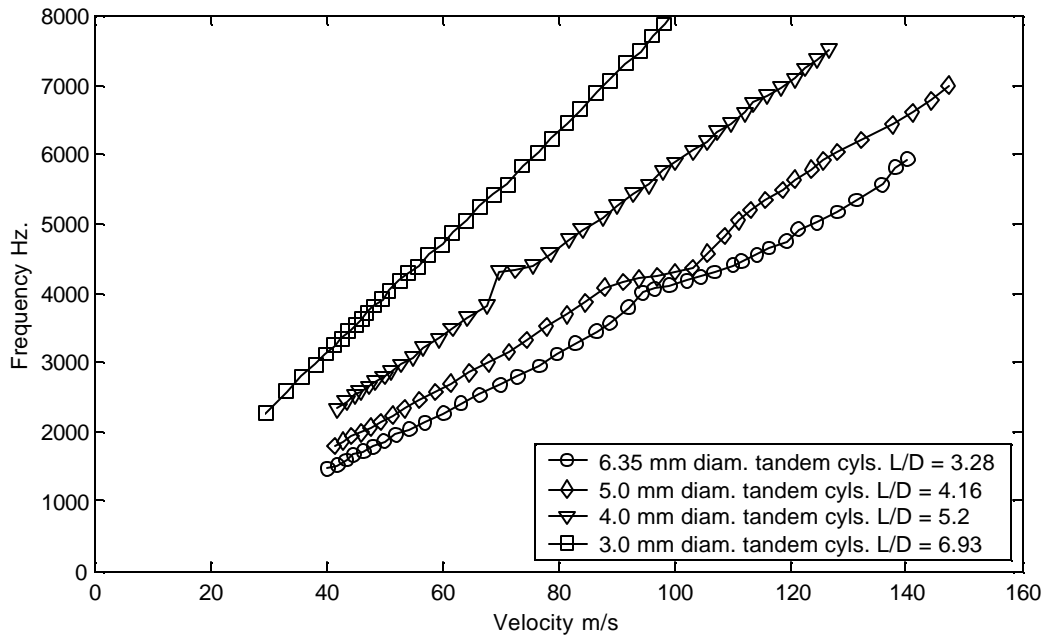


Figure 5.44 Comparison of frequency of dominant peak in spectra vs. average flow velocity in the duct.

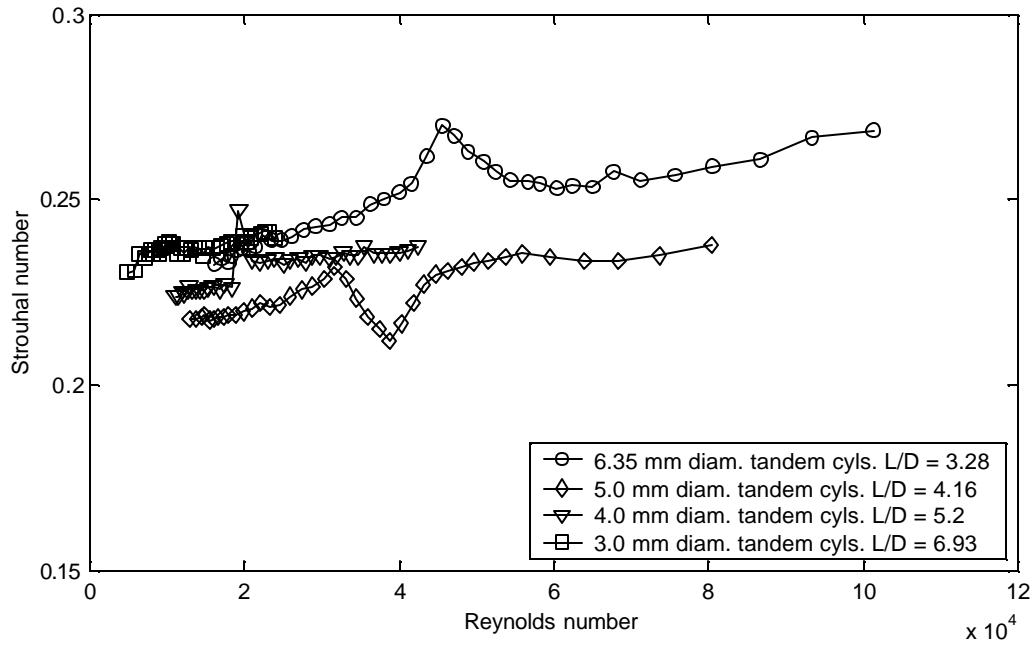


Figure 5.45 Comparison of Strouhal vs. Reynolds numbers from experiments on cylinders in tandem.

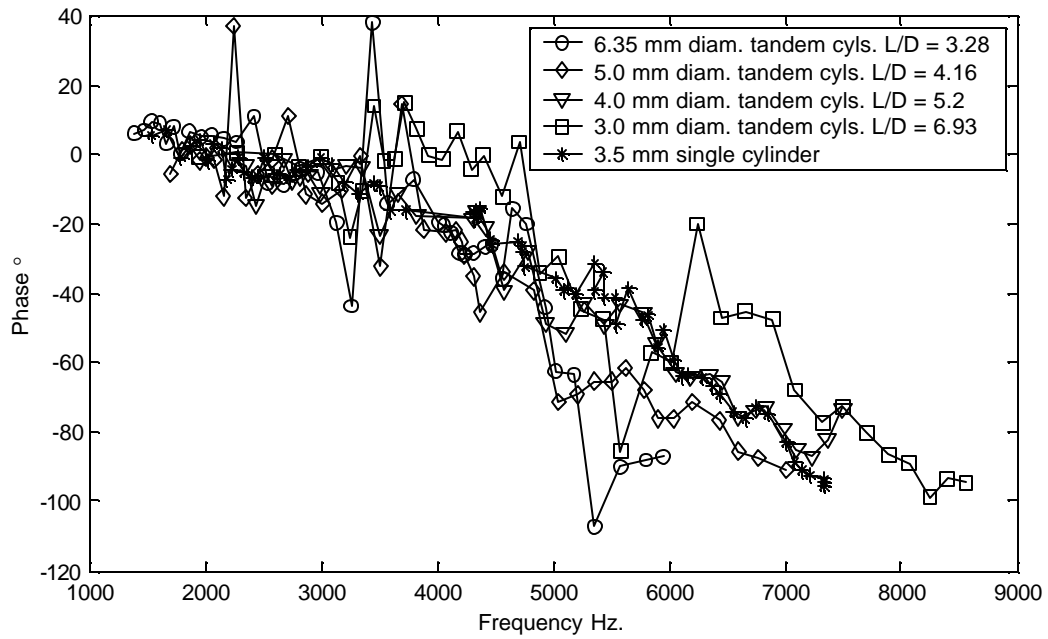


Figure 5.46 Comparison of phase angle vs. frequency of dominant peak in spectra for cylinders in tandem tests. Microphone pair 2a-4a. 3.5 mm single cylinder results also plotted for comparison.

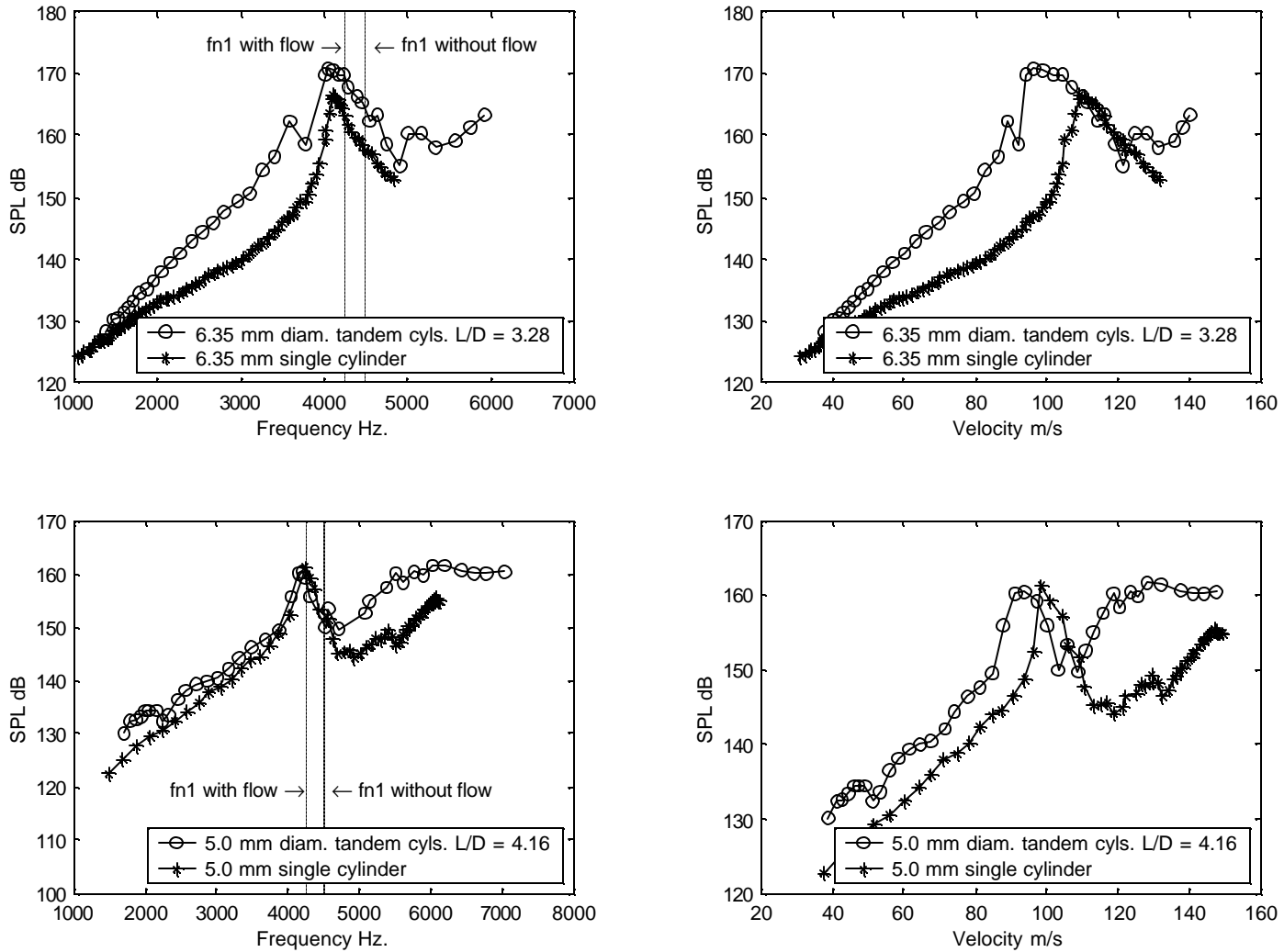


Figure 5.48 Comparisons of sound pressure level vs. frequency and sound pressure level vs. velocity of single cylinder results with results from the cylinders in tandem tests. Microphone position 2a. Acoustic resonance estimated with flow velocity at resonance condition (fn1 with flow).

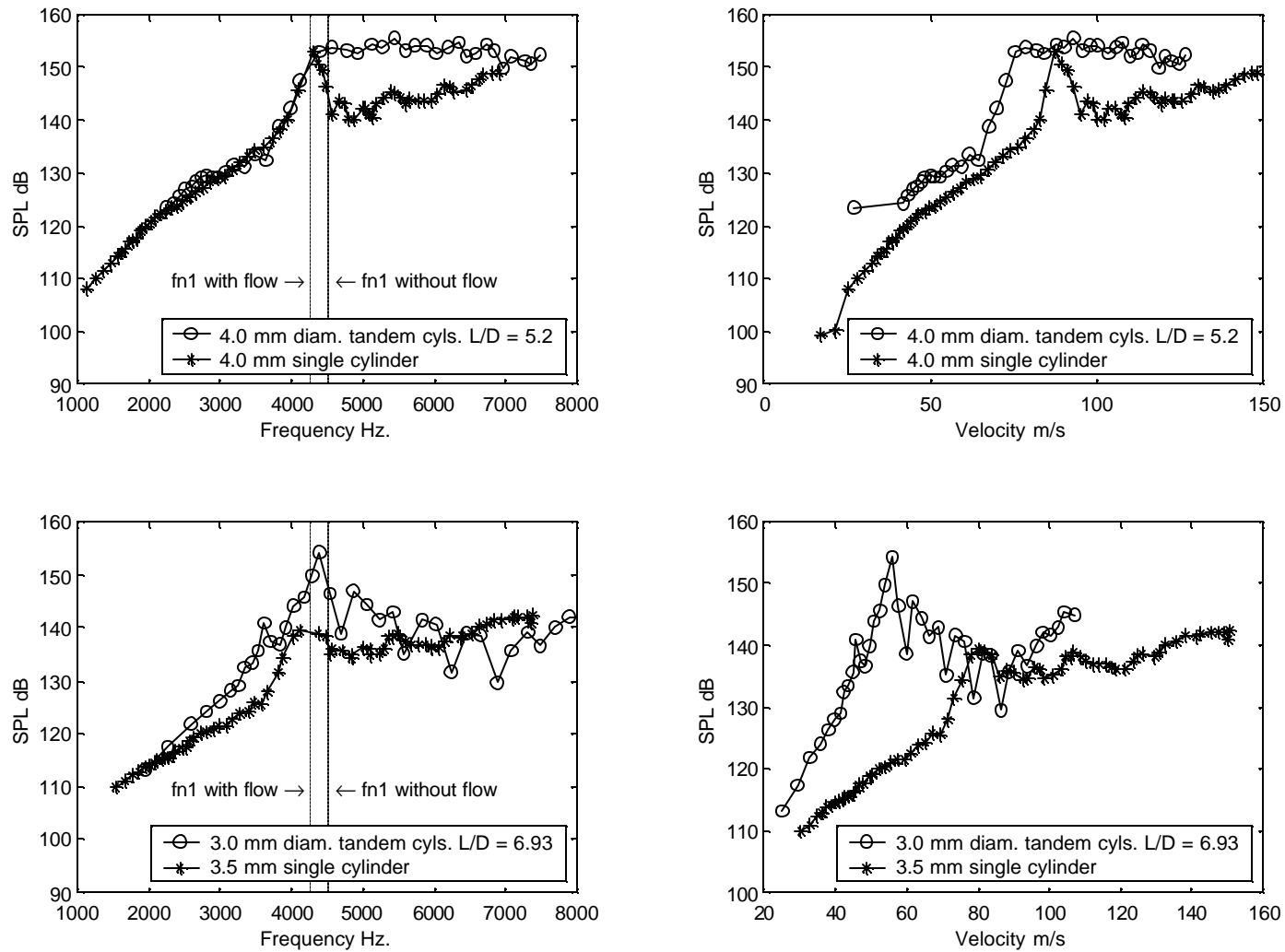


Figure 5.49 Comparisons of sound pressure level vs. frequency and sound pressure level vs. velocity of single cylinder results with results from the cylinders in tandem tests. Microphone position 2a. Acoustic resonance estimated with flow velocity at resonance condition (fn1 with flow)

## Chapter 6: Acoustic Model Based Inferences Using Experimental Results

### 6.1 Introduction

In this Chapter, the model presented in Chapter 3 will be used to try to explain the experimental results presented in Chapter 5.

### 6.2 Dipole source strength from cylinders in cross-flows

In order to obtain a solution from the theoretical model that is comparable to results obtained from experiments it is necessary to characterize the noise source strength and the system damping. On the other hand, if the model could predict reasonably well the behavior of the flow-induced acoustic field from cylinders in a duct, then the model could be applied using an inverse acoustic analogy approach to obtain both dipole source excitation and system damping.

Dipole source strength in the case of cylinders in cross-flows is a direct function of the fluctuating flow-induced forces that are created by the vortex shedding phenomena. These forces have been defined in equation (3.27) and as shown are a function of density, flow velocity, cylinder dimensions, and a nondimensional constant  $C'_L$  defined as the fluctuating lift coefficient. The fluctuating lift coefficient is used to approximate the estimated fluctuating force from the true or real fluctuating force since there are other parameters that affect these forces as seen in section 2.6.

The nondimensional monochromatic body force per unit of mass, which is equivalent to the dipole source strength needed in equation (3.90), is derived starting from the magnitude of equation (3.27):

$$|\mathbf{F}'_L| = \frac{C'_L \rho_0 V^2 D L}{2} \quad (6.1)$$

The magnitude of equation (3.27) is only important since it is assumed that the fluctuating forces behave in a sinusoidal manner. This assumption permitted the simplification of the wave equation shown in equation (3.43) that transformed it to the inhomogeneous convected Helmholtz equation shown in equation (3.44). This assumption is valid since in this work we are interested in the tonal noise sources only. Equation (6.1) is then divided by  $\rho_0 L_c^3$  to express the force per unit of mass:

$$F_y = \frac{C'_L V^2 D L}{2 L_c^3} \quad (6.2)$$

Where  $L_c$  represents the characteristic length used in equations (3.42). Finally, equation (6.2) is nondimensionalized by multiplying it by  $L_c / c_0^2$  as shown in equations (3.42) to obtain:

$$F_{y\text{nd}} = \frac{C'_L V^2 D L}{2 L_c^2 c_0^2} \quad (6.3)$$

Equation (6.3) hides the importance of the density of the fluid in the final determination of the sound pressure levels from equation (3.90). The importance of the density is realized once the non-dimensional pressure is dimensionalized as shown in equations (3.42).

The use of equation (6.3) in equation (3.90) assumes that the fluctuating forces produced along the cylinder length will be concentrated at the center of the cylinder. Equation (6.3) also assumes that the full length of the cylinder is important in the estimation of the fluctuating force. Reports in the literature support this assumption [Szepessy and Bearman]. For cylinders with aspect ratios less than approximately 4, the vortex shedding from the cylinder can be considered to be in phase along the cylinder length [Zdravkovich 1997]. In our case the cylinder aspect ratios were always less than one.

### 6.3 Methodology used in the application of the acoustic model

The model can be used directly as presented by equation (3.90) (and its auxiliary equations and forms depending on the case) to determine the acoustic field of dipole sources inside a duct with uniform flow. However two main difficulties make this direct approach not suitable in our case. 1) The fluctuating lift forces are not known. The source strength is linked to the fluctuating lift forces of the cylinders, but as described in Chapter 2, there are different factors that influence these forces. Even if these factors could be controlled, the fluctuating lift forces also vary depending on the Reynolds number regime present. 2) Damping is not known. Damping can have a very significant effect in the acoustic field produced in a duct. For these two reasons a different approach was used in the validation of the acoustic model.

In our case the measurements of the acoustic field produced by single cylinders in cross-flows inside a duct presented in Chapter 5 were used in optimization procedures that attempted to minimize the difference between the results from experiments and the results of the model. These optimization procedures used the experimentally determined values of density, frequency, and flow velocity in addition to the acoustic field measurements. The results of these optimization procedures are damping coefficients and fluctuating lift coefficients.

The approach initially attempted was to first obtain acoustic damping for a constant source strength or fluctuating lift coefficient. To accomplish this, the minimization of the difference between the experimental and theoretical complex acoustic pressure ratios between a series of microphone pairs was performed. This approach used experimentally obtained amplitude and phase information at all microphone positions upstream from the cylinder. The minimization function used in this approach is of the form:

$$\text{Minimize } F(x_h, y_h, z_h, x_1, y_1, z_1, C_L', \rho_o, V, f, z_y, z_z, Q_{nd}) = \sum_{h=1}^N \left( \frac{P_{\text{model}_h}}{P_{\text{model}_1}} - \frac{P_{\text{exp}_h}}{P_{\text{exp}_1}} \right)^2 \quad (6.4)$$

where  $N$  is the number of positions in the acoustic field where measurements were taken;  $(x_h, y_h, z_h)$  are the coordinates of microphone position  $h$ ;  $(x_1, y_1, z_1)$  are the coordinates of the reference microphone;  $C_L', \rho_o, V, f, z_y, z_z,$  and  $Q_{nd}$  are the fluctuating lift coefficient, density, velocity, frequency, specific acoustic impedance in the  $y$  and  $z$  walls, and volumetric damping, respectively. The estimated and measured acoustic pressures at position  $h$  are referred as  $P_{\text{model}_h}$  and  $P_{\text{exp}_h}$ , respectively. From equation (3.90)  $P_{\text{model}_h}$  is obtained. The implementation of the minimization procedure presented in equation (6.4) was made using Matlab version 5.3 optimization toolbox function `fminimax`. This function utilizes a sequential quadratic programming method [Brayton et al.]. This function was used since it could be used with complex arguments. Two programs to implement the minimization procedure described in equation (6.2) were made. One program was used to solve for the value of complex volumetric



damping and the other program was used to obtain the complex wall acoustic impedance. These two very similar procedures are presented in Appendix I.

The second part of the procedure consists of the minimization of a function that groups the normalized square of the error between the experimental rms pressure readings and the rms pressures calculated using the model at the same microphone positions. In this part, acoustic damping determined from step one was used and the fluctuating lift coefficient ( $C_L'$ ) was allowed to vary. The general problem can be expressed as:

$$\text{Minimize } F(x_h, y_h, z_h, C_L', r_o, V, f, z_y, z_z, Q_{nd}) = \sum_{h=1}^N \left( \frac{P_{\text{model}_h} - P_{\text{exp}_h}}{P_{\text{exp}_h}} \right)^2 \quad (6.5)$$

Sections I.6, I.7, and I.8 in Appendix I show the Matlab programs that implement the optimization procedure presented in equation (6.5).

This two-step method to obtain first the acoustic damping and then the fluctuating lift coefficient proved not the best approach for two reasons. 1) Acoustic damping effects are negligible at off-resonance conditions. 2) The two damping mechanisms included in our model do not appear to be capable of explaining the phase differences seen in our experimental measurements. In Chapter 7, results of numerical experiments using the model with different values of the complex damping coefficients are presented. These results show why the minimization procedure shown in equation (6.4) was not successful.

Instead of this two-step approach, it was decided to obtain the fluctuating lift coefficients assuming very rigid walls and zero volumetric damping. This approach was implemented using the minimization procedure described in equation (6.5). Later, an improved approach that consists of solving for the fluctuating lift coefficient and damping coefficients at the same time was tried. This new approach used only the resistive components of the wall impedance coefficients and the real part of the volumetric damping. However, the results obtained by this approach only confirmed that damping is negligibly small at off-resonance conditions and show inconclusive results at close to resonance conditions.

The general procedures described in this section were used only with single cylinders. The approach used to compare the results of the model with pairs of cylinders and multiple cylinders will be described in the respective sections.

#### **6.4 Inverse acoustic analogy approach**

Lighthill in his groundbreaking work in the 1950s established the relationships between the acoustic wave equation and the fluid dynamic equations. The nonlinear terms of the fluid dynamic equations were grouped as noise sources on the right side of the inhomogeneous wave equation [Norton]. This approach implies that if the flow field is known the noise sources are known. The inhomogeneous wave equation would be valid near the sources and far from the sources the homogeneous wave equation could be used. Using this approach the acoustic field produced by the known noise sources confined to a small region of sound generation in a larger region where acoustic propagation is possible could be estimated in theory. This approach is known as Lighthill's acoustic analogy.

In this study the measurements of the acoustic field would be used to infer the noise source strength. This approach is therefore an inverse approach to the one described in the previous paragraph. The use of measurements

of the acoustic field to determine properties of the noise source is for this reason referred in this work as an inverse acoustic analogy approach.

### **6.5 Single cylinder experimental and modeling results**

Fluctuating lift coefficients were obtained using the minimization procedure presented in equation (6.5) for all single cylinder results. These fluctuating lift coefficients were then compared to fluctuating lift coefficients obtained from the literature to validate the procedure. Finally, fluctuating lift coefficients were used with the model to calculate sound pressure levels to compare with experimental results.

Figure 6.1 shows the results obtained from the optimization procedure. As mentioned in section 6.3, these results assume that the full length of the cylinder contributes in the determination of the fluctuating lift forces. Additionally, the maximum velocity at the duct was used in the calculations. These two factors might explain the slightly lower fluctuating lift coefficients obtained than those reported in the literature as shown in Figure 6.2. Figure 6.2 only presents the set of results for four of our cylinders to avoid clutter.

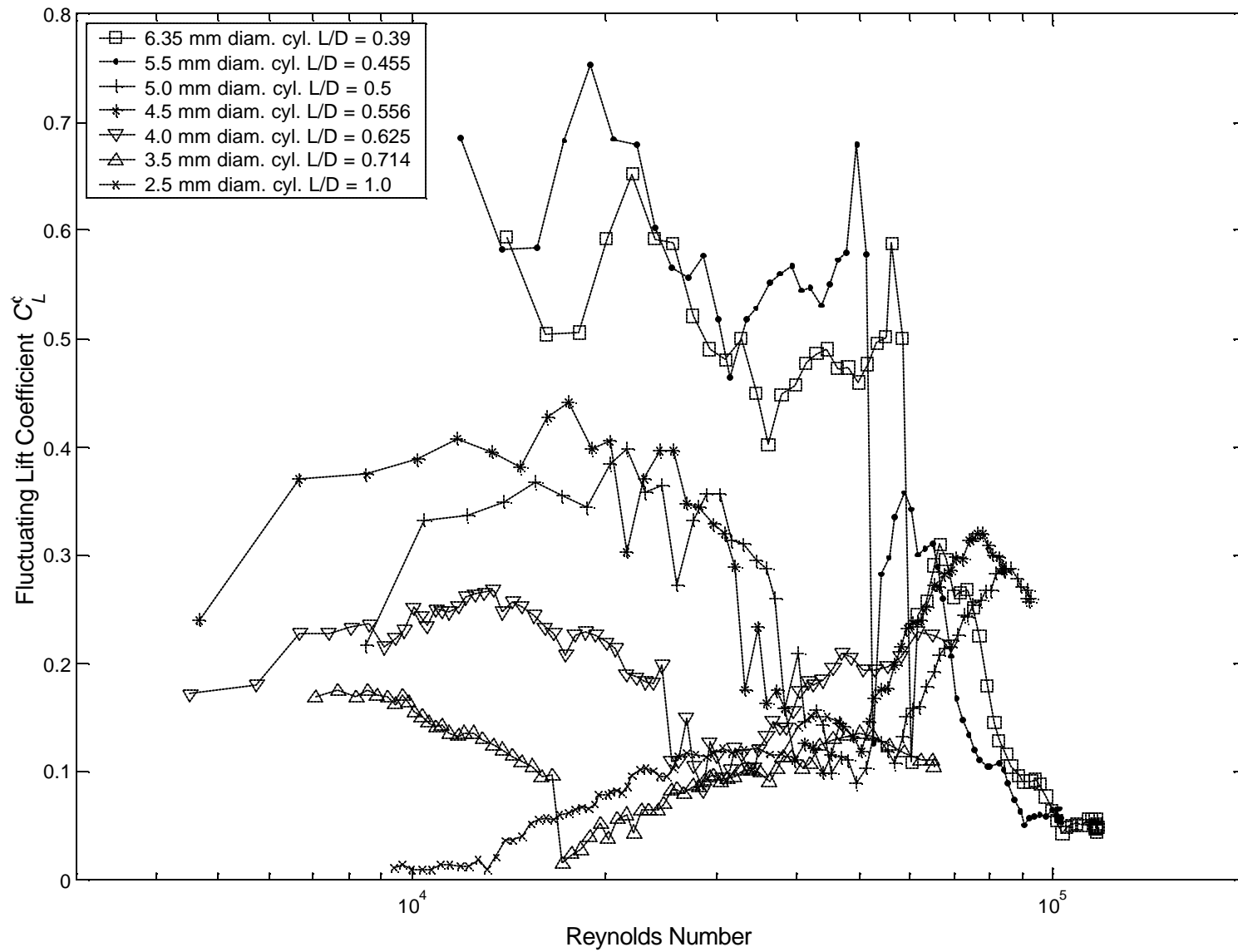


Figure 6.1 Fluctuating lift coefficients obtained using acoustic field measurements of single cylinders in a duct.

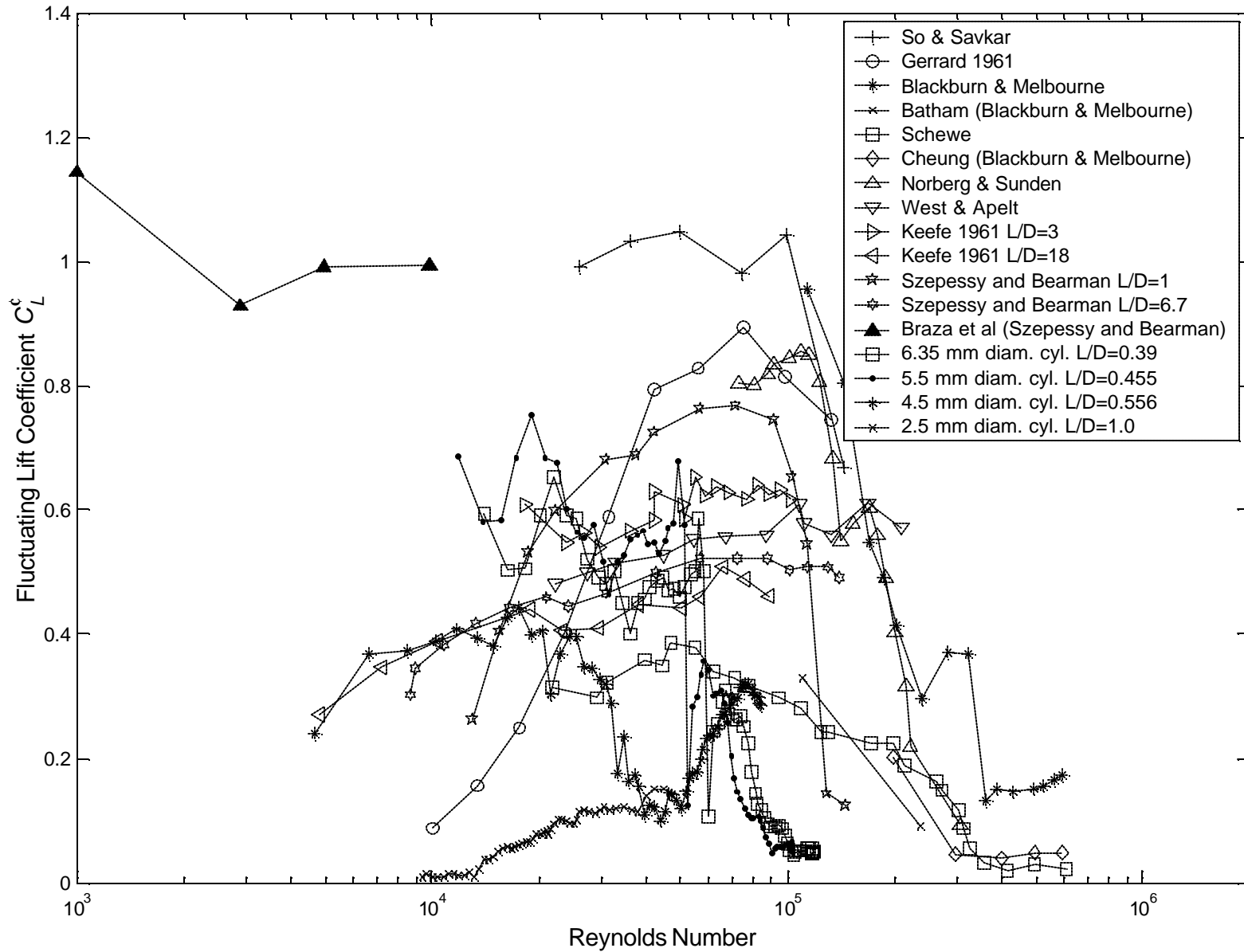


Figure 6.2 Fluctuating lift coefficients from the literature obtained with nominally smooth flows.

Figure 6.1 shows that at lower Reynolds numbers the smaller the diameter (or the larger the aspect ratio), the smaller the fluctuating lift coefficients. Between Reynolds numbers of 30,000 and 70,000, fluctuating lift coefficients no longer follow any noticeable trend with respect to aspect ratio. Only the work by Szepessy and Bearman show a few results of fluctuating lift coefficients for aspect ratios smaller than one. For this reason, the trends presented in Figure 6.1 could not be checked against results from the literature. The comparisons made in Figure 6.2 show that the fluctuating lift coefficients obtained with our inverse acoustic analogy type approach follow closely results from the literature obtained for smooth flows. Most of the data found was concentrated in the upper subcritical and critical flow regimes while our results cover most of the subcritical flow regime. All the results presented in Figure 6.2 except those of Braza et al. are experimental results. Braza et al.'s results, obtained from the paper by Szepessy and Bearman, were obtained by a two-dimensional direct simulation of the Navier-Stokes equations.

Figure 6.3 compares results obtained with the 6.35 mm and 5.5 mm diameter cylinders with results from the literature obtained with turbulent flows. The percentage indicated in the caption is the turbulence intensity reported. The addition of turbulence lowers the transition to the critical regime and apparently uniformize the trends observed by many researchers on the fluctuating lift coefficient. Our data follows closely the same trends. In our case, turbulence intensity was not directly measured but using measurements of the hydrodynamic pressure fluctuations reported in section 4.10, it was estimated to be of the order of 1%.

Figure 6.4 shows the fluctuating lift coefficients obtained for the different tests performed on the 6.35 mm diameter cylinders. The figure shows for all the tests that the fluctuating lift coefficients are declining as a function of Reynolds number. Tests 1 and 2 results are very close to each other. Similarly, test 3 and the stereolithography cylinder results are very similar. As can be seen in Figure 5.23 the results of test 3 and the stereolithography test produce similar sound pressure levels while tests 1 and 2 are similar and slightly higher. These differences cause the difference seen in Figure 6.4. Figure 6.4 shows that there is a discontinuity in the fluctuating lift trends for Reynolds number in the 60,000 to 70,000 range. Test 3 results are shown with solid black markers to help in observing this behavior. At this value of Reynolds number the resonance condition is established. It was found that the fluctuating lift coefficient increased above what the normal trend would predict just below resonance. Similarly it decreases more than expected at frequencies slightly larger than the resonance frequency. This behavior was not observed for other cylinder diameters. Originally, it was thought that this behavior was caused by fluid-acoustic coupling effects. It was believed that it appeared only on the larger cylinders since the larger cylinders produce stronger acoustic fields inside the duct. Although this is a possible explanation, this result could also be caused by the reduced robustness of the minimization procedure close to the resonance point where differences in the acoustic field measurements are harder to detect and more difficult to differentiate by the model.

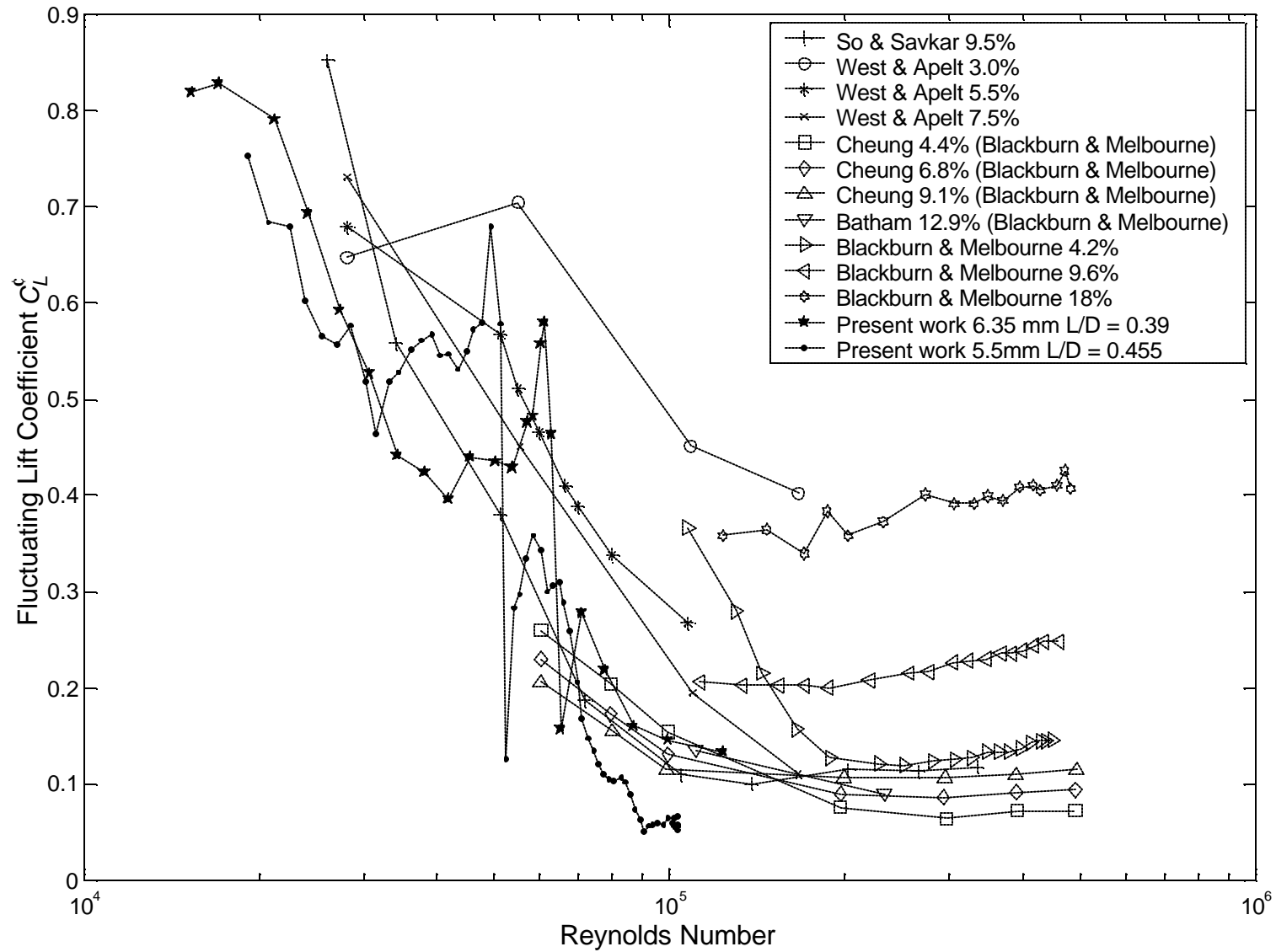


Figure 6.3 Fluctuating lift coefficients from the literature obtained with turbulent flows. Turbulent intensities reported shown to the right of the names in percentages.

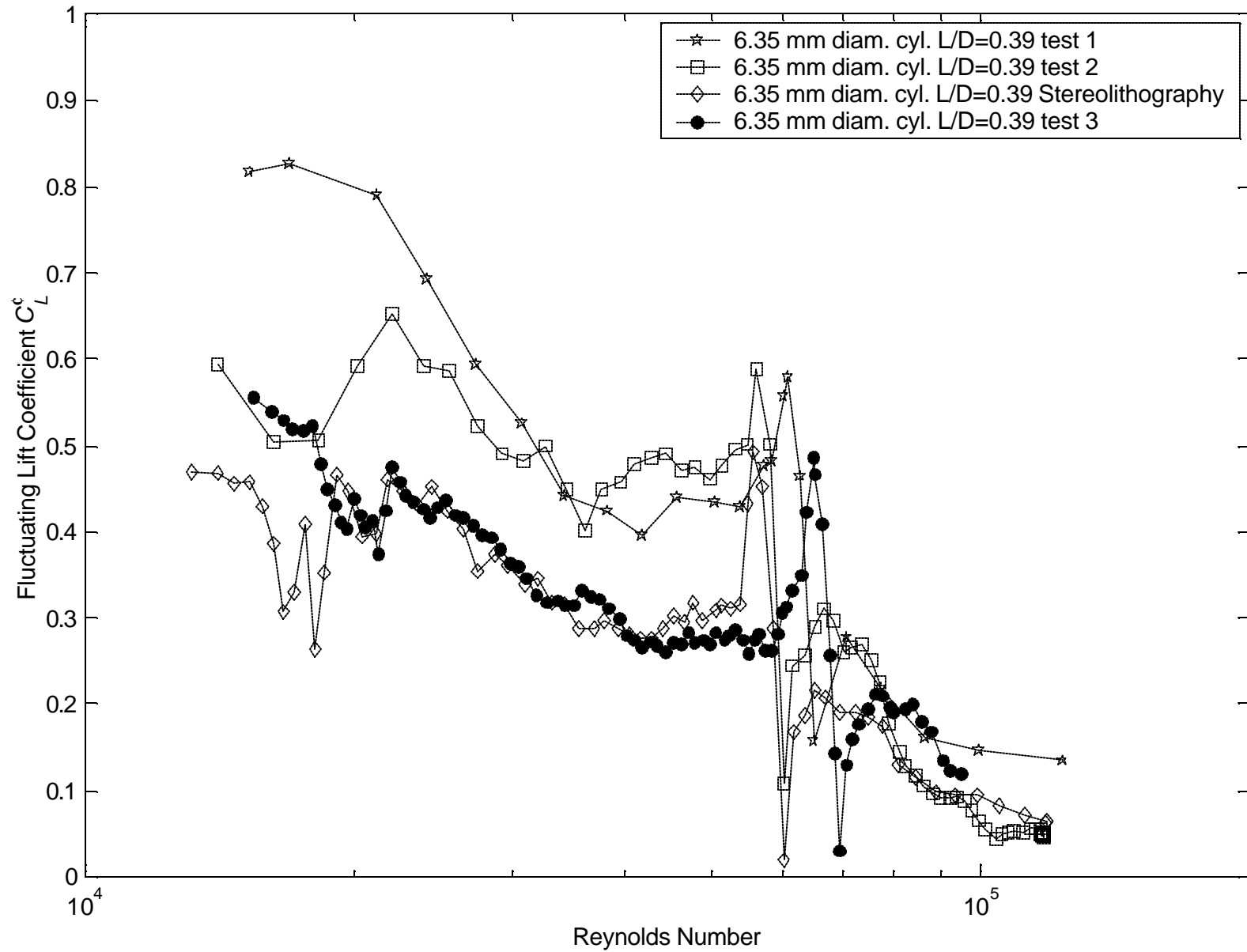


Figure 6.4 Comparison of fluctuating lift coefficients obtained using different experimental data sets

Fluid-acoustic coupling effects are difficult to determine because there are many parameters that affect the flow phenomena created by circular cylinder in cross-flows inside a duct and, therefore, make the separation of effects difficult. Figure 6.1 shows that the fluctuating lift coefficients increase with cylinder diameter for the lower Reynolds numbers. This behavior could be explained as the results of the positive feedback of the stronger acoustic field created by the larger diameter cylinders. However, it is not known if the aspect ratio, blockage, or other variable that affects single cylinder flow phenomena is responsible for the observed behavior. Further research is needed as described in Chapter 8 to fully separate fluid-acoustic coupling effects from purely fluid mechanic effects.

As mentioned in section 6.4 an improved optimization approach was tried to find fluctuating lift coefficient and damping parameters jointly. The results of this approach are presented in Figures 6.5 through 6.7. This approach was tried with one of the 6.35 mm data sets only. Figure 6.5 shows the results of the fluctuating lift coefficients found. It can be seen, as expected, that now the fluctuating lift coefficients increase as soon as damping starts to play a role. Once damping is allowed to vary in the modeling equations, the minimization procedure finds a better fit to the data with the use of the extra degree of freedom, and this leads to the increase in the fluctuating lift coefficient in comparison to the one found when damping was neglected.

Figure 6.6 shows the values of the nondimensional damping coefficients found (only real values of these coefficients were used). It can be seen that only when the fluctuating lift coefficient vary damping parameter are nonzero. Figure 6.7 shows similar results, but here the procedure was tried with the specific acoustic resistance as the damping parameter. In this case, zero damping would be for very large specific acoustic resistance. The figure includes only the range of interest.

The final step in the validation of the procedure is the use of the fluctuating lift coefficients found with the optimization procedure to verify that they can be used to accurately predict sound pressure levels. Figure 6.8 presents the results of the sound pressure levels measured at different positions with results obtained with the model for a 6.35 mm diameter cylinder. The model uses measured values of flow velocity, frequency, density and the fluctuating lift coefficients found. Figure 6.8 show a very good agreement between the experimental and measured results.

The model was also used to determine the phase angle between different microphone pairs. Figure 6.9 compares the measured and model results of phase angle between the microphone pairs. Phase angles obtained from the model, unlike acoustic pressures, are not affected by the fluctuating coefficients found in the optimization procedure used. Phase angle can be affected by damping as will be see in the next chapter. However, Figure 6.9 does not show these damping effects on phase angle. Figure 6.9 shows greater differences between experimental and measured results but the model follows closely the trends of the experiments.



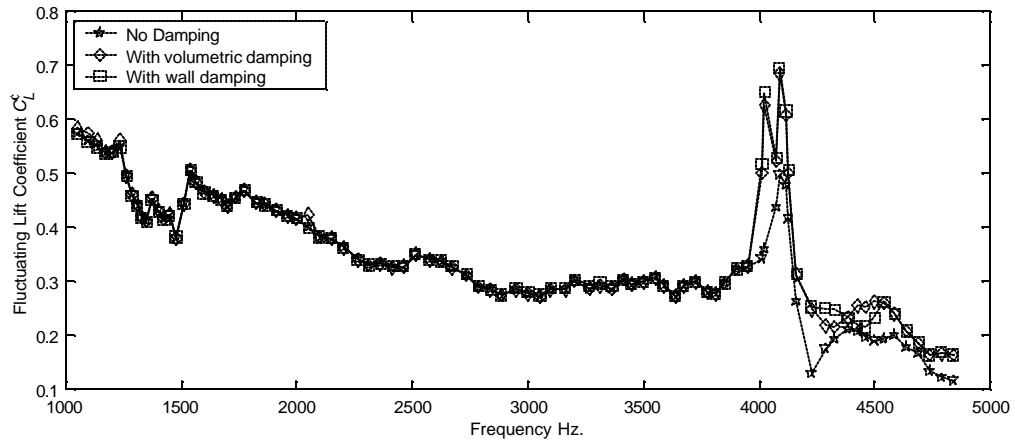


Figure 6.5 Fluctuating lift coefficients obtained in conjunction with damping coefficients.

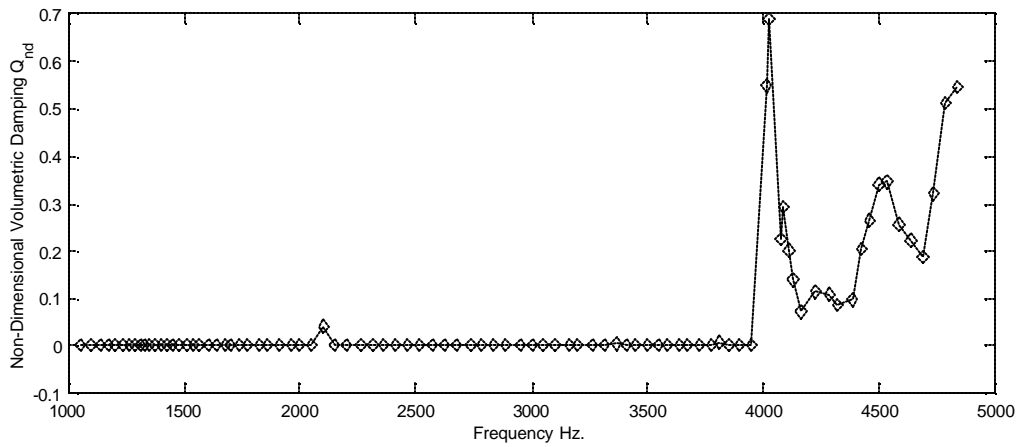


Figure 6.6 Non-dimensional volumetric damping coefficients obtained with results from Figure 6.5.

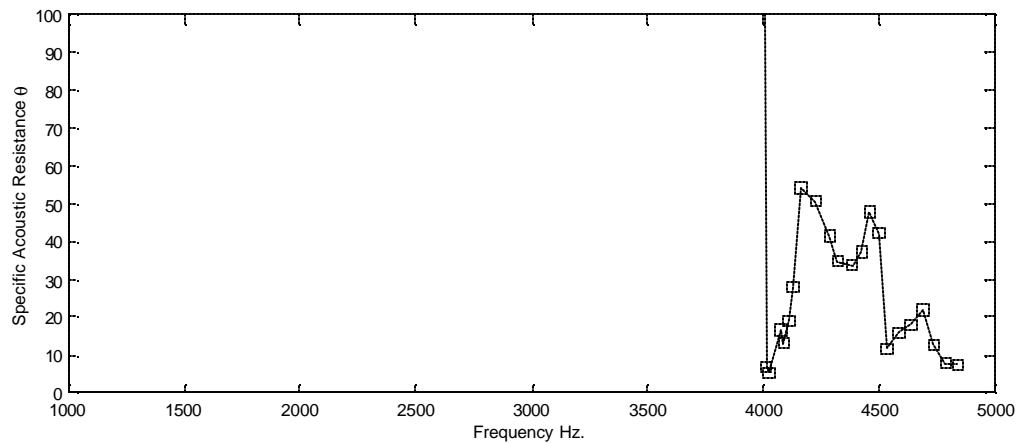


Figure 6.7 Wall damping coefficients obtained with results from Figure 6.5

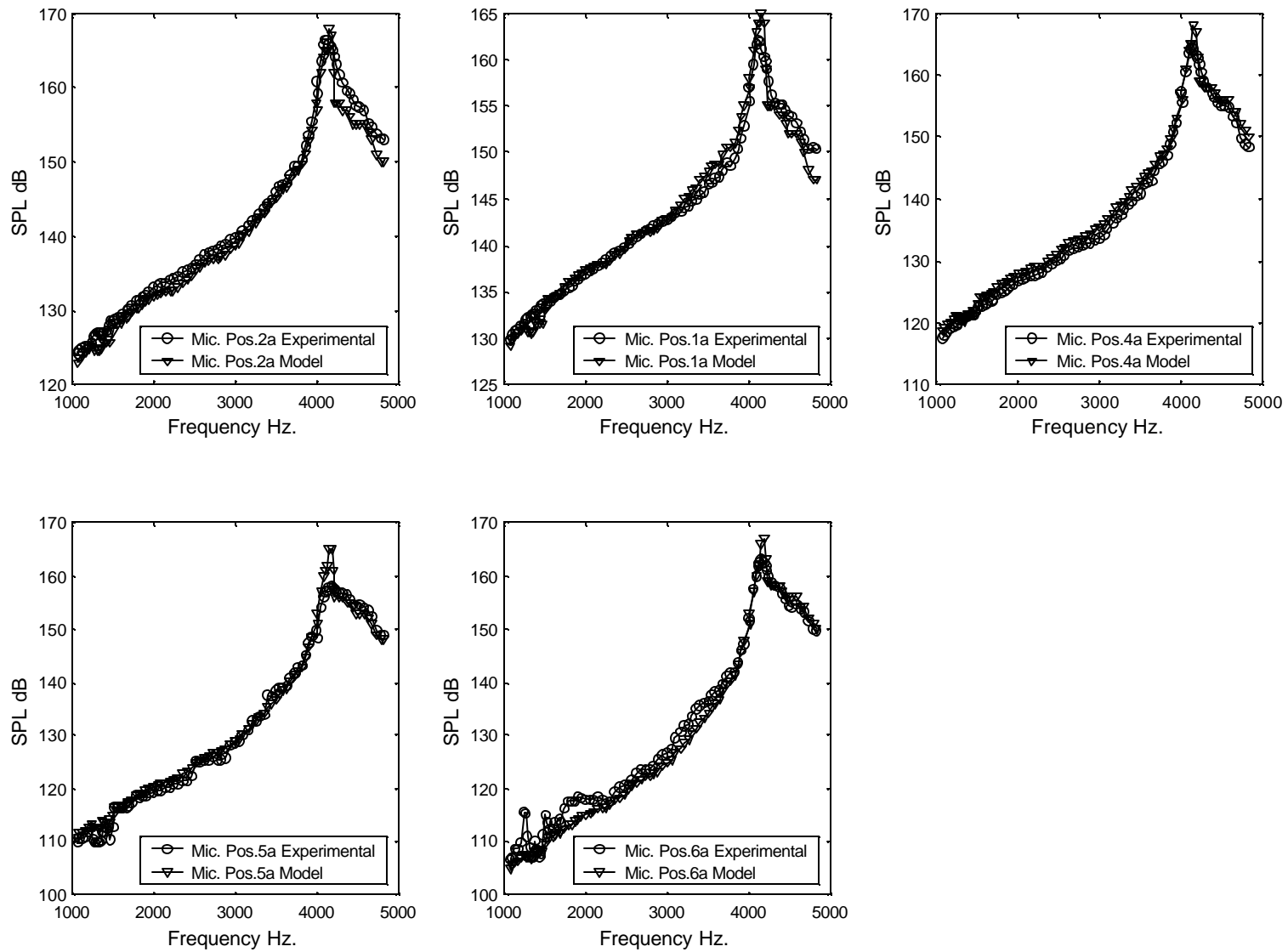


Figure 6.8 Comparison of experimental and model sound pressure levels as a function of tone frequency at different microphone positions. Cylinder diameter = 6.35 mm.

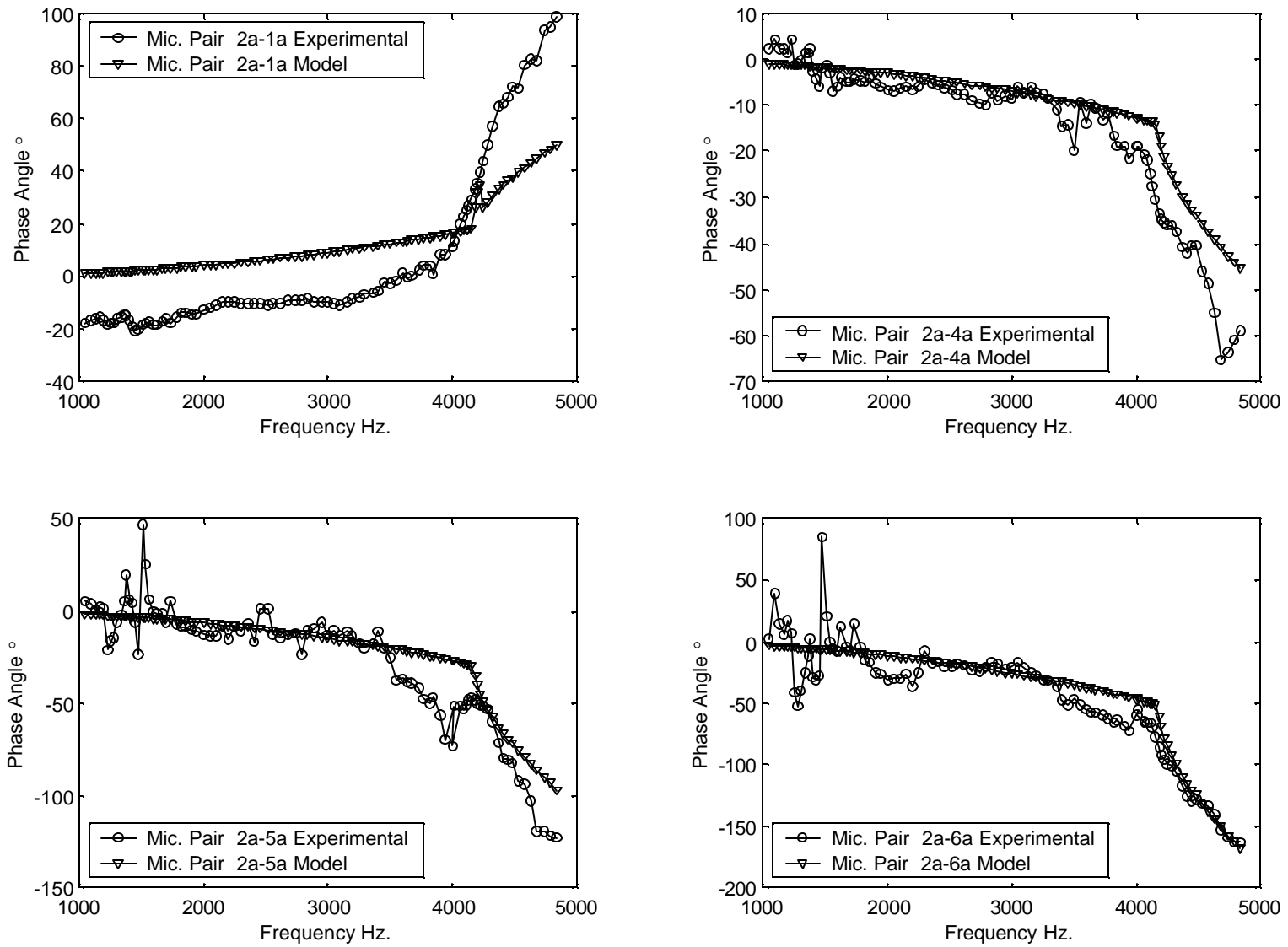


Figure 6.9 Comparison of experimental and modeling results of phase angle between microphone pairs as a function of tone frequency. Cylinder diameter = 6.35 mm.

### 6.6 Hourglass single cylinder experimental and modeling results

The modeling approach described in the previous sections for cylinders of constant diameter was also tried on one hourglass-shaped cylinder. The cylinder used had 3.8 mm cylinder diameter and 1 mm radius of curvature (see Figures 4.20 and 4.21).

Figure 6.10 presented the fluctuating lift coefficients found using the optimization procedure described in equation (6.5) on this cylinder. Measured values of the tone frequency, flow velocity, and fluid density were used in the calculations. In the calculations, it was assumed that the cylinder had a constant diameter of 3.8 mm and a length of 2.5 mm. These assumptions were made to determine an estimate of the dipole source strength for this cylinder. With these assumptions, the fluctuating lift coefficients found are reasonable in comparison to results from the literature.

Once the fluctuating lifts were obtained, they were used directly in the modeling equations to determine the sound pressure levels predicted at the measurement locations. Figure 6.11 compares the results obtained from the measurements of the acoustic field with those found by the model using these fluctuating lift coefficients. As can be seen, there is very good agreement between experimental and modeling results.

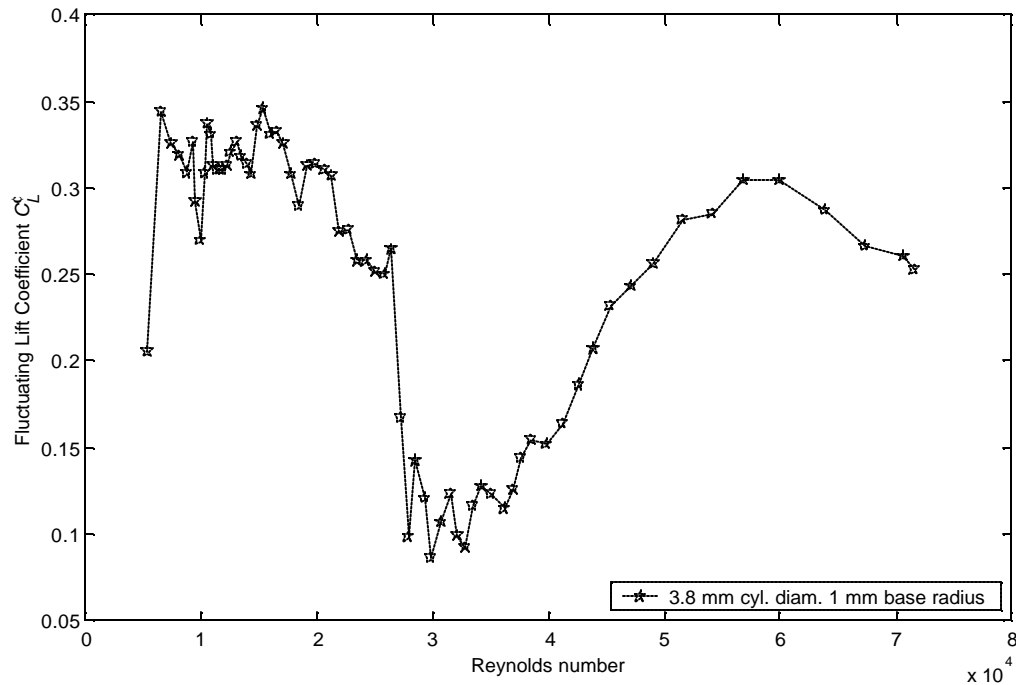


Figure 6.10 Fluctuating lift coefficients obtained using the model and measurements of the acoustic field produced by an hourglass shaped cylinder inside a duct.

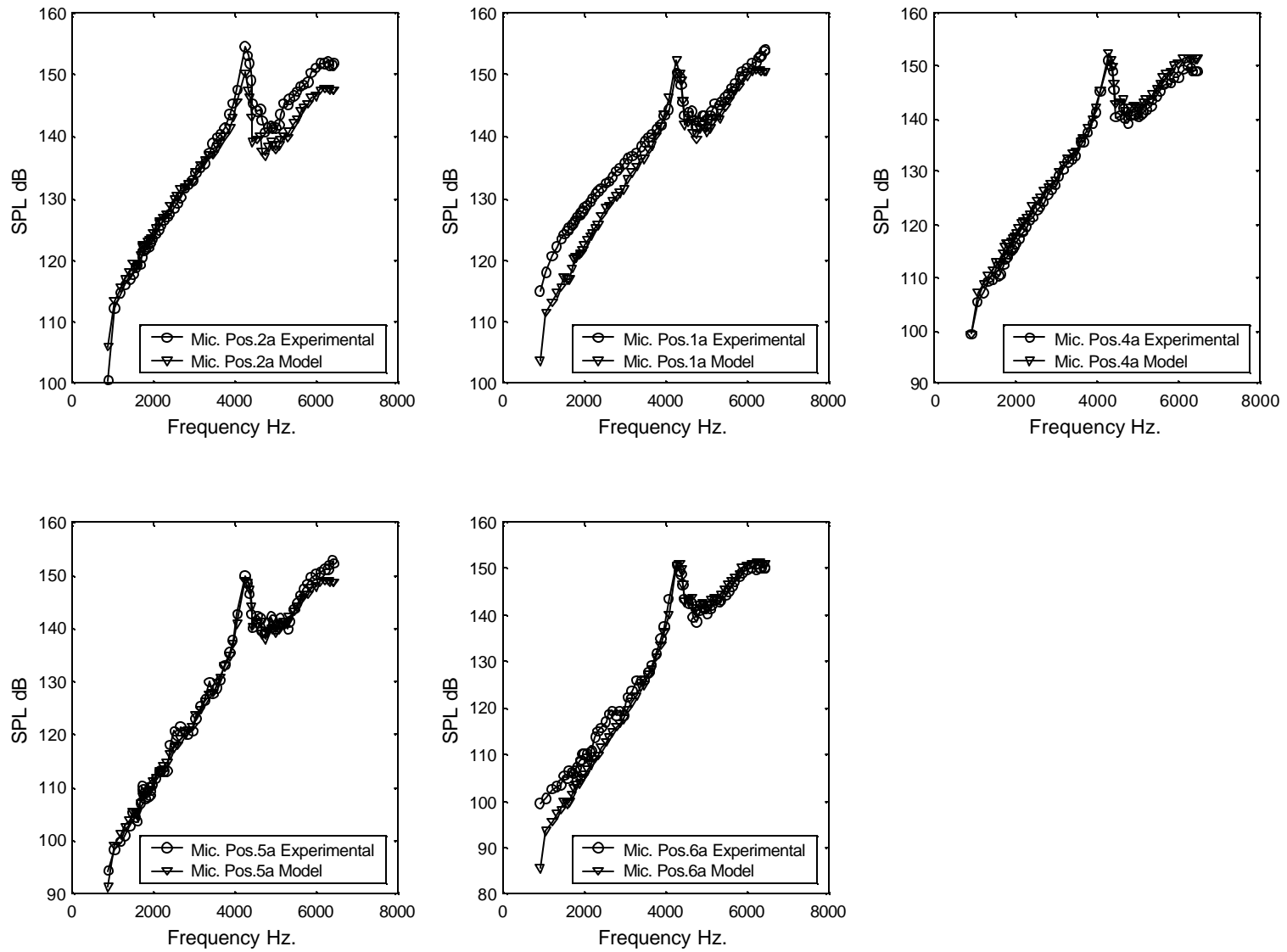


Figure 6.11 Comparison of experimental and model sound pressure levels as a function of tone frequency at different microphone positions. Hourglass cylinder 3.8 mm cylinder diameter and 1 mm base curvature.

### 6.7 Single cylinder with acoustic foam at y-walls experimental and modeling results

As described in section 5.4.1.1, measurements were made of the acoustic field produced by a single cylinder in a duct with acoustic foam on some of its walls. The purpose of these experiments was in general to explore the effects of the foam material on the sound field and to test the model with wall damping.

Since the values of the fluctuating lift coefficients are not known a fluctuating lift coefficient of 0.5 was assumed. This value is in the range found for rigid walls as presented in section 6.5. Since fluctuating forces were assumed this procedure to determine wall damping coefficients will not provide the correct or real values of the acoustic impedances but only an estimate.

To obtain wall impedances the objective function presented in equation (6.5) was changed to minimize the sum of the differences of the squares between the model and experimentally determined sound pressure levels. This objective function provided a better estimate of the specific acoustic resistances. The very nonlinear nature of the objective function made the search for the best wall damping coefficient very difficult. The results found by the nonlinear regression procedure are very dependent on the initial value and upper and lower bound imposed to limit the search space. Figure 6.12 shows values of the specific acoustic resistances found for the y-walls (the walls that support the resonance) where the foam was installed. Figure 6.12 also includes results found by Chung and Blaser 1980b for 19 mm acoustic foam samples for comparison. The 2.5 mm foam acoustic impedance values were then used with the model to find the sound pressure levels at the different microphone positions to compare to the experimental results. This comparison is shown in Figure 6.13.

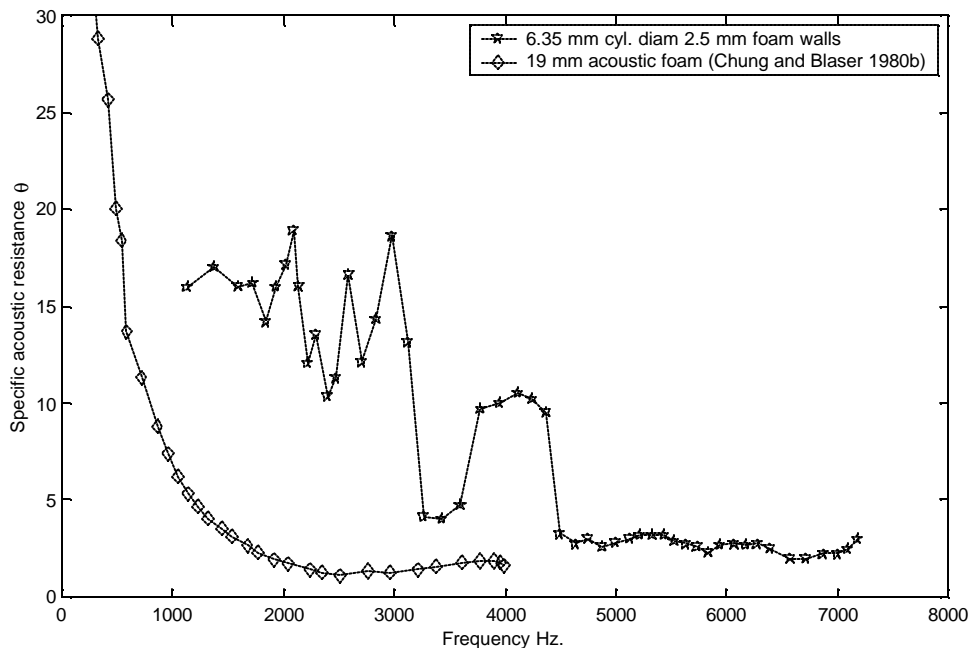


Figure 6.12 Wall damping coefficients obtained for 2.5 mm acoustic foam on duct walls.

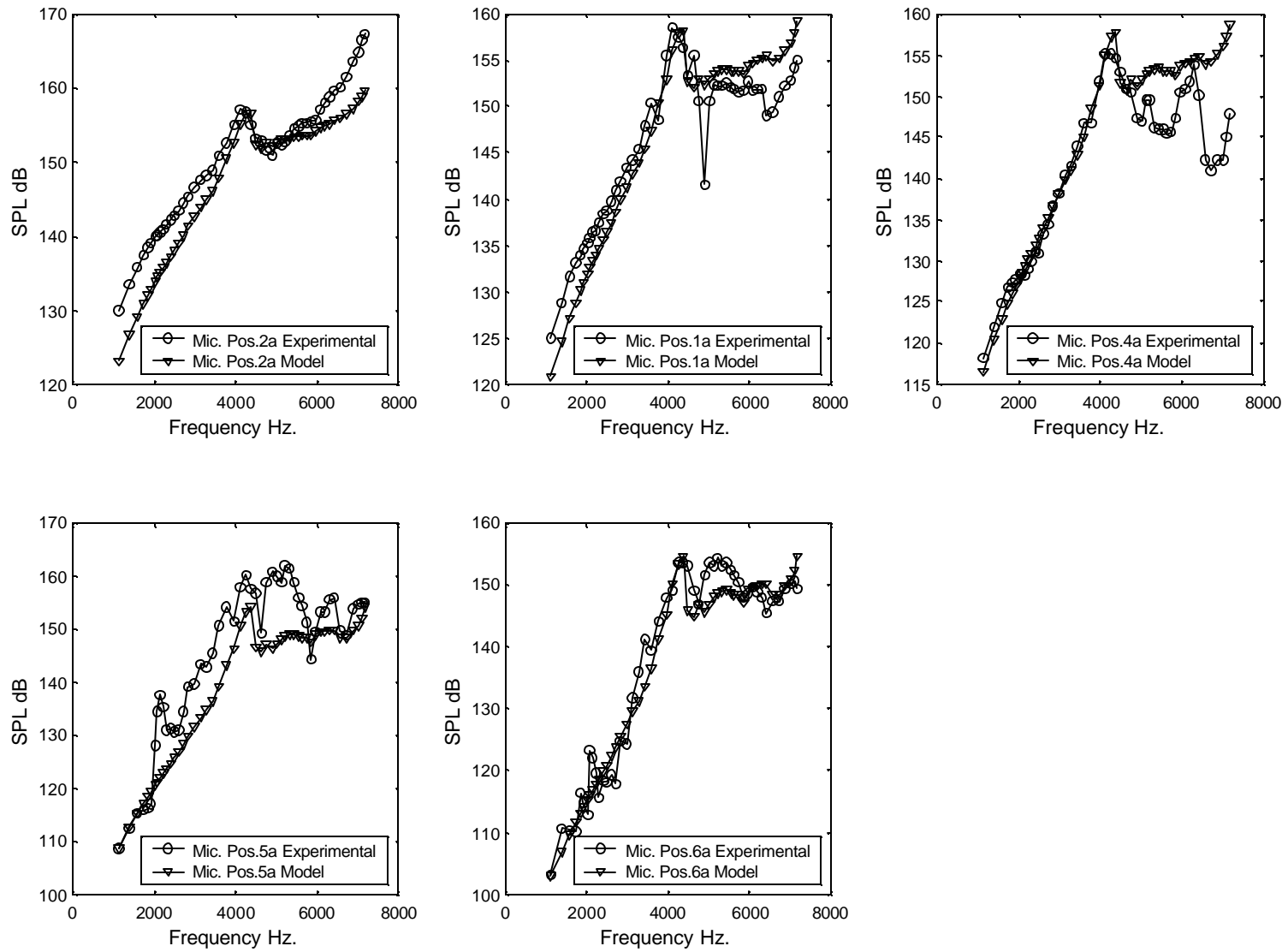


Figure 6.13 Comparison of experimental and model sound pressure levels as a function of tone frequency at different microphone positions. Using a 6.35 mm cylinder in duct with 2.5 mm acoustic foam on duct walls.

## 6.8 Tandem cylinders experimental and modeling results

The model was used in different optimization procedures to try to validate its use when multiple cylinders are present in the duct and to attempt to explain the behavior of the measured acoustic field.

First, a similar procedure to the one used to find the fluctuating lift coefficient for single cylinders as described in equation (6.5) was tried. In this case  $P_{\text{model}_h}$  was equivalent to the sum of the acoustic pressures produced by the two dipole sources at the cylinders positions, assuming that the dipoles were in phase. Damping was also assumed negligible. In this optimization procedure, instead of solving for a single fluctuating lift coefficient, the minimization algorithm was allowed to vary this parameter independently for each cylinder. With this procedure, pairs of fluctuating lift coefficients that minimize the error were found. In many cases, the best fit implied the dominance of only one of the dipole sources. For this reason a new approach was pursued. The new approach assumed that the fluctuating lift coefficient for the upstream cylinder would remain identical to the single cylinder case. The downstream cylinder fluctuating lift coefficient would then be found so that the modified objective function would be minimized.

Figure 6.14 shows the values of the fluctuating lift coefficients used and found. The downstream cylinder fluctuating lift coefficient was found as described above. The upstream cylinder fluctuating lift coefficient was obtained from an equation fit of data obtained for single cylinders. The single cylinder fluctuating lift coefficient is shown only for comparison purposes. The same procedure was repeated for the 4 mm tandem cylinders. Figure 6.15 compares the results of the downstream fluctuating lift coefficients obtained by the optimization procedure. Figure 6.15 also shows fluctuating lift coefficient measurements on the downstream cylinder reported by Savkar.

Once the fluctuating lift coefficients were obtained the model sound pressure level predictions were compared to the measurements. Figures 6.16 and 6.17 show the results of these comparisons. In these figures the single cylinder values were also plotted for reference.

The values of the fluctuating lift coefficients found are significantly higher than for the upstream cylinder. Arie et al. found that the fluctuating lift coefficients of the downstream cylinders in a tandem arrangement were approximately double the values of the upstream cylinders for  $L/D$  values between 3 and 7. But the coefficients never exceeded the value of 1. Their tests were made at a Reynolds number of  $1.57 \times 10^5$ . Savkar, on the other hand, reported values slightly higher than 1 that are closer to the results found using our inverse acoustic analogy approach. Figure 6.14 also shows that the maximum and minimum values of the fluctuating lift coefficients are found near to the resonance frequency.

The over and under prediction of the fluctuating lift coefficient just prior and after the resonance could be caused by the model inaccuracies in predicting experimentally observed natural frequencies. Figure 6.18 compares results obtained by the model assuming fluctuating lift coefficients of 0.5 for both 6.35 mm diameter cylinders. The figure shows that the resonance frequency in this case is predicted at a slightly higher frequency. This condition causes a shift in the curve profile to a higher frequency. Therefore, when the optimization procedure is used slightly higher values of the fluctuating lift coefficients are predicted than



would otherwise be. For this reason the fluctuating lift coefficients are also underpredicted at the resonance point found by the model.

It is critical to establish the correct value of the effective speed of sound, the convection effects on natural frequencies and any other factor that affect the acoustic natural frequency. If this is not done correctly, then the behavior of the solution shifts, and the prediction suffers inaccuracies. As a last resort, the speed of sound should be adjusted to match observed resonances so that the predictions obtained by the optimization procedures will be the result of the physical phenomena and not just a mathematical adjustment to the data.

Figure 6.18 shows also the sound pressure levels at position 1a that would be predicted by the model if each cylinder acted independently of the other. In this case, the distance from the cylinders to the measurement point is such that only at higher frequencies the sound pressure levels of the two cylinders are significant at this measurement location. Only when this happens are phase effects important since otherwise the sound pressure level of the closer cylinder dominates. An additional condition for noticeable changes in the sound pressure level is that the phase should be close to completely reversed.

Figure 6.19 is similar to 6.18, but in this case the fluctuating lift coefficients used were those presented in Figure 6.14. Figure 6.19 shows that when there are large discrepancies in source strength phase effects are not as significant as expected.

In tandem cylinders, the downstream cylinder SPL is not important at our measurements points until the frequency of the tone is close to the resonance or an extremely strong dipole source strength is assumed. For this reason, very large values of  $C_L'$  are required to explain any differences in the sound pressure level induced by the downstream cylinder alone. If, on the other hand, there is an increase in the dipole strength by fluid-acoustic coupling (of one or two dipoles) significantly more modest increases in  $C_L'$  would be needed.

The shift in the sound pressure level curves predicted by the model alone cannot explain the large fluctuating lift coefficients found at off resonance conditions. Additionally as seen in Figure 6.15 the fluctuating lift coefficients found for the 6.35 mm diameter cylinders are significantly larger than that those for the 4 mm diameter cylinders. It is more likely, due to their spacing, that the 4 mm diameter cylinders shed vortices out of phase; thus, the dipole sources produced by them would be out of phase. The 6.35 mm cylinders have a spacing that is more favorable to in-phase noise emitting as described by Morse and Ingard. During the optimization procedure used to determine fluctuating lift coefficients, it was assumed that both pairs of cylinders were in phase. For the 4 mm diameter cylinder pair, the fluctuation lift coefficients found with this assumption would be less than if the correct phasing were used. If the discrepancies in the fluctuating lift between the 4 mm and 6.35 mm diameter cylinders pairs could be explained by the out of phase noise emission, their large values would need to be explained. The best way to resolve this problem would be to measure the fluctuating forces in conjunction with measurements of the acoustic field.

There appears to be two types of fluid-acoustic coupling possible for two cylinders in tandem in a duct. The first fluid-acoustic coupling happens when the sound reflected from the duct walls and the fluid phenomena close to the cylinder interact. Judging from the single cylinders results, this scenario is not likely. During single cylinder testing, fluctuating lift coefficients showed no difference close to or far from the

resonance. Only in the case of the 6.35 mm diameter cylinder does the the fluctuating lift coefficient appear to be affected near a resonance. This, however, could be explained by the shift in the model predicted sound pressure level curve as described above.

The second type of fluid or fluid-acoustic coupling has been reported by Morse and Ingard and Johnson and Loehrke for two cylinders and plates in tandem, respectively. For two cylinders in tandem, the interactions can lead to a type of resonance present in a free field. This resonance condition happens when the spacing between cylinders in tandem is the same as the spacing between two consecutive vortices in the wake [see Morse and Ingard, page 757, also described in section 5.5]. Stoneman et al. show that this interaction is due to noise sources and sinks created in the downstream plate depending on the plate spacing. Their explanation is valid when a strong acoustic field such as the one present in their investigations exists. This does not fully explain the causes of these interactions in free field where a strong transverse resonance does not exist.

The fluctuating lift coefficients found for the 6.35 mm cylinders pair are significantly larger than those presented in the limited data available in the literature. This could be caused by other effects like fluid-acoustic coupling. But as mentioned above further work is needed to resolve this situation.

The model was also used to visualize the acoustic field produced by the two 6.35 mm diameter cylinders in tandem. Figure 6.20 shows the predicted acoustic field at three different frequencies. The frequencies chosen were below, close and above the first transverse acoustic resonance. There are large changes in the acoustic field as a function of frequency as shown. The acoustic fields in Figure 6.20 were calculated using the fluctuating lift coefficients presented in Figure 6.14. The values of other variables needed in the calculations such as air density and fluid velocity were taken from experimental measurements at those frequencies.

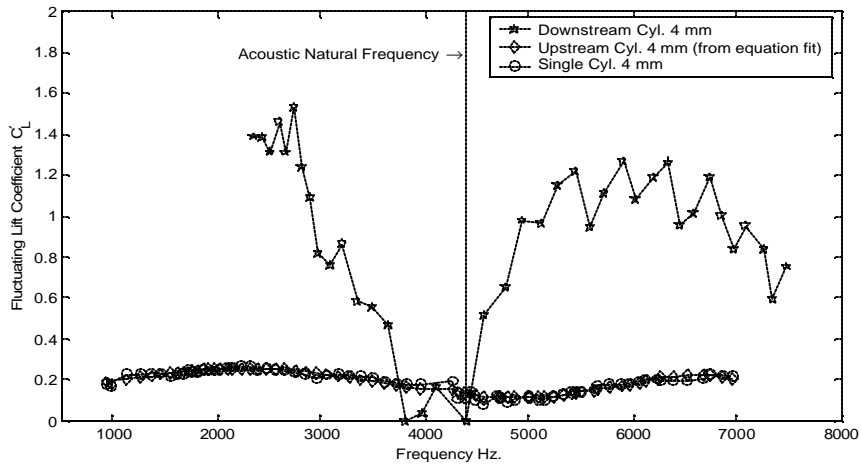
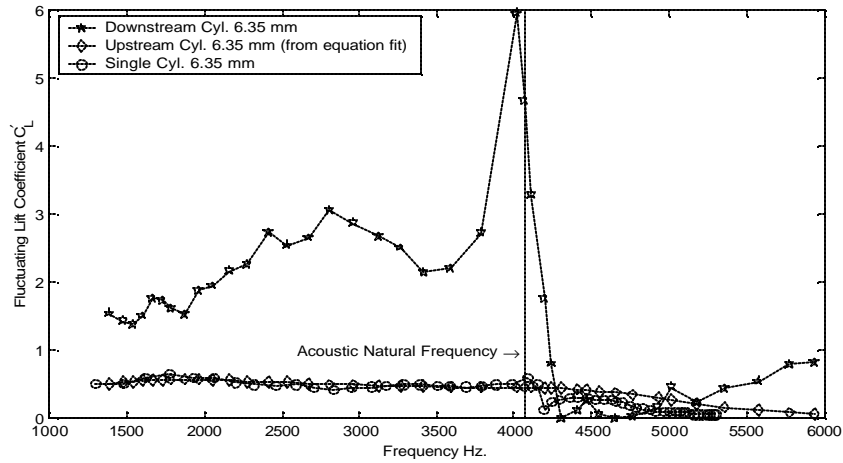


Figure 6.14 Fluctuating lift coefficients of cylinders in tandem and single cylinder.

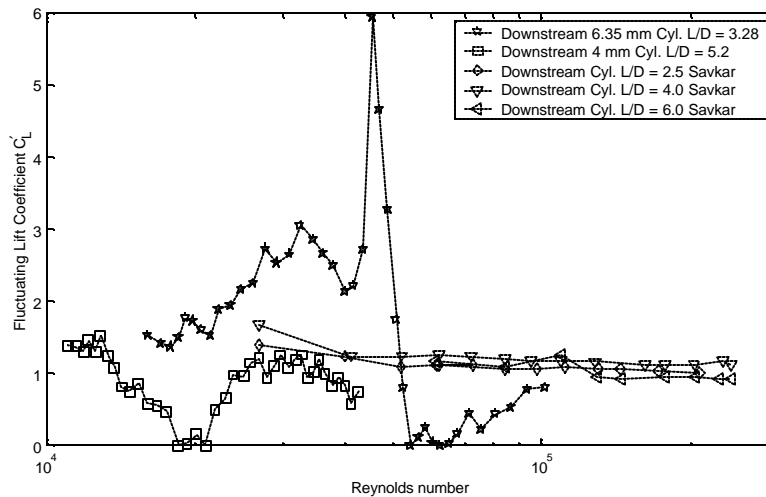


Figure 6.15 Comparison of fluctuating lift coefficients found for the downstream cylinder using the model for the 6.35 mm and 4 mm diameter cylinders in tandem.

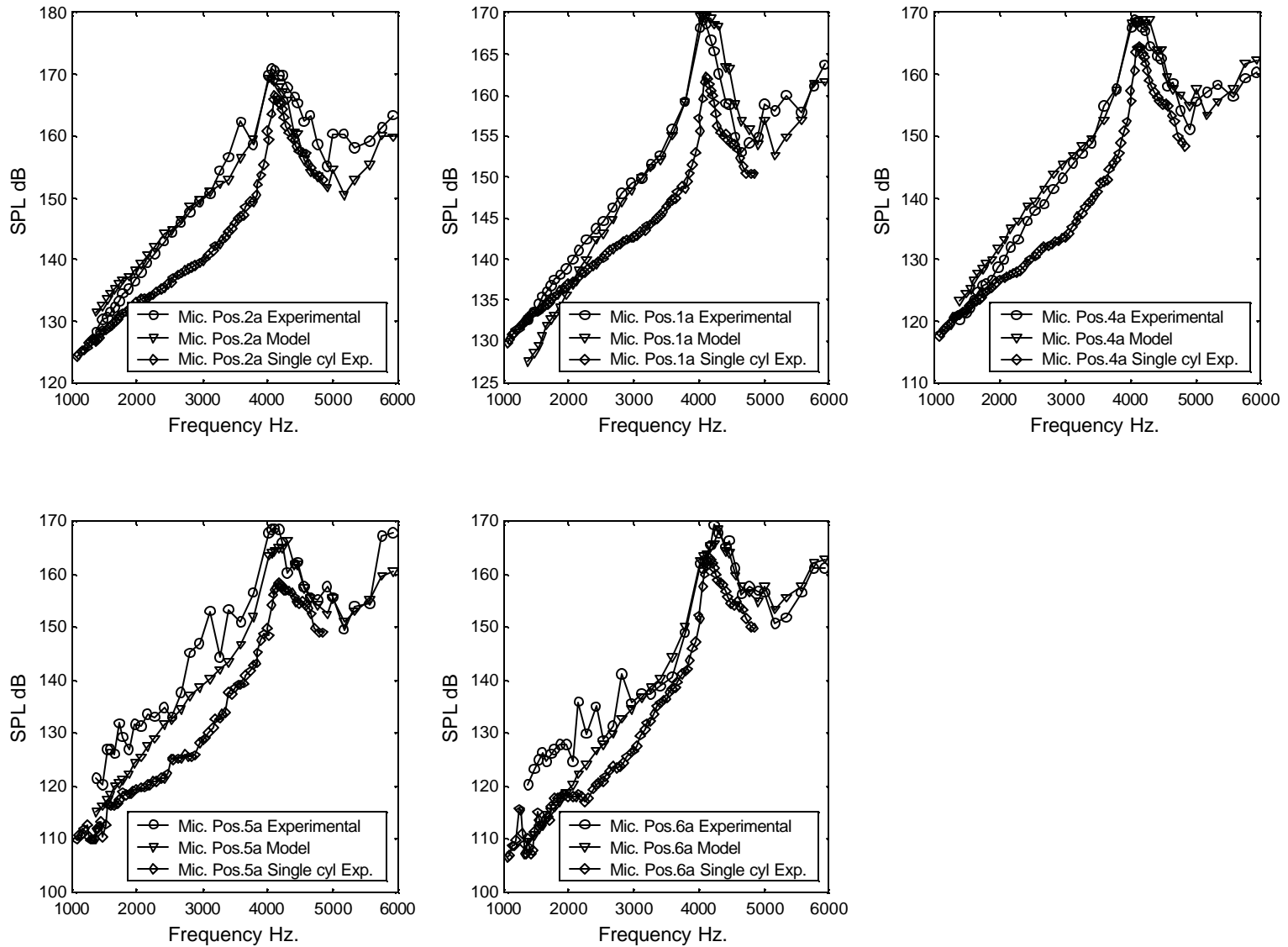


Figure 6.16 Comparison of measured and model sound pressure levels estimated for 6.35 mm diameter cylinders in tandem arrangement.

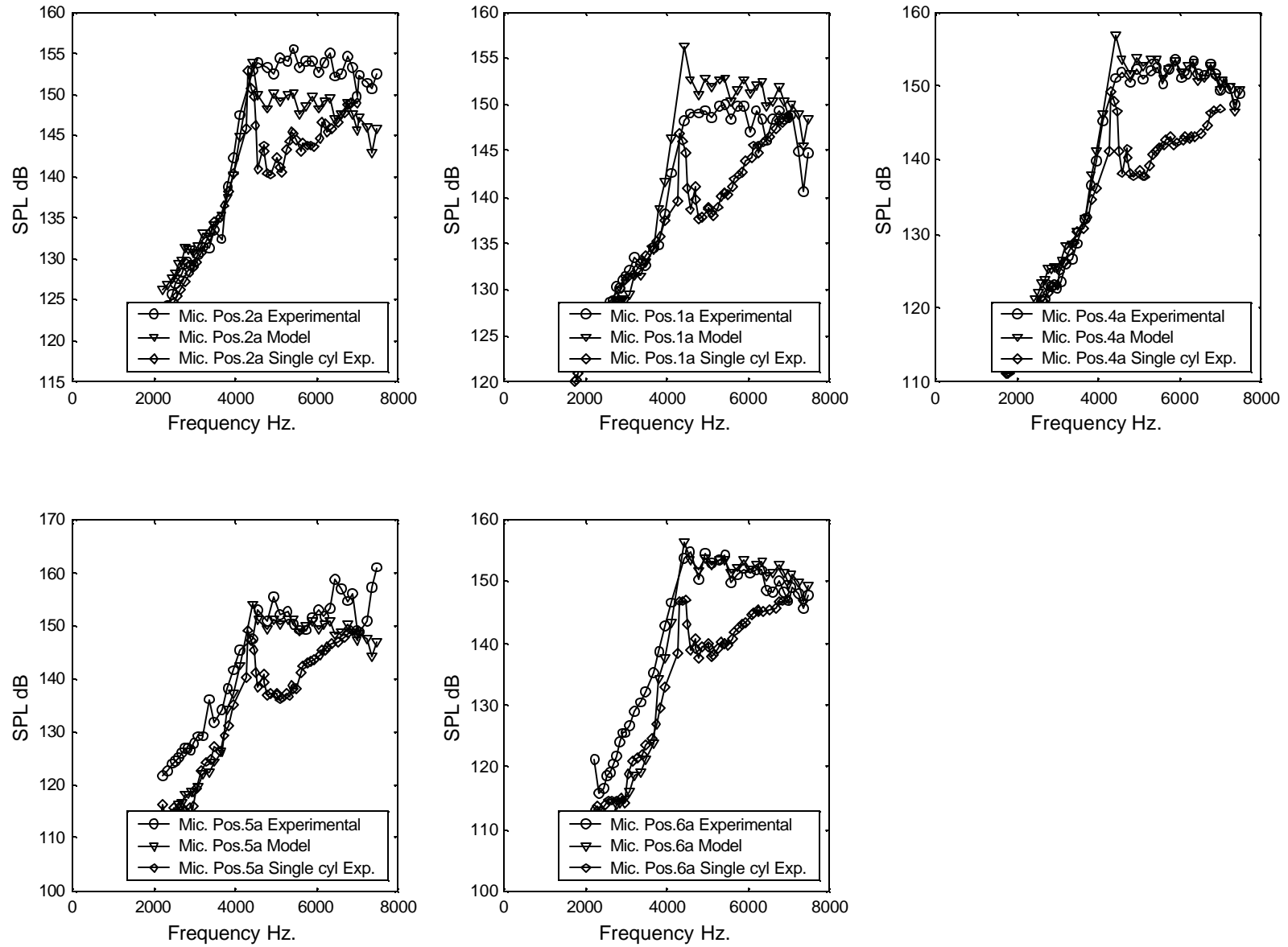


Figure 6.17 Comparison of measured and model sound pressure levels estimated for 4 mm diameter cylinders in tandem arrangement.

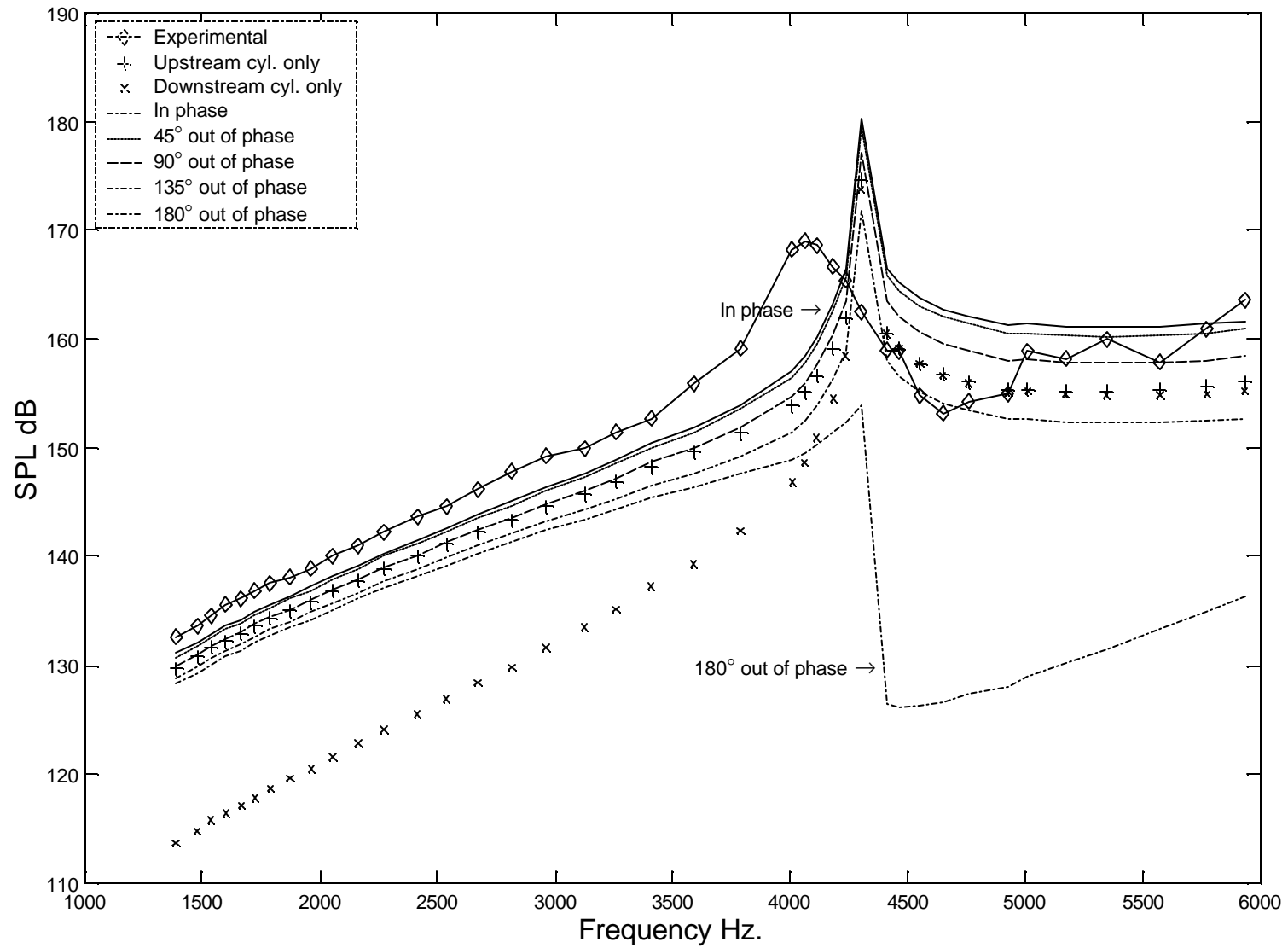


Figure 6.18 Sound pressure levels for 6.35 mm diameter cylinders in tandem arrangement. Experimental and model results at position 1a. Model results calculated assuming  $C_L' = 0.5$  for both cylinders.

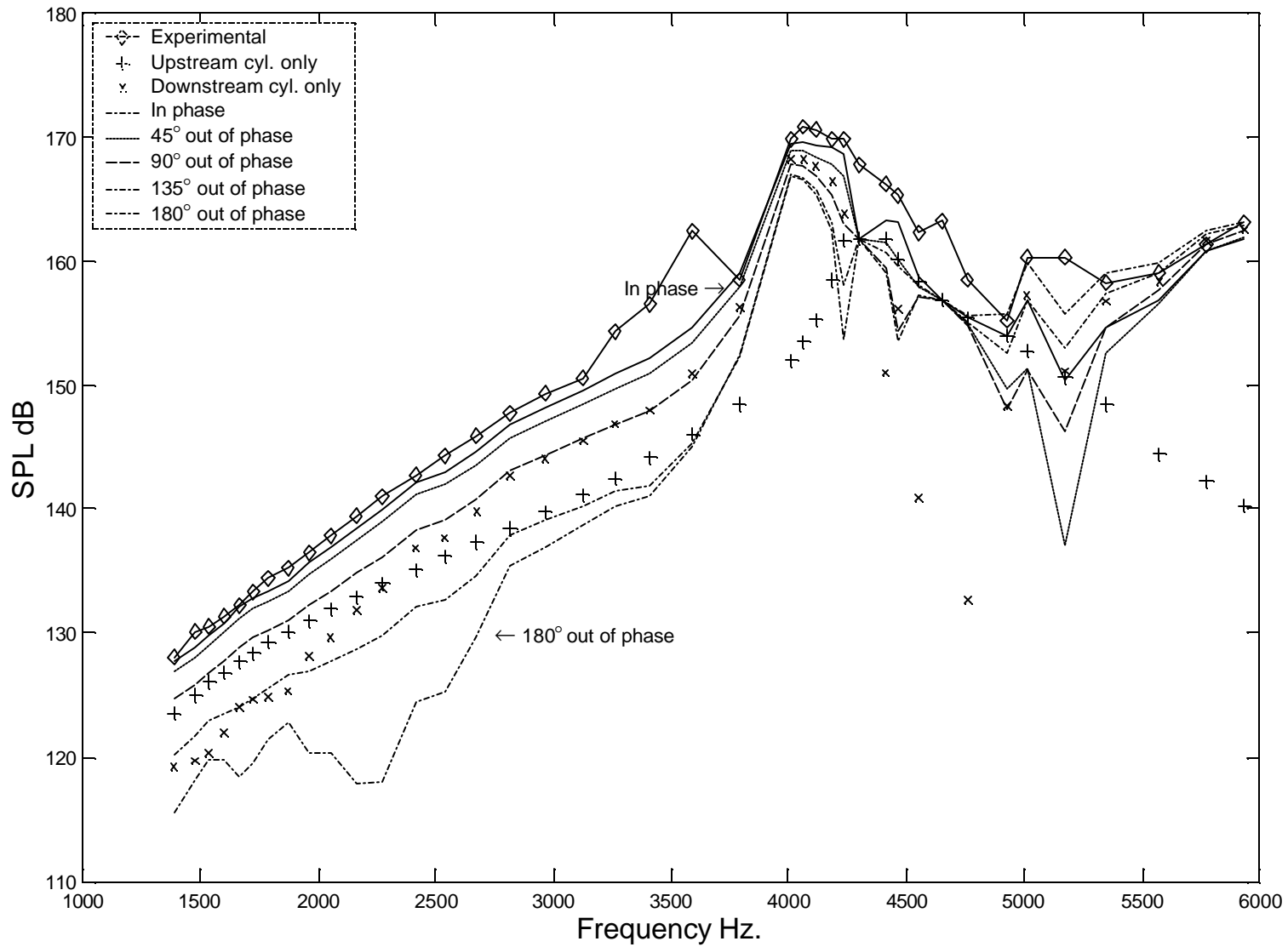


Figure 6.19 Sound pressure levels for 6.35 mm diameter cylinders in tandem arrangement. Experimental and model results at position 2a. Model results calculated assuming  $C_L'$  from Figure 6.14 for each cylinder.

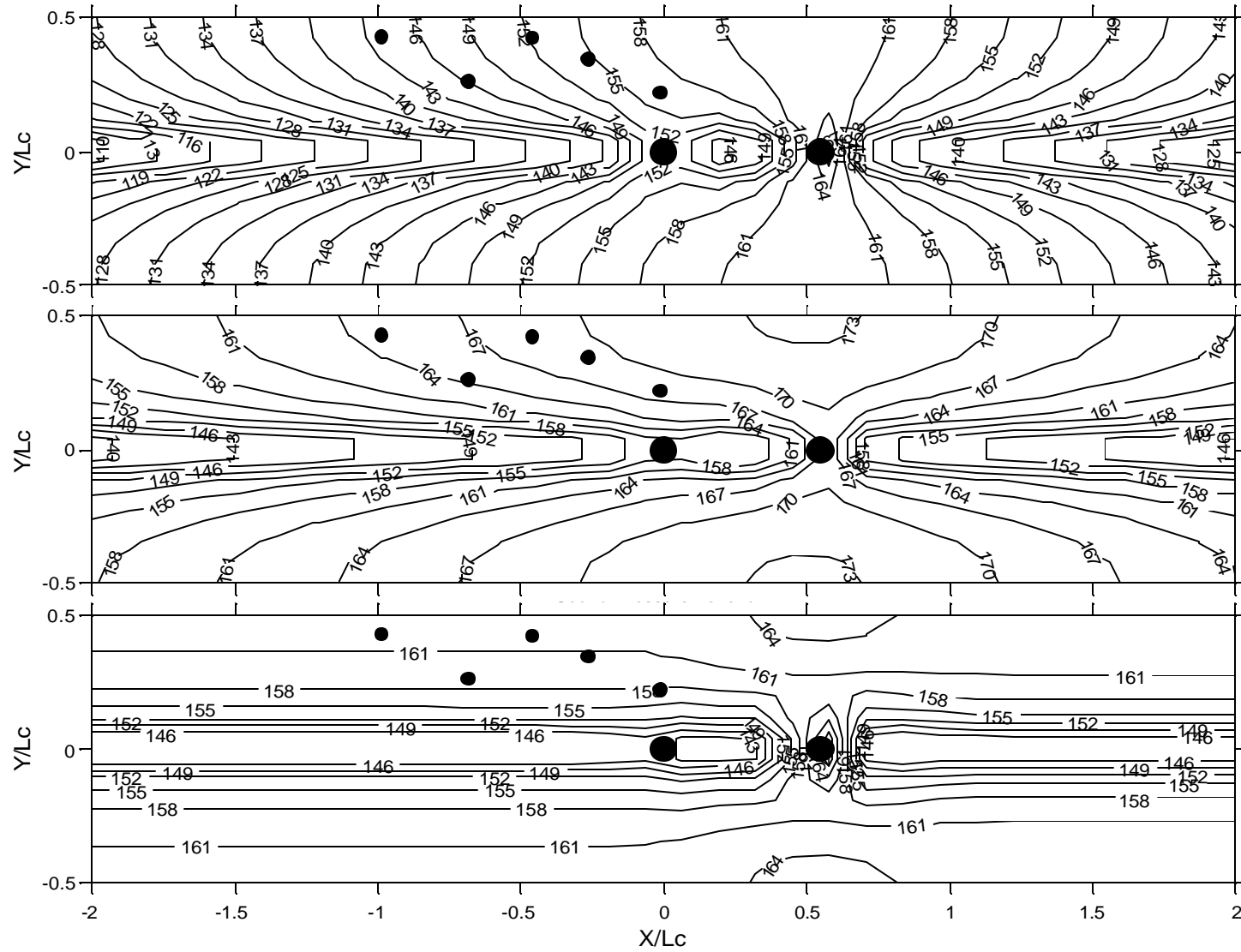


Figure 6.20 Sound pressure levels (dB) of cylinders in tandem arrangement obtained from the model. Small circles represent measurement positions. Large circles represent cylinders. The 6.35 mm diameter cylinders with  $C_L'$  from Figure 6.14. Top 3562 Hz, middle 4187 Hz, bottom 5800 Hz.



## 6.9 Side-by-side cylinders experimental and modeling results

Side-by-side cylinders test results showed that pairs of cylinders in this configuration produced significantly lower sound pressure levels in comparison to single cylinders and cylinders in tandem. In many cases, as seen in the representative spectra taken during these tests and shown in Appendix H, there is not a clear relationship between frequency and velocity, as is the case for single cylinders and cylinders in tandem. For this reason it was more difficult to use the model in the same way that it was used for single cylinders or cylinders in tandem. In this section the model was used directly, assuming values of the fluctuating lift coefficients and neglecting damping.

The spacing for side-by-side cylinders was chosen in part so that the cylinders would be located in a region where the flow velocity would be close to that at the center of the duct (see Figures 4.7 and 4.27). The other consideration for its spacing was to have a T/D ratio in the range that would produce out of phase vortex shedding from the cylinders.

To compare modeling results to those from experiments, fluctuating lift coefficients from single cylinders tests were used. The fluctuating lift coefficients used in this case were obtained from the same curve fit used for the upstream cylinder in the cylinders in tandem configuration that is shown in Figure 6.14. In this case, as it was also the norm for the other model results, flow velocity, frequency of the tone, and density values were taken from measurements. In this case, the frequency of the dominant peak in the spectra varied significantly depending on where the spectra was measured. Measurements at position d3 downstream of the cylinders were used. At this position the more typical vortex shedding relation between frequency and velocity was observed. This indicated also that there was vortex shedding present but that it was not necessarily responsible for the dominant noise measured upstream from the cylinders. In the sound pressure level graphs presented in Appendix H the sound pressure levels shown are the maximum values found in the spectra and not necessarily the sound pressure component at the frequency of vortex shedding. For this reason, in order to correctly compare the results of the model to the experiments, the sound pressure level from experiments was obtained at the frequency of vortex shedding regardless if it was the maximum in the spectra at that location or not.

Figure 6.21 show the results found with the model and compares them to those found experimentally for the 6.35 mm diameter cylinder. This cylinder diameter gives a T/D ratio that is slightly less than that reported to produce out of phase vortex shedding. However, for other cylinder diameters in which the T/D ratio fell in the range of interest, the results were similar. The model was solved for each of the two cylinders, and then the results were added assuming different source phases. Figure 6.21 was made only for the range of flow velocities that produced a close to linear frequency–velocity relationship (see Figure H.3). The results show that there is a good agreement between the experimental and modeling results when the sources at each cylinder are added in anti-phase as expected. However, these results are very close to the maximum tonal hydrodynamic fluctuating pressures discussed in section 4.10; thus, the signal to noise ratio is significantly reduced. In this case, however, the frequencies of interest are significantly higher than those at which the maximum tonal

components were found in the hydrodynamic pressure fluctuations. Thus, the results of Figure 4.40 represent an upper maximum sensitivity on the tonal sound pressure level.

Figure 6.22 shows the acoustic field found by the model at one particular frequency for the 6.35 mm diameter cylinders in side-by-side configuration. The acoustic field produced by only one of the cylinders is also plotted so that interference effects can be visualized. The constant sound pressure level lines are plotted only between 100 and 160 dB in increments of 5 dB. In the top figure the lack of constant sound pressure level lines means that the sound pressure level is below 100 dB. As can be seen, the effects of the source phase are very important.

### **6.10 Cylinder array model and comparison with experimental results**

The model was also used to estimate the sound pressure levels produced by cylinder arrays inside a duct. It was decided to try a stereolithography staggered cylinder array with  $T/D = L/D = 3.0$ . This decision was based on the fact that this array was among the ones that had a smaller number of cylinders. Additionally, this array followed a close to linear frequency-velocity relationship of the dominant peaks in the spectra. The experimental results for this array are shown in Appendix F. The model was used to estimate the sound pressure level at the upstream microphone position to avoid the hydrodynamic pressure fluctuations created by the flow over the cylinders inside the array (See Figure F.1). To do this, it was initially assumed that each cylinder produced an acoustic dipole at the cylinder center location with the dipole strength estimated using its cylinder diameter, the measured upstream flow velocity, and density, and assuming the value of the fluctuating lift coefficient equal for all cylinders. Additionally, it was assumed that all the sources were in phase. The sound pressure levels at the upstream microphone position would then be the sum of the complex acoustic pressures produced by each of the dipole sources at the upstream position. Later, the effects of the changes in flow velocity and density were crudely accounted for in the model by dividing the array in four sections, each one assigned the closest flow velocity and density measurement point. Appendix I sections I.11 and I.12 show the programs used to make these calculations.

Figures 6.23 and 6.24 plot the results of the model and compare them to the measurements. The figures present results from the model calculated using constant fluctuating lift coefficients of 0.1 (using upstream velocity and density for all cylinders), 0.1 (with corrected velocity and density as described above) and adjusted to match the measured sound pressure levels values. Fluctuating lift coefficient reports for cylinders inside arrays are not abundant in the literature. The works by Chen 1972b, Chen 1987, Oengören and Ziada 1998, and Savkar 1984 indicate that the fluctuating lift coefficients are in general significantly larger for staggered arrays than for in-line arrays. Only Savkar reports similar values of fluctuating lift coefficients between staggered and inline arrays. He found fluctuating lift coefficients as large as 3 for normal triangular arrays with a pitch to diameter ratio  $P/D$  of 1.2. Savkar measured fluctuating lift coefficients for normal triangular arrays with  $P/D = 1.2, 1.5, \text{ and } 1.71$ . Savkar indicated that the maximum fluctuating lift coefficients were measured at the first row of the array with  $P/D = 1.5$ , at the second row for  $P/D = 1.2$ , and at the third row for  $P/D = 1.71$ . The fluctuating drag coefficient, on the other hand, always peaked at the second row. Oengören and Ziada 1998 also report measurements of fluctuating lift coefficients for normal triangular arrays. They performed measurements on

arrays with P/D ratios of 1.61, 2.08, and 3.41. Oengören and Ziada also found that the fluctuating lift coefficient peaked in the first three rows as observed by Savkar. However, they report increases in fluctuating lift coefficient with increasing P/D ratio, unlike Savkar's results that show the opposite trend. Maximum fluctuating lift coefficients reported by Savkar for arrays with P/D ratios of 1.5 and 1.71 are in the range between 0.5 to 1.6, depending on the Reynolds number. Oengören and Ziada report values of these coefficients in the range of 0.02 to 0.07 for the array with P/D ratio of 1.61 for similar Reynolds numbers. These large discrepancies point to the complexities involved in measuring dynamic forces produced in cylinders, inside arrays and to the many different factors that affect these forces.

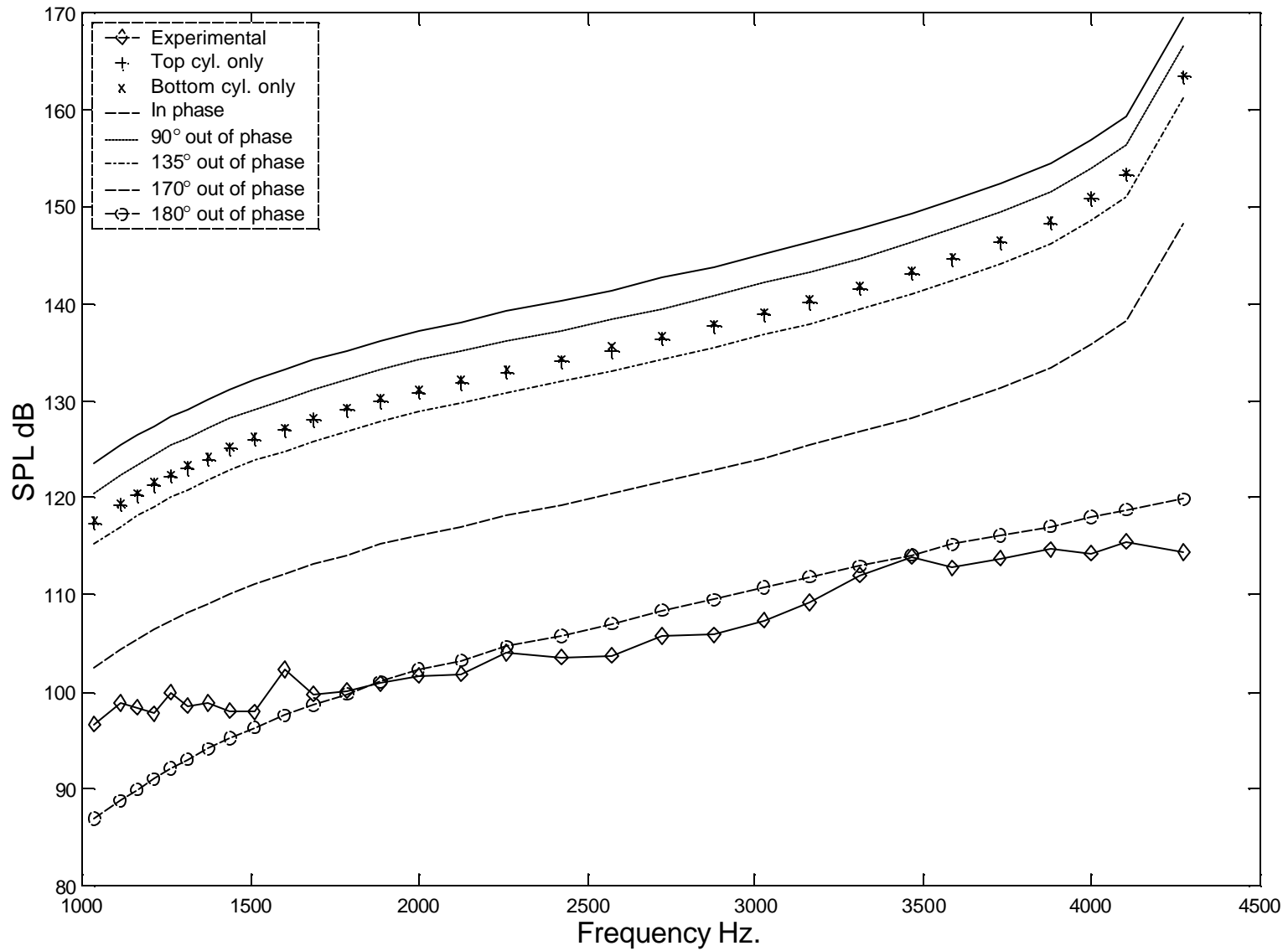


Figure 6.21 Side-by-side cylinders modeling and experimental results comparisons.  $CL'$  assumed equal to single cylinder (shown in Figure 6.14). Measurements and calculations at microphone position 1a. Cylinder diameters = 6.35 mm.

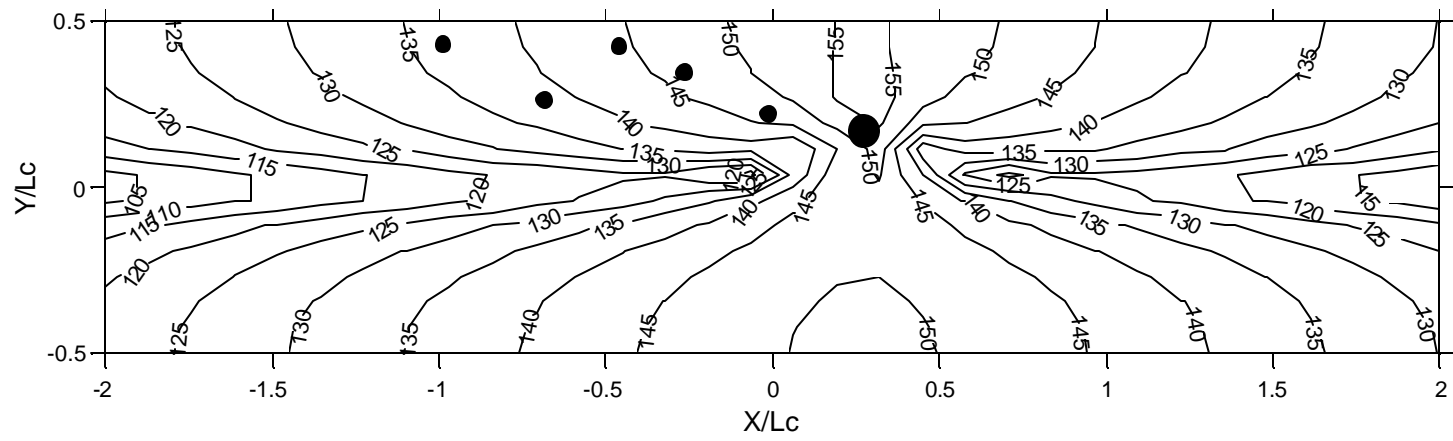
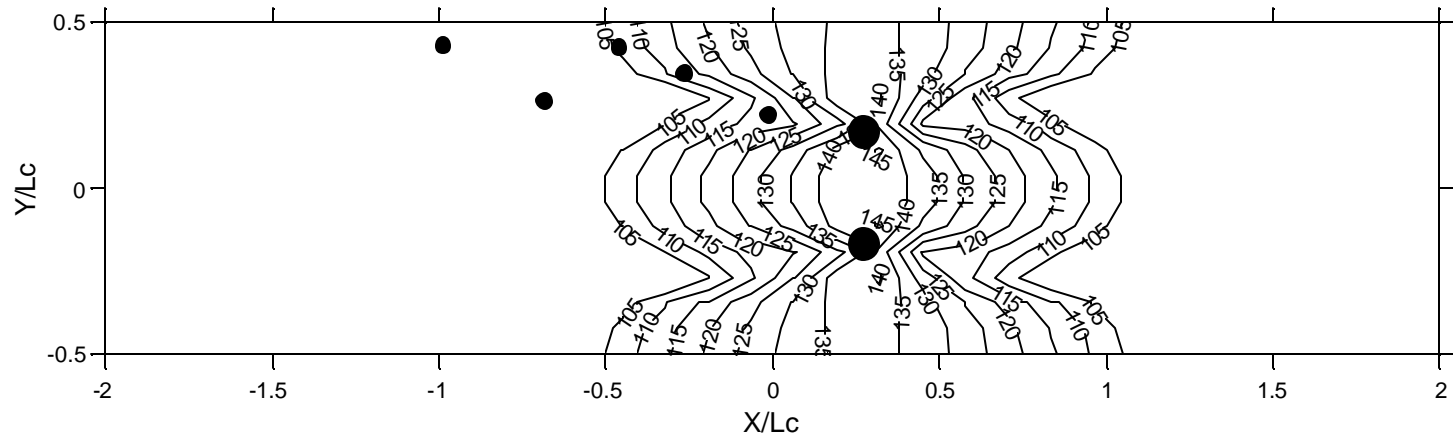


Figure 6.22 Sound pressure levels field produced by two identical dipoles sources out of phase (top) and by only one of the dipole source present (bottom). Frequency 3725Hz. Small circles represent measurement positions. Large circles represent cylinders. Dipole source strength using 6.35 mm diameter cylinders data.

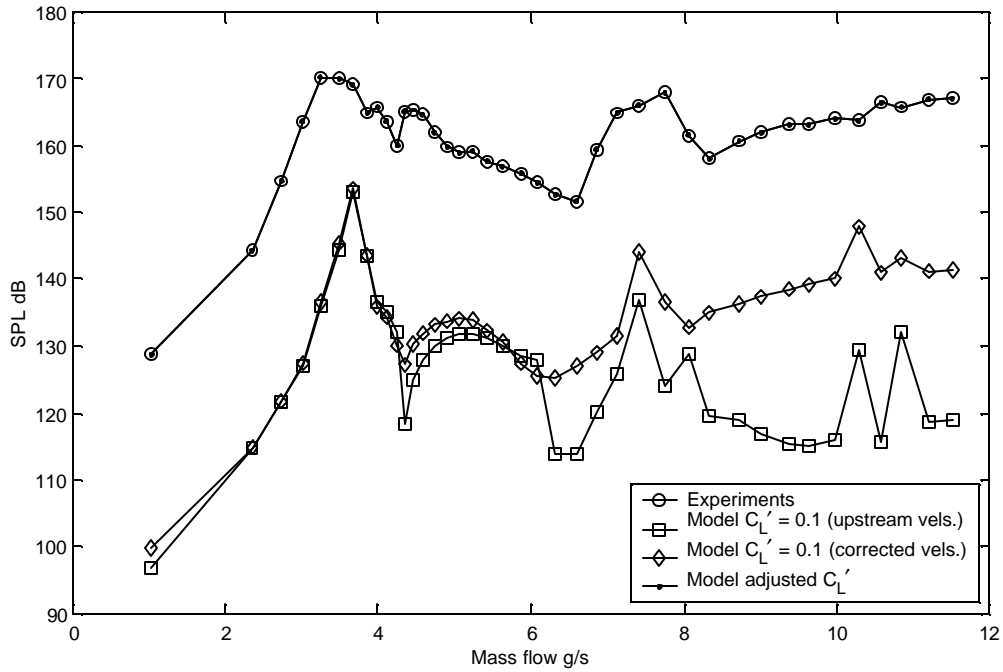


Figure 6.23 Comparison of sound pressure levels calculated using our model assuming two different fluctuating lift coefficients and noise sources to be in phase against results from measurements upstream of cylinder array. Staggered array with  $T/D = L/D = 3.0$

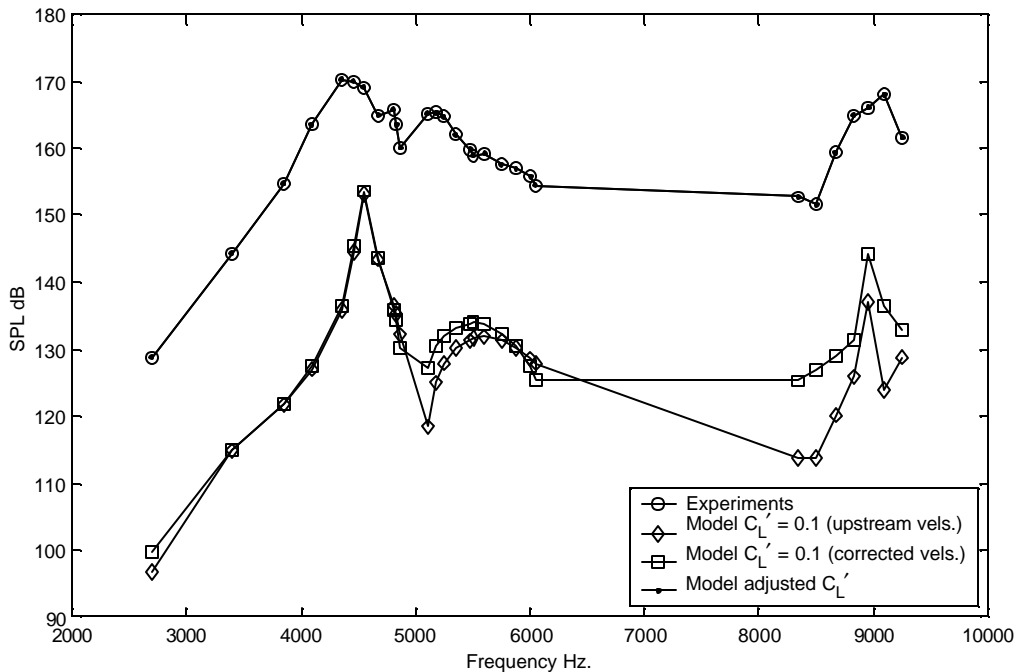


Figure 6.24 Similar to Figure 6.23 but plotted against frequency and for a reduced number of data points.

An interesting observation made by Savkar is that the fluctuating drag forces' oscillating frequency was the same as those for the fluctuating lift forces. In single cylinders the drag forces oscillate at double the lift force

frequency due to vortex shedding. For this reason, Savkar believed that other fluid phenomenon and not vortex shedding was responsible for creating the dynamic forces on the cylinders in arrays. How the fluctuating forces are created is not important for determining the strength of the acoustic dipole produced by the cylinders but the flow field around the cylinders is very important for fluid-acoustic coupling effects.

Figures 6.23 and 6.24 show that the sound pressure level results obtained by the model for constant fluctuating lift coefficients follow in general the same trends of the measured values. At the higher mass flows were the velocity differences in the array are more significant, the sound pressure levels found using the corrected velocity and density values follow significantly better the measurements trend. These graphs also show that the model curves were slightly shifted to the right thus over predicting the first transverse acoustic natural frequency of the duct. The perfect results obtained using the adjusted values of the fluctuating lift coefficient were possible since in this case only one measurement location was used to find these values. The procedure to determine these coefficients was to first calculate the sound pressure levels assuming a constant value of the fluctuating lift coefficients. Since there is a linear relationship between acoustic pressure and fluctuating lift coefficient, the difference in sound pressure levels between the measured and estimated values was used to obtain the fluctuating lift coefficient that would be needed to eliminate the discrepancies between the model and measured results. In equation form this would be:

$$SPL_1 = 20 \cdot \text{Log} \left( \frac{C'_{L1} P_{aux}}{20 \cdot 10^{-6}} \right) \quad (6.6)$$

$$SPL_m = 20 \cdot \text{Log} \left( \frac{C'_{Ladj} P_{aux}}{20 \cdot 10^{-6}} \right)$$

where  $SPL_1$  and  $SPL_m$  represent the estimated and measured sound pressure levels, respectively.  $C'_{L1}$  and  $C'_{Ladj}$  are the assumed fluctuating lift coefficient used in the initial estimation of sound pressure levels and the fluctuating lift coefficient that would be needed for the model to return identical results to the measured sound pressure levels respectively. The variable  $P_{aux}$  is auxiliary and cancels out. The  $C'_{Ladj}$  needed to move the model solution from the value of  $SPL_1$  to  $SPL_m$  is then found

$$C'_{Ladj} = C'_{L1} 10^{\frac{SPL_m - SPL_1}{20}} \quad (6.7)$$

The results found by equation (6.7) are plotted in Figures 6.25 and 6.26. Below a Reynolds number of approximately 7000, the fluctuating lift coefficient needed to fit the data is, with some exceptions, around 2-3. These values and especially the larger values of these coefficients below this Reynolds number will be reduced if the model sound pressure level curve would not be shifted. In this Reynolds number range, our results are close to the results found by Savkar for normal triangular arrays. Savkar's results were found at higher Reynolds numbers. His results decrease with increasing Reynolds number. At higher Reynolds numbers if the velocity/density effects are not accounted for unrealistic values of fluctuating lift coefficients are needed to correct the sound pressure levels.

Figure 6.26 is similar to 6.25, but in this case the fluctuating lift coefficients were found once the crude velocity corrections were made. Once these corrections were made, significantly lower values of the fluctuating lift coefficients were found. This result shows that the model can predict the trends in the sound pressure levels produced by cylinder arrays.

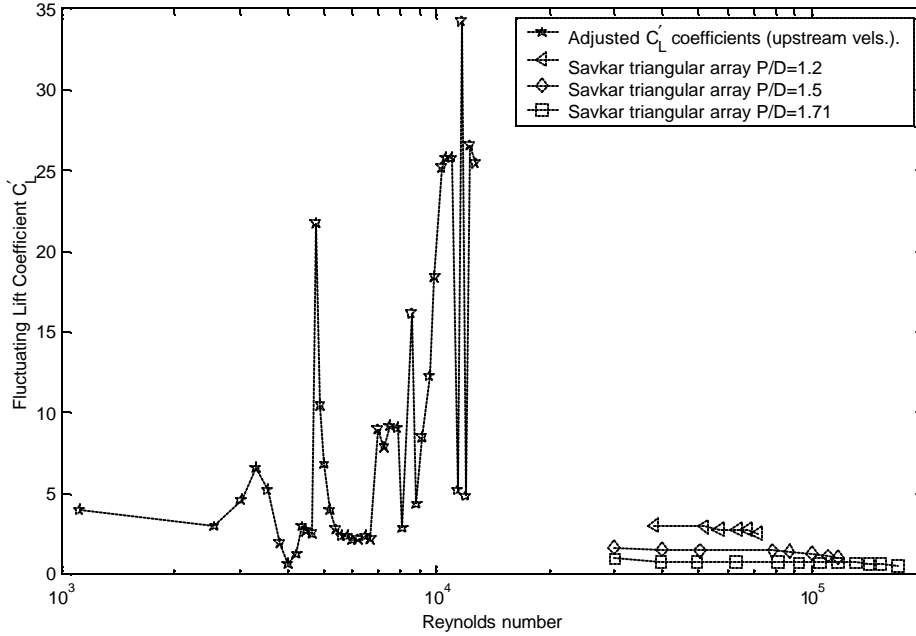


Figure 6.25 Fluctuating lift coefficients needed to adjust model results to be equal to measured results. Without velocity/density corrections.



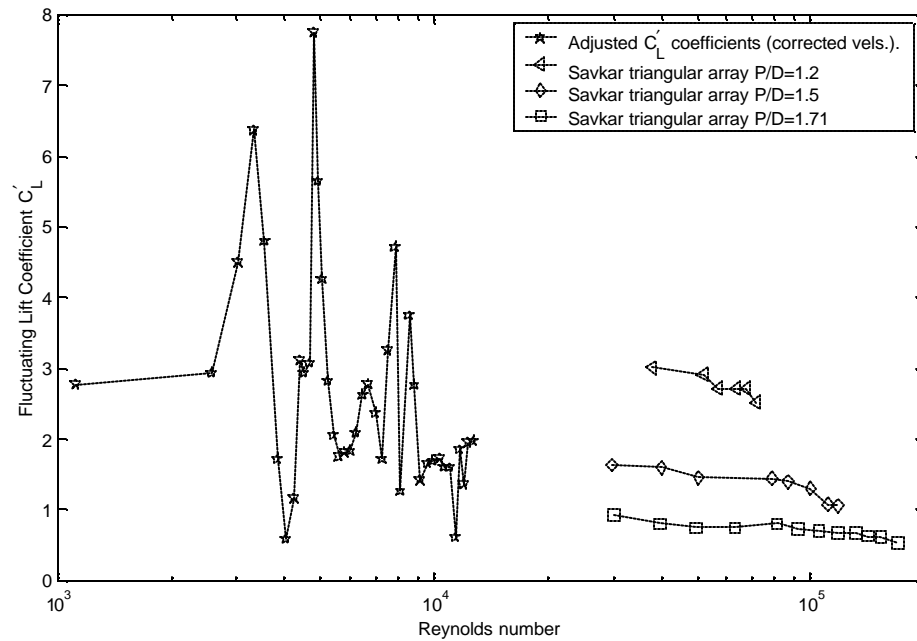


Figure 6.26 Fluctuating lift coefficients needed to adjust model results to be equal to measured results. With velocity/density corrections.

### 6.11 Convection effects on first transverse acoustic resonance frequency

In Chapter 3, using relations developed from the modeling equations, resonant frequency estimation equations that accounted for convection and damping effects were derived. In this section, the measured acoustic resonances produced by single cylinders inside our test section were used to validate them.

Figure 6.27 compares the estimations made using equation (3.98) and the single cylinder tests measured results. To determine the Mach number needed in equation (3.98) the flow velocity in the duct was estimated assuming a constant Strouhal number of 0.2. Since the real Strouhal number varied for the different cylinders there are small errors associated to the correct value of the flow velocity present when the cylinder tonal noise reached the resonance frequency. The experimentally determined resonance frequency was chosen to be the peak at any of the measured locations that was clearly a resonance condition. In many cases there were very clear resonant peaks in the sound pressure level graphs that differ slightly in frequency. In this case, the frequency that was closer to the predicted value was chosen. The errors in the experimental frequency results are estimated at less than 100 Hz. These results show the importance of accounting for convection effects in any model especially when relatively large flow velocities are involved.

The acoustic resonance predictions for multiple cylinders were in general not as accurate as those for single cylinders. These inaccuracies might be linked to the disruption of the flow field. In the case of cylinder arrays, other mechanism that alter the effective speed of sound might be present. The correct estimation of the natural frequencies is essential for the model to be used accurately.

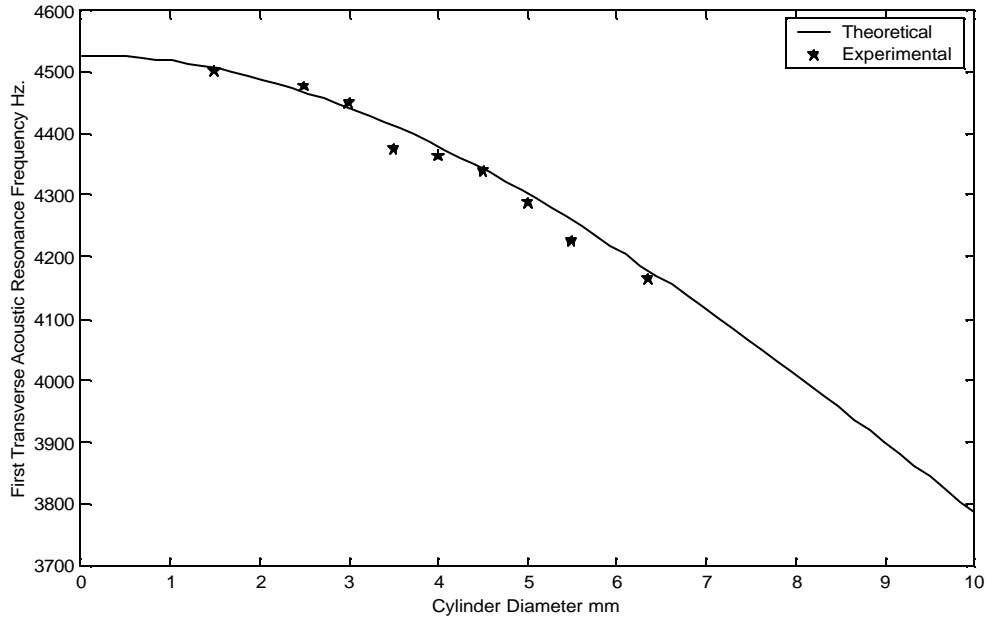


Figure 6.27 Comparison of measurements and predictions of acoustic resonance frequency accounting for convection effects

## Chapter 7: Numerical Experiments

### 7.1 Introduction

The purpose of this chapter is to use our acoustic model to explore some of the effects that different variables of relevance have on the acoustic field produced by bluff bodies in cross-flows inside a duct. In particular, the effects of volumetric damping, specific wall acoustic impedances, and the parameters that affect the dipole source strength will be explored.

### 7.2 Effect of volumetric damping on acoustic field

The effect of volumetric damping on the acoustic field produced by a point dipole source inside a duct with flow was explored using the model. The model was used to solve for the sound pressure levels at the five microphone positions upstream of the cylinders where most of our experimental measurements were made (positions 1a, 2a, 4a, 5a and 6a, see Figure 4.22). Additionally, the phase between the four different microphone pair combination previously used was also included. The dipole was positioned in the center of the duct where the cylinder in Figure 4.22 is shown. The calculations of the dipole source strength were made assuming a 6.35 mm diameter cylinder was the source of the acoustic dipole. Additionally, constant values of the air density ( $1.3 \text{ kg/m}^3$ ), fluctuating lift coefficient (0.4) and Strouhal number (0.2) were assumed. The solutions cover the range of 1000 to 9000 Hz and were made varying the frequency in 10 Hz increments. The flow velocity was then calculated using the Strouhal number definition. Solutions are reported for seven different values of purely real and seven different values of purely imaginary nondimensional volumetric damping coefficient.

It is believed that nondimensional volumetric damping could be caused by scattering due to other cylinders, flow turbulence or visco-thermal processes. There are different physical mechanisms by which each of these processes could affect the propagation of acoustic waves inside the duct. However, in this work these factors have not been explored. The effects of nondimensional volumetric damping were explored only by changing the numerical values of this parameter in our model without regard to a possible physical mechanism. For this reason, it is not known what would be a good range of nondimensional volumetric damping coefficients to explore. In the results presented in this section, the nondimensional volumetric damping coefficients were changed between 0 and 10 and were assumed purely real or purely imaginary.

Figure 7.1 shows the results for the real nondimensional volumetric damping coefficients. There are several interesting features of the results. In general, the increase in damping value produced a reduction in sound pressure level for any given frequency. This behavior, however, is reversed between 6000 and 8000 Hz at microphone position 1a. Other typical and expected results include the increase in sound pressure levels when the resonance frequency gets close to a duct resonance frequency. For some values of damping and in the second excited mode at around 8000 Hz, Figure 7.1 shows that at resonance, the sound pressure levels are actually less than at nonresonance conditions! This can be seen at microphone positions 4a, 5a, and 6a.

Figure 7.2 is similar to 7.1, but in this case the nondimensional volumetric damping coefficients were purely imaginary with the same absolute values as those used in Figure 7.1. The introduction of these coefficients shifts the acoustic natural frequencies found by the model to higher frequencies without changing the sound pressure

levels found at the resonance. The small differences seen in the sound pressure levels at resonance are attributable to how close was the frequency used during the calculations to the acoustic natural frequencies predicted by the model. The calculations were performed at discrete frequency intervals. Depending on how close the actual acoustic resonance frequency is to these discrete values, the solution would be affected. This condition is also experienced with the experimental data since the data is discretized by the dynamic signal analyzer in 800 points. This means that in our single cylinders tests where a frequency span of 10 kHz was used the data was returned in 12.5 Hz packets. This observation points out again the experimental and theoretical difficulties of determining the dipole source strength and acoustic damping very close to the resonance condition.

It would also be of interest to observe the changes introduced by volumetric damping on the acoustic field. Appendix J presents contour plots of the acoustic field produced by the cylinder for different values of volumetric damping at 4000 and 5000 Hz. All contour plots presented in this work are cross sections of the acoustic field at the duct wall.

Figure 7.3 presents the changes introduced by the different real nondimensional volumetric damping coefficients on the phase angle between different microphone pairs. In this case the differences are not as dramatic as the differences that they produce on the sound pressure levels. The increases in damping in this case tend to lower the phases found with no damping except for the 2a-1a cylinder pair in which it has the inverse effect. This is caused by the change in direction between the microphone for this microphone pair.

Figure 7.4 is similar to Figure 7.3 but was made using purely imaginary coefficients. While Figure 7.3 showed relatively smooth changes in the phase angle as the frequency varied, Figure 7.4 shows a very well defined discontinuity in the phase angle curves that appears at the resonance condition predicted by the model using the given damping values. Similar to the effects of these damping coefficients on sound pressure levels, the changes on phase angle cause a shift in the phase angle curves to higher frequencies as damping is increased.

It is important to note that the results presented here might not be representative of actual conditions. As mentioned before, a constant value of density was assumed when making these calculations. At the higher frequencies (and therefore higher flow velocities) the pressure drop down the duct causes significant variation in density.

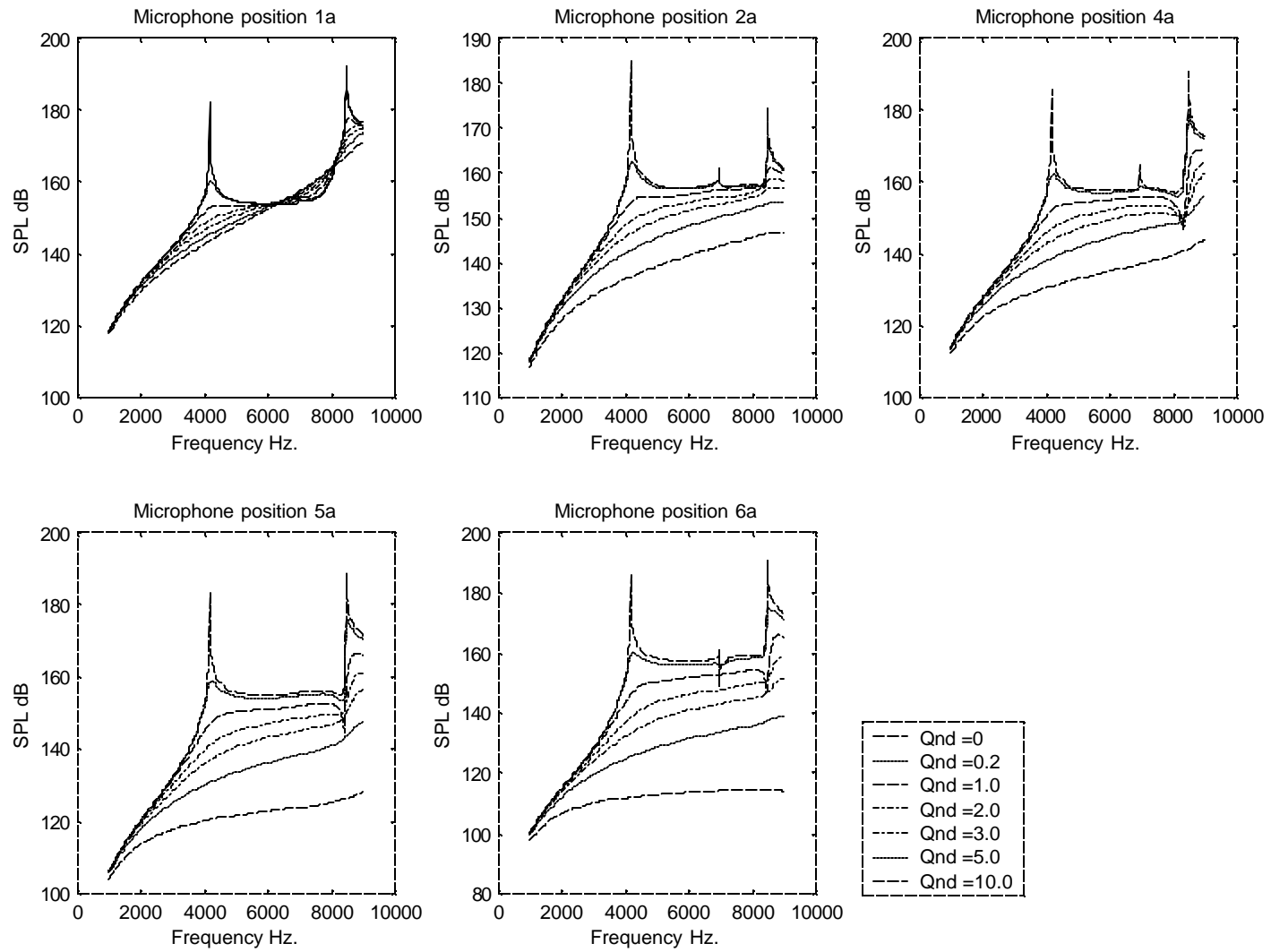


Figure 7.1 Sound pressure levels at different microphone positions as a function of frequency for different values of real nondimensional volumetric damping coefficient.

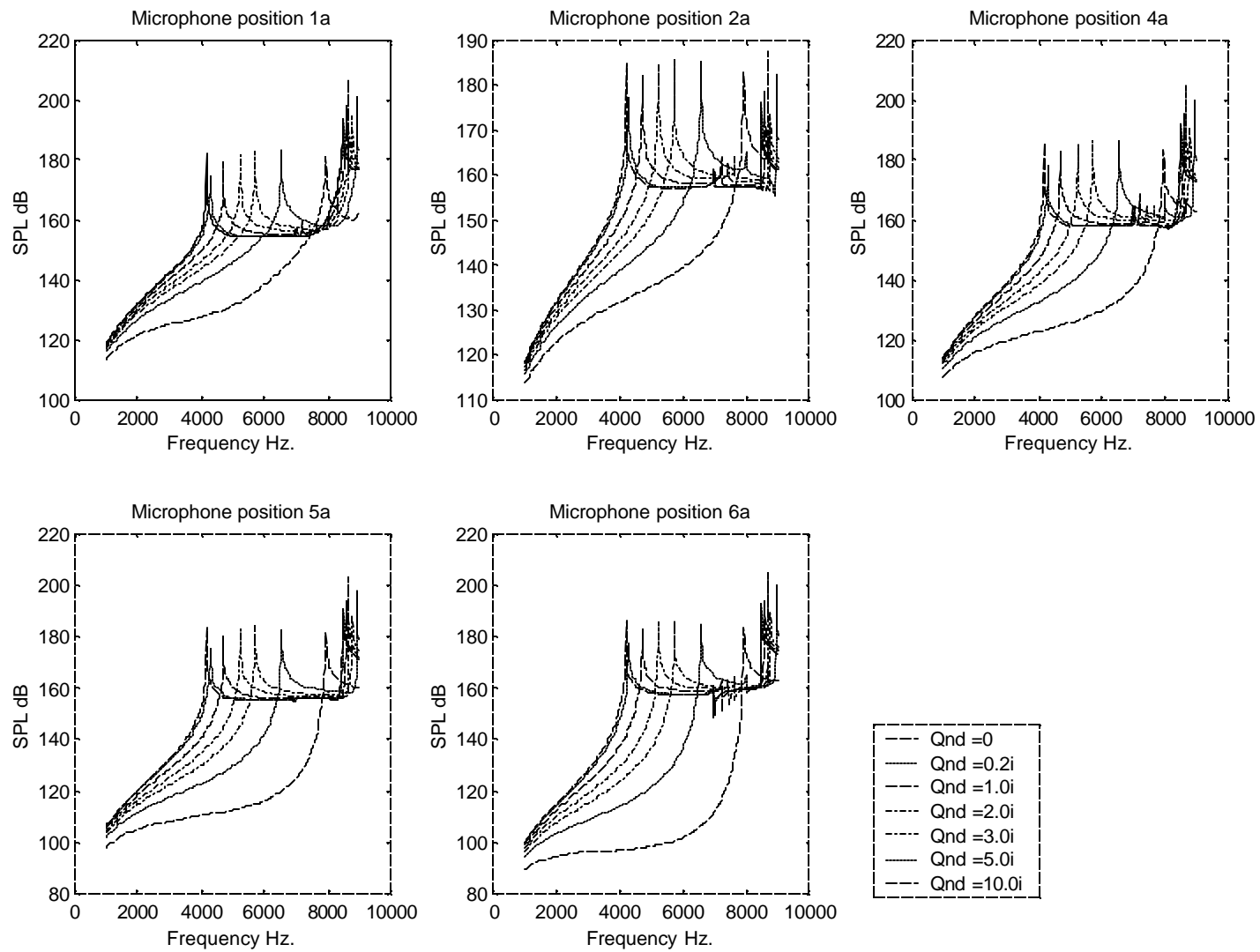


Figure 7.2 Sound pressure levels at different microphone positions as a function of frequency for different values of imaginary nondimensional volumetric damping coefficient.

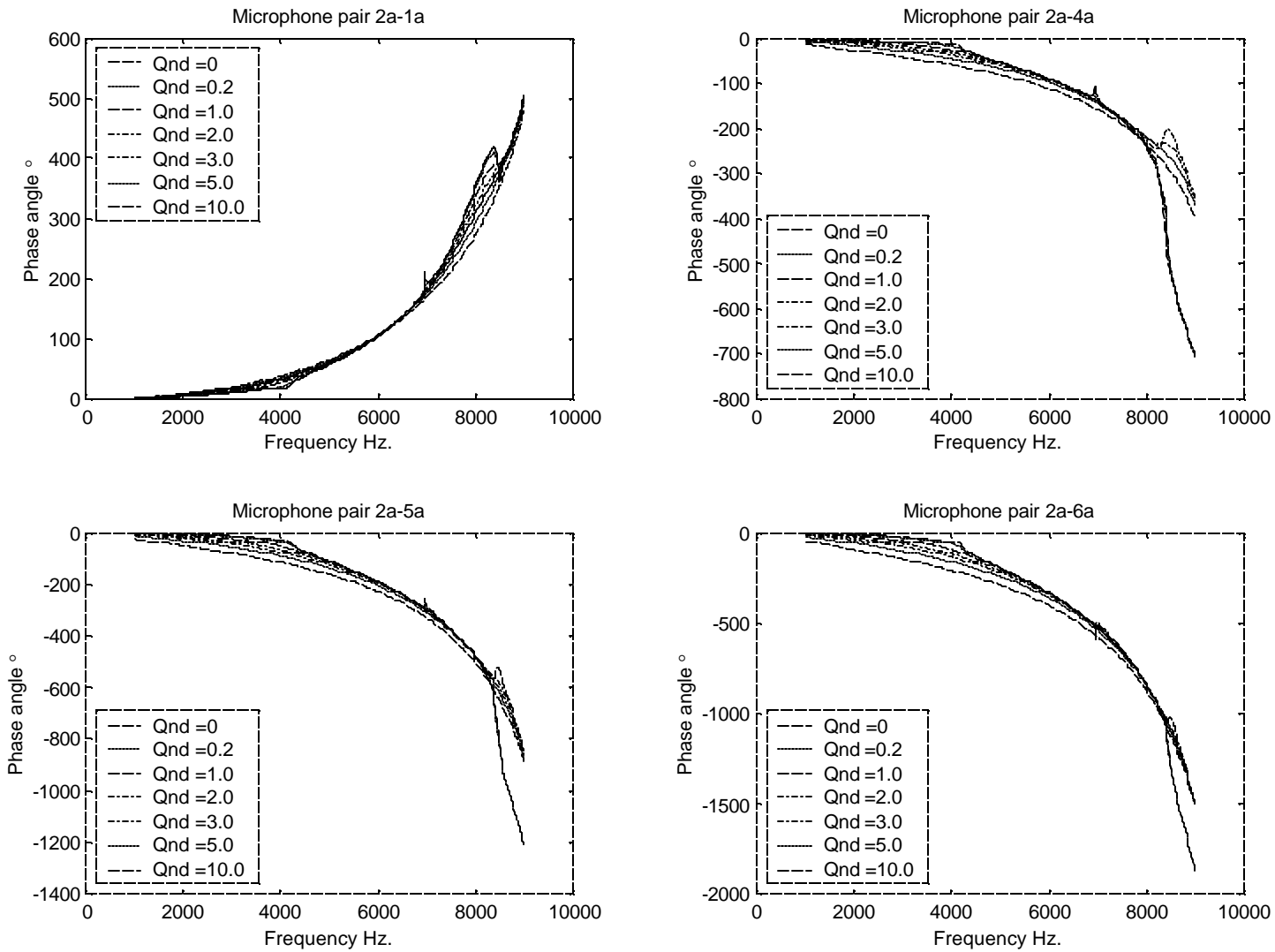


Figure 7.3 Phase angle between different microphone pairs as a function of frequency for different values of real nondimensional volumetric damping coefficient.

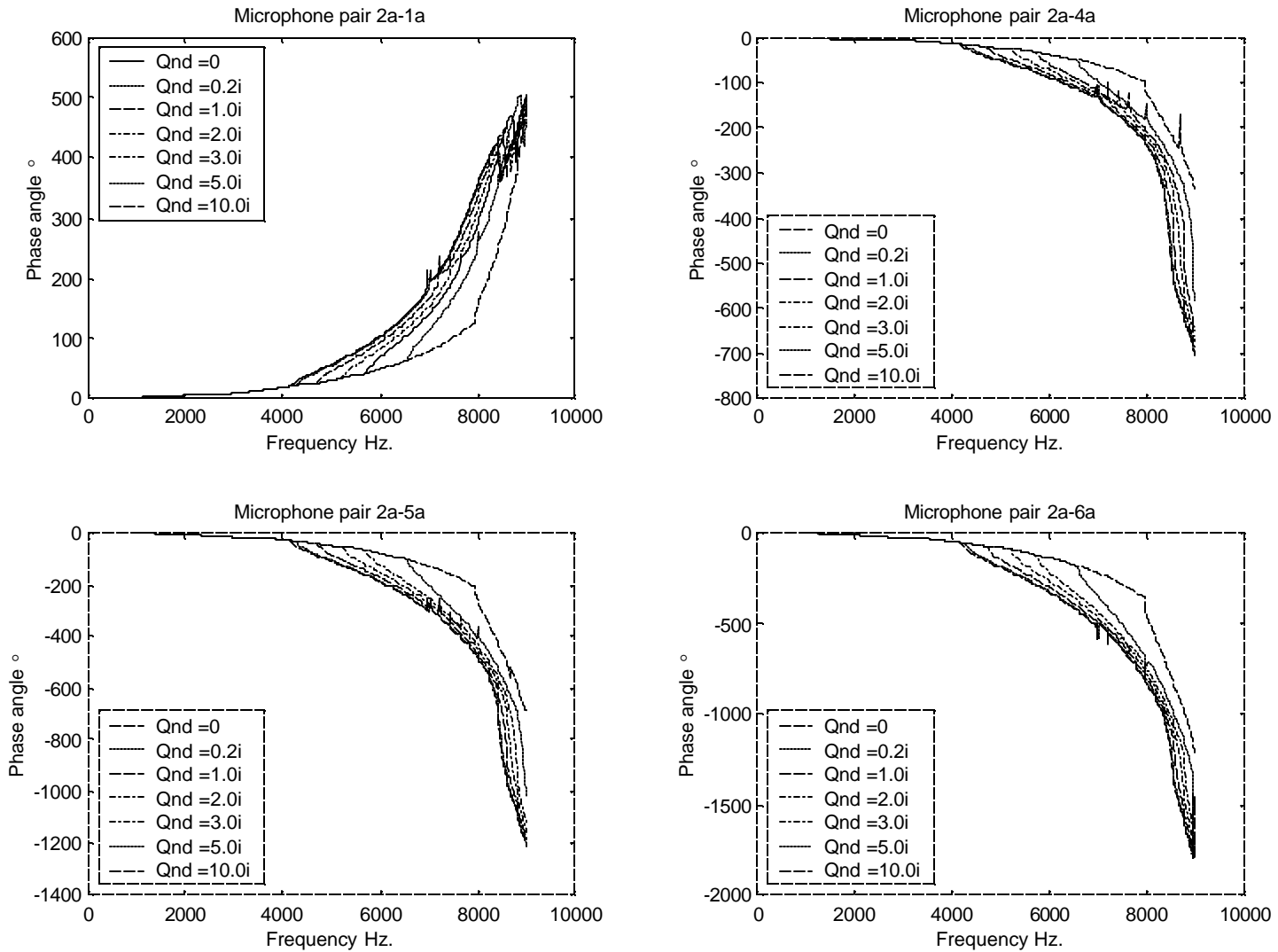


Figure 7.4 Phase angle between different microphone pairs as a function of frequency for different values of imaginary nondimensional volumetric damping coefficient.



### 7.3 Effect of walls acoustic impedance on acoustic field

The effects of changes in the y-walls specific acoustic impedance were explored in the same way, as was the case for the nondimensional volumetric damping coefficients. The test results shown in section 7.2 were made assuming very rigid walls in the duct. In this section this assumption remains for the z-walls. Volumetric damping is neglected. Similarly, in the results found in this section, the same assumptions introduced in section 7.2 were made, and the same frequency range was explored.

The specific acoustic impedance values used were  $1 \times 10^5$ , 15, 5, 3, 2, 1, and 0.5. Similarly as was the case in the previous section, the tests were repeated using purely imaginary coefficients for the specific acoustic impedances with the same absolute values.

Figure 7.5 shows the sound pressure level curves calculated at each of the different microphone positions used throughout this work. The results in many ways are similar to the results found in section 7.2 for the real nondimensional volumetric damping coefficients. Figure 7.5 also shows the increase in sound pressure level as the damping increases in the 6-8 kHz region for microphone position 1a and the reductions in sound pressure level at resonance at microphone positions 4a, 5a, and 6a.

Figure 7.6 is similar to Figure 7.5 but was obtained with the purely imaginary y-wall specific acoustic impedance. These imaginary values of impedance cause changes in both the magnitudes of the sound pressure levels at resonance conditions as well as on the frequency at which these resonances develop.

Plots of the acoustic field for different values of real and imaginary acoustic impedance are also presented in Appendix J.

Figure 7.7 presents the results that the changes in real y-walls specific acoustic impedance produce in the phase angle predicted by the model between the microphone pairs. The results of Figure 7.7 are very similar to the results of Figure 7.3. Damping in this case also tends to shift the curves slightly downwards in general.

Figure 7.8 is similar to Figure 7.7, but in this case presents the results obtained using the imaginary values of the y-walls specific acoustic impedance. These graphs also shows similarities to Figure 7.4 obtained for the imaginary values of the nondimensional volumetric acoustic damping. There are also discontinuities present in the phase angle curves at the resonance condition but in this case damping reduces the natural frequency instead of increasing it as was the case in Figure 7.4.

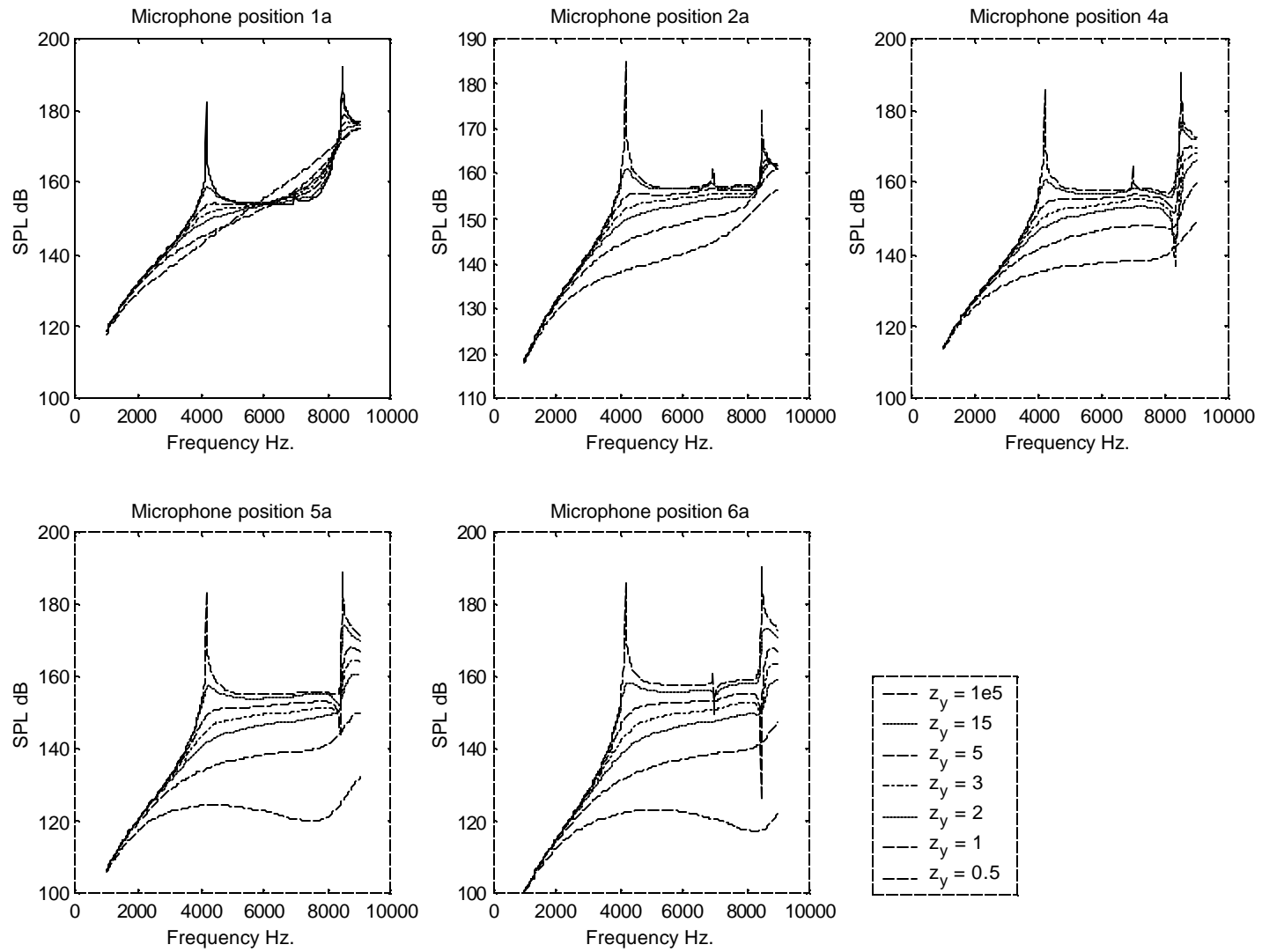


Figure 7.5 Sound pressure levels at different microphone positions as a function of frequency for different values of real y-walls specific acoustic impedance.

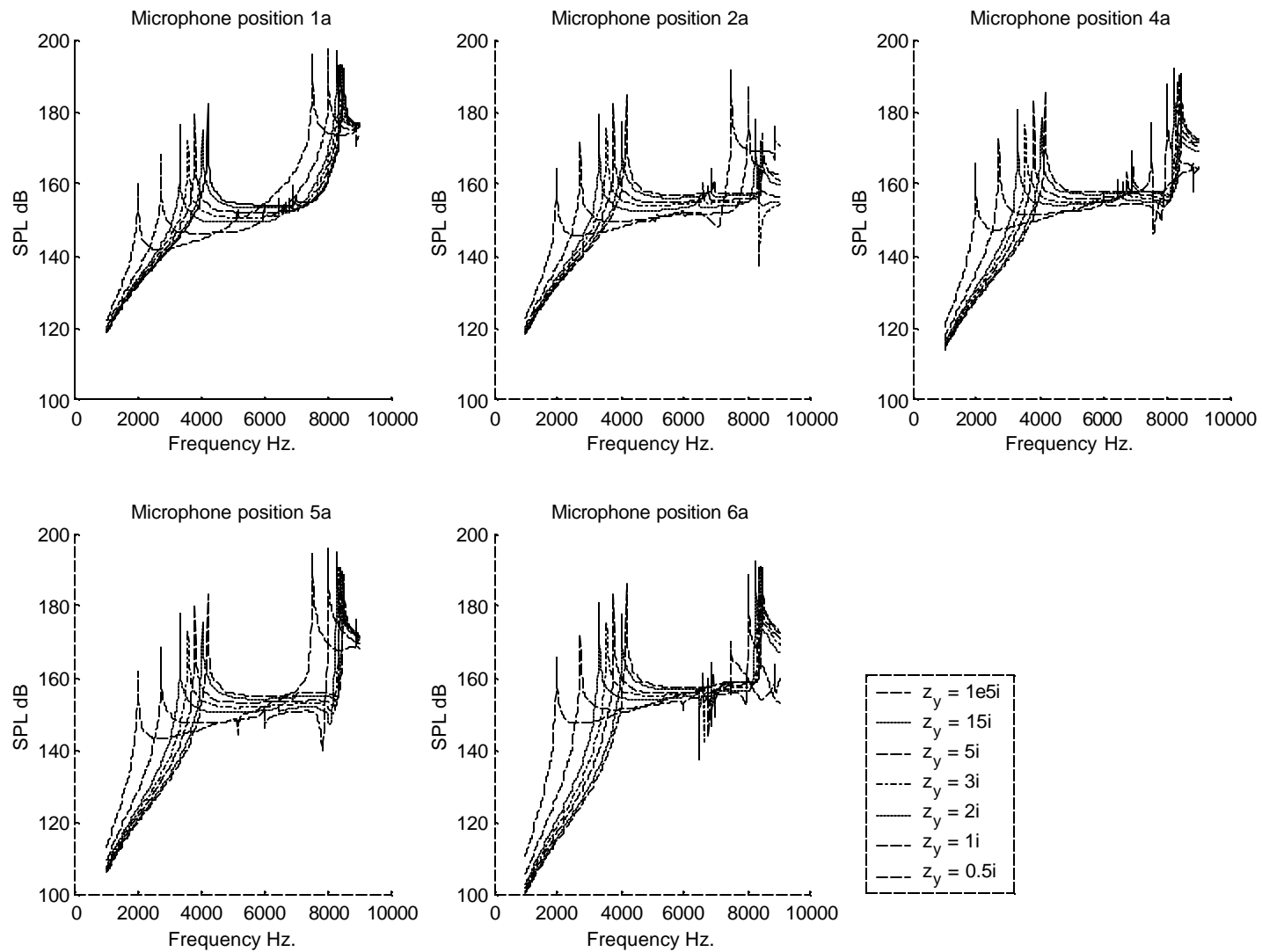


Figure 7.6 Sound pressure levels at different microphone positions as a function of frequency for different values of imaginary y-walls specific acoustic impedance.

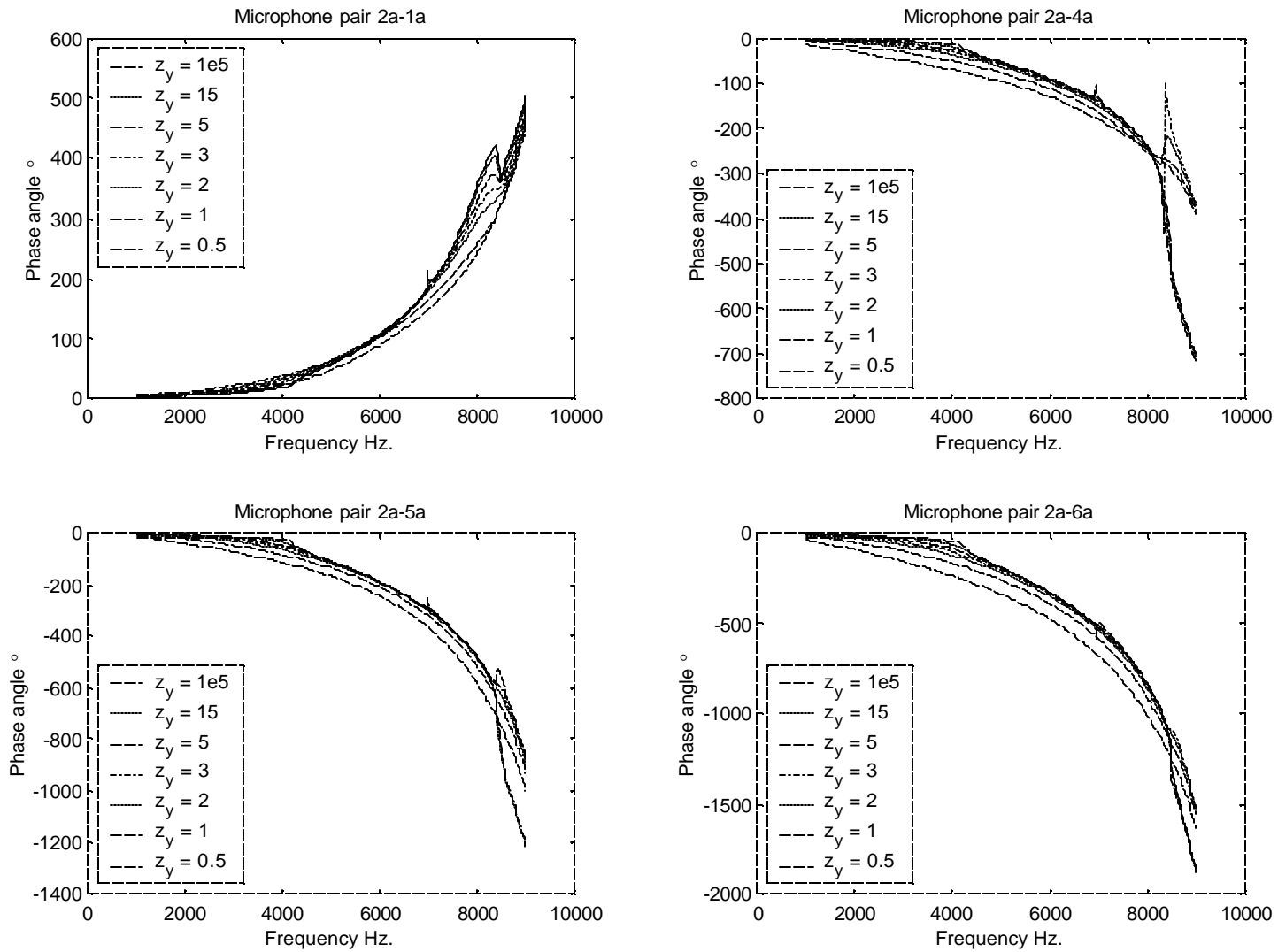


Figure 7.7 Phase angle between different microphone pairs as a function of frequency for different values of real  $y$ -walls specific acoustic impedance.

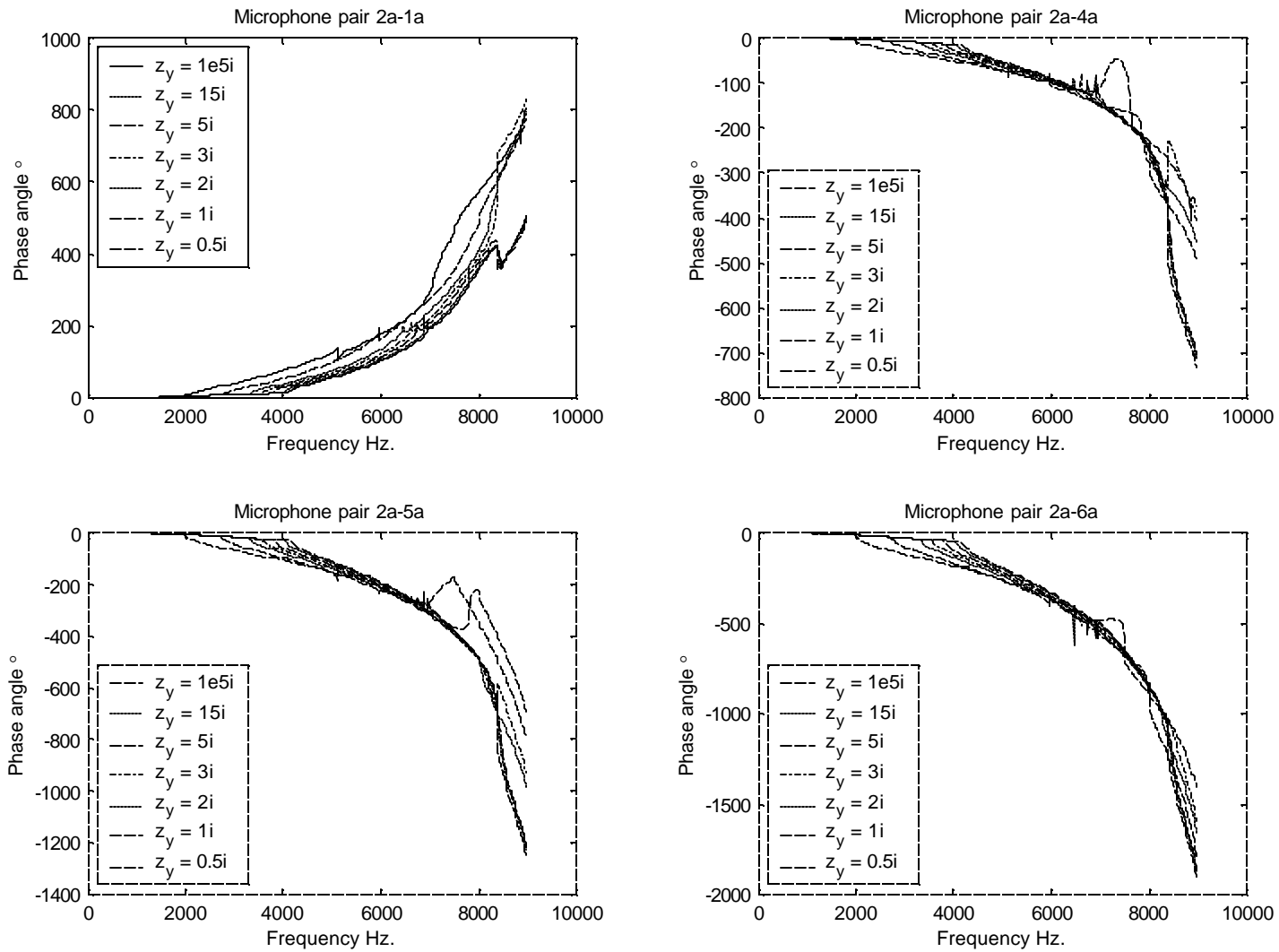


Figure 7.8 Phase angle between different microphone pairs as a function of frequency for different values of imaginary y-walls specific acoustic impedance.

#### **7.4 Effect of density, flow velocity, fluctuating lift coefficient, and cylinder dimensions (Parameters that influence dipole source strength)**

In this work density, flow velocity, fluctuating lift coefficient, and cylinder dimensions have been identified as the important parameters in the generation of sound from cylinders in cross-flow inside a duct. In this section, the effects of changes in these parameters on the sound pressure level will be discussed.

The sound pressure levels produced for any given case depend strongly, as has been shown in chapters 5 and 6, on the position where the measurements/estimations are made, the closeness of the frequency of interest to a resonance frequency, the damping of the system and the strength, and directionality of the source of noise. Due to all these complexities, it is very difficult to obtain a general solution to the problem that could be universally applied to every case without recurring to solving the full acoustic equations. It is useful to understand how changes in the main variables affect the measurements.

With the above in mind, it is interesting to see the effects of changes in dipole source strength. The parameters that influence dipole source strength are fluid density, flow velocity, fluctuating lift coefficients, and cylinder dimensions. All of these variables have a linear dependence on the strength of the fluid forces, except the fluid velocity, which has a square dependence. These dependencies can therefore be used to determine the effects on sound pressure level directly. Figure 7.9 shows how changes in these variables would increase a given sound pressure level. Figure 7.9 shows that an order of magnitude change in any of the linearly dependent variables results in an increase of 20 dB in the sound pressure level with respect to the initial value. Order of magnitude changes in these variables are possible. Fluctuating lift coefficients are usually found between values of 0.1 and 1 and can fluctuate considerably as seen in chapter 6. Gas density values during tests with superheated R134a refrigerant were around  $20 \text{ kg/m}^3$  while during tests using compressed air or nitrogen density values were around  $1.3 \text{ kg/m}^3$ . Changes in flow velocity, on the other hand, are double the other variables due to the quadratic dependence as can be seen in Figure 7.9. Notice that changes in cylinder diameter and flow velocity, in addition to modifying the dipole source strength, alter the analytic series solution since these changes influence the frequency of the source. This double effect makes the direct prediction of the effects of changes in these variables more difficult.

In sections 2.4 and 2.5 the effects of different variables on the sound pressure level and acoustic resonance in heat exchangers was discussed. Several researchers [Blevins and Bressler 1993, Ziada et al. 1989a,b] expressed the important effects of Mach number and Reynolds number on the sound pressure levels. Ziada et al. 1989a,b in particular mention the importance of the Reynolds number and described how, for an otherwise identical test, by doubling the Reynolds number a resonance that was not present now materialized. Blevins and Bressler 1993 believed that the Reynolds number was a secondary parameter in comparison to the Mach number. Reynolds number is linearly dependent on density, diameter and flow velocity, all of which are very important variables that affect the noise source strength as described in this work. Mach number also is linearly dependent on flow velocity, which as described earlier have a quadratic dependence on dipole source strength. These results show why the dependence on Reynolds and Mach number was noted by these researchers.

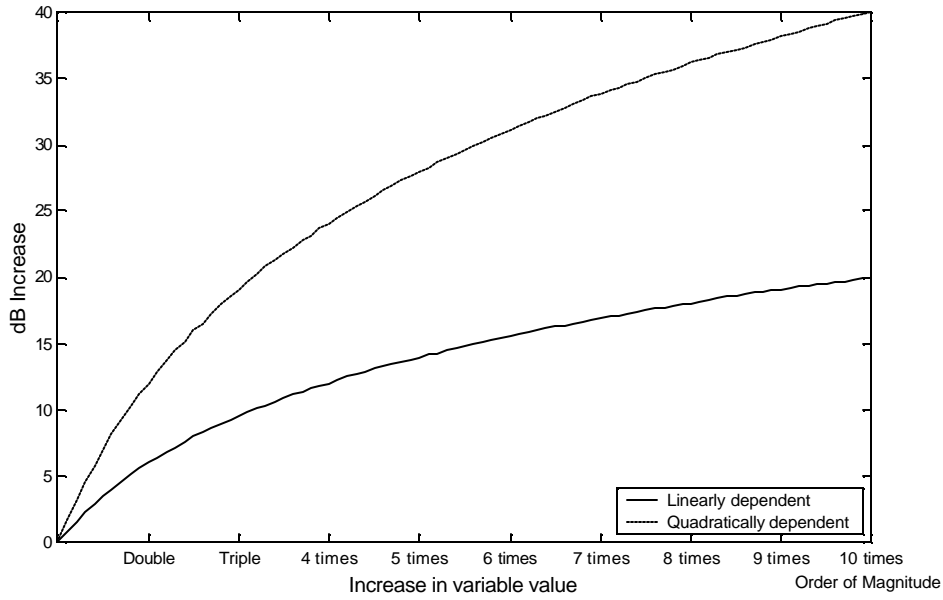


Figure 7.9 Effect of changes in the variables that affect the dipole source strength on sound pressure levels.

### 7.5 Effect of nondimensional volumetric damping and finite y-wall specific acoustic impedance on the first transverse acoustic resonance frequency of a duct with flow

The effect of damping on the acoustic natural frequency was explored by plotting the results of equation (3.100). In the results of the calculations presented in this section, a 6.35 mm diameter cylinder with a Strouhal number of 0.2 was assumed to determine the values of flow velocity and Mach number at the coincidence condition.

Figure 7.10 shows the results obtained assuming purely real or purely imaginary nondimensional volumetric damping coefficients. The same ranges for the values of these coefficients as used in section 7.2 were also used here. Figure 7.10 shows, as was suggested by Figure 7.2, that imaginary nondimensional volumetric damping coefficients increase the acoustic resonance frequencies. On the other hand, real values of these coefficients tend to lower the natural frequencies of the system. It is interesting to note that for values slightly higher than 6 the natural frequencies predicted by equation (3.100) are zero. This condition can be interpreted as the point where a discontinuity in the analytic series solutions is no longer present. Therefore, for real nondimensional volumetric damping coefficients larger than this value, the solutions are expected to be continuous.

Figure 7.11 is similar to 7.10, but in this case the effects of the changes in the y-wall specific acoustic impedance on the first acoustic natural frequency are presented. Figure 7.11 shows that purely resistive specific acoustic impedances do not have an effect on resonant frequency. The purely reactive impedances have an effect only for very large damping values (small acoustic impedances). This is supported in the results found in section 5.4.1.1 where it can be seen that the introduction of open cell acoustic foam changes the sound pressure levels but not the frequency of the acoustic resonance. This indicates that this material can be characterized by purely resistive impedance.

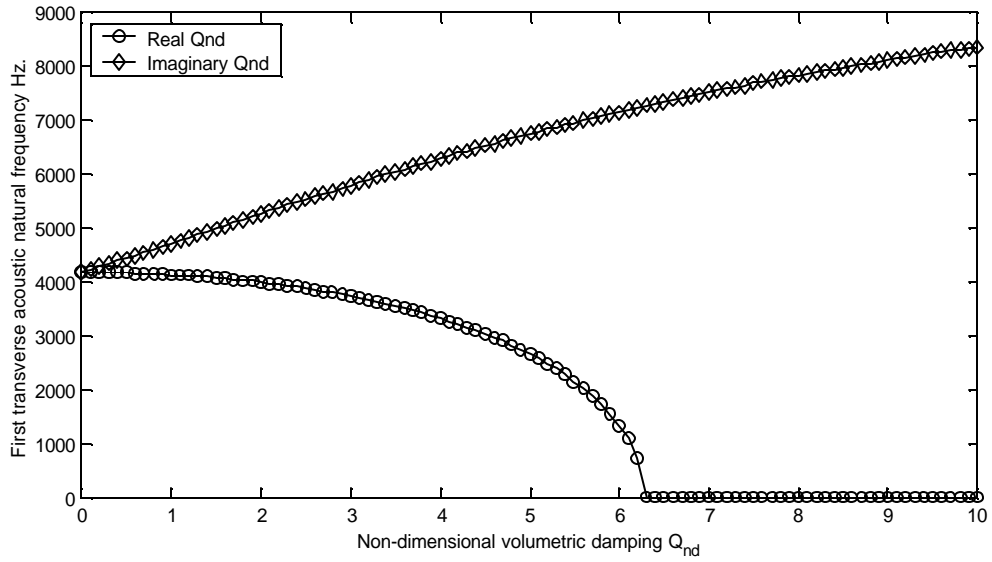


Figure 7.10 Effect of changes in non-dimensional volumetric damping on first transverse acoustic resonance frequency of duct.

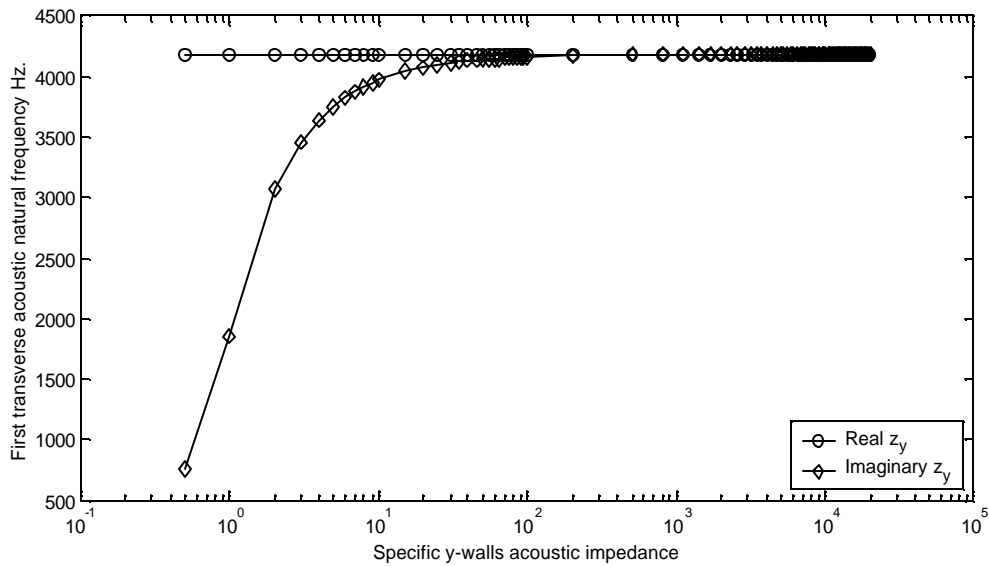


Figure 7.11 Effect of changes in y-walls specific acoustic impedance on first transverse acoustic resonance frequency of duct.



## Chapter 8: Summary and Suggestions for Future Work

### 8.1 Summary of results

The goal of this study was to gain a better understanding of the tonal flow-induced noise problems of plate heat exchangers. This led to a study of the noise produced by cylinders in cross-flows inside a rectangular duct. To our knowledge, this work links for the first time the experimentally measured acoustic field produced by cylinders in cross-flow inside a rectangular duct to a theoretically based acoustic model. Some of the main results of this study are summarized in this chapter.

### 8.2 Summary of results for single cylinders

#### 8.2.1 Constant diameter cylinders

The experiments on single cylinders showed that the results of the sound pressure levels were consistent for all cylinder diameters. By consistency in this case we are referring to the trends observed for all cylinder diameters on the sound pressure level curves when plotted either versus frequency or flow velocity. Sound pressure levels varied significantly depending on cylinder diameter. The larger the cylinder diameter, the clearer the tonal noise observed, and the higher the sound pressure levels. This behavior was successfully modeled with an acoustic model based on the inhomogeneous convected Helmholtz equation with a point dipole source term.

Measured transfer function phase angles between microphone pairs showed a similar consistency for all the tests made on single cylinders. In this case the phase angle curves are not affected by changes in cylinder diameter nor any other variable that affects dipole source strength. Phase angle changes only as the frequency of the source is changed. Phase angle is not affected by changes in source strength. These results are consistent with the results of the acoustic model. The acoustic model also successfully predicts the trends seen in the detailed experimental measurements.

The introduction of convection effects in the modeling equations improved the model accuracy by minimizing the shifts in the measured and predicted sound pressure level curves. The elimination of the shifts is crucial to obtain better fluctuating lift coefficient predictions using the model in the optimization procedures described in Chapter 6. Although the flow velocity profile assumed in the derivation of the model is assumed flat and constant, the flow profile is actually three dimensional. This assumption proved adequate in this study. Convection effects on the acoustics of the duct modeled were able to predict relatively well the reductions in first transverse acoustic natural frequency with the increase in flow velocity. These effects were more noticeable for larger cylinder diameters, since for these cylinders larger flow velocities are needed to excite the resonance frequency.

Strouhal number measurements for very short aspect ratio cylinders showed that as the diameter was reduced or the aspect ratio increased the measured Strouhal number decreased in value.

Fluctuating lift coefficients obtained using our inverse acoustic analogy approach are in agreement with experimentally determined values of these coefficients by other researchers.

Tests using acoustic foam on the side walls of the chamber showed that sound pressure levels can be effectively reduced by changing the acoustic impedance of the walls.

### 8.2.2 “Hourglass” shaped cylinders

Tests on hourglass-shaped cylinders showed that in general these types of cylinders behave in the same way as constant diameter cylinders both in regard to sound pressure level and phase angle. However, these cylinders showed stronger sound pressure level fields than constant diameter cylinders with diameters of dimension close to the diameter seen at the center of the hourglass cylinders. This type of cylinder also exhibits reduced values of Strouhal numbers. These observations point out that these cylinders can be treated as constant diameter cylinders if a larger diameter is used. Unfortunately, it appears that two different “effective” diameters are necessary. One to estimate noise source strength and the other to account for noise frequency.

The increased diameter at the cylinder base in conjunction with the flow velocity profile inside the duct are believed responsible for the observed behavior. The effects of the curvatures of the cylinders tested are not differentiable except for the smaller diameter cylinders where they produce noticeable differences on Strouhal number. This fact implies that these effects could be more dependent on the velocity profile in the duct than on cylinder curvature. The horseshoe vortex may also play a role in the observed behavior of this type of cylinder. Szepessy 1993 (see section 2.6.2) concluded that the horseshoe vortex depends on aspect ratio for aspect ratios less than one (the range covered in this study). Similarly, the observed variation of Strouhal number with aspect ratio in constant diameter cylinders could be caused by horse shoe vortex effects. Further work is needed in this area.

## **8.3 Summary of results for multiple cylinders**

### 8.3.1 Side-by-side cylinders

Side by side cylinders showed significantly reduced sound pressure levels in comparison to single cylinders or cylinders in tandem. This behavior could be attributable to two conditions 1) The proximity of the cylinders to each other affect their vortex shedding generation process and therefore the magnitudes of the fluctuating forces sustained by the cylinders. 2) The acoustic field produced by these cylinders is significantly diminished due to the out of phase characteristics of the dipole sources created by each cylinder. The comparison between measured sound pressure levels and sound pressure levels estimated using our model (assuming out of phase point dipole sources using fluctuating lift coefficients from the single cylinder tests) supports the latter scenario, although it is not a sufficient condition to eliminate the former scenario. If the former scenario is the actual case, on the other hand, our proposed model is not invalidated. Measurements of the fluctuating forces while simultaneously measuring the acoustic field can provide the answer to this problem.

### 8.3.2 Tandem cylinders

Cylinders in tandem tested in this study behaved similarly to single cylinders. Cylinders in tandem showed, especially for the 6.35 mm and 3 mm diameter cylinder pairs, significant increases in sound pressure level in comparison to single cylinder tests. The large fluctuating lift coefficients for the downstream cylinders found using our acoustic model and optimization procedure (inverse acoustic analogy approach) and the measurements of the acoustic field at several positions in the duct do not agree with the limited data available in the literature. In contrast, the fluctuating lift coefficients found for single cylinders agree relatively well with results from the literature.

The additional difficulty of finding the fluctuating lift coefficient of two instead of one cylinder complicates the problem. This complication is caused by the sensitivity of the measured and estimated results to the cylinder and microphone measurement positions.

Tandem-cylinder Strouhal numbers are slightly higher than 0.2 and did not follow any noticeable trend as a function of cylinders diameter. For single cylinders, it was observed that the smaller the cylinder diameter, the smaller the Strouhal number. This trend was not observed for cylinders in tandem.

### 8.3.3 Cylinder arrays

Cylinder array tests performed on normal triangular, square in-line and staggered arrays showed that these short aspect ratio cylinder arrays have similar Strouhal numbers to their large aspect ratio counterparts. One of the main differences between the larger aspect ratio arrays and the arrays tested in this work is the very large pressure drop down the duct for the short aspect ratio arrays. The large pressure drop creates significant gradients in density and velocity along the length of the arrays. Flow velocity and density are some of the main parameters that influence the fluctuating forces that produce the dipole noise source from cylinders. The large gradient in velocity cause cylinders in different regions of the arrays to generate noise at significantly different frequencies and with different source strength even if similar fluctuating lift coefficients could be assumed for all cylinders. The differences in frequency do not change considerably when any of the noise source frequencies pass through a resonance. In many cases the sound pressure level at resonant and nonresonant conditions was comparable. For this reason, an acoustic model to predict the flow-induced noise behavior of heat exchangers should be able to predict noise levels at off resonance conditions. The model based on fundamental acoustic principles and validated with the results of single and multiple cylinders presented in this work provides for the first time the basis of such a model.

### 8.3.4 Plate heat exchangers

The initial work on plate heat exchangers prompted our investigation on the flow-acoustic phenomena of bluff bodies in cross-flow inside a duct. Measurements of the flow-induced noise of plate heat exchangers taken using R134a and nitrogen confirmed that the acoustic resonances present in this type of heat exchanger were of the same nature as those reported in the literature. The results of the tests performed on them also indicated that the general flow-acoustic behavior for staggered and in-line arrays is also experienced by plate heat exchangers. The results of the tests on plate heat exchangers are difficult to generalize since the design of these heat exchangers is very complex, not likely to be repeated and proprietary.

## **8.4 Design recommendations to avoid flow-induced tonal noise in plate evaporators**

There are several areas of opportunity for utilizing results from this work to better design a plate evaporator for the reduction or elimination of tonal noise problems. This objective can be achieved in three ways: 1) modifying the design to alter the flow-induced noise generation, 2) changing the acoustics of the duct containing the sound sources, or 3) altering the refrigerant flow dynamics in the refrigeration system, but mainly in the expansion valve/plate evaporator assembly.

Flow-induced tonal noise from bluff bodies is directly related to vortex shedding that causes the fluctuating pressure around bluff bodies responsible for this phenomenon. For this reason, if vortex shedding can be eliminated or reduced, this problem could be minimized. There are 8 different proven ways to eliminate vortex shedding from

cylinders [Blevins 1994]. Of these eight, only using streamlined shapes could be implemented in the manufacture of the aluminum plate heat exchangers. Finding a manufacturable streamlined shape that can still produce good heat transfer performance would be the problem to solve if this approach is chosen.

The important parameters in generating tonal noise have been identified (see section 7.4). It has been found that flow velocity is the dominant parameter that affects the strength of the dipole source with a square dependence (see equation (6.3)). Reducing the flow velocity in the duct—by increasing the duct height, for example (and thus increasing the cross-sectional area)—will reduce the tonal noise produced by the cylinders significantly, even when the length of the cylinders increases. Similarly, design changes that reduce any of the other four main parameters directly linked to the strength of the source (fluctuating lift coefficient, cylinder diameter, cylinder length, or fluid density) will help reduce the tonal noise problems. Since these four parameters are in many cases directly interrelated, it is necessary that the effects of these parameters be reduced overall to consider the design a better one from the flow-induced noise viewpoint.

Additionally, a reduction in the number of bluff bodies will generally reduce the number of sound sources with its consequent reduction in tonal noise. There are exemptions to this rule, as was shown with the side-by-side cylinder tests.

A well-known method of eliminating acoustic resonance is introducing baffles to increase the acoustic resonance frequency of the duct. Since this approach does not alter the flow velocity in the duct (and thus the frequency of the tonal noise sources), the shift in frequency allows for a significant reduction in the tonal noise (which in many cases is greater than 20 dB) by eliminating this coincidence condition. The introduction of baffles could also shift the resonance frequencies to a range of frequencies to which the human ear is not as sensitive. The introduction of baffles is a feasible alternative in plate heat exchangers.

Other ways of altering the acoustics of the duct involve modifying its acoustic resonance supporting walls. Figures C.11 and D.1, for example, show that in these designs the side walls also contained stamped protuberances. These designs in general showed broader spectra at the dominant frequency than did designs in which flat walls were present. Broadband noise is not perceived to be as annoying as tonal noise.

Flow-induced tonal noise problems in plate heat exchangers are caused by the flow of gases. This condition occurs only transiently. If two-phase refrigerant could always be present in the heat exchanger, not only would the flow induced noise problem be significantly reduced, but also the heat transfer capacity of the heat exchanger would be increased. This alternative could in principle be the best approach of the three discussed in this section.

## **8.5 Contributions of present study**

To our knowledge this study is the first to:

4. Present a systematic investigation of the correlation between the acoustic sound field generated by small aspect ratio cylinders of different diameters in cross-flow inside a rectangular duct and an acoustic model driven by point dipole sources.
5. Use an inverse acoustic analogy approach. That is, measurements of the acoustic field have been used to obtain properties of the flow-induced sound sources.
6. Correlate the effects of fluid and geometric variables on the noise source strength produced by small aspect ratio cylinders inside a duct.

7. Present estimations of the source strength and acoustic damping for small aspect ratio cylinders inside a rectangular duct using experimental measurements of the acoustic field inside a duct and an acoustic model.
8. Present results of measurements and modeling of the acoustic field produced by two small aspect ratio cylinders side by side and in tandem configurations inside a channel.
9. Use a model based on fundamental acoustics to predict the flow-induced noise behavior of a cylinder array at resonant and non-resonant conditions.
10. Show that cylinder shape (hourglass cylinders) and flow velocity profile inside the duct affect the flow induced noise produced by this type of cylinder.
11. Use rapid prototyping techniques to study the flow-induced noise of cylinder arrays inside a duct. The results obtained for stereolithography cylinders led us to believe that this technique can now be used more confidently as a design verification tool. These techniques could greatly reduce cost and simplify testing of cylinder arrays.
12. Present results of measurements of flow-induced noise in plate heat exchangers and links this problem to the well known problem of acoustic resonance in large heat exchangers.

Some additional contributions of this study include:

13. Present a very large data set of results of Strouhal number for small aspect ratio cylinders, tandem cylinders, side by side cylinders and cylinder arrays.
14. Show results of detailed measurements of the velocity profile inside a very small rectangular channel.
15. Present results of measurements of hydrodynamic pressure fluctuations produced by the turbulent flow at the walls of a very small rectangular duct.
16. Develop a technique to estimate microphone pair phase angle mismatch.
17. Create a modified two-microphone technique to measure the acoustic properties of very small acoustic terminations.

### **8.6 Recommendations for future work**

Measurements of fluctuating forces and acoustic field simultaneously with single cylinders, side-by-side cylinders, cylinders in tandem, and cylinder arrays are needed to confirm that the fluctuating lift coefficients obtained using the procedures described in this work are accurate. These measurements would also help to establish whether the results seen for the side-by-side tests are caused by dipole cancellation effects or occur because the cylinders are no longer producing strong fluctuating forces due to the fluid mechanic interactions caused by their proximity. The measurement of the phases between the fluctuating forces of multiple cylinders can also be used to improve the model prediction capabilities and better understand the interactions between the different sound sources. The simultaneous measurements of fluctuating forces and the acoustic field and the use of the acoustic model in combination with the measurement results can help to provide a better understanding of the relationships between the fluid mechanics of circular cylinders in cross-flow inside a duct and its noise generation effects.

Simultaneously measuring the fluctuating lift forces and acoustic field can help to establish the influence of fluid-acoustic coupling effects. It is believed that fluid-acoustic coupling, if present will affect the fluctuating lift forces. By noticing the trends in the fluctuating lift coefficients measured at different conditions and with different cylinders, it should be possible to determine the importance of this phenomenon.

Tests on larger aspect ratio cylinders would be necessary to extend the use of the acoustic modeling technique used herein. For cylinders with aspect ratios large enough that vortex shedding is not in phase along the cylinder length, acoustic point dipoles could be spaced at appropriate locations throughout the cylinder to represent the acoustic sources. The use of this approach introduces the need to determine the phases between dipoles located in the same cylinder and on different cylinders. Tests on larger aspect ratio cylinders is a necessary step towards extending this modeling scheme for use on larger heat exchangers.

Due to time limitations, tests placing single cylinders at different positions in the duct were not made in this study. These tests can be used to further validate the model when the source is not present in the center of the duct.

The effects of cylinder curvature and duct velocity profile on the flow-induced noise behavior of hourglass-shaped cylinders needs further investigation. The measurements performed in this study show the importance of these effects both on sound pressure level and on source frequency. Velocity profile effects might also be responsible for the Strouhal number reductions seen as the cylinder diameter was reduced during single cylinder tests. Horseshoe vortex from small aspect ratio cylinders is not fully understood. The horseshoe vortex could also be influenced by cylinder curvature and flow velocity profile. Its effect on the Strouhal vortex shedding is unclear. Further work is needed on this complex flow interaction.

Although damping proved to be negligible in this case, further work to determine the correct values of system damping (volumetric or at the walls) for different duct/cylinder systems or working fluids is necessary. Until physical or empirically based models or data are available it will be very difficult to use these parameters adequately in acoustic models.

The large gradients seen in the acoustic field predicted by the model introduce the possibility of choosing the microphone mounting positions optimally to more accurately compute parameters such as the fluctuating lift coefficient. More appropriate microphone mounting positions and/or using more microphones might also help improve the estimations made for cylinders in tandem.

## Appendix A: Acoustic Impedance and Reflections Coefficients of Different Duct Terminations

### A.1 Introduction

A standard procedure to measure acoustic properties of materials was used in the design of the acoustic terminations placed in the pre and post conditioning test sections of our wind tunnel. The procedure is commonly known as the two-microphone technique or the transfer function method of determining acoustic properties inside ducts. This technique is used to determine the reflection coefficients from which other properties can be obtained. Originally developed by Chung and Blaser 1980a, b, it has been now established as an ASTM standard [ASTM standard E1050-90].

This method to determine acoustic properties is based on measurements by two microphones that are installed flush to an impedance tube and are spaced a distance  $s$  between them. The tube can be circular or rectangular with constant cross sectional area along its length. In one side of this tube is installed a broadband noise source and at the other end is installed the material/termination to be tested. Figure A.1 shows a schematic of the required setup.

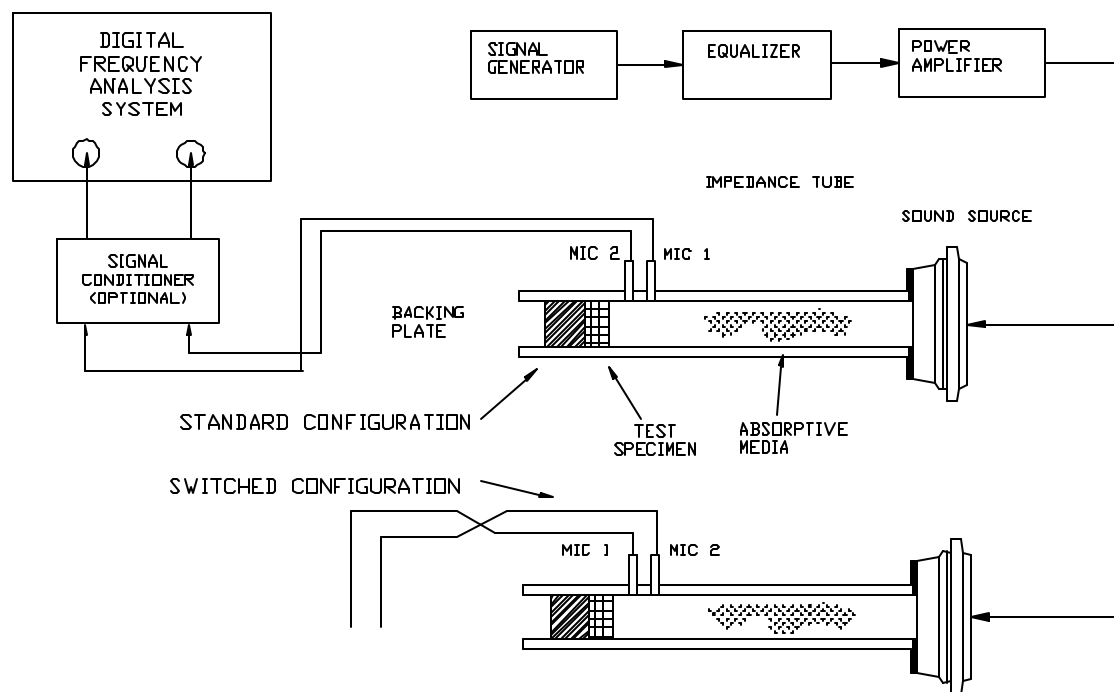


Figure A.1 Schematic of experimental apparatus needed to determine acoustic impedance and reflections coefficients using ASTM standard E1050-90.

### A.2 Formulation and limitations

This method determines properties at a range of frequencies. The dimensions of the impedance tube and the microphone spacing limit the frequency range of the measurements. Impedance tube geometry limits the propagation of purely plane waves to below the first cutoff frequency of the duct. After the first cutoff frequency of

the duct plane waves and higher order modes are present. Since this method assumes only plane wave propagation inside the impedance tube this method is no longer applicable for frequencies greater than the first cutoff frequency of the duct since higher order waves can alter the results if present. The range of frequencies is defined as:

$$f_l < f < f_u$$

$$f_u = \frac{c_o}{2W} \quad (A.1)$$

In equations (A.1)  $f_u$  represents the first cutoff frequency for a rectangular duct where  $W$  should be the larger side of the rectangular cross section, in our case this side is the width  $W$ . According to the ASTM standard,  $f_l$  is a lower limit that depends on the microphone spacing and the accuracy of the analysis system. The standard states that currently there is no method to determine this limit [ASTM standard E1050-XX draft 5].

The microphone spacing limits the maximum frequency at which the incident and reflected waves can be effectively separated. The microphone spacing distance should be specified in order that this distance is less than 80% the shortest half wavelength of interest.

$$s \leq 0.80 \frac{c_o}{2 f_u} \quad (A.2)$$

Chung and Blaser 1980a developed from first principles and without mathematical simplifications a relationship to determine the reflection coefficient from a test sample or termination by using the transfer function between the two microphones. This relationship is shown in equation (A.3).

$$R = \frac{H_{12} - e^{-ik s}}{e^{ik s} - H_{12}} e^{i2k(s+1)} \quad (A.3)$$

The specific acoustic impedance from the test sample/termination can be determined using the results from equation (A.3) as shown below.

$$z = \frac{(1+R)}{(1-R)} \quad (A.4)$$

For our purposes, the implementation of the two-microphone method to determine the acoustic properties of different duct terminations required that the impedance tube used be of the same dimensions as our wind tunnel. Additionally a strong broadband acoustic source of very small size that fits the impedance tube is needed. To solve the first problem the wind tunnel was used as the impedance tube. The only modification required was to drill holes on the walls of the test section to place the microphones. These holes however could also be used later to measure the acoustic field during the single cylinder tests. The second problem was solved by using an orifice tube as a source of sound instead of using a speaker. Orifice tubes are known sound generators that produce broadband noise [Rodarte et al. 1999a,b]. Figure A.2 shows this arrangement.



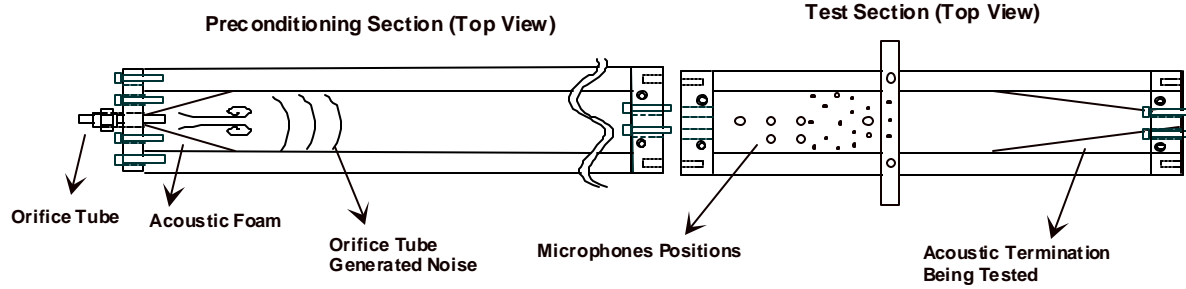


Figure A.2 Schematic of impedance tube arrangement used to measure acoustic impedance and reflection coefficients from different possible acoustic terminations.

The introduction of flow in the duct requires a correction of equation (A.3) to:

$$R = \frac{H_{12} - e^{-ik_i s}}{e^{ik_r s} - H_{12}} e^{i2k(s+1)} \quad (\text{A.5})$$

The value of  $k_i$  and  $k_r$  refer to the corrected wavenumbers that should be used if uniform flow can be assumed in the impedance tube. The values of  $k_i$  and  $k_r$  are obtain from:

$$k_i = \frac{k}{(1+M)} = \frac{2 p f}{c_0(1+M)} \quad (\text{A.6})$$

$$k_r = \frac{k}{(1-M)} = \frac{2 p f}{c_0(1-M)}$$

The determination of the correct value of the transfer function  $H_{12}$  requires the perfect phase matching of the microphones and instrumentation as well as correct amplitude calibration. To reduce these sources of error the transfer function  $H_{12}$  is corrected before use in equations (A.3) and (A.5). The correction factor is obtained from the transfer functions measured in the original and switched configurations (see Figure A.1). This is expressed as:

$$H_{12} = \frac{H_{\text{meas}}}{(H_o H_s)^{0.5}} \quad (\text{A.7})$$

### A.3 Technique validation

To test this procedure it was used to measure the reflection coefficient from the open wind tunnel rectangular termination. This termination has the advantage that the reflection coefficient can be determined from analytical relations. The radiation impedance of rectangular pistons determined from the formulations by Levine, Morse and Ingard and Mechel were used to compare the results of our measurements. The equations to determine the specific acoustic impedance for each of these formulations is presented below.

Formulation by Levine:

$$z \approx 1 - \frac{2i}{p abk} (a+b) - \sqrt{\frac{2}{p}} \frac{e^{i(ka-p/4)}}{(ka)^{3/2}} \left(1 - \frac{9i}{8ka}\right) - \sqrt{\frac{2}{p}} \frac{e^{i(kb-p/4)}}{(kb)^{3/2}} \left(1 - \frac{9i}{8kb}\right) -$$

ka >> 1 (A.8)

$$\frac{2i}{p abk^2} - \frac{2i}{p abk^2} (e^{ika} + e^{ikb}) - \frac{2i}{p} e^{ik\sqrt{a^2+b^2}} \frac{(a^2+b^2)^{3/2}}{(kab)^3} + O(k^{-7/2})$$

Formulation by Morse and Ingard:

$$z \approx \frac{a^2 q_M(ka) - a^2 q_M(kb) - ia^2 c_M(ka) + ib^2 c_M(kb)}{(a^2 - b^2)} \quad b \rightarrow a$$

where :

$$q_M(x) = \left[ 1 - 4 \frac{1 - J_0(x)}{x^2} \right] \quad (A.9)$$

$$c_M(x) = \frac{8}{p x} \left[ 1 - \frac{p}{2x} M_0(x) \right]$$

$$M_0(x) = \frac{2}{p} \int_0^{p/2} \sin(x \cos u) du$$

Formulation by Mechel:

$$\text{Real}(z) = 1 - \frac{2}{p k^2 ab} \left[ \frac{1 + \cos(k\sqrt{a^2+b^2}) + k\sqrt{a^2+b^2} \sin(k\sqrt{a^2+b^2})}{\cos(ka) - \cos(kb)} \right] + \frac{2}{p} I_1'$$

(A.10)

$$\text{Im ag}(z) = \frac{2}{p k^2 ab} \left[ \frac{k(a+b) + \sin(k\sqrt{a^2+b^2}) - k\sqrt{a^2+b^2} \cos(k\sqrt{a^2+b^2})}{\sin(ka) - \sin(kb)} \right] - \frac{2}{p} I_2'$$

where :

$$I_1' = \int_1^{\sqrt{1+(b/a)^2}} \sqrt{1-1/x^2} \cos(xka) dx + \int_1^{\sqrt{1+(a/b)^2}} \sqrt{1-1/x^2} \cos(xkb) dx$$

$$I_2' = \int_1^{\sqrt{1+(b/a)^2}} \sqrt{1-1/x^2} \sin(xka) dx + \int_1^{\sqrt{1+(a/b)^2}} \sqrt{1-1/x^2} \sin(xkb) dx$$

The above equations were solved using Mathematica version 4.0 and compared to measurements taken.

Figure A.3 shows the comparison.

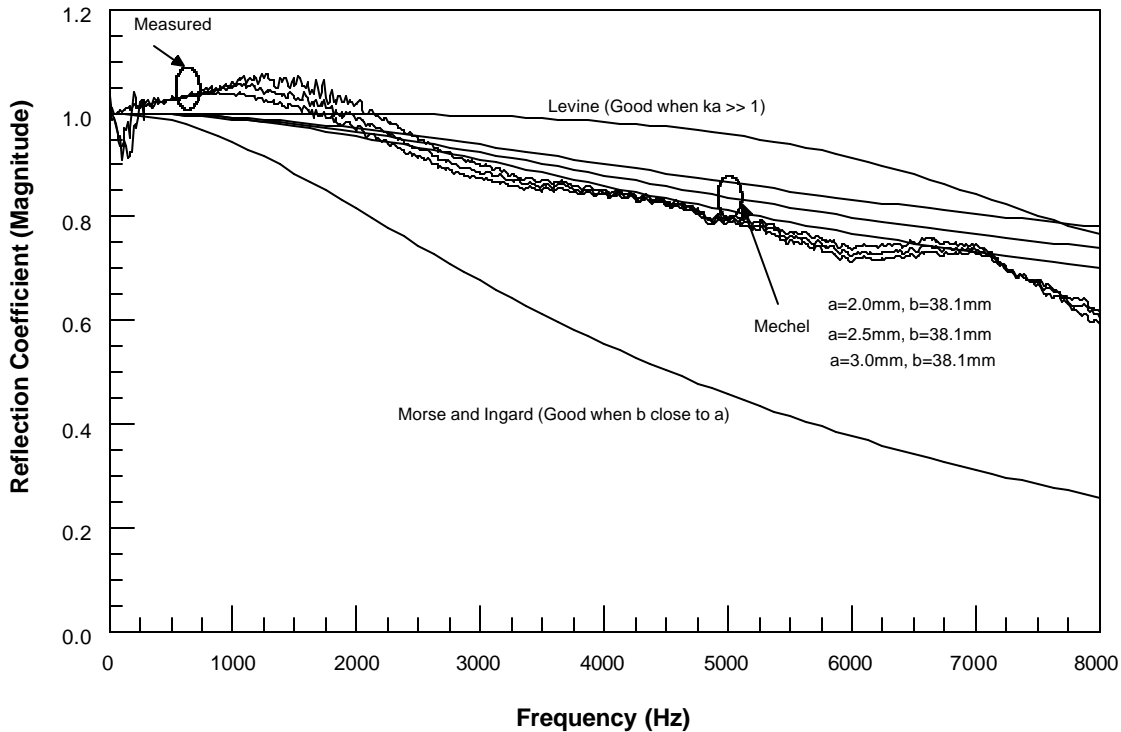


Figure A.3 Reflection coefficient of rectangular wind tunnel termination open to the atmosphere.

The measured reflection coefficient below about 2 kHz were actually larger than 1. This fact could not be explained. For larger frequencies, the measured reflection coefficient seems to follow approximately the results predicted by the more accurate Mechel formulation.

#### A.4 Evaluation of different acoustic terminations

Three different acoustic terminations were tested. The acoustic terminations were made from acoustic foam used for anechoic chambers. The acoustic open cell foam was made by Illbruck-Sonex under the commercial name sonex wedges.

Figures A.4, A.6 and A.7 present the schematics of the different terminations tested. Figures A.5, A.7 and A.9 present the measured reflection coefficients.

Figure A.5 shows the results of measurements taken with different microphone spacing. Microphone spacing is limited in the standard by the first cutoff frequency of the duct. If it can be assumed that orifice tube noise does not excite higher order modes, then the frequency limit of the two-microphone technique are imposed by the microphone phase matching. Measurements of the sound pressure level produced by orifice tubes inside 1/2" copper tubes with refrigerant in general do not show a significant increase in sound pressure level after the first cutoff frequency [Rodarte et al.1999a,b]. This find supports this assumption. In our case the microphones used are very good quality phase matched microphones used for sound intensity measurements. Microphone calibration presented in section 4.8 show that these microphones maintain their phase matching characteristics at very high frequencies. For these reasons it was decided to use smaller microphone spacings and estimate the reflections coefficients at

higher frequencies. Figure A.5 shows the results for 3 different microphone spacings. The results overlap each other at the lower frequencies. The three different traces measured at the smaller spacing represent two different noise source levels and measurements taken at a high noise source level with the 4 mm foam sections shown removed. This was done to reduce the pressure drop introduced by the acoustic termination. The noise source level nor the modifications to the acoustic termination modify significantly the measured reflection coefficient.

Similarly Figure A.7 shows three traces that correspond to two different noise source levels with the foam at the center of the duct and one with high noise source level and the middle section of the foam removed as shown in Figure A.6. Again the reflection coefficient of this termination is independent of these factors.

Figure A.9 shows also three traces which correspond again to measurements at two different noise source levels with foam at the center and with a high noise source level with a hole in the center as shown in Figure A.8. In this case they are more easily distinguishable from each other. The introduction of the hole in the center of this termination slightly increases the reflection coefficient at all frequencies.

From these measurements it was decided that any of the acoustic terminations presented in Figures A.4 and A.6 could be used. The termination shown in Figure A.6 was used in our wind tunnel.

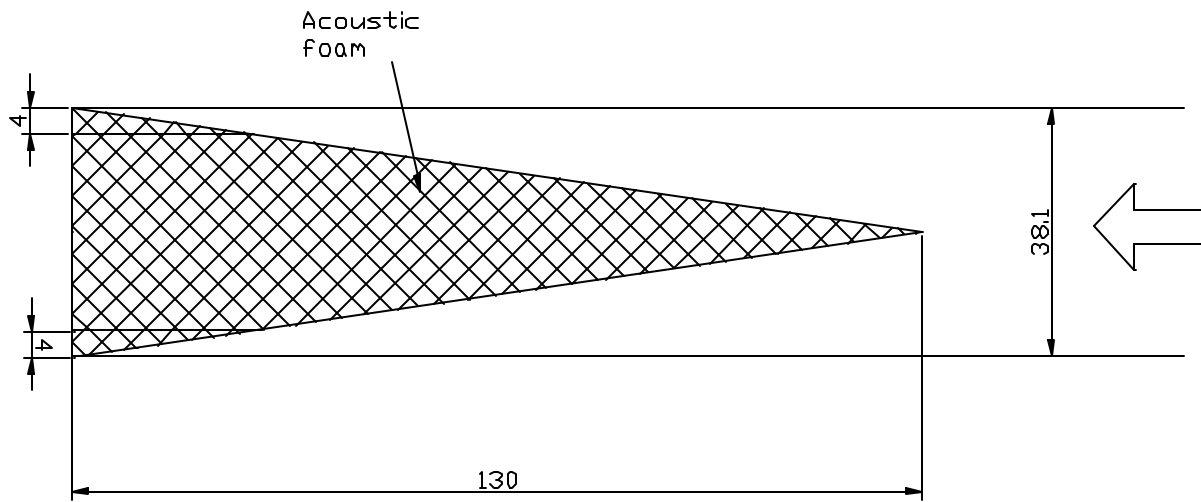


Figure A.4 Schematic of acoustic foam termination with foam at center of duct. Drawing to scale. Dimensions in mm.

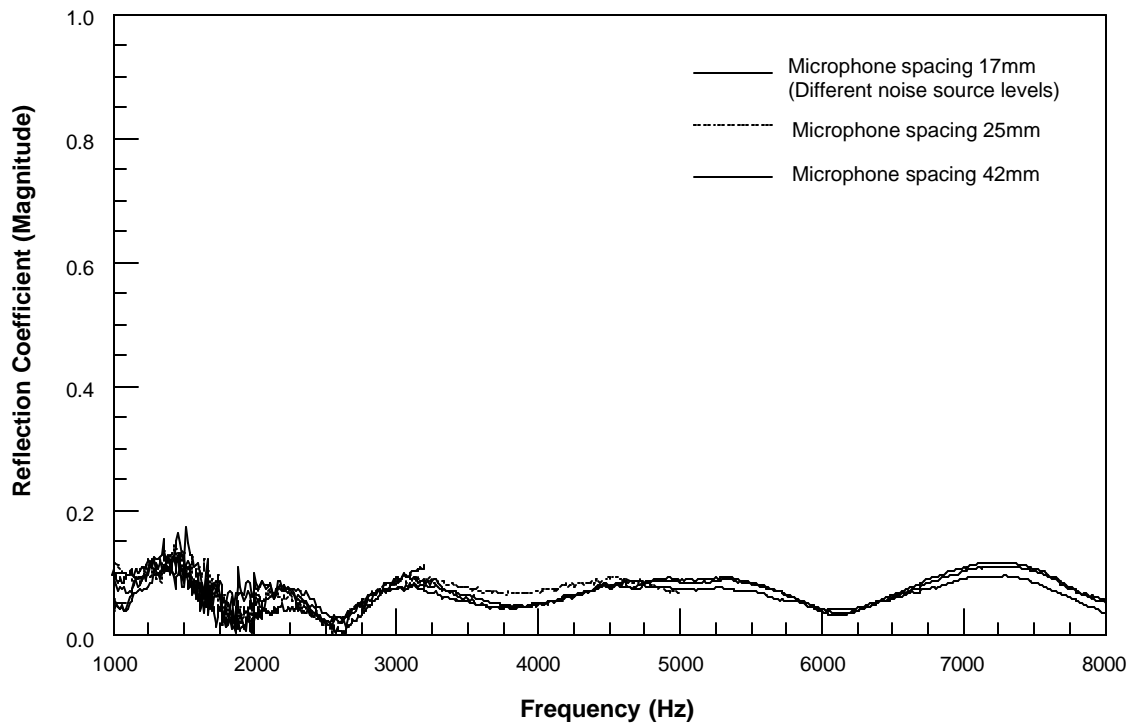


Figure A.5 Reflection coefficient measured for acoustic termination shown in Figure A.4.

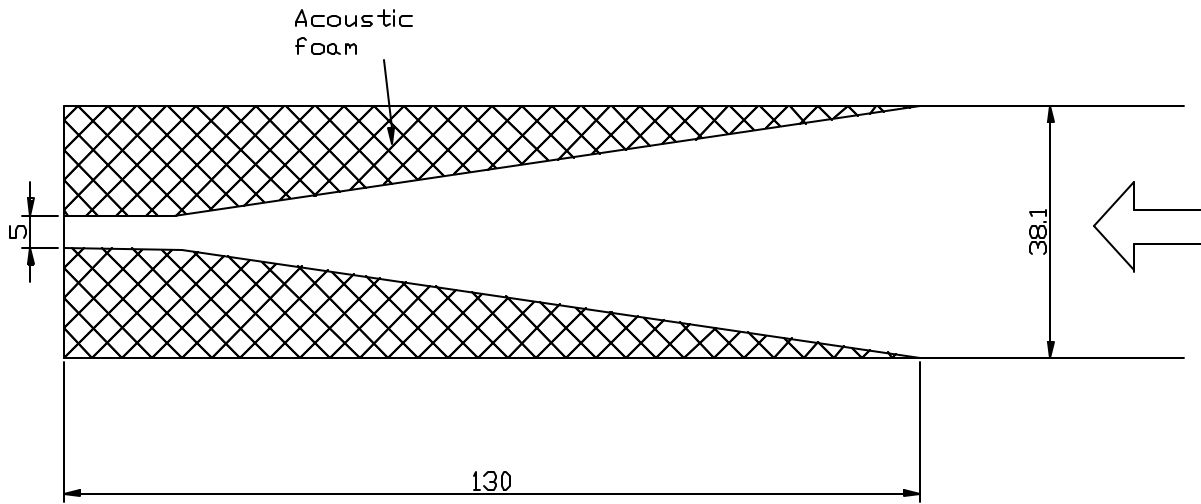


Figure A.6 Schematic of acoustic foam termination with foam at sides of duct. Drawing to scale. Dimensions in mm.

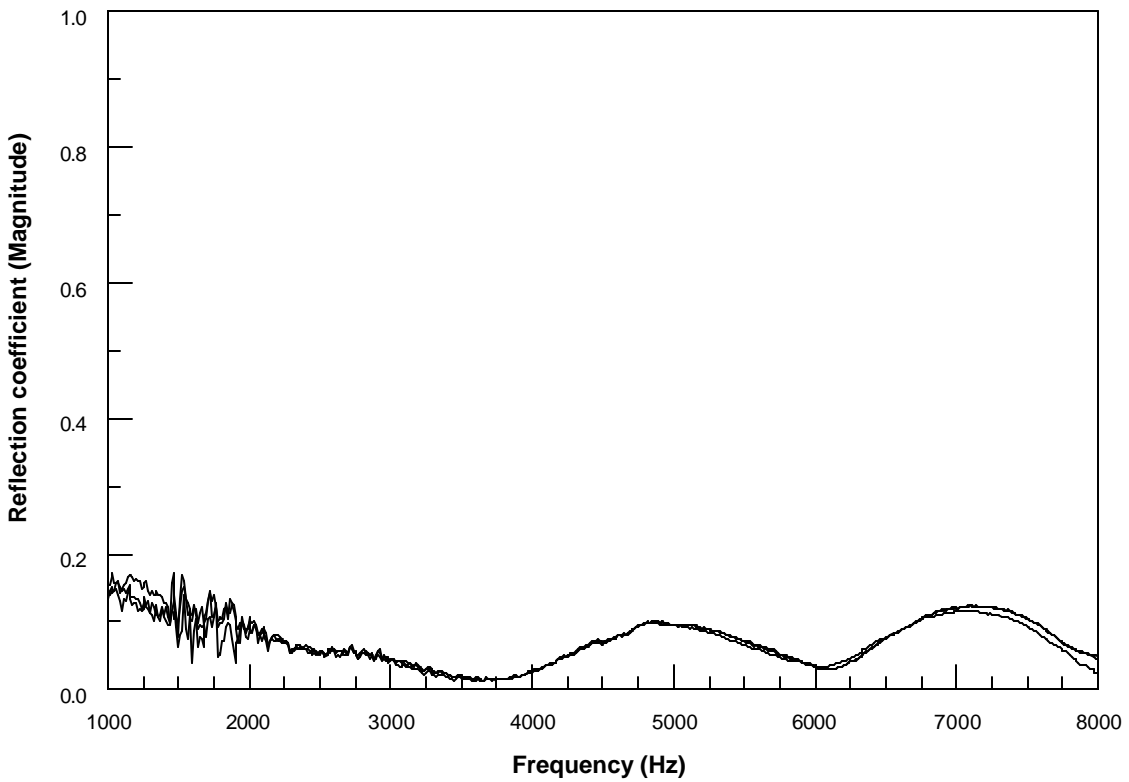


Figure A.7 Reflection coefficient measured for acoustic termination shown in Figure A.6.

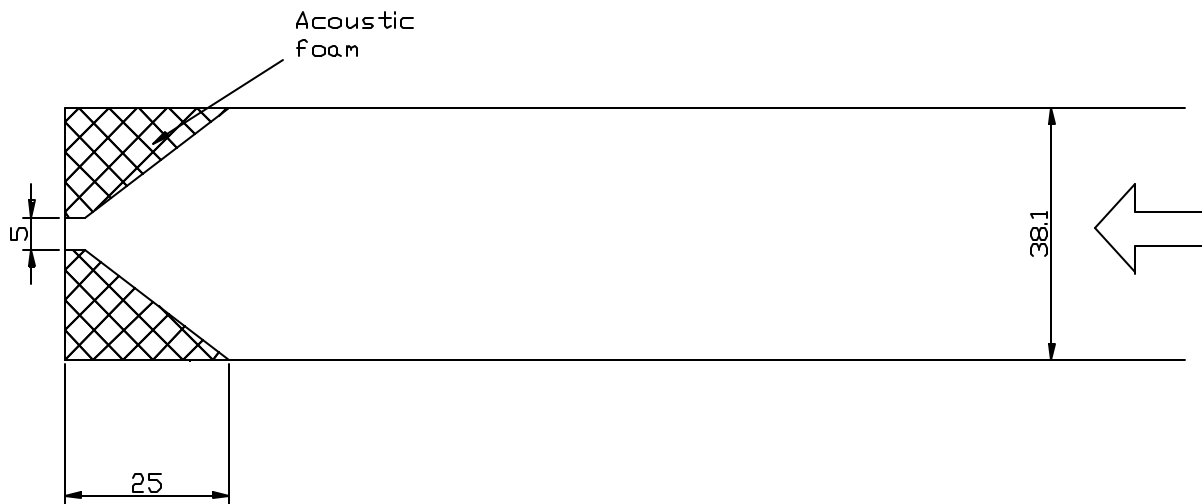


Figure A.8 Schematic of acoustic foam termination with foam at sides of duct. Drawing to scale. Dimensions in mm.

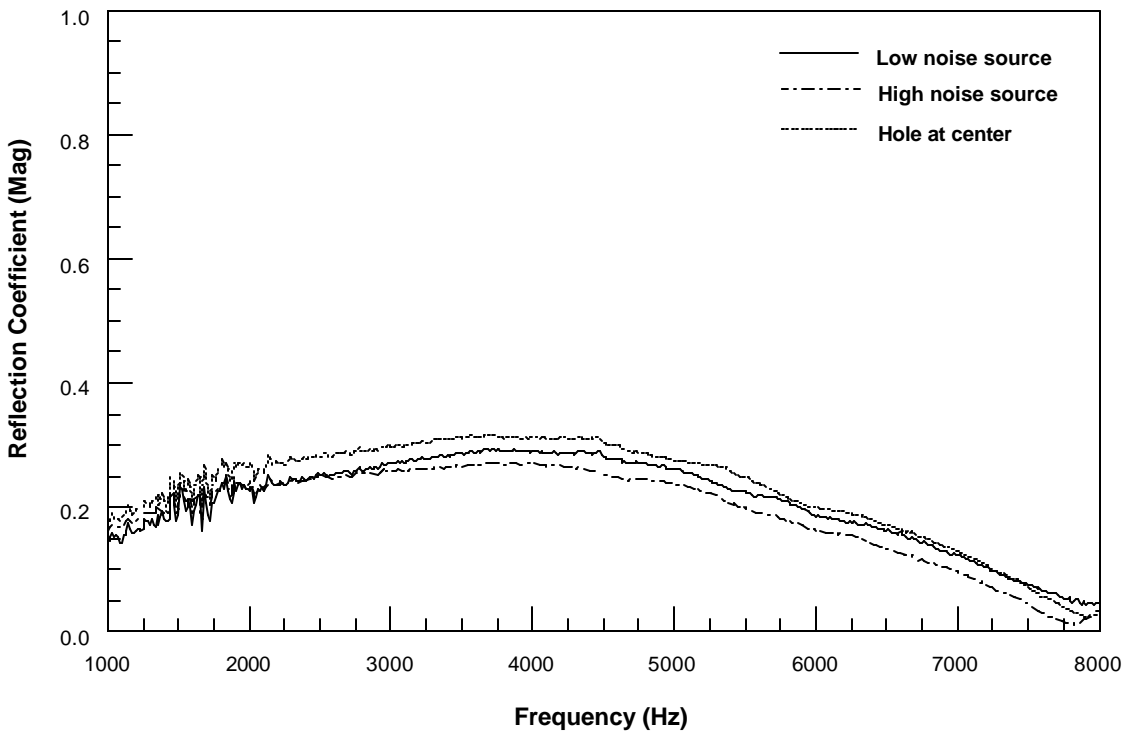


Figure A.9 Reflection coefficient measured for acoustic termination shown in Figure A.8.

## Appendix B: Flow Velocity Mapping Inside 2.5 x 38.1 mm Test Section

### B.1 Introduction

This appendix describes the procedure and relevant information used to measure and compare the velocity profile inside our wind tunnel section.

### B.2 Description of measurements

Using two 24 gauge Luer lock type syringe needles that were modified for use as a Pitot tube the velocity profile was determined for several different values of Reynolds number using both air and nitrogen. The open loop setup used to take these measurements was described in chapter 4.

The procedure involved measuring the velocity at several positions along the channel cross section. Different positions equally spaced were chosen along the width and then the Pitot tube probe was moved to different locations vertically. Figure 4.5 shows a photograph of the test section with the assembly used to position the Pitot tube. The assembly is positioned accurately with the use of micrometers. Figure 4.6 presents a schematic drawing that shows the measurement positions inside the wind tunnel.

Two different fluids were used in the initial flow velocity measurements inside the channel. Air measurements were taken at all positions shown in Figure 4.6. Nitrogen measurements were only taken at the center of the wind tunnel along the wind tunnel height. When nitrogen was used a heat exchanger was required to raise the temperature of the fluid to ambient conditions. The flow velocity was controlled for the two fluids with pressure regulators.

### B.3 Flow velocity using a Pitot tube

Pitot tubes are devices that can translate the difference in the static and stagnation pressures to a flow velocity. The relationship between these two pressures is described below:

$$P_T = P_o + \frac{\rho_o V^2}{2} \quad (\text{B.1})$$

Equation (B.1) can be rearranged so that the velocity at the Pitot tube tip can be determined from the pressure difference as shown in equation (B.2).

$$V = \sqrt{\frac{2(P_T - P_o)}{\rho_o}} \quad (\text{B.2})$$

There are two Correction factors that should be used with equation (B.2). The first of these correction factors is needed only if the fluid in which the measurements are made is a compressible gas. This gas compressibility factor is determined assuming isentropic compression at the probe tip. Equation (B.3) presents this compressibility factor (Miller R.W.).

$$\Gamma_{\text{Pitot}} = \sqrt{1 - \frac{1}{2k} \frac{(P_T - P_o)}{P_o} + \frac{(k-1)}{6k^2} \left( \frac{(P_T - P_o)}{P_o} \right)^2} \quad (\text{B.3})$$



The other correction factor is a Pitot tube coefficient that corrects for the differences in Pitot tube design. This correction factor lay in the range between 0.8 and 1.0 depending on the particular design. The velocity at the tip of the Pitot tube can therefore be estimated as:

$$V = K_{\text{Pitot}} \Gamma_{\text{Pitot}} \sqrt{\frac{2(P_T - P_o)}{r_o}} \quad (\text{B.4})$$

The calibration of the Pitot tube consists in finding the value of the coefficient  $K_{\text{Pitot}}$ .

The procedure to calibrate Pitot tube follows:

18. Determine average velocity through the channel

Measure mass flow using a venturi and/or Coriolis flow meter. Determine the fluid density at the measurement point from temperature and pressure readings. Using this information and the cross sectional area an average velocity is determined.

19. Estimate average velocity measured with Pitot tube readings

Using area averaging, the Pitot tube measurements are used in an optimization procedure to determine the best value of the constant  $K_{\text{Pitot}}$  that minimizes the error between the area averaged flow velocity and the average flow velocity determined as described in step 1.

20. Correct the Pitot tube constant  $K_{\text{Pitot}}$

The procedure described in step 2 was repeated for the 5 different flow velocity mappings made in the wind tunnel with compressed air. The  $K_{\text{Pitot}}$  constants determined for the 5 different cases did not vary significantly. These five constants were then averaged to get the final  $K_{\text{Pitot}}$  coefficient used. The value determined in this way was  $K_{\text{pitot}} = 0.9$ . This value lays right in the middle of the range of values for this parameter as described above.

#### B.4 Velocity profile estimation using the logarithmic overlap law

Two different empirical correlations derived from dimensional analysis have been used to describe the velocity profile in turbulent flow inside pipes and ducts. These correlations are known as the “logarithmic overlap law” and the “power law”. In this work the logarithmic overlap law was chosen to compare the flow velocity measurements inside the channel to predictions for turbulent flow inside a duct.

The logarithmic overlap law was an extension to the work by Prandtl and Kármán by Millikan who proved that the wall layer and outer layer for turbulent flow near a wall could only overlap smoothly by following a logarithmic relationship [White].

This logarithmic relationship is shown in equation (B.5).

$$\frac{u(z)}{u^*} \approx \frac{1}{k} \ln\left(\frac{z u^*}{n}\right) + B \quad 0 < z < \frac{\text{height}}{2} \quad (\text{B.5})$$

This logarithmic overlap law turned out to be more than a short overlapping link and can actually be used to approximate the entire flow velocity profile [White].

The constant  $k$  and  $B$  are 0.41 and 5.0 respectively. The variable  $z$  represents the height in the channel,  $u^*$  is the frictional velocity,  $\nu$  is the kinematic viscosity and  $u$  is the local velocity at the  $z$  location.

To determine the value of  $u^*$  there are two possible methods. One requires measuring the pressure drop in the channel section. The other method involves finding an average velocity expression from equation (B.5), equating this expression to the measured average velocity and solving for  $u^*$ . The second method was used since the logarithmic law was used only as a mean of comparing our measurements and since pressure drop measurements were not taken, additionally measurements of average velocities were already available. Average velocity can be estimated using equation (B.5).

$$U_{ave} = \frac{2}{H} \int_0^{H/2} u dz = u^* \left( \frac{1}{k} \ln \left( \frac{Hu^*}{2n} \right) + B - \frac{1}{k} \right) \quad (B.6)$$

Equation (B.6) assumes that the velocity profile is two-dimensional. This implies that there is an error associated with this procedure to determine the frictional velocity. Measurements made using the Pitot tube show that the flow velocity is two-dimensional for a significant portion of the duct. Additionally as shown in Figure 4.9 very significant variations in the estimated profile for widely different Reynolds number do not deviate appreciably. For these reasons and since the logarithmic overlap law is used only for comparative purposes the small errors associated with this procedure have not been considered.

### B.5 Description of included material

Tables B.1 to B.5 show the measured flow velocities taken inside the channel for 5 different values of Reynolds numbers or mass flow rates.

Table B.6 presents the temperatures and pressures measured at the test point that were used to determine density. Mass flow measurements are also presented in this table.

Table B.7 shows the flow velocity measurements at the center of the channel taken using nitrogen instead of air.

Figures B.1 to B.4 show the velocity profiles inside the duct for the first 4 Reynolds numbers presented in tables B.1 to B.5. These graphs were made assuming symmetry in the flow inside the duct. The higher Reynolds number graph was not included in the Appendix since is already presented as Figure 4.6. The flow velocity measurements experienced for all Reynolds number a small drop in the velocity at the center of the duct. This drop is more noticeable for the lower Reynolds number flows. The reduction in the flow at the center of the duct is attributable to the not perfect covering of the 1/4" (6.35 mm) holes upstream of the Pitot tube. These holes were made to insert the single cylinders in the test section and were blocked for the flow velocity measurements. They were blocked inserting a 1/4" (6.35 mm) cylinder until it was flush to the inside of the duct. This method however seems to affect the uniformity of the flow.

Finally an EES program (Engineering equation solver) is included. This program can be used to determine the mass flow rate using the Venturi flow meter equations, the flow velocity profile estimation using the logarithmic overlap law, the Pitot tube flow velocity estimations and other auxiliary calculations.

Table B.1 Local flow velocities in m/s measured inside test section for nominal Reynolds number of 2125.

Width mm → Height mm ↓	0.7	2.8	4.9	7	9.1	11.2	13.3	15.4	17.5
1.2	18.46	26.18	28.14	29.56	30.91	31.30	31.24	31.19	30.02
1	18.37	25.39	27.27	28.62	30.02	30.41	30.30	30.30	29.09
0.8	18.08	24.21	26.18	27.52	28.86	29.27	29.21	29.15	28.07
0.6	17.56	22.68	24.70	25.99	27.33	27.71	27.77	27.58	26.83
0.4	16.90	21.03	23.42	24.35	25.79	26.25	26.31	26.05	24.98
0.2	16.92	19.07	21.44	22.53	24.00	24.63	24.70	24.35	22.76

Table B.2 Local flow velocities in m/s measured inside test section for nominal Reynolds number of 3170.

Width mm → Height mm ↓	0.7	2.8	4.9	7	9.1	11.2	13.3	15.4	17.5
1.2	29.46	39.23	42.61	45.60	46.04	46.48	46.19	47.83	45.45
1	29.46	38.31	41.53	44.17	44.36	45.56	45.08	46.77	44.32
0.8	29.17	36.91	40.08	42.45	42.73	44.09	43.55	45.23	42.77
0.6	28.28	34.79	38.00	40.12	40.54	41.65	41.53	42.97	40.83
0.4	27.30	32.57	35.80	37.86	38.26	39.35	39.31	40.62	38.35
0.2	26.42	29.69	33.55	35.42	35.80	36.82	36.78	37.91	35.42

Table B.3 Local flow velocities in m/s measured inside test section for nominal Reynolds number of 4415.

Width mm → Height mm ↓	0.7	2.8	4.9	7	9.1	11.2	13.3	15.4	17.5
1.2	40.01	55.71	60.52	62.63	64.26	63.75	64.44	64.26	63.58
1	40.01	54.17	58.89	60.92	62.63	62.26	62.99	62.81	61.98
0.8	39.89	51.83	56.41	58.39	60.14	59.98	60.71	60.36	59.79
0.6	38.76	49.48	53.38	55.51	57.30	57.41	58.47	57.86	57.38
0.4	37.73	46.63	50.40	52.30	53.99	54.20	55.12	54.44	54.23
0.2	37.25	43.28	46.98	48.58	50.20	50.53	51.27	50.30	49.98

Table B.4 Local flow velocities in m/s measured inside test section for nominal Reynolds number of 5860.

Width mm → Height mm ↓	0.7	2.8	4.9	7	9.1	11.2	13.3	15.4	17.5
1.2	55.45	73.34	79.18	81.88	84.63	84.68	85.52	85.37	85.46
1	55.76	71.64	77.05	79.82	82.50	82.59	83.49	83.32	82.63
0.8	55.27	68.61	73.85	76.42	79.22	79.71	80.62	80.21	79.77
0.6	53.32	64.99	70.21	73.36	75.93	76.59	77.87	77.01	76.40
0.4	51.51	61.18	66.52	69.04	71.47	71.92	73.19	72.08	72.18
0.2	50.01	57.13	62.05	64.21	66.35	66.92	67.94	66.38	66.52

Table B.5 Local flow velocities in m/s measured inside test section for nominal Reynolds number of 7280.

Width mm → Height mm ↓	0.7	2.8	4.9	7	9.1	11.2	13.3	15.4	17.5
1.2	67.44	87.63	94.73	99.30	101.30	102.10	102.50	102.70	102.30
1	67.64	85.33	91.94	96.54	98.71	99.82	100.30	100.40	100.10
0.8	66.37	81.45	88.04	92.43	94.91	96.31	97.21	96.75	96.49
0.6	64.03	77.10	84.07	88.40	90.93	92.70	93.84	92.77	107.10
0.4	61.99	72.52	79.05	83.03	85.51	87.05	88.08	86.71	86.88
0.2	58.56	67.19	73.39	77.19	79.26	80.77	81.51	79.70	79.75

Table B. Flow conditions at the test section during flow velocity profile measurements

Reynolds number	Temperature °C	Pressure Psig (kPa g)	Mass Flow g/s
2125	22.12	0.00 (0.00)	2.96
3170	22.02	0.10 (0.69)	4.42
4415	22.15	0.55 (3.79)	6.15
5860	22.15	1.00 (6.89)	8.17
7280	21.81	1.45 (10.00)	10.17

Table B.7 Flow velocities in m/s measured at center of test section using nitrogen.

Reynolds Number → Height mm ↓	1540	2660	3915	5240	6115
1.24	22.22	37.62	54.26	71.16	83.40
1	22.13	37.80	53.75	72.40	83.52
0.76	21.64	37.16	52.63	70.86	80.68
0.52	20.55	35.39	50.06	66.27	76.03
0.28	19.16	32.47	46.52	60.96	69.13

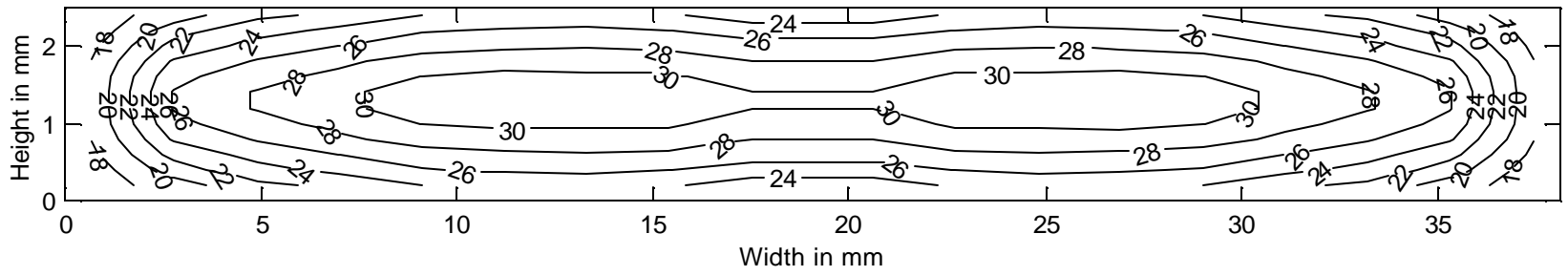


Figure B.1 Contour plot showing velocity profile measured using compressed air at a Reynolds number (based on half the duct height and average velocity) of 2125. Height scale twice width scale. Contours in m/s.

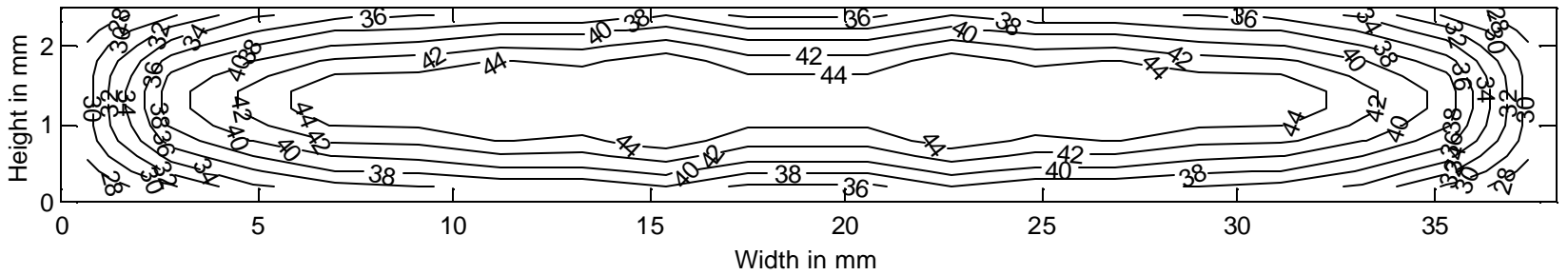


Figure B.2 Contour plot showing velocity profile measured using compressed air at a Reynolds number (based on half the duct height and average velocity) of 3170. Height scale twice width scale. Contours in m/s.

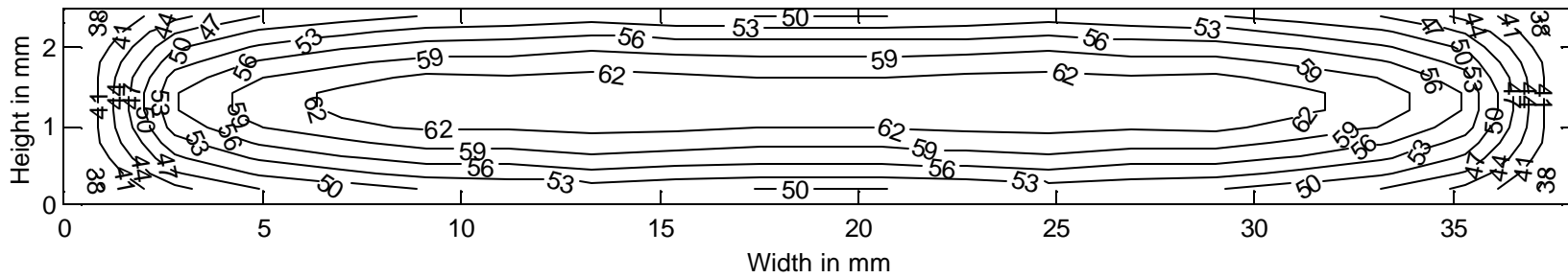


Figure B.3 Contour plot showing velocity profile measured using compressed air at a Reynolds number (based on half the duct height and average velocity) of 4415. Height scale twice width scale. Contours in m/s.

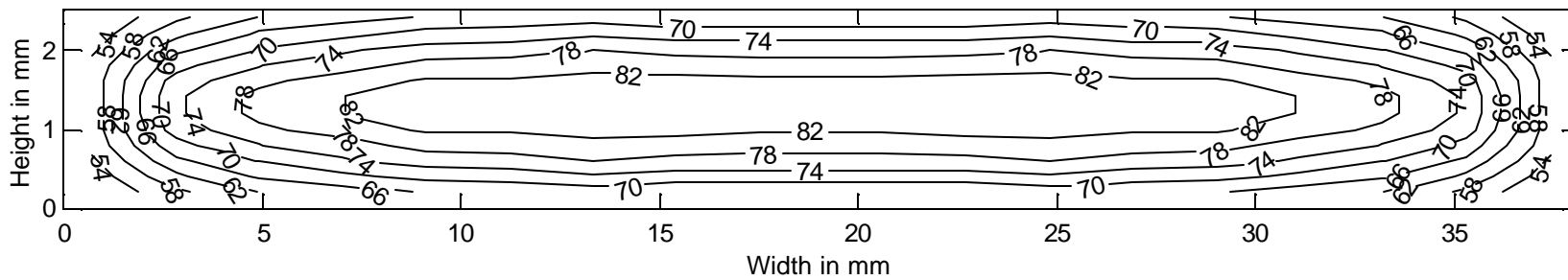


Figure B.4 Contour plot showing velocity profile measured using compressed air at a Reynolds number (based on half the duct height and average velocity) of 5860. Height scale twice width scale. Contours in m/s.

## Flow velocity data reduction program for EES (engineering equation solver) Ver 6.026.

(This program requires the creation of a parametric table with the Pitot tube measured differential pressures in inches of water (deltaP\_pitot))

### "Input data"

DPinh2o=20 "Venturi differential pressure in inH2O 3, 6, 10, 15, 20"  
PventInReal=15.7 "Venturi manometric pressure in psig 2.27, 4.3, 7.46, 11.44, 15.7"  
T1=22.12 "Air temperature in C"  
Pitotpress=1.45 "Pitot tube static pressure in psig 0, 0.1, 0.55, 1.0, 1.45"

### "Massflow section"

Patm=747 "mmHg"  
Pabs=Patm\*convert(mmHg,kPa) "kPa"  
Dt=0.375\*0.0254 "m"  
Di=0.8\*0.0254 "m"  
Ck=0.948

### "Areas"

At\_venturi=pi\*Dt^2/4 "m^2"  
Ai\_venturi=pi\*Di^2/4 "m^2"

### "Mass flow calculations"

Delta\_P=DPinh2o\*convert(inH2O,Pa) "Pa"  
rho\_i=DENSITY(air,T=T1,P=P1) "kg/m^3"  
P1=Pabs+PventInReal\*convert(psi,kPa) "kPa"  
P2=P1-delta\_P\*convert(Pa,kPa) "kPa"  
E=sqrt(Beta^4/(1-Beta^4))  
Beta=Dt/Di  
mdot=(Ck/1.05)\*Y\*At\_venturi\*sqrt((2\*Delta\_p\*rho\_i)/(1-beta^4)) "kg/s"  
Y=((1-(Dt/Di)^4)\*(k/(k-1))\*(P2/P1)^(2/k)\*(1-(P2/P1)^(k-1)/k))/((1-(Dt/Di)^4\*(P2/P1)^(2/k))\*(1-P2/P1))^(1/2)  
mdotg=1000\*mdot "g/s"

### "Channel average velocity"

Vel\_chan=mdot/(rho\_o\*A\_channel) "m/s"  
width=0.0381 "m"  
Height=0.0025 "m"  
A\_channel=width\*height "m^2"  
P\_pitot=Pabs+pitotpress\*convert(psi,kPa) "kPa"  
rho\_o=density(air,T=T1,P=P\_pitot) "kg/m^3"

### "Channel section"

B=5 "Logarithmic velocity profile constant"  
kk=0.41 "Logarithmic velocity profile constant"  
Perim=2\*(height+width) "Perimeter in m"  
mu=VISCOSITY(air,T=T1) "Dynamic viscosity kg/(m s)"  
rho=DENSITY(air,T=T1,P=P\_pitot) "Density in kg/m^3"  
nu=mu/rho "Kinematic viscosity in m^2/s^2"  
Le=4.4\*Dh\*Re\_Dh^(1/6) "Entrance length in m"  
Re\_Dh=(Dh\*Vel\_Chan)/nu "Reynolds Number based on hydraulic diamter and average velocity"  
Re\_h2=(Height/2)\*Vel\_Chan/nu "Reynolds number based on channel half height and average velocity"  
Dh=(0.64)^4\*A\_channel/(Perim) "Corrected hydraulic diameter (see With Fluid mechanics)"  
Dh2=2\*Height "hydraulic diameter for parallel plates flow"  
Vel\_Chan=u\_star\*((1/kk)\*ln((height\*u\_star)/(2\*nu))+B-(1/kk)) " Average velocity equation to obtain value of u\* avergae velocity from mass flow measurements"

Vmax=Vel\_chan\*u[30] *"Maximum velocity at center of channel m/s"*

Duplicate j=1,30

Pos[j]=((height/2)\*j)/30 *"Position where u(y) is calculated in m"*

u[j]=u\_star\*((1/kk)\*ln((Pos[j]\*u\_star)/(nu))+B) /Vel\_Chan *"Normalized velocity profile"*

Posmm[j]=Pos[j]\*1000 *"Position where u(y) is calculated in mm"*

End

*"Pitot tube equations"*

DELTAP=deltaP\_pitot\*convert(inH2O,kpa) *"kPa"*

K\_pitot= 0.9 *"Pitot constant"*

GAMMA\_pitot=sqrt(1-(1/(2\*k))\*(DELTAP/P\_pitot)+((k-1)/(6\*k^2))\*(DELTAP/P\_pitot)^2) *"Gas compressibility constant"*

Vel=K\_pitot\*GAMMA\_pitot\*sqrt(2\*DELTAP\*1000/rho) *"Velocity m/s"*

*"Auxiliary information"*

*"Speed of sound calculation"*

c\_ideal=sqrt(k\*R\*1000\*(T1+273.15)) *"ideal gas approximation m/s"*

c=sqrt(dp\*convert(kPa,Pa)/drho) *"m/s"*

dp=0.01 *"kPa"*

drho=density2-density1 *"kg/m^3"*

density1=density(air,P=P1,T=T1) *"kg/m^3"*

entropy1=entropy(air,P=P1,T=T1) *"kJ/(kg K)"*

density2=density(air,P=P1+dp,s=entropy1) *"kg/m^3"*

*"This section is to obtain the value of the isentropic coefficient k"*

Cv=Cp-R *"kJ/(kg K)"*

Mm=MOLARMASS(air) *"kg/kmol"*

Ru=8.3144 *"kJ/(kmol K)"*

R=Ru/Mm *"kJ/(kg K)"*

Cp=SPECHEAT(air,T=T1) *"kJ/(kg K)"*

k=Cp/Cv



## Appendix C: Plate Sample Acceleration Measurement Test Results

### Plate Evaporator A

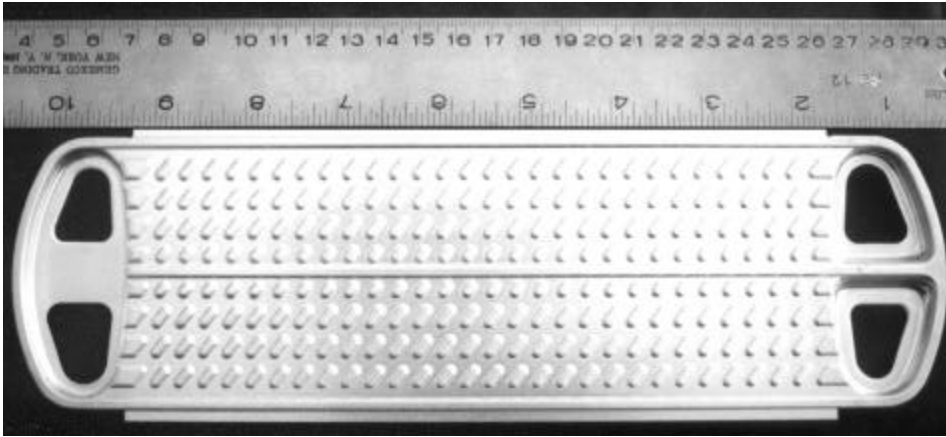


Figure C.1 Photograph of plate A showing details of internal structure. The flow enters one side and exits the other side. The two passages are not connected. For our testing only one passage was used.

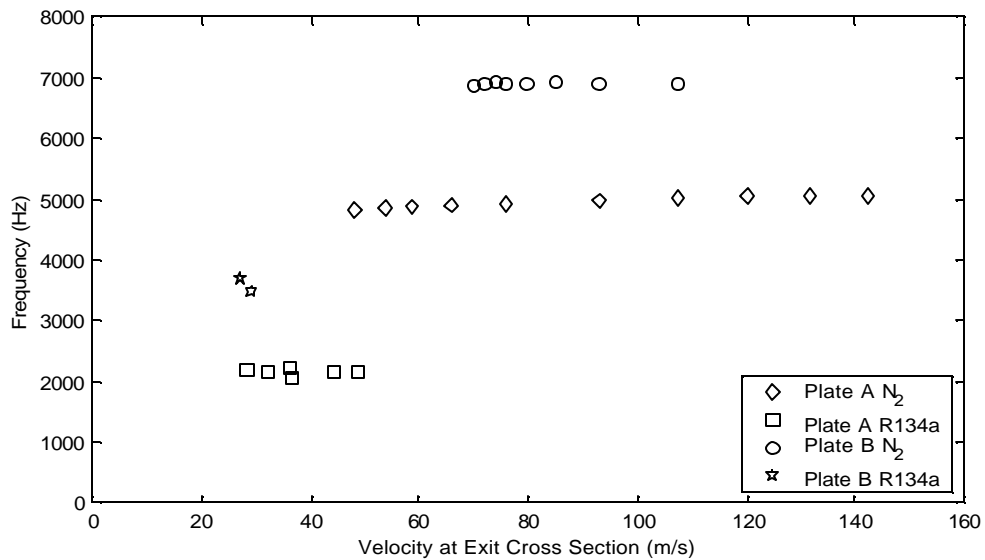


Figure C.2 Frequencies at peaks in acceleration spectra for nitrogen and R134a tests. Differences in the frequencies caused by variations in speed of sound for the two fluids. Plate B identical to plate A except that a wire (baffle) was introduced in the center of the plates.

# Plate Evaporator C

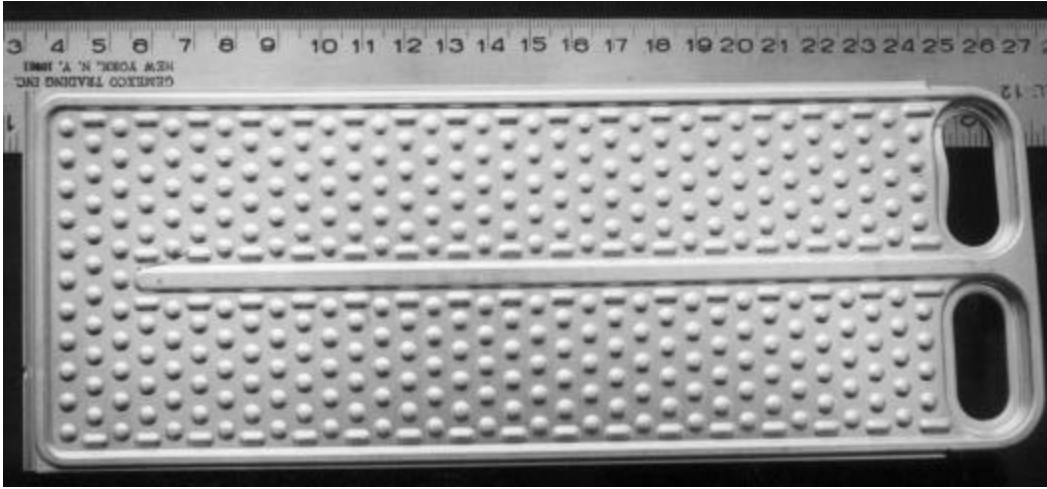


Figure C.3 Photograph of plate C showing details of internal structure.

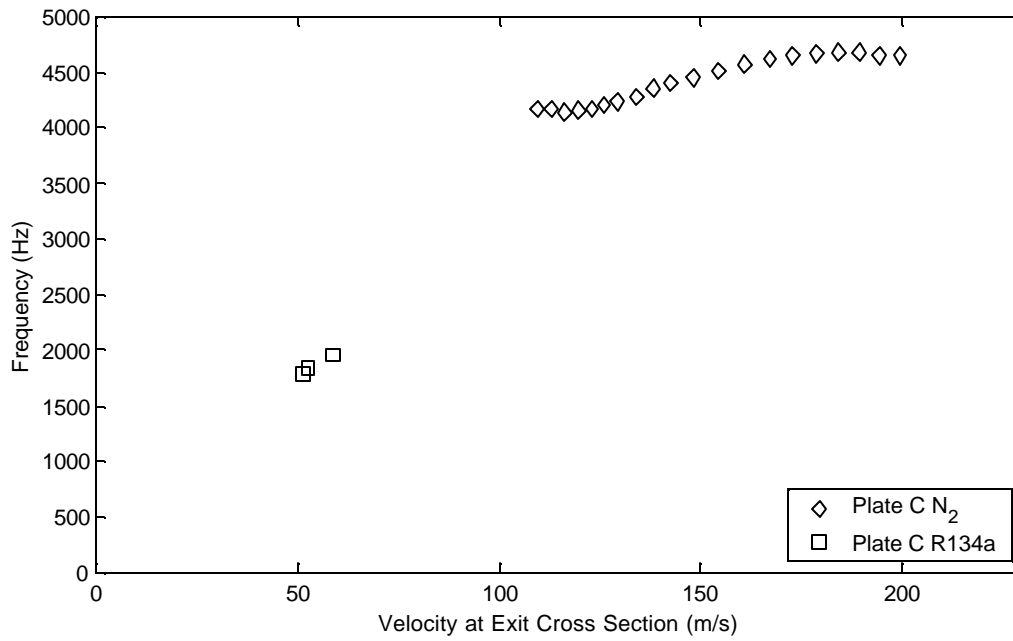


Figure C.4 Frequencies at peaks in acceleration spectra for nitrogen and R134a tests. Plate C.

## Plate Evaporator D

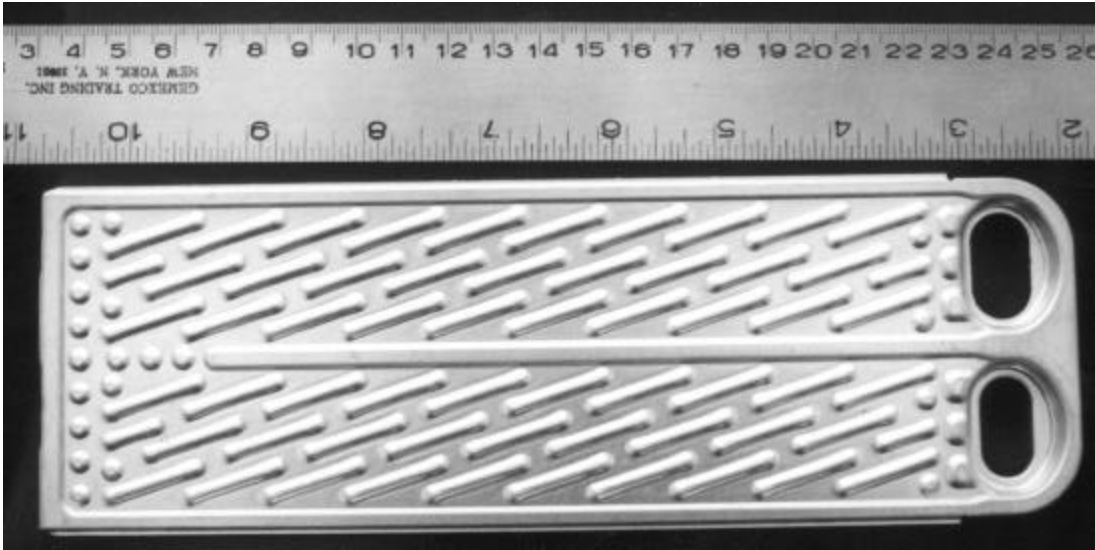


Figure C.5 Photograph of plate D showing details of internal structure.

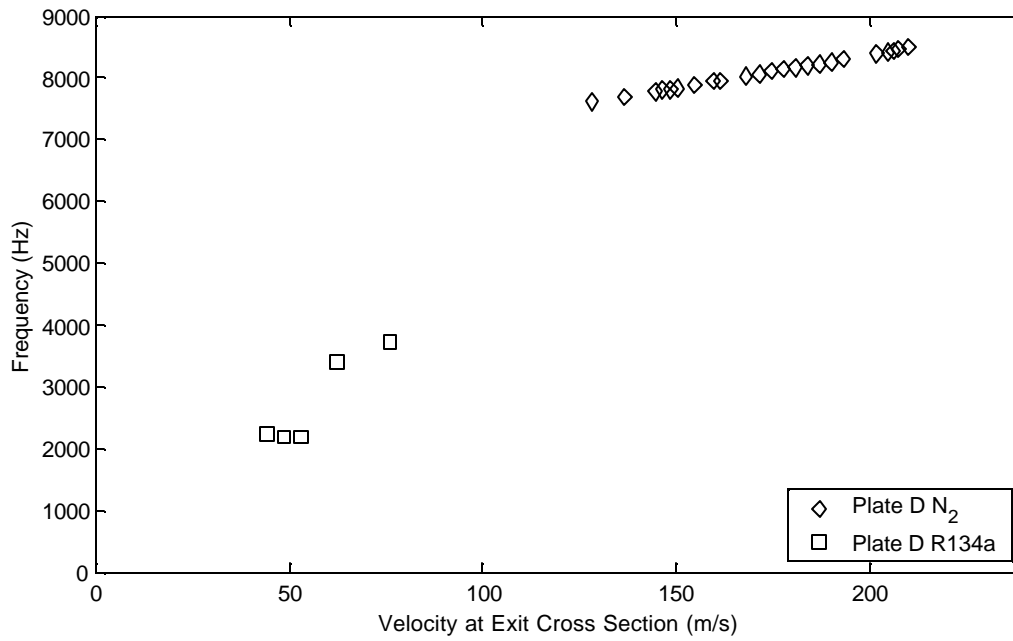


Figure C.6 Frequencies at peaks in acceleration spectra for nitrogen and R134a tests. Plate D.

# Plate Evaporator E

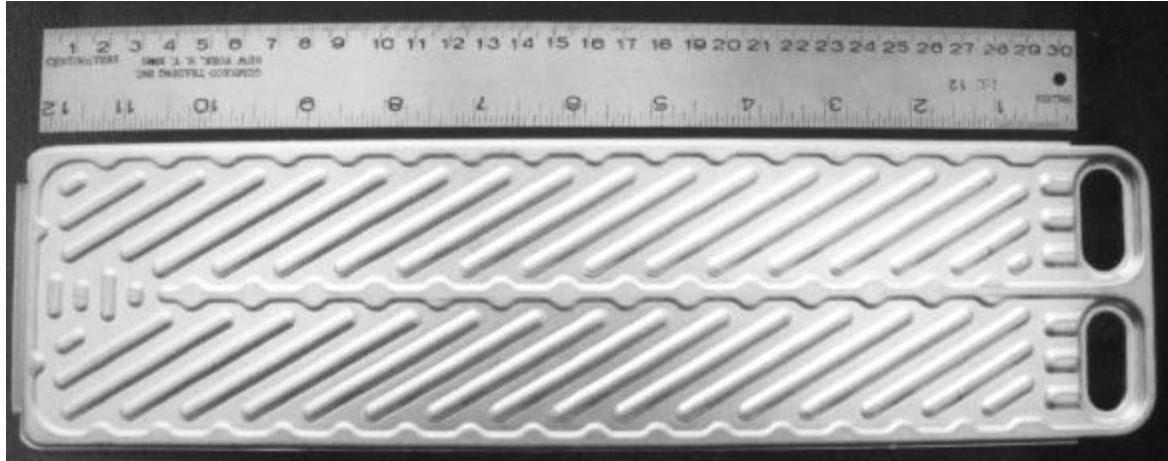


Figure C.7 Photograph of plate E showing details of internal structure.

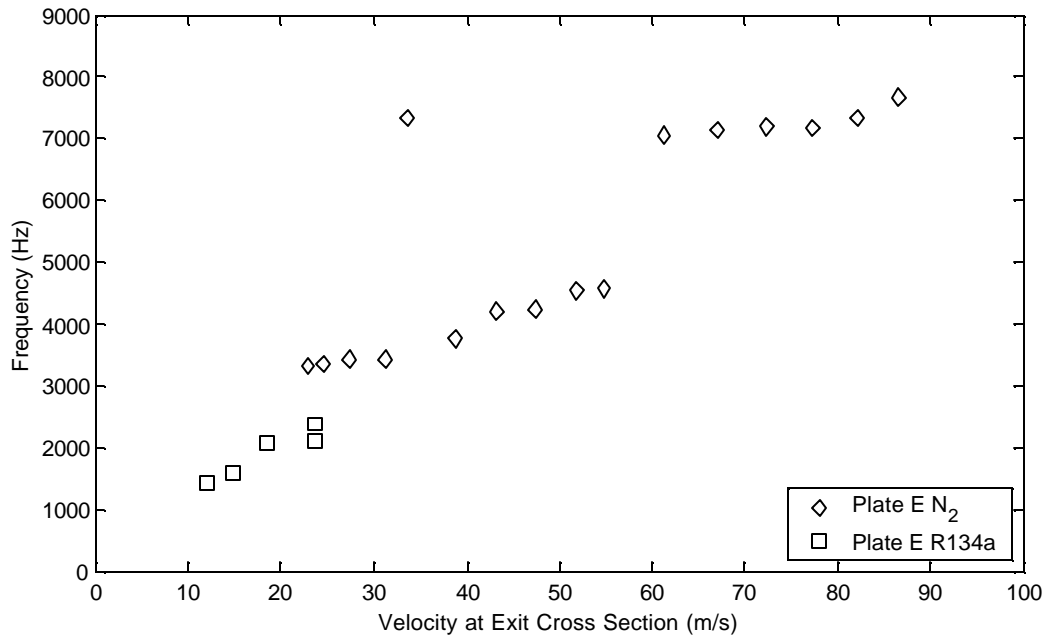


Figure C.8 Frequencies at peaks in acceleration spectra for nitrogen and R134a tests. Plate E.

## Plate Evaporator F

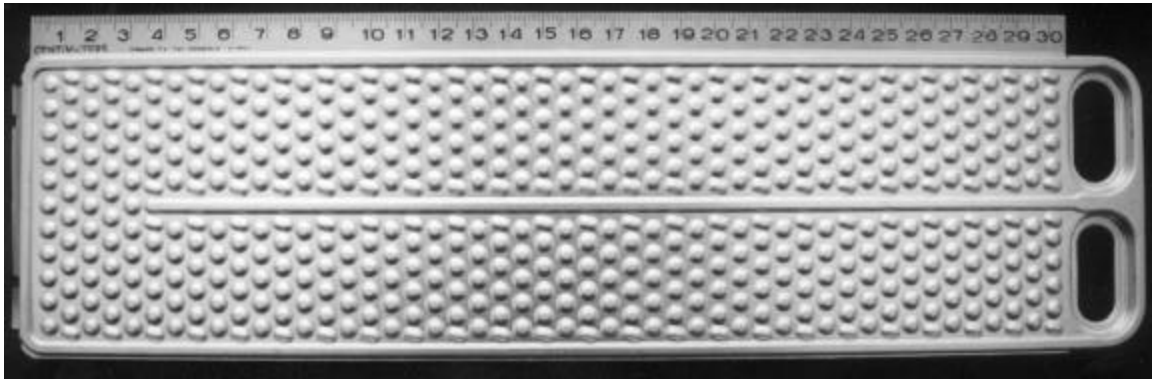


Figure C.9 Photograph of plate F showing details of internal structure.

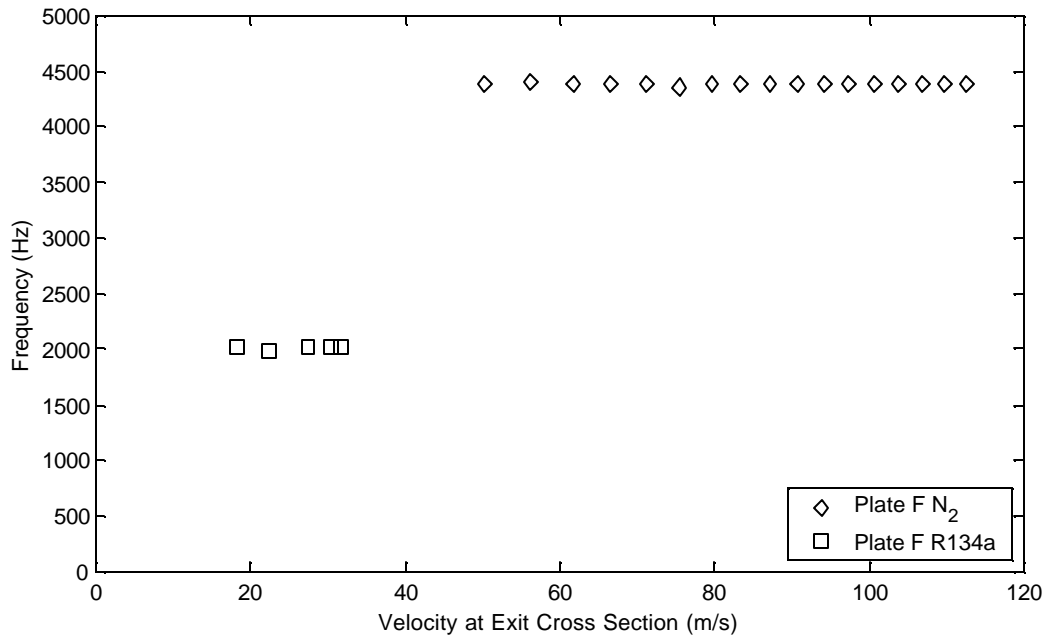


Figure C.10 Frequencies at peaks in acceleration spectra for nitrogen and R134a tests. Plate F.

## Plate Evaporator G

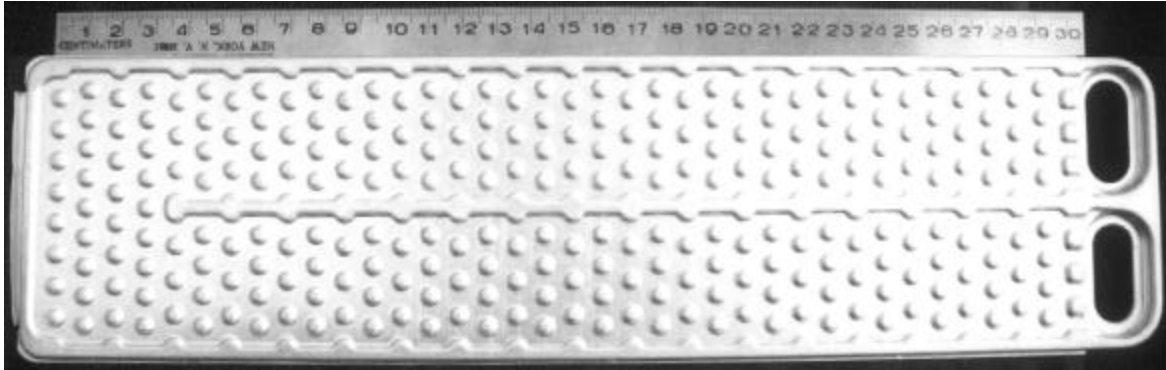


Figure C.11 Photograph of plate G showing details of internal structure.

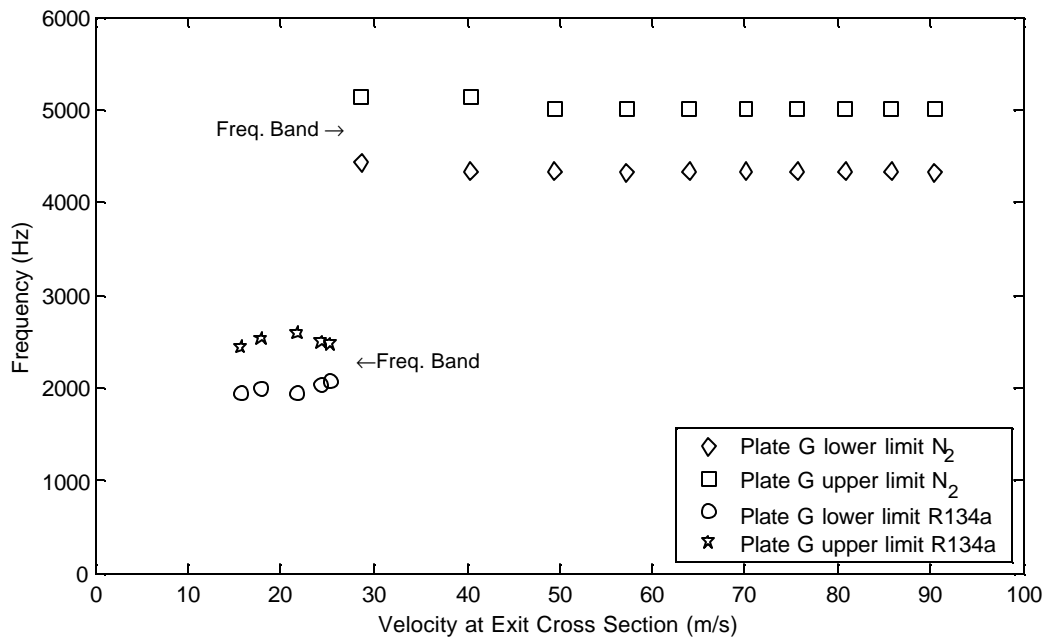


Figure C.12 Frequencies at peaks in acceleration spectra for nitrogen and R134a tests. The spectra exhibit closely spaced peaks indicated as “frequency bands” in figure above. Plate G.

## Appendix D: Plate Sample Dynamic Pressure Test Results

### Plate Evaporator A2

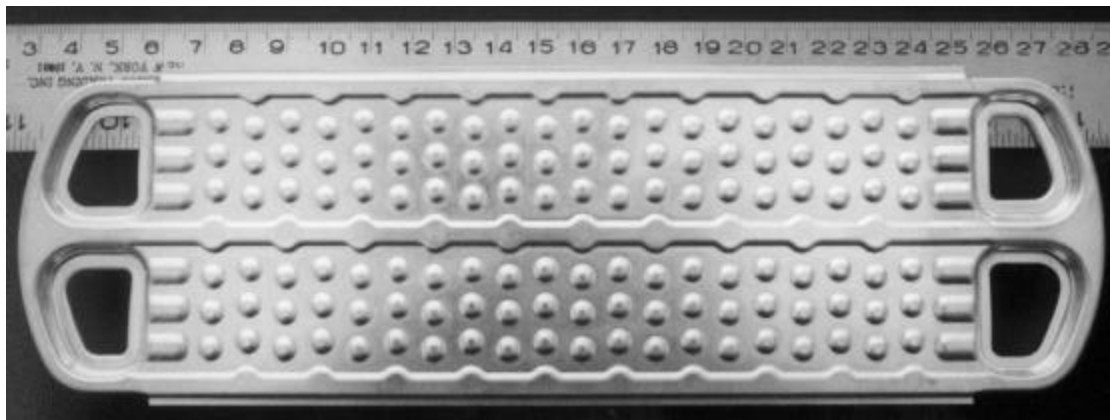


Figure D.1 Photograph of plate A2 showing details of internal structure.

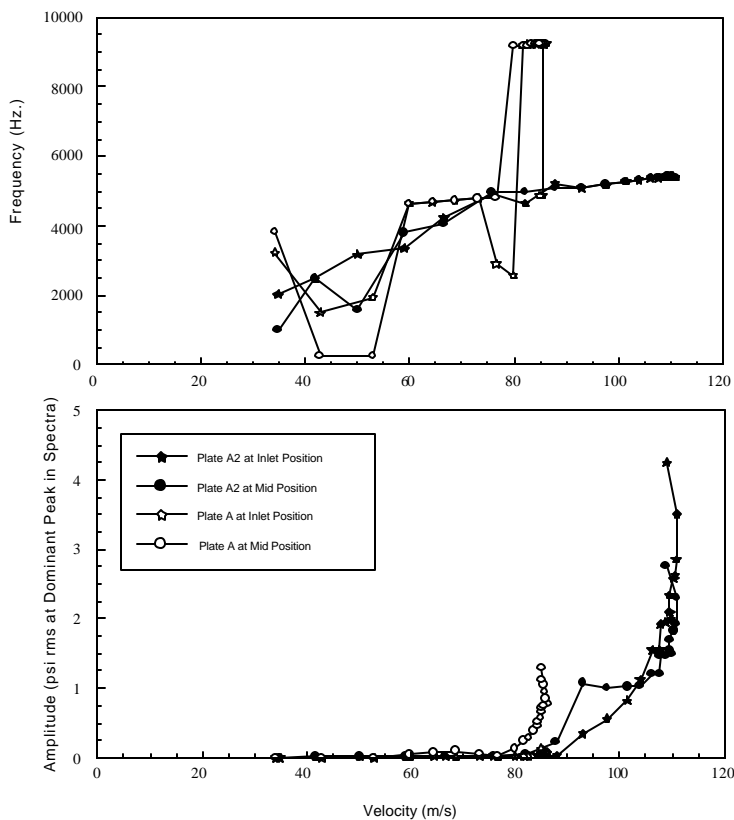


Figure D.2 Frequency-velocity and amplitude-velocity plots made from values of peaks in dynamic pressure spectra obtained using nitrogen for plates A and A2.

# Plate Evaporator C2

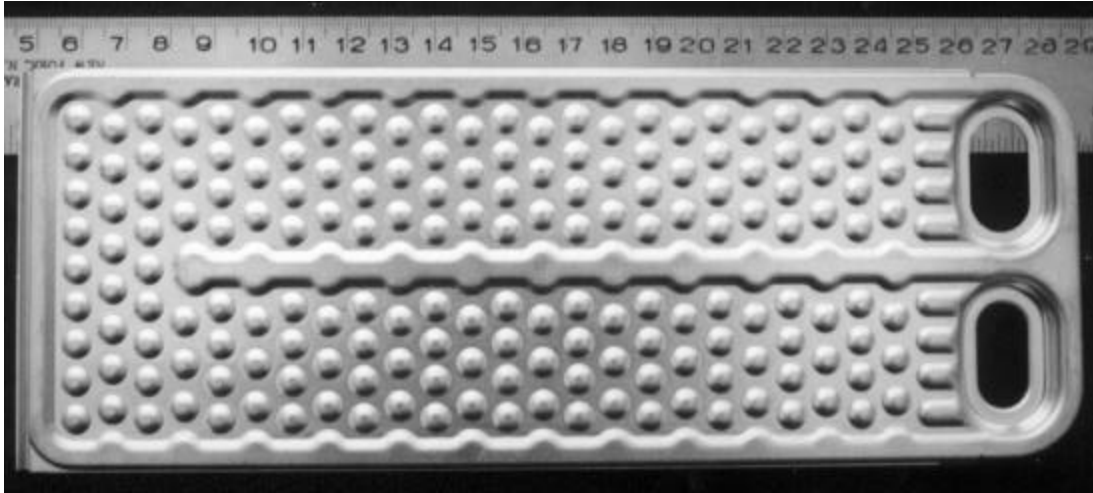


Figure D.3 Photograph of plate C2 showing details of internal structure.

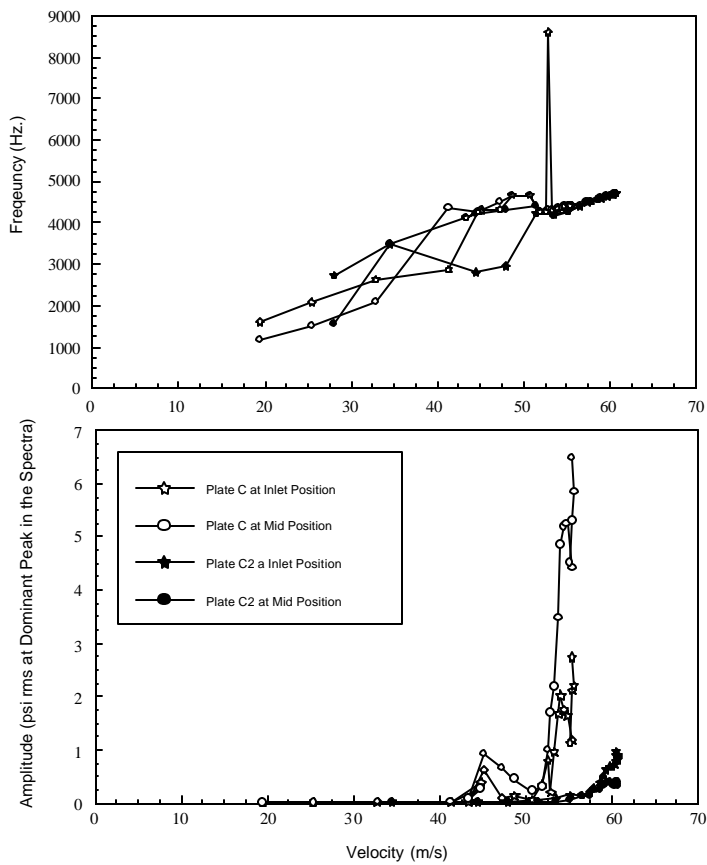


Figure D.4 Frequency-velocity and amplitude-velocity plots made from values of peaks in dynamic pressure spectra obtained using nitrogen for plates C and C2.



## Plate Evaporator F2

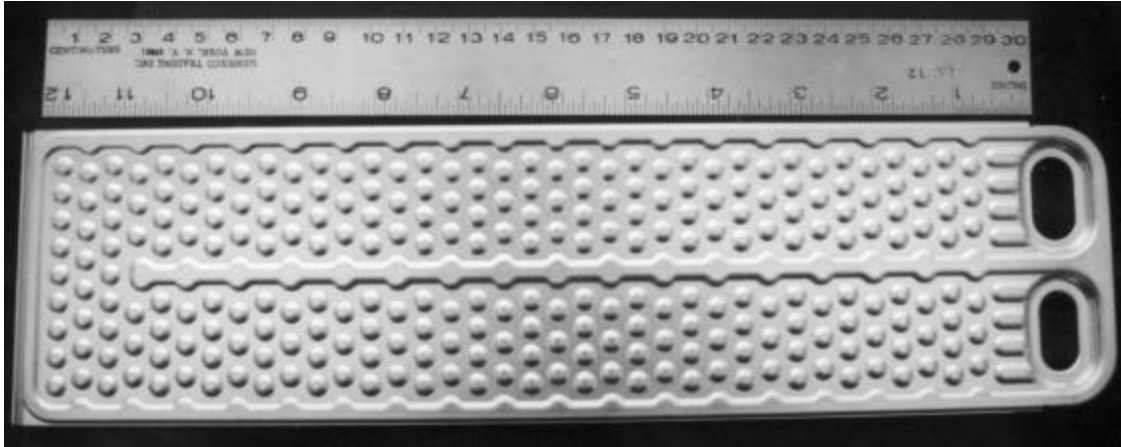


Figure D.5 Photograph of plate F2 showing details of internal structure.

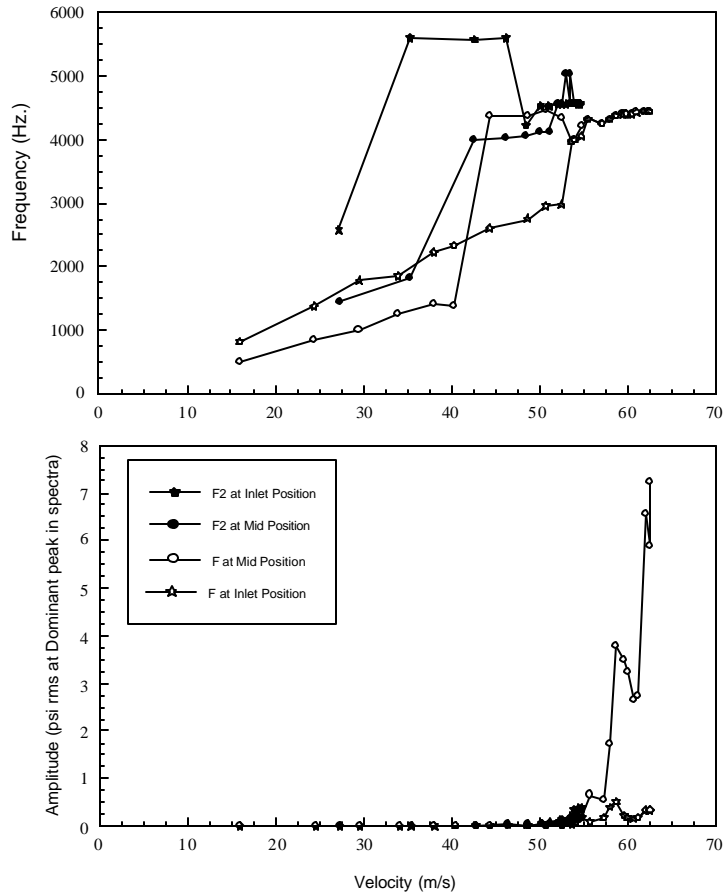


Figure D.6 Frequency-velocity and amplitude-velocity plots made from values of peaks in dynamic pressure spectra obtained using nitrogen for plates F and F2.

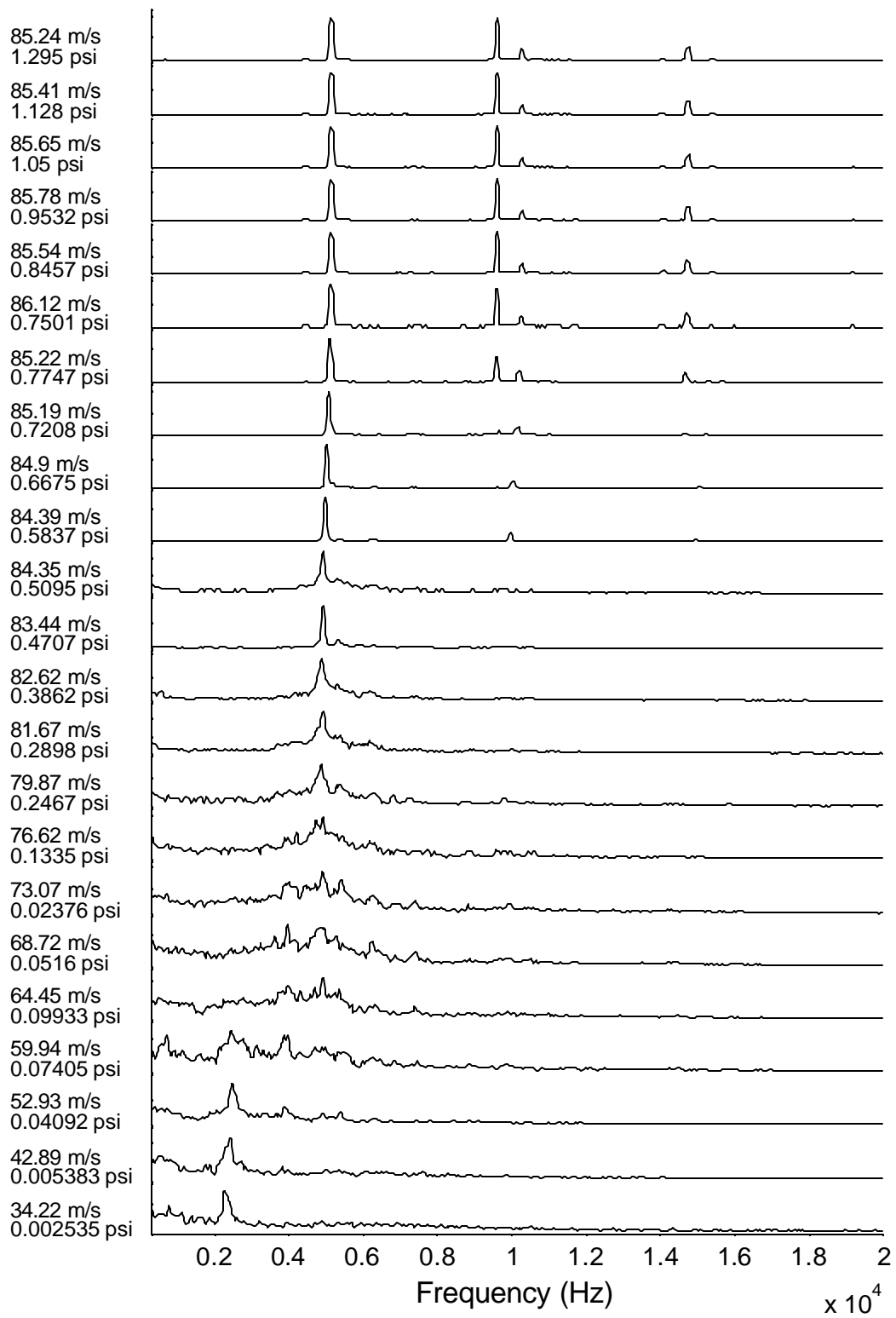


Figure D.7 Dynamic pressure spectrum of plate sample A taken at inlet position. Inlet velocity and maximum pressure are plotted on the left.

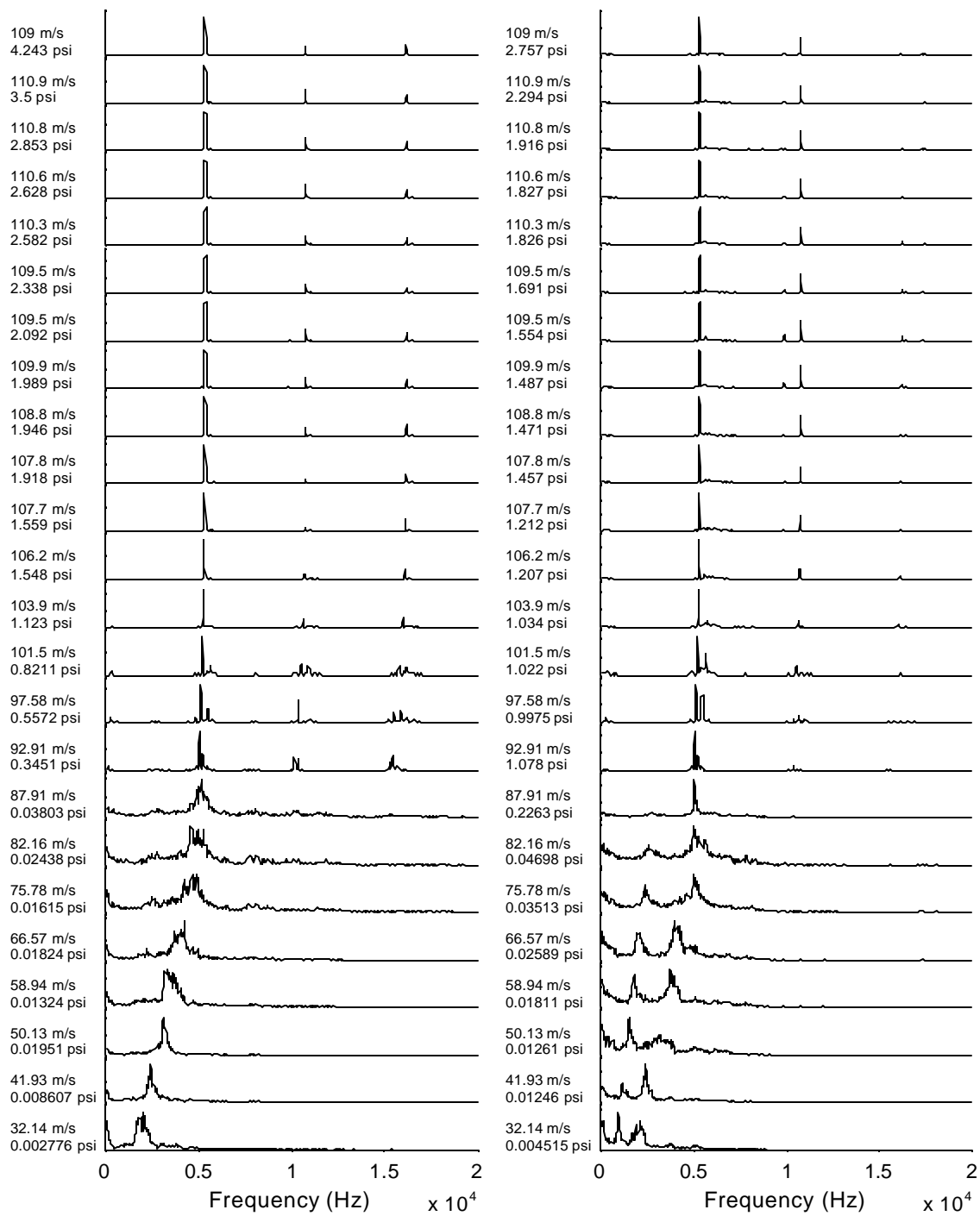


Figure D.8 Dynamic pressure spectrum of plate sample A2 taken at inlet and mid positions (left and right plots respectively). Inlet velocity and maximum pressure are plotted on the left.

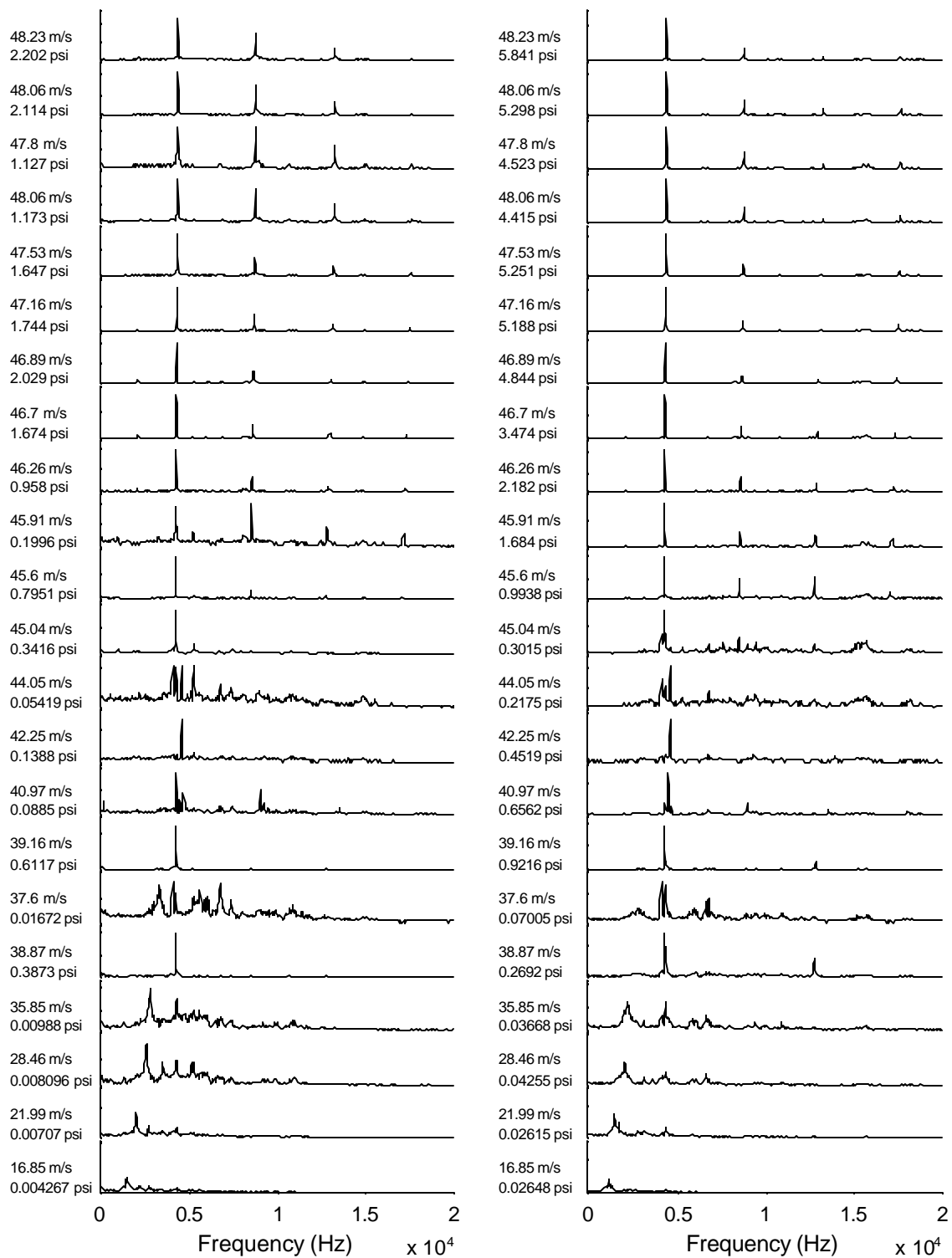


Figure D.9 Dynamic pressure spectrum of plate sample C taken at inlet and mid positions (left and right plots respectively). Inlet velocity and maximum pressure are plotted on the left.

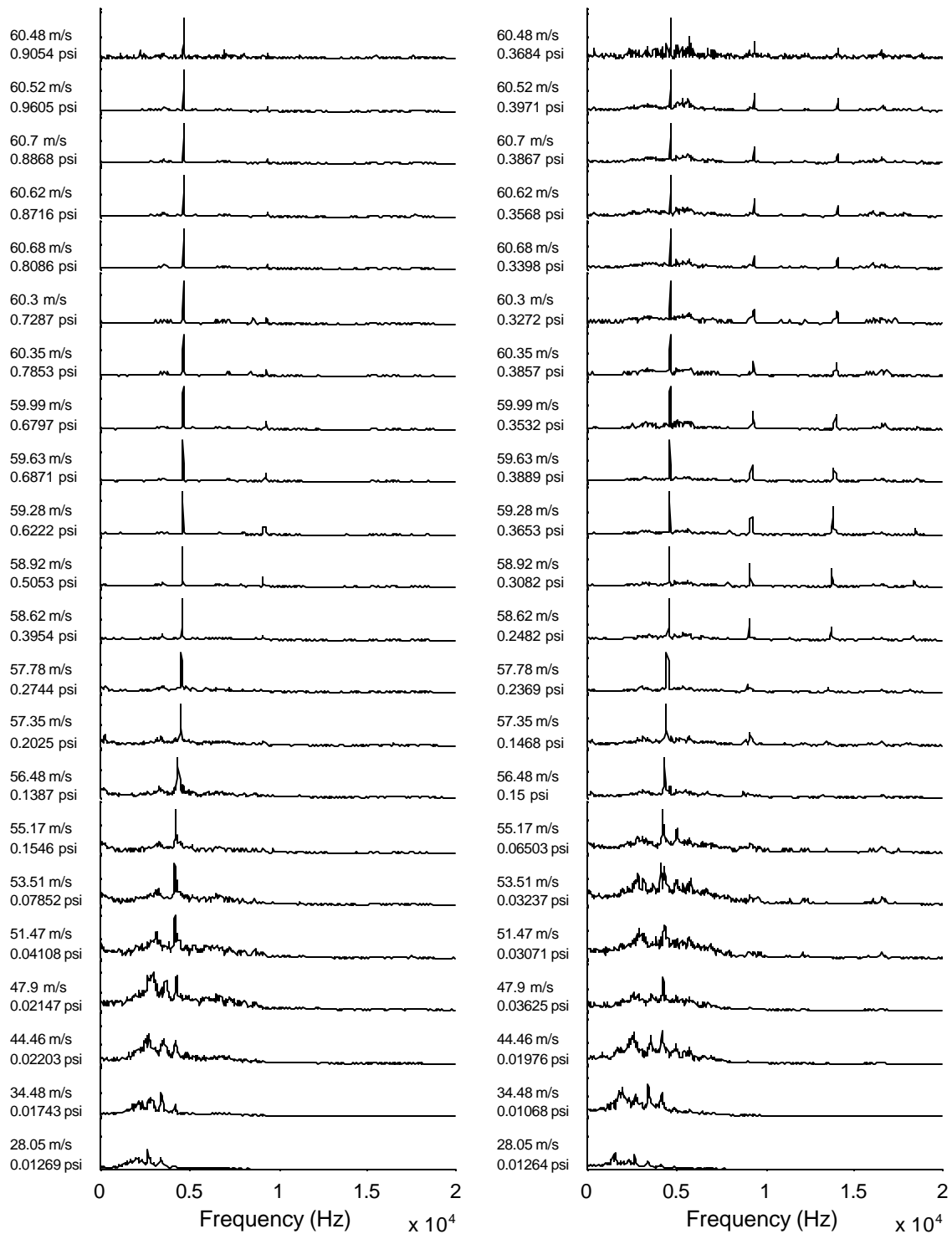


Figure D.10 Dynamic pressure spectrum of plate sample C2 taken at inlet and mid positions (left and right plots respectively). Inlet velocity and maximum pressure are plotted on the left.

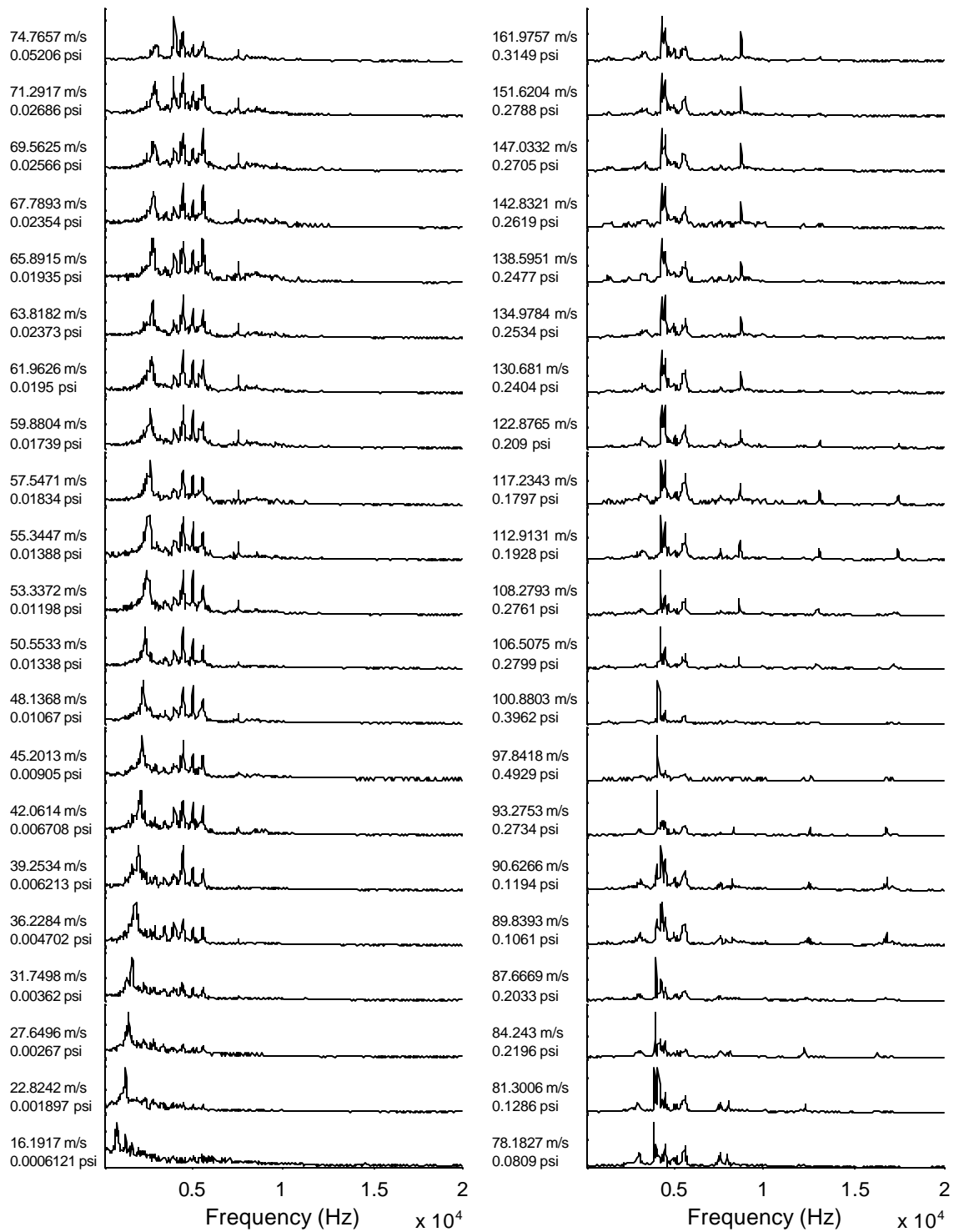


Figure D.11 Dynamic pressure spectrum of plate sample F taken at mid position (right plots continue from end of left plots). Outlet velocity and maximum pressure are plotted on the left.

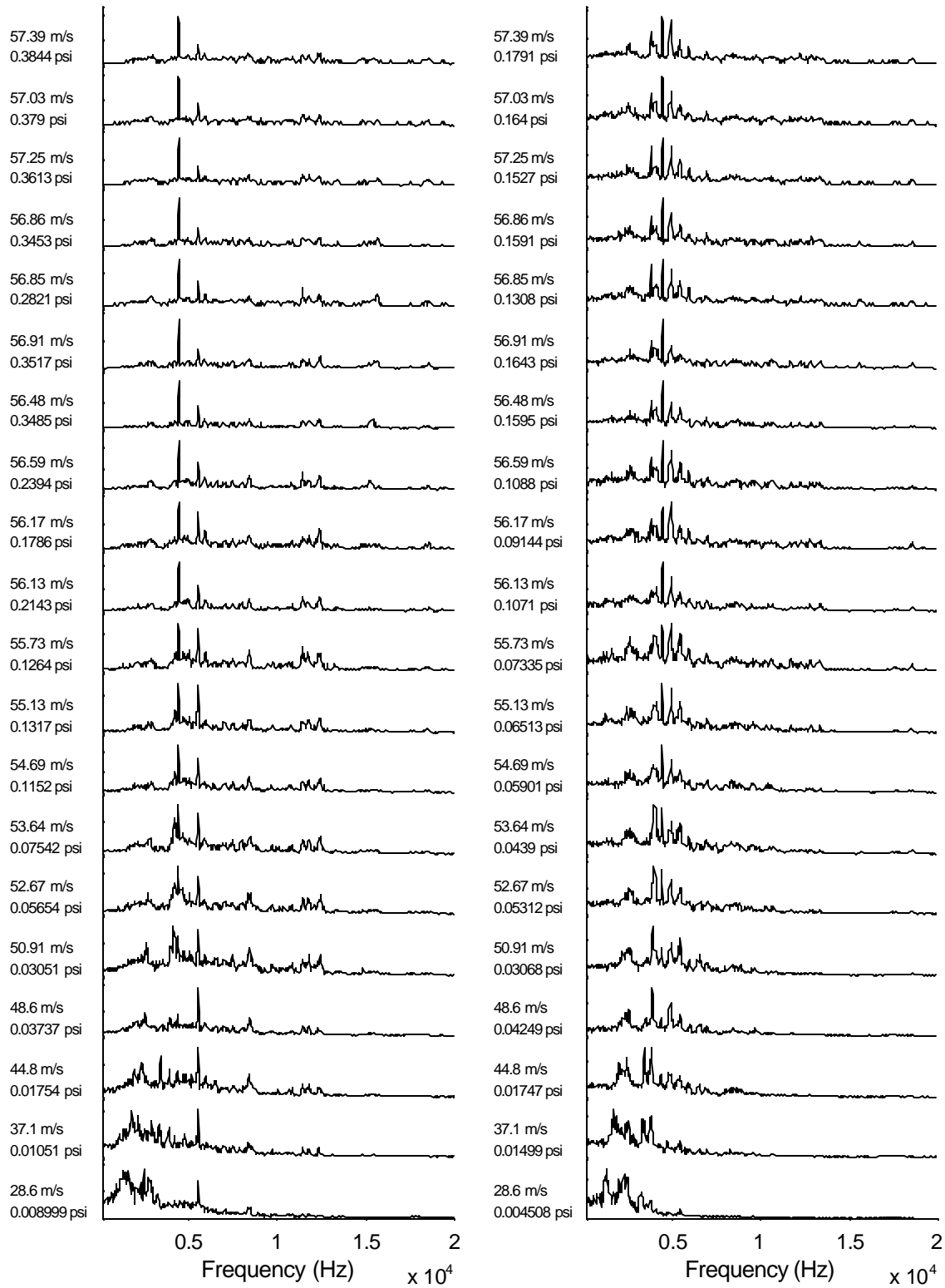


Figure D.12 Dynamic pressure spectrum of plate sample F2 taken at inlet and mid positions (left and right plots respectively). Inlet velocity and maximum pressure are plotted on the left.

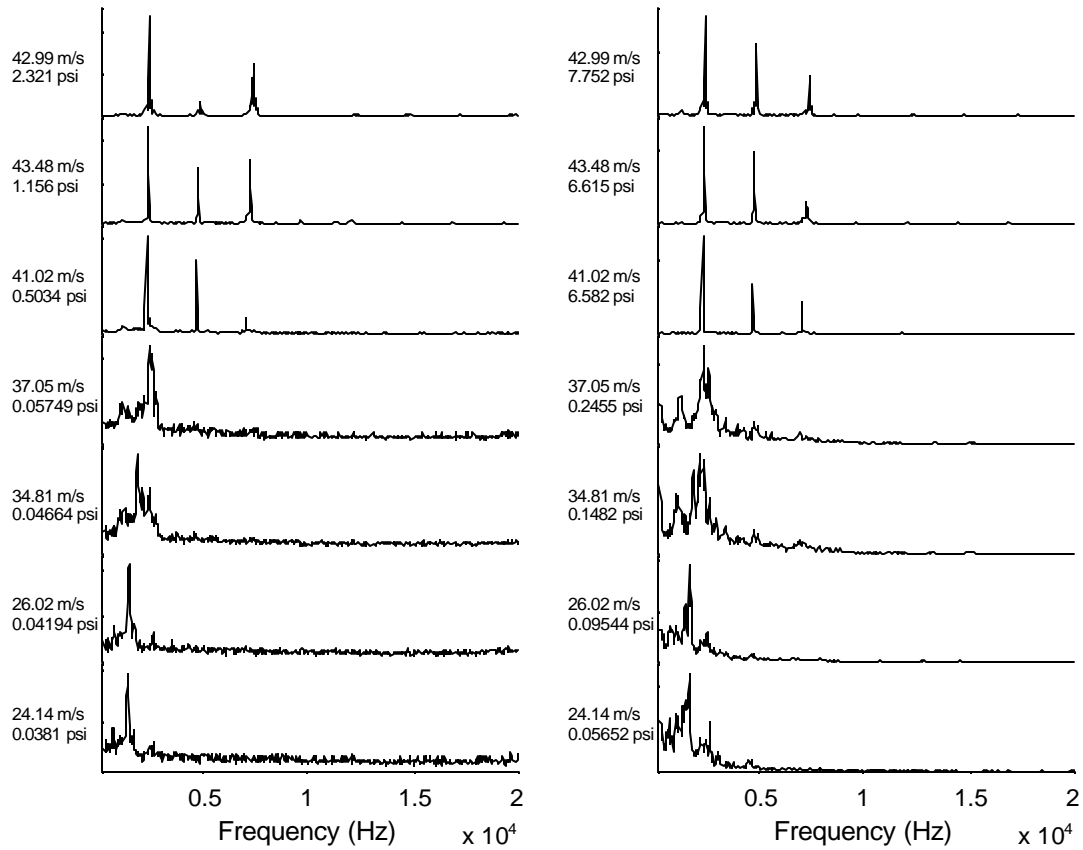


Figure D.13 Dynamic pressure spectrum of plate sample A2 taken using R134a refrigerant. Inlet and mid positions (left and right plots respectively). Inlet velocity and maximum pressure are plotted on the left.

Table D.1. R134a Refrigerant test conditions plate A2 tests.

P in bars	P out bars	T in °C	T out °C	Mass Flow lb/h	Vel In m/s	Vel out m/s	Inlet Super Heat °C	Outlet Super Heat °C	Inlet Density kg/m <sup>3</sup>	Outlet Density kg/m <sup>3</sup>	Pres. Drop psi	Inlet Sound Speed m/s	Outlet Sound Speed m/s
4.60	4.19	22.7	22.0	80.6	24.14	26.69	9.7	11.7	21.37	19.32	5.904	150.1	151.1
4.93	4.48	38.9	34.5	86.9	26.02	28.36	23.7	22.2	21.37	19.6	6.571	155.7	155.2
5.15	4.35	56.5	51.1	113.1	34.81	40.94	39.8	39.7	20.79	17.67	11.68	161.6	161.5
5.35	4.32	61.0	56.4	123.1	37.05	45.80	43.2	45.2	21.25	17.19	14.9	162.8	163.4
5.84	4.37	60.3	55.9	150.5	41.02	55.28	39.6	44.3	23.47	17.42	21.41	161.5	163.1
6.30	4.46	61.2	56.2	172.8	43.48	62.12	38.1	44.0	25.42	17.79	26.76	160.9	163
6.61	4.52	55.9	52.3	184.2	42.99	64.23	31.2	39.7	27.41	18.34	30.23	158.2	161.6



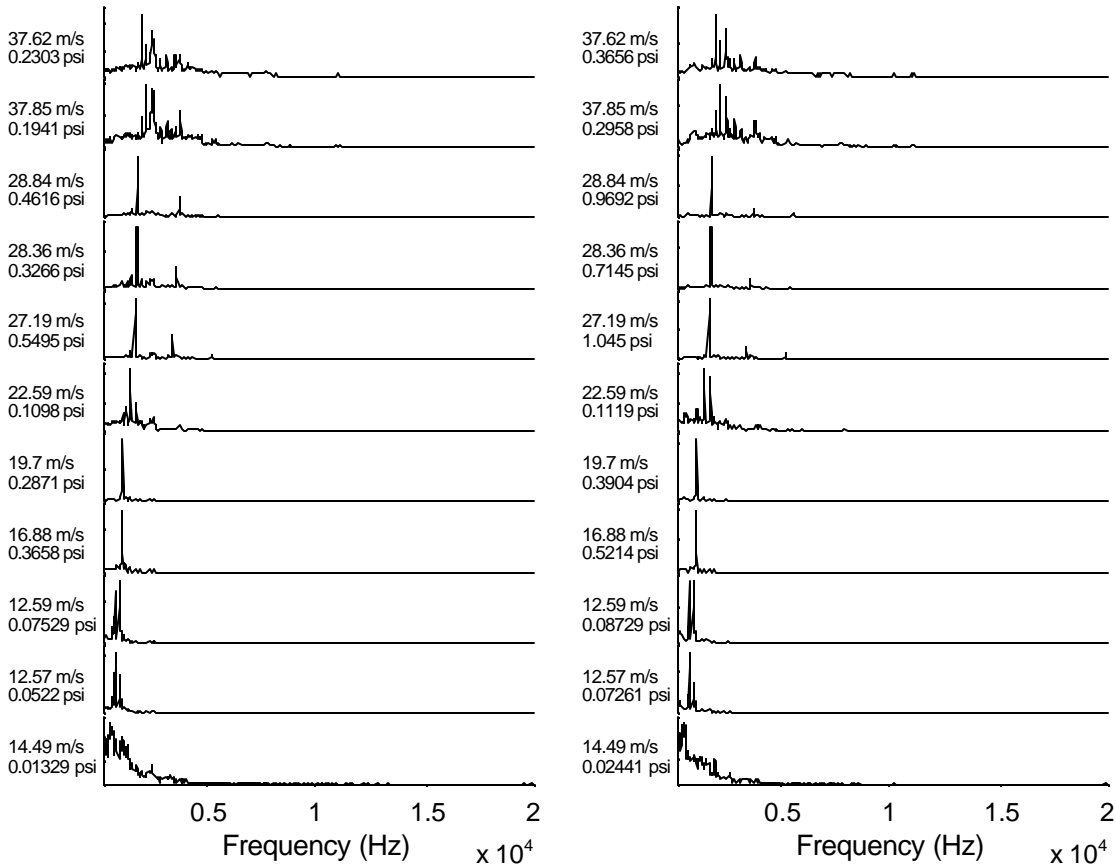


Figure D.14 Dynamic pressure spectrum of plate sample F2 taken using R134a refrigerant. Mid and outlet positions (left and right plots respectively). Outlet velocity and maximum pressure are plotted on the left.

Table D.2. R134a Refrigerant test conditions plate F2 tests.

P in bars	P out bars	T in °C	T out °C	Mass Flow lb/h	Vel In m/s	Vel out m/s	Inlet Super Heat °C	Outlet Super Heat °C	Inlet Density kg/m <sup>3</sup>	Outlet Density kg/m <sup>3</sup>	Pres. Drop psi	Inlet Sound Speed m/s	Outlet Sound Speed m/s
5.28	4.66	17.3	13.9	79.4	0.27	14.49	Sat.	Sat.		22.79	8.988		145.9
4.75	4.43	28.6	25.8	61.0	11.77	12.57	14.5	13.8	20.18	21.55	4.707	152	151.9
4.76	4.45	25.4	22.8	62.3	11.80	12.59	11.2	10.7	20.57	21.96	4.619	150.6	150.6
4.90	4.42	40.0	37.1	77.6	15.29	16.88	25.0	25.2	19.11	21.09	6.826	156.2	156.4
5.09	4.47	44.5	41.4	89.8	17.32	19.70	28.3	29.2	18.96	21.56	8.963	157.4	157.8
5.51	4.61	49.0	44.2	105.4	18.99	22.59	30.3	31.0	19.4	23.08	12.96	158.1	158.5
5.87	4.50	29.8	26.5	134.0	20.43	27.19	9.0	14.0	20.49	27.27	19.84	149.1	151.9
5.71	4.38	51.8	46.9	123.7	21.67	28.36	31.9	35.2	18.14	23.74	19.28	158.7	160
6.04	4.64	62.9	58.5	127.8	22.08	28.84	41.2	45.1	18.42	24.07	20.19	162.1	163.4
6.53	4.35	51.0	46.1	164.2	24.65	37.85	26.6	34.7	18.04	27.7	31.71	156.4	159.8
6.73	4.37	47.3	43.4	166.1	23.69	37.62	22.0	31.8	18.36	29.15	34.17	154.4	158.8

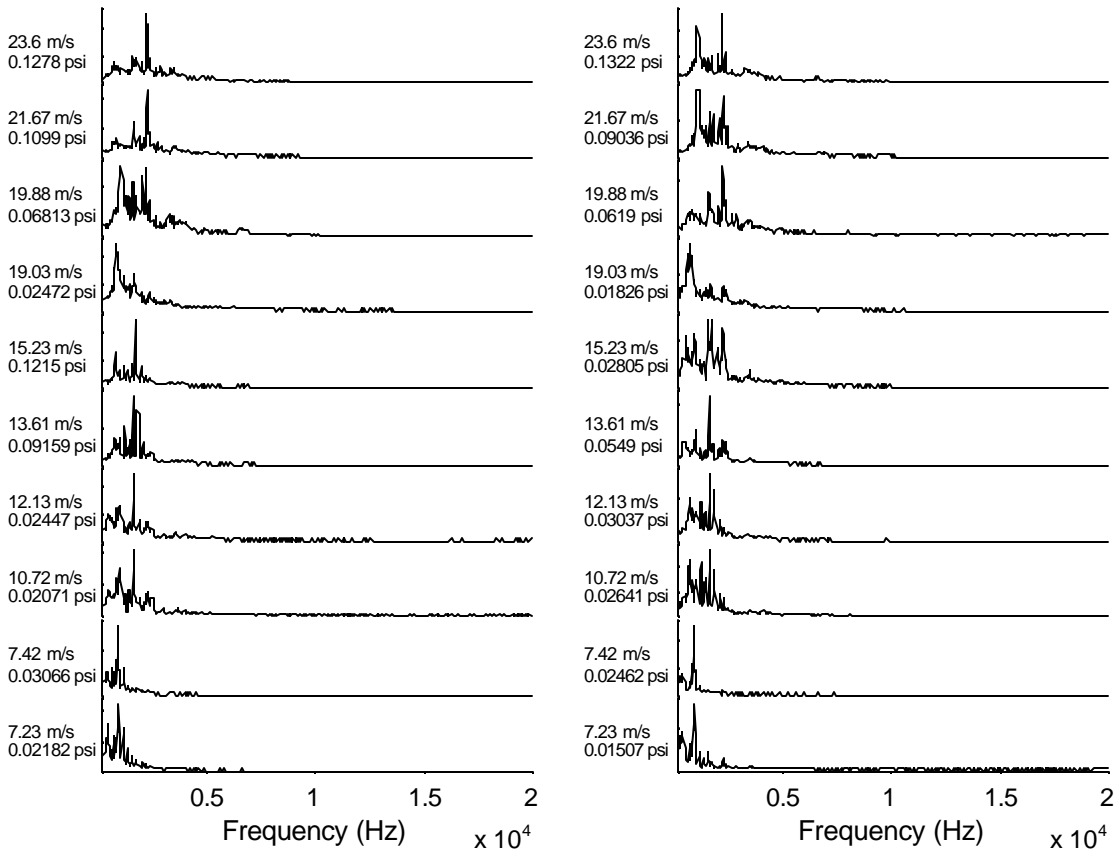


Figure D.15 Dynamic pressure spectrum of plate sample F taken using R134a refrigerant. Inlet and mid positions (left and right plots respectively). Outlet velocity and maximum pressure are plotted on the left.

Table D.3. R134a Refrigerant test conditions plate F tests.

P in bars	P out bars	T in °C	T out °C	Mass Flow lb/h	Vel In m/s	Vel out m/s	Inlet Super Heat °C	Outlet Super Heat °C	Inlet Density kg/m <sup>3</sup>	Outlet Density kg/m <sup>3</sup>	Pres. Drop psi	Inlet Sound Speed m/s	Outlet Sound Speed m/s
5.14	4.86	23.0	15.3	48.8	7.09	7.23	6.4	0.5	23.76	24.24	3.964	148.4	145.8
6.08	5.82	36.3	20.1	59.9	7.68	7.42	14.4	Sat.	28.4	27.42	3.735	151.4	145
4.12	3.63	31.9	8.0	53.9	10.47	10.72	22.1	2.0	17.68	18.11	7.197	155.2	147.2
4.11	3.63	32.0	7.9	61.0	11.88	12.13	22.2	1.9	17.69	18.06	7.06	155.3	147.2
6.83	5.91	41.7	19.1	111.4	12.84	13.61	15.8	Sat.	28.81	30.53	13.44	151.6	144.9
5.94	5.00	21.8	13.6	105.7	12.86	15.23	0.6	Sat.	24.43	28.92	13.5	145	145.7
6.70	5.18	17.1	14.3	136.6	14.71	19.03	Two- phase	Two- Phase	25.27	32.69	22.09	144.2	145.5
6.07	4.59	24.3	10.0	126.7	15.24	19.88	2.4	Sat.	22.42	29.24	21.46	145.7	146
6.19	4.52	32.0	9.3	135.9	16.70	21.67	9.4	Sat.	22.08	28.65	24.24	149	146
6.20	4.48	21.8	9.0	146.8	17.09	23.60	Sat.	Sat.	21.89	30.23	24.98	144.6	146.1

## Appendix E: In-line Square Arrays Test Results

### In-line Square Array with P/D = 2.0

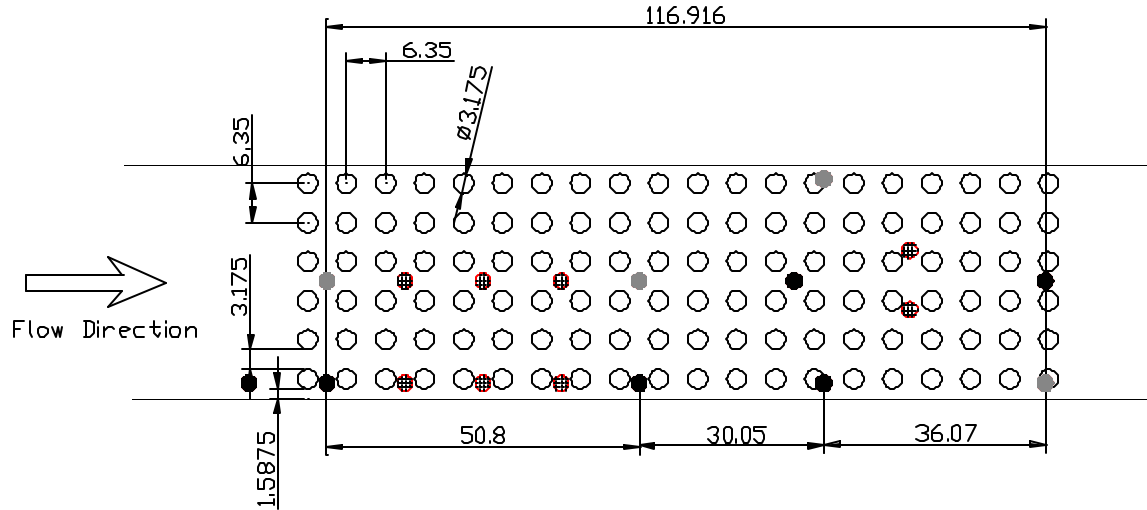


Figure E.1 Schematic of in-line square array tested with  $P/D = T/D = L/D = 2.0$ . Black dots represent microphone positions. Gray dots represent positions where static pressure measurements were made. Hatched dots are plugged microphone locations. Dimensions in mm. Drawing to scale.

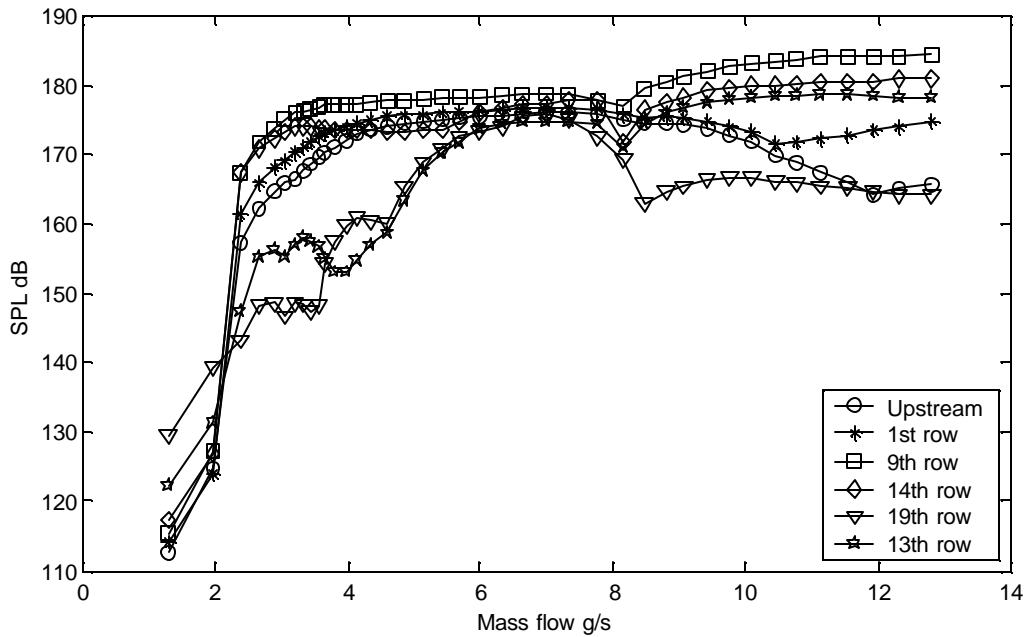


Figure E.2 Sound pressure level of dominant peak in spectra. Microphone positions shown in Figure E.1. Inline array with  $T/D = L/D = 2.0$ .

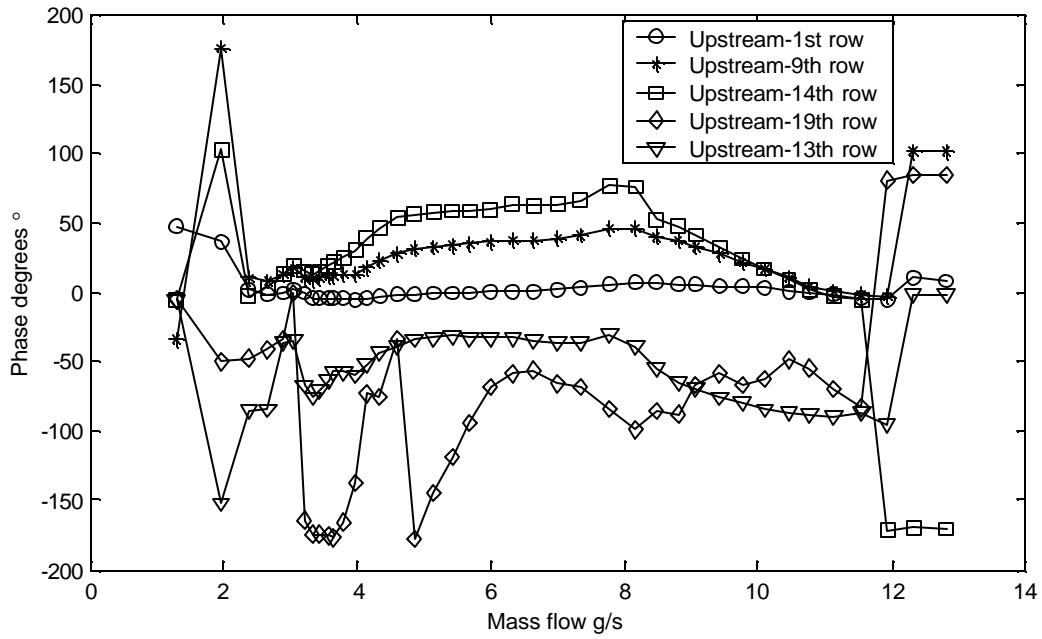


Figure E.3 Transfer function phase between microphone pairs shown at frequency of dominant peak in spectra of upstream microphone. Microphone positions shown in Figure E.1. Inline array with  $T/D = L/D = 2.0$ .

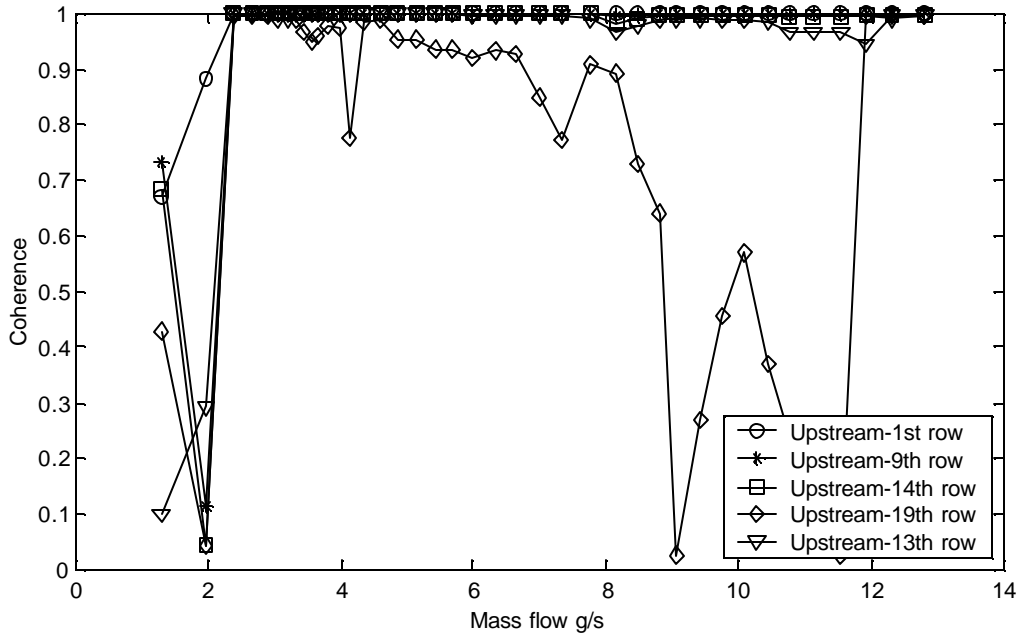
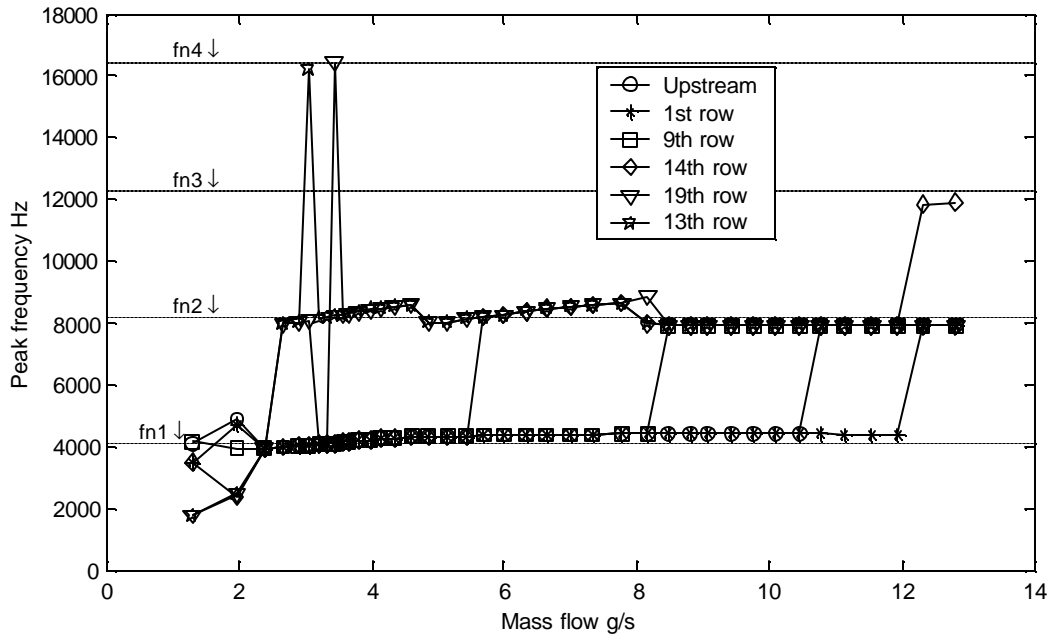
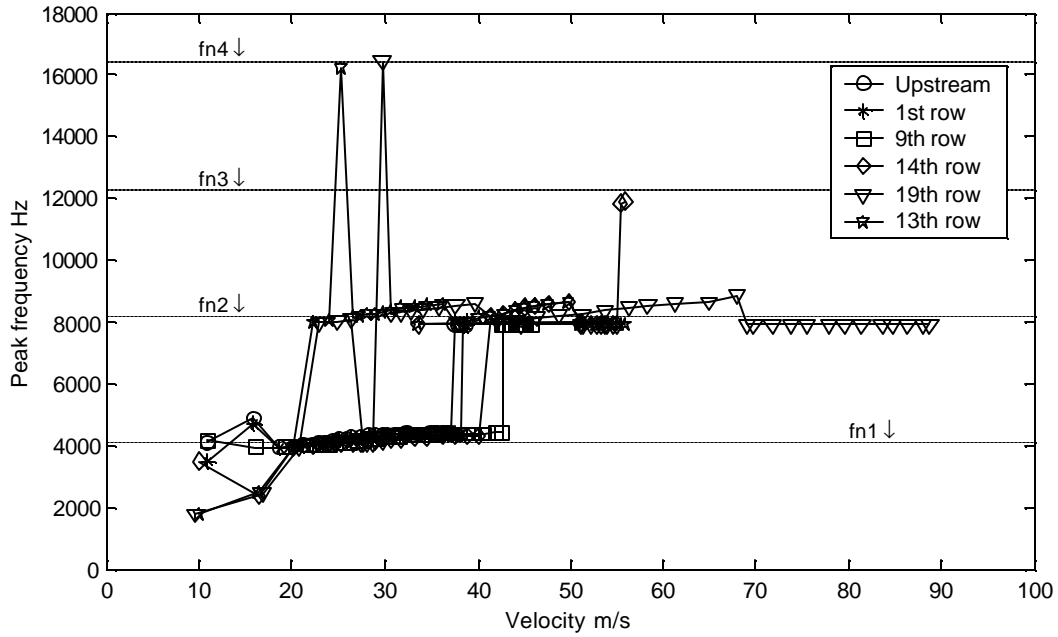


Figure E.4 Coherence between microphone pairs at frequency of dominant peak in spectra of upstream microphone. Phase measurements presented in Figure E.3 prone to error if coherence not close to one. Inline array with  $T/D = L/D = 2.0$ .



E.5 Plot of frequency of dominant peak in spectra vs. mass flow. Inline array with  $T/D = L/D = 2.0$ .  $fn1$ ,  $fn2$ ...acoustic natural frequencies with solidity effect.



E.6 Plot of frequency of dominant peak in spectra vs. flow velocity. Velocity estimated using density at measurement location and empty duct cross sectional area. Inline array with  $T/D = L/D = 2.0$ .  $fn1$ ,  $fn2$ ...acoustic natural frequencies with solidity effect.

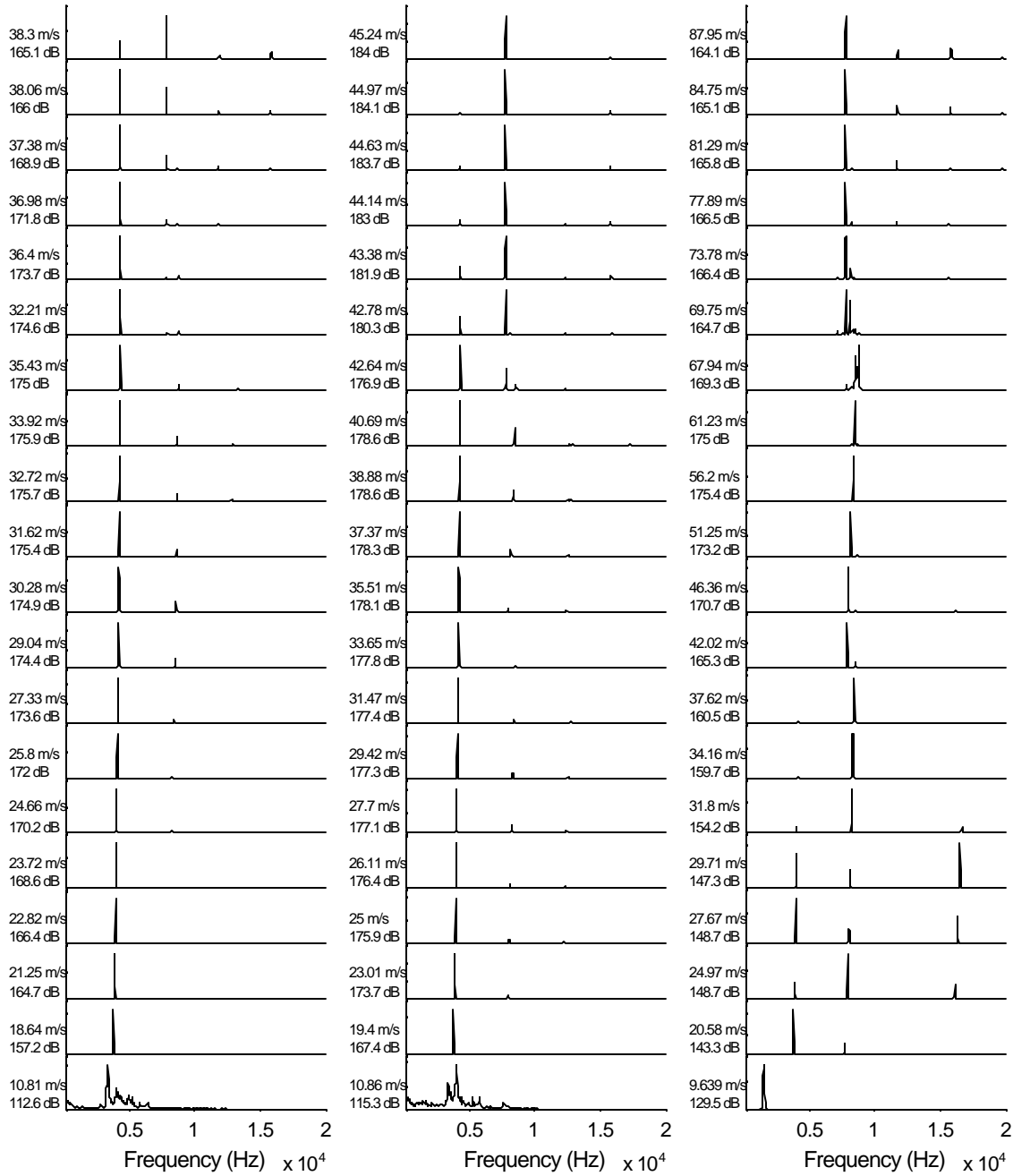


Figure E.7 Representative spectra taken at upstream position, after 9 row and after 19 row (left, center and right respectively). Spectra in same line taken at identical mass flow conditions. Velocity estimated using density at measurement location and empty duct cross sectional area. Sound pressure level shown at left calculated for dominant peak in spectra. Inline array with  $T/D = L/D = 2.0$ .

### In-line Square Array with $P/D = 1.5$

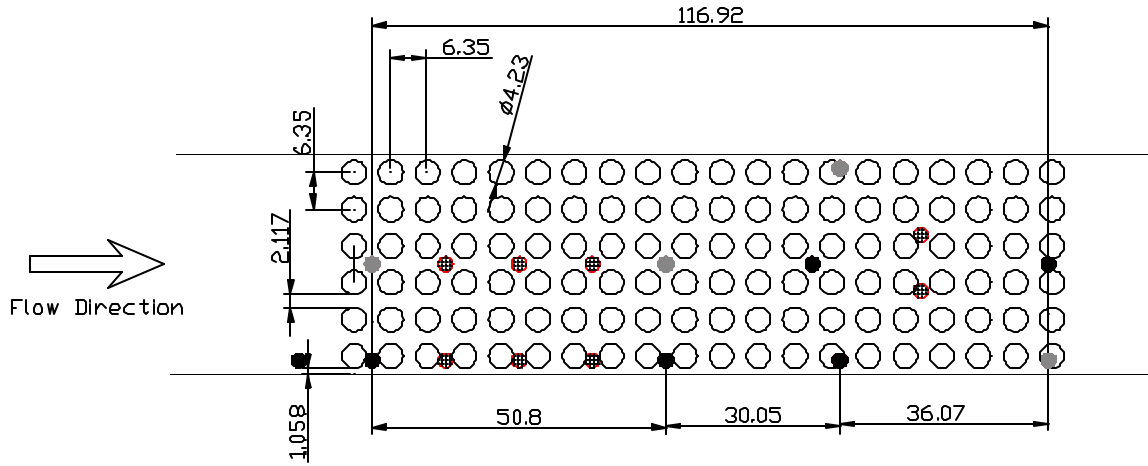


Figure E.8 Schematic of in-line square array tested with  $P/D = T/D = L/D = 1.5$ . Black dots represent microphone positions. Gray dots represent positions where static pressure measurements were made. Hatched dots are plugged microphone locations. Dimensions in mm. Drawing to scale.

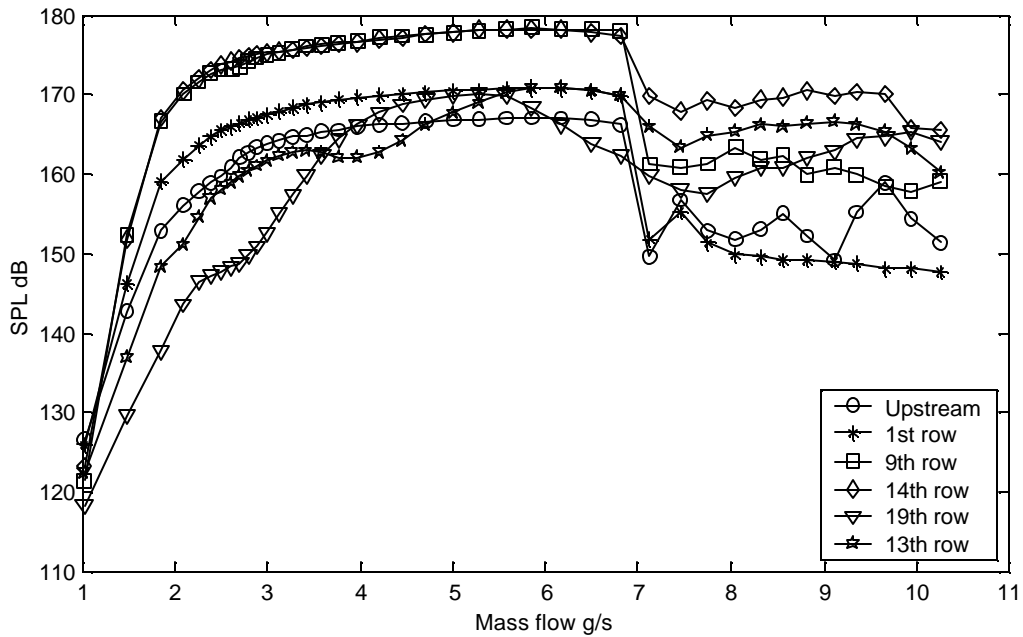


Figure E.9 Sound pressure level of dominant peak in spectra. Microphone positions shown in Figure E.8. Inline array with  $T/D = L/D = 1.5$ .

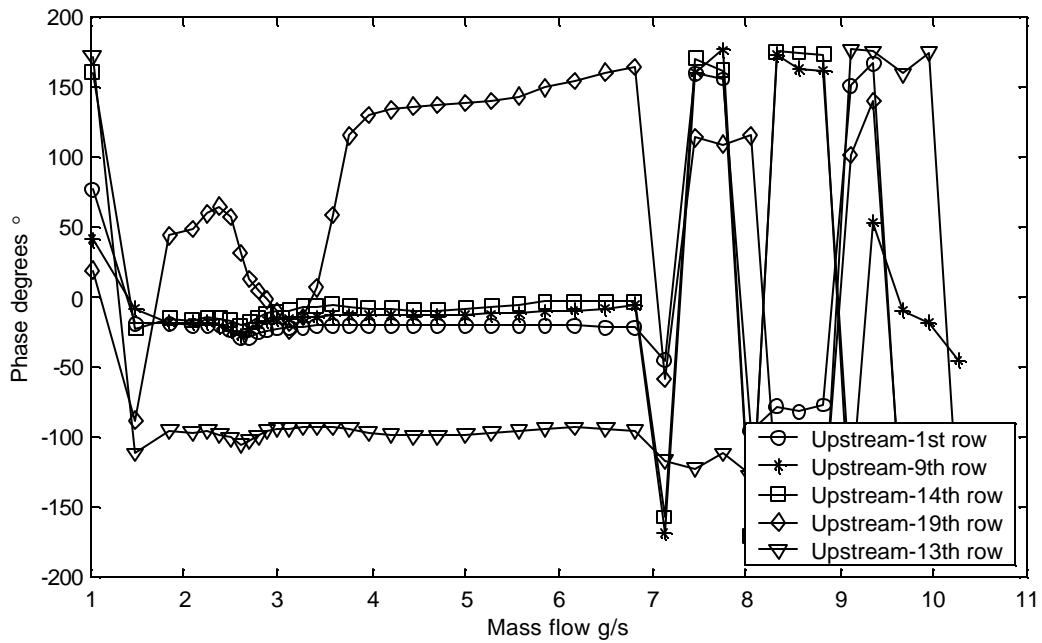


Figure E.10 Transfer function phase between microphone pairs shown at frequency of dominant peak in spectra of upstream microphone. Microphone positions shown in Figure E.8. Inline array with  $T/D = L/D = 1.5$ .

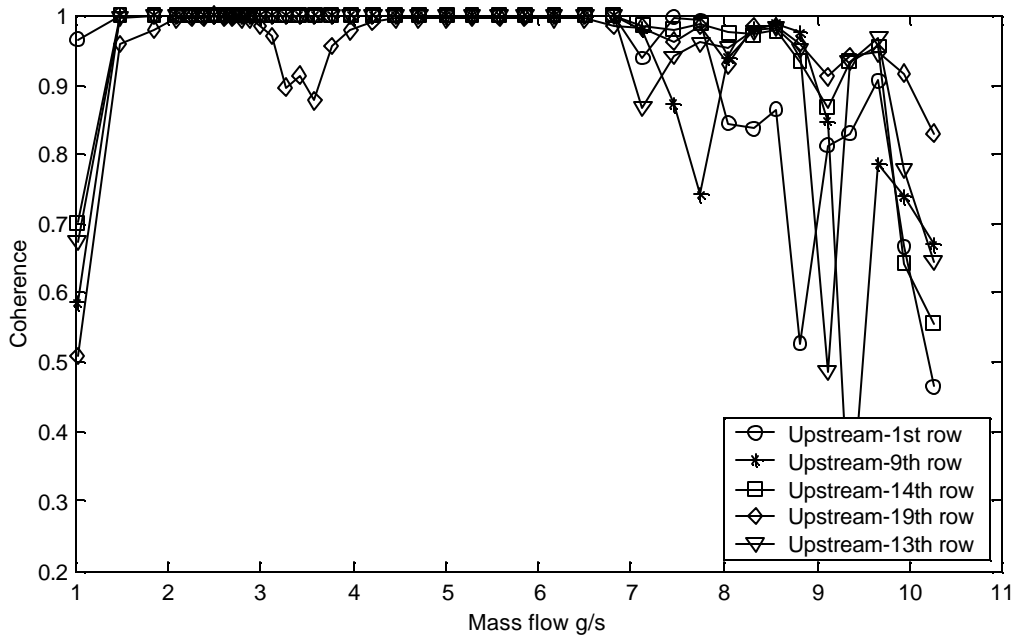
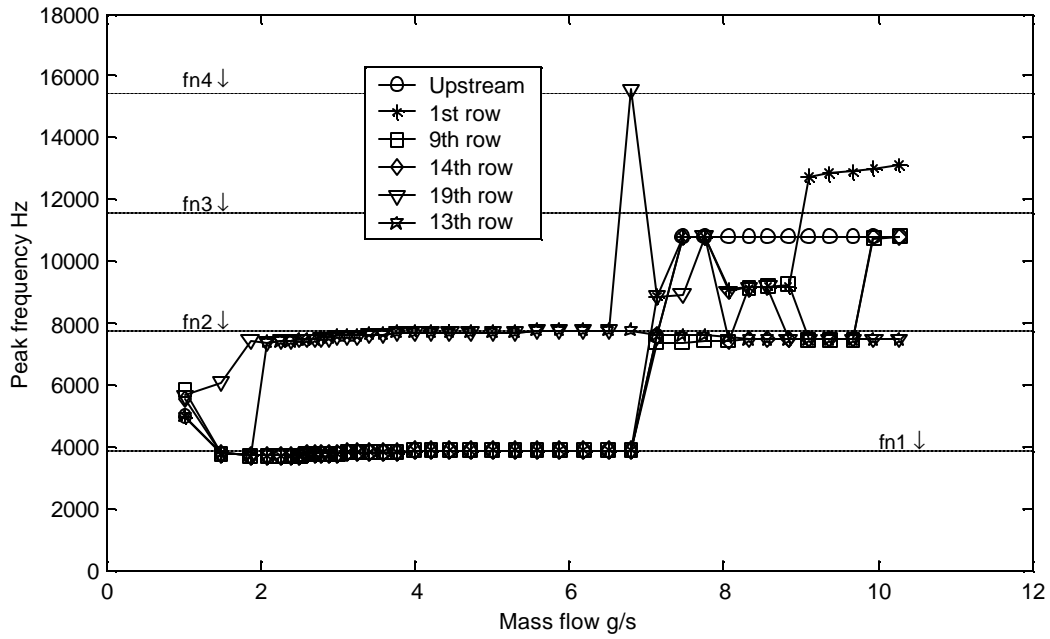
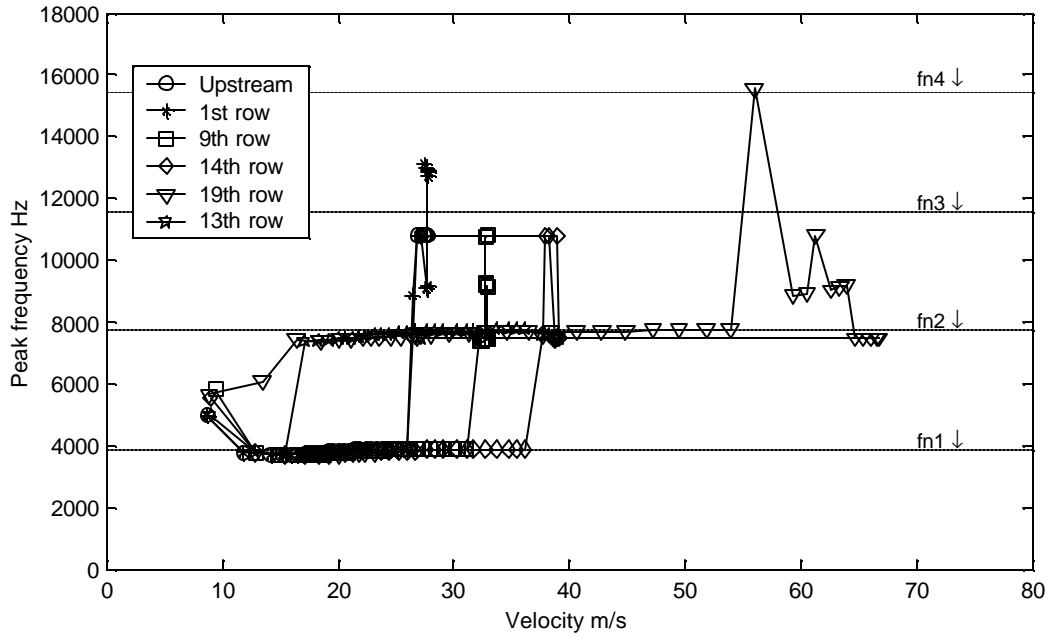


Figure E.11 Coherence between microphone pairs shown at frequency of dominant peak in spectra of upstream microphone. Phase measurements presented in Figure E.10 prone to error if coherence not close to one. Inline array with  $T/D = L/D = 1.5$ .





E.12 Plot of frequency of dominant peak in spectra vs. mass flow. Inline array with  $T/D = L/D = 1.5$ . fn1, fn2...acoustic natural frequencies with solidity effect.



E.13 Plot of frequency of dominant peak in spectra vs. flow velocity. Velocity estimated using density at measurement location and empty duct cross sectional area. Inline array with  $T/D = L/D = 1.5$ . fn1, fn2...acoustic natural frequencies with solidity effect.

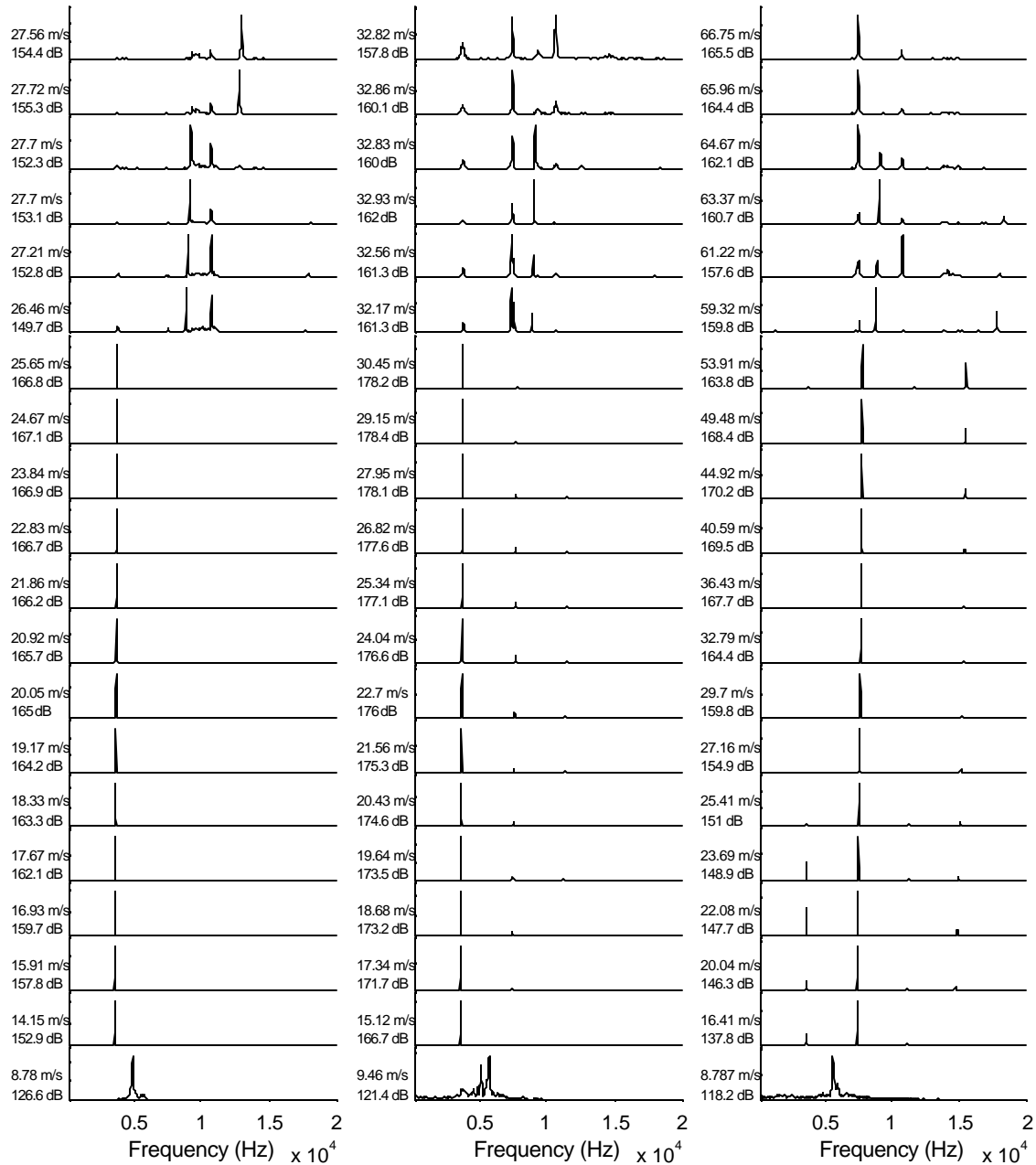


Figure E.14 Representative spectra taken at upstream position, after 9<sup>th</sup> row and after 19<sup>th</sup> row (left, center and right respectively). Spectra in same line taken at identical mass flow conditions. Velocity estimated using density at measurement location and empty duct cross sectional area. Sound pressure level shown at left calculated for dominant peak in spectra. Inline array with  $T/D = L/D = 1.5$ .

## Appendix F: Staggered Arrays Test Results

### Staggered Array with $T/D = 3.0$ and $L/D = 3.0$

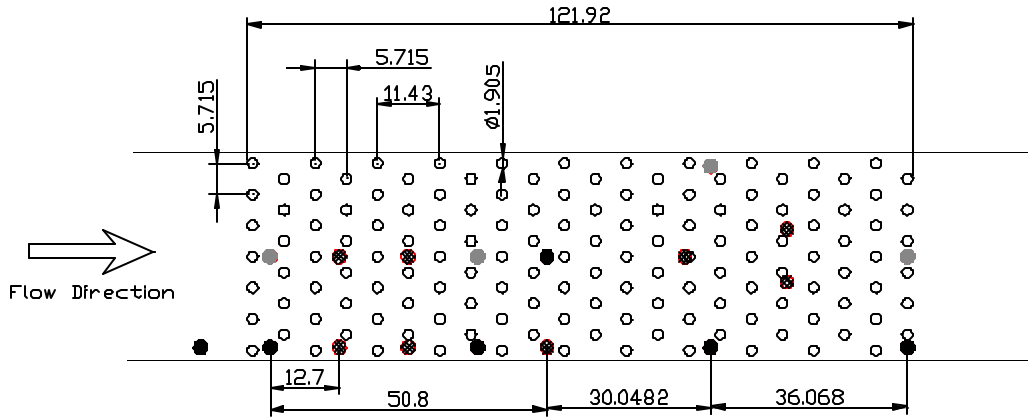


Figure F.1 Schematic of staggered array tested with  $T/D = 3.0$  and  $L/D = 3.0$ . Black dots represent microphone positions. Gray dots represent positions where static pressure measurements were made. Hatched dots are plugged microphone locations. Dimensions in mm. Drawing to scale.

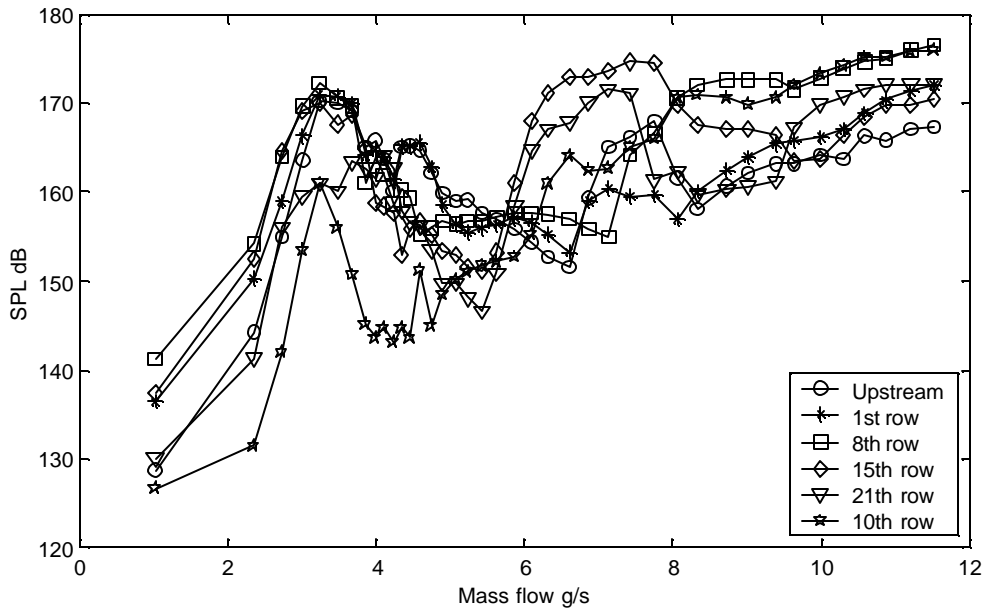


Figure F.2 Sound pressure level of dominant peak in spectra. Microphone positions shown in Figure F.1. Staggered array with  $T/D = 3.0$  and  $L/D = 3.0$ .

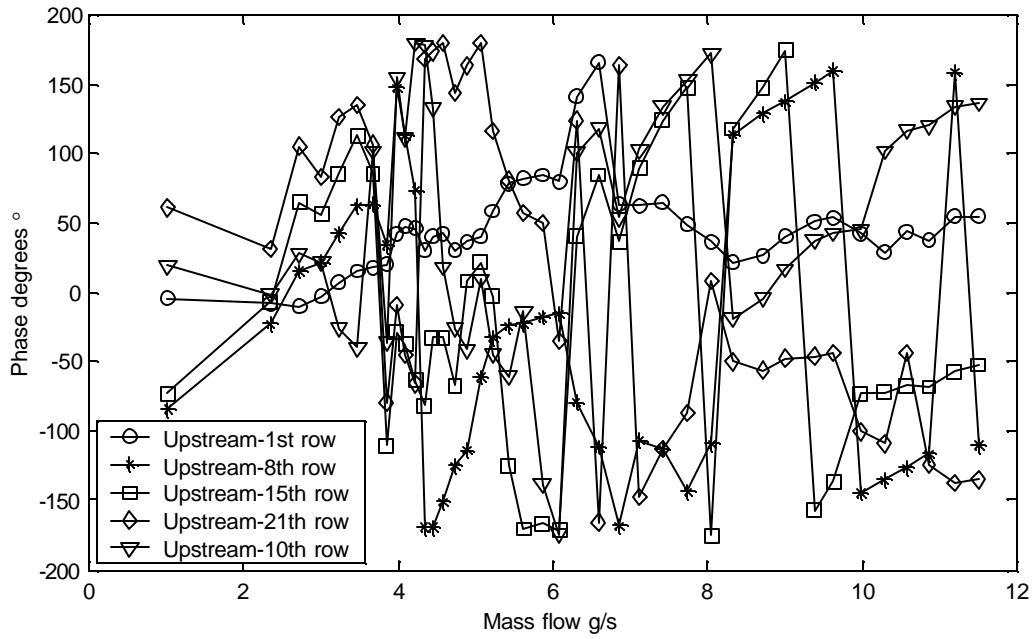


Figure F.3 Transfer function phase between microphone pairs shown at frequency of dominant peak in spectra of upstream microphone. Microphone positions shown in Figure F.1. Staggered array with  $T/D = 3.0$  and  $L/D = 3.0$ .

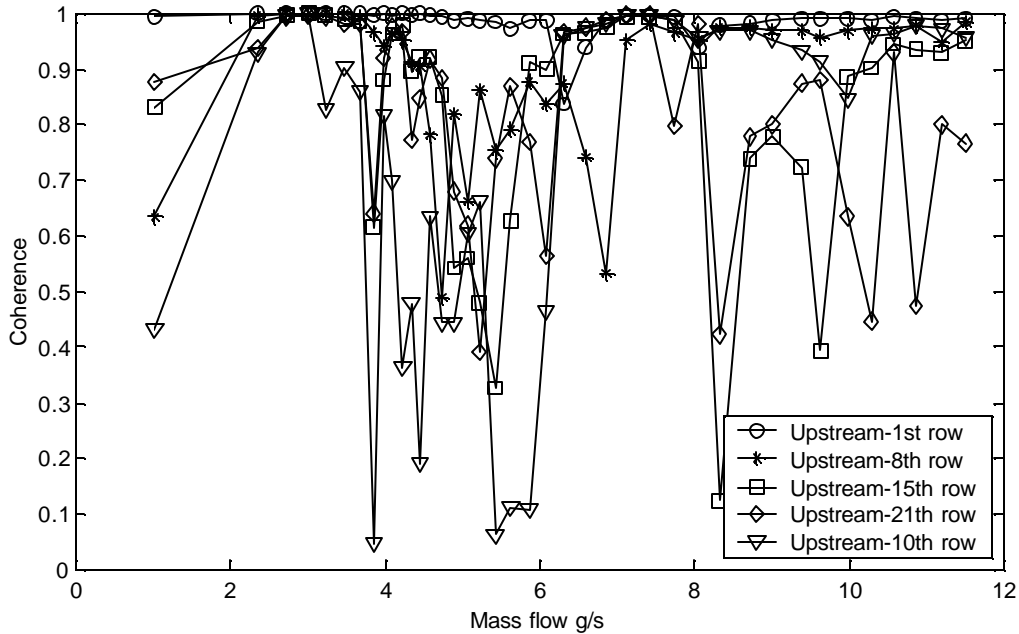
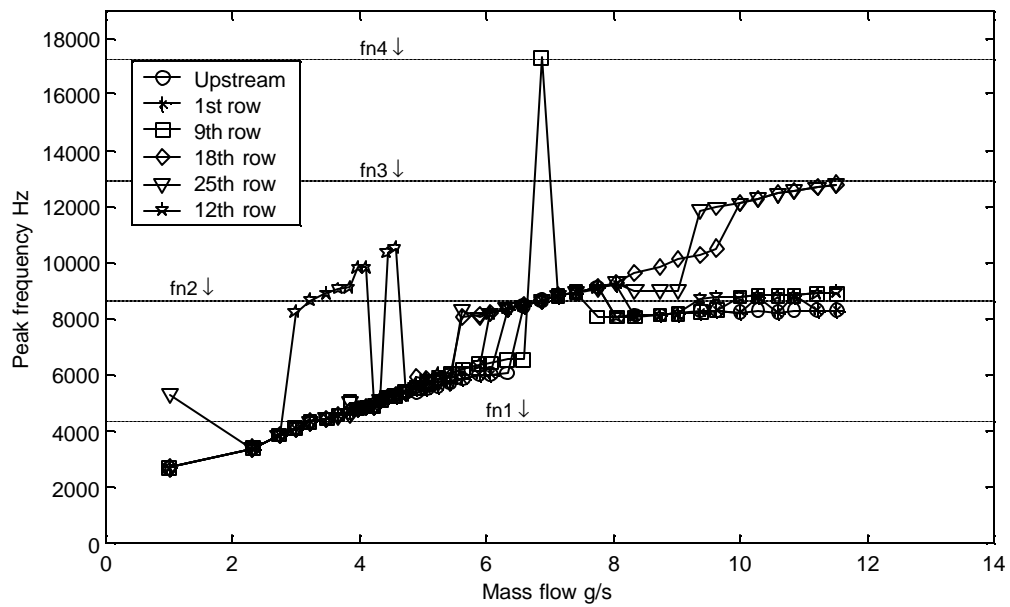
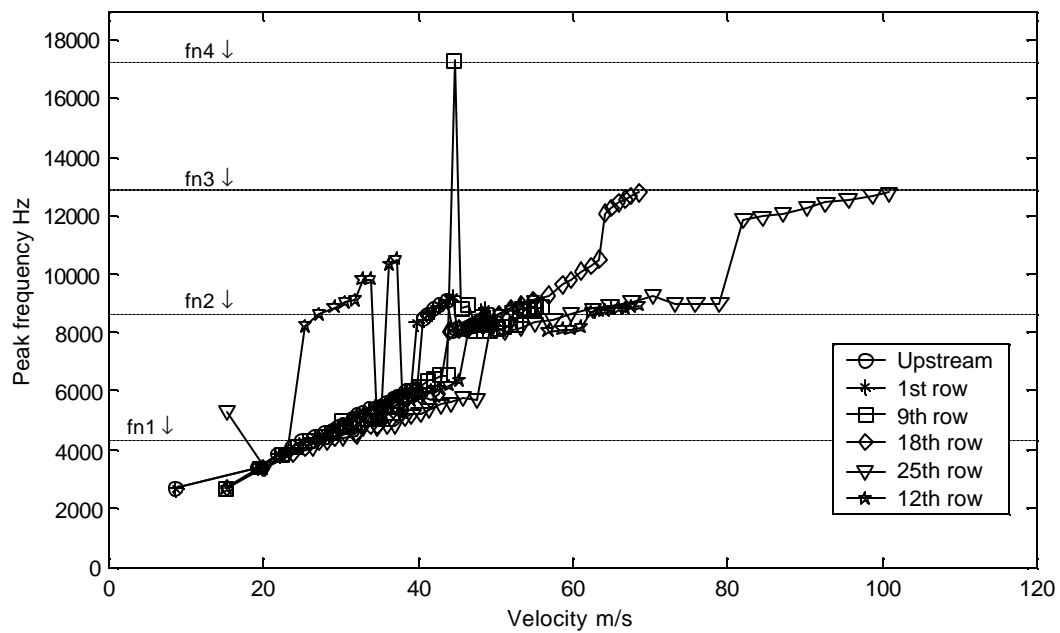


Figure F.4 Coherence between microphone pairs at frequency of dominant peak in spectra of upstream microphone. Phase measurements presented in Figure F.3 prone to error if coherence not close to one. Staggered array with  $T/D = 3.0$  and  $L/D = 3.0$ .



F.5 Plot of frequency of dominant peak in spectra vs. mass flow. Staggered array with  $T/D = 3.0$  and  $L/D = 3.0$ .  $fn1$ ,  $fn2$ ... acoustic natural frequencies with solidity effect.



F.6 Plot of frequency of dominant peak in spectra vs. flow velocity. Velocity estimated using density at measurement location and empty duct cross-sectional area. Staggered array with  $T/D = 3.0$  and  $L/D = 3.0$ .  $fn1$ ,  $fn2$ ... acoustic natural frequencies with solidity effect.

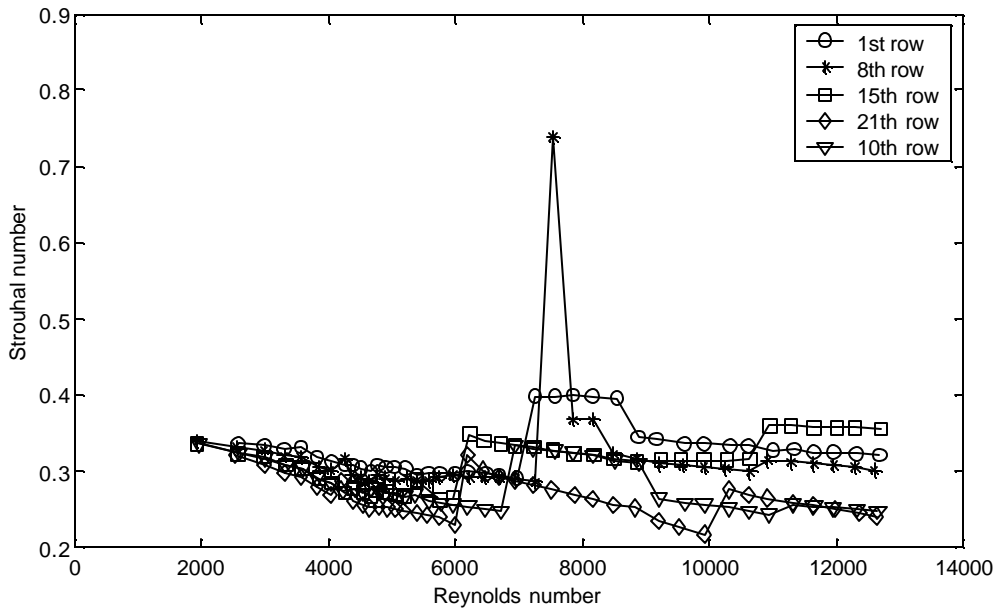


Figure F.7 Strouhal numbers determined at different positions throughout the array using dominant peak in spectra. Velocity estimated using density at measurement location and full duct cross-sectional area. Staggered array with  $T/D = 3.0$  and  $L/D = 3.0$ .

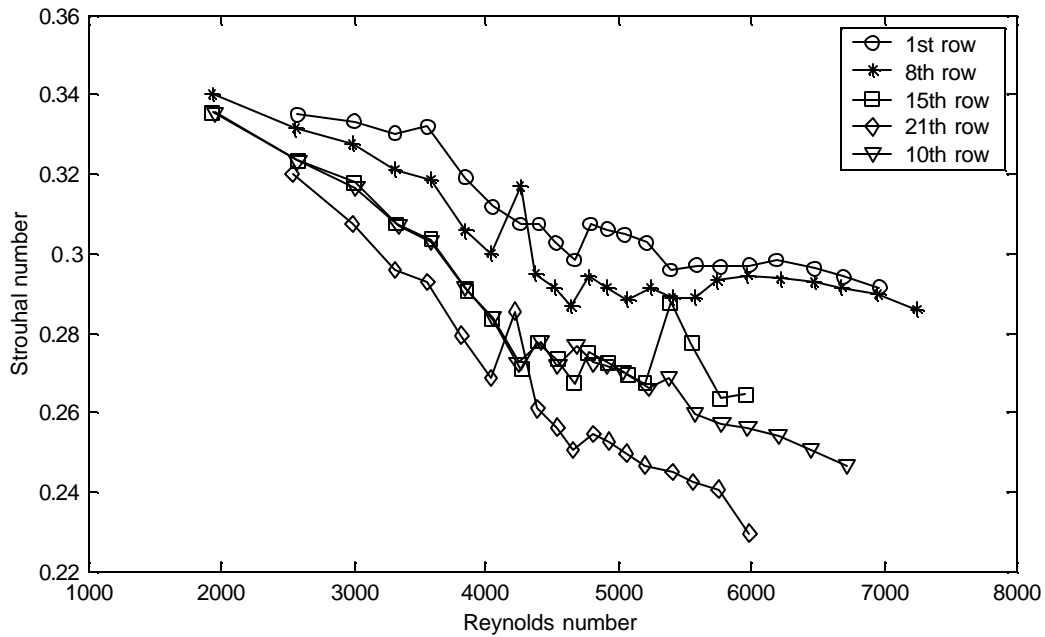


Figure F.8 Zoom in of Figure F.7 showing Strouhal numbers behavior when frequencies of dominant peak in spectra below second transverse acoustic natural frequency of duct. Staggered array with  $T/D = 3.0$  and  $L/D = 3.0$ .

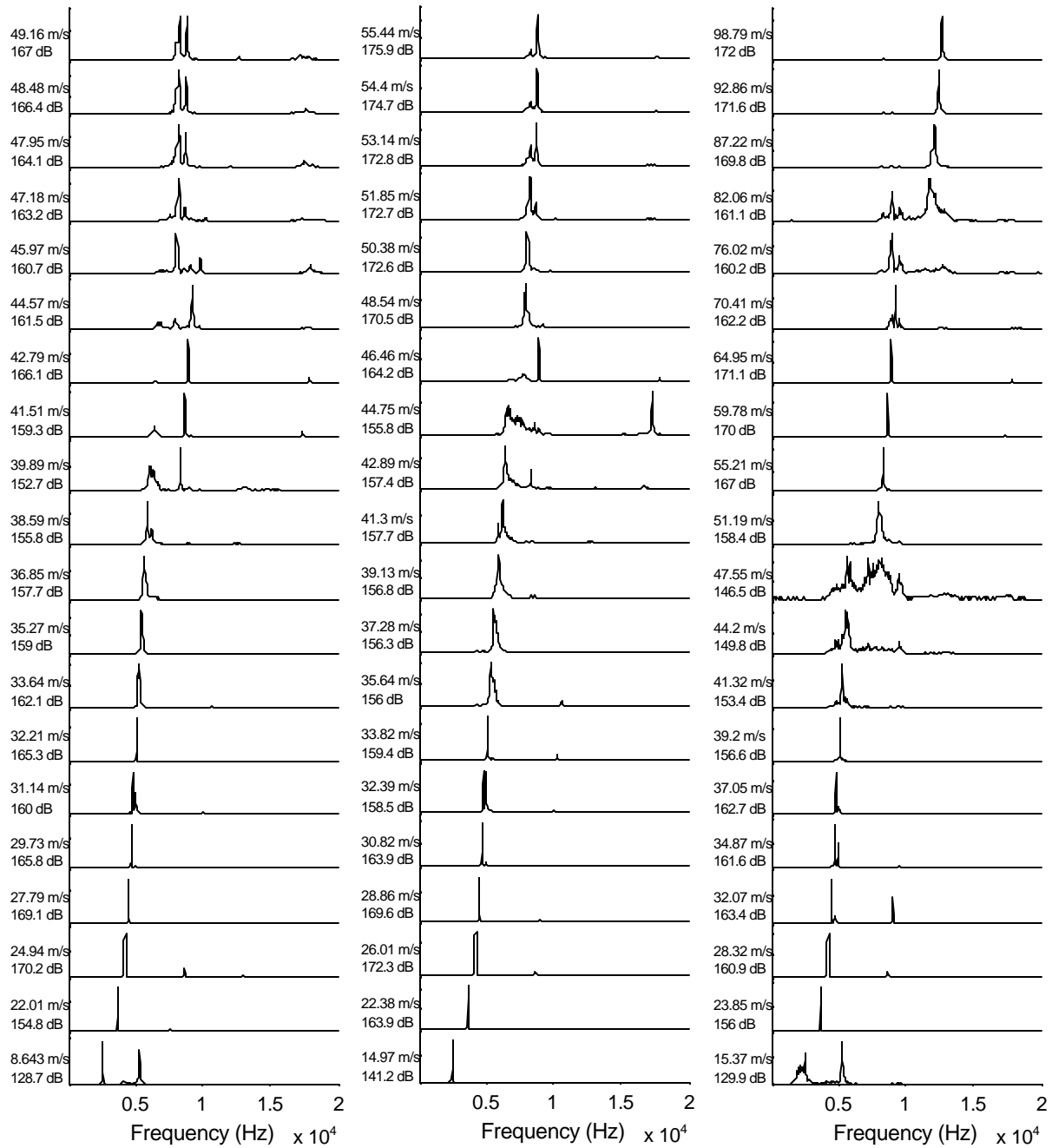


Figure F.9 Representative spectra taken at upstream position, after 8<sup>th</sup> row and after 21<sup>st</sup> row (left, center and right respectively). Spectra in same line taken at identical mass flow conditions. Velocity estimated using density at measurement location and empty duct cross-sectional area. Sound pressure level shown at left calculated for dominant peak in spectra. Staggered array with T/D = 3.0 and L/D = 3.0.

### Staggered Array with T/D = 3.0 and L/D = 2.5

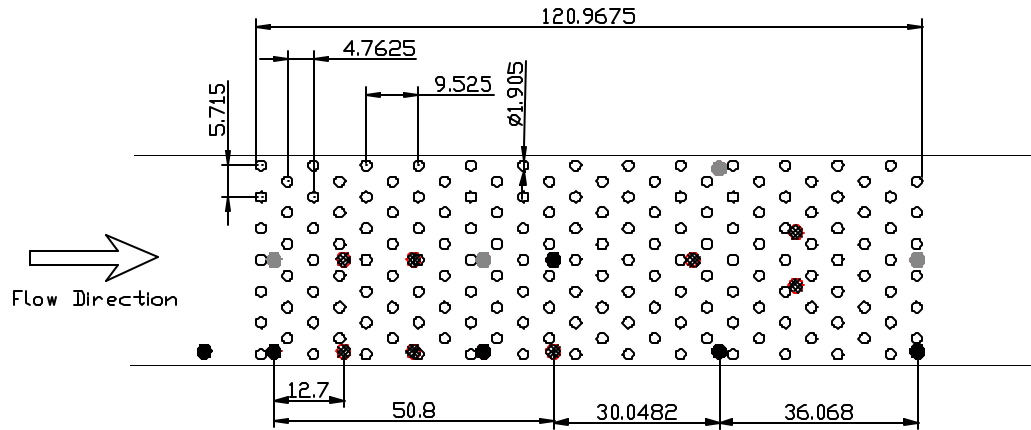


Figure F.10 Schematic of staggered array tested with  $T/D = 3.0$  and  $L/D = 2.5$ . Black dots represent microphone positions. Gray dots represent positions where static pressure measurements were made. Hatched dots are plugged microphone locations. Dimensions in mm. Drawing to scale.

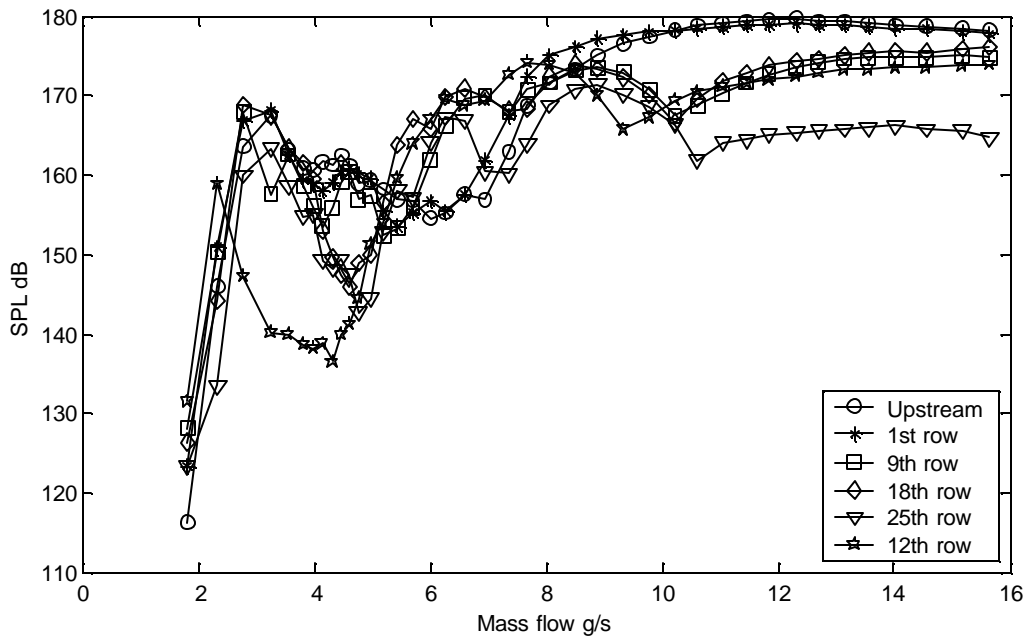


Figure F.11 Sound pressure level of dominant peak in spectra. Microphone positions shown in Figure F.10. Staggered array with  $T/D = 3.0$  and  $L/D = 2.5$ .



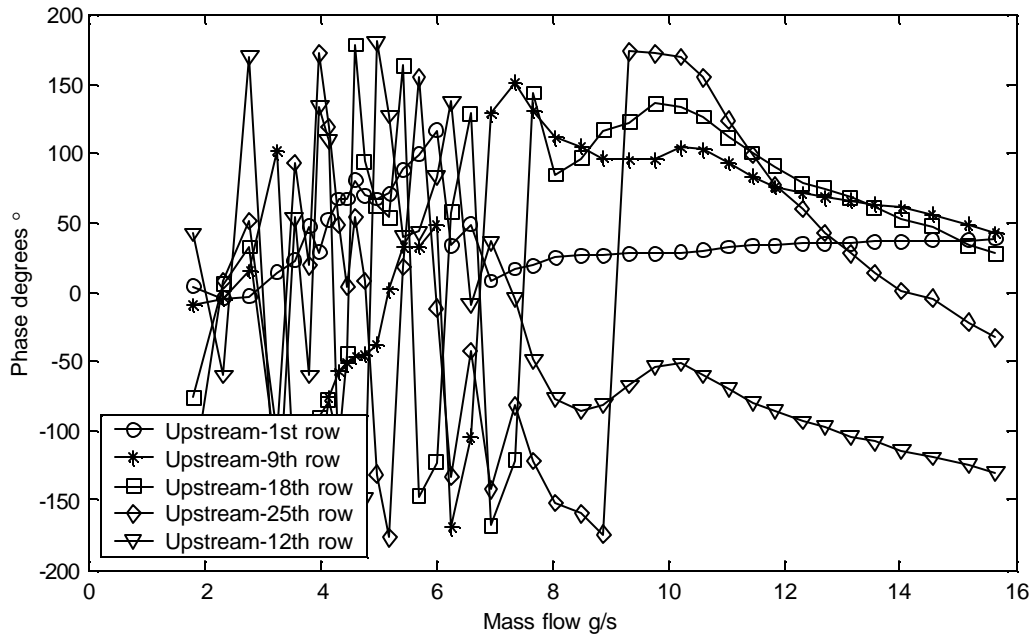


Figure F.12 Transfer function phase between microphone pairs shown at frequency of dominant peak in spectra of upstream microphone. Microphone positions shown in Figure F.10. Staggered array with  $T/D = 3.0$  and  $L/D = 2.5$ .

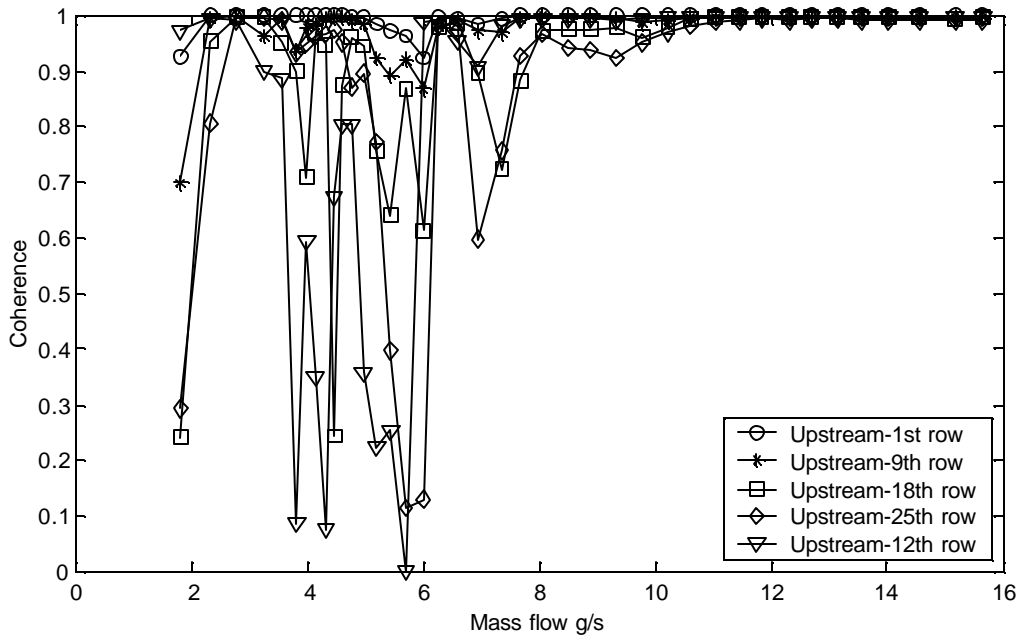


Figure F.13 Coherence between microphone pairs at frequency of dominant peak in spectra of upstream microphone. Phase measurements presented in Figure F.12 prone to error if coherence not close to one. Staggered array with  $T/D = 3.0$  and  $L/D = 2.5$ .

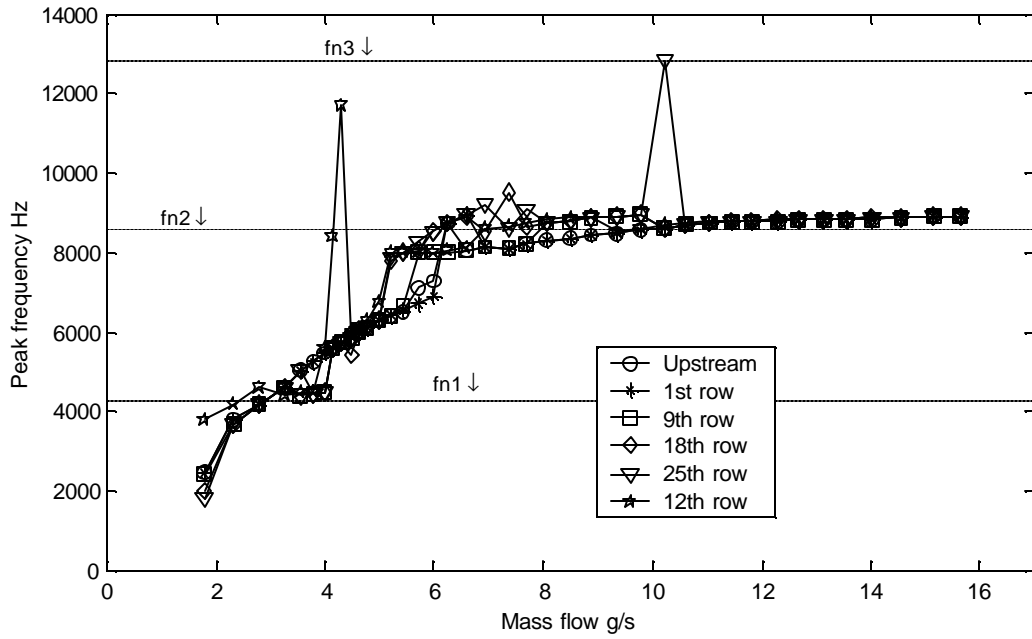


Figure F.14 Plot of frequency of dominant peak in spectra vs. mass flow. Staggered array with  $T/D = 3.0$  and  $L/D = 2.5$ .  $fn_1, fn_2, \dots$  acoustic natural frequencies with solidity effect.

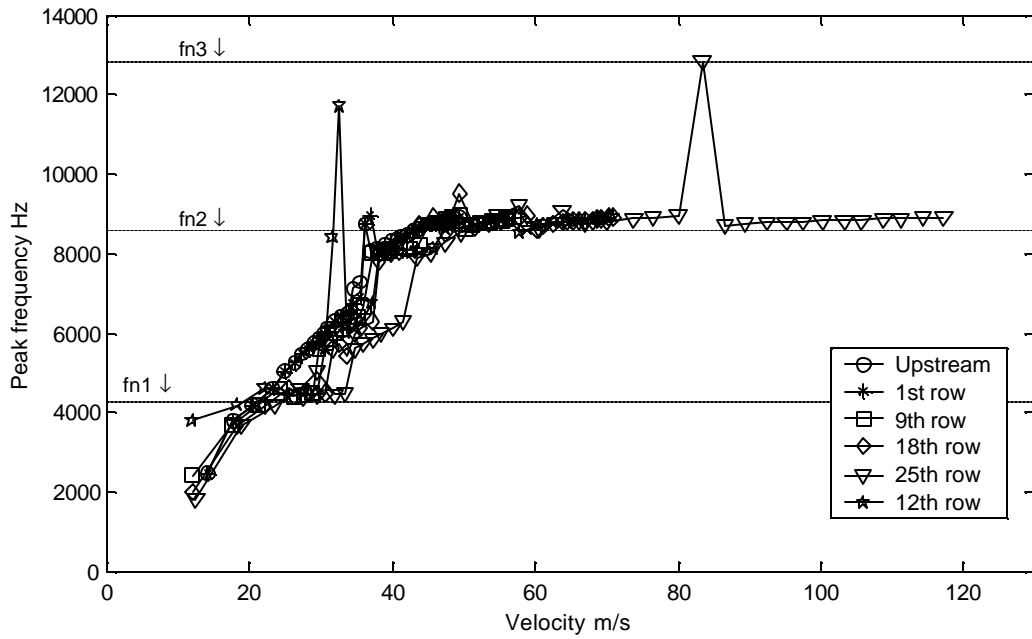


Figure F.15 Plot of frequency of dominant peak in spectra vs. flow velocity. Velocity estimated using density at measurement location and empty duct cross-sectional area. Staggered array with  $T/D = 3.0$  and  $L/D = 2.5$ .  $fn_1, fn_2, \dots$  acoustic natural frequencies with solidity effect.

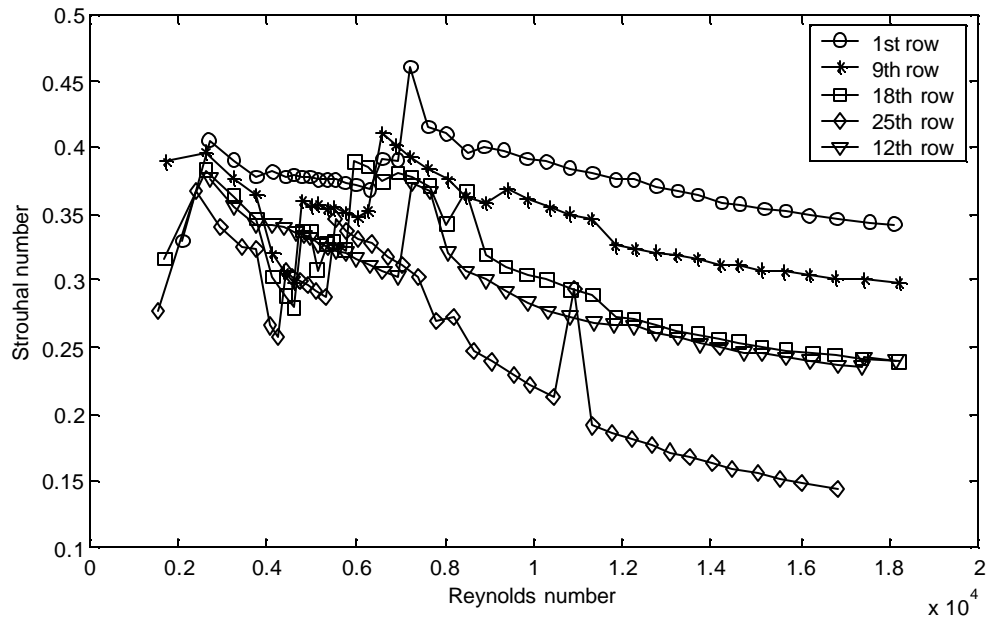


Figure F.16 Strouhal numbers determined at different positions throughout the array using dominant peak in spectra. Velocity estimated using density at measurement location and full duct cross-sectional area. Staggered array with  $T/D = 3.0$  and  $L/D = 2.5$ .

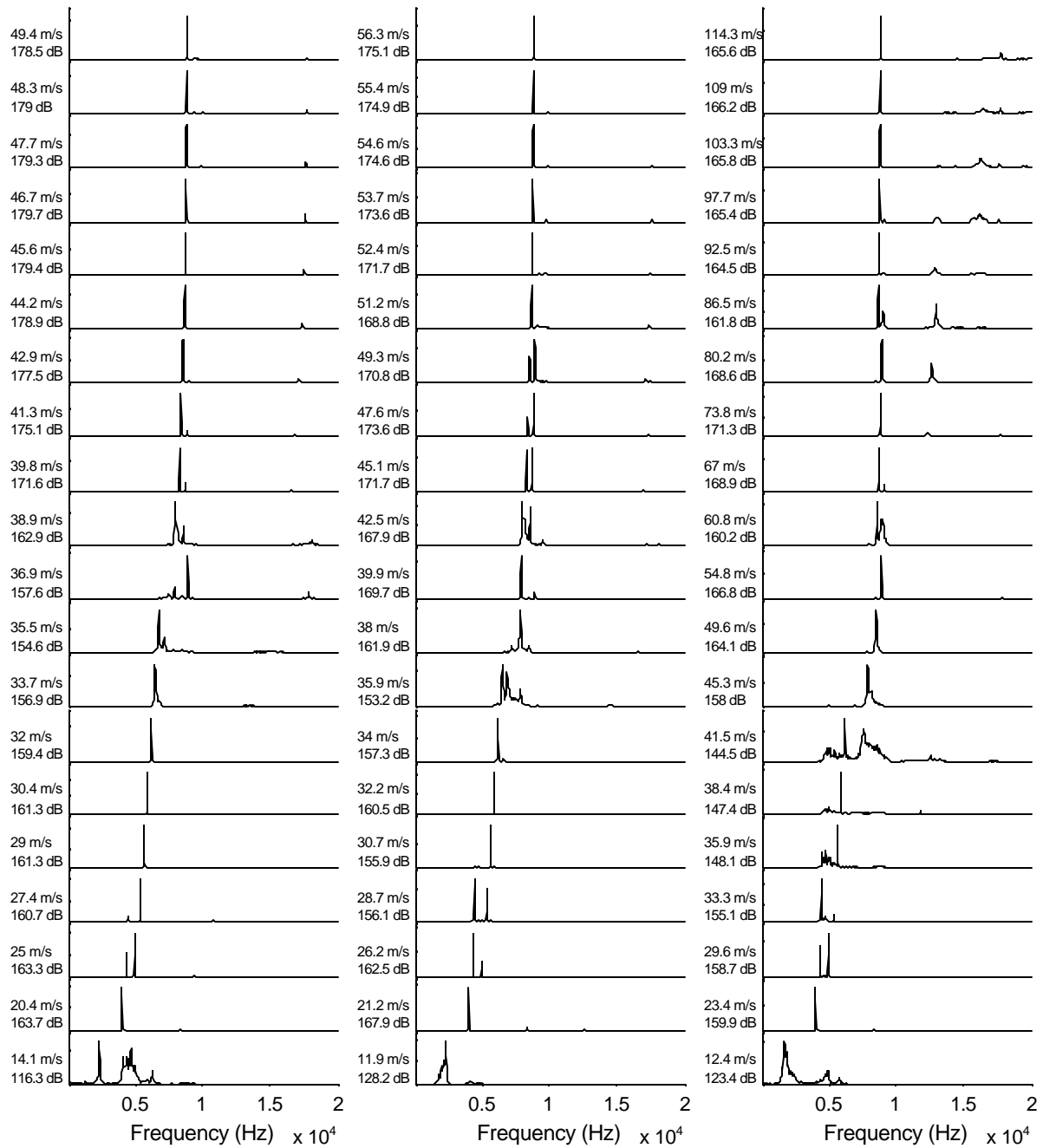


Figure F.17 Representative spectra taken at upstream position, after 9<sup>th</sup> row and after 25<sup>th</sup> row (left, center and right respectively). Spectra in same line taken at identical mass flow conditions. Velocity estimated using density at measurement location and empty duct cross-sectional area. Sound pressure level shown at left calculated for dominant peak in spectra. Staggered array with T/D = 3.0 and L/D = 2.5.

### Staggered Array with T/D = 3.0 and L/D = 2.0

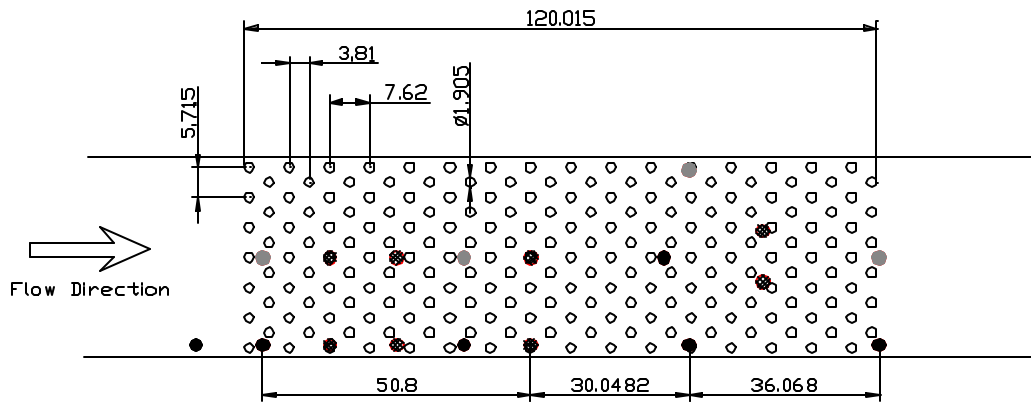


Figure F.18 Schematic of staggered array tested with T/D = 3.0 and L/D = 2.0. Black dots represent microphone positions. Gray dots represent positions where static pressure measurements were made. Hatched dots are plugged microphone locations. Dimensions in mm. Drawing to scale.

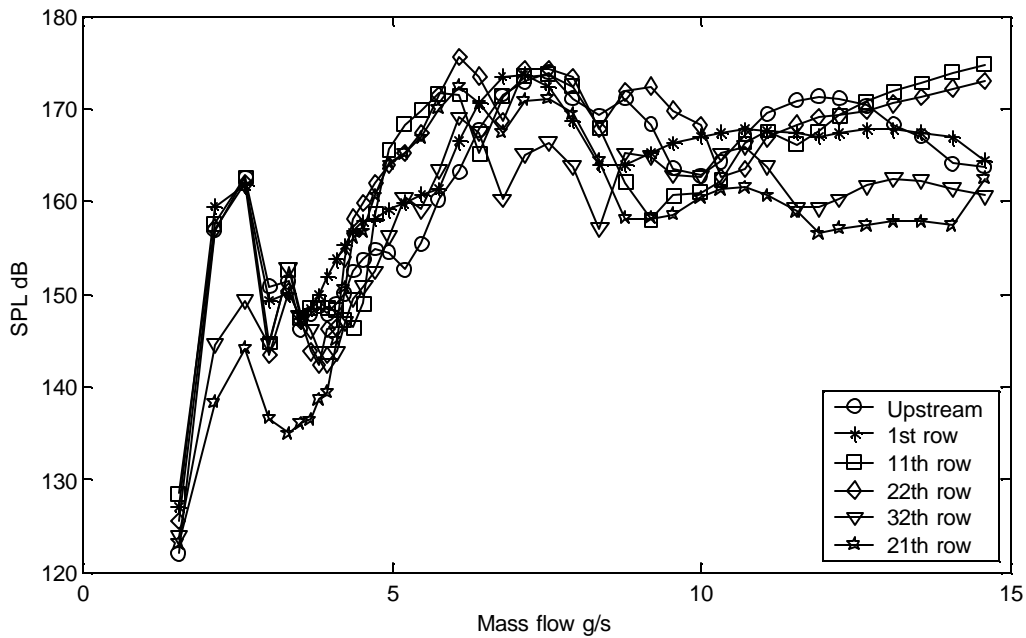


Figure F.19 Sound pressure level of dominant peak in spectra. Microphone positions shown in Figure F.18. Staggered array with T/D = 3.0 and L/D = 2.0.

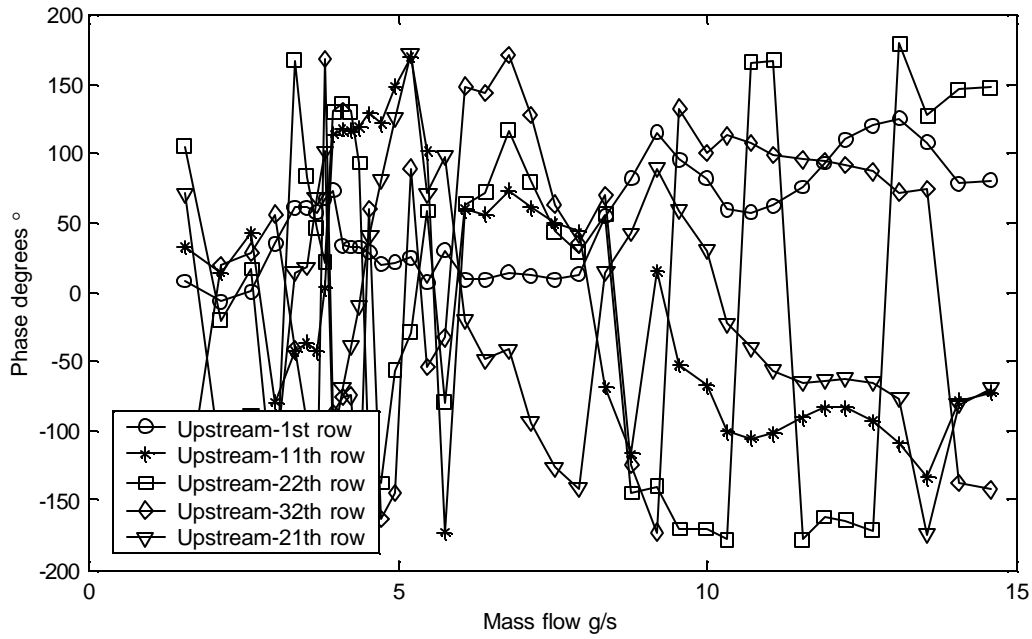


Figure F.20 Transfer function phase between microphone pairs shown at frequency of dominant peak in spectra of upstream microphone. Microphone positions shown in Figure F.18. Staggered array with  $T/D = 3.0$  and  $L/D = 2.0$ .

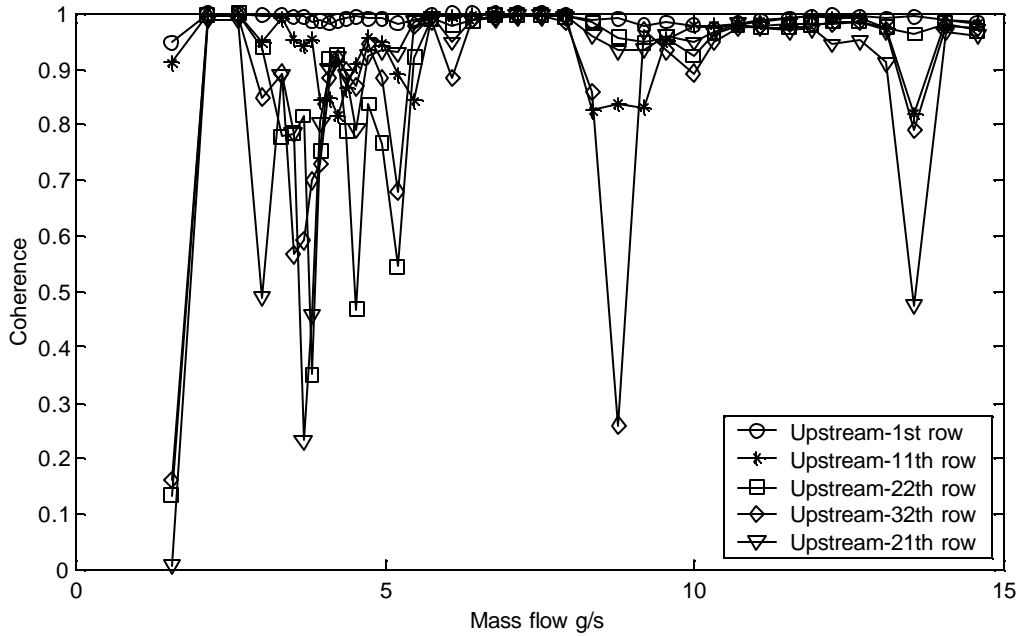


Figure F.21 Coherence between microphone pairs at frequency of dominant peak in spectra of upstream microphone. Phase measurements presented in Figure F.20 prone to error if coherence not close to one. Staggered array with  $T/D = 3.0$  and  $L/D = 2.0$ .

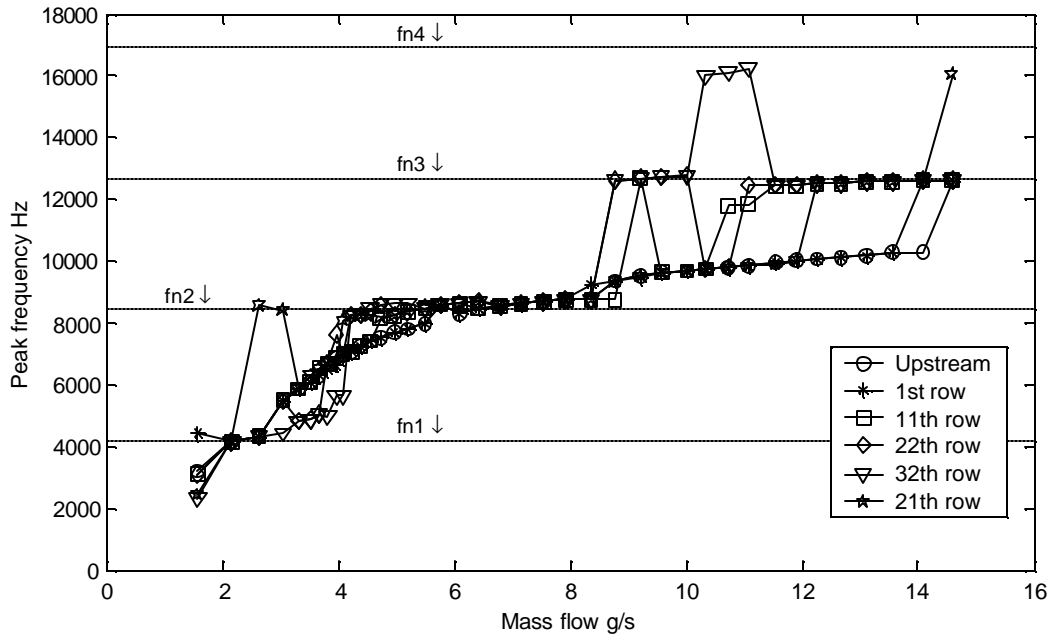


Figure F.22 Plot of frequency of dominant peak in spectra vs. mass flow. Staggered array with  $T/D = 3.0$  and  $L/D = 2.0$ .  $fn_1, fn_2, \dots$  acoustic natural frequencies with solidity effect.

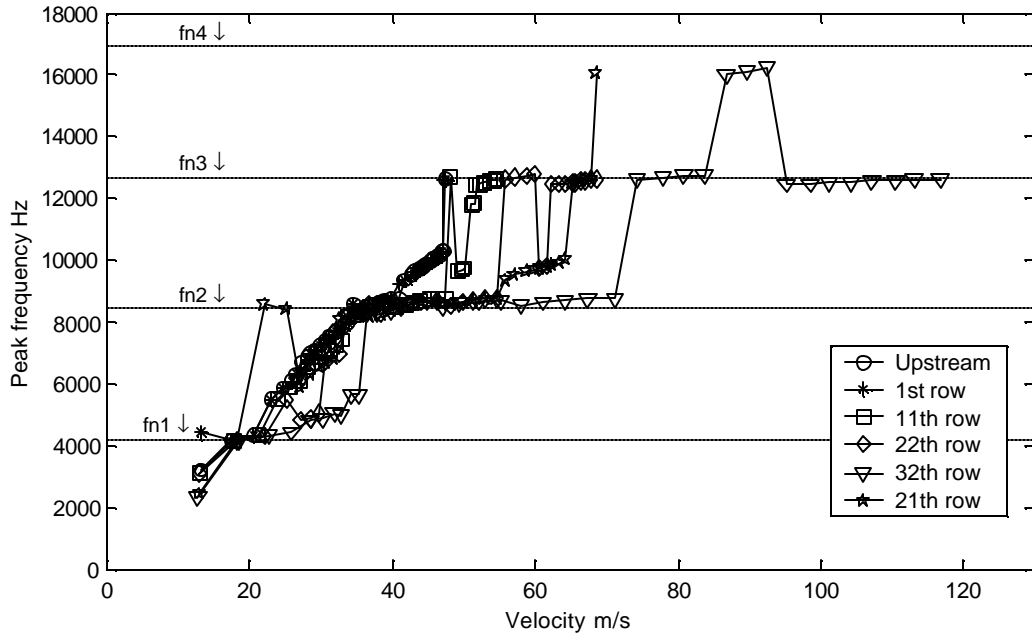


Figure F.23 Plot of frequency of dominant peak in spectra vs. flow velocity. Velocity estimated using density at measurement location and empty duct cross-sectional area. Staggered array with  $T/D = 3.0$  and  $L/D = 2.0$ .  $fn_1, fn_2, \dots$  acoustic natural frequencies with solidity effect.

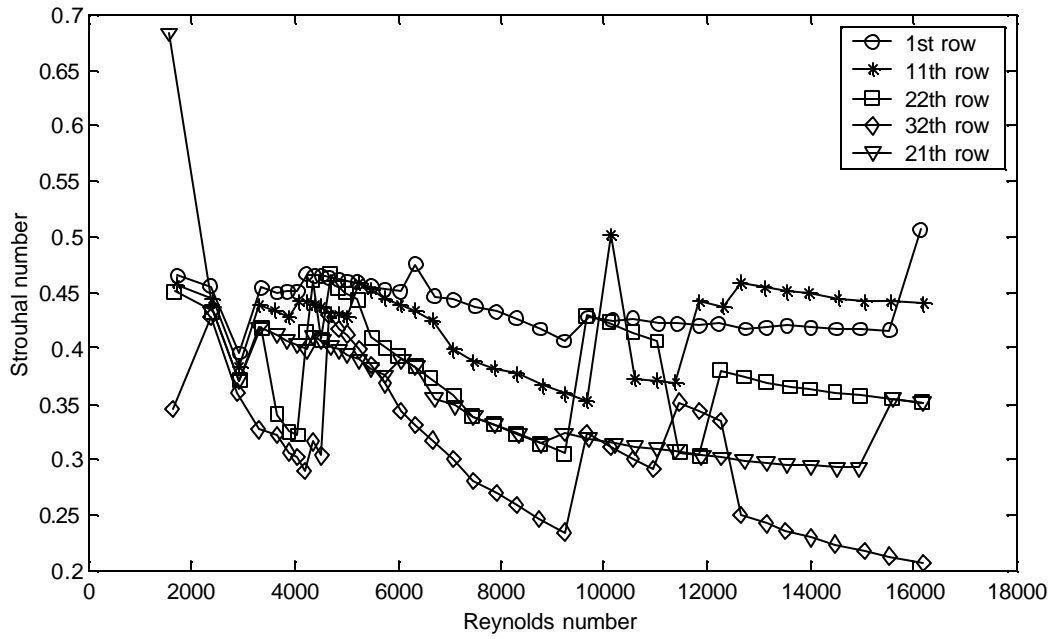


Figure F.24 Strouhal numbers determined at different positions throughout the array using dominant peak in spectra. Velocity estimated using density at measurement location and full duct cross-sectional area. Staggered array with  $T/D = 3.0$  and  $L/D = 2.0$ .



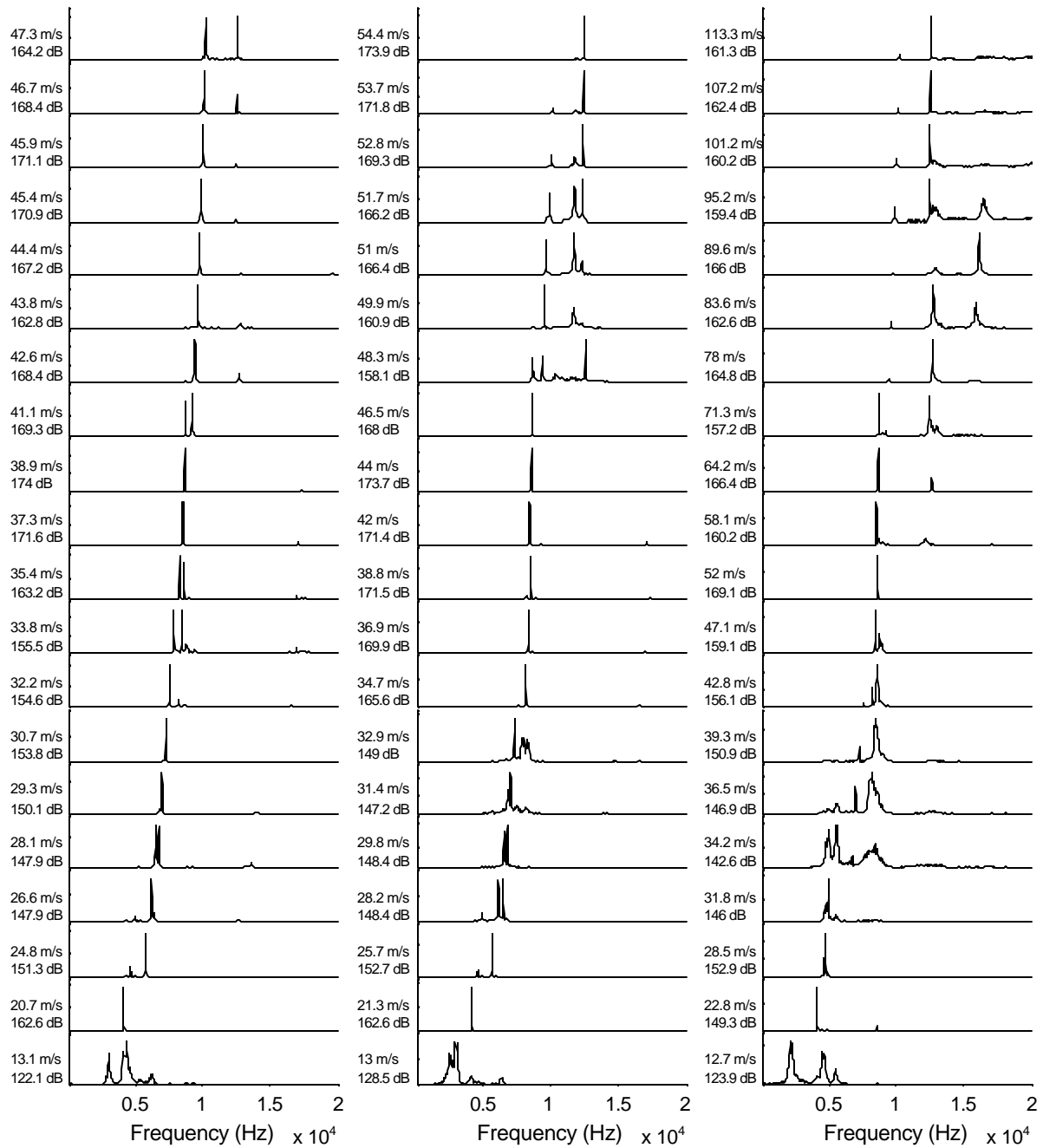


Figure F.25 Representative spectra taken at upstream position, after 11<sup>th</sup> row and after 32<sup>nd</sup> row (left, center, and right, respectively). Spectra in same line taken at identical mass flow conditions. Velocity estimated using density at measurement location and empty duct cross-sectional area. Sound pressure level shown at left calculated for dominant peak in spectra. Staggered array with T/D = 3.0 and L/D = 2.0.

Staggered Array with T/D = 3.0 and L/D = 1.8

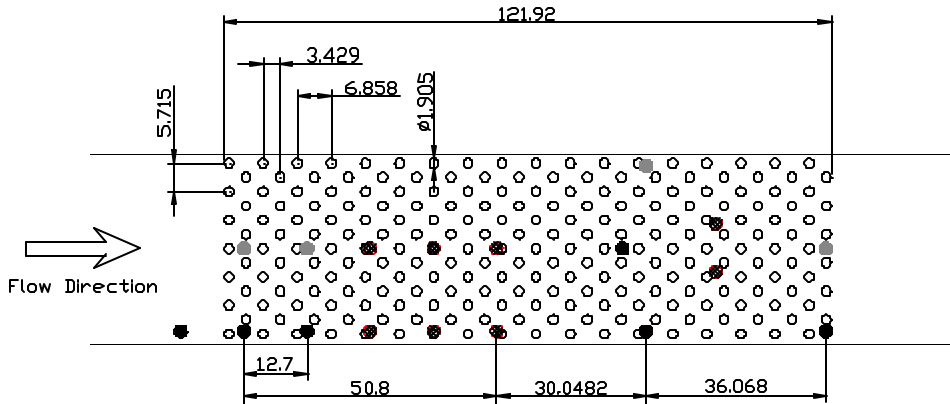


Figure F.26 Schematic of staggered array tested with T/D = 3.0 and L/D = 1.8. Black dots represent microphone positions. Gray dots represent positions where static pressure measurements were made. Hatched dots are plugged microphone locations. Dimensions in mm. Drawing to scale.

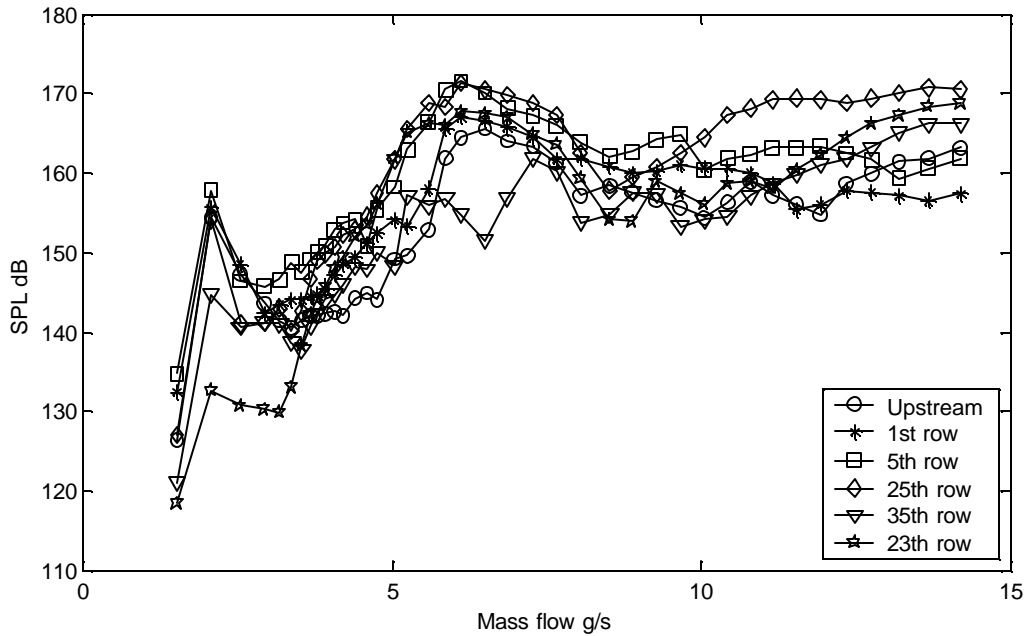


Figure F.27 Sound pressure level of dominant peak in spectra. Microphone positions shown in Figure F.26. Staggered array with T/D = 3.0 and L/D = 1.8.

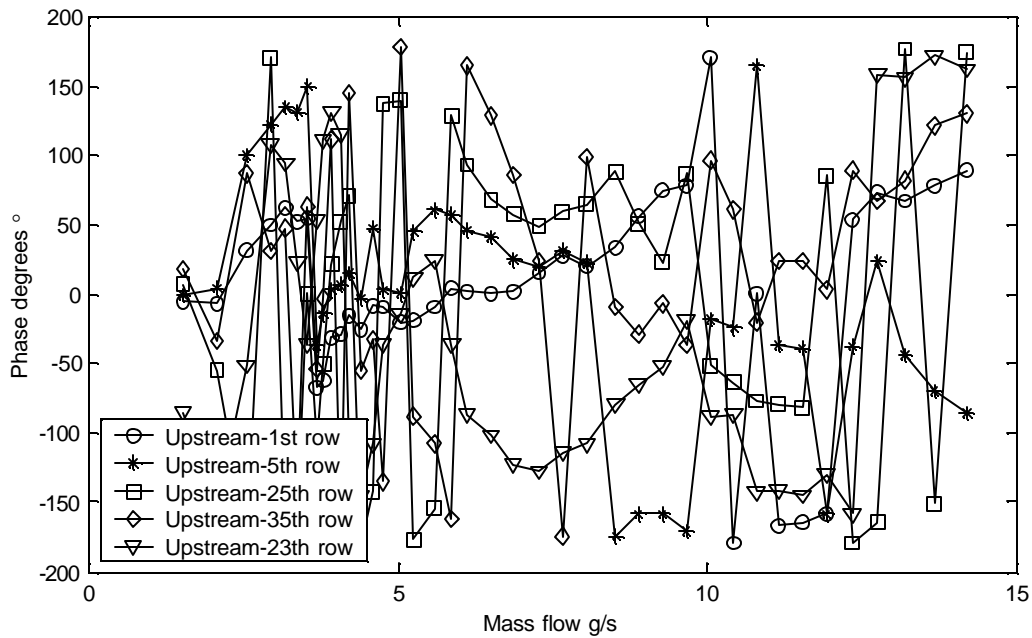


Figure F.28 Transfer function phase between microphone pairs shown at frequency of dominant peak in spectra of upstream microphone. Microphone positions shown in Figure F.26. Staggered array with  $T/D = 3.0$  and  $L/D = 1.8$ .

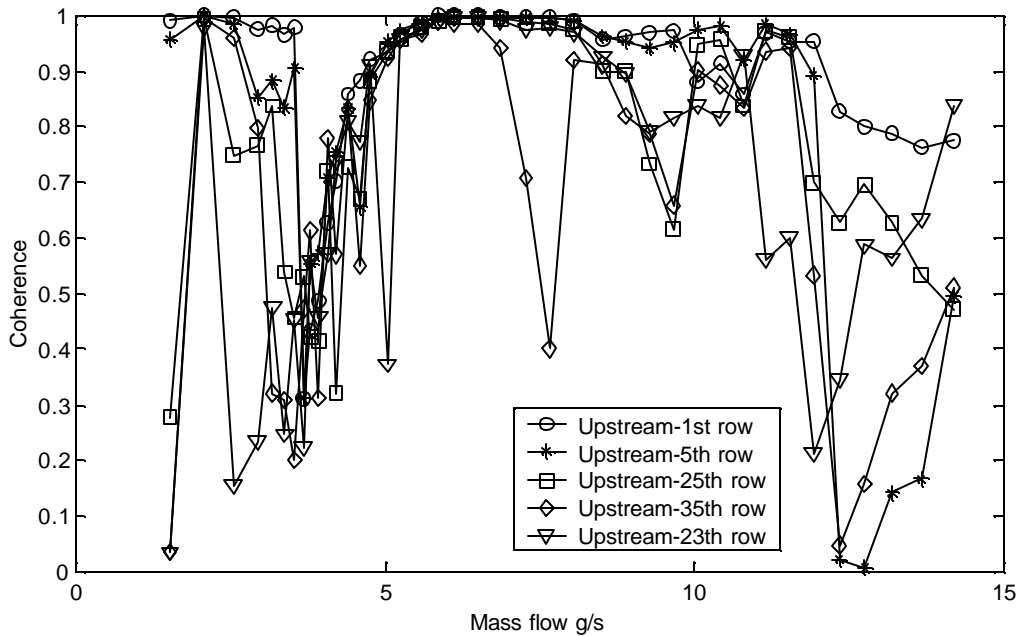


Figure F.29 Coherence between microphone pairs at frequency of dominant peak in spectra of upstream microphone. Phase measurements presented in Figure F.28 prone to error if coherence not close to one. Staggered array with  $T/D = 3.0$  and  $L/D = 1.8$ .

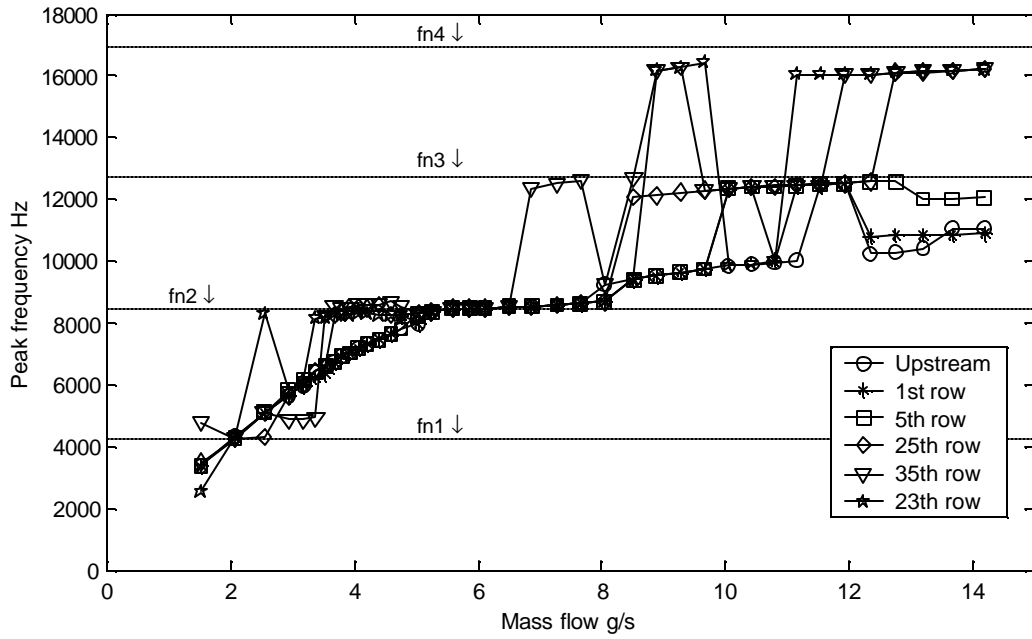


Figure F.30 Plot of frequency of dominant peak in spectra vs. mass flow. Staggered array with  $T/D = 3.0$  and  $L/D = 1.8$ .  $fn_1, fn_2, \dots$  acoustic natural frequencies with solidity effect.

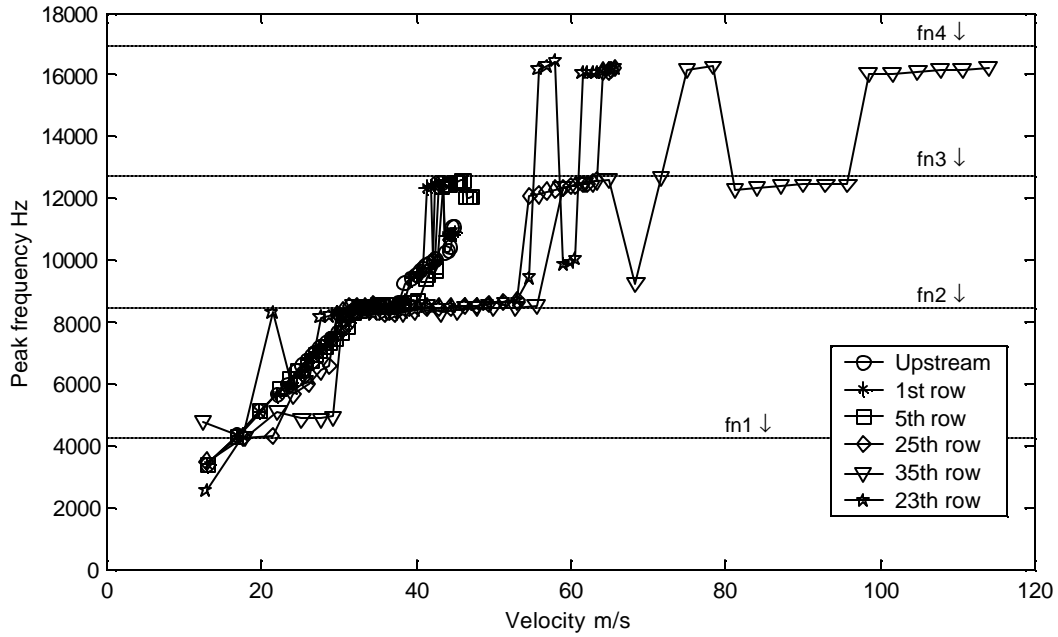


Figure F.31 Plot of frequency of dominant peak in spectra vs. flow velocity. Velocity estimated using density at measurement location and empty duct cross-sectional area. Staggered array with  $T/D = 3.0$  and  $L/D = 1.8$ .  $fn_1, fn_2, \dots$  acoustic natural frequencies with solidity effect.

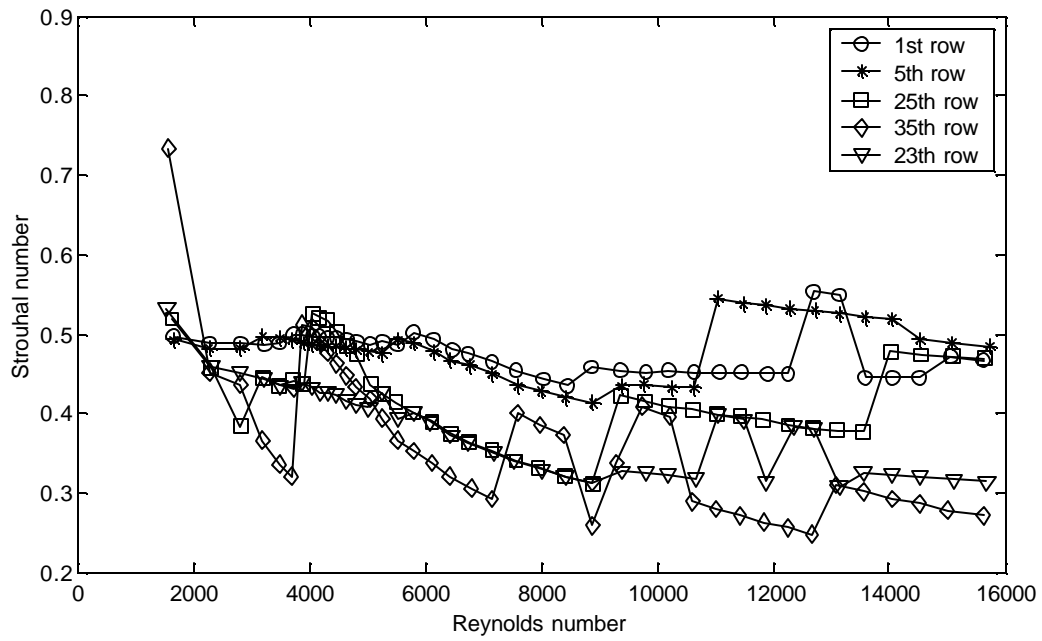


Figure F.32 Strouhal numbers determined at different positions throughout the array using dominant peak in spectra. Velocity estimated using density at measurement location and full duct cross-sectional area. Staggered array with  $T/D = 3.0$  and  $L/D = 1.8$ .

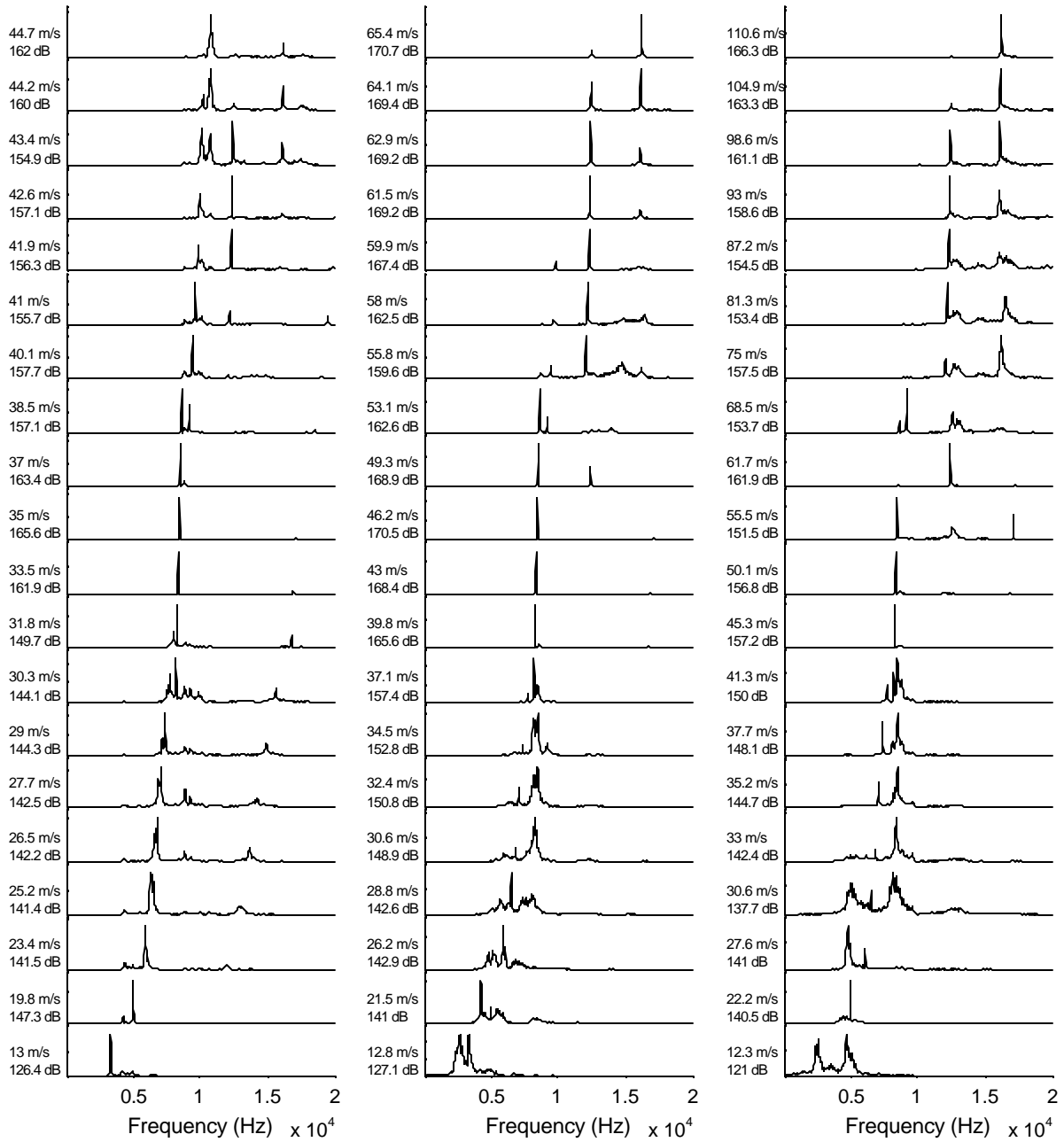


Figure F.33 Representative spectra taken at upstream position, after 25<sup>th</sup> row and after 35<sup>th</sup> row (left, center and right respectively). Spectra in same line taken at identical mass flow conditions. Velocity estimated using density at measurement location and empty duct cross-sectional area. Sound pressure level shown at left calculated for dominant peak in spectra. Staggered array with T/D = 3.0 and L/D = 1.8.

### Staggered Array with T/D = 3.0 and L/D = 1.6

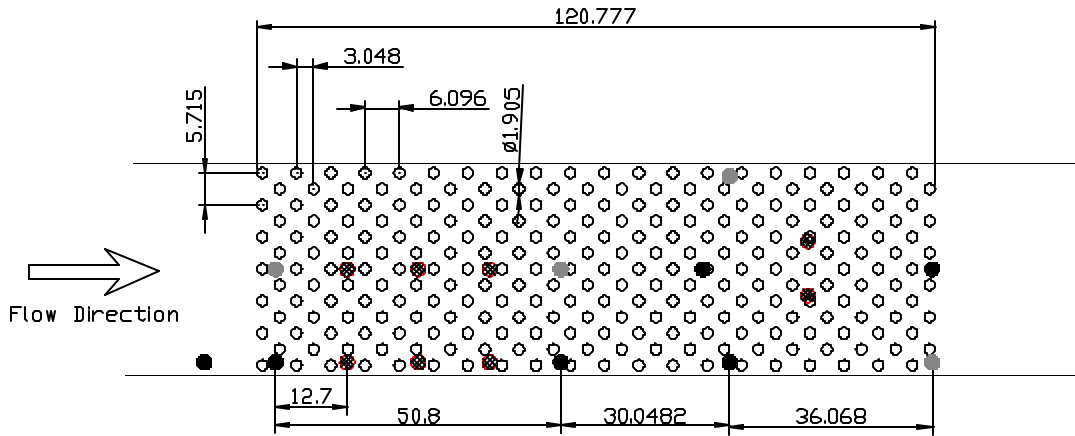


Figure F.34 Schematic of staggered array tested with T/D = 3.0 and L/D = 1.6. Black dots represent microphone positions. Gray dots represent positions where static pressure measurements were made. Hatched dots are plugged microphone locations. Dimensions in mm. Drawing to scale.

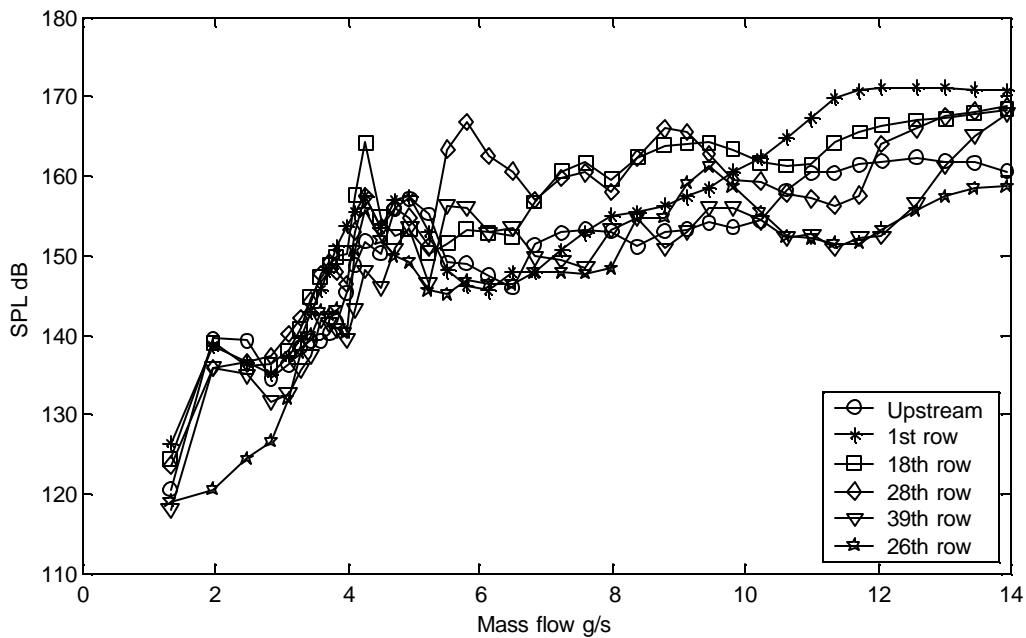


Figure F.35 Sound pressure level of dominant peak in spectra. Microphone positions shown in Figure F.34. Staggered array with T/D = 3.0 and L/D = 1.6.

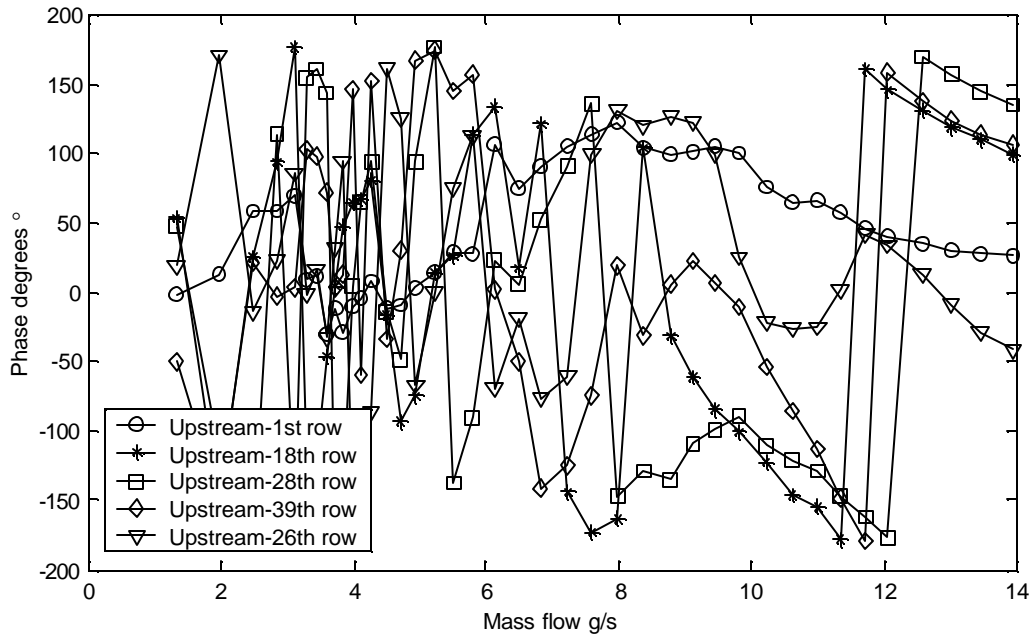


Figure F.36 Transfer function phase between microphone pairs shown at frequency of dominant peak in spectra of upstream microphone. Microphone positions shown in Figure F.34. Staggered array with  $T/D = 3.0$  and  $L/D = 1.6$ .

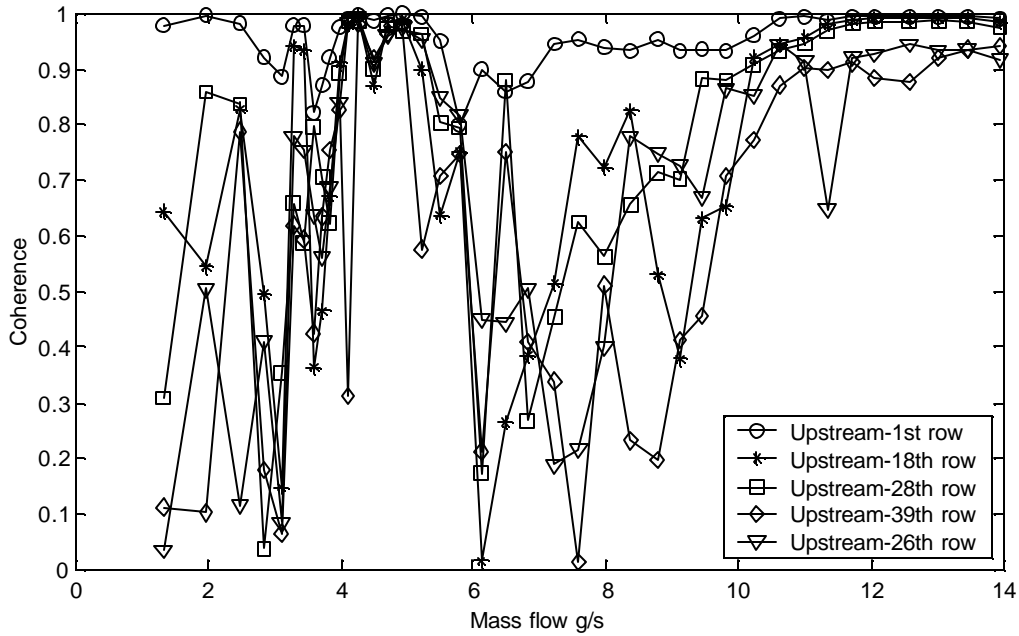


Figure F.37 Coherence between microphone pairs at frequency of dominant peak in spectra of upstream microphone. Phase measurements presented in Figure F.36 prone to error if coherence not close to one. Staggered array with  $T/D = 3.0$  and  $L/D = 1.6$ .



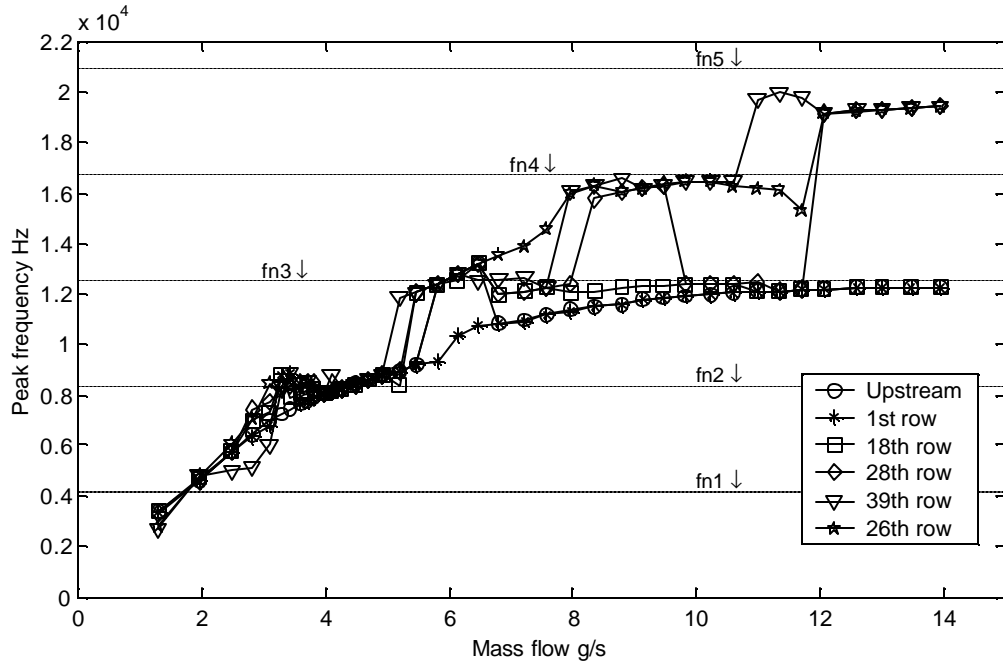
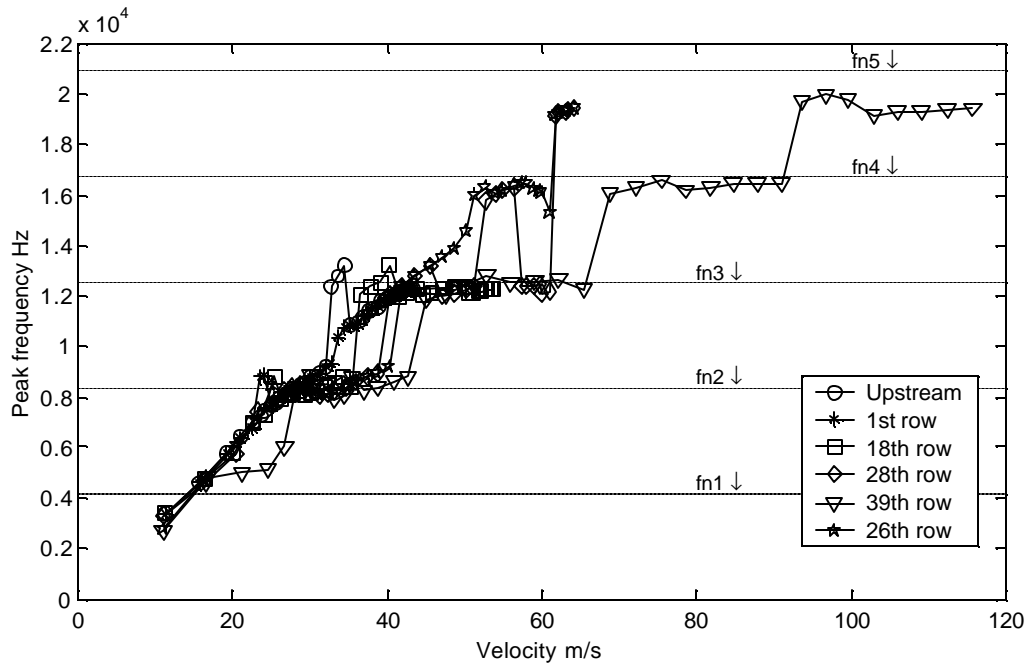


Figure F.38 Plot of frequency of dominant peak in spectra vs. mass flow. Staggered array with  $T/D = 3.0$  and  $L/D = 1.6$ .  $fn_1, fn_2, \dots$  acoustic natural frequencies with solidity effect.



F.39 Plot of frequency of dominant peak in spectra vs. flow velocity. Velocity estimated using density at measurement location and empty duct cross-sectional area. Staggered array with  $T/D = 3.0$  and  $L/D = 1.6$ .  $fn_1, fn_2, \dots$  acoustic natural frequencies with solidity effect.

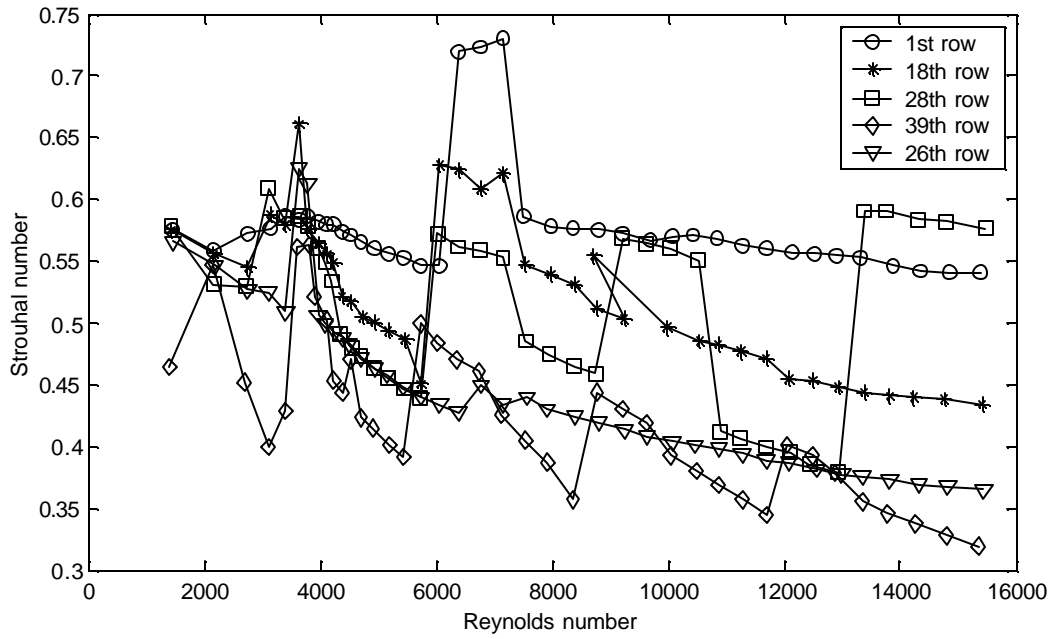


Figure F.40 Strouhal numbers determined at different positions throughout the array using dominant peak in spectra. Velocity estimated using density at measurement location and full duct cross-sectional area. Staggered array with  $T/D = 3.0$  and  $L/D = 1.6$ .

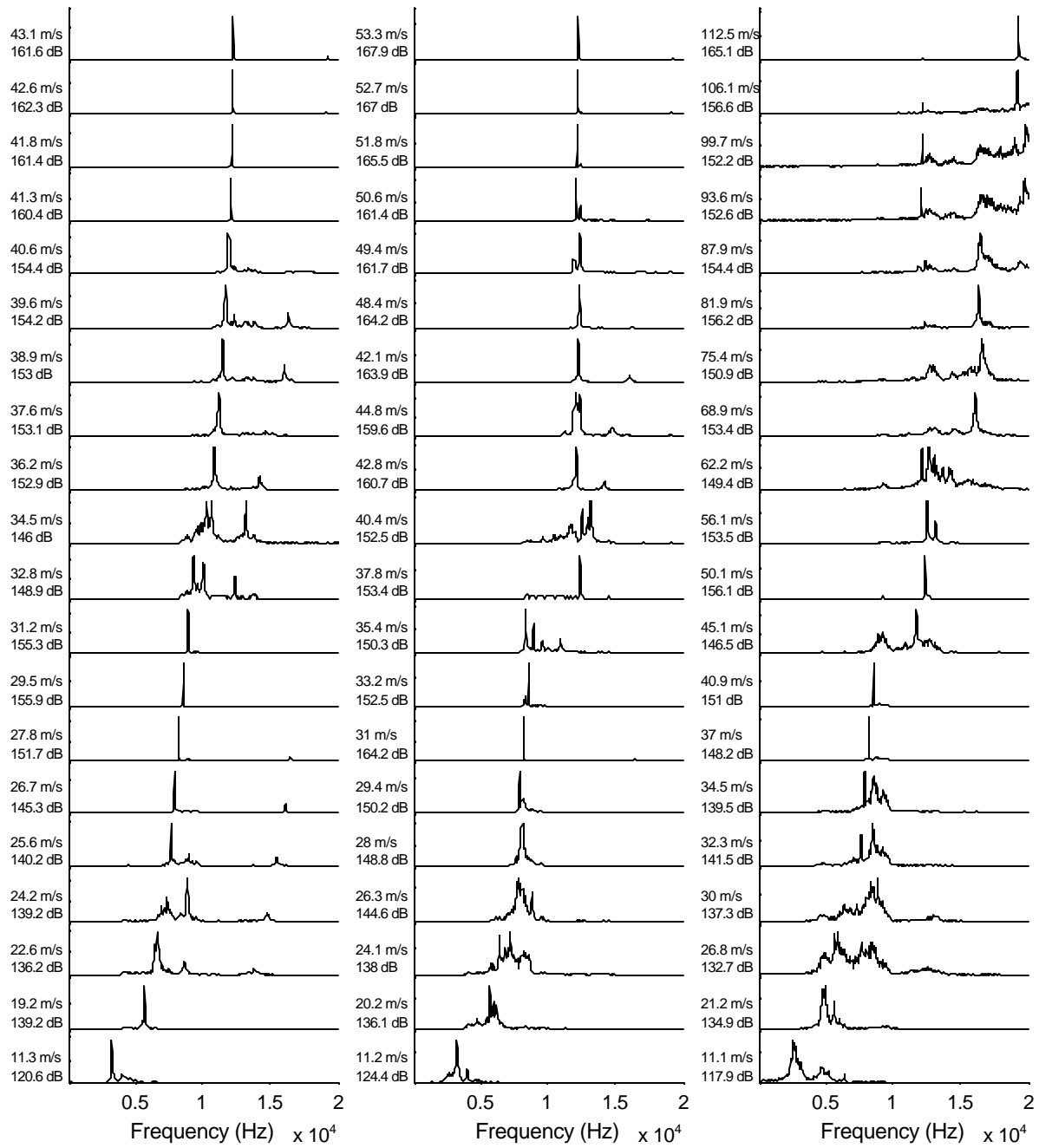


Figure F.41 Representative spectra taken at upstream position, after 18<sup>th</sup> row and after 39<sup>th</sup> row (left, center and right respectively). Spectra in same line taken at identical mass flow conditions. Velocity estimated using density at measurement location and empty duct cross-sectional area. Sound pressure level shown at left calculated for dominant peak in spectra. Staggered array with T/D = 3.0 and L/D = 1.6.

### Staggered Array with T/D = 3.0 and L/D = 1.4

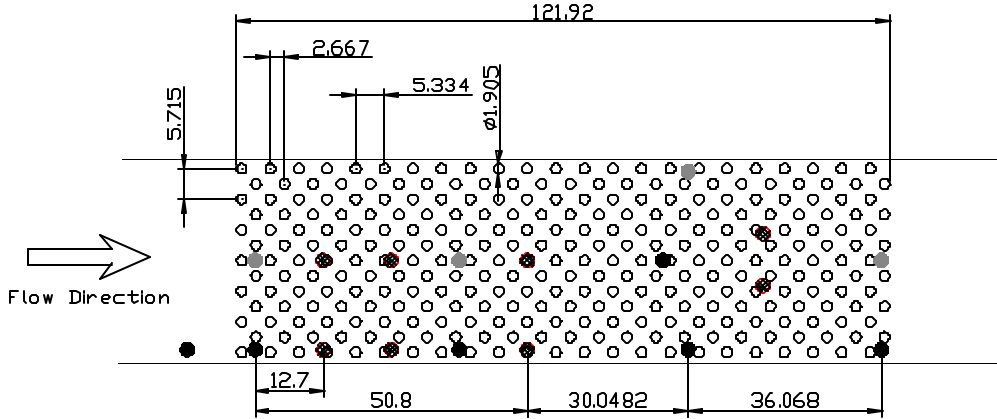


Figure F.42 Schematic of staggered array tested with  $T/D = 3.0$  and  $L/D = 1.4$ . Black dots represent microphone positions. Gray dots represent positions where static pressure measurements were made. Hatched dots are plugged microphone locations. Dimensions in mm. Drawing to scale.

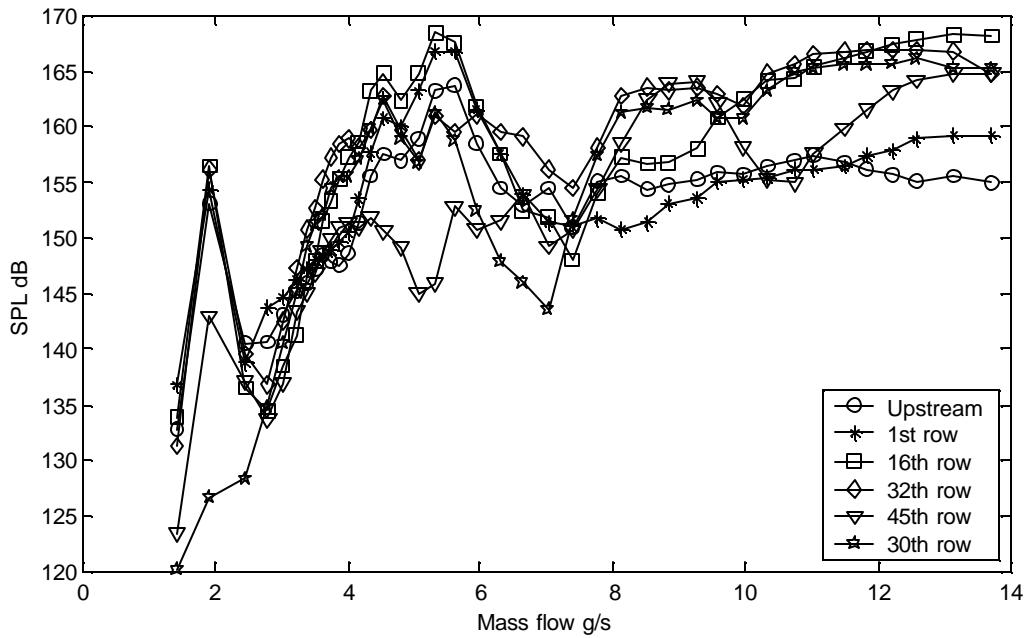


Figure F.43 Sound pressure level of dominant peak in spectra. Microphone positions shown in Figure F.42. Staggered array with  $T/D = 3.0$  and  $L/D = 1.4$ .

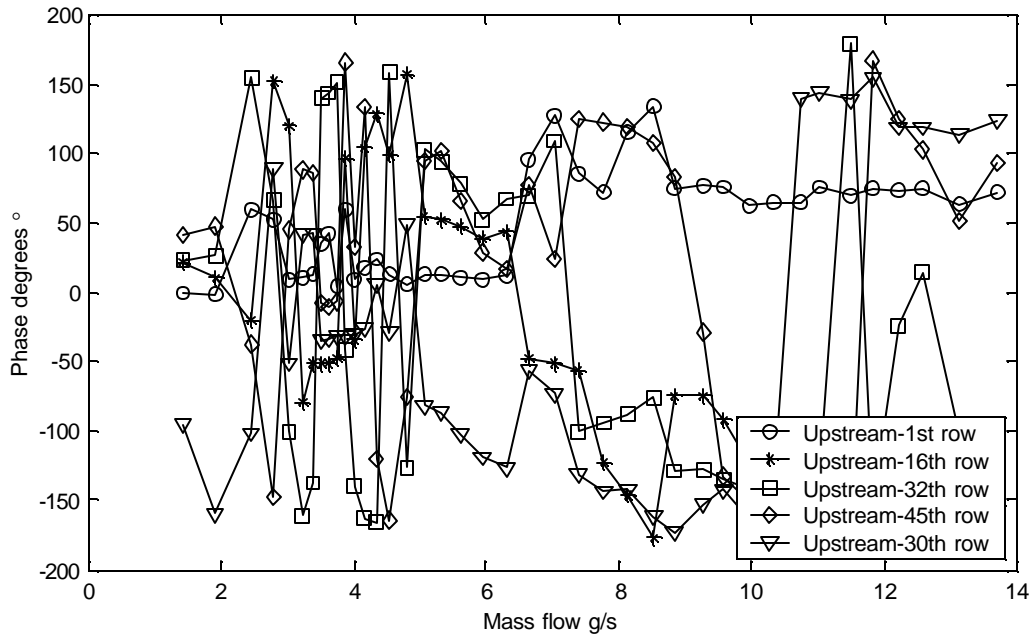


Figure F.44 Transfer function phase between microphone pairs shown at frequency of dominant peak in spectra of upstream microphone. Microphone positions shown in Figure F.42. Staggered array with  $T/D = 3.0$  and  $L/D = 1.4$ .

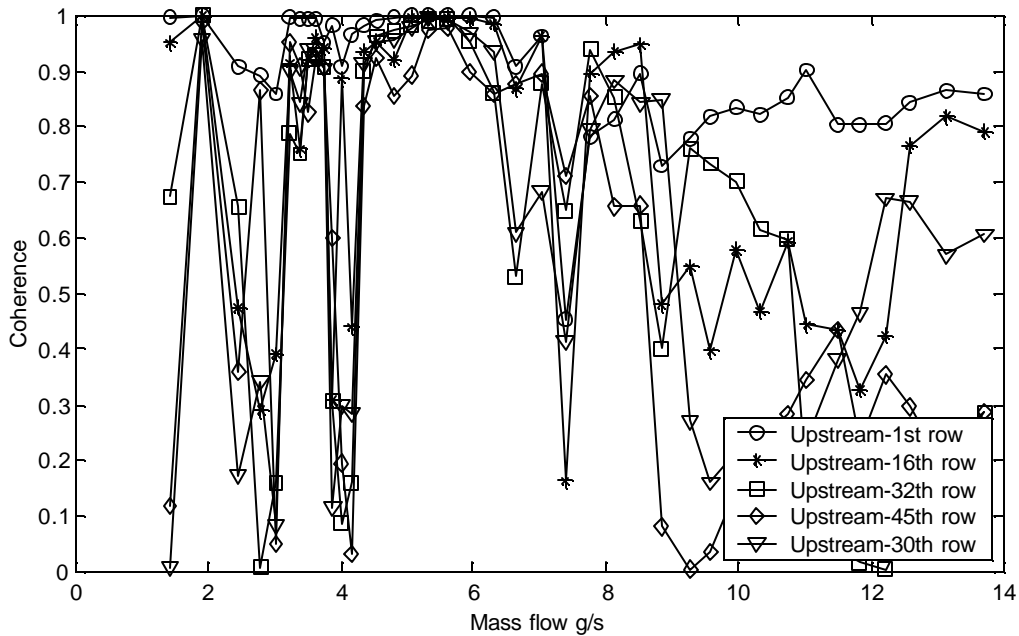


Figure F.45 Coherence between microphone pairs at frequency of dominant peak in spectra of upstream microphone. Phase measurements presented in Figure F.44 prone to error if coherence not close to one. Staggered array with  $T/D = 3.0$  and  $L/D = 1.4$ .

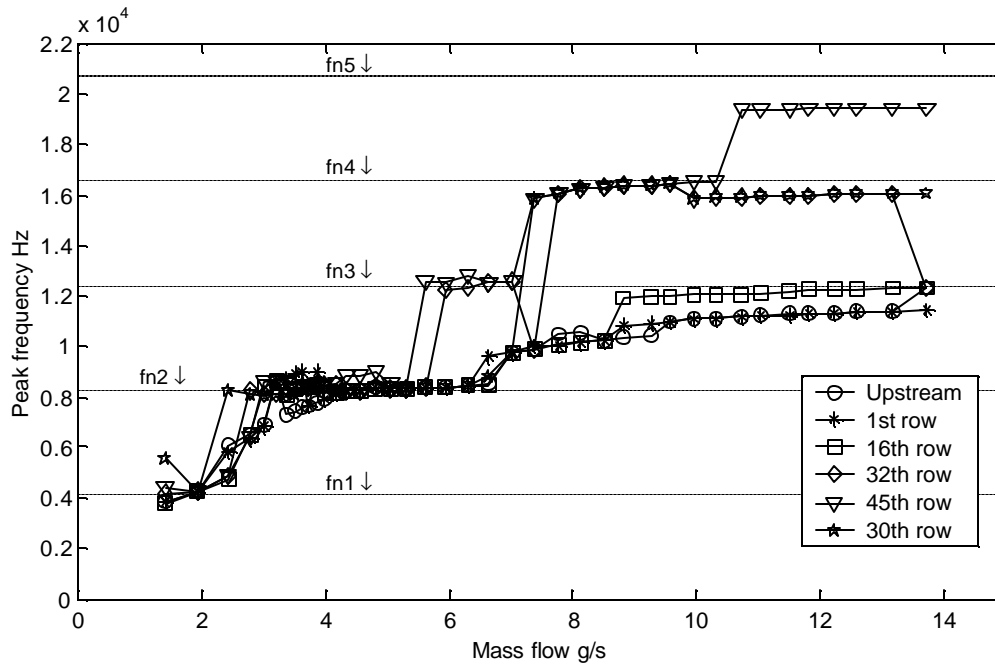


Figure F.46 Plot of frequency of dominant peak in spectra vs. mass flow. Staggered array with  $T/D = 3.0$  and  $L/D = 1.4$ .  $fn_1, fn_2, \dots$  acoustic natural frequencies with solidity effect.

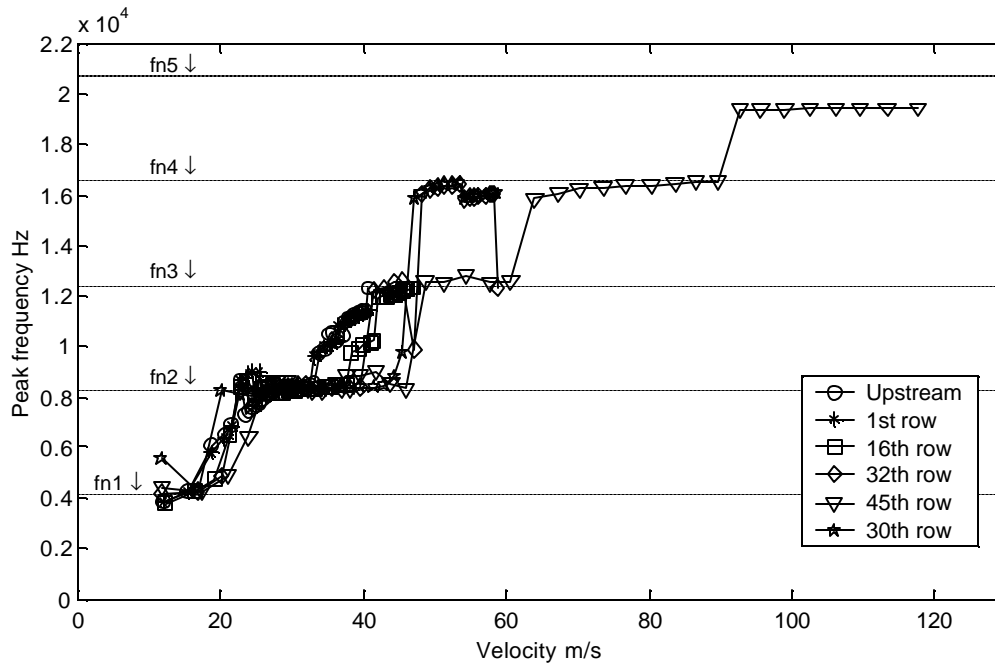


Figure F.47 Plot of frequency of dominant peak in spectra vs. flow velocity. Velocity estimated using density at measurement location and empty duct cross-sectional area. Staggered array with  $T/D = 3.0$  and  $L/D = 1.4$ .  $fn_1, fn_2, \dots$  acoustic natural frequencies with solidity effect.

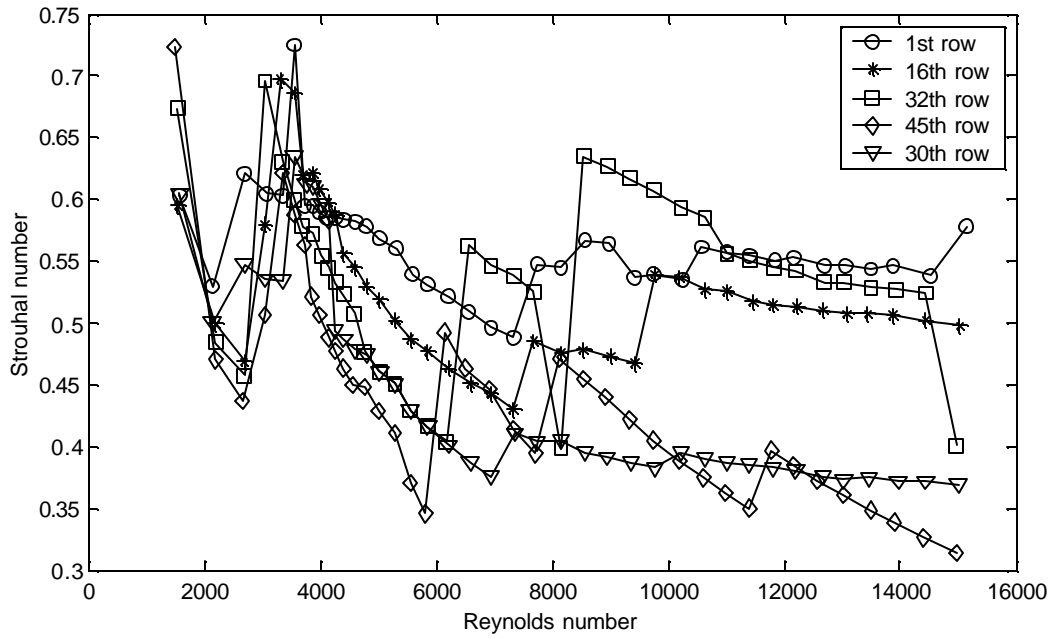


Figure F.48 Strouhal numbers determined at different positions throughout the array using dominant peak in spectra. Velocity estimated using density at measurement location and full duct cross-sectional area. Staggered array with  $T/D = 3.0$  and  $L/D = 1.4$ .

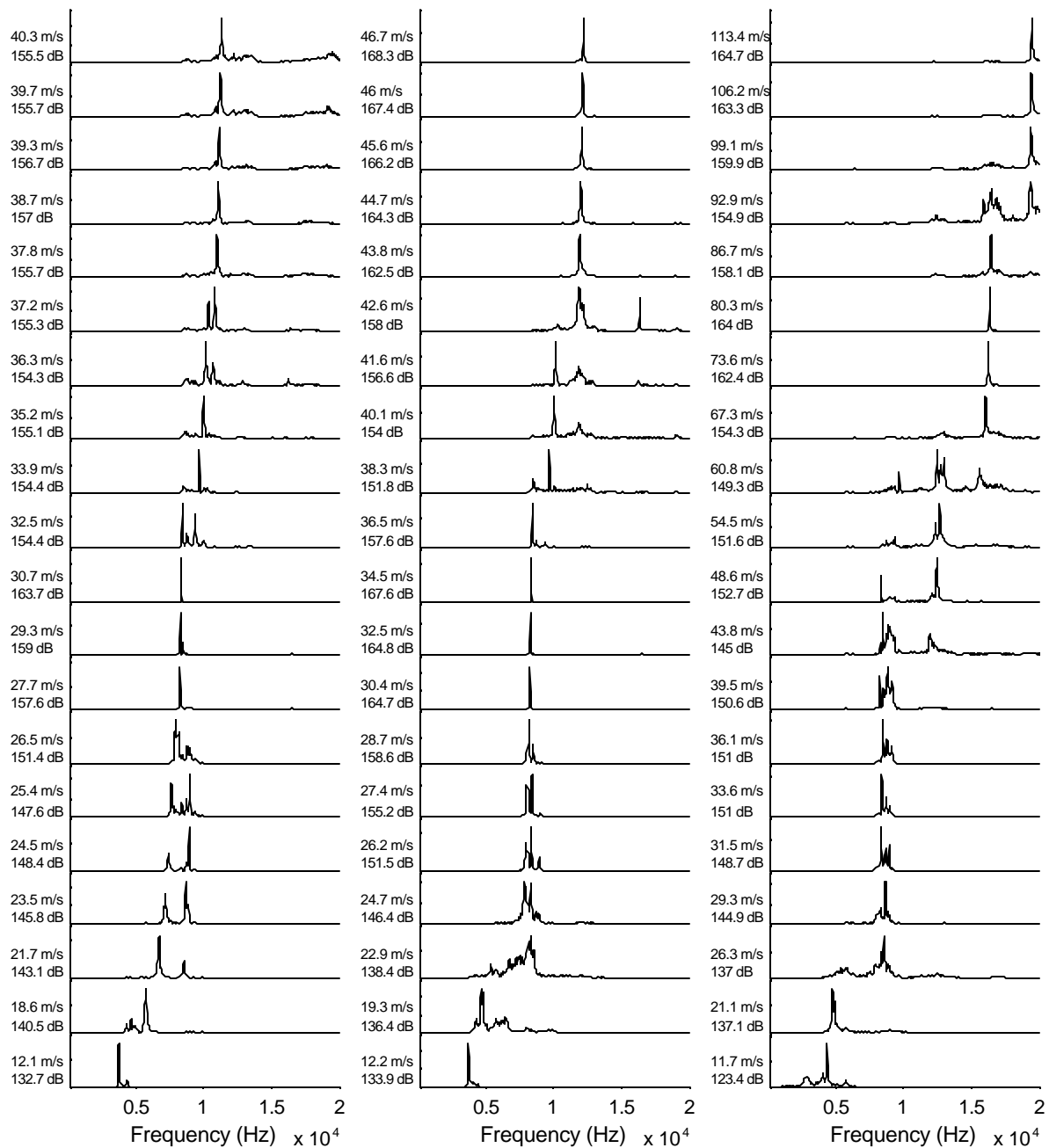


Figure F.49 Representative spectra taken at upstream position, after 16<sup>th</sup> row and after 45<sup>th</sup> row (left, center and right respectively). Spectra in same line taken at identical mass flow conditions. Velocity estimated using density at measurement location and empty duct cross-sectional area. Sound pressure level shown at left calculated for dominant peak in spectra. Staggered array with T/D = 3.0 and L/D = 1.4.



### Staggered Array with T/D = 3.0 and L/D = 1.2

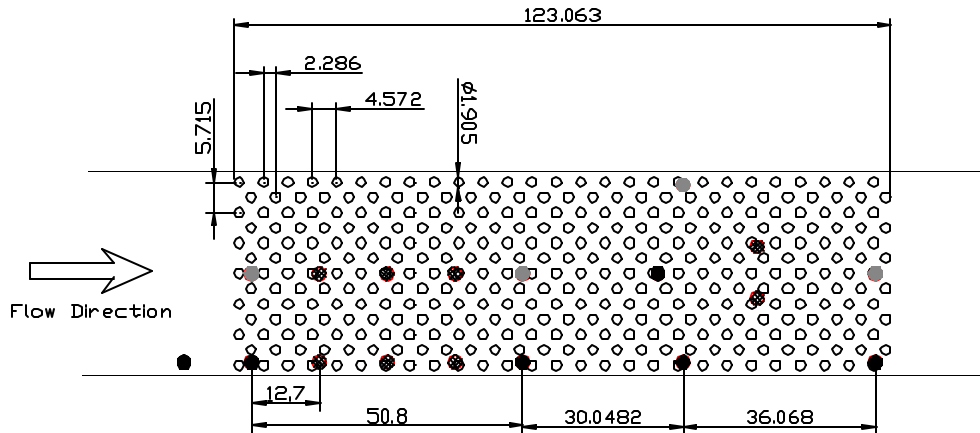


Figure F.50 Schematic of staggered array tested with  $T/D = 3.0$  and  $L/D = 1.2$ . Black dots represent microphone positions. Gray dots represent positions where static pressure measurements were made. Hatched dots are plugged microphone locations. Dimensions in mm. Drawing to scale.

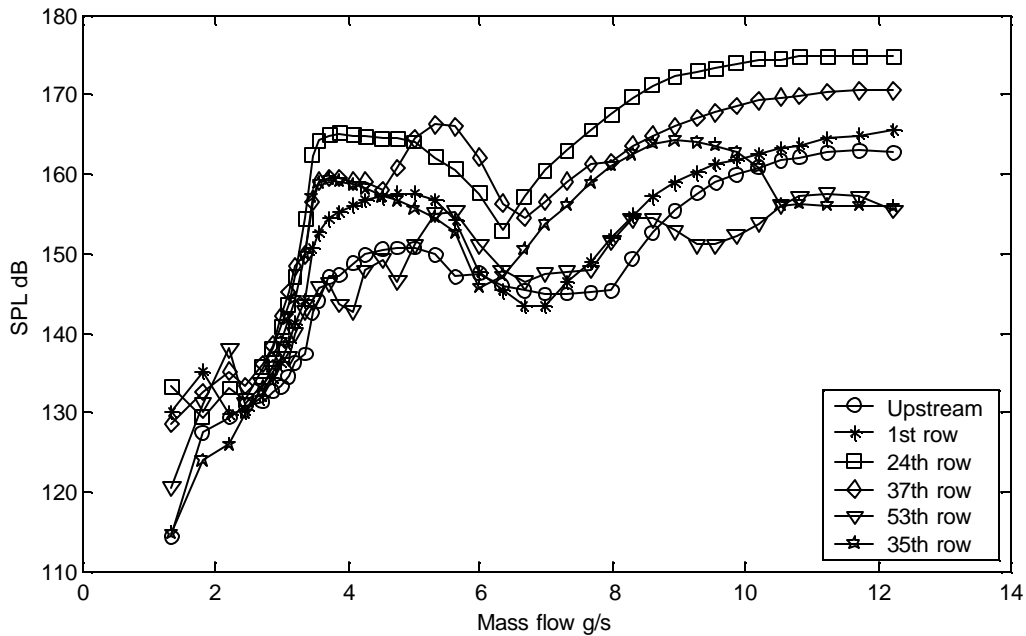


Figure F.51 Sound pressure level of dominant peak in spectra. Microphone positions shown in Figure F.50. Staggered array with  $T/D = 3.0$  and  $L/D = 1.2$ .

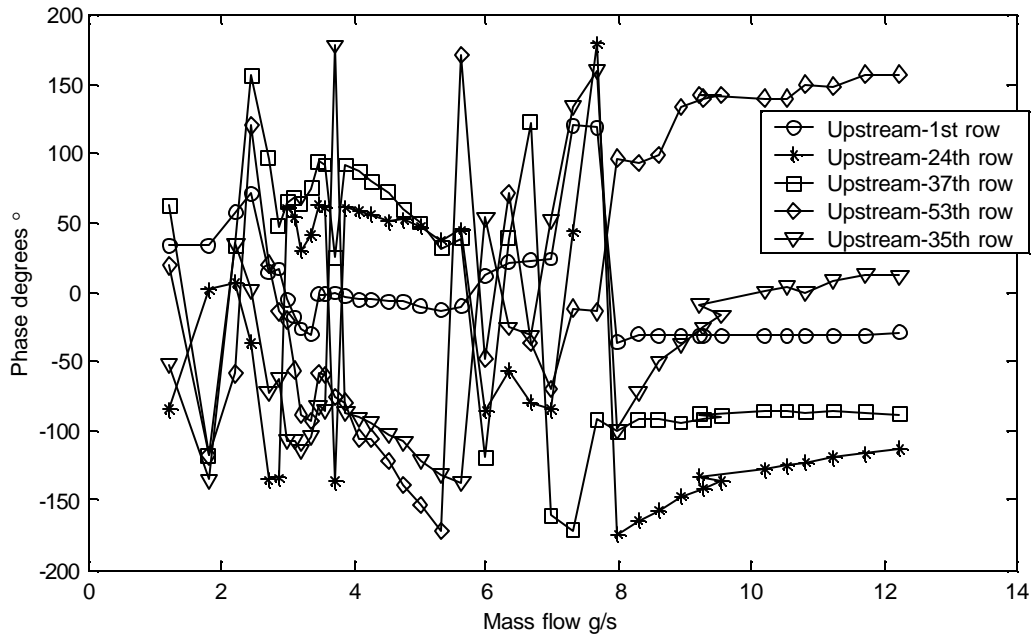


Figure F.52 Transfer function phase between microphone pairs shown at frequency of dominant peak in spectra of upstream microphone. Microphone positions shown in Figure F.50. Staggered array with  $T/D = 3.0$  and  $L/D = 1.2$ .

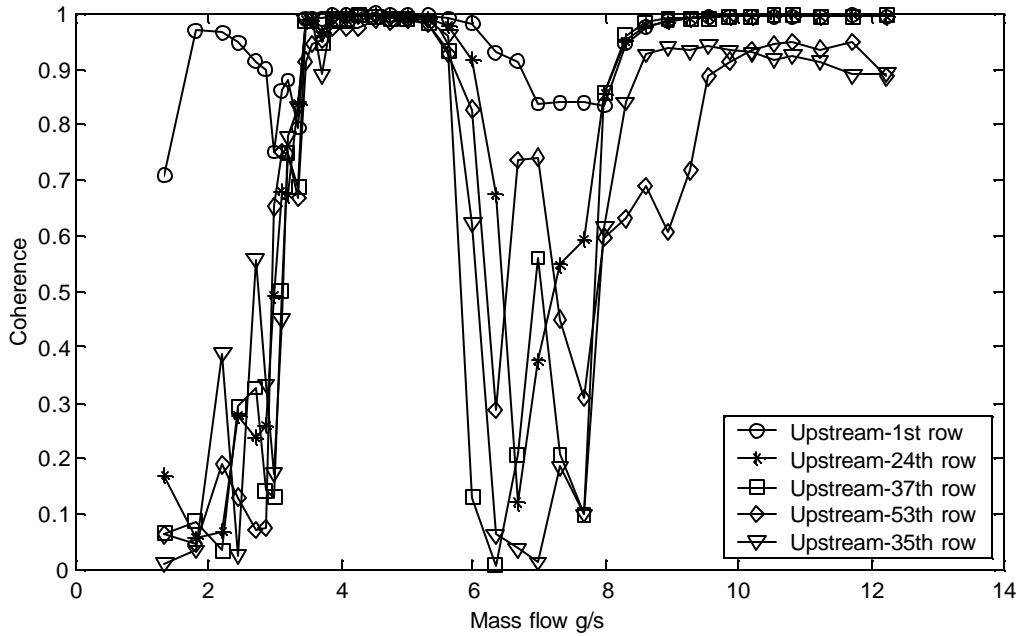


Figure F.53 Coherence between microphone pairs at frequency of dominant peak in spectra of upstream microphone. Phase measurements presented in Figure F.52 prone to error if coherence not close to one. Staggered array with  $T/D = 3.0$  and  $L/D = 1.2$ .

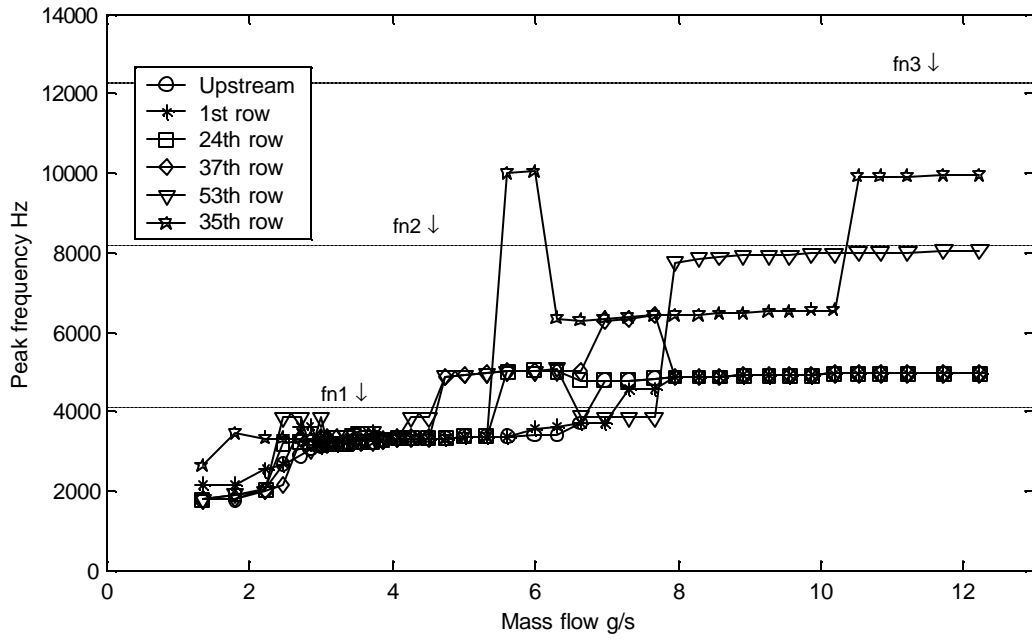


Figure F.54 Plot of frequency of dominant peak in spectra vs. mass flow. Staggered array with  $T/D = 3.0$  and  $L/D = 1.2$ .  $fn_1, fn_2, \dots$  acoustic natural frequencies with solidity effect.

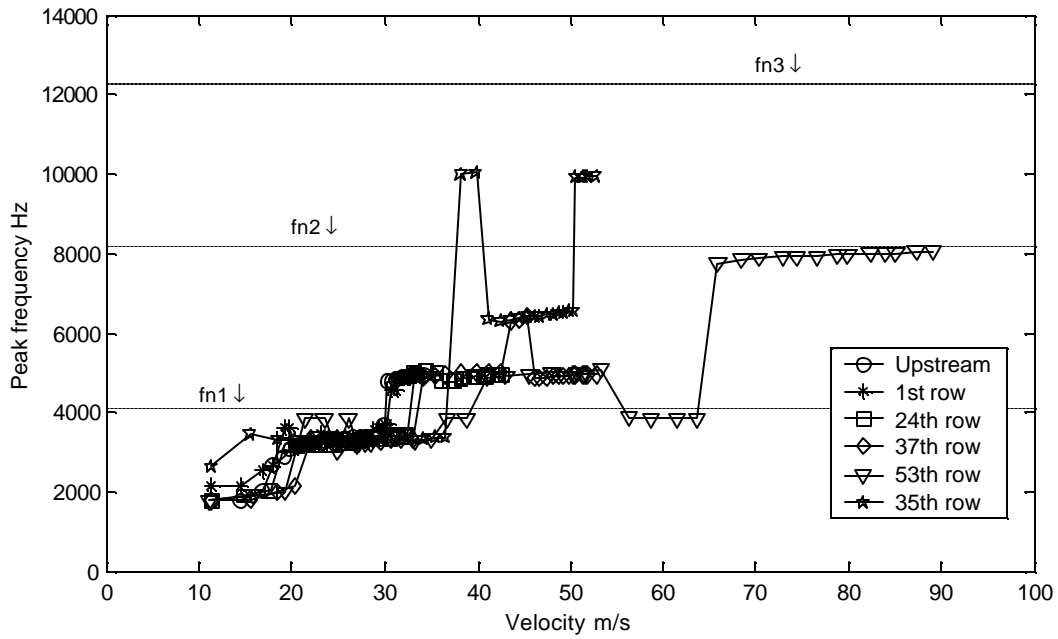


Figure F.55 Plot of frequency of dominant peak in spectra vs. flow velocity. Velocity estimated using density at measurement location and empty duct cross-sectional area. Staggered array with  $T/D = 3.0$  and  $L/D = 1.2$ .  $fn_1, fn_2, \dots$  acoustic natural frequencies with solidity effect.

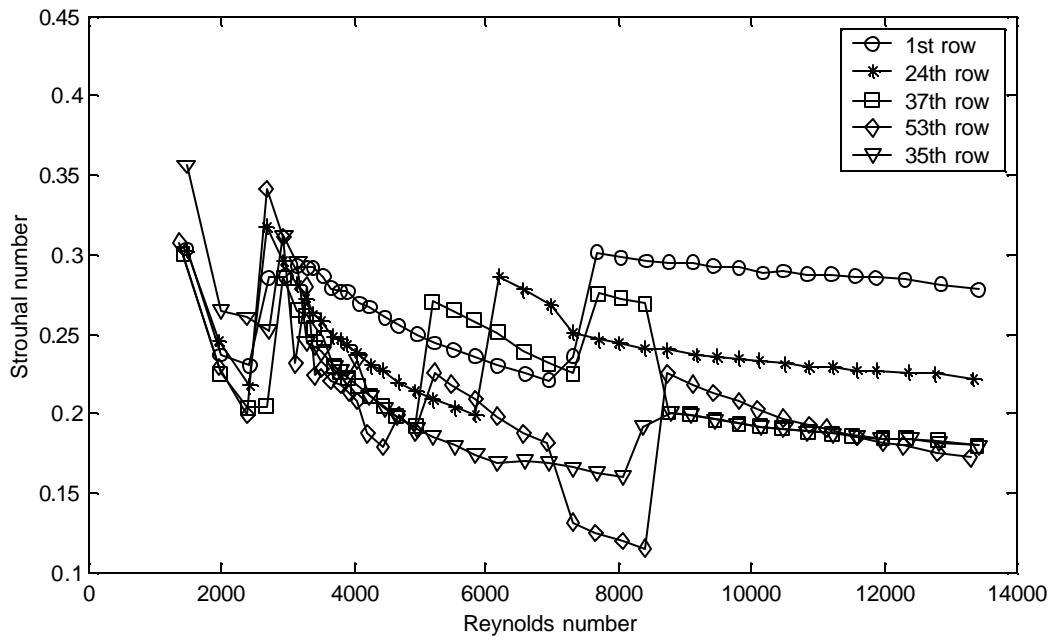


Figure F.56 Strouhal numbers determined at different positions throughout the array using dominant peak in spectra. Velocity estimated using density at measurement location and full duct cross-sectional area. Staggered array with  $T/D = 3.0$  and  $L/D = 1.2$ .

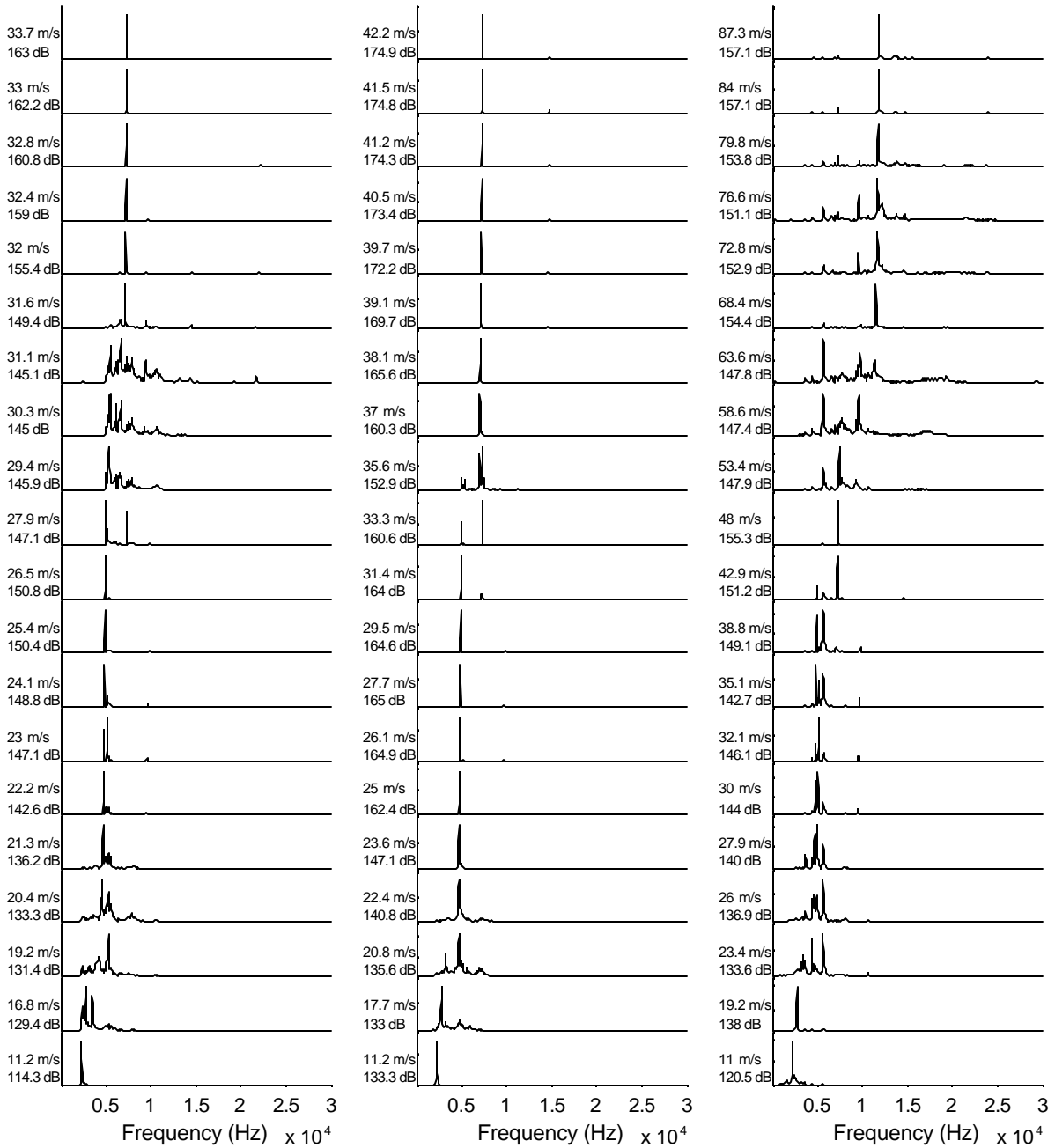


Figure F.57 Representative spectra taken at upstream position, after 24<sup>th</sup> row and after 53<sup>rd</sup> row (left, center and right respectively). Spectra in same line taken at identical mass flow conditions. Velocity estimated using density at measurement location and empty duct cross-sectional area. Sound pressure level shown at left calculated for dominant peak in spectra. Staggered array with T/D = 3.0 and L/D = 1.2.

### Staggered Array with T/D = 3.0 and L/D = 1.1

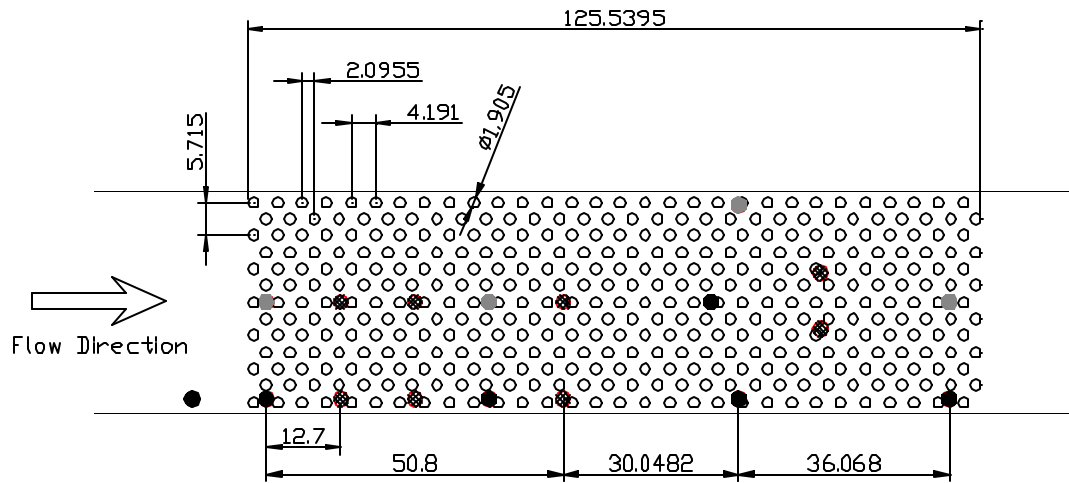


Figure F.58 Schematic of staggered array tested with T/D = 3.0 and L/D = 1.1. Black dots represent microphone positions. Gray dots represent positions where static pressure measurements were made. Hatched dots are plugged microphone locations. Dimensions in mm. Drawing to scale.

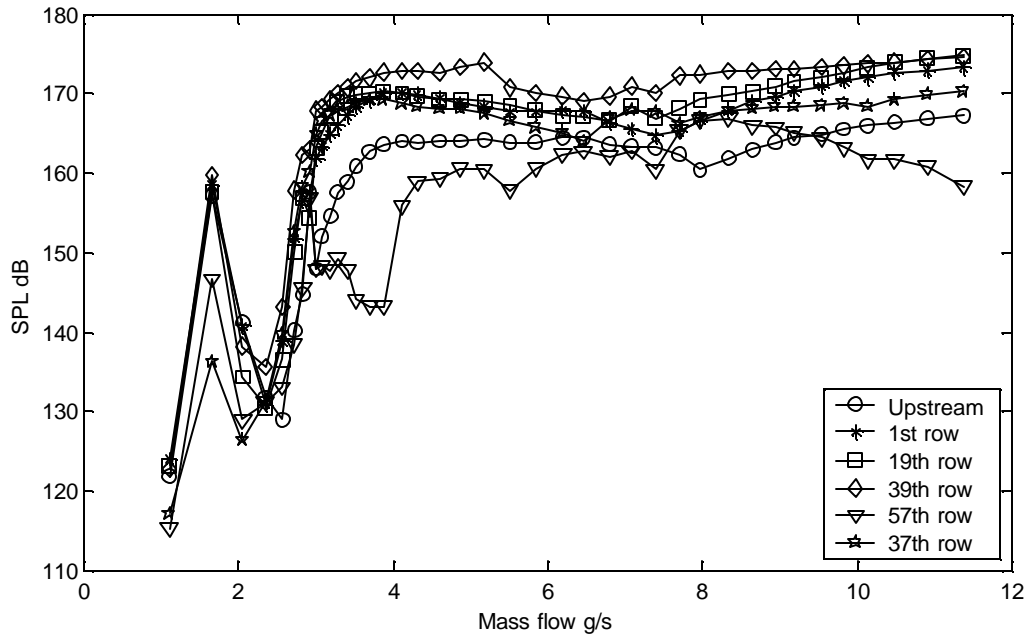


Figure F.59 Sound pressure level of dominant peak in spectra. Microphone positions shown in Figure F.58. Staggered array with T/D = 3.0 and L/D = 1.1.

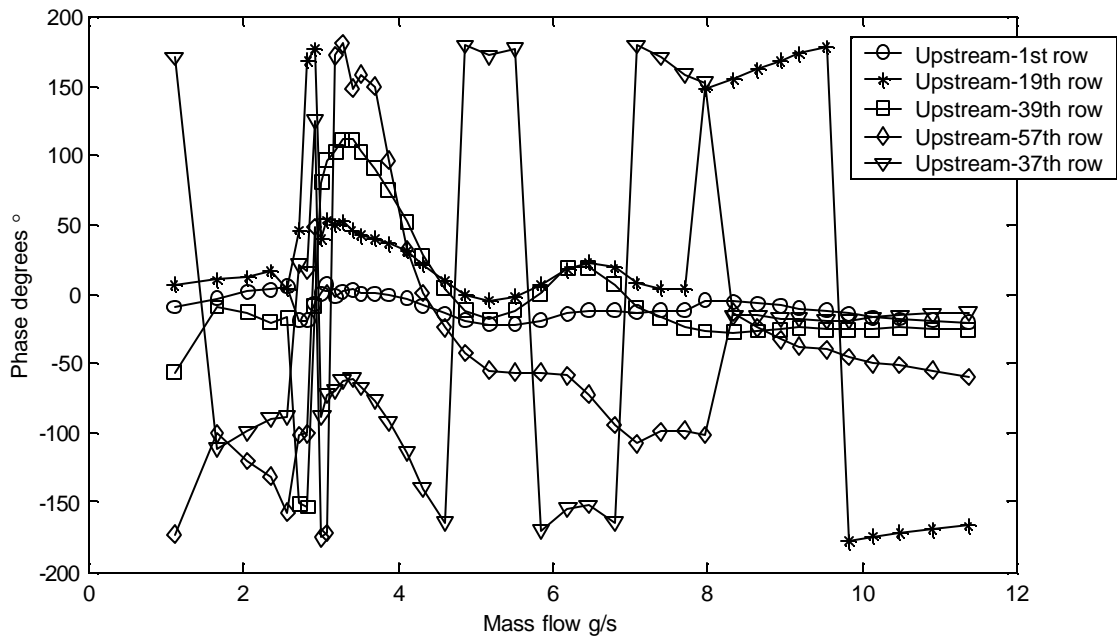


Figure F.60 Transfer function phase between microphone pairs shown at frequency of dominant peak in spectra of upstream microphone. Microphone positions shown in Figure F.58. Staggered array with  $T/D = 3.0$  and  $L/D = 1.1$ .

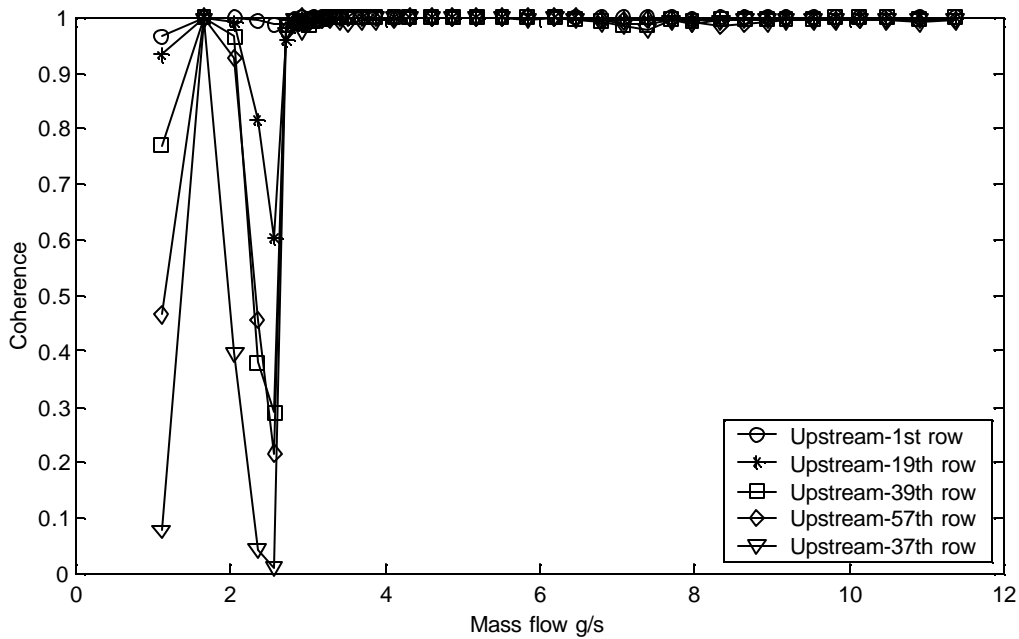


Figure F.61 Coherence between microphone pairs at frequency of dominant peak in spectra of upstream microphone. Phase measurements presented in Figure F.60 prone to error if coherence not close to one. Staggered array with  $T/D = 3.0$  and  $L/D = 1.1$ .

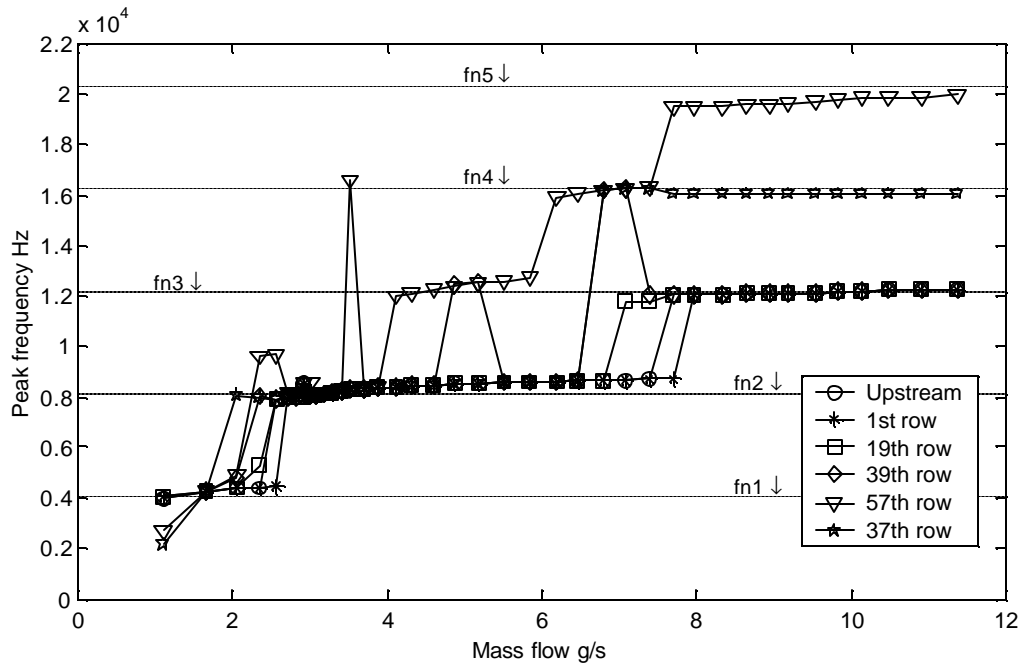


Figure F.62 Plot of frequency of dominant peak in spectra vs. mass flow. Staggered array with  $T/D = 3.0$  and  $L/D = 1.1$ .  $fn_1, fn_2, \dots$  acoustic natural frequencies with solidity effect.

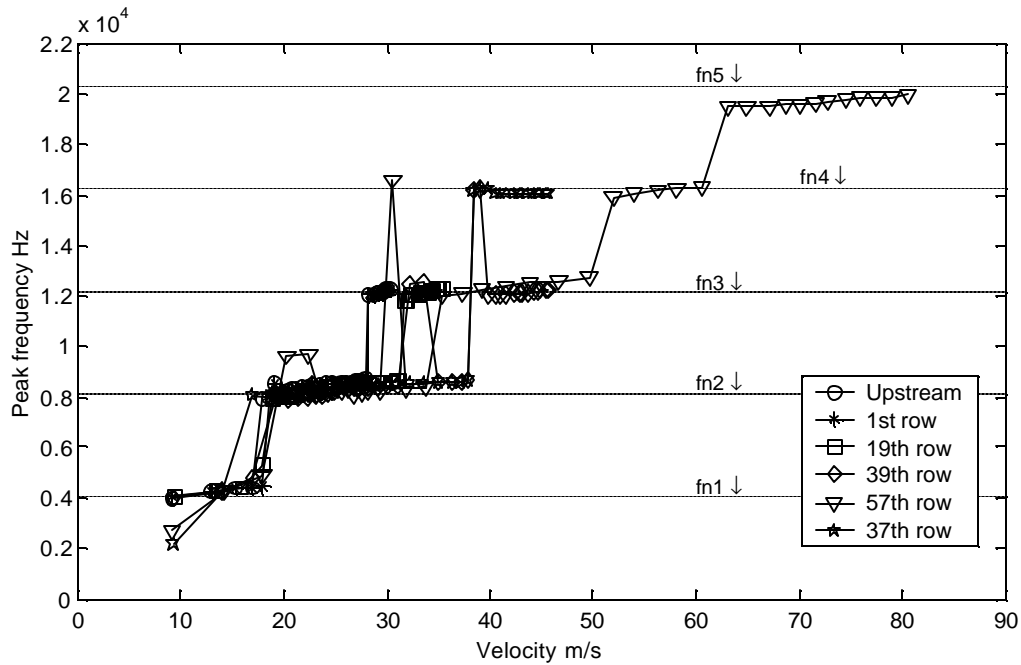


Figure F.63 Plot of frequency of dominant peak in spectra vs. flow velocity. Velocity estimated using density at measurement location and empty duct cross-sectional area. Staggered array with  $T/D = 3.0$  and  $L/D = 1.1$ .  $fn_1, fn_2, \dots$  acoustic natural frequencies with solidity effect.



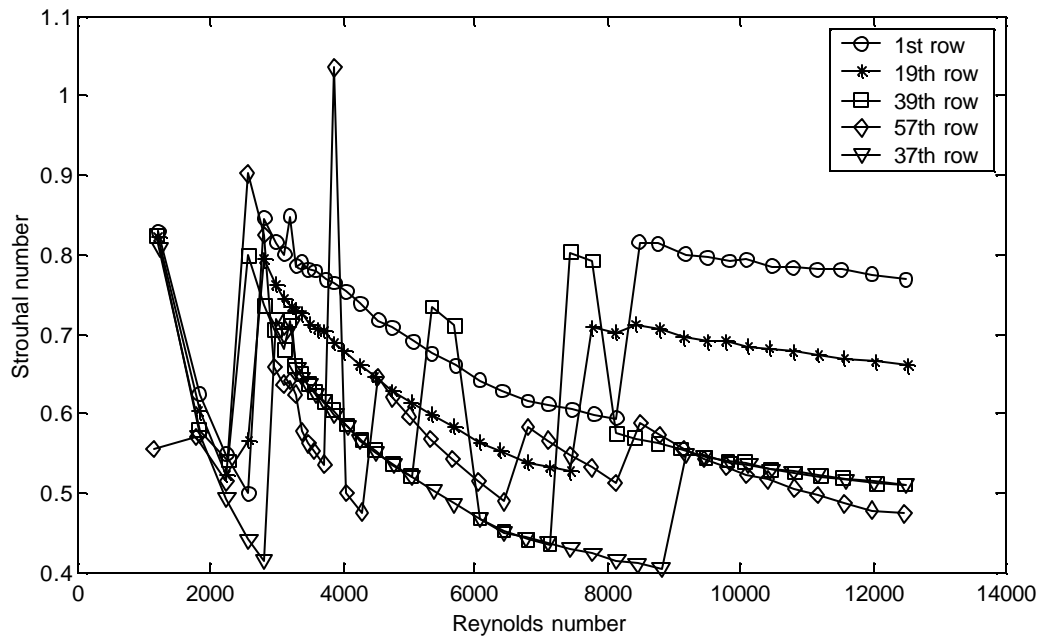


Figure F.64 Strouhal numbers determined at different positions throughout the array using dominant peak in spectra. Velocity estimated using density at measurement location and full duct cross-sectional area. Staggered array with  $T/D = 3.0$  and  $L/D = 1.1$ .

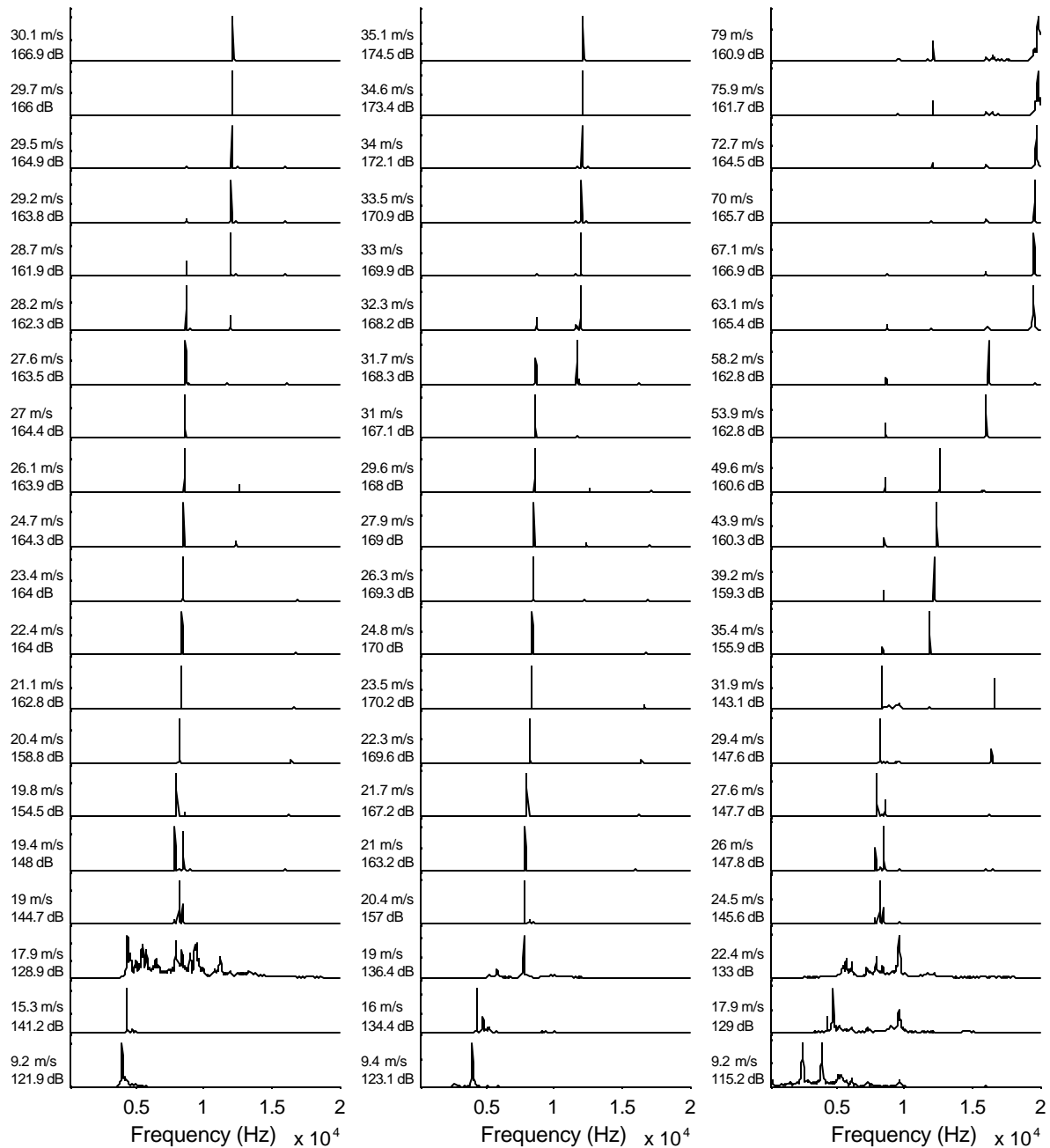


Figure F.65 Representative spectra taken at upstream position, after 19<sup>th</sup> row and after 57<sup>th</sup> row (left, center and right respectively). Spectra in same line taken at identical mass flow conditions. Velocity estimated using density at measurement location and empty duct cross-sectional area. Sound pressure level shown at left calculated for dominant peak in spectra. Staggered array with T/D = 3.0 and L/D = 1.1.

### Staggered Array with T/D = 3.0 and L/D = 1.0

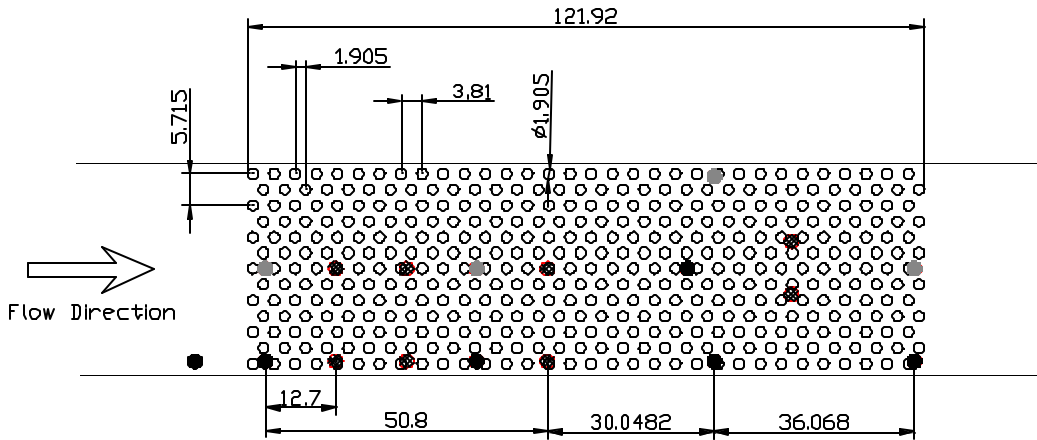


Figure F.66 Schematic of staggered array tested with T/D = 3.0 and L/D = 1.0. Black dots represent microphone positions. Gray dots represent positions where static pressure measurements were made. Hatched dots are plugged microphone locations. Dimensions in mm. Drawing to scale.

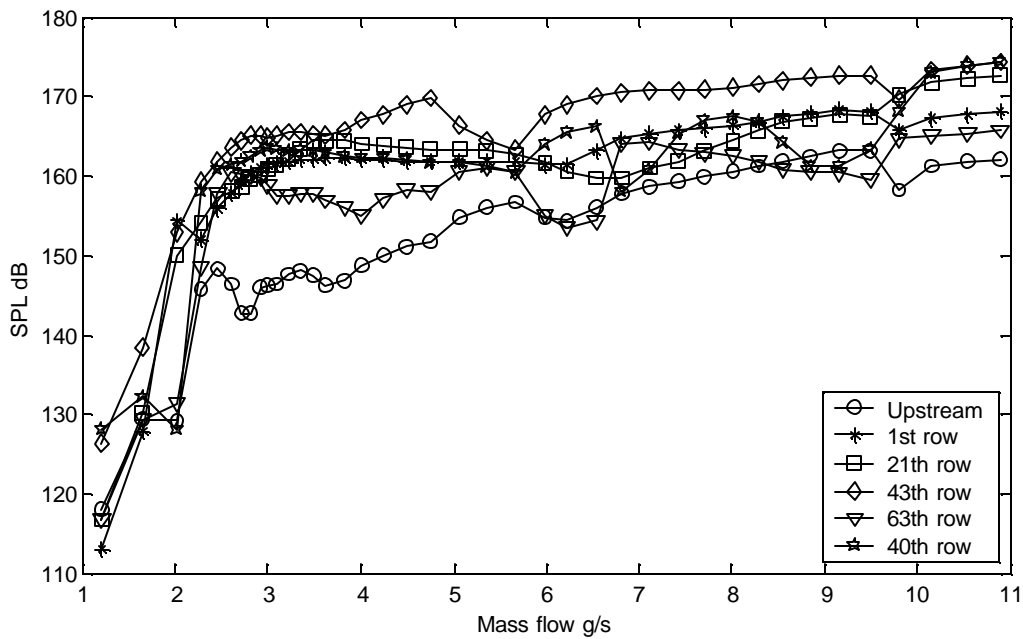


Figure F.67 Sound pressure level of dominant peak in spectra. Microphone positions shown in Figure F.66. Staggered array with T/D = 3.0 and L/D = 1.0.

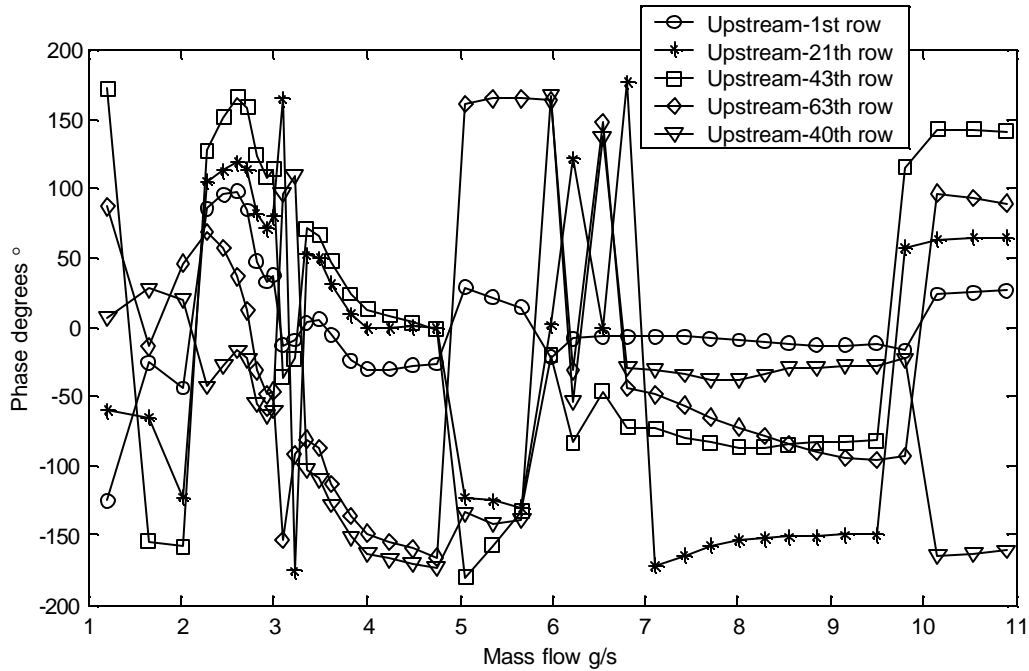


Figure F.68 Transfer function phase between microphone pairs shown at frequency of dominant peak in spectra of upstream microphone. Microphone positions shown in Figure F.66. Staggered array with  $T/D = 3.0$  and  $L/D = 1.0$ .

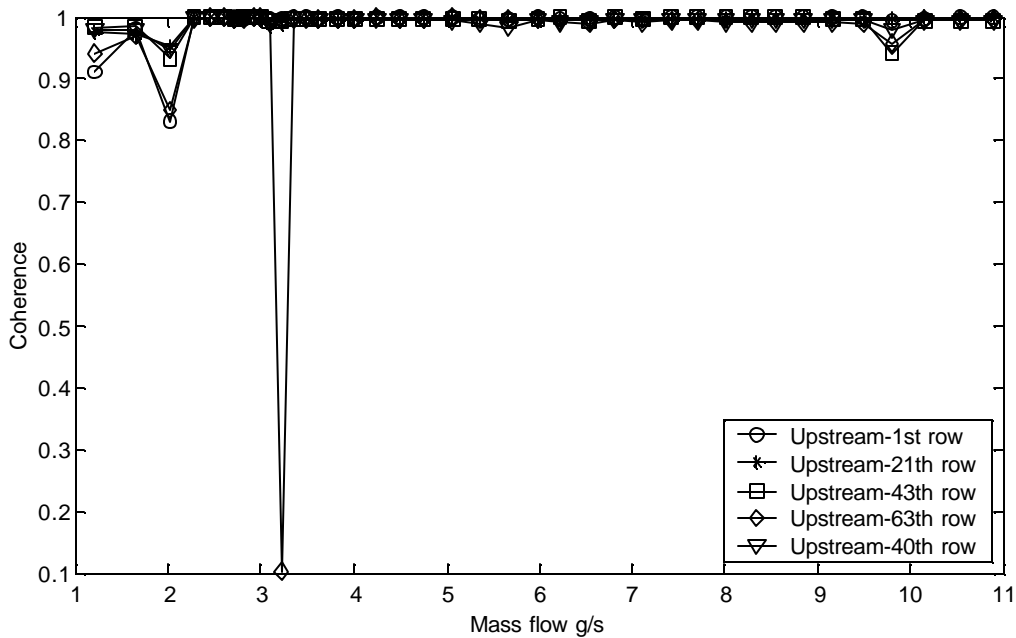


Figure F.69 Coherence between microphone pairs at frequency of dominant peak in spectra of upstream microphone. Phase measurements presented in Figure F.68 prone to error if coherence not close to one. Staggered array with  $T/D = 3.0$  and  $L/D = 1.0$ .

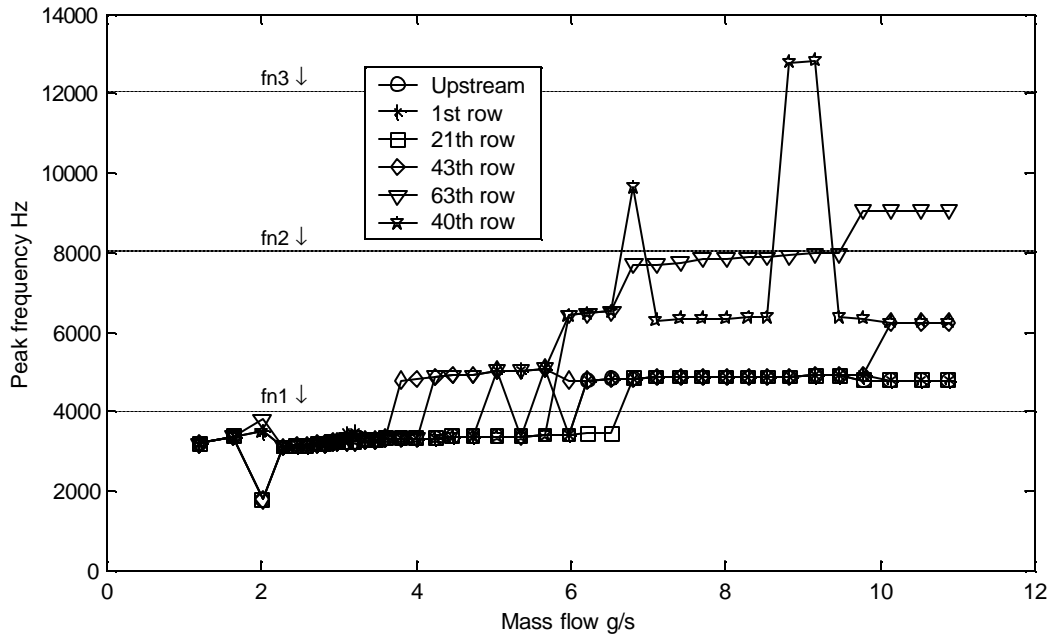


Figure F.70 Plot of frequency of dominant peak in spectra vs. mass flow. Staggered array with  $T/D = 3.0$  and  $L/D = 1.0$ .  $fn_1, fn_2, \dots$  acoustic natural frequencies with solidity effect.

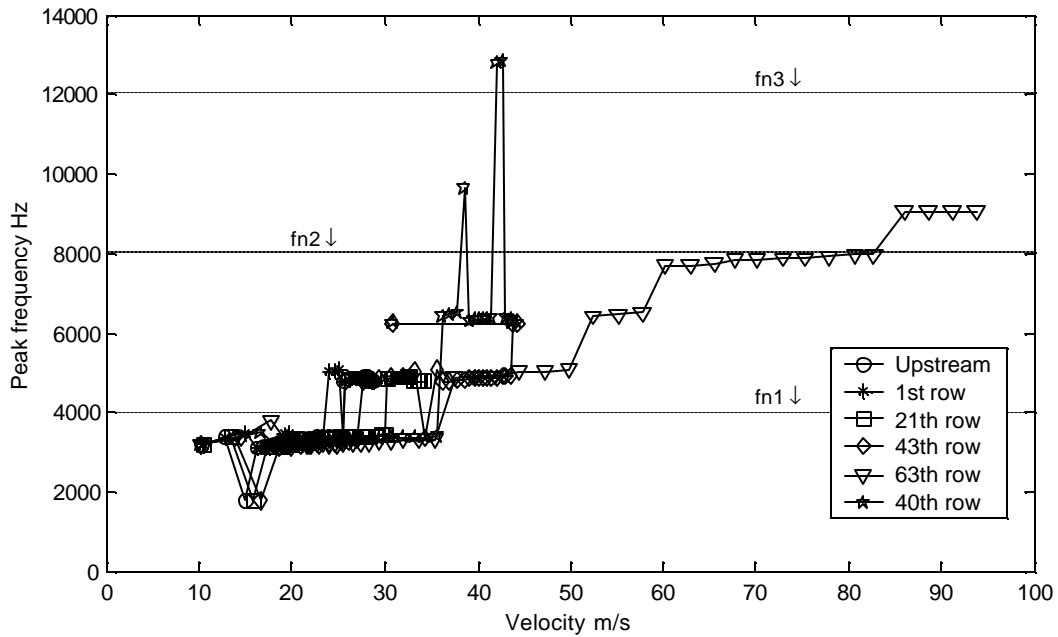


Figure F.71 Plot of frequency of dominant peak in spectra vs. flow velocity. Velocity estimated using density at measurement location and empty duct cross-sectional area. Staggered array with  $T/D = 3.0$  and  $L/D = 1.0$ .  $fn_1, fn_2, \dots$  acoustic natural frequencies with solidity effect.

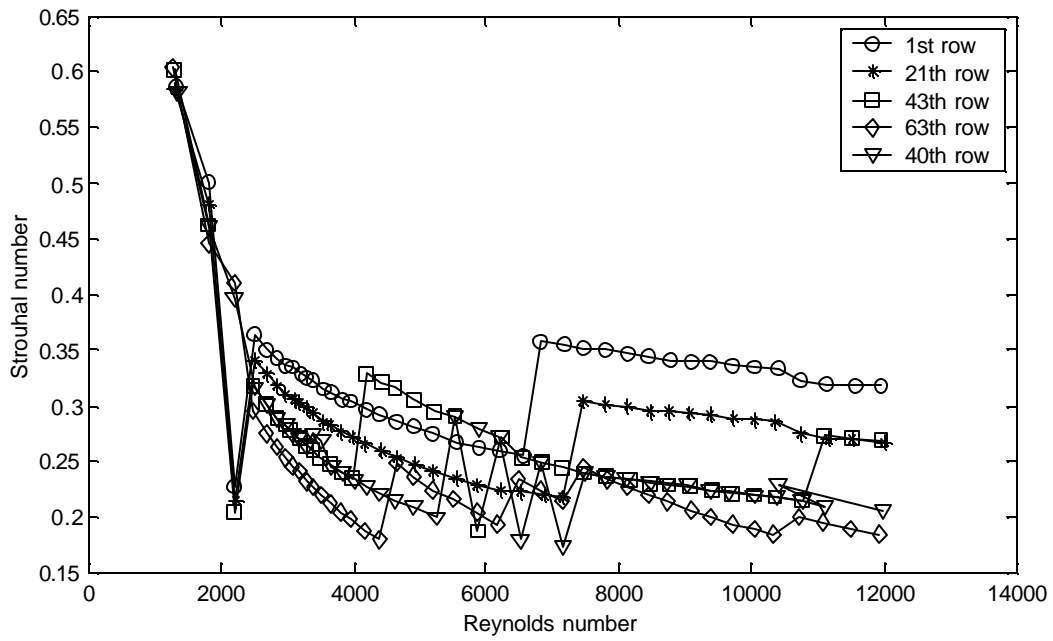


Figure F.72 Strouhal numbers determined at different positions throughout the array using dominant peak in spectra. Velocity estimated using density at measurement location and full duct cross-sectional area. Staggered array with  $T/D = 3.0$  and  $L/D = 1.0$ .

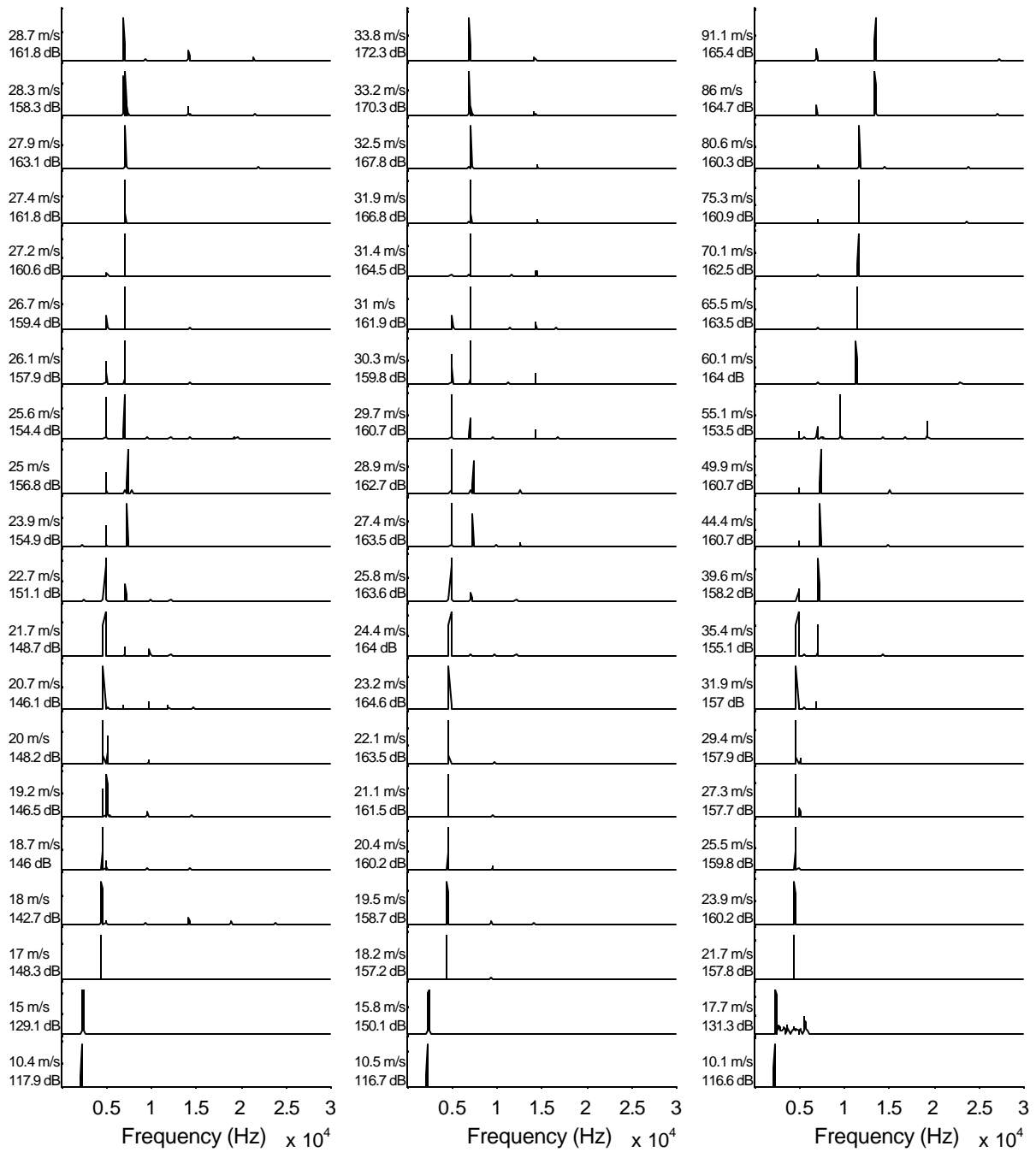


Figure F.73 Representative spectra taken at upstream position, after 21<sup>st</sup> row and after 63<sup>rd</sup> row (left, center and right respectively). Spectra in same line taken at identical mass flow conditions. Velocity estimated using density at measurement location and empty duct cross-sectional area. Sound pressure level shown at left calculated for dominant peak in spectra. Staggered array with T/D = 3.0 and L/D = 1.0.

### Staggered Array with T/D = 3.0 and L/D = 0.9

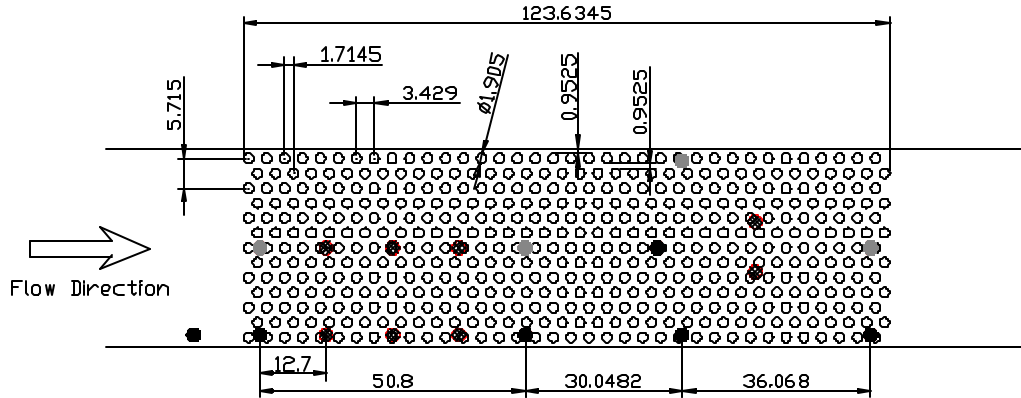


Figure F.74 Schematic of staggered array tested with  $T/D = 3.0$  and  $L/D = 0.9$ . Black dots represent microphone positions. Gray dots represent positions where static pressure measurements were made. Hatched dots are plugged microphone locations. Dimensions in mm. Drawing to scale.

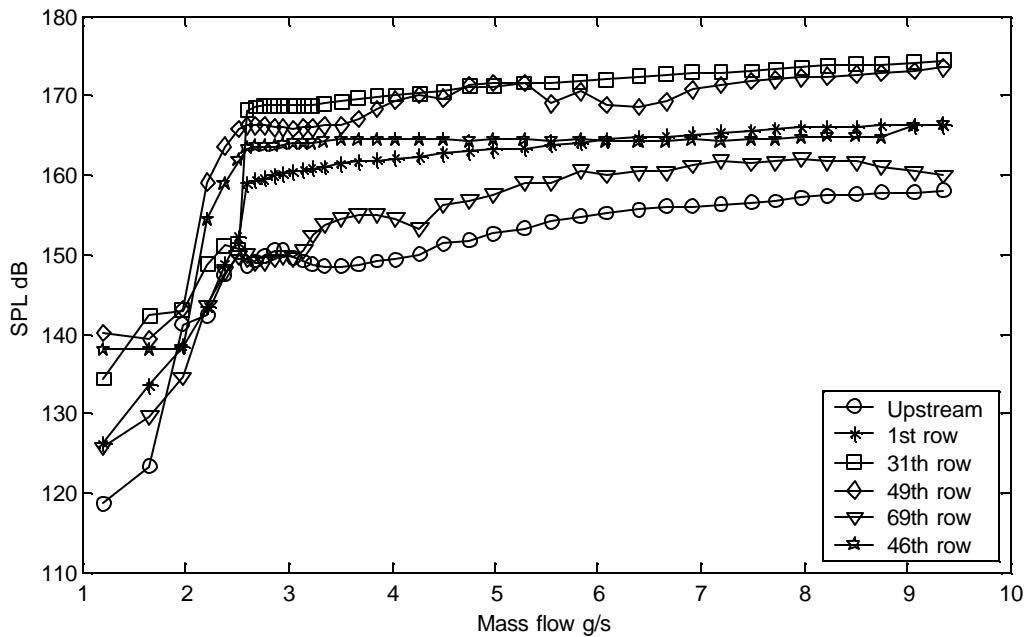


Figure F.75 Sound pressure level of dominant peak in spectra. Microphone positions shown in Figure F.74. Staggered array with  $T/D = 3.0$  and  $L/D = 0.9$ .



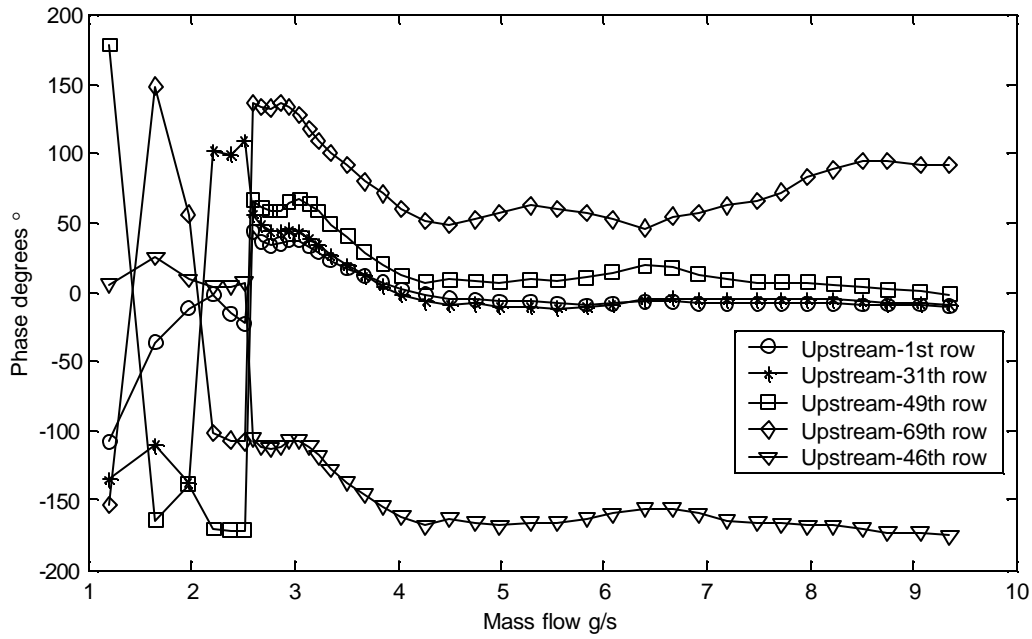


Figure F.76 Transfer function phase between microphone pairs shown at frequency of dominant peak in spectra of upstream microphone. Microphone positions shown in Figure F.74. Staggered array with  $T/D = 3.0$  and  $L/D = 0.9$ .

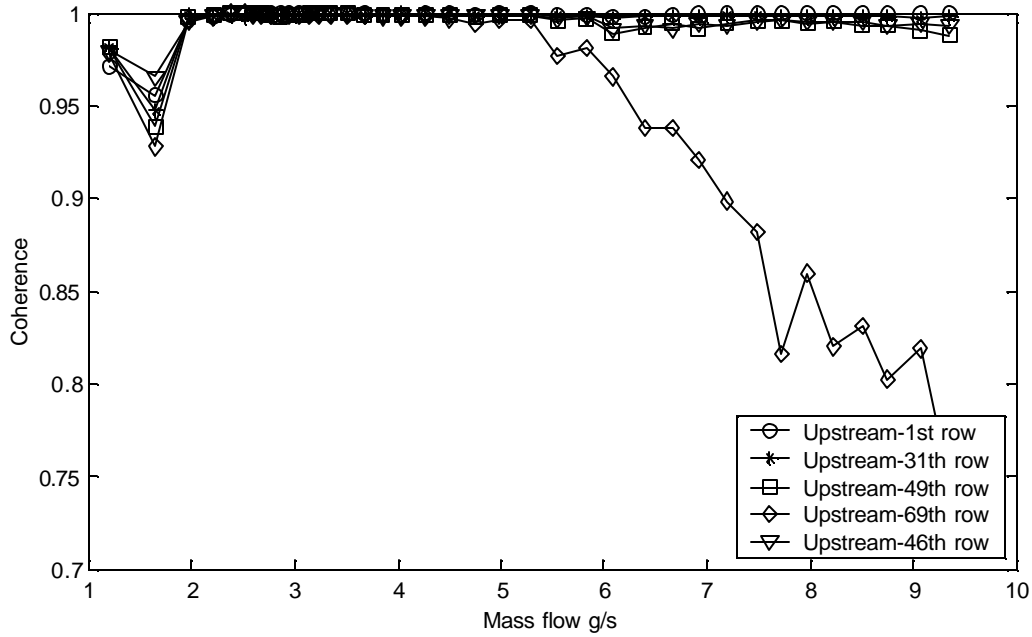


Figure F.77 Coherence between microphone pairs at frequency of dominant peak in spectra of upstream microphone. Phase measurements presented in Figure F.76 prone to error if coherence not close to one. Staggered array with  $T/D = 3.0$  and  $L/D = 0.9$ .

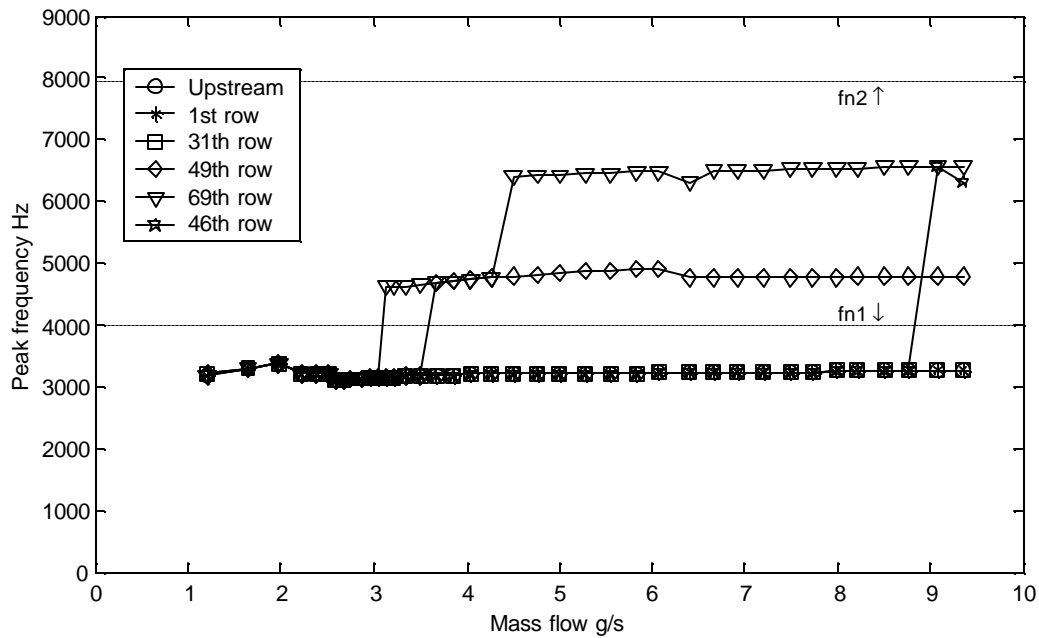


Figure F.78 Plot of frequency of dominant peak in spectra vs. mass flow. Staggered array with  $T/D = 3.0$  and  $L/D = 0.9$ .  $fn_1, fn_2 \dots$  acoustic natural frequencies with solidity effect.

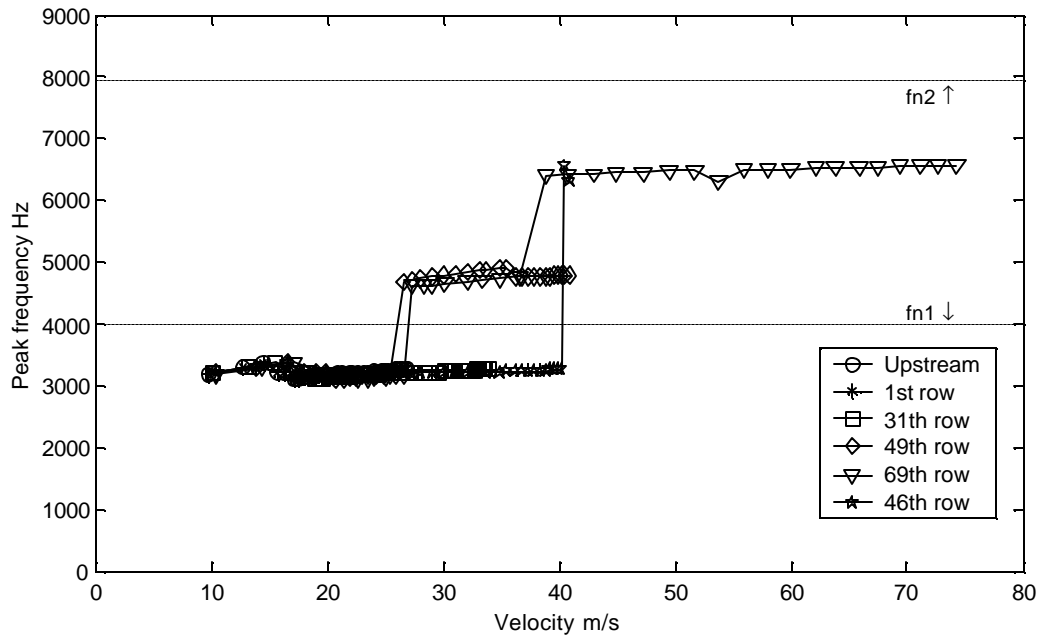


Figure F.79 Plot of frequency of dominant peak in spectra vs. flow velocity. Velocity estimated using density at measurement location and empty duct cross sectional area. Staggered array with  $T/D = 3.0$  and  $L/D = 0.9$ .  $fn_1, fn_2 \dots$  acoustic natural frequencies with solidity effect.

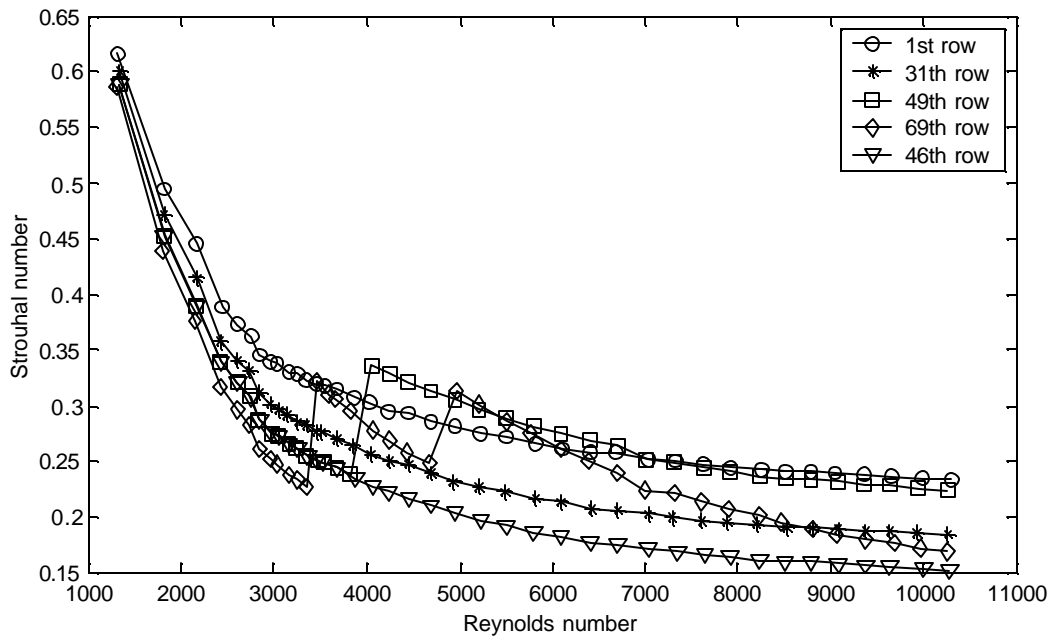


Figure F.80 Strouhal numbers determined at different positions throughout the array using dominant peak in spectra. Velocity estimated using density at measurement location and full duct cross sectional area. Staggered array with  $T/D = 3.0$  and  $L/D = 0.9$ .

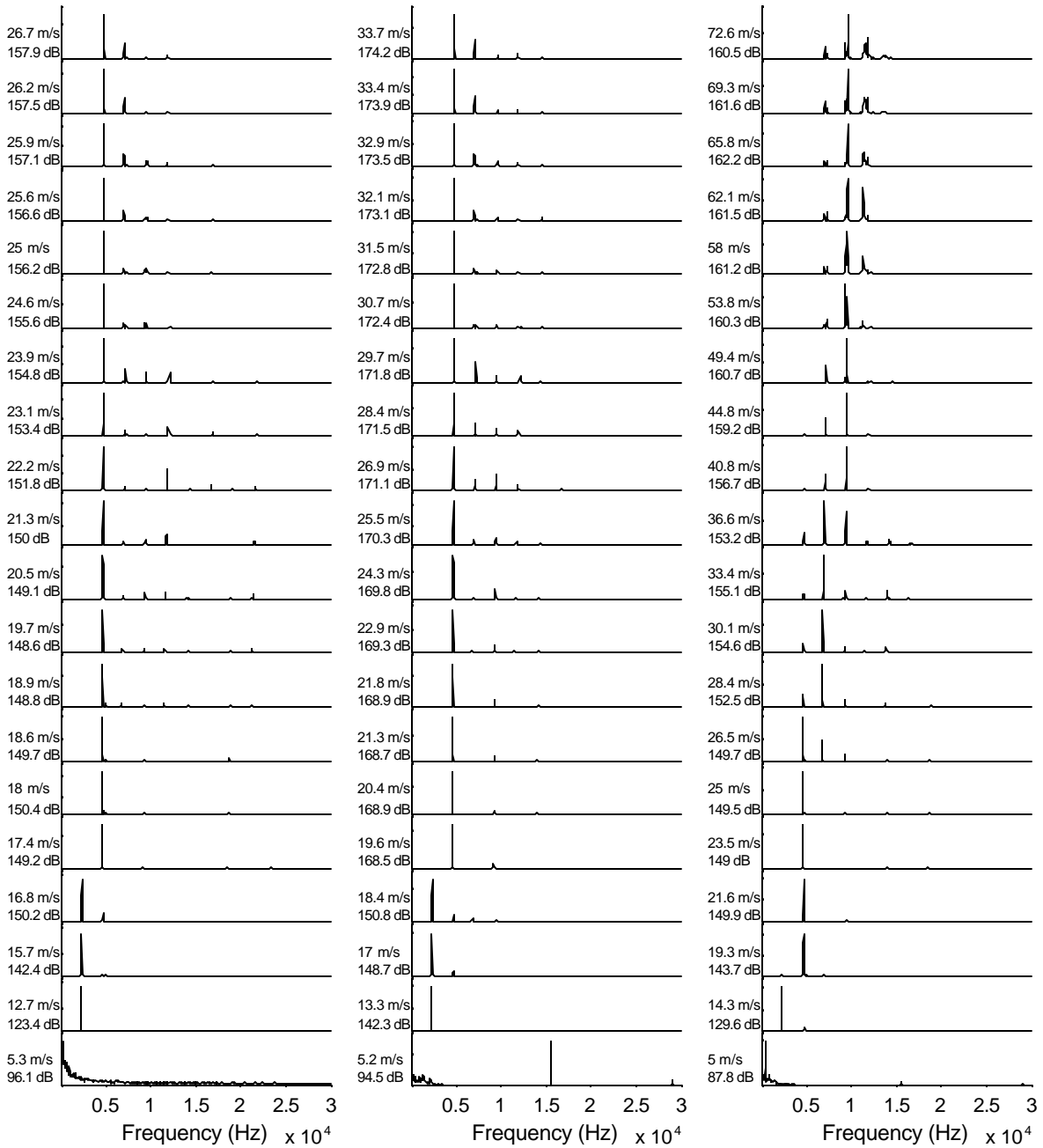


Figure F.81 Representative spectra taken at upstream position, after 31<sup>st</sup> row and after 69<sup>th</sup> row (left, center and right respectively). Spectra in same line taken at identical mass flow conditions. Velocity estimated using density at measurement location and empty duct cross sectional area. Sound pressure level shown at left calculated for dominant peak in spectra. Staggered array with T/D = 3.0 and L/D = 0.9.

# Appendix G: Single Cylinders Test Results

## 6.35 mm Diameter Aluminum Cylinder

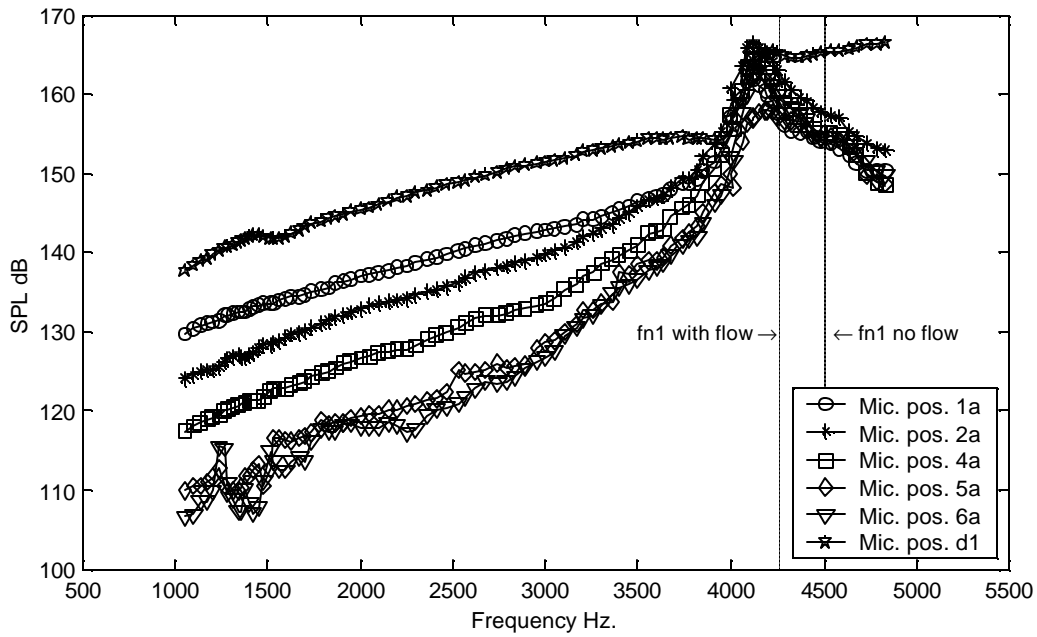


Figure G.1 Sound pressure level of dominant peak in spectra as a function of frequency. Microphones and cylinder positions shown in Figure 4.22.(fn1 with flow) acoustic resonance estimated with flow velocity at resonance condition.

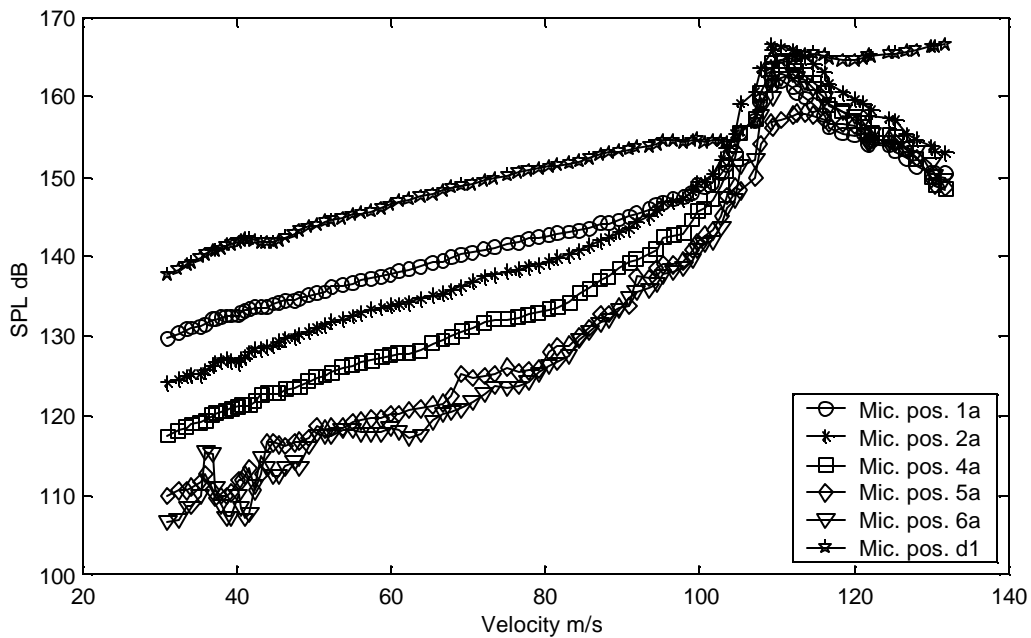


Figure G.2 Sound pressure level as a function of average flow velocity.

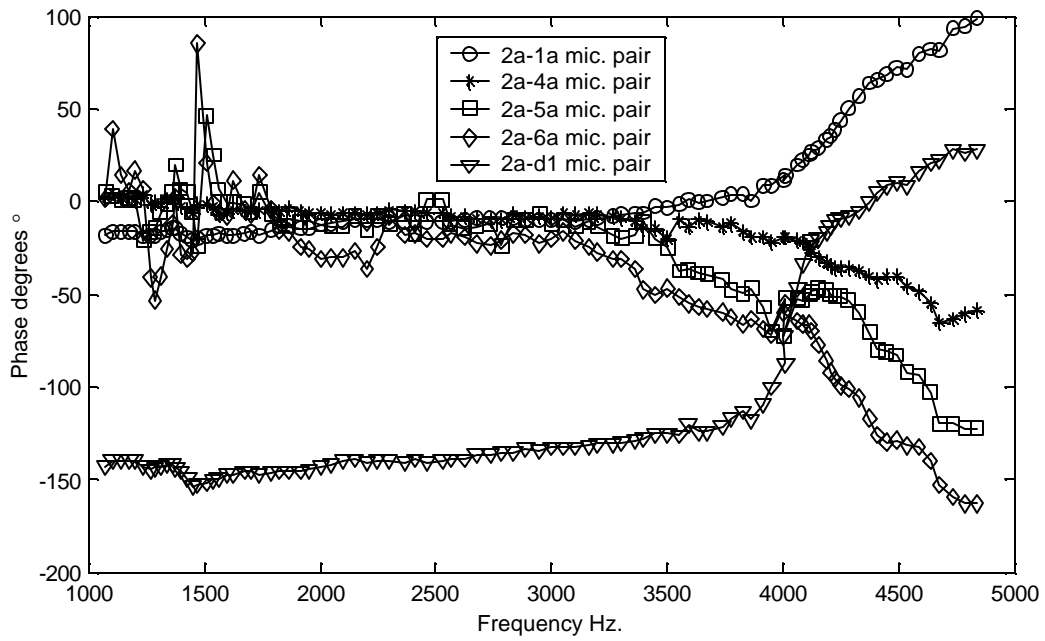


Figure G.3 Transfer function phase angle at frequency of dominant peak in spectra between microphone pairs shown.

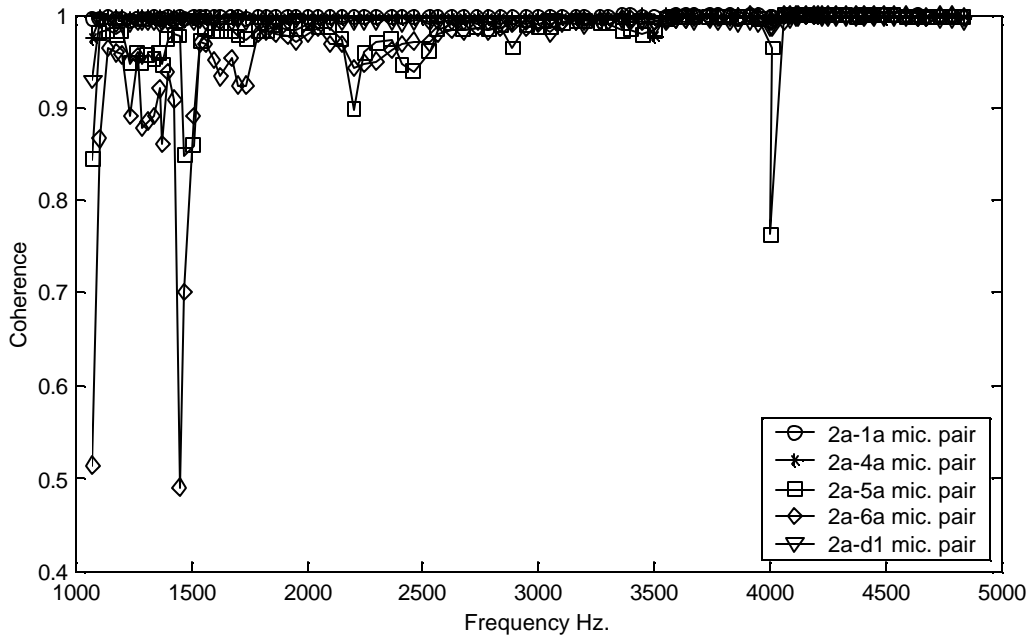


Figure G.4 Coherence at frequency of dominant peak in spectra between microphone pairs shown. Phase angle shown in figure above prone to error if coherence not close to one.

### 6.35 mm Diameter Stereolithography Cylinder

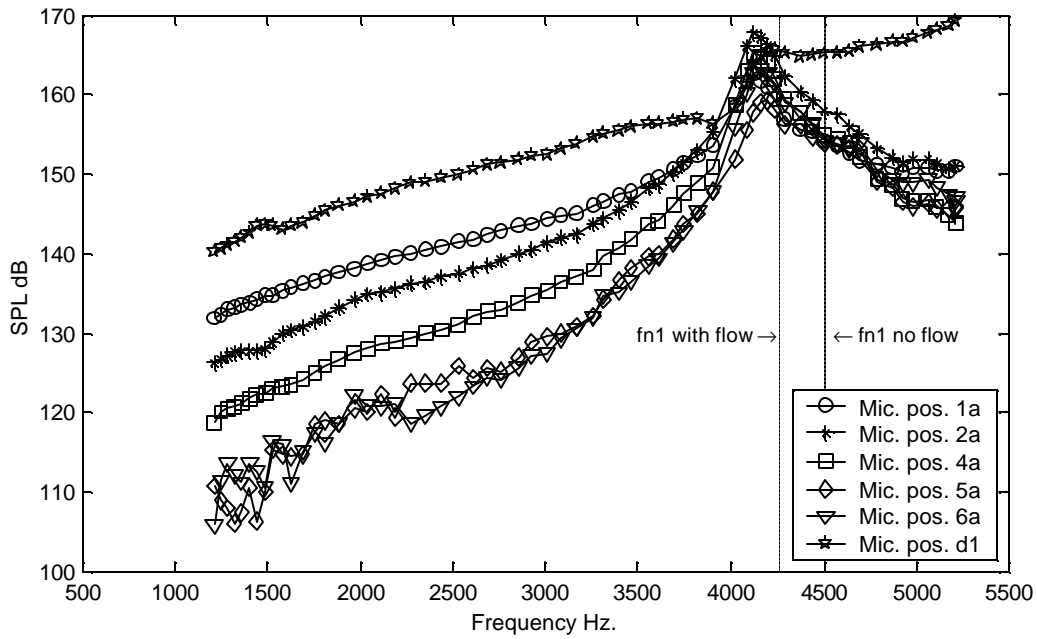


Figure G.5 Sound pressure level of dominant peak in spectra as a function of frequency. Microphones and cylinder positions shown in Figure 4.22. (fn1 with flow) acoustic resonance estimated with flow velocity at resonance condition.

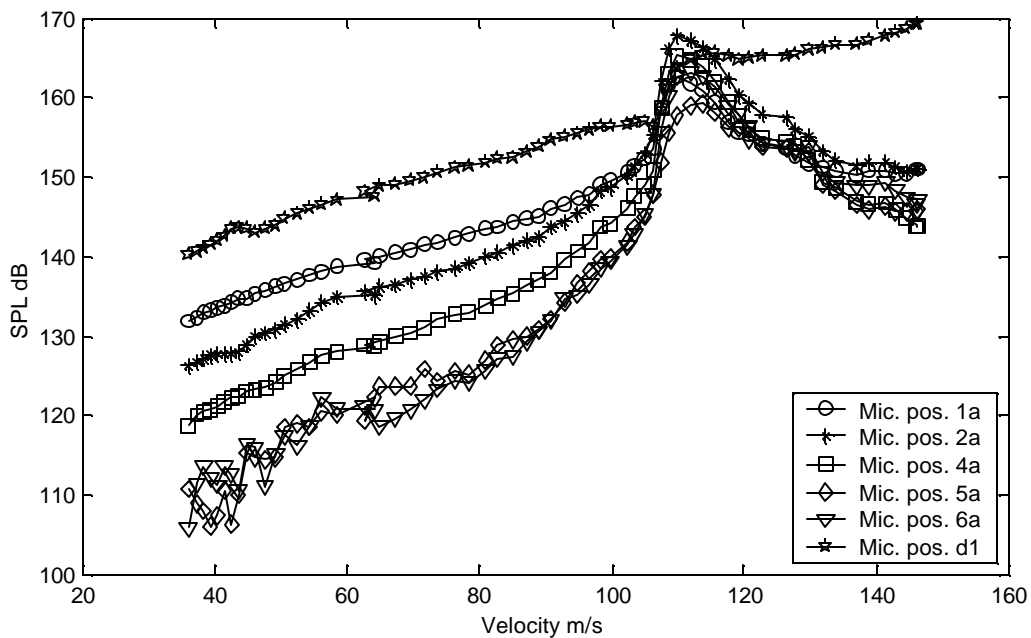


Figure G.6 Sound pressure level as a function of average flow velocity.

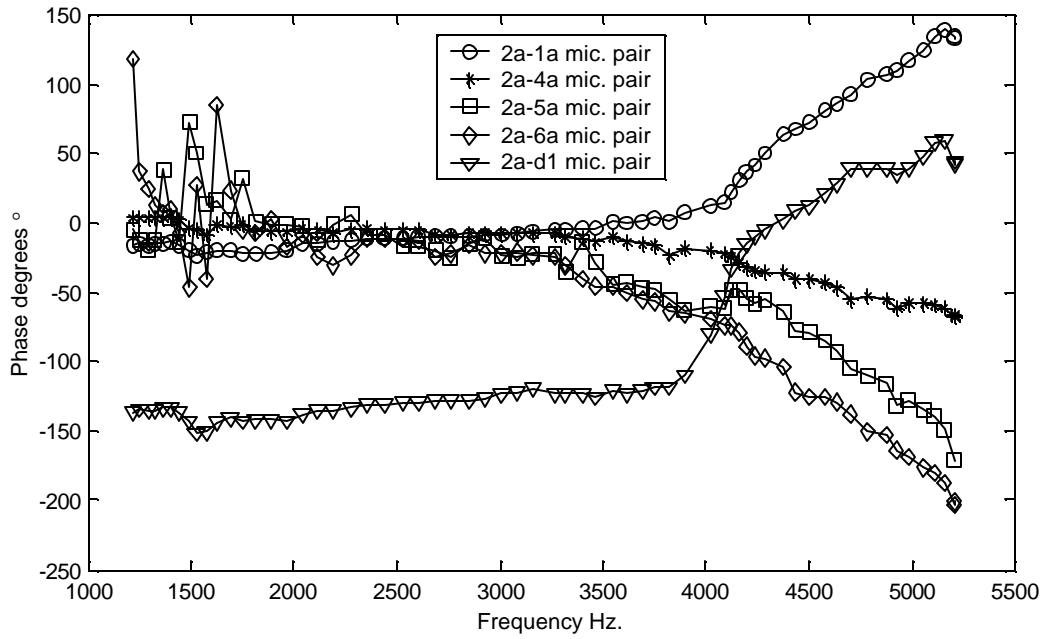


Figure G.7 Transfer function phase angle at frequency of dominant peak in spectra between microphone pairs shown.

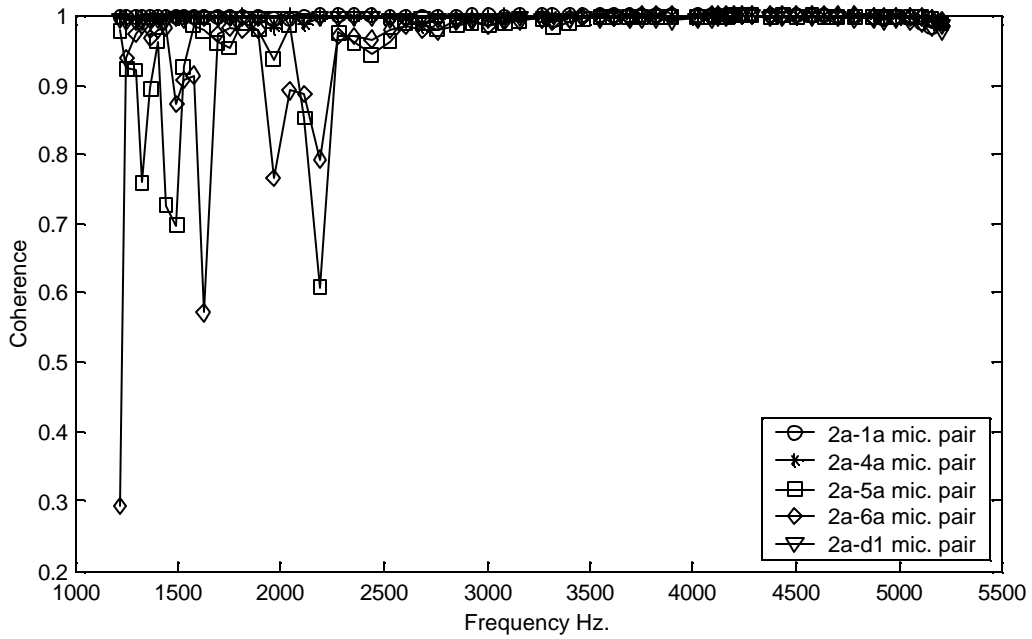


Figure G.8 Coherence at frequency of dominant peak in spectra between microphone pairs shown. Phase angle shown in figure above prone to error if coherence not close to one.



### 5.5 mm Diameter Aluminum Cylinder

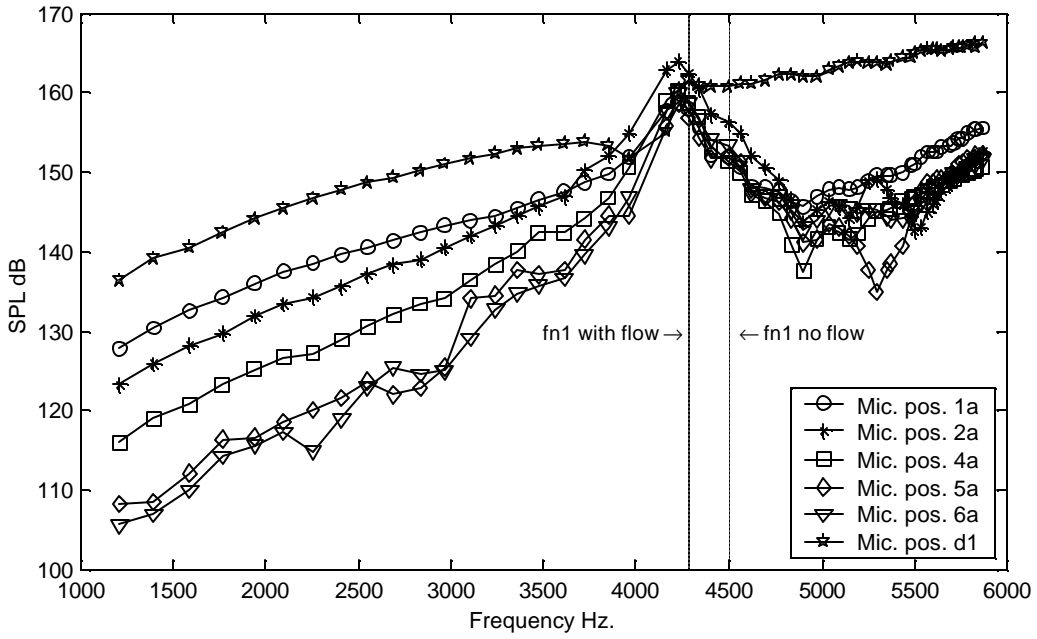


Figure G.9 Sound pressure level of dominant peak in spectra as a function of frequency. Microphones and cylinder positions shown in Figure 4.22. (fn1 with flow) acoustic resonance estimated with flow velocity at resonance condition.

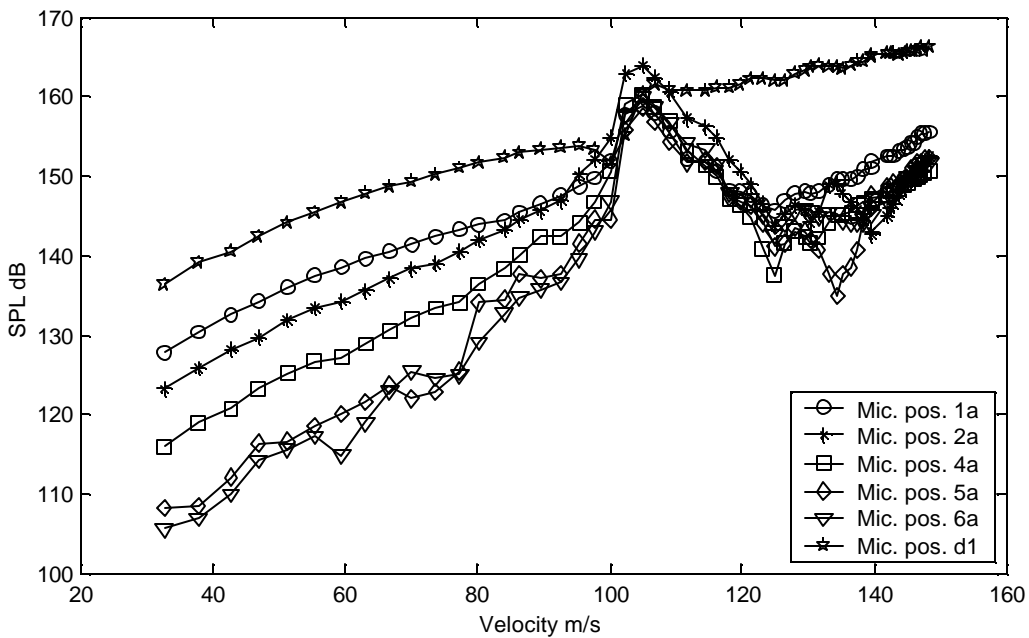


Figure G.10 Sound pressure level as a function of average flow velocity.

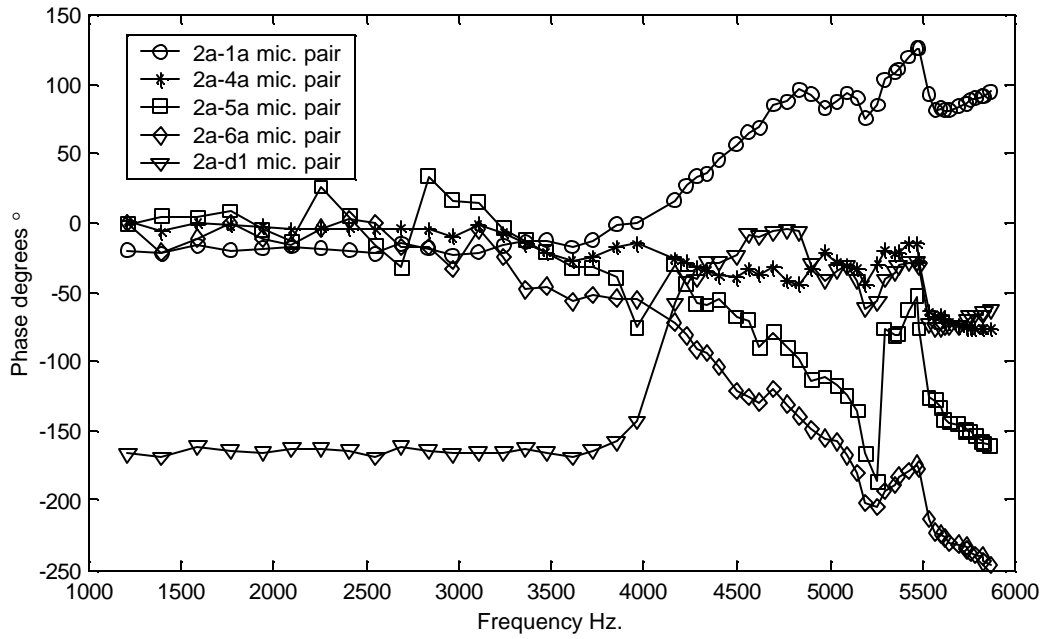


Figure G.11 Transfer function phase angle at frequency of dominant peak in spectra between microphone pairs shown.

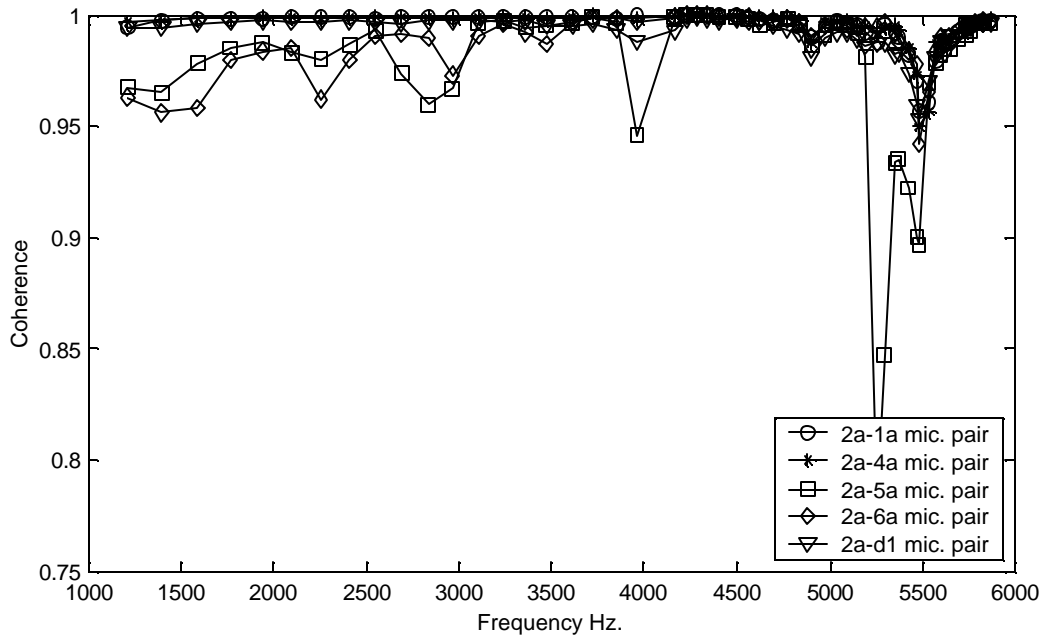


Figure G.12 Coherence at frequency of dominant peak in spectra between microphone pairs shown. Phase angle shown in figure above prone to error if coherence not close to one.

### 5.0 mm Diameter Aluminum Cylinder

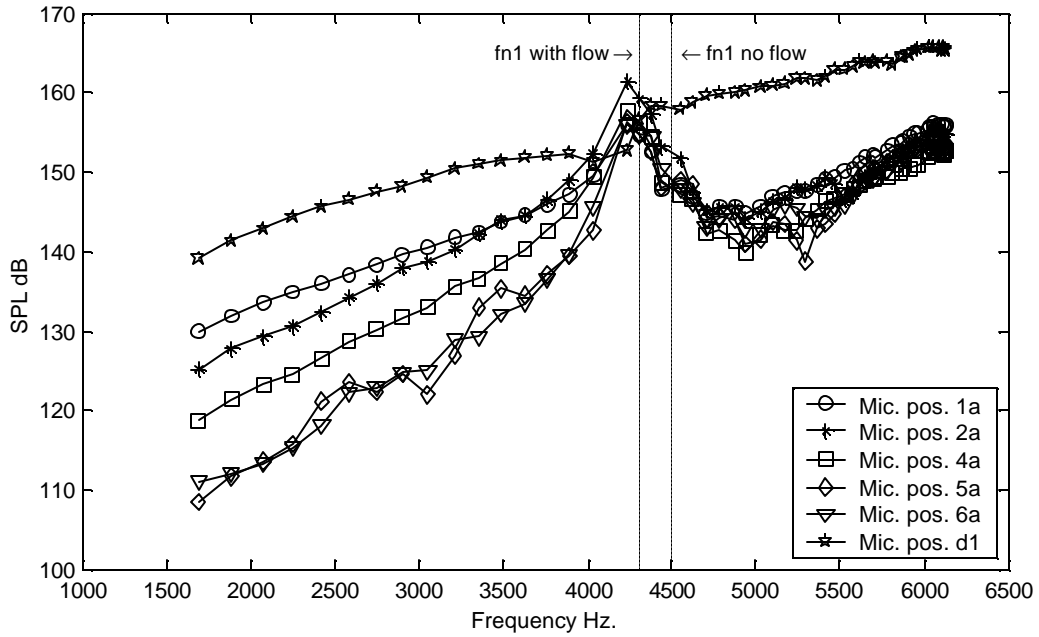


Figure G.13 Sound pressure level of dominant peak in spectra as a function of frequency. Microphones and cylinder positions shown in Figure 4.22. (fn1 with flow) acoustic resonance estimated with flow velocity at resonance condition.

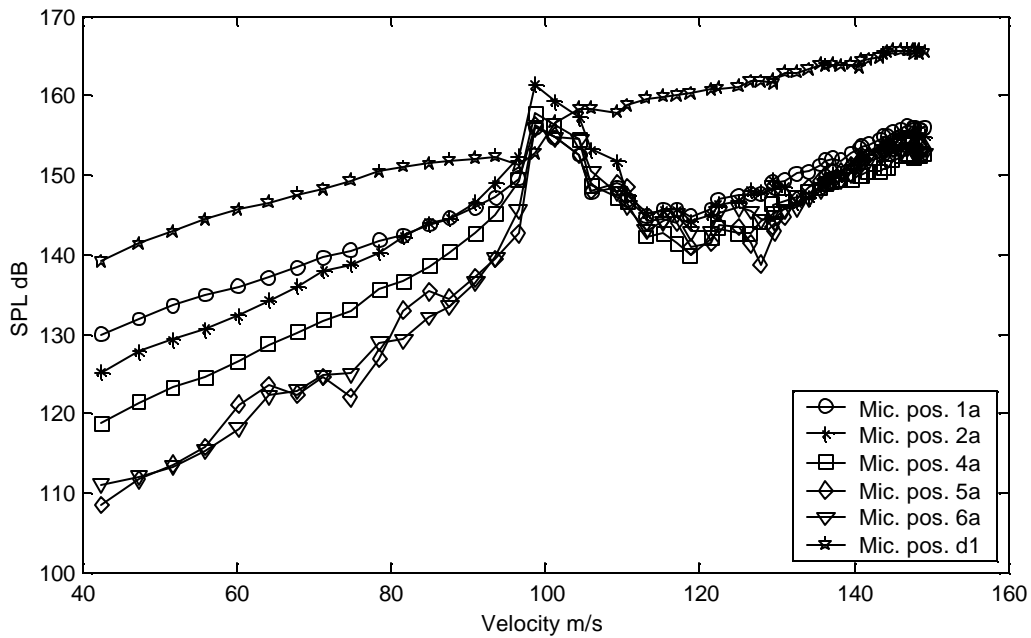


Figure G.14 Sound pressure level as a function of average flow velocity.

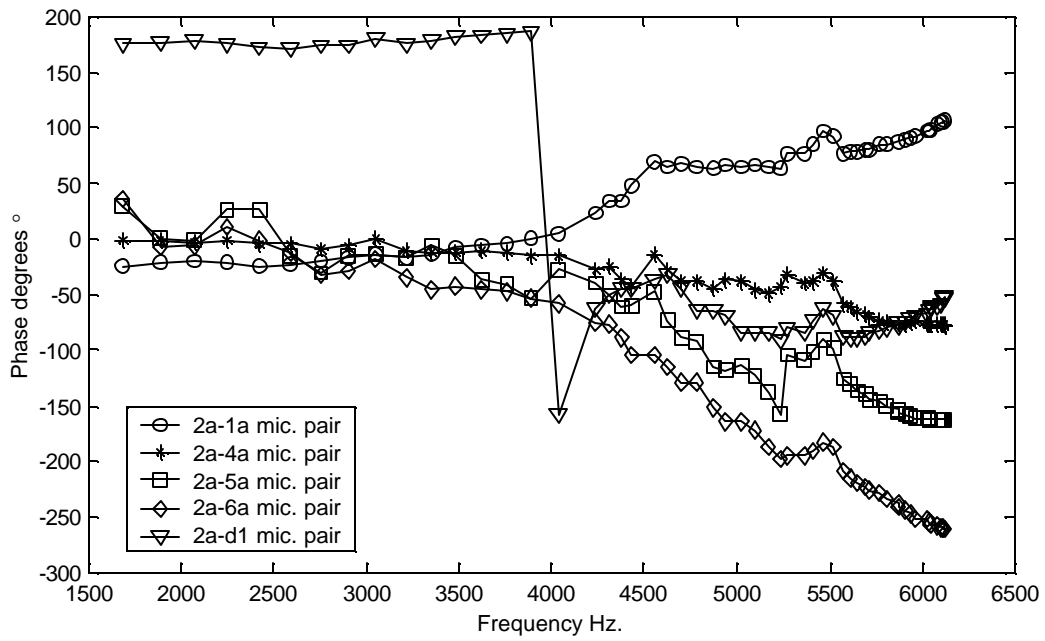


Figure G.15 Transfer function phase angle at frequency of dominant peak in spectra between microphone pairs shown.

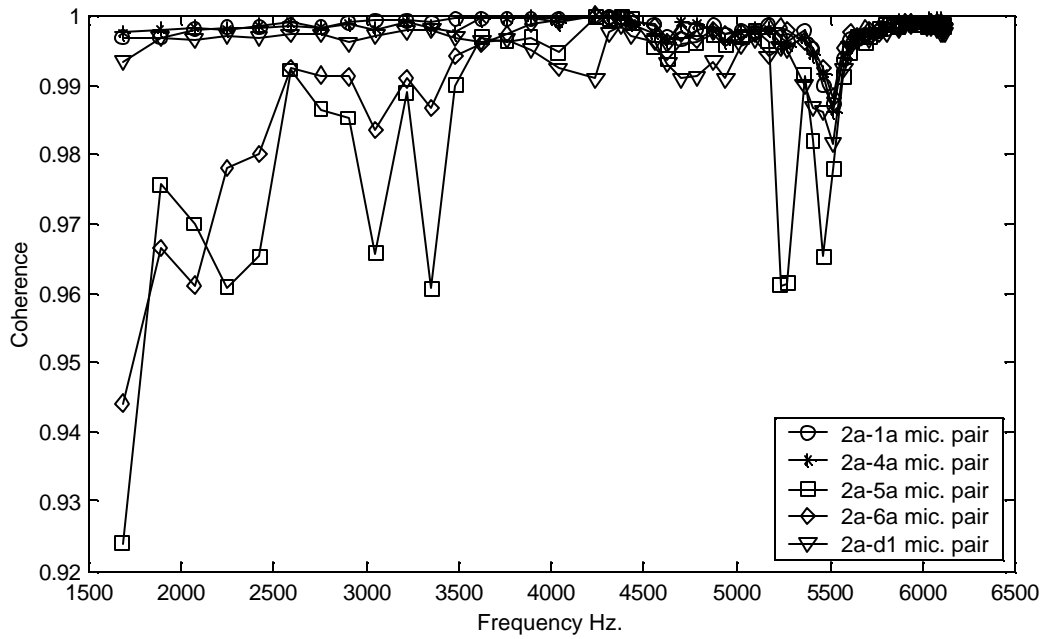


Figure G.16 Coherence at frequency of dominant peak in spectra between microphone pairs shown. Phase angle shown in figure above prone to error if coherence not close to one.

### 4.5 mm Diameter Aluminum Cylinder

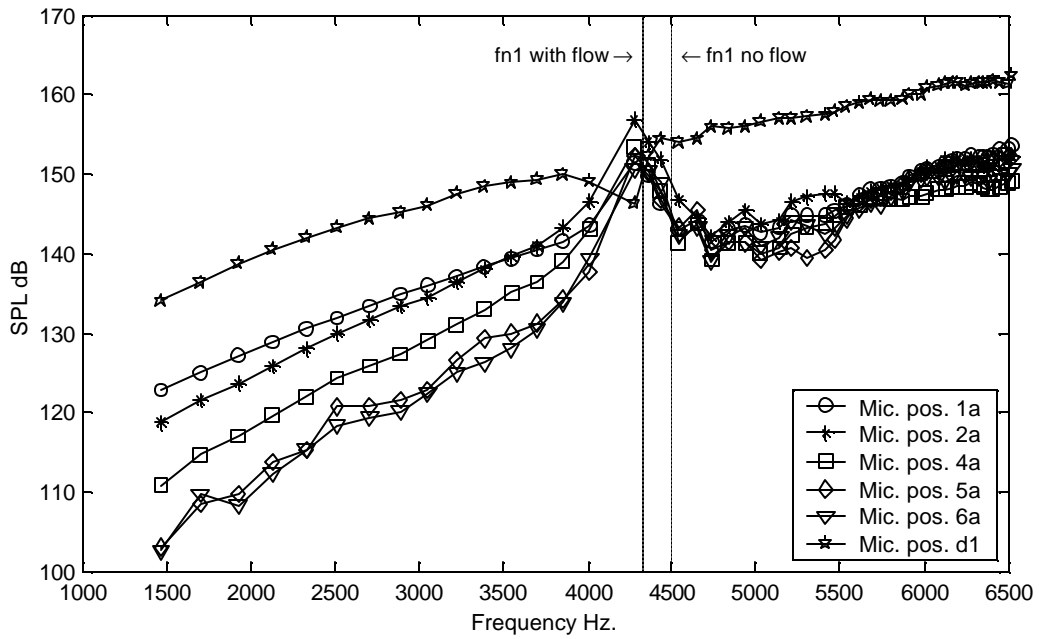


Figure G.17 Sound pressure level of dominant peak in spectra as a function of frequency. Microphones and cylinder positions shown in Figure 4.22. (fn1 with flow) acoustic resonance estimated with flow velocity at resonance condition.

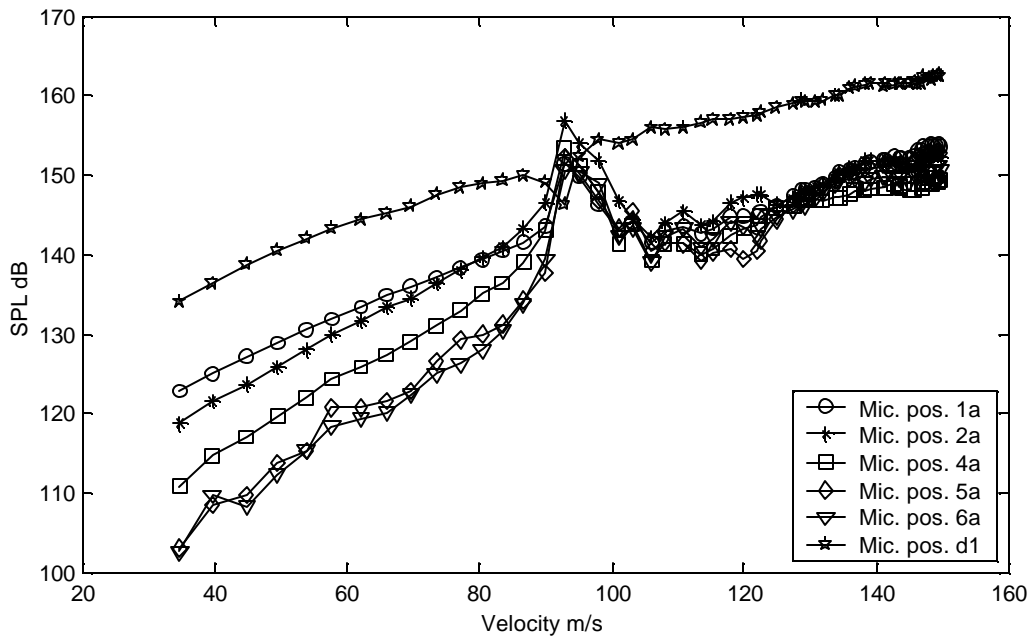


Figure G.18 Sound pressure level as a function of average flow velocity.

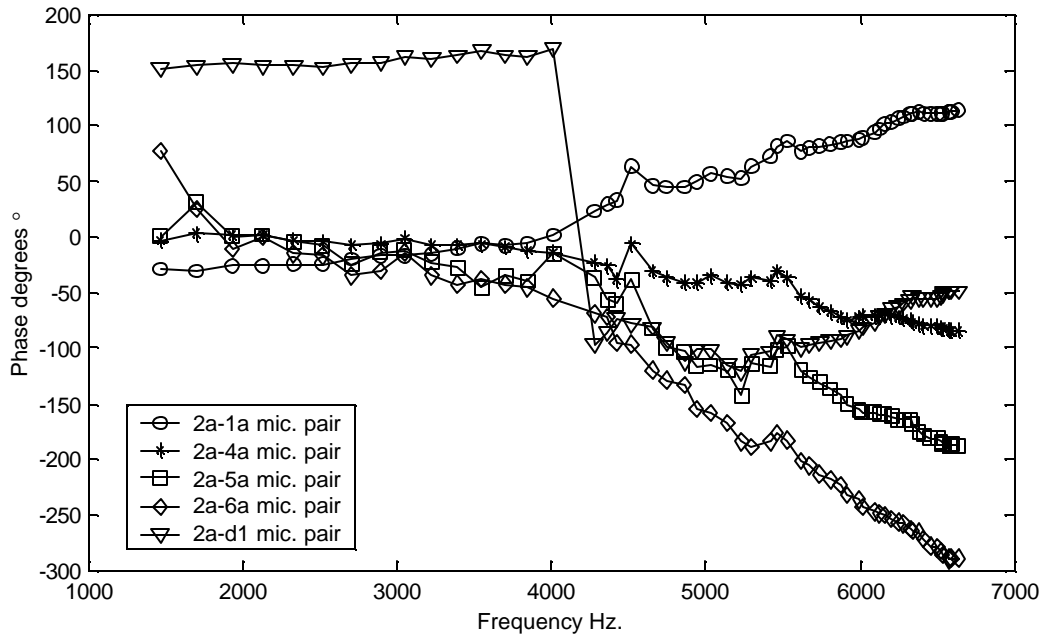


Figure G.19 Transfer function phase angle at frequency of dominant peak in spectra between microphone pairs shown.

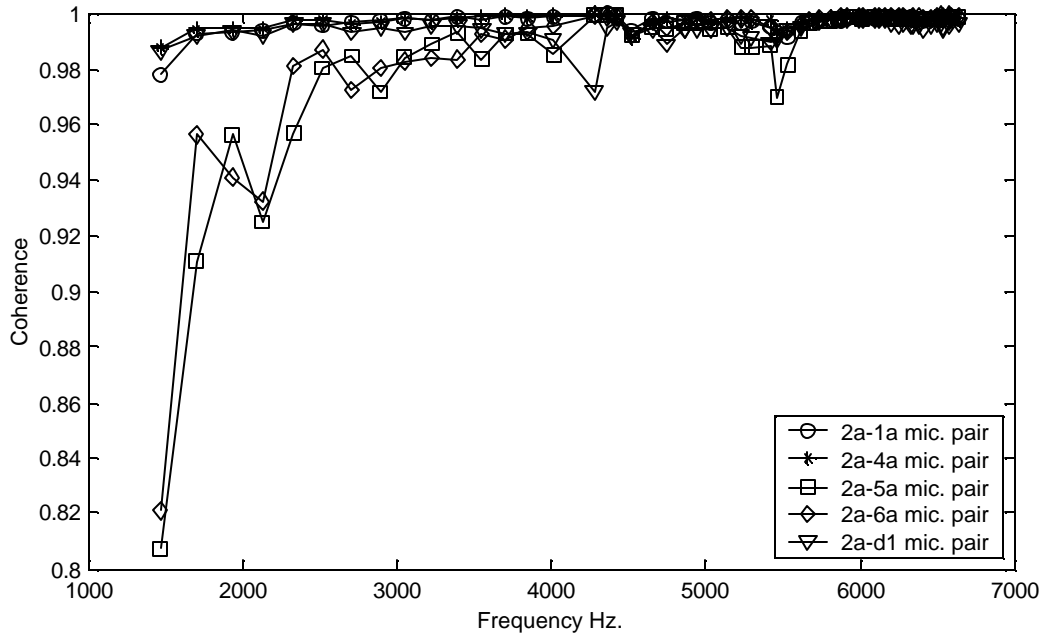


Figure G.20 Coherence at frequency of dominant peak in spectra between microphone pairs shown. Phase angle shown in figure above prone to error if coherence not close to one.

### 4.0 mm Diameter Aluminum Cylinder

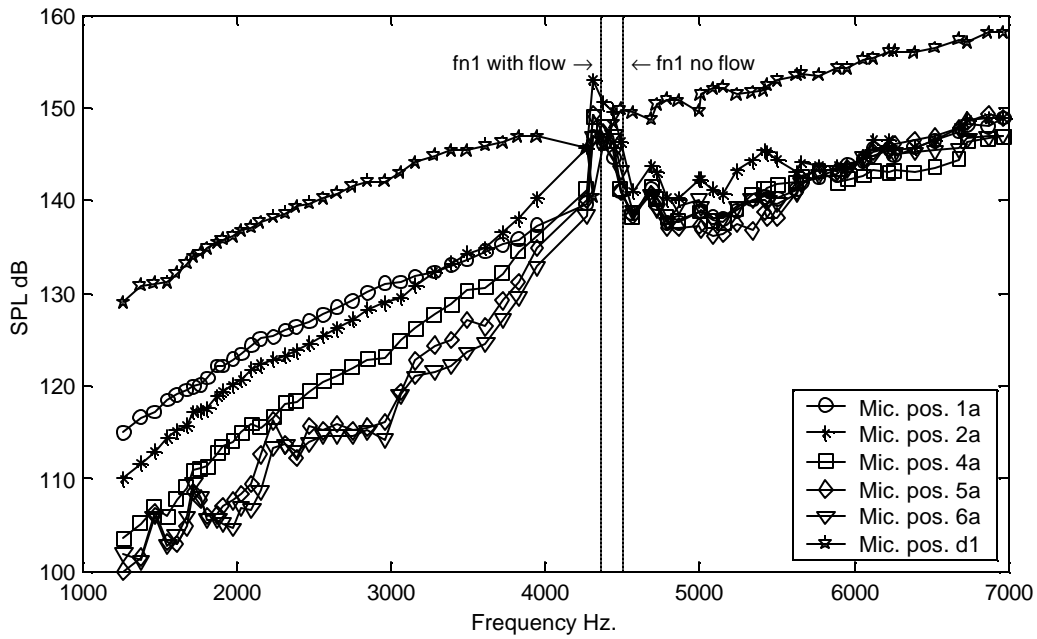


Figure G.21 Sound pressure level of dominant peak in spectra as a function of frequency. Microphones and cylinder positions shown in Figure 4.22.(fn1 with flow) acoustic resonance estimated with flow velocity at resonance condition.

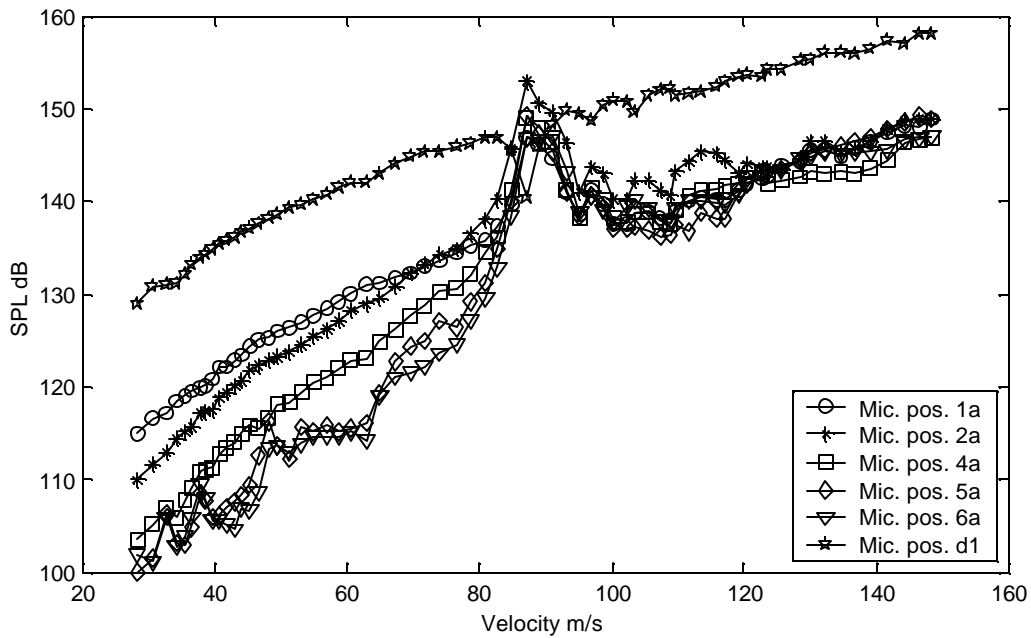


Figure G.22 Sound pressure level as a function of average flow velocity.

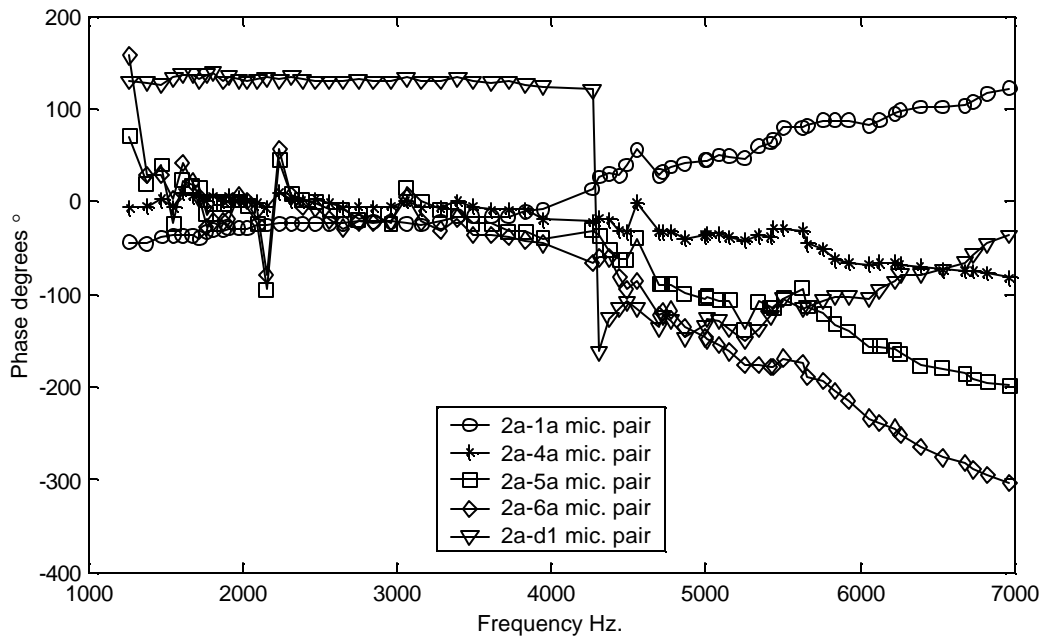


Figure G.23 Transfer function phase angle at frequency of dominant peak in spectra between microphone pairs shown.

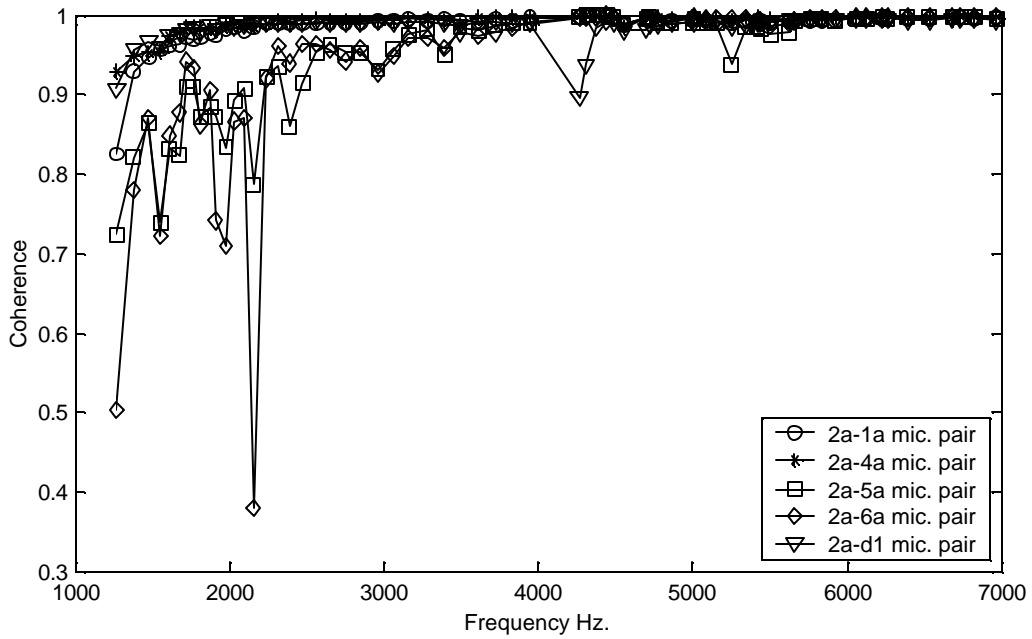


Figure G.24 Coherence at frequency of dominant peak in spectra between microphone pairs shown. Phase angle shown in figure above prone to error if coherence not close to one.



### 3.5 mm Diameter Aluminum Cylinder

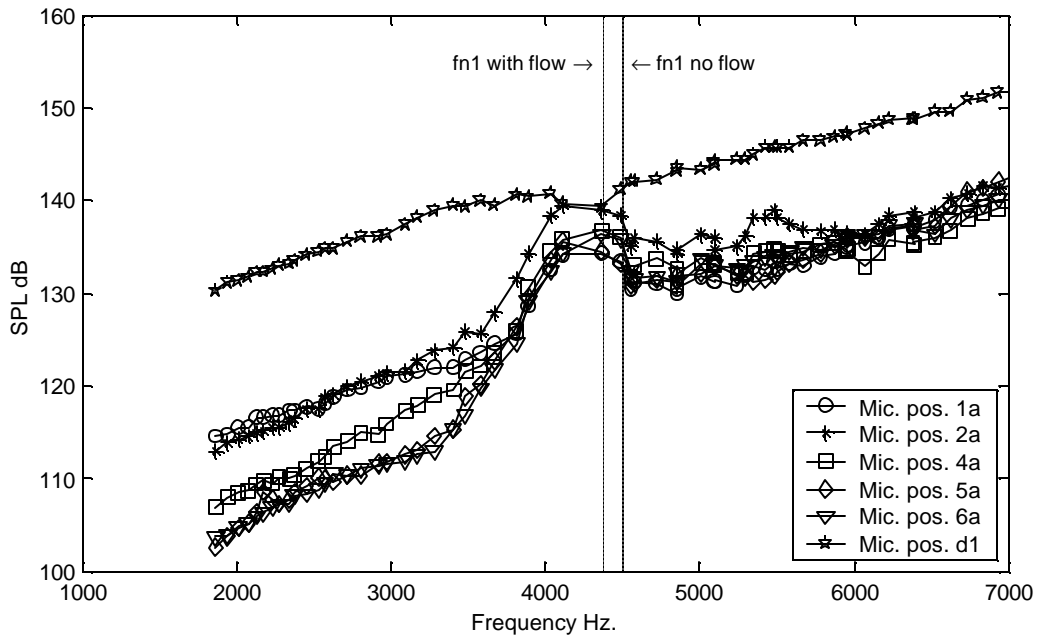


Figure G.25 Sound pressure level of dominant peak in spectra as a function of frequency. Microphones and cylinder positions shown in Figure 4.22. (fn1 with flow) acoustic resonance estimated with flow velocity at resonance condition.

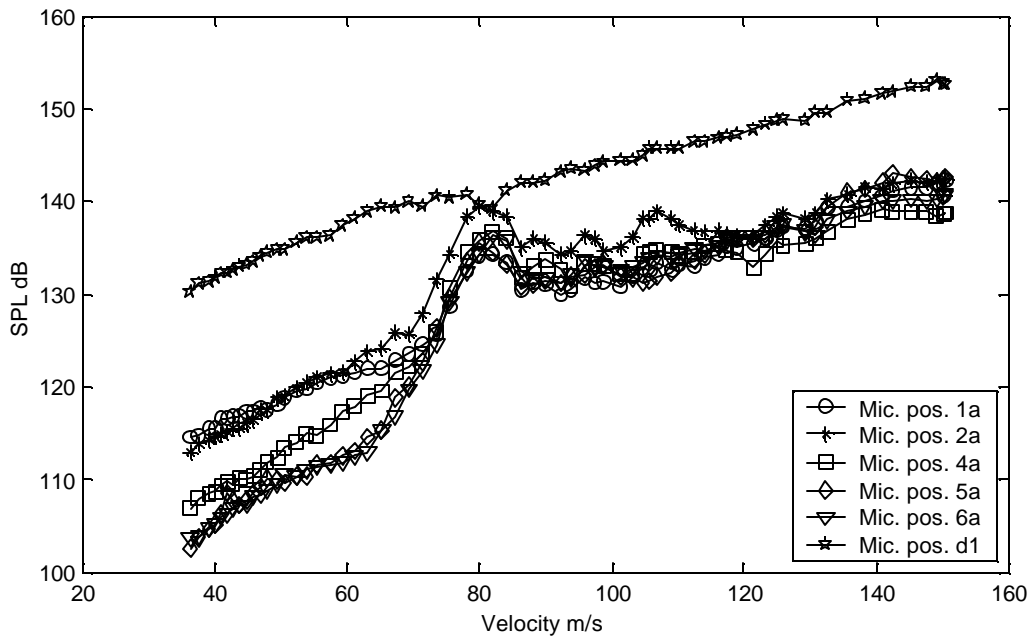


Figure G.26 Sound pressure level as a function of average flow velocity.

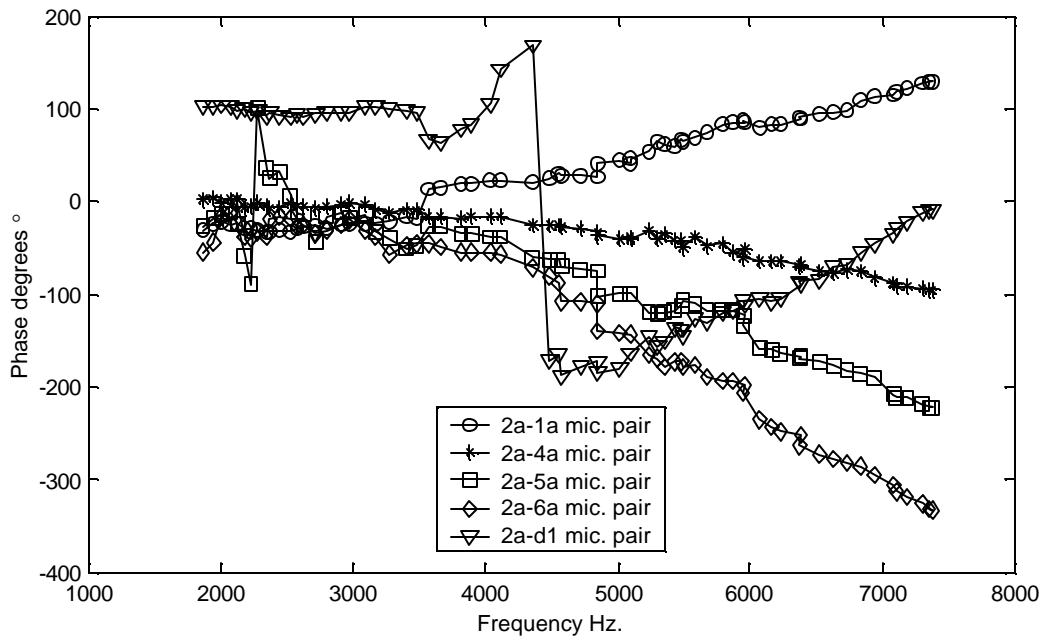


Figure G.27 Transfer function phase angle at frequency of dominant peak in spectra between microphone pairs shown.

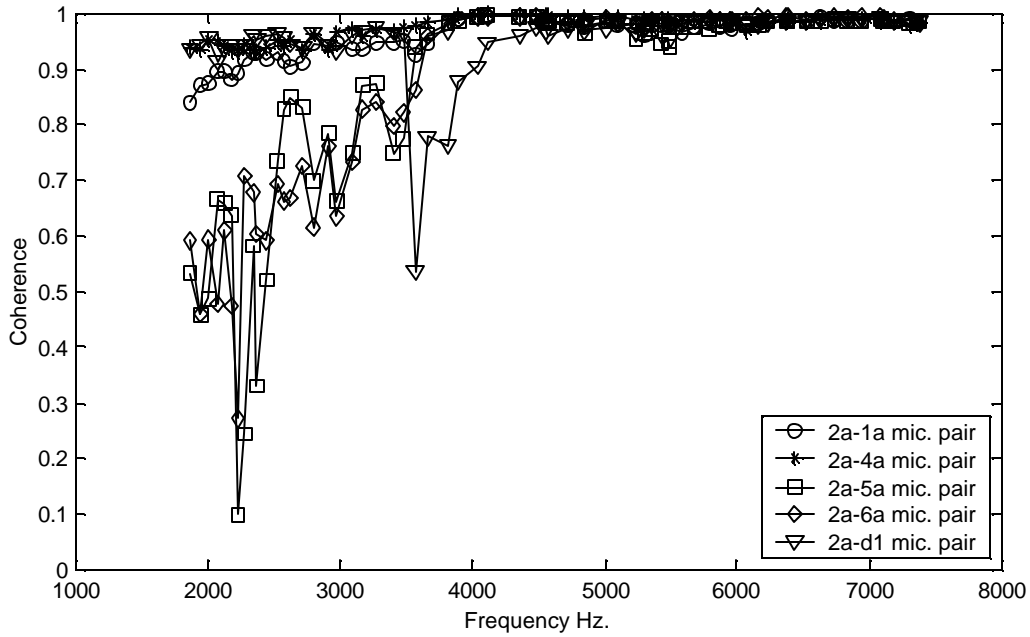


Figure G.28 Coherence at frequency of dominant peak in spectra between microphone pairs shown. Phase angle shown in figure above prone to error if coherence not close to one.

### 2.5 mm Diameter Aluminum Cylinder

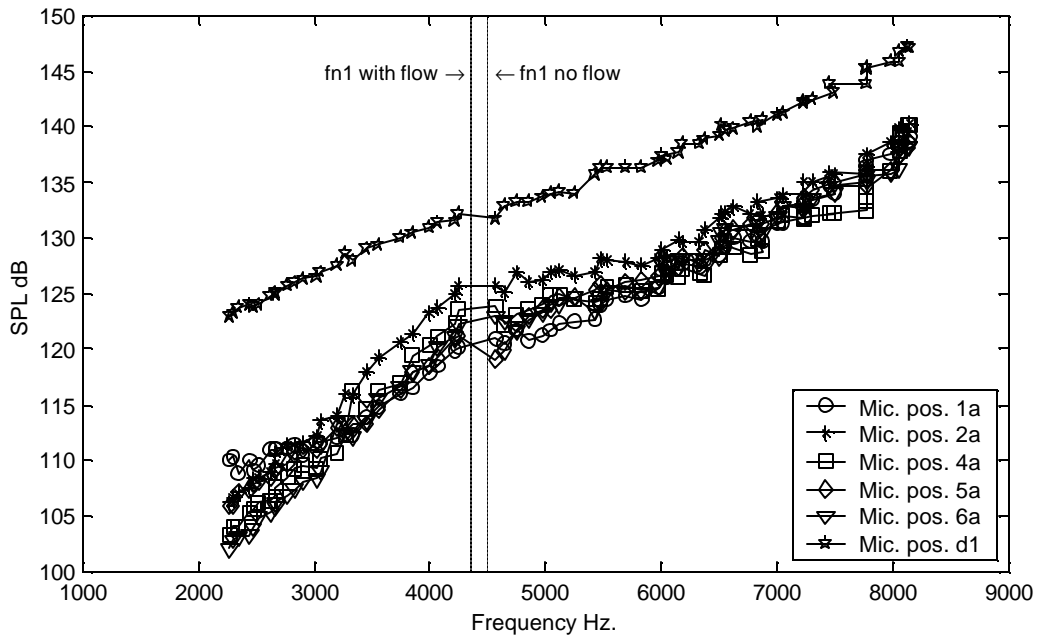


Figure G.29 Sound pressure level of dominant peak in spectra as a function of frequency. Microphones and cylinder positions shown in Figure 4.22. (fn1 with flow) acoustic resonance estimated with flow velocity at resonance condition.

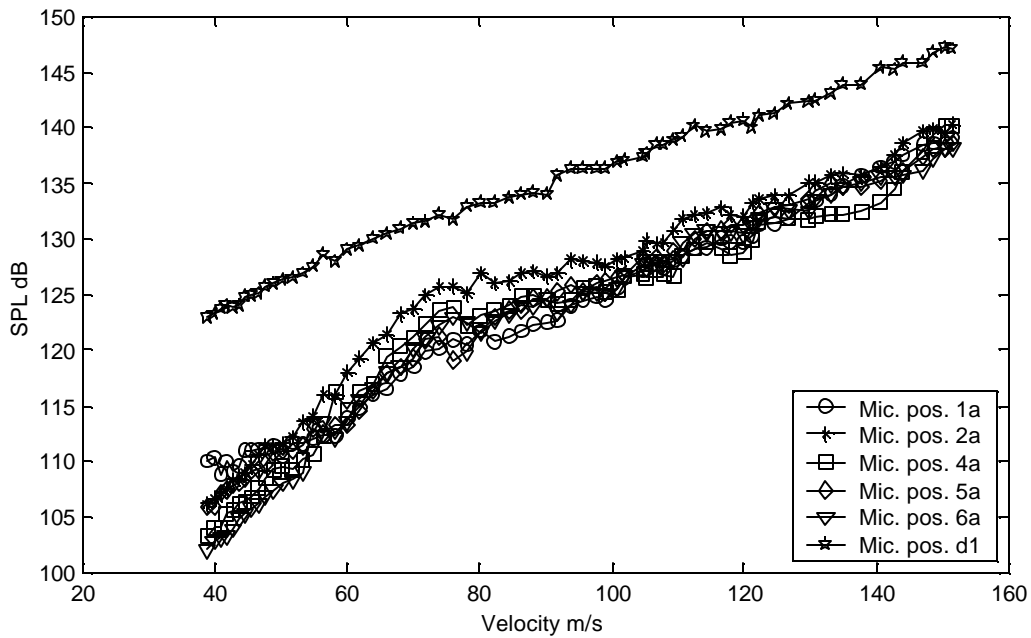


Figure G.30 Sound pressure level as a function of average flow velocity.

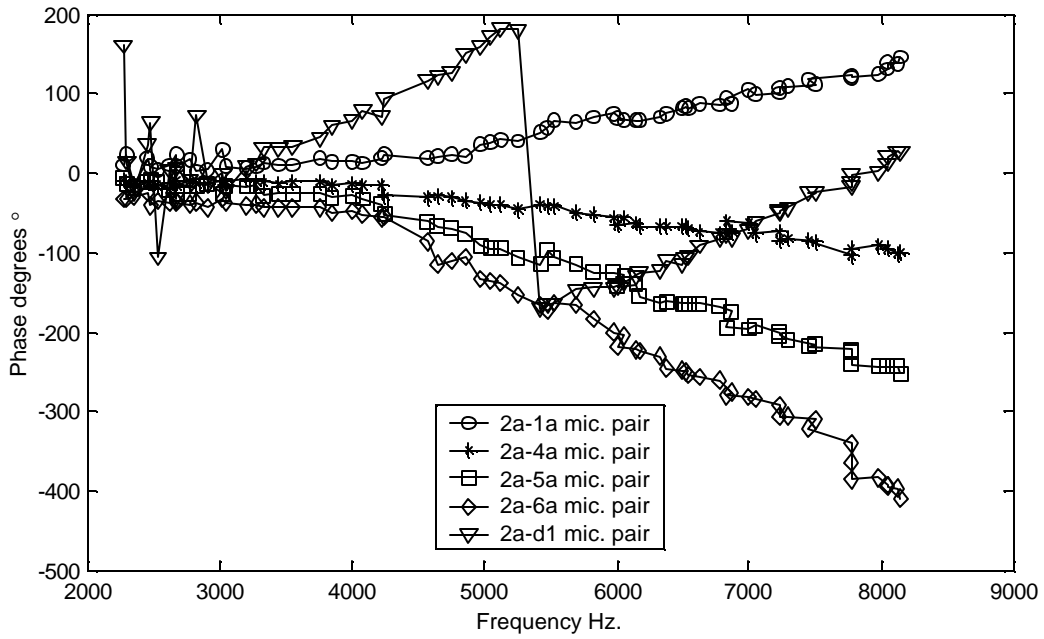


Figure G.31 Transfer function phase angle at frequency of dominant peak in spectra between microphone pairs shown.

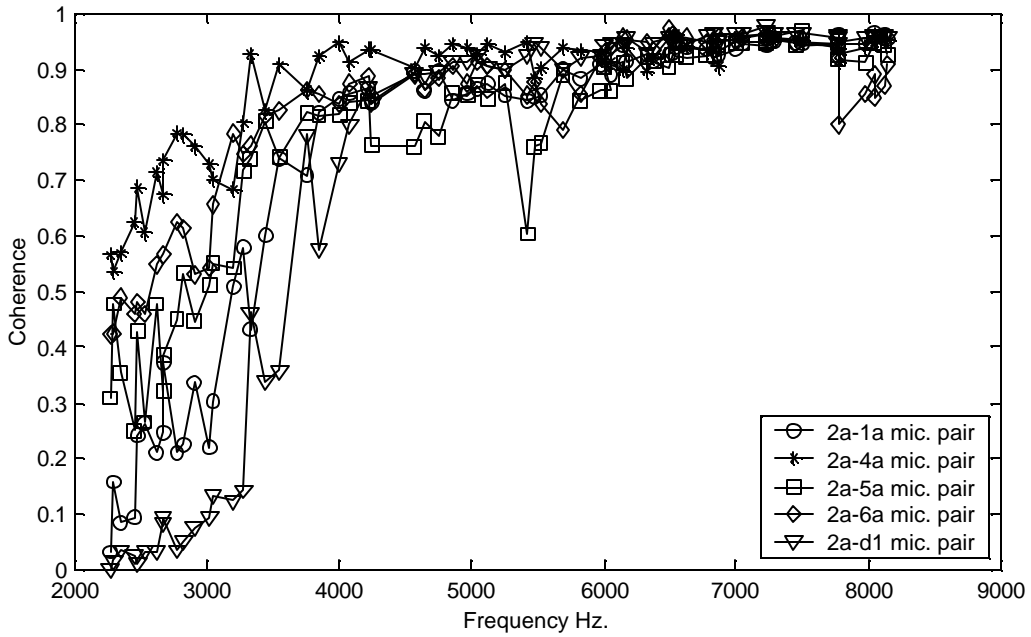


Figure G.32 Coherence at frequency of dominant peak in spectra between microphone pairs shown. Phase angle shown in figure above prone to error if coherence not close to one.

6.35 mm Diameter Aluminum Cylinder with 1.5mm Closed Cell Foam on Resonance Walls

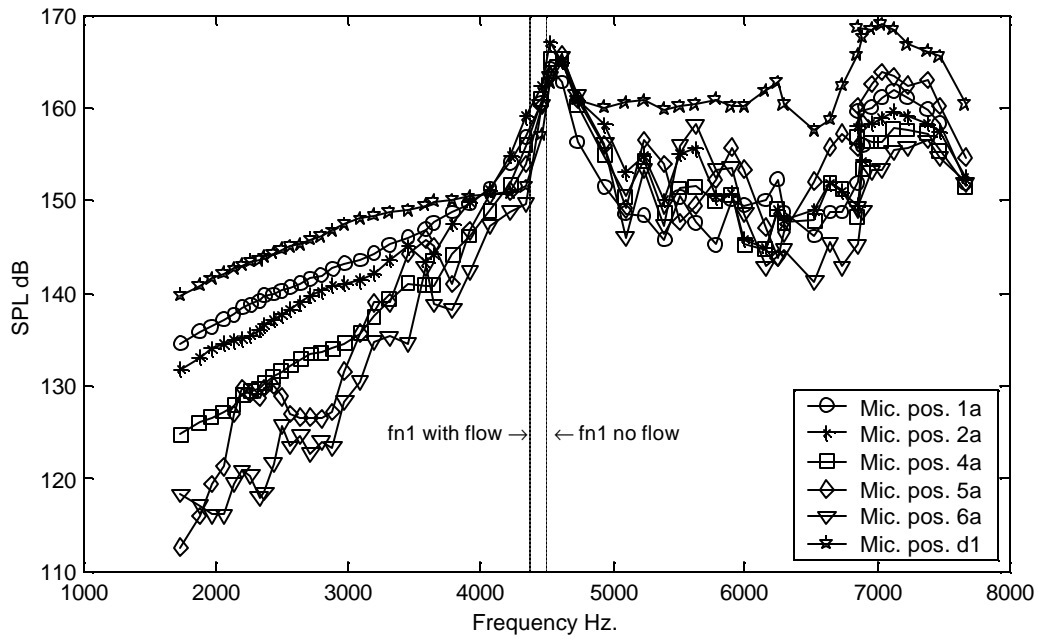


Figure G.33 Sound pressure level of dominant peak in spectra as a function of frequency. Microphones and cylinder positions shown in Figure 4.22. (fn1 with flow) acoustic resonance estimated with flow velocity at resonance condition.

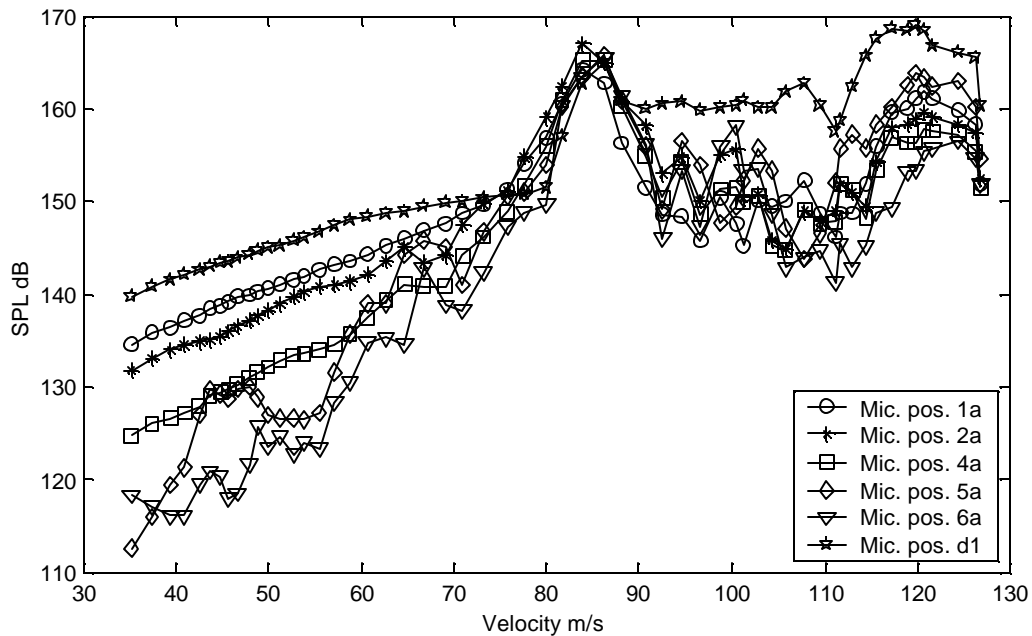


Figure G.34 Sound pressure level as a function of average flow velocity.

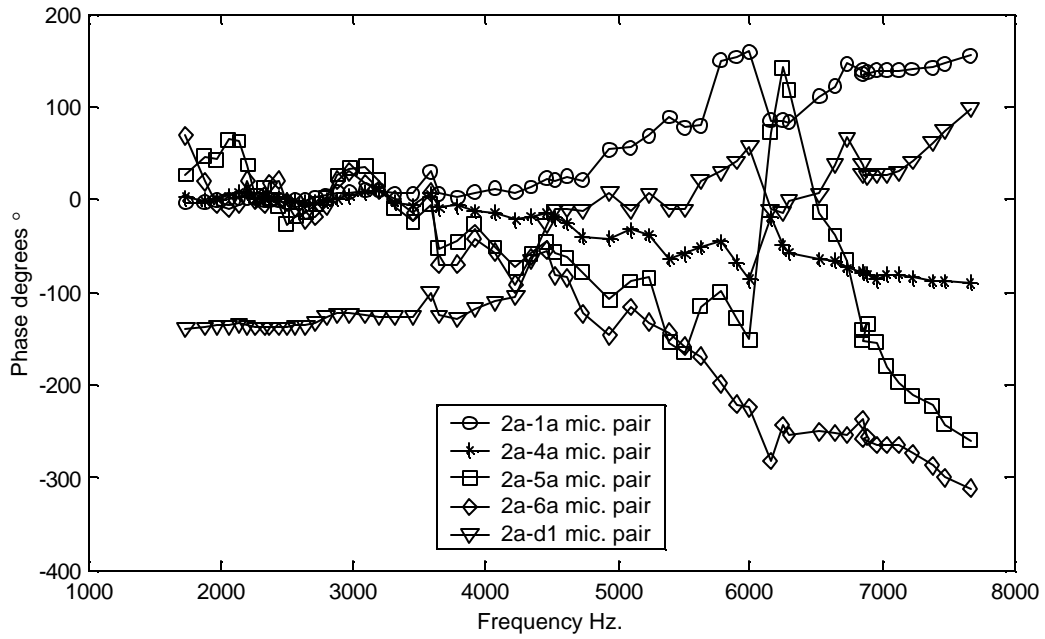


Figure G.35 Transfer function phase angle at frequency of dominant peak in spectra between microphone pairs shown.

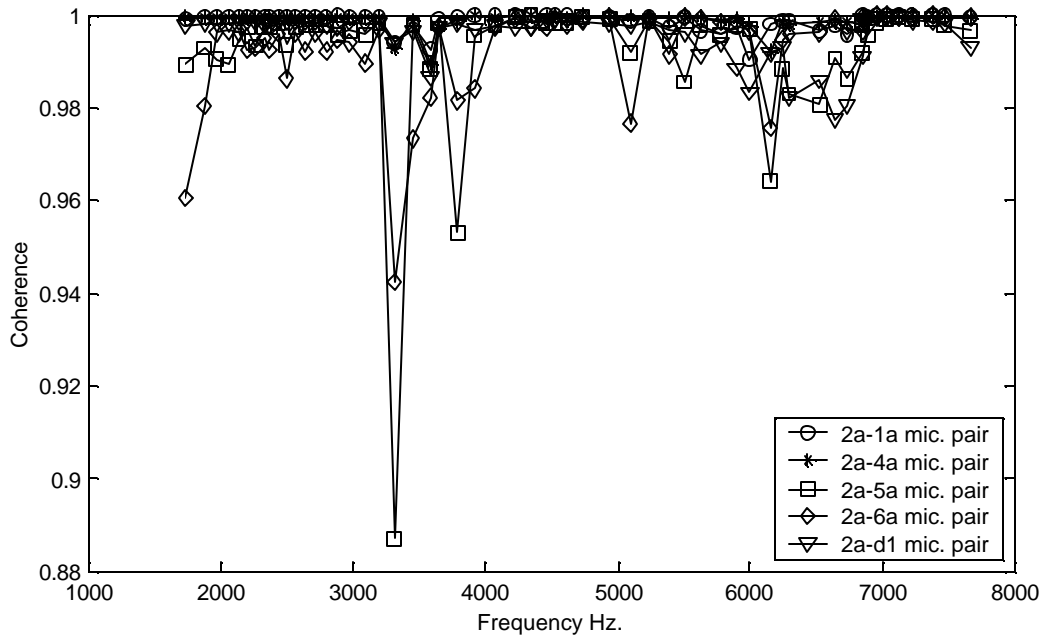


Figure G.36 Coherence at frequency of dominant peak in spectra between microphone pairs shown. Phase angle shown in figure above prone to error if coherence not close to one.

**6.35 mm Diameter Aluminum Cylinder with 2.5mm Open Cell Foam on Resonance Walls**

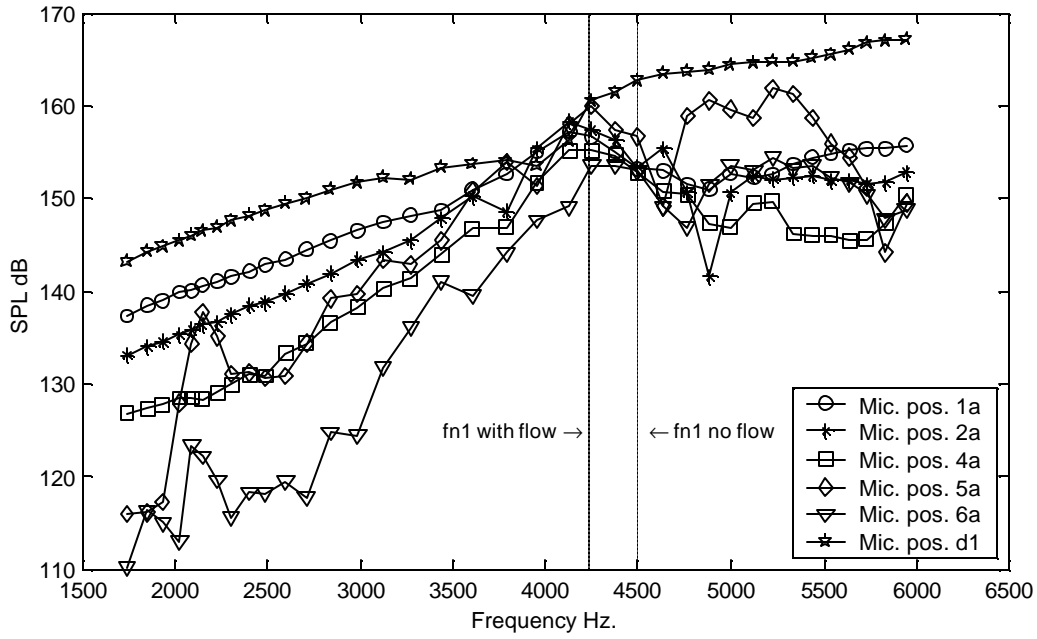


Figure G.37 Sound pressure level of dominant peak in spectra as a function of frequency. Microphones and cylinder positions shown in Figure 4.22. (fn1 with flow) acoustic resonance estimated with flow velocity at resonance condition.

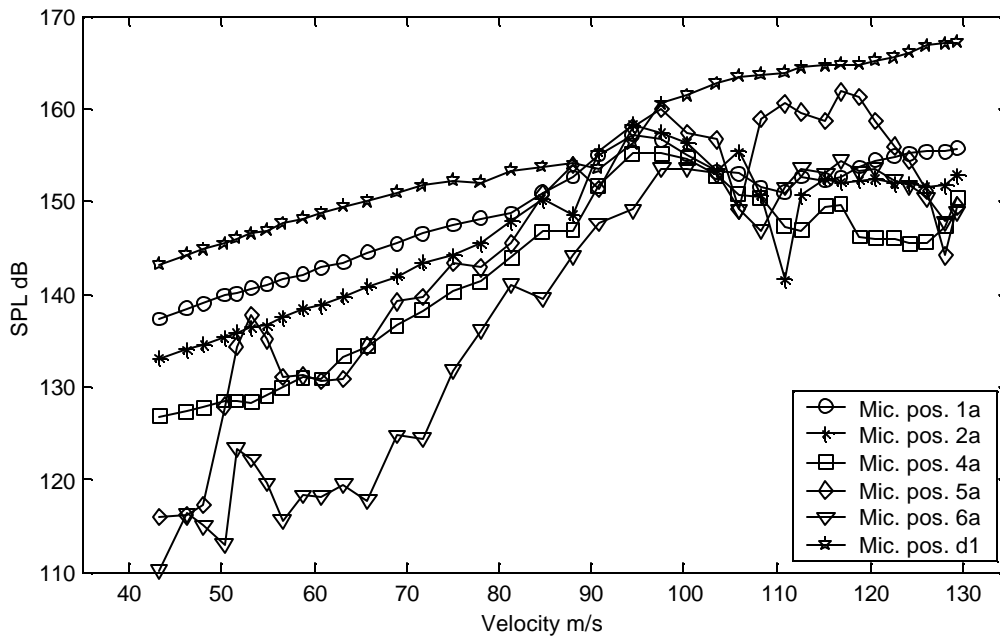


Figure G.38 Sound pressure level as a function of average flow velocity.

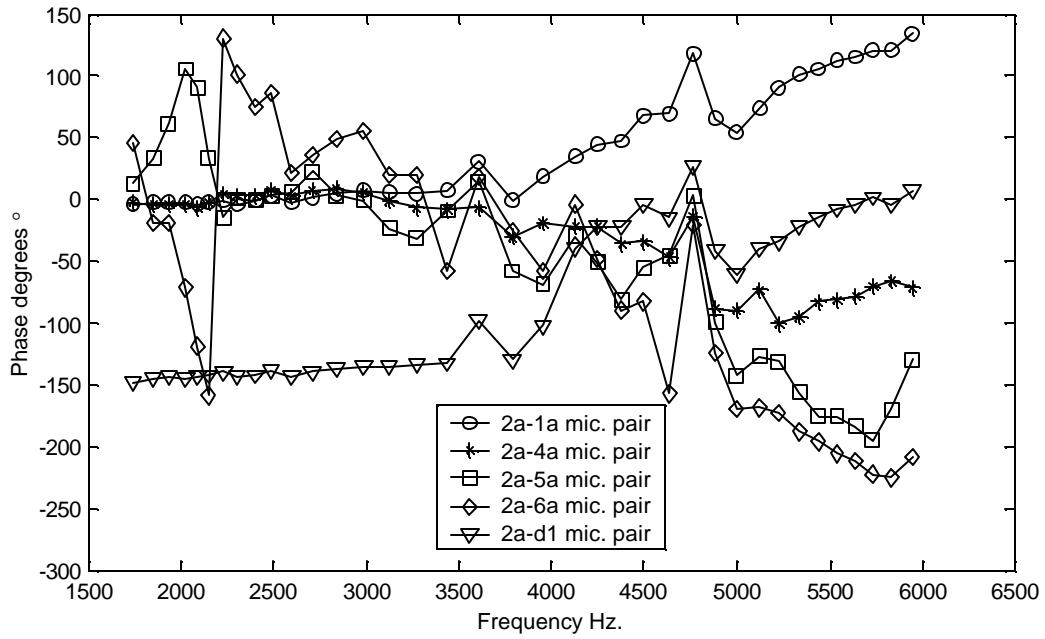


Figure G.39 Transfer function phase angle at frequency of dominant peak in spectra between microphone pairs shown.

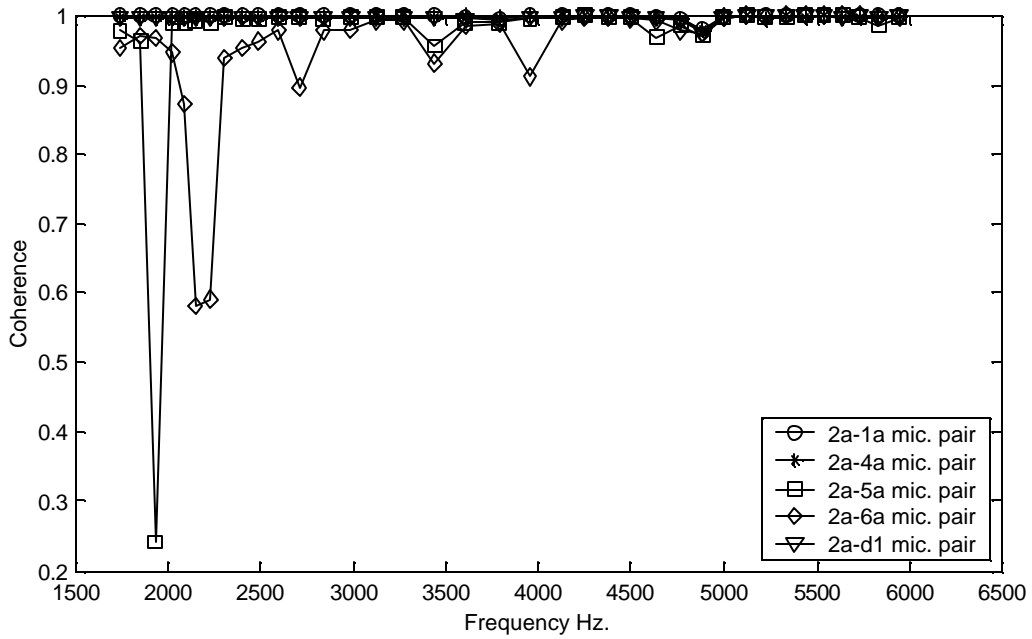


Figure G.40 Coherence at frequency of dominant peak in spectra between microphone pairs shown. Phase angle shown in figure above prone to error if coherence not close to one.



### 3.8 mm Diameter "Hourglass" Shaped Cylinders

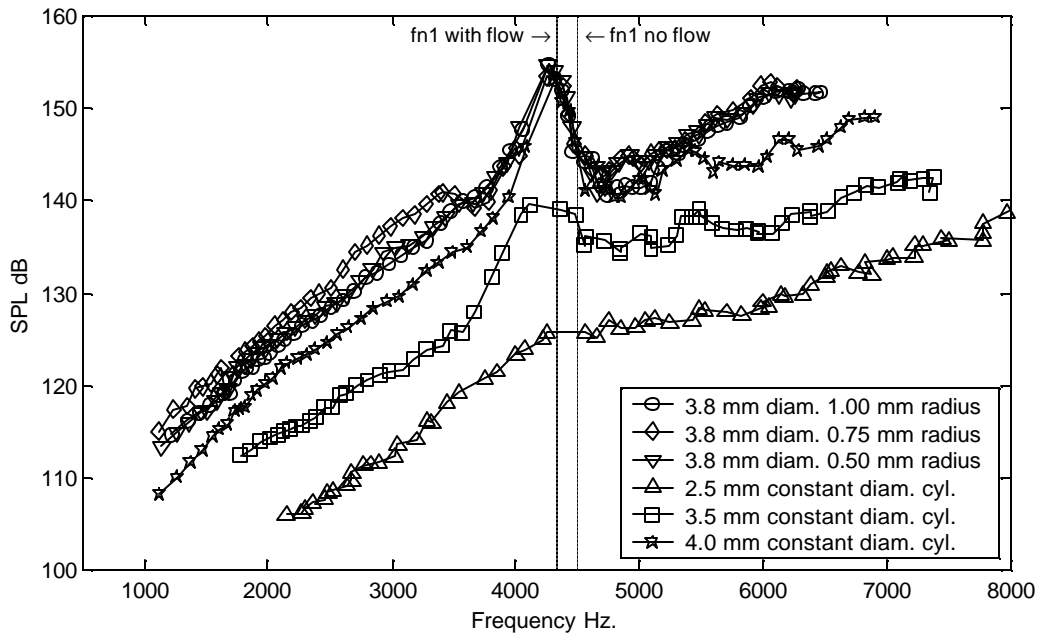


Figure G.41 Comparison of sound pressure levels produced by cylinders of different shape against results from regular cylinders (see Figure 4.21). Measurements at microphone position 1a. (fn1 with flow) acoustic resonance estimated with flow velocity at resonance condition.

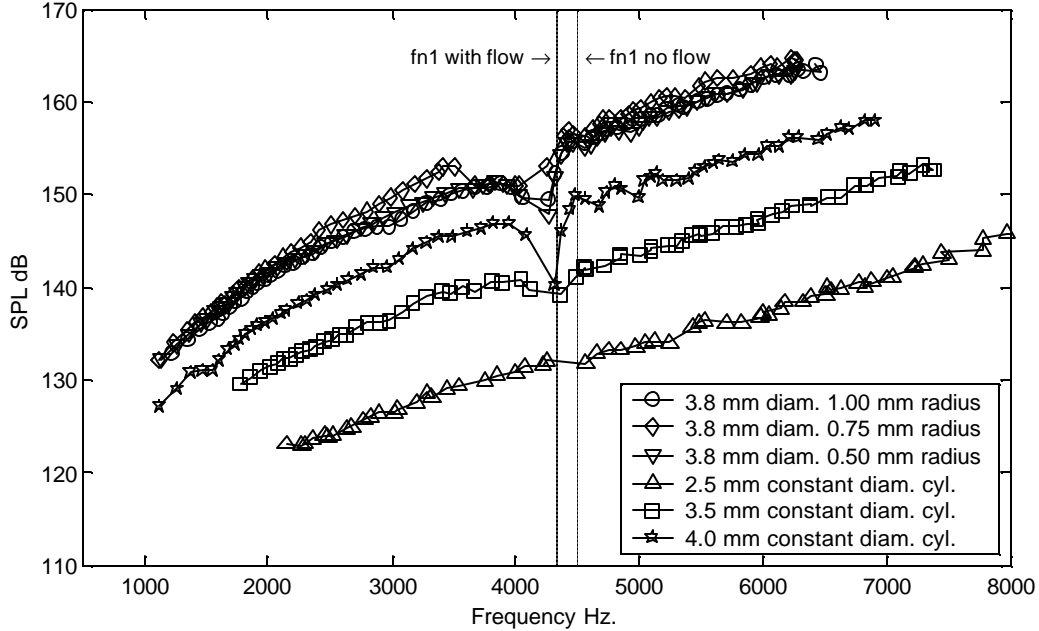


Figure G.42 Comparison of sound pressure levels produced by cylinders of different shape against results from regular cylinders (see Figure 4.21). Measurements at microphone position d1. (fn1 with flow) acoustic resonance estimated with flow velocity at resonance condition.

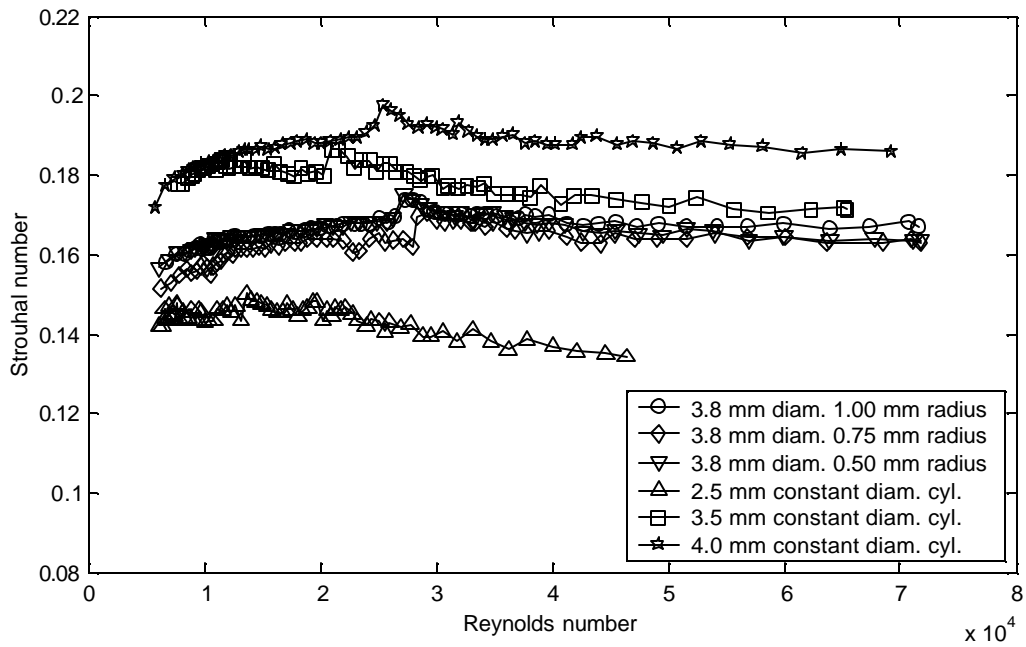


Figure G.43 Comparison of Strouhal vs. Reynolds number for cylinders of different shape against results from regular cylinders.

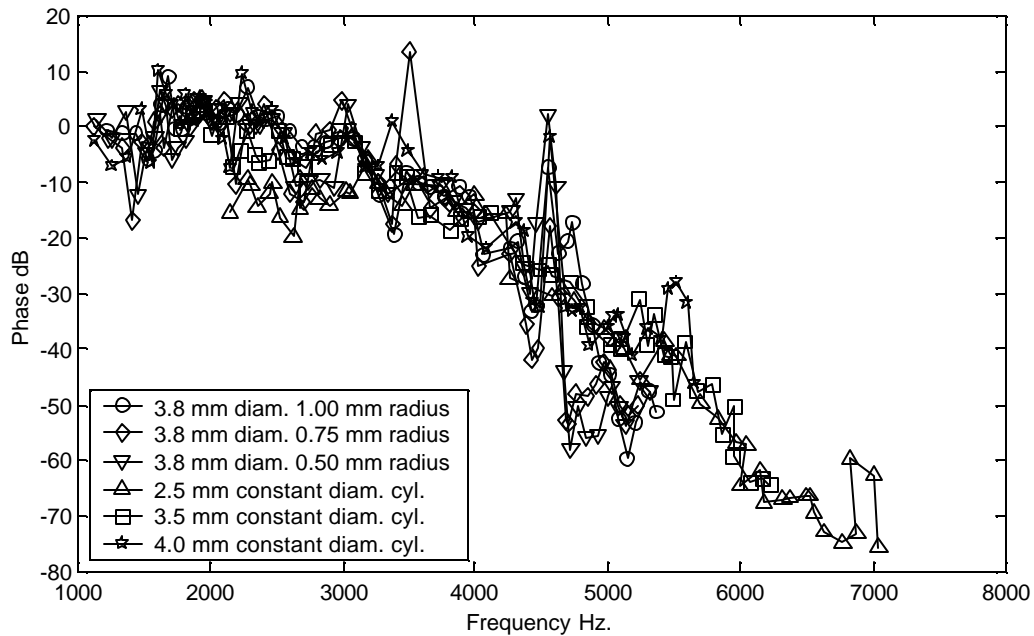


Figure G.44 Comparison of transfer function phase angle between microphone pair 2a -4a for cylinders of different shape against results from regular cylinders.

### 3.3 mm Diameter "Hourglass" Shaped Cylinders

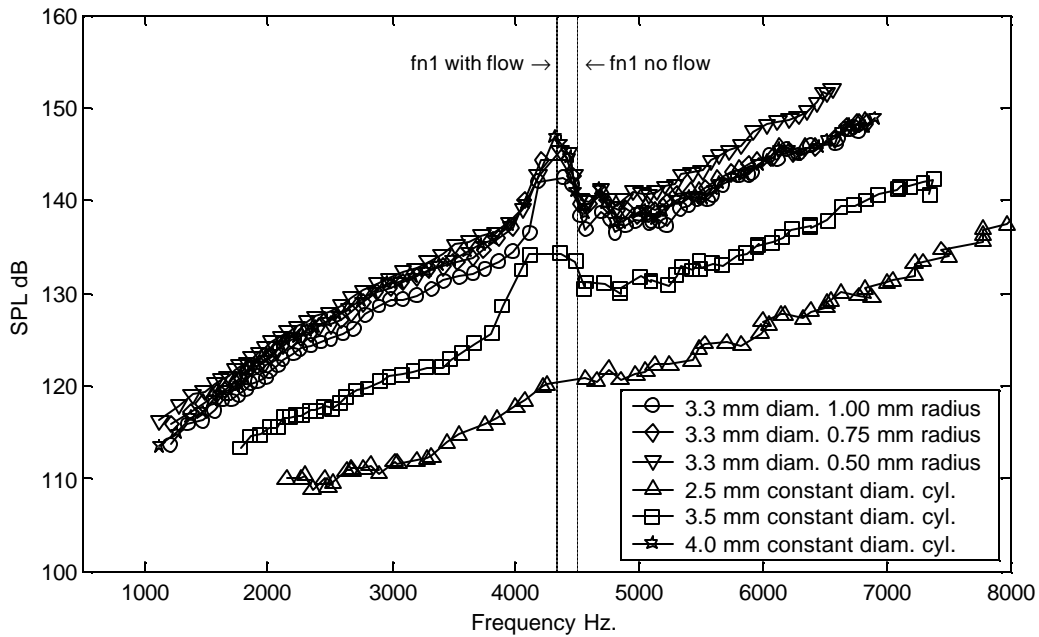


Figure G.45 Comparison of sound pressure levels produced by cylinders of different shape against results from regular cylinders (see Figure 4.21). Measurements at microphone position 1a. (fn1 with flow) acoustic resonance estimated with flow velocity at resonance condition.

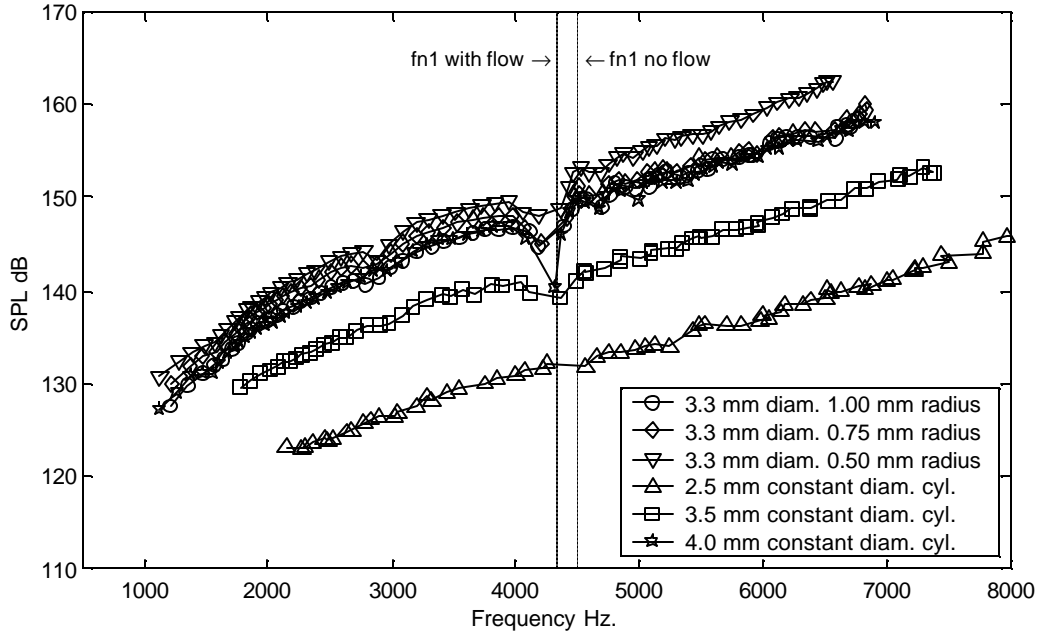


Figure G.46 Comparison of sound pressure levels produced by cylinders of different shape against results from regular cylinders (see Figure 4.21). Measurements at microphone position d1. (fn1 with flow) acoustic resonance estimated with flow velocity at resonance condition.

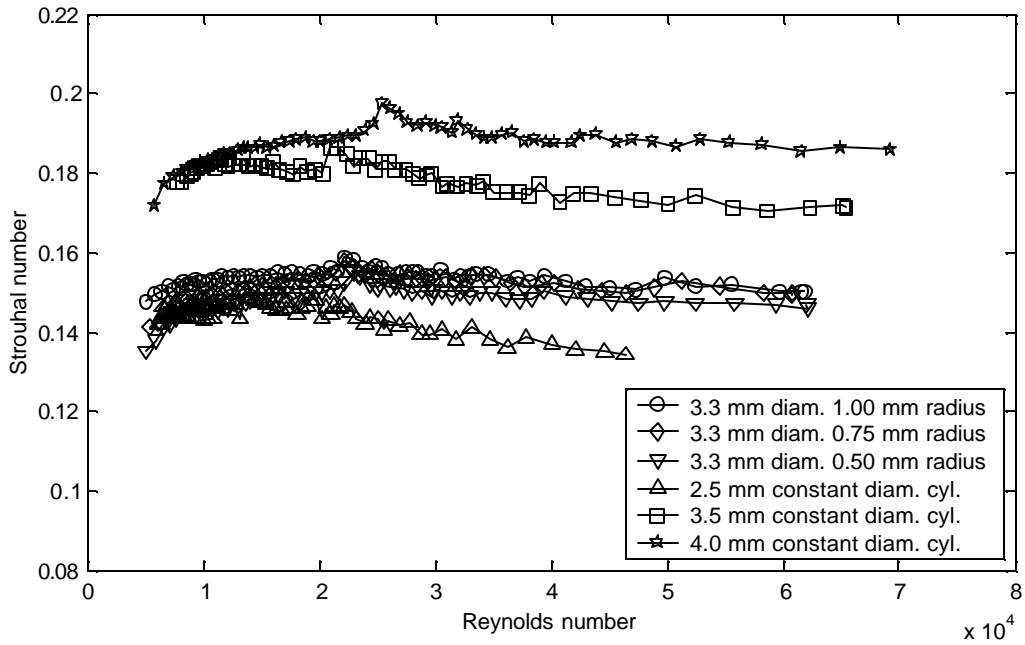


Figure G.47 Comparison of Strouhal vs. Reynolds number for cylinders of different shape against results from regular cylinders.

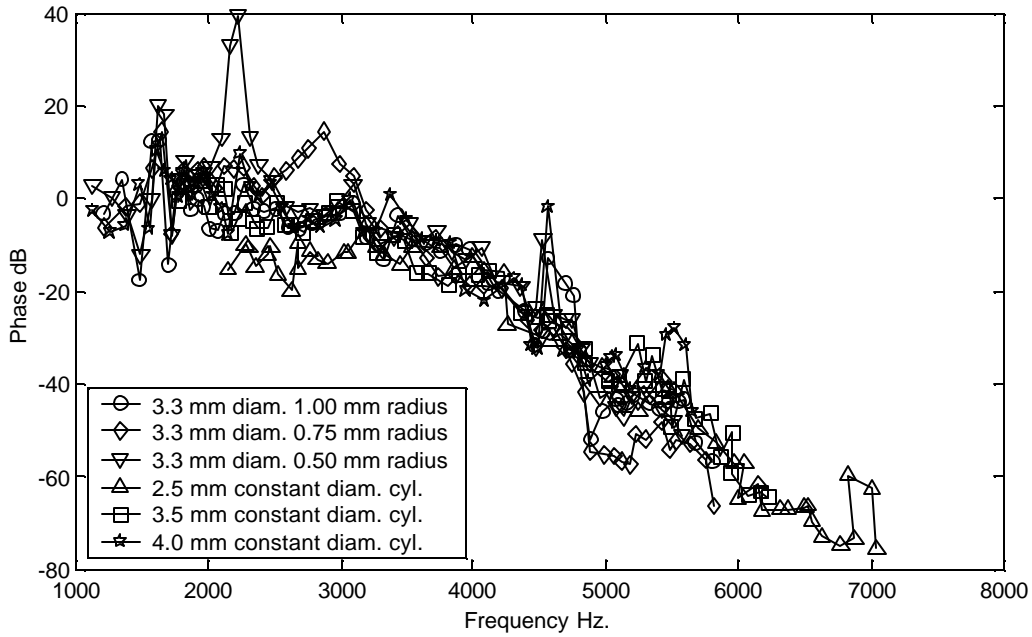


Figure G.48 Comparison of transfer function phase angle between microphone pair 2a -4a for cylinders of different shape against results from regular cylinders.

### 2.85 mm Diameter "Hourglass" Shaped Cylinders

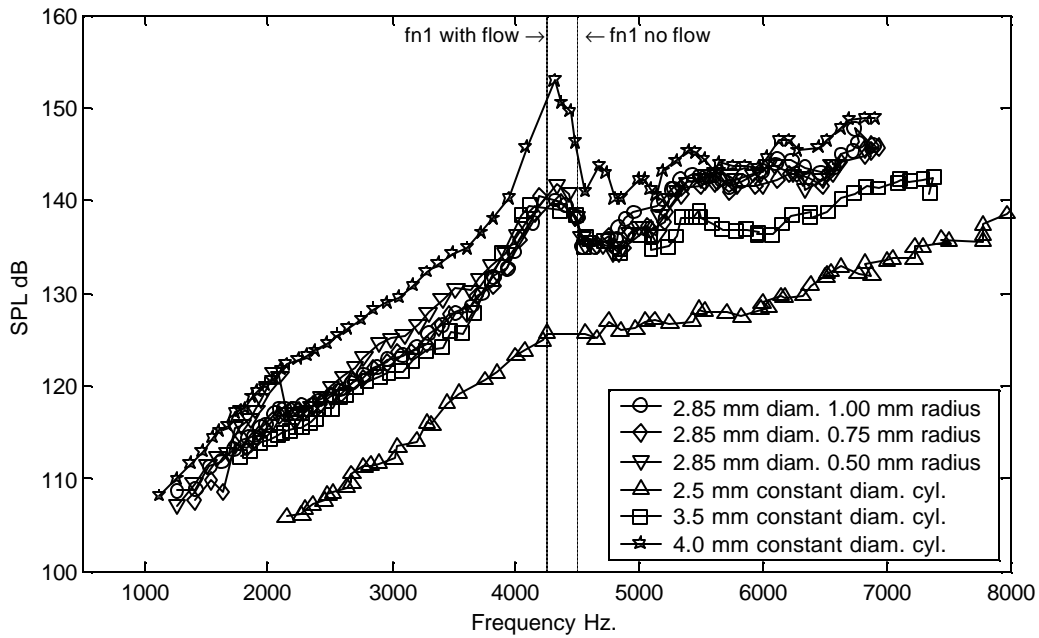


Figure G.49 Comparison of sound pressure levels produced by cylinders of different shape against results from regular cylinders (see Figure 4.21). Measurements at microphone position 1a. (fn1 with flow) acoustic resonance estimated with flow velocity at resonance condition.

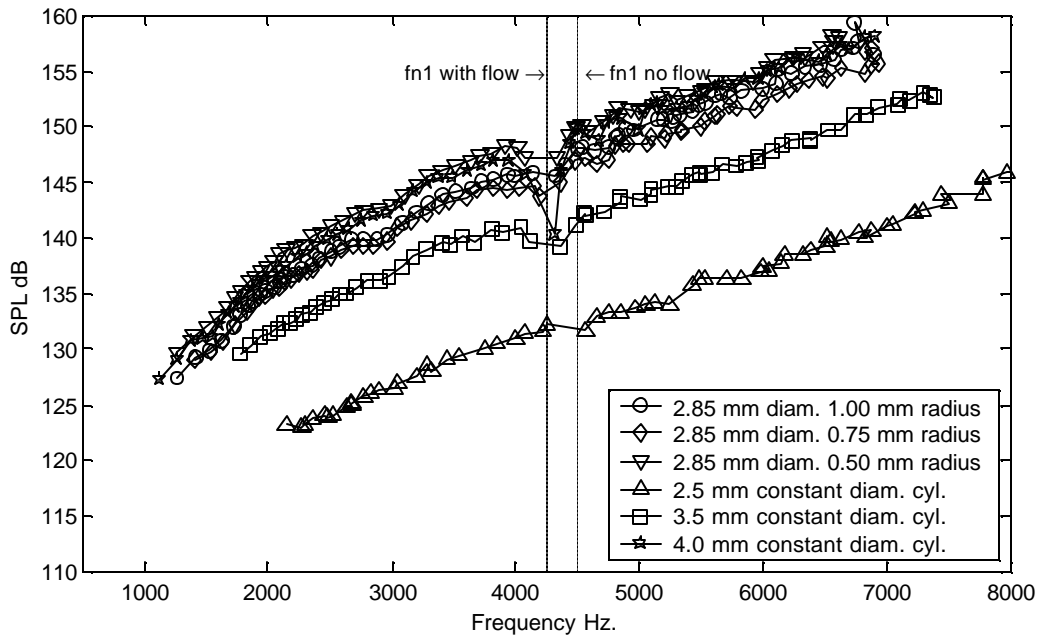


Figure G.50 Comparison of sound pressure levels produced by cylinders of different shape against results from regular cylinders (see Figure 4.21). Measurements at microphone position d1. (fn1 with flow) acoustic resonance estimated with flow velocity at resonance condition.

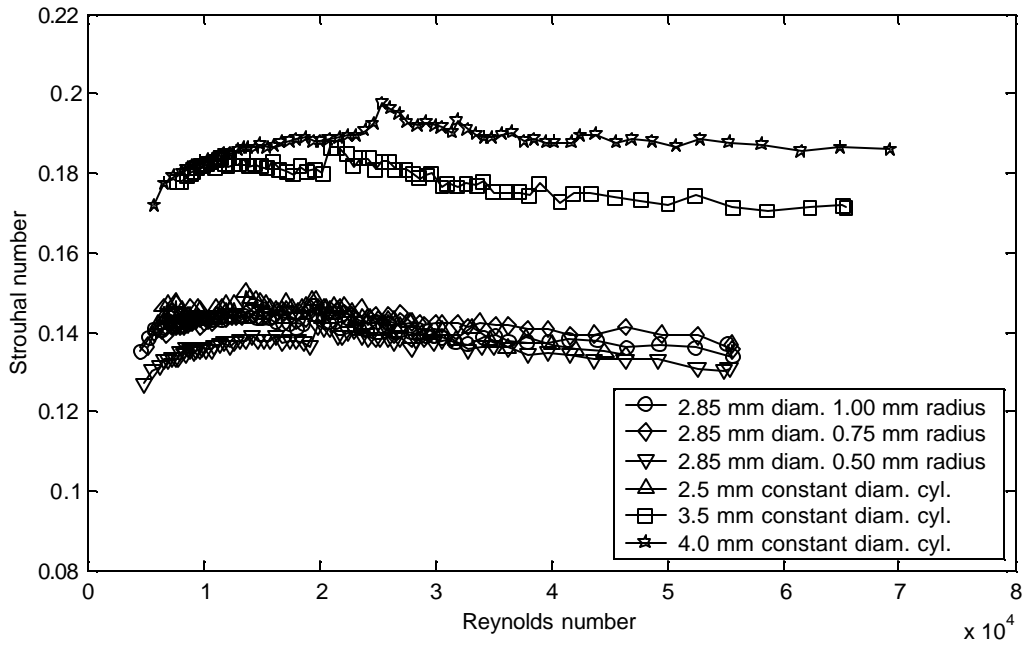


Figure G.51 Comparison of Strouhal vs. Reynolds number for cylinders of different shape against results from regular cylinders.

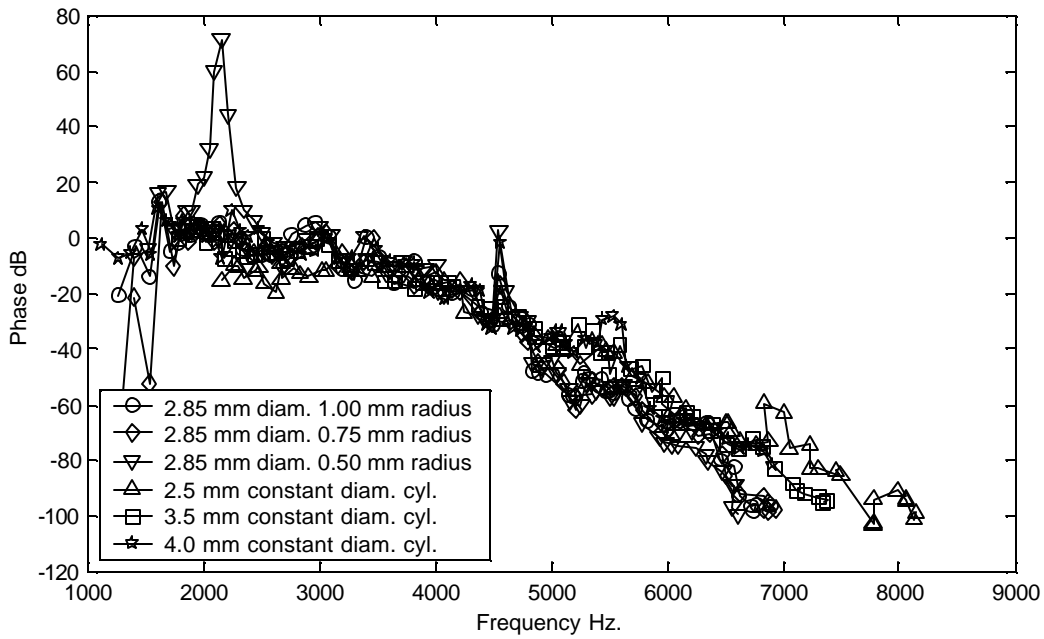


Figure G.52 Comparison of transfer function phase angle between microphone pair 2a -4a for cylinders of different shape against results from regular cylinders.

### 2.35 mm Diameter "Hourglass" Shaped Cylinders

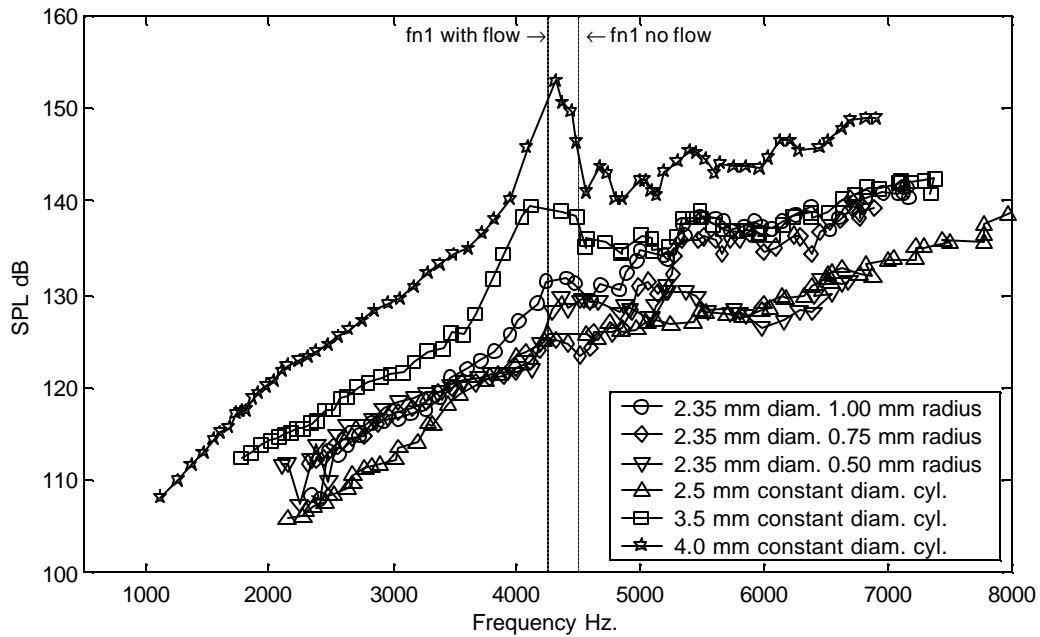


Figure G.53 Comparison of sound pressure levels produced by cylinders of different shape against results from regular cylinders (see Figure 4.21). Measurements at microphone position 1a. (fn1 with flow) acoustic resonance estimated with flow velocity at resonance condition.

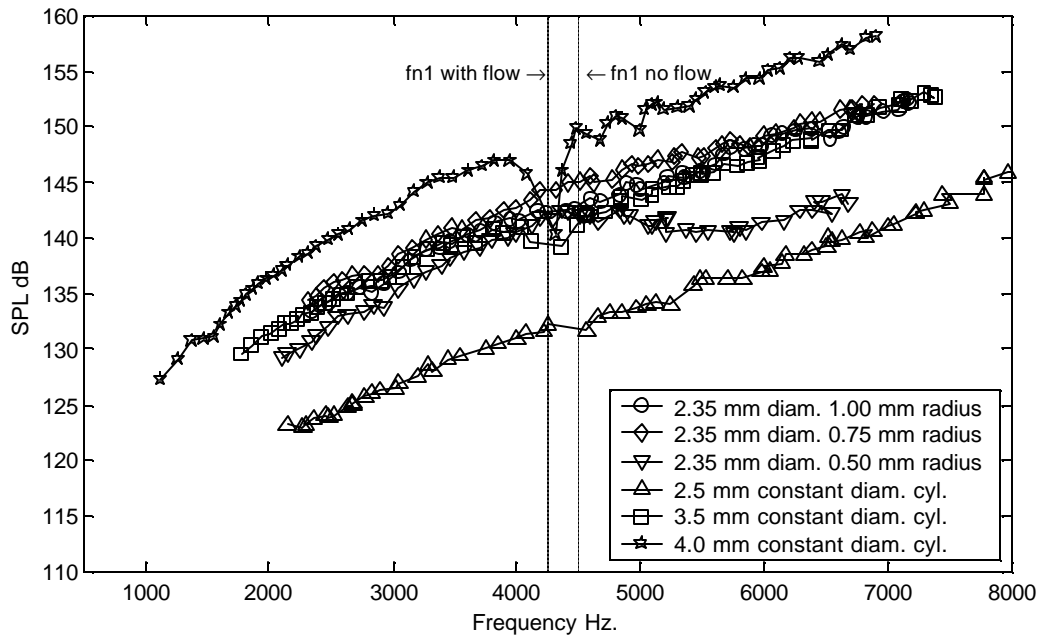


Figure G.54 Comparison of sound pressure levels produced by cylinders of different shape against results from regular cylinders (see Figure 4.21). Measurements at microphone position d1. (fn1 with flow) acoustic resonance estimated with flow velocity at resonance condition.

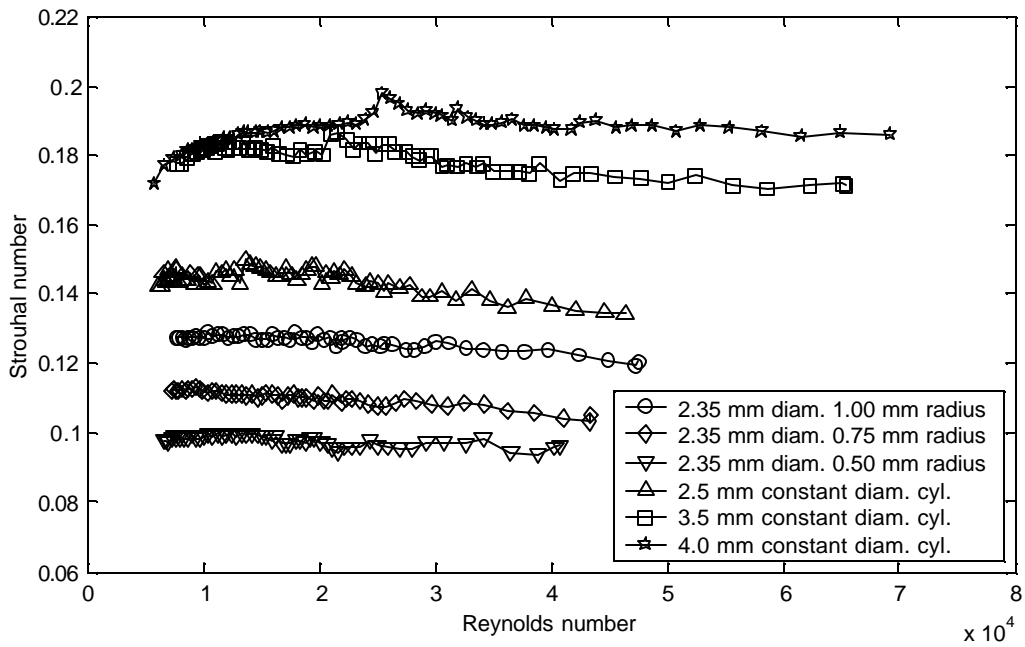


Figure G.55 Comparison of Strouhal vs. Reynolds number for cylinders of different shape against results from regular cylinders.

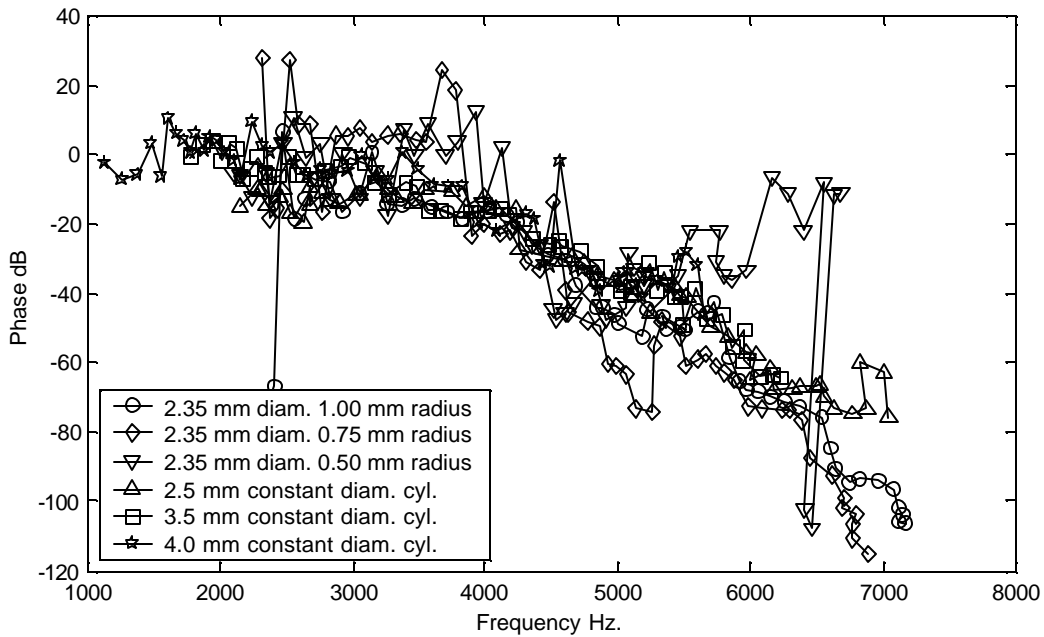


Figure G.56 Comparison of transfer function phase angle between microphone pair 2a -4a for cylinders of different shape against results from regular cylinders.



### 1.8 mm Diameter "Hourglass" Shaped Cylinders

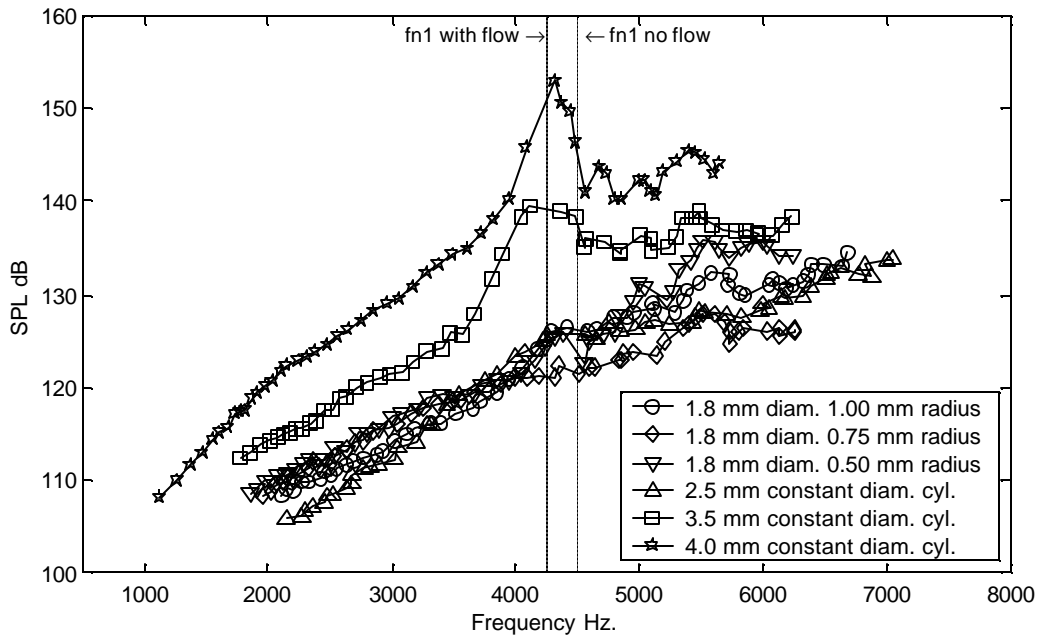


Figure G.57 Comparison of sound pressure levels produced by cylinders of different shape against results from regular cylinders (see Figure 4.21). Measurements at microphone position 1a. (fn1 with flow) acoustic resonance estimated with flow velocity at resonance condition.

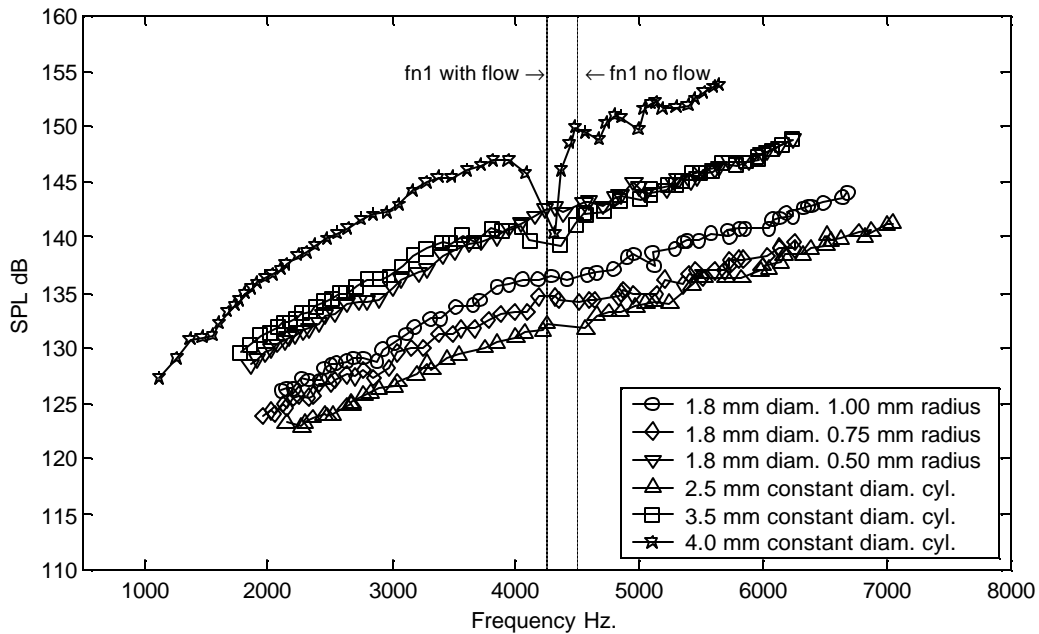


Figure G.58 Comparison of sound pressure levels produced by cylinders of different shape against results from regular cylinders (see Figure 4.21). Measurements at microphone position d1. (fn1 with flow) acoustic resonance estimated with flow velocity at resonance condition.

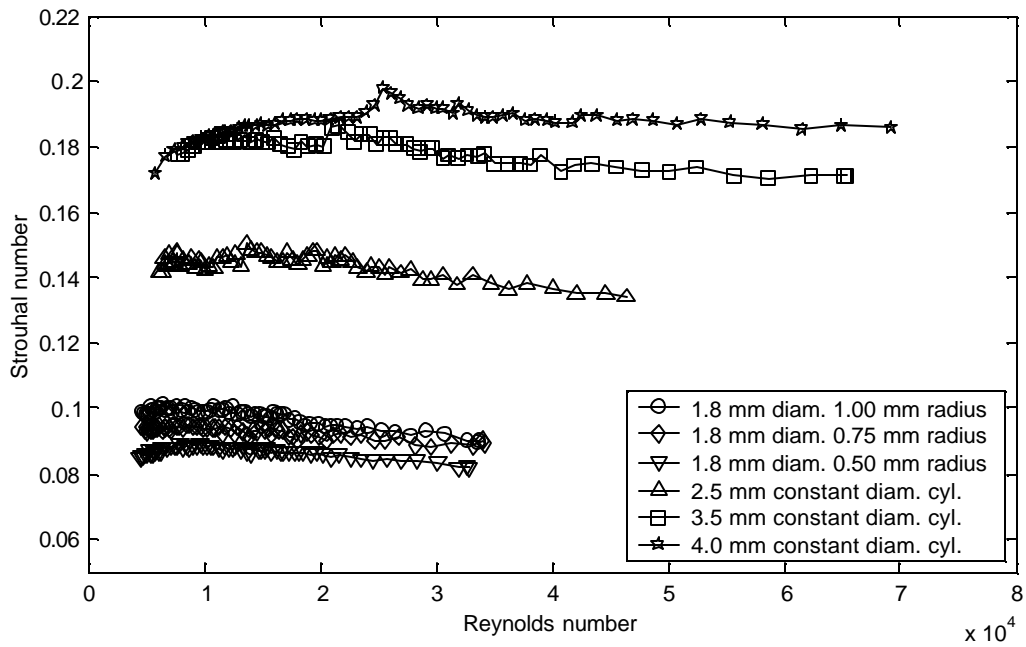


Figure G.59 Comparison of Strouhal vs. Reynolds number for cylinders of different shape against results from regular cylinders.

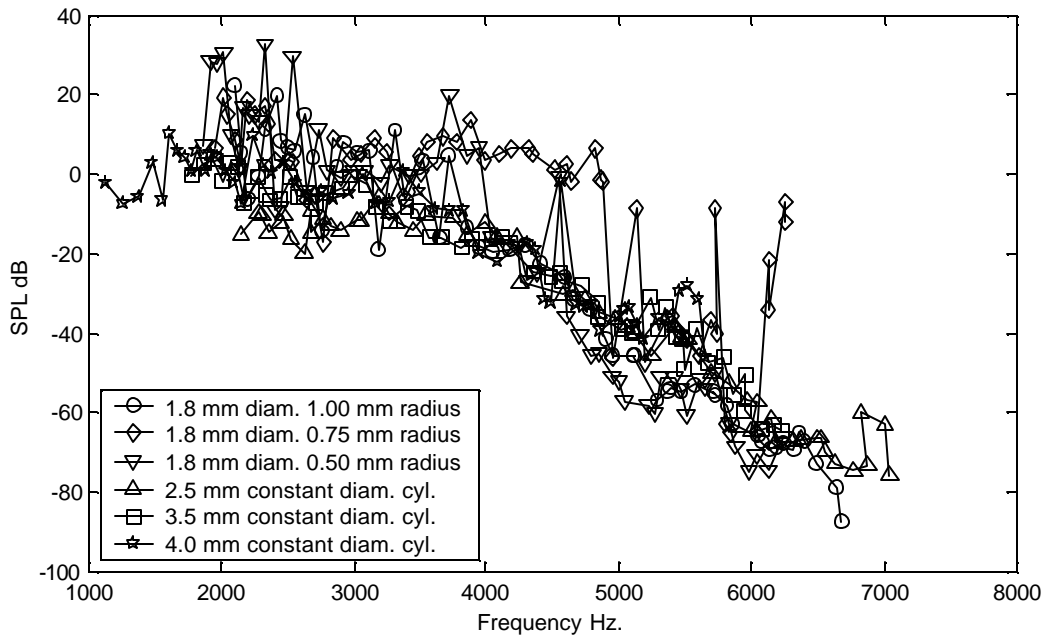


Figure G.60 Comparison of transfer function phase angle between microphone pair 2a -4a for cylinders of different shape against results from regular cylinders.

## Appendix H: Pairs of Cylinders Test Results

### 6.35 mm Diameter Cylinders Side-by-Side Configuration

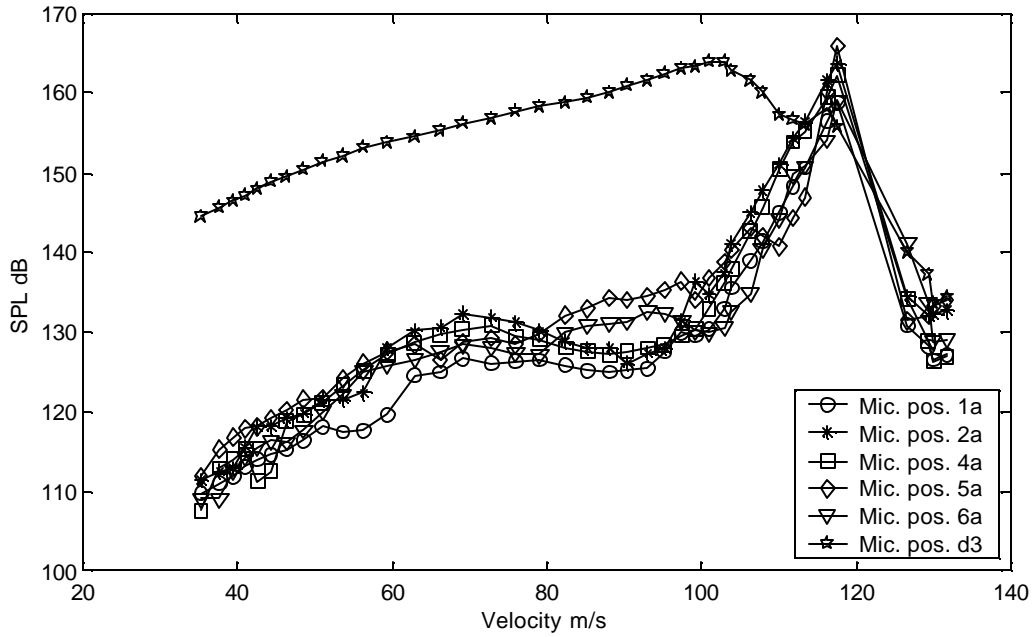


Figure H.1 Sound pressure level at dominant peak in spectra vs. average flow velocity. Microphones and cylinders positions shown in Figures 4.22 and 4.27.

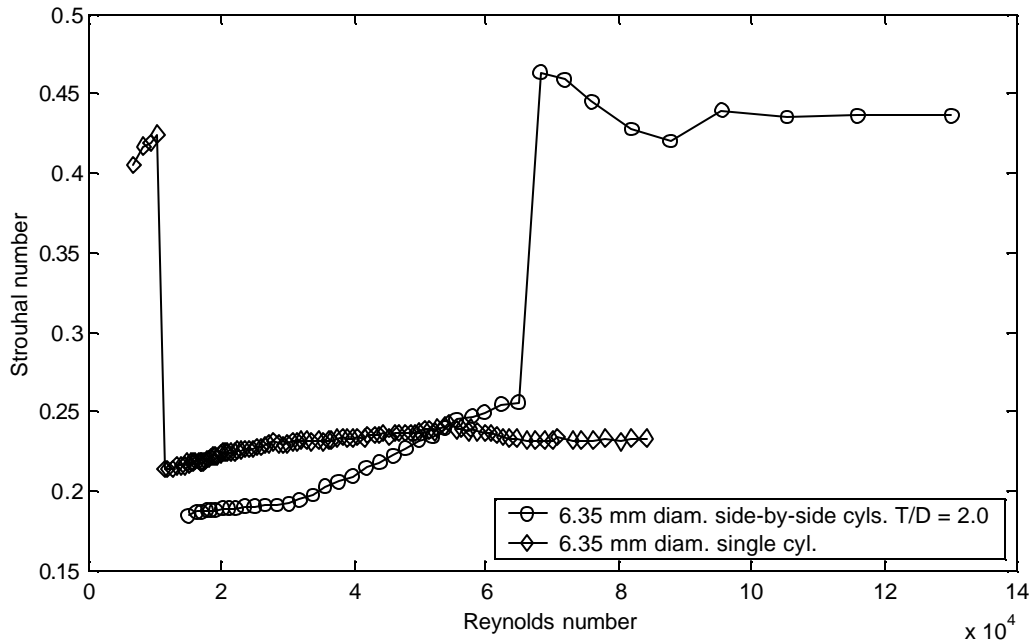


Figure H.2 Comparison of single cylinder and side-by-side cylinders Strouhal numbers as a function of Reynolds number. Strouhal number for side-by-side cylinders estimated using measurements at position d3.

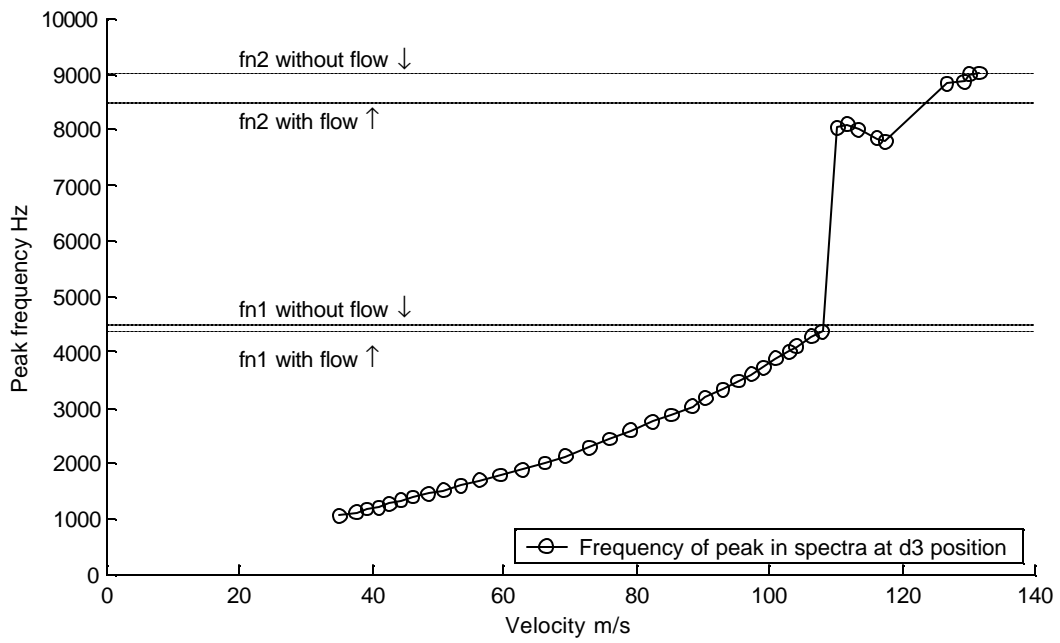


Figure H.3 Frequency of dominant peak in spectra at position d3 vs. average flow velocity. 6.35 mm side-by-side cylinders.

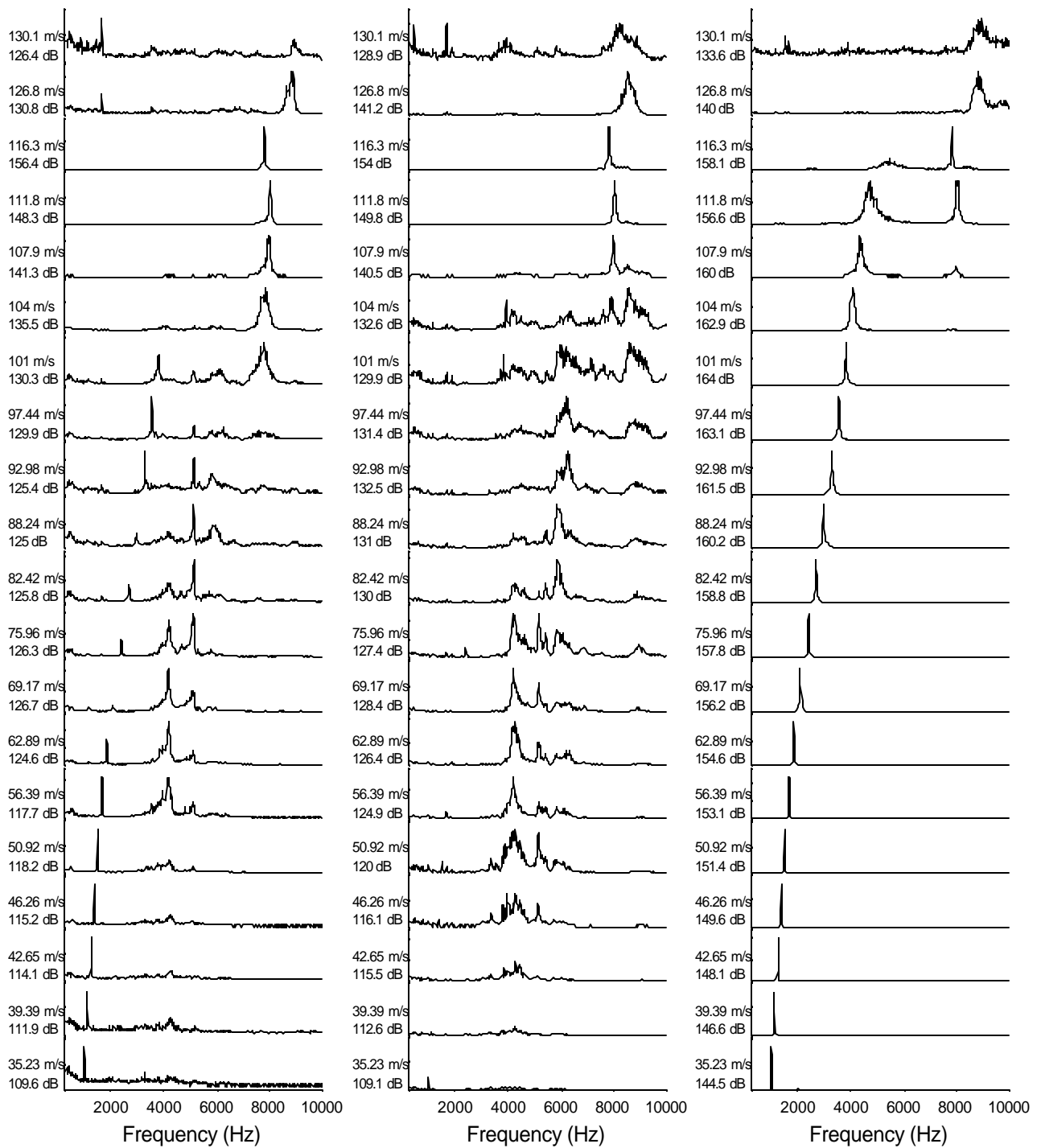


Figure H.4 Representative spectra taken at microphone positions 1a, 6a and d3 (left, center and right respectively). 6.35 mm side-by-side cylinders.

### 5.0 mm Diameter Cylinders Side-by-Side Configuration

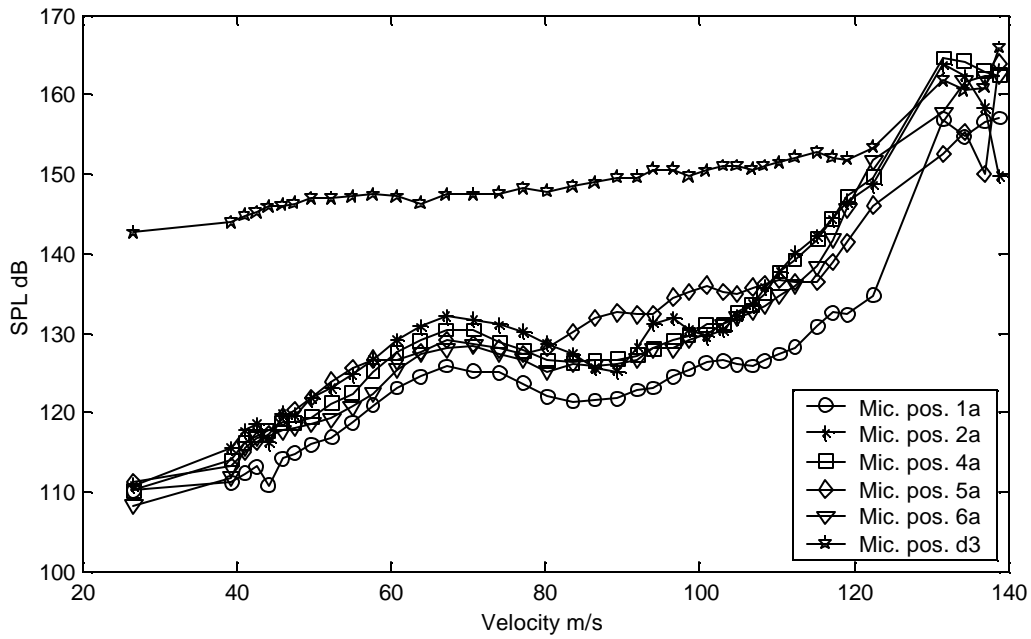


Figure H.5 Sound pressure level at dominant peak in spectra vs. average flow velocity. Microphones and cylinders positions shown in Figures 4.22 and 4.27.

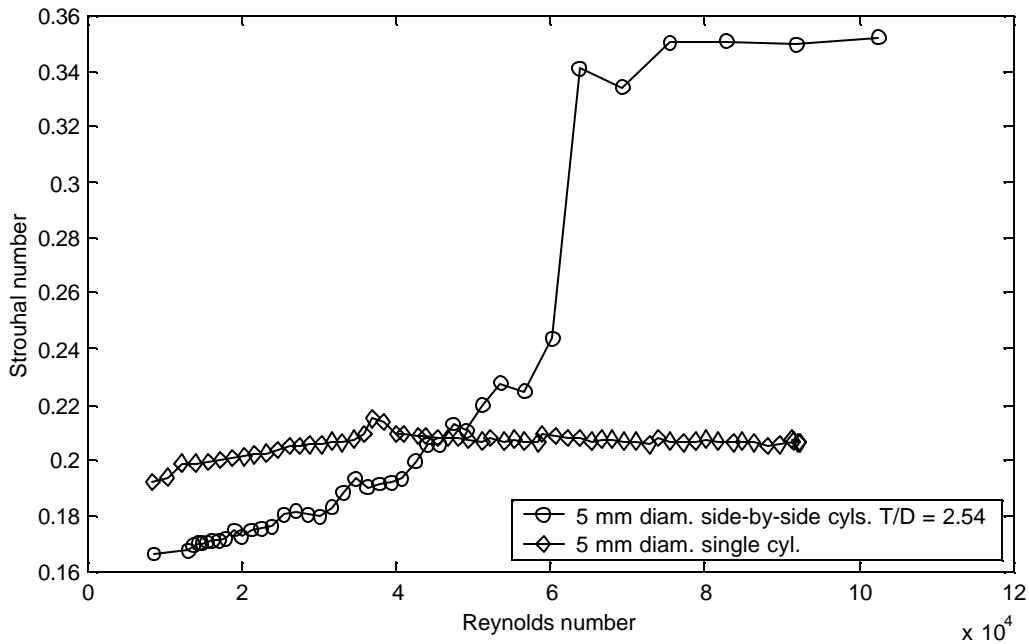


Figure H.6 Comparison of single cylinder and side-by-side cylinders Strouhal numbers as a function of Reynolds number. Strouhal number for side-by-side cylinders estimated using measurements at position d3.

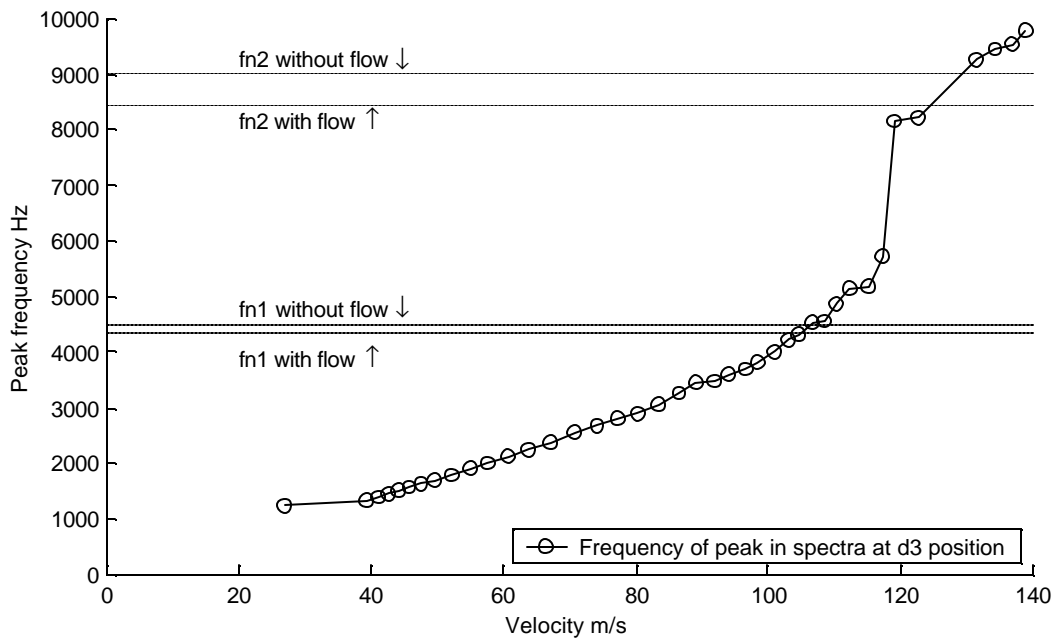


Figure H.7 Frequency of dominant peak in spectra at position d3 vs. average flow velocity. 5.0 mm side-by-side cylinders.

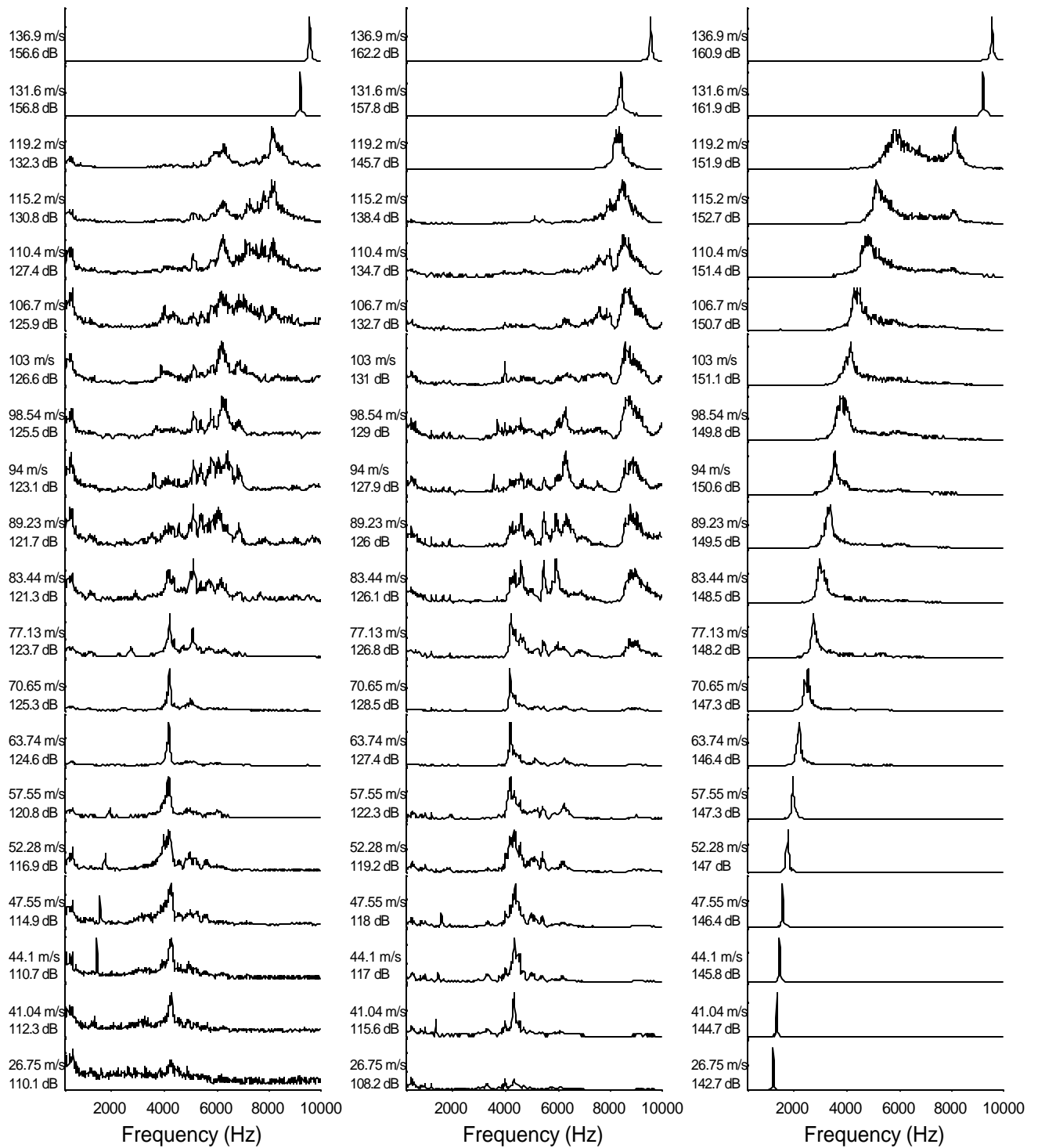


Figure H.8 Representative spectra taken at microphone positions 1a, 6a and d3 (left, center and right respectively). 5.0 mm side-by-side cylinders.



### 4.0 mm Diameter Cylinders Side-by-Side Configuration

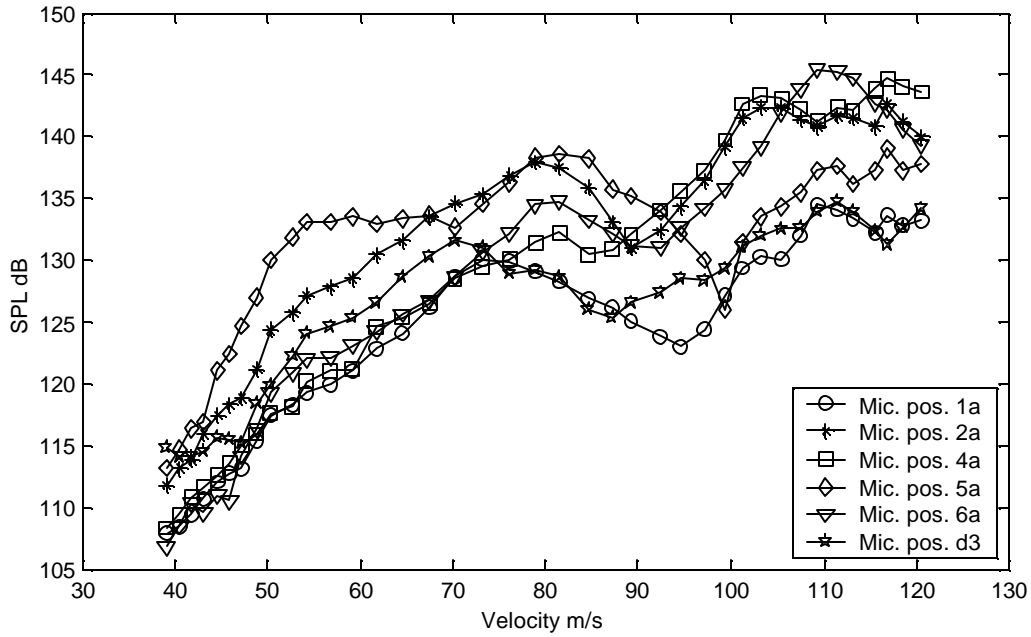


Figure H.9 Sound pressure level at dominant peak in spectra vs. average flow velocity. Microphones and cylinders positions shown in Figures 4.22 and 4.27.

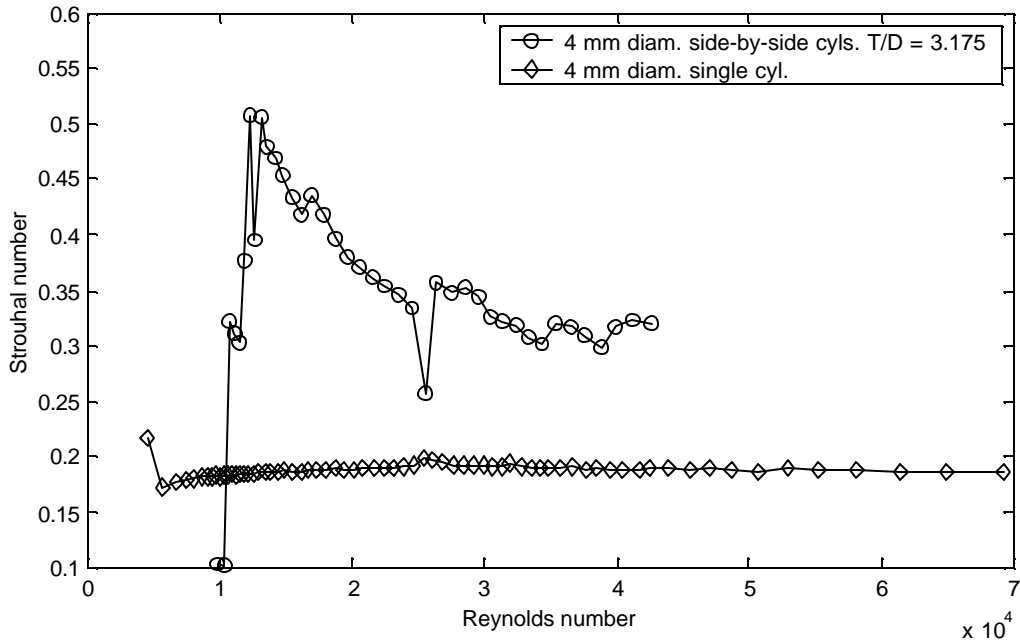


Figure H.10 Comparison of single cylinder and side-by-side cylinders Strouhal numbers as a function of Reynolds number. Strouhal number for side-by-side cylinders estimated using measurements at position d3.

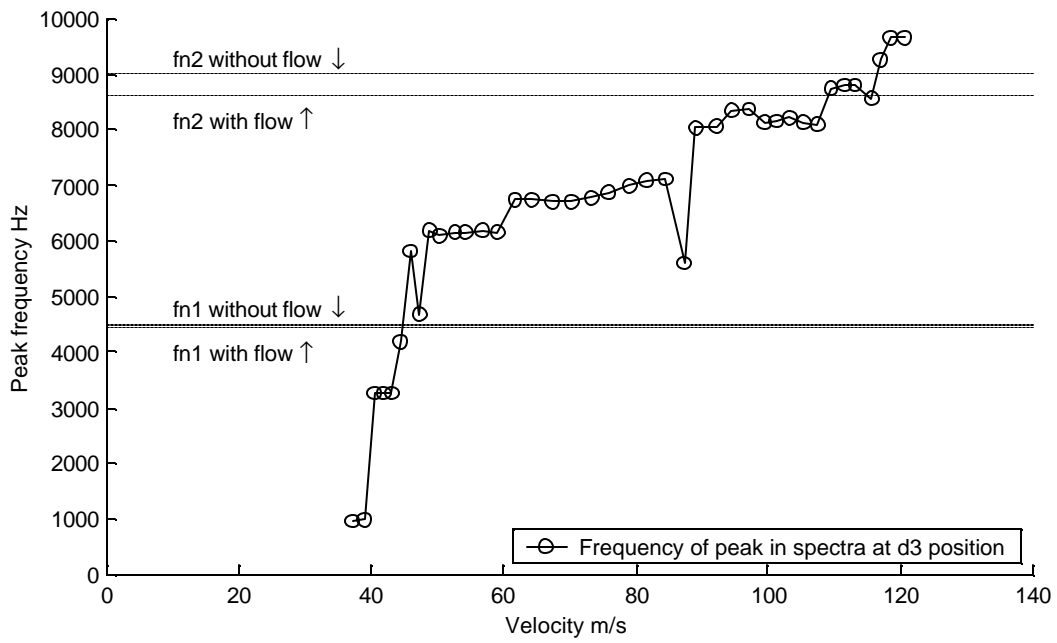


Figure H.11 Frequency of dominant peak in spectra at position d3 vs. average flow velocity. 4.0 mm side-by-side cylinders.

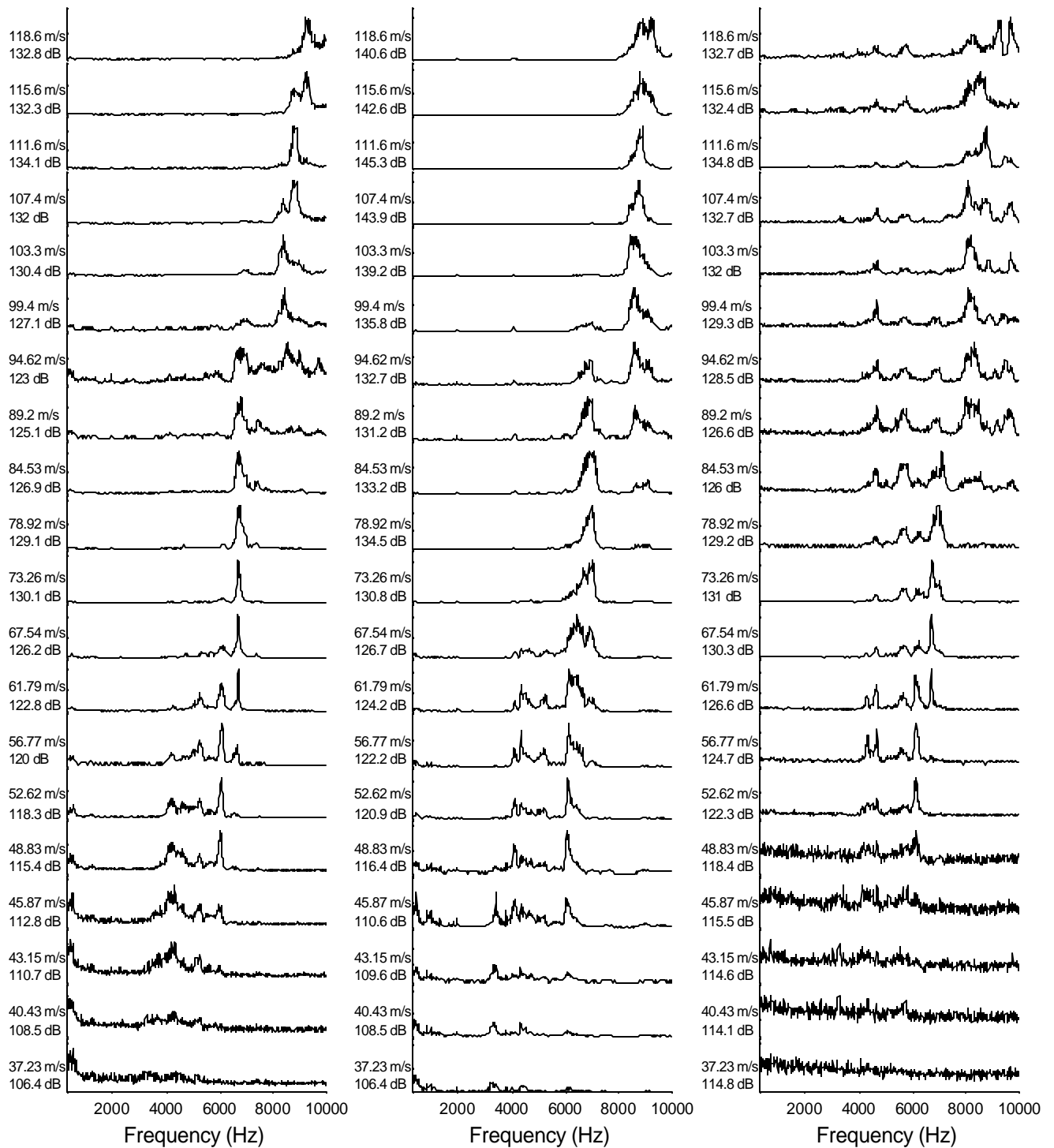


Figure H.12 Representative spectra taken at microphone positions 1a, 6a and d3 (left, center and right respectively). 4.0 mm side-by-side cylinders.

### 3.0 mm Diameter Cylinders Side-by-Side Configuration

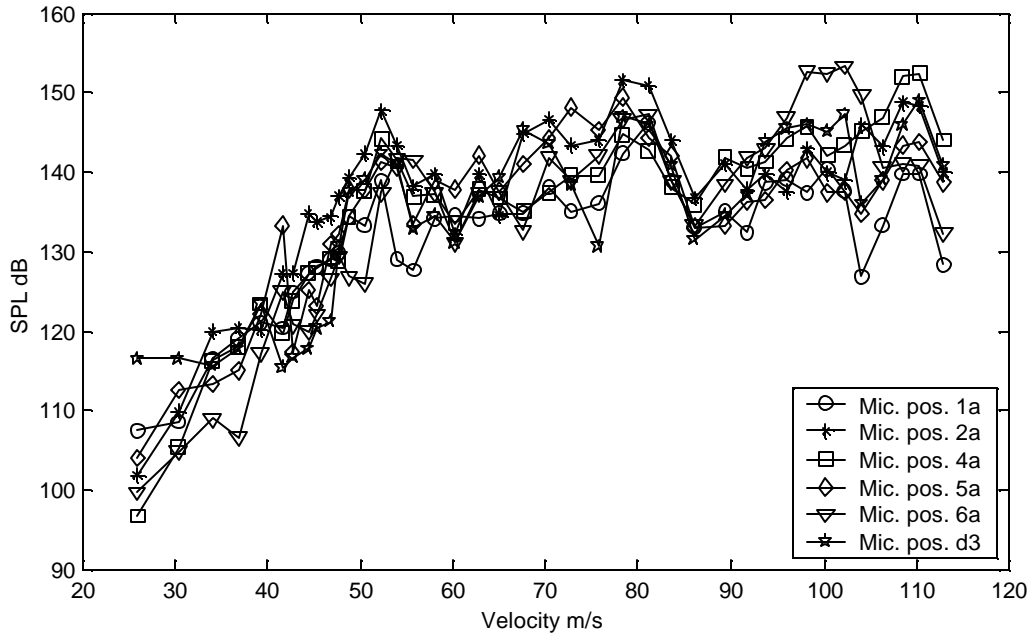


Figure H.13 Sound pressure level at dominant peak in spectra vs. average flow velocity. Microphones and cylinders positions shown in Figures 4.22 and 4.27.

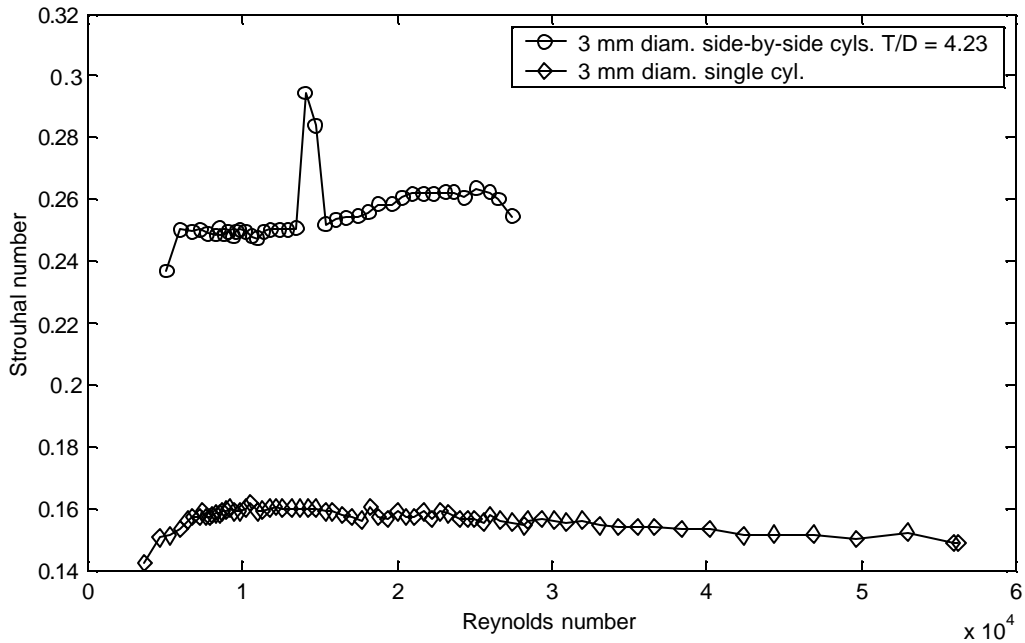


Figure H.14 Comparison of single cylinder and side-by-side cylinders Strouhal numbers as a function of Reynolds number. Strouhal number for side-by-side cylinders estimated using measurements at position d3.

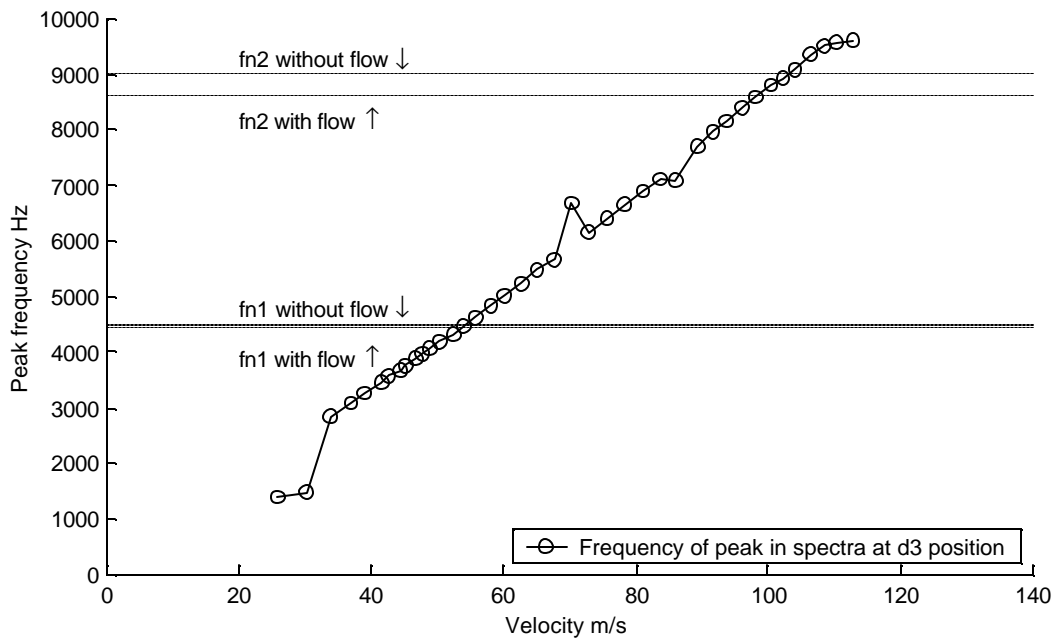


Figure H.15 Frequency of dominant peak in spectra at position d3 vs. average flow velocity. 3.0 mm side-by-side cylinders.

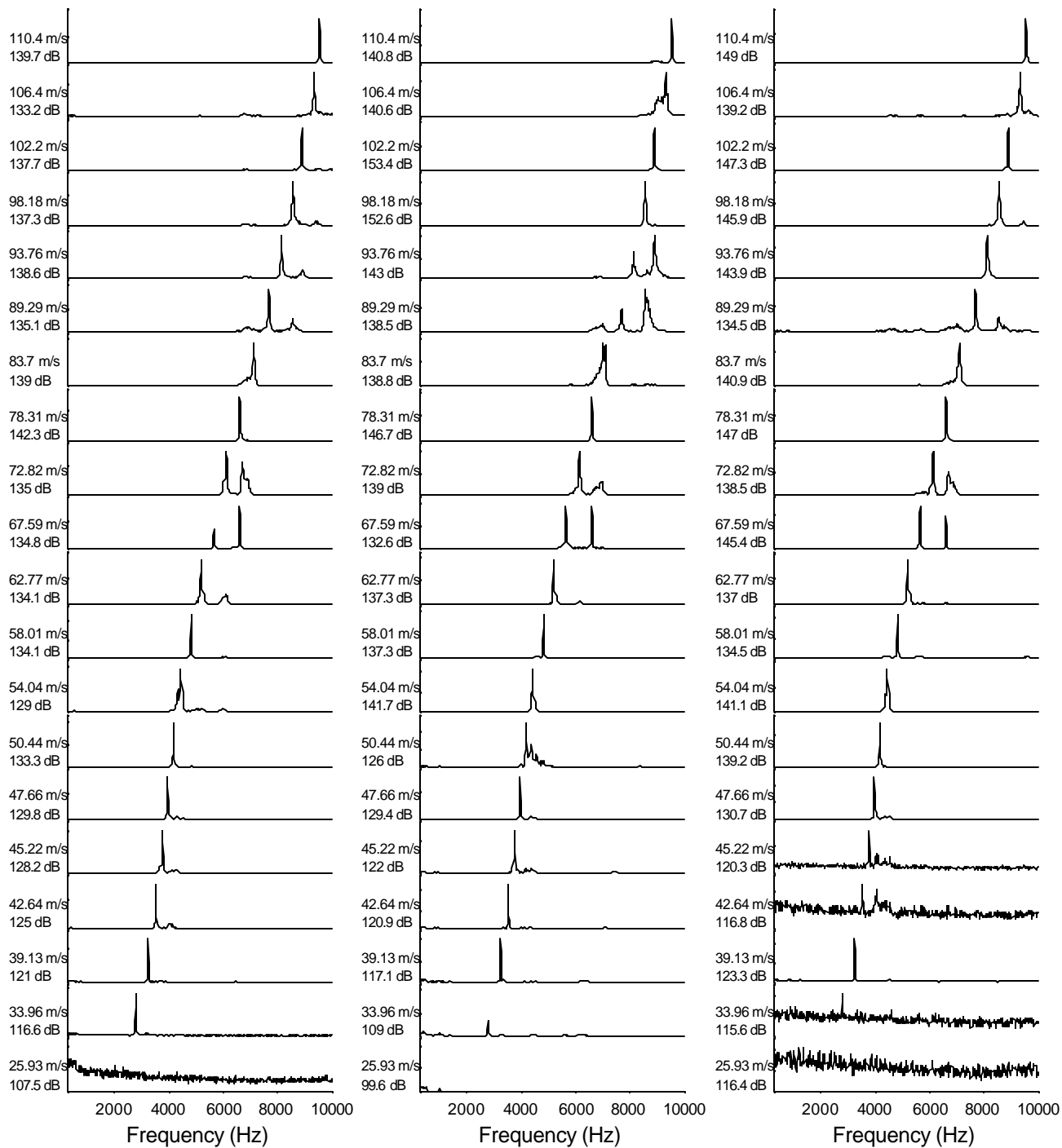


Figure H.16 Representative spectra taken at microphone positions 1a, 6a and d3 (left, center and right respectively). 3.0 mm side-by-side cylinders.

### 6.35 mm Diameter Cylinders Tandem Configuration

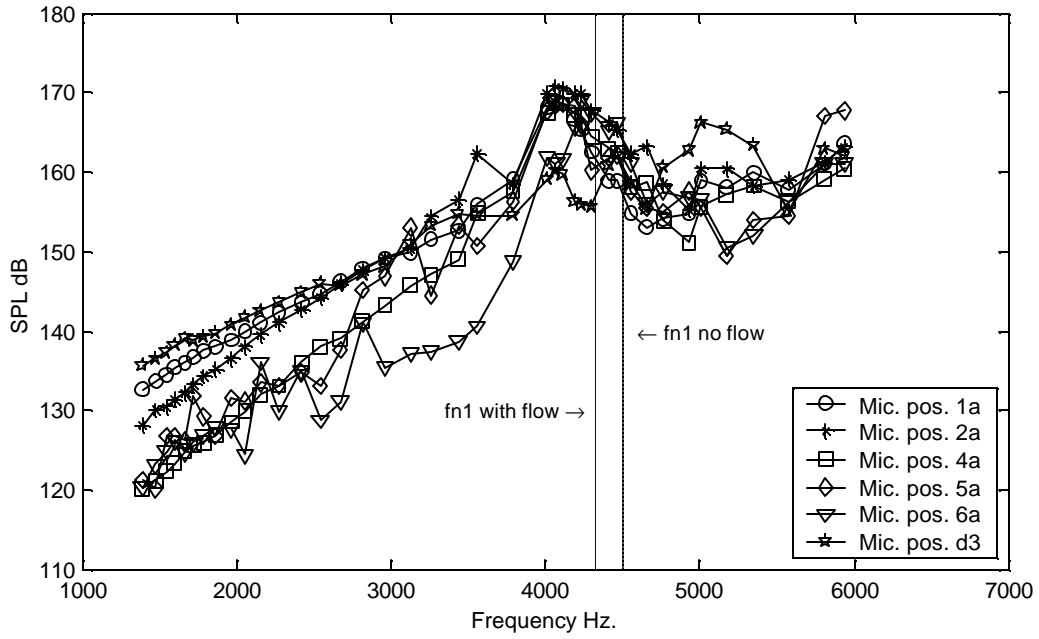


Figure H.17 Sound pressure level at dominant peak in spectra vs. frequency. Microphones and cylinders positions shown in Figures 4.22 and 4.27.

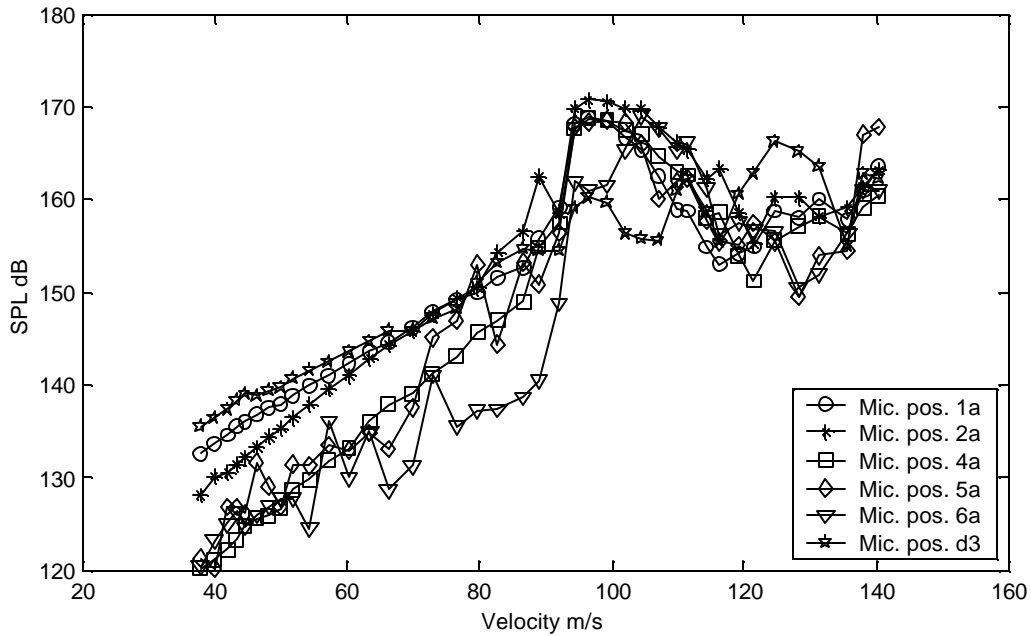


Figure H.18 Sound pressure level at dominant peak in spectra vs. average flow velocity. Microphones and cylinders positions shown in Figures 4.22 and 4.27.

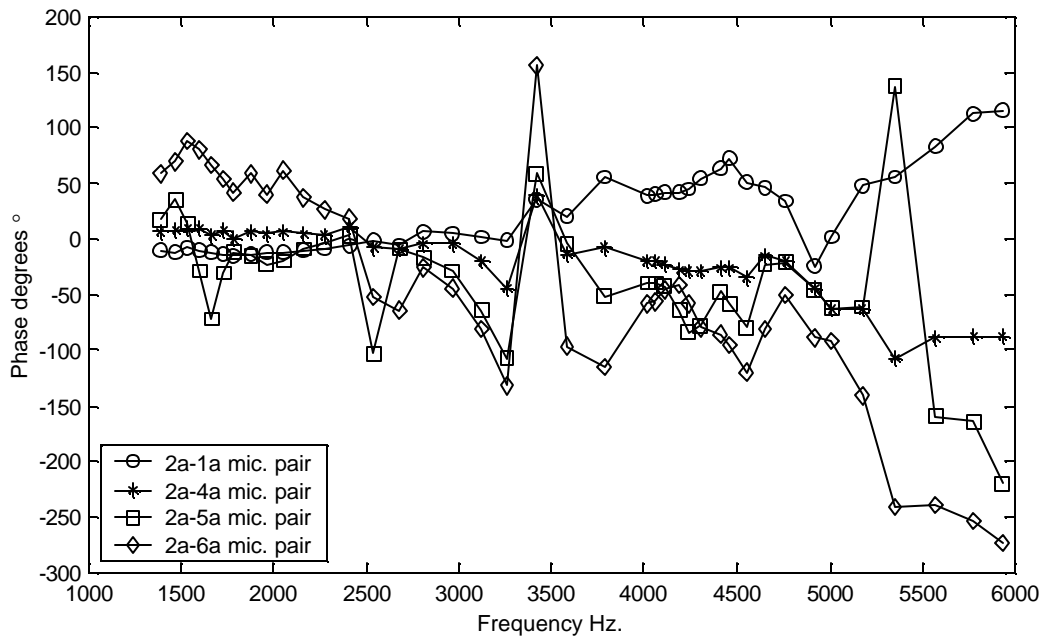


Figure H.19 Transfer function phase angle at frequency of dominant peak in spectra between microphone pairs shown.

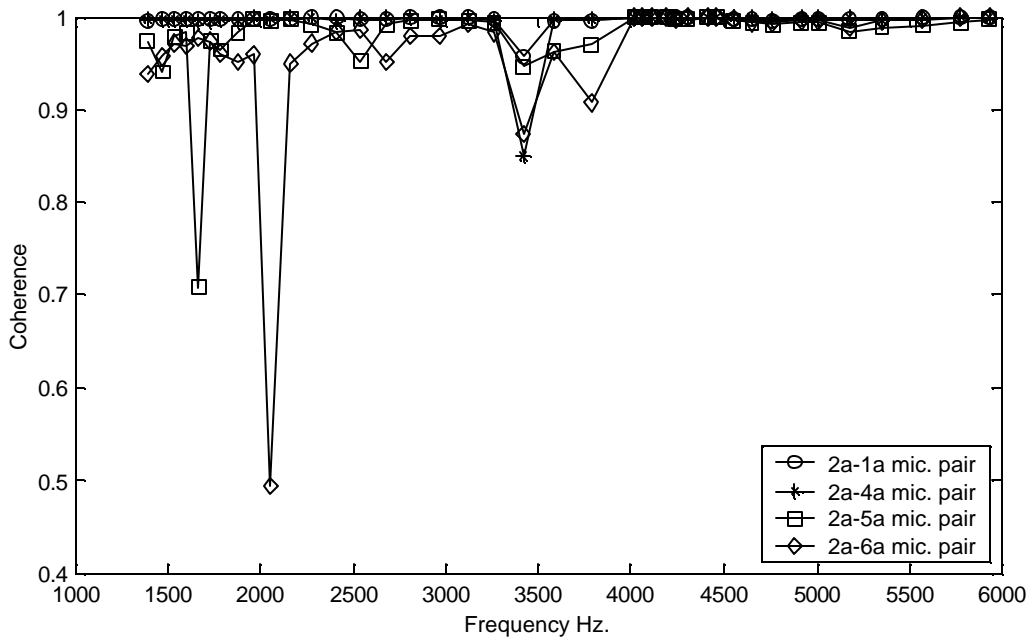


Figure H.20 Coherence at frequency of dominant peak in spectra between microphone pairs shown. Phase angle shown in figure above prone to error if coherence not close to one.



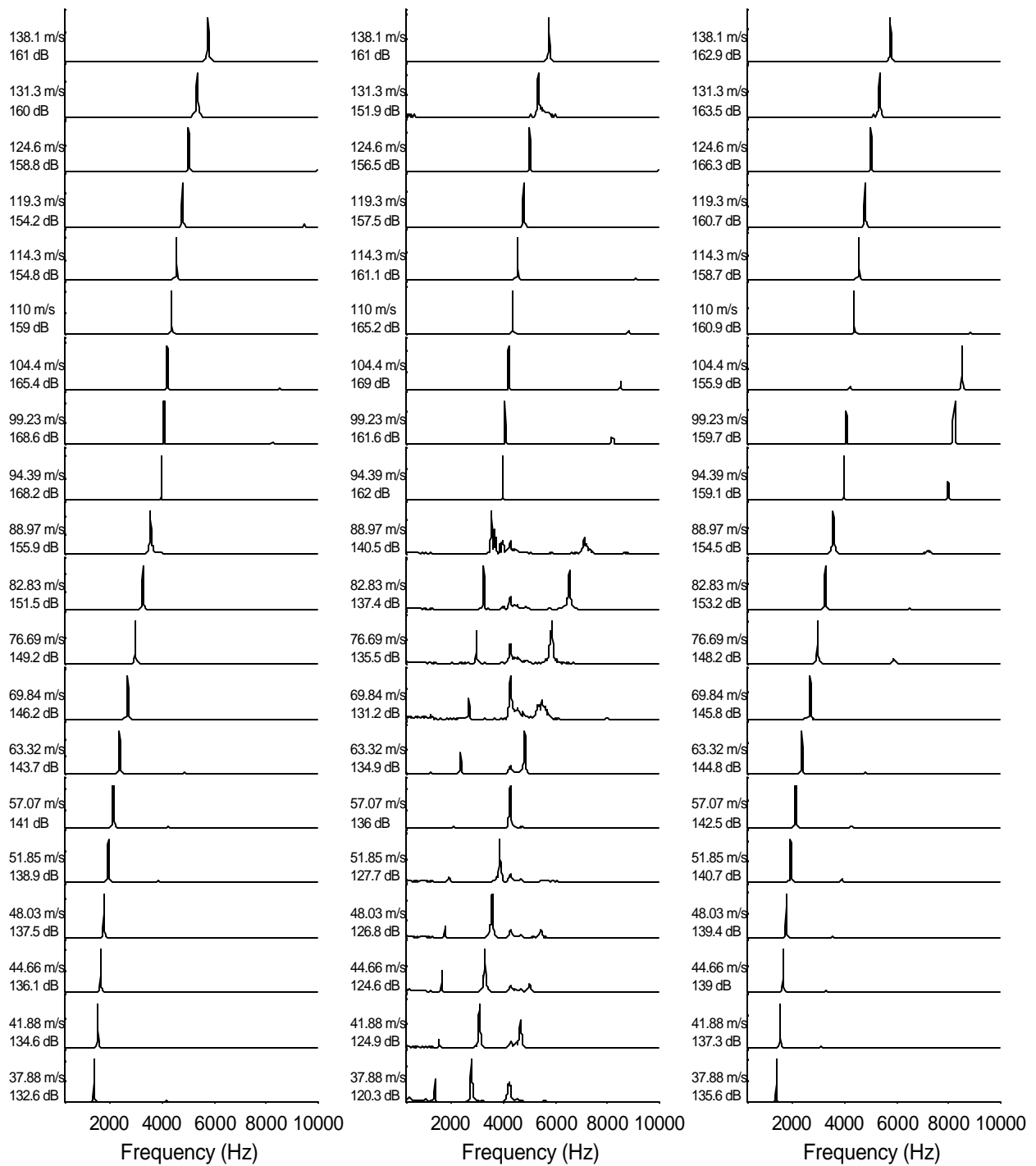


Figure H.21 Representative spectra taken at microphone positions 1a, 6a and d3 (left, center and right respectively). 6.35 mm tandem cylinders.

### 5.0 mm Diameter Cylinders Tandem Configuration

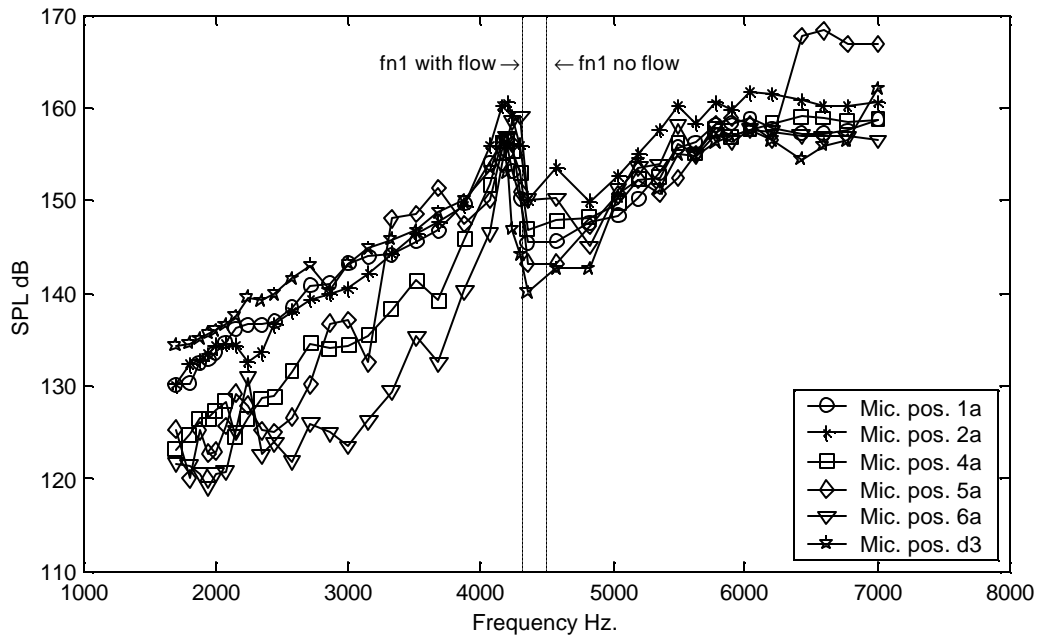


Figure H.22 Sound pressure level at dominant peak in spectra vs. frequency. Microphones and cylinders positions shown in Figures 4.22 and 4.27.

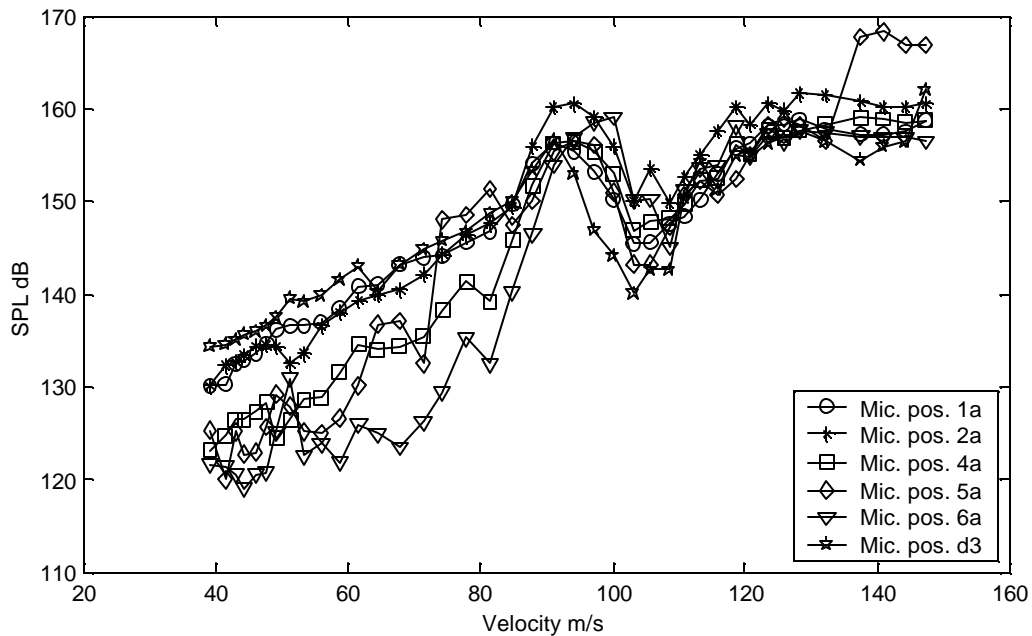


Figure H.23 Sound pressure level at dominant peak in spectra vs. average flow velocity. Microphones and cylinders positions shown in Figures 4.22 and 4.27.

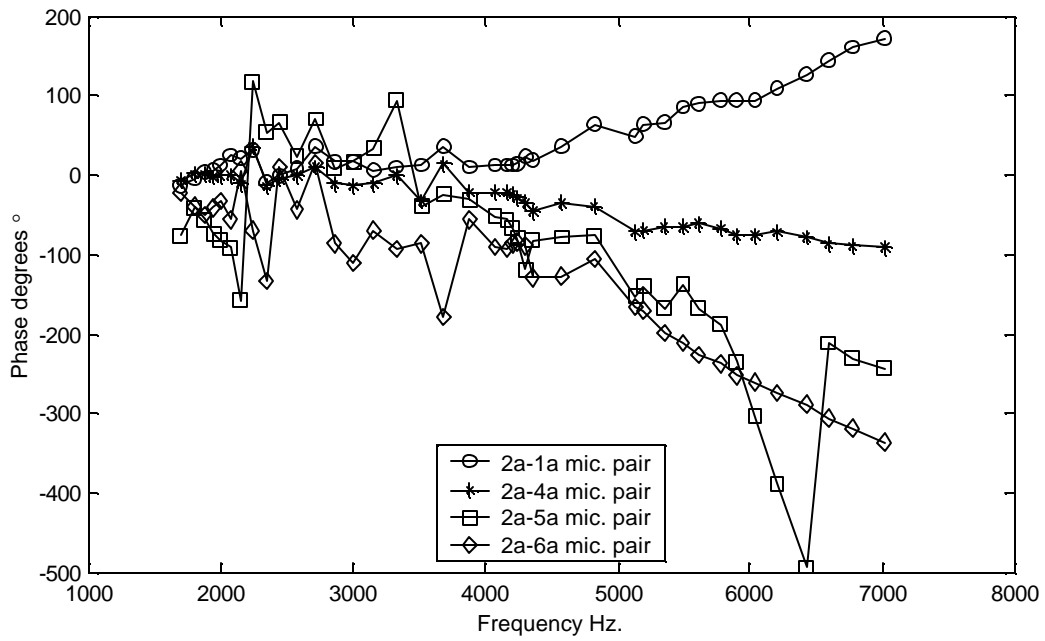


Figure H.24 Transfer function phase angle at frequency of dominant peak in spectra between microphone pairs shown.

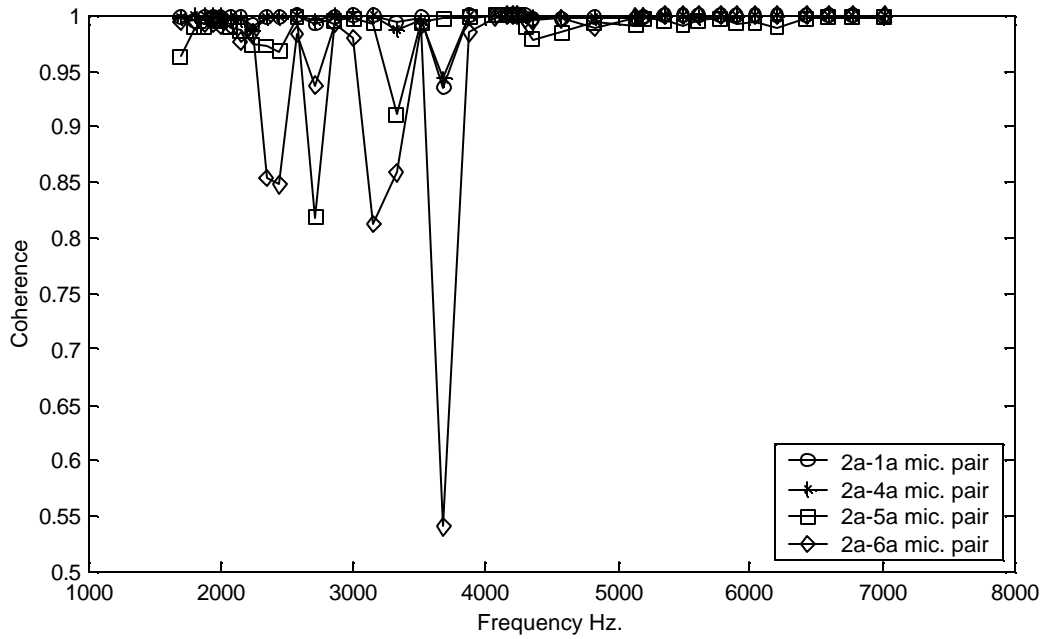


Figure H.25 Coherence at frequency of dominant peak in spectra between microphone pairs shown. Phase angle shown in figure above prone to error if coherence not close to one.

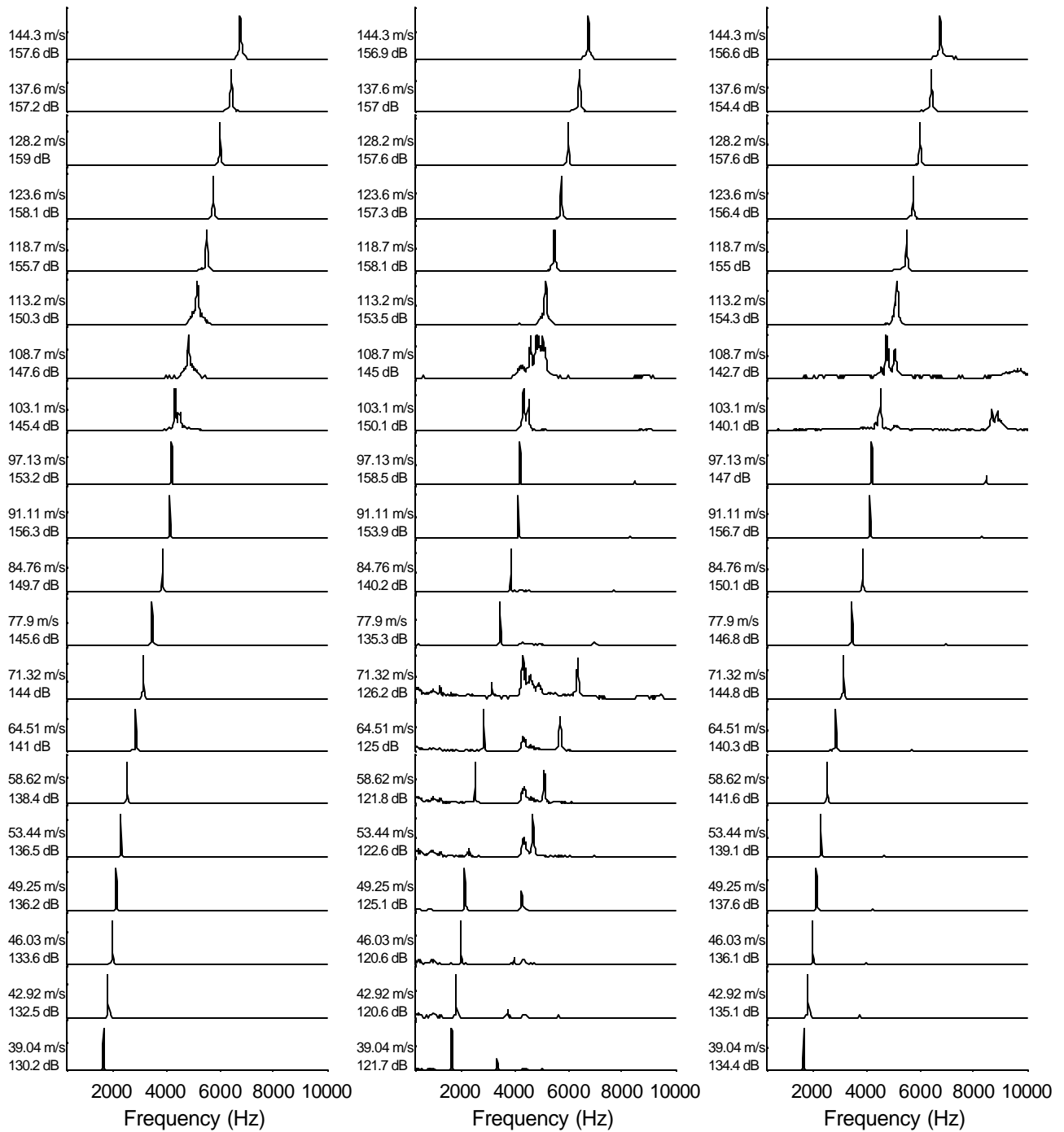


Figure H.26 Representative spectra taken at microphone positions 1a, 6a and d3 (left, center and right respectively). 5.0 mm tandem cylinders.

### 4.0 mm Diameter Cylinders Tandem Configuration

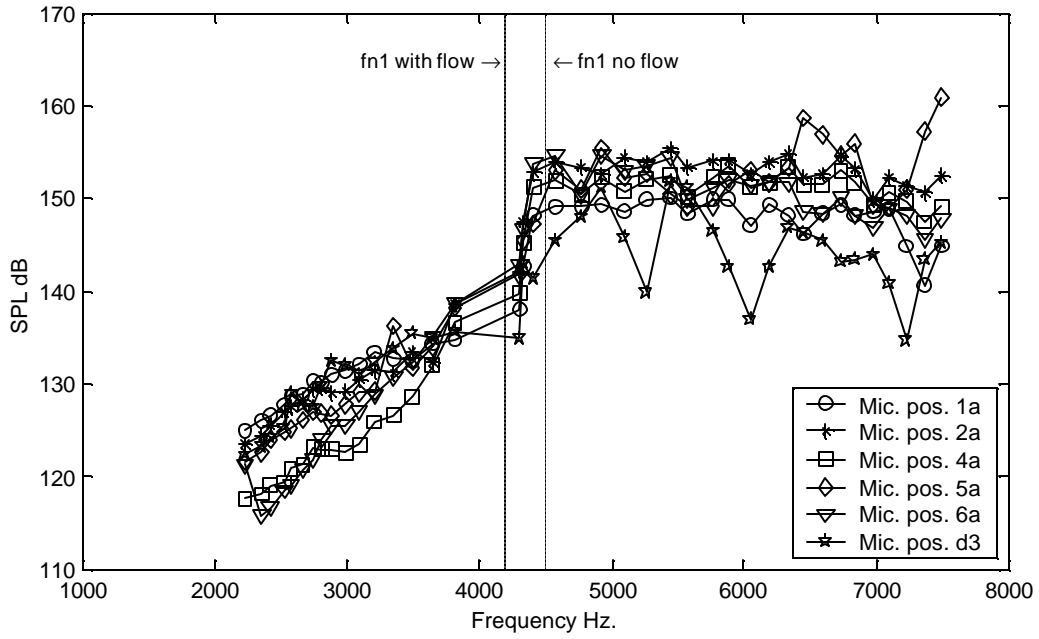


Figure H.27 Sound pressure level at dominant peak in spectra vs. frequency. Microphones and cylinders positions shown in Figures 4.22 and 4.27.

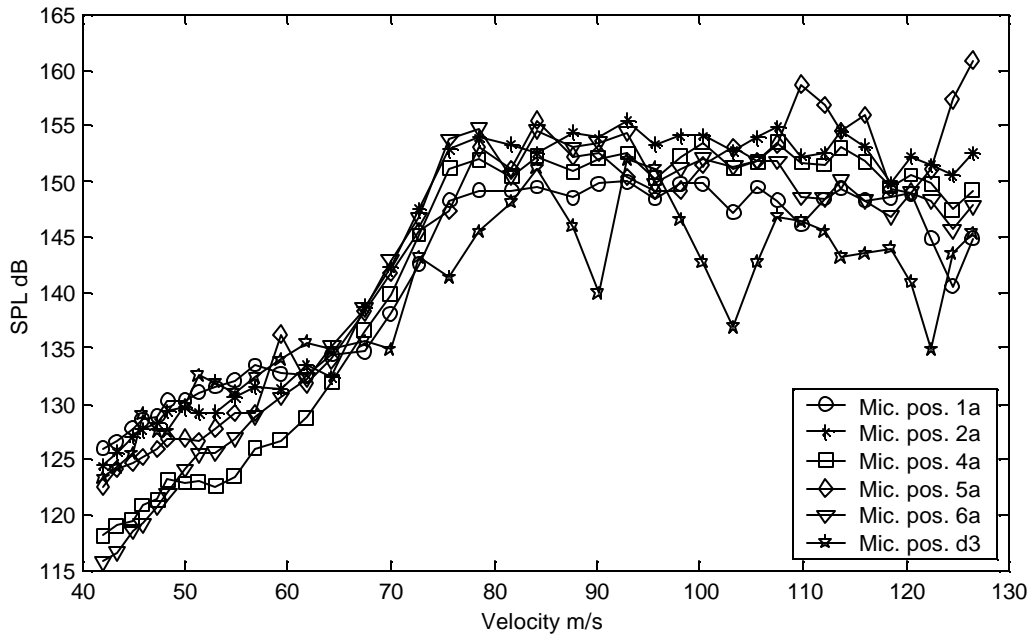


Figure H.28 Sound pressure level at dominant peak in spectra vs. average flow velocity. Microphones and cylinders positions shown in Figures 4.22 and 4.27.

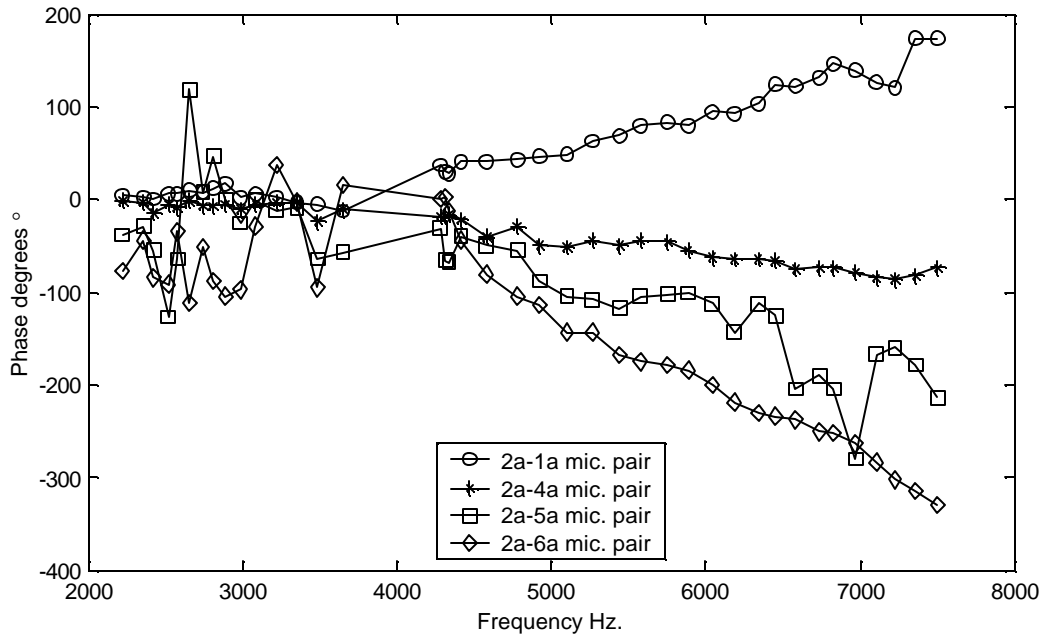


Figure H.29 Transfer function phase angle at frequency of dominant peak in spectra between microphone pairs shown.

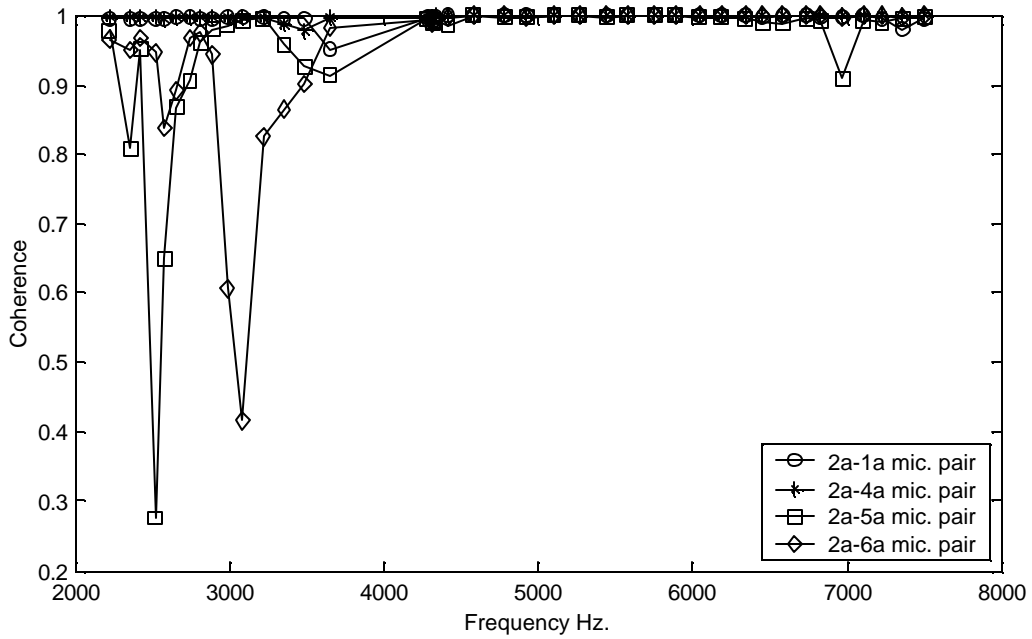


Figure H.30 Coherence at frequency of dominant peak in spectra between microphone pairs shown. Phase angle shown in figure above prone to error if coherence not close to one.

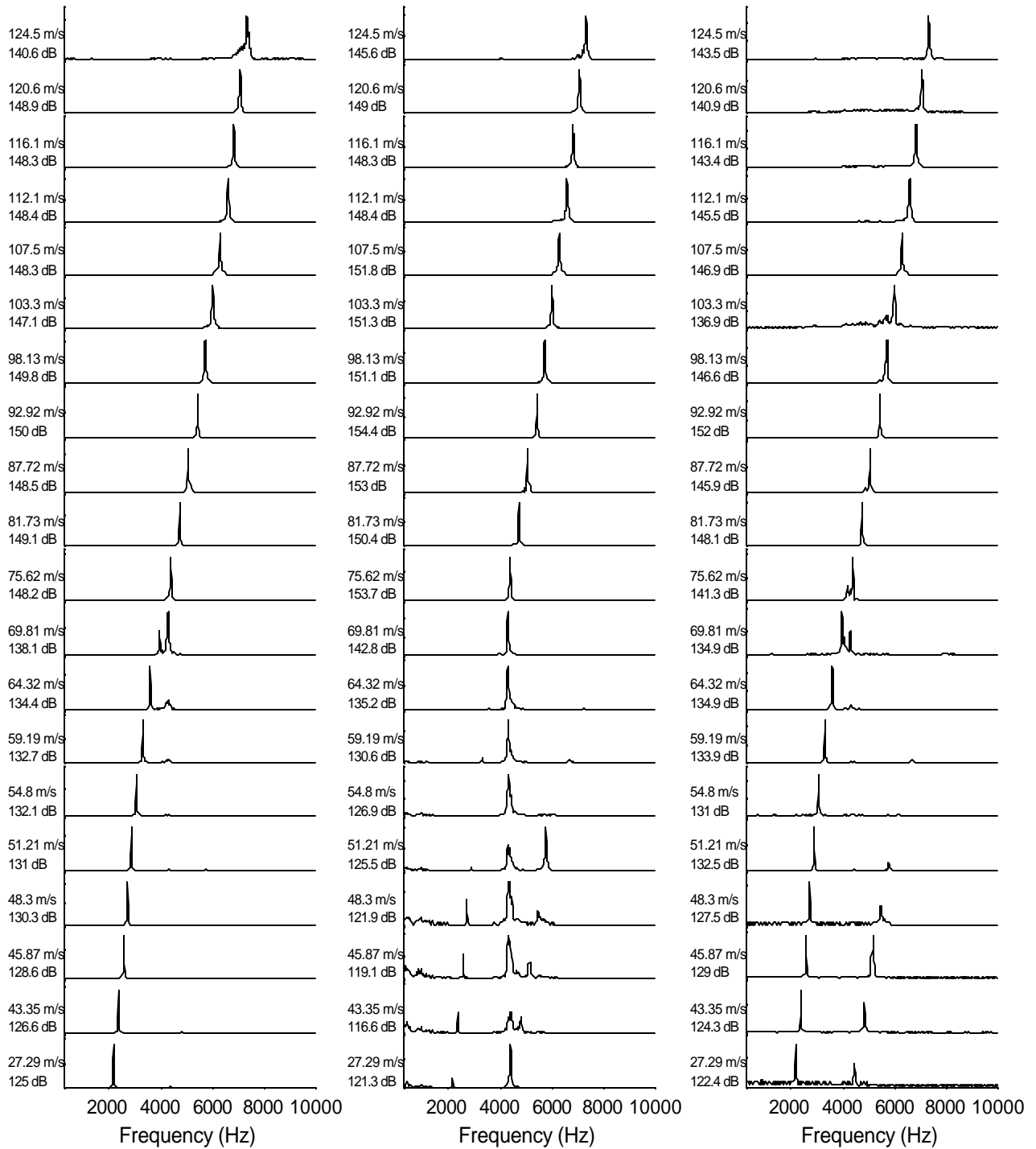


Figure H.31 Representative spectra taken at microphone positions 1a, 6a and d3 (left, center and right respectively). 4.0 mm tandem cylinders.

### 3.0 mm Diameter Cylinders Tandem Configuration

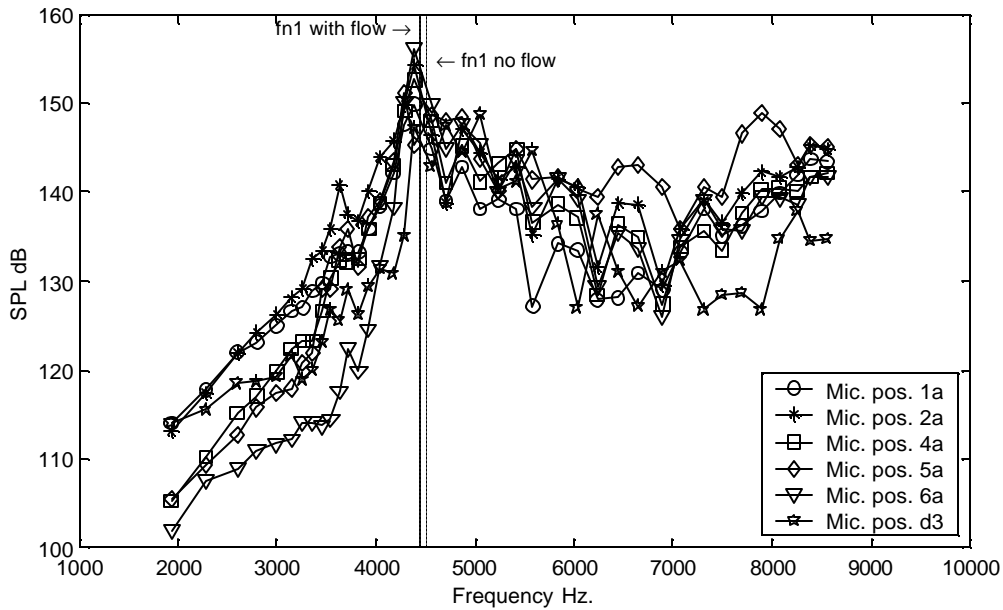


Figure H.32 Sound pressure level at dominant peak in spectra vs. frequency. Microphones and cylinders positions shown in Figures 4.22 and 4.27.

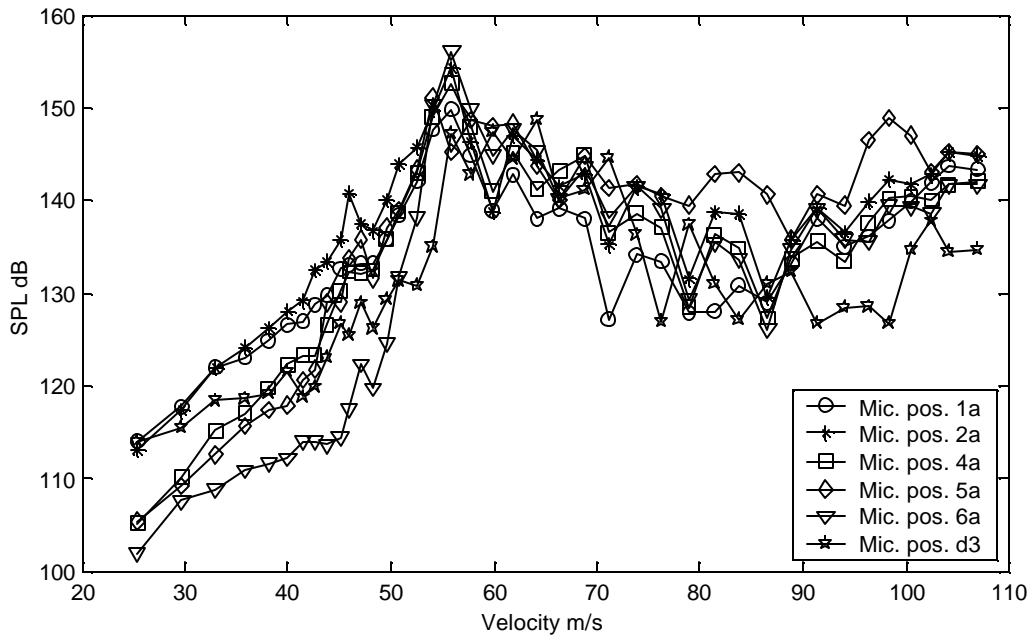


Figure H.33 Sound pressure level at dominant peak in spectra vs. average flow velocity. Microphones and cylinders positions shown in Figures 4.22 and 4.27.



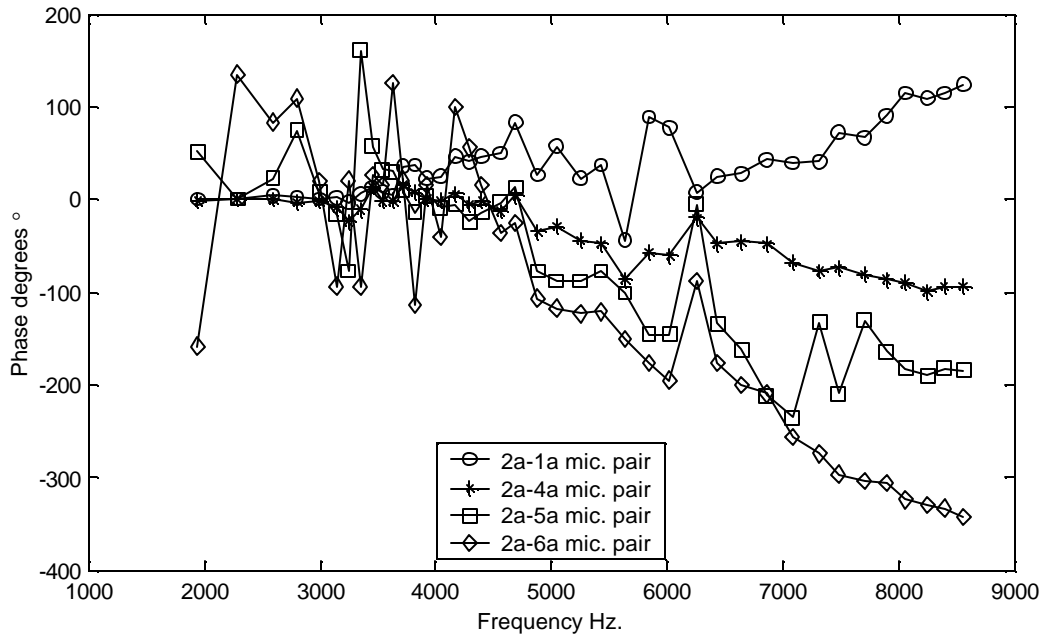


Figure H.34 Transfer function phase angle at frequency of dominant peak in spectra between microphone pairs shown.

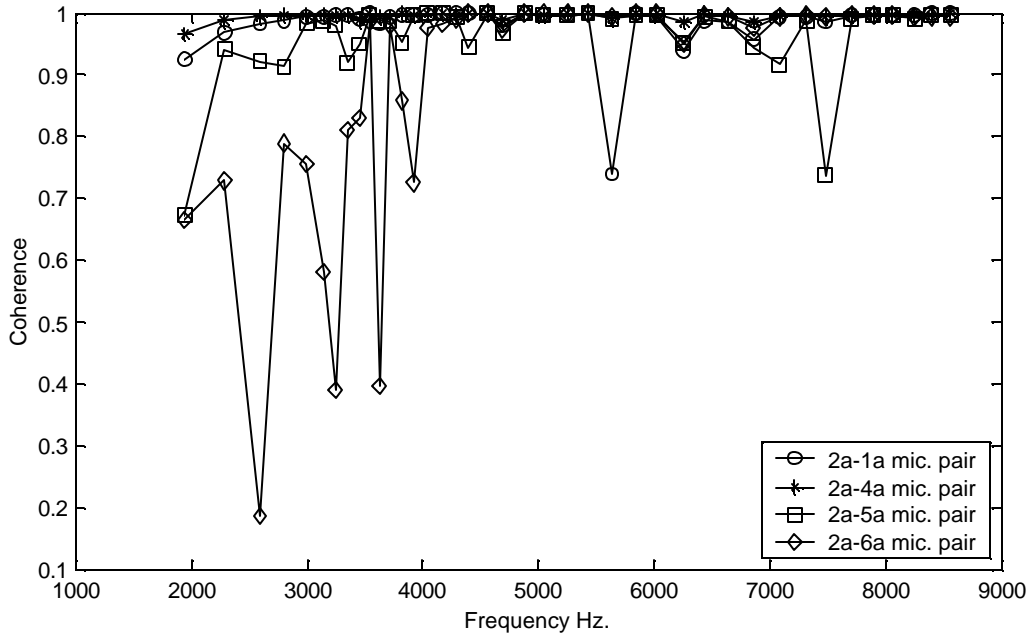


Figure H.35 Coherence at frequency of dominant peak in spectra between microphone pairs shown. Phase angle shown in figure above prone to error if coherence not close to one.

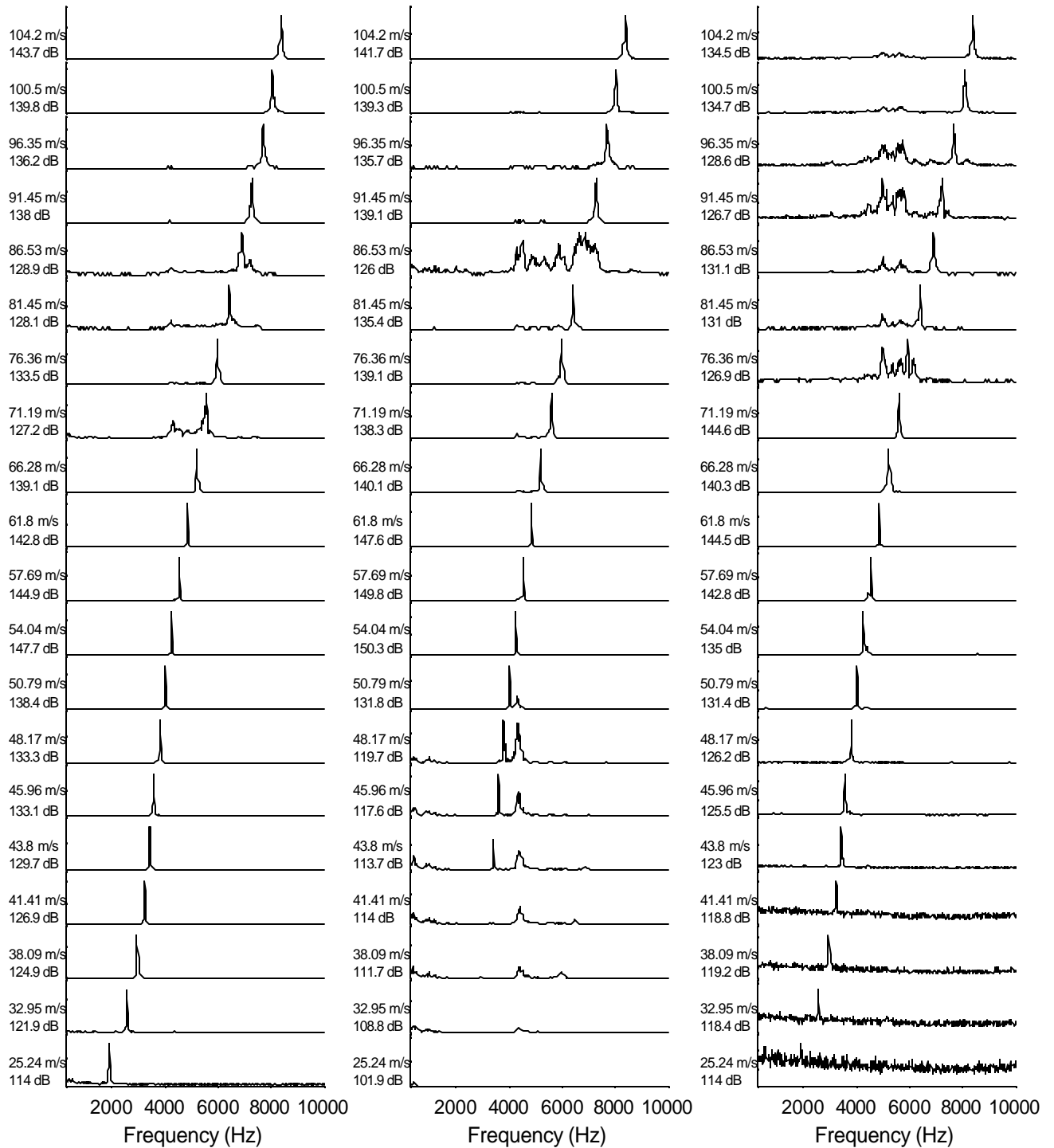


Figure H.36 Representative spectra taken at microphone positions 1a, 6a and d3 (left, center and right respectively). 3.0 mm tandem cylinders.

## Appendix I: Matlab Programs to Solve Modeling and Optimization Equations

### I.1 Main optimization program to find complex wall impedance coefficients

```
clear;
clc;
tic;
p12456=dlmread('c:\aprelimprop\tests\testcyl2\Cyl635mm2\text files\p12456_635mm.txt','t');
frpairs=dlmread('c:\aprelimprop\tests\testcyl2\Cyl635mm2\frpairs.txt','t');
frq=dlmread('c:\aprelimprop\tests\testcyl2\Cyl635mm2\text files\Freqtot_635mm2.txt','t');
rhoall=dlmread('c:\aprelimprop\tests\testcyl2\Cyl635mm2\text files\rho_635mm.txt','t');
vel=dlmread('c:\aprelimprop\tests\testcyl2\Cyl635mm2\text files\Vel_635mm2.txt','t');
points=dlmread('c:\aprelimprop\tests\testcyl\Cyl635mm\text files\points.txt','t');

global frq ii rhoall vel points frpairs
options=optimset('largescale','off');

for uu=1:100
    ii=uu;
    x0=[1e5+0.5i];
    [xsol,fval,exitflag,output]=fminimax('ObjectiveZyDamp',x0,[],[],[],[],[],[],[],options)
    Qsol(uu,1)=xsol;
    Qsol(uu,2)=fval;
    Qsol(uu,3)=exitflag;
    Qsol(uu,4)=output;
    save Zysol_635mm Qsol -ascii

end
time=toc
save Zysol_635mm Qsol -ascii
save time_635mm time -ascii
```

### I.2 Objective function used by complex wall impedance coefficients main program

```
function fu = ObjectiveZyDamp(vals)

global frq ii rhoall vel points frpairs

fq=frq(ii);
vl=vel(ii);
ro=rhoall(ii);
waiz=1e5+0i;

Qqnd=0;
fl=0.4;

fr2a1a=frpairs(ii,1);
fr2a4a=frpairs(ii,2);
fr2a5a=frpairs(ii,3);
fr2a6a=frpairs(ii,4);

fu1=(DampNew(points(2,1),points(2,2),points(1,1),points(1,2),fq,vl,ro,fl,vals(1),waiz,Qqnd)-fr2a1a)^2;
fu2=(DampNew(points(2,1),points(2,2),points(4,1),points(4,2),fq,vl,ro,fl,vals(1),waiz,Qqnd)-fr2a4a)^2;
```

```

fu3=(DampNew(points(2,1),points(2,2),points(5,1),points(5,2),fq,v1,ro,fl,vals(1),waiz,Qqnd)-fr2a5a)^2;
fu4=(DampNew(points(2,1),points(2,2),points(6,1),points(6,2),fq,v1,ro,fl,vals(1),waiz,Qqnd)-fr2a6a)^2;

fu=abs(fu1+fu2+fu3+fu4);

```

### I.3 Function that solves for the complex acoustic pressure ratio for microphone pairs

```

function [Pmod]=DampNew(xp1,yp1,xpi,yipi,ffreq,Vo,ro,Clp,zzzy,zzz,qnd)

c=345;
D=0.00635;
W=0.0381;
H=0.0025;
LL=0.0025;
L=5*W;
Lc=W;
xs=0.00/Lc;
ys=-0.0002/Lc;
zs=0.000/Lc;
z=0.00124/Lc;
CL=Clp;
freq=ffreq;
w=freq*2*pi;
kLc=w*Lc/c;
V=Vo;
Qnd=qnd;
rho=ro;
M=V/c;
Fy=CL*D*LL*V^2/(2*(Lc^2)*(c^2));
zy=zzzy;
zz=zzz;
betay=1/zy;
betaz=1/zz;
alphay=-i*kLc*betay;
alphaz=-i*kLc*betaz;
zetay0=(2*Lc*alphay/W)^0.5;
zetaz0=(2*Lc*alphaz/H)^0.5;
points=[xp1 yp1;xpi ypi];
x=points(1,1)/Lc;
y=points(1,2)/Lc;

if x>-0.001 mmax=50; namx=50; else mmax=20; nmax=20; end;

for m=0:mmax
    if m==0 kym=zetay0; else zetaym=2*alphay/(pi*m); kym=m*pi*Lc/W+zetaym; end
    if m==0 Am=W/Lc; else Am=W/(2*Lc)+((-1)^m)*sin(kym*W/Lc)/(2*kym); end
    if mod(m,2)==0; csy=cos(kym*y); else csy=sin(kym*y); end
    if mod(m,2)==0; csysp=-kym*sin(kym*ys); else csysp=kym*cos(kym*ys); end
    for n=0:nmax
        if n==0 knz=zetaz0; else zetazn=2*alphaz/(pi*n); knz=n*pi*Lc/H+zetazn; end
        if n==0 An=H/Lc; else An=H/(2*Lc)+((-1)^n)*sin(kzn*H/Lc)/(2*kzn); end
        if mod(n,2)==0; csz=cos(kzn*z); else csz=sin(kzn*z); end
        if mod(n,2)==0; cszs=cos(kzn*zs); else cszs=sin(kzn*zs); end
        kxnmP1=(-kLc*M+sqrt(kLc^2-(1-M^2)*(kym^2+kzn^2-i*Qnd*kLc)))/(1-M^2);

```

```

kxmnP2=(-kLc*M-sqrt(kLc^2-(1-M^2)*(kym^2+kzn^2-i*Qnd*kLc)))/(1-M^2);
QmnP=-i*Fy*csysp*cszs*exp(i*kxmnP1*(x-xs))/((1-M^2)*Am*An*(kxmnP1-kxmnP2));
QmnM=-i*Fy*csysp*cszs*exp(i*kxmnP2*(x-xs))/((1-M^2)*Am*An*(kxmnP1-kxmnP2));
if x>xs Qmn=QmnP; else Qmn=QmnM; end
P(m+1,n+1)=csy*csz*Qmn;
end
end
Pxyz(1)=(sum(sum(P)))*rho*c^2;
clear P;

x=points(2,1)/Lc;
y=points(2,2)/Lc;

for m=0:mmax
if m==0 kym=zeta0; else zetaym=2*alphay/(pi*m); kym=m*pi*Lc/W+zetaym; end
if m==0 Am=W/Lc; else Am=W/(2*Lc)+((-1)^m)*sin(kym*W/Lc)/(2*kym); end
if mod(m,2)==0; csy=cos(kym*y); else csy=sin(kym*y); end
if mod(m,2)==0; csysp=-kym*sin(kym*ys); else csysp=kym*cos(kym*ys); end
for n=0:nmax
if n==0 kzn=zeta0; else zetazn=2*alphaz/(pi*n); kzn=n*pi*Lc/H+zetazn; end
if n==0 An=H/Lc; else An=H/(2*Lc)+((-1)^n)*sin(kzn*H/Lc)/(2*kzn); end
if mod(n,2)==0; csz=cos(kzn*z); else csz=sin(kzn*z); end
if mod(n,2)==0; cszs=cos(kzn*zs); else cszs=sin(kzn*zs); end
kxmnP1=(-kLc*M+sqrt(kLc^2-(1-M^2)*(kym^2+kzn^2-i*Qnd*kLc)))/(1-M^2);
kxmnP2=(-kLc*M-sqrt(kLc^2-(1-M^2)*(kym^2+kzn^2-i*Qnd*kLc)))/(1-M^2);
QmnP=-i*Fy*csysp*cszs*exp(i*kxmnP1*(x-xs))/((1-M^2)*Am*An*(kxmnP1-kxmnP2));
QmnM=-i*Fy*csysp*cszs*exp(i*kxmnP2*(x-xs))/((1-M^2)*Am*An*(kxmnP1-kxmnP2));
if x>xs Qmn=QmnP; else Qmn=QmnM; end
P(m+1,n+1)=csy*csz*Qmn;
end
end
Pxyz(2)=(sum(sum(P)))*rho*c^2;
clear P;

Pmod=Pxyz(2)/Pxyz(1);

```

#### 1.4 Main optimization program to find complex volumetric damping coefficients

```

clear;
clc;
tic;
p12456=dlmread('c:\aprelimprop\tests\testcyl2\Cyl635mm2\text files\p12456_635mm.txt','t');
frpairs=dlmread('c:\aprelimprop\tests\testcyl2\Cyl635mm2\frpairs.txt','t');
frq=dlmread('c:\aprelimprop\tests\testcyl2\Cyl635mm2\text files\Freqtot_635mm2.txt','t');
rhoall=dlmread('c:\aprelimprop\tests\testcyl2\Cyl635mm2\text files\rho_635mm.txt','t');
vel=dlmread('c:\aprelimprop\tests\testcyl2\Cyl635mm2\text files\Vel_635mm2.txt','t');
points=dlmread('c:\aprelimprop\tests\testcyl\Cyl635mm\text files\points.txt','t');

global frq ii rhoall vel points frpairs
options=optimset('largescale','off');

for uu=83:83
ii=uu;

```

```

x0=[7];
[xsol,fval,exitflag,output]=fminimax('ObjectiveQDamp',x0,[],[],[],[],[],[],[],options)
Qsol(uu,1)=xsol;
Qsol(uu,2)=fval;
Qsol(uu,3)=exitflag;
Qsol(uu,4)=output;
save qsol_635mm Qsol -ascii

end
time=toc
save qsol_635mm Qsol -ascii
save time_635mm time -ascii

```

### I.5 Objective function used by complex volumetric damping coefficients main program

```

function fu = ObjectiveQDamp(vals)

global frq ii rhoall vel points frpairs

frq=frq(ii);
vl=vel(ii);
ro=rhoall(ii);
waiz=1e5+0i;
fl=0.4;

fr2a1a=frpairs(ii,1);
fr2a4a=frpairs(ii,2);
fr2a5a=frpairs(ii,3);
fr2a6a=frpairs(ii,4);

fu1=(DampNew(points(2,1),points(2,2),points(1,1),points(1,2),frq,vl,ro,fl,waiz,waiz,vals(1))-fr2a1a)^2;
fu2=(DampNew(points(2,1),points(2,2),points(4,1),points(4,2),frq,vl,ro,fl,waiz,waiz,vals(1))-fr2a4a)^2;
fu3=(DampNew(points(2,1),points(2,2),points(5,1),points(5,2),frq,vl,ro,fl,waiz,waiz,vals(1))-fr2a5a)^2;
fu4=(DampNew(points(2,1),points(2,2),points(6,1),points(6,2),frq,vl,ro,fl,waiz,waiz,vals(1))-fr2a6a)^2;
fu=abs(fu1+fu2+fu3+fu4);

```

### I.6 Main optimization program to find fluctuating lift coefficient when values of acoustic damping are known or assumed

```

clear;
clc;
tic
p12456=dlmread('c:\aprelimprop\testcyl2\Cyl635mm\text files\p12456_635mm.txt','t');
frq=dlmread('c:\aprelimprop\testcyl2\Cyl635mm\text files\Freqtot_635mm.txt','t');
rhoall=dlmread('c:\aprelimprop\testcyl2\Cyl635mm\text files\rho_635mm.txt','t');
vel=dlmread('c:\aprelimprop\testcyl2\Cyl635mm\text files\Vel_635mm.txt','t');
points=dlmread('c:\aprelimprop\testcyl2\Cyl635mm\text files\points.txt','t');

global p12456 frq ii rhoall vel points
options=optimset('largescale','off');

```

```

for uu=1:70
ii=uu;
x0=[0.5];
A=[-1;1];
b=[-0.01;1.0 ];
[xsol,fval,exitflag,output]=fminimax('CLpObjectiveF_635mm',x0,A,b,[],[],[],[],[],options);
Clsol(uu,1)=xsol;
Clsol(uu,2)=fval;
Clsol(uu,3)=exitflag;
Clsol(uu,4)=output;
save clsol_635mm Clsol -ascii

end
time=toc
save clsol_635mm Clsol -ascii
save time_635mm time -ascii

```

### I.7 Objective function used by fluctuating lift coefficients main program

```

function fu = CLpObjectiveF_635mm(vals)
global p12456 frq ii rhoall vel points

fq=frq(ii);
vl=vel(ii);
ro=rhoall(ii);
waireal=1e5;
waiimag=0;
Qqnd=0;
Pexp1=p12456(ii,1); %Pascals
Pexp2=p12456(ii,2);
Pexp4=p12456(ii,3);
Pexp5=p12456(ii,4);
Pexp6=p12456(ii,5);

fu1=((CLp3_635mm(points(1,1),points(1,2),fq,vals(1),vl,ro,waireal,waiimag,waireal,waiimag,Qqnd)-
Pexp1)/Pexp1)^2;
fu2=((CLp3_635mm(points(2,1),points(2,2),fq,vals(1),vl,ro,waireal,waiimag,waireal,waiimag,Qqnd)-
Pexp2)/Pexp2)^2;
fu3=((CLp3_635mm(points(4,1),points(4,2),fq,vals(1),vl,ro,waireal,waiimag,waireal,waiimag,Qqnd)-
Pexp4)/Pexp4)^2;
fu4=((CLp3_635mm(points(5,1),points(5,2),fq,vals(1),vl,ro,waireal,waiimag,waireal,waiimag,Qqnd)-
Pexp5)/Pexp5)^2;
fu5=((CLp3_635mm(points(6,1),points(6,2),fq,vals(1),vl,ro,waireal,waiimag,waireal,waiimag,Qqnd)-
Pexp6)/Pexp6)^2;

fu=fu1+fu2+fu3+fu4+fu5;

```

### I.8 Function that solves for the acoustic pressures at each microphone position

```

function [Pmod]=CLp3_635mm(xp,yp,freq,CL,V,rho,zzyr,zzyi,zzzr,zzzi,qnd)

```

```

c=345;
W=0.0381;
H=0.0025;
L=5*W;
Lc=W;
xs=0.00/Lc;
ys=-0.0002/Lc;
zs=0.000/Lc;

z=0.00124/Lc;
D=0.003;
LL=0.0025;
Qnd=qnd;
zyr=zzyr;
zyi=zzyi;
z zr=zzr;
z zi=zzzi;
zy=zyr+zyi*i;
zz=zzr+zzi*i;
betay=1/zy;
betaz=1/zz;

x=xp/Lc;
y=yp/Lc;

w=freq*2*pi;
kLc=w*Lc/c;
M=V/c;
Fy=CL*D*LL*V^2/(2*(Lc^2)*(c^2));
alphay=-i*kLc*betay;
alphaz=-i*kLc*betaz;
zetay0=(2*Lc*alphay/W)^0.5;
zetaz0=(2*Lc*alphaz/H)^0.5;
bb=3;
aa=3;
dB(1)=1;
terms=aa-1;

for m=0:1
    if m==0 kym=zetay0; else zetaym=2*alphay/(pi*m); kym=m*pi*Lc/W+zetaym; end
    if m==0 Am=W/Lc; else Am=W/(2*Lc)+((-1)^m)*sin(kym*W/Lc)/(2*kym); end
    if mod(m,2)==0; csy=cos(kym*y); else csy=sin(kym*y); end
    if mod(m,2)==0; csysp=-kym*sin(kym*ys); else csysp=kym*cos(kym*ys); end

    for n=0:1
        if n==0 kzn=zetaz0; else zetazn=2*alphaz/(pi*n); kzn=n*pi*Lc/H+zetazn; end
        if n==0 An=H/Lc; else An=H/(2*Lc)+((-1)^n)*sin(kzn*H/Lc)/(2*kzn); end
        if mod(n,2)==0; csz=cos(kzn*z); else csz=sin(kzn*z); end
        if mod(n,2)==0; cszs=cos(kzn*zs); else cszs=sin(kzn*zs); end
        kxmnP1=(-kLc*M+sqrt(kLc^2-(1-M^2)*(kym^2+kzn^2-i*Qnd*kLc)))/(1-M^2);
        kxmnP2=(-kLc*M-sqrt(kLc^2-(1-M^2)*(kym^2+kzn^2-i*Qnd*kLc)))/(1-M^2);

        QmnP=-i*Fy*csysp*cszs*exp(i*kxmnP1*(x-xs))/((1-M^2)*Am*An*(kxmnP1-kxmnP2));
        QmnM=-i*Fy*csysp*cszs*exp(i*kxmnP2*(x-xs))/((1-M^2)*Am*An*(kxmnP1-kxmnP2));
        if x>xs Qmn=QmnP; else Qmn=QmnM; end
        P(m+1,n+1)=csy*csz*Qmn;
    end
end

```



```

end
end
Pmod=abs(sum(sum(P)))*rho*c^2;
dB(2)=20*log10(Pmod/20e-6);
clear P;

for m=0:2
    if m==0 kym=zeta0; else zetaym=2*alpha/(pi*m); kym=m*pi*Lc/W+zetaym; end
    if m==0 Am=W/Lc; else Am=W/(2*Lc)+((-1)^m)*sin(kym*W/Lc)/(2*kym); end
    if mod(m,2)==0; csy=cos(kym*y); else csy=sin(kym*y); end
    if mod(m,2)==0; csysp=-kym*sin(kym*ys); else csysp=kym*cos(kym*ys); end

    for n=0:2
        if n==0 kzn=zeta0; else zetazn=2*alpha/(pi*n); kzn=n*pi*Lc/H+zetazn; end
        if n==0 An=H/Lc; else An=H/(2*Lc)+((-1)^n)*sin(kzn*H/Lc)/(2*kzn); end
        if mod(n,2)==0; csz=cos(kzn*z); else csz=sin(kzn*z); end
            if mod(n,2)==0; cszs=cos(kzn*zs); else cszs=sin(kzn*zs); end
        kxmnP1=(-kLc*M+sqrt(kLc^2-(1-M^2)*(kym^2+kzn^2-i*Qnd*kLc)))/(1-M^2);
        kxmnP2=(-kLc*M-sqrt(kLc^2-(1-M^2)*(kym^2+kzn^2-i*Qnd*kLc)))/(1-M^2);

        QmnP=-i*Fy*csysp*cszs*exp(i*kxmnP1*(x-xs))/((1-M^2)*Am*An*(kxmnP1-kxmnP2));
        QmnM=-i*Fy*csysp*cszs*exp(i*kxmnP2*(x-xs))/((1-M^2)*Am*An*(kxmnP1-kxmnP2));
        if x>xs Qmn=QmnP; else Qmn=QmnM; end
        P(m+1,n+1)=csy*csz*Qmn;
    end
end
Pmod=abs(sum(sum(P)))*rho*c^2;
dB(3)=20*log10(Pmod/20e-6);
clear P;

while abs(dB(bb)-dB(bb-1)) > 0.1 | abs(dB(bb-1)-dB(bb-2)) > 0.1
nmax=aa;
mmax=aa;
bb=bb+1;
terms=aa;
if aa>10 nume=10; else nume=1; end
aa=aa+nume;

for m=0:mmax
    if m==0 kym=zeta0; else zetaym=2*alpha/(pi*m); kym=m*pi*Lc/W+zetaym; end
    if m==0 Am=W/Lc; else Am=W/(2*Lc)+((-1)^m)*sin(kym*W/Lc)/(2*kym); end
    if mod(m,2)==0; csy=cos(kym*y); else csy=sin(kym*y); end
    if mod(m,2)==0; csysp=-kym*sin(kym*ys); else csysp=kym*cos(kym*ys); end

    for n=0:nmax
        if n==0 kzn=zeta0; else zetazn=2*alpha/(pi*n); kzn=n*pi*Lc/H+zetazn; end
        if n==0 An=H/Lc; else An=H/(2*Lc)+((-1)^n)*sin(kzn*H/Lc)/(2*kzn); end
        if mod(n,2)==0; csz=cos(kzn*z); else csz=sin(kzn*z); end
            if mod(n,2)==0; cszs=cos(kzn*zs); else cszs=sin(kzn*zs); end
        kxmnP1=(-kLc*M+sqrt(kLc^2-(1-M^2)*(kym^2+kzn^2-i*Qnd*kLc)))/(1-M^2);
        kxmnP2=(-kLc*M-sqrt(kLc^2-(1-M^2)*(kym^2+kzn^2-i*Qnd*kLc)))/(1-M^2);

        QmnP=-i*Fy*csysp*cszs*exp(i*kxmnP1*(x-xs))/((1-M^2)*Am*An*(kxmnP1-kxmnP2));
        QmnM=-i*Fy*csysp*cszs*exp(i*kxmnP2*(x-xs))/((1-M^2)*Am*An*(kxmnP1-kxmnP2));
        if x>xs Qmn=QmnP; else Qmn=QmnM; end
        P(m+1,n+1)=csy*csz*Qmn;
    end
end

```

```

    end
end
Pmod=abs(sum(sum(P)))*rho*c^2;
dB(bb)=20*log10(Pmod/20e-6);
clear P;

end

```

### I.9 Main optimization program to find fluctuating lift coefficients and Non-dimensional volumetric damping simultaneously

```

clear;
clc;

tic
p12456=dlmread('p12456_635mm.txt','t');
frq=dlmread('Frequot_635mm2.txt','t');
rhoall=dlmread('rho_635mm.txt','t');
vel=dlmread('Vel_635mm2.txt','t');
points=dlmread('points.txt','t');

global p12456 frq ii rhoall vel points
options=optimset('largescale','off');

for uu=1:100
ii=uu;
x0=[0.5 0.001];
lb=[.01;-1e5];
ub=[2;1e5];
[xsol,fval,exitflag,output]=fminimax('CLpObjectiveF_635mmQCL',x0,[],[],[],[],lb,ub,[],options);
Clsol(uu,1)=xsol(1);
Clsol(uu,2)=xsol(2);
Clsol(uu,3)=fval;
Clsol(uu,4)=exitflag;
Clsol(uu,5)=output;
ii
toc
save clsol_635mmQCL Clsol -ascii
end
time=toc;
save clsol_635mmQCL Clsol -ascii
save time_635mmQCL time -ascii

```

### I.10 Objective function used by fluctuating lift coefficient and volumetric damping main program

```

function fu = CLpObjectiveF_635mmQCL(vals)

global p12456 frq ii rhoall vel points

fq=frq(ii);
vl=vel(ii);

```

```

ro=rhoall(ii);
wairreal=1e5;
waiimag=0;
%Qqnd= -405.0806;

Pexp1=p12456(ii,1); % Pascals
Pexp2=p12456(ii,2);
Pexp4=p12456(ii,3);
Pexp5=p12456(ii,4);
Pexp6=p12456(ii,5);

fu1=((CLp_635mmQCL(-0.0003,0.0084,fq,vals(1),vl,ro,wairreal,waiimag,wairreal,waiimag,vals(2))-
Pexp1)/Pexp1)^2;
fu2=((CLp_635mmQCL(-0.010,0.0131,fq,vals(1),vl,ro,wairreal,waiimag,wairreal,waiimag,vals(2))-
Pexp2)/Pexp2)^2;
fu3=((CLp_635mmQCL(-0.0175,0.016,fq,vals(1),vl,ro,wairreal,waiimag,wairreal,waiimag,vals(2))-
Pexp4)/Pexp4)^2;
fu4=((CLp_635mmQCL(-0.0259,0.010,fq,vals(1),vl,ro,wairreal,waiimag,wairreal,waiimag,vals(2))-
Pexp5)/Pexp5)^2;
fu5=((CLp_635mmQCL(-0.0376,0.0162,fq,vals(1),vl,ro,wairreal,waiimag,wairreal,waiimag,vals(2))-
Pexp6)/Pexp6)^2;

fu=fu1+fu2+fu3+fu4+fu5;

```

### I.11 Main program to find acoustic pressures produced by staggered cylinder array with $T/D=L/D=3.0$

```

clear;
clc;
tic

frq=dlmread('FreqPeaks.txt','t');
rhoall=dlmread('Rhos.txt','t');
vel=dlmread('Vels.txt','t');

c=345;
W=0.0381;
H=0.0025;
L=4*W;
Lc=W;

wairreal=1e5;
waiimag=0;
Qqnd=0;

xsstag3_1=[0:11.43:114.3]/(1000*Lc);
ysstag3_1=[-17.145:5.715:17.145]/(1000*Lc);
xsstag3_2=[5.715:11.43:120.015]/(1000*Lc);
ysstag3_2=[-14.2875 -8.5725 -2.8575 2.8575 8.5725 14.2875]/(1000*Lc);

yup=-16.675/(1000*Lc);
xup=-9.5551/(1000*Lc);

```

```

for ii=1:40
    ii
    fq=frq(ii,2);

    cl1=1;
    for xxs=1:11
        vl=vel(ii,1);
        ro=rhoall(ii,1);
        if ((xxs>2) & (xxs<=6)) vl=vel(ii,2); ro=rhoall(ii,2);
        elseif ((xxs>6) & (xxs<=9)) vl=vel(ii,3); ro=rhoall(ii,3);
        elseif (xxs>9) vl=vel(ii,4); ro=rhoall(ii,4);
        end

    for yys=1:7

        pup1(xxs,yys)=CLp_1905mmxs(xup,yup,xssttag3_1(xxs),yssttag3_1(yys),fq,cl1,vl,ro,wairreal,waiimag,wairreal,
waiimag,Qqnd);
        end
        for yys=1:6

            pup2(xxs,yys)=CLp_1905mmxs(xup,yup,xssttag3_2(xxs),xssttag3_2(yys),fq,cl1,vl,ro,wairreal,waiimag,wairreal,
waiimag,Qqnd);
            end
            end
            pupabs(ii)=abs(sum(sum(pup1)))+abs(sum(sum(pup2)));
            pupang(ii)=angle(sum(sum(pup1)))+angle(sum(sum(pup2)));

            name=strcat('PupSttagTDLD3_2');
            dlmwrite(name,pupabs,'\t');
            name=strcat('AngSttagTDLD3_2');
            dlmwrite(name,pupang,'\t');
            end

```

## I.12 Function to determine acoustic pressure of each source at desired location used by main program shown in section I.11

```

function [Pmod]=CLp_1905mmxs(xpp,ypp,xss,yss,freq,CL,V,rho,zzyr,zzyi,zzzr,zzzi,Qnd)

c=345;
W=0.0381;
H=0.0025;
L=4*W;
Lc=W;
xs=xss;
ys=yss;
zs=0.000/Lc;

z=0.00124/Lc;
D=0.001905;
LL=0.0025;

zyr=zzyr;

```

```

zyi=zzyi;
zzr=zzzr;
zzi=zzzi;
zy=zyr+zyi*i;
zz=zzr+zzi*i;
betay=1/zy;
betaz=1/zz;

point(1)=xpp;
point(2)=ypp;
x=point(1);
y=point(2);

w=freq*2*pi;
kLc=w*Lc/c;
M=V/c;
Fy=CL*D*LL*V^2/(2*(Lc^2)*(c^2));
alphay=-i*kLc*betay;
alphaz=-i*kLc*betaz;
zetay0=(2*Lc*alphay/W)^0.5;
zetaz0=(2*Lc*alphaz/H)^0.5;

if abs(x*Lc-xs*Lc)<0.005 mmax=30; nmax=30; else mmax=10; nmax=10; end;

for m=0:mmax
  if m==0 kym=zetay0; else zetaym=2*alphay/(pi*m); kym=m*pi*Lc/W+zetaym; end
  if m==0 Am=W/Lc; else Am=W/(2*Lc)+((-1)^m)*sin(kym*W/Lc)/(2*kym); end
  if mod(m,2)==0; csy=cos(kym*y); else csy=sin(kym*y); end
  if mod(m,2)==0; csysp=-kym*sin(kym*ys); else csysp=kym*cos(kym*ys); end
  for n=0:nmax
    if n==0 kzn=zetaz0; else zetazn=2*alphaz/(pi*n); kzn=n*pi*Lc/H+zetazn; end
    if n==0 An=H/Lc; else An=H/(2*Lc)+((-1)^n)*sin(kzn*H/Lc)/(2*kzn); end
    if mod(n,2)==0; csz=cos(kzn*z); else csz=sin(kzn*z); end
    if mod(n,2)==0; cszs=cos(kzn*zs); else cszs=sin(kzn*zs); end
    kxmnP1=(-kLc*M+sqrt(kLc^2-(1-M^2)*(kym^2+kzn^2-i*Qnd*kLc)))/(1-M^2);
    kxmnP2=(-kLc*M-sqrt(kLc^2-(1-M^2)*(kym^2+kzn^2-i*Qnd*kLc)))/(1-M^2);
    QmnP=-i*Fy*csysp*cszs*exp(i*kxmnP1*(x-xs))/((1-M^2)*Am*An*(kxmnP1-kxmnP2));
    QmnM=-i*Fy*csysp*cszs*exp(i*kxmnP2*(x-xs))/((1-M^2)*Am*An*(kxmnP1-kxmnP2));
    if x>xs Qmn=QmnP; else Qmn=QmnM; end
    P(m+1,n+1)=csy*csz*Qmn;
  end
end

Pmod=(sum(sum(P)))*rho*c^2;
clear P;

```

## Appendix J: Contour Plots of Acoustic Field

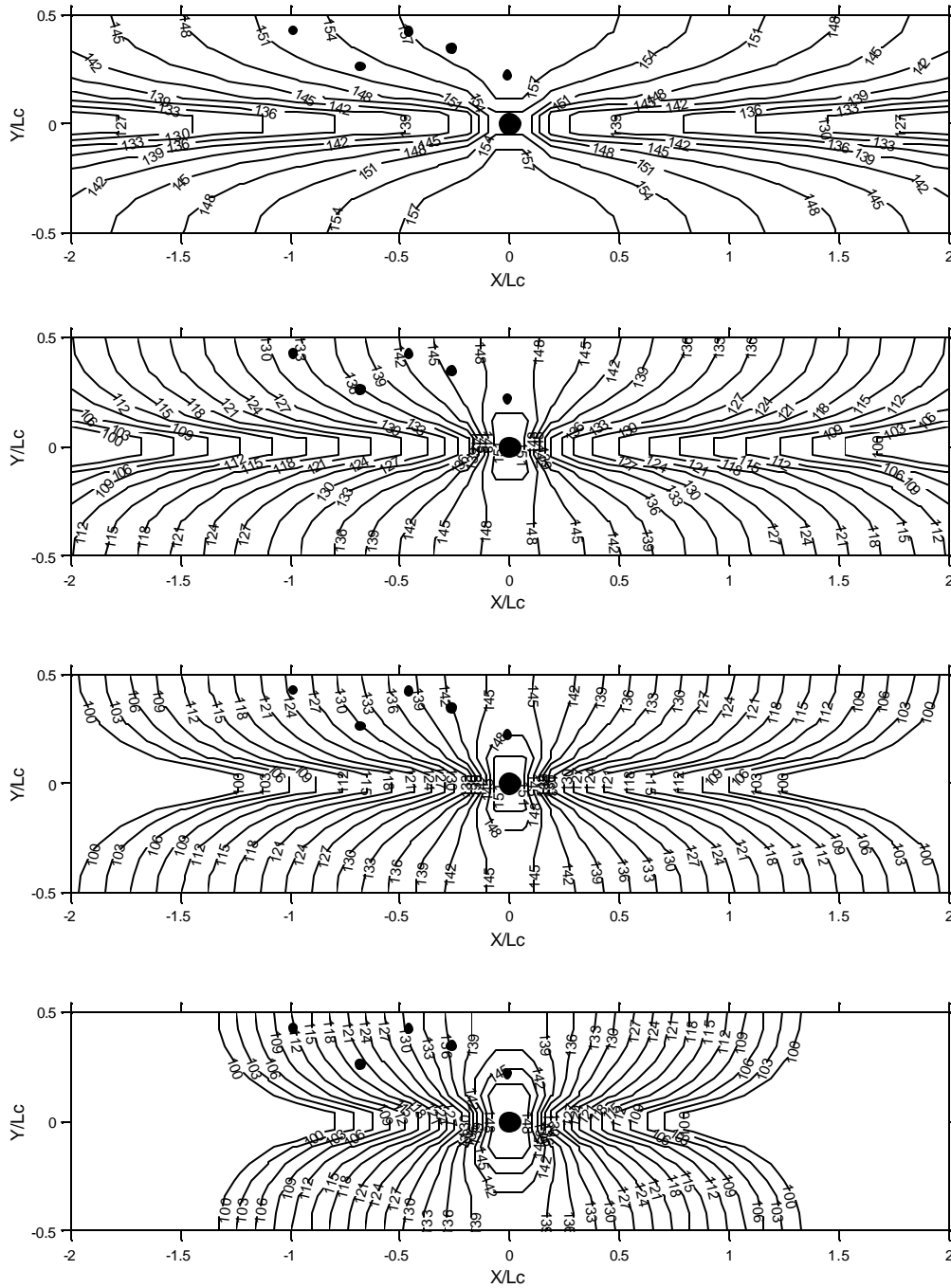


Figure J.1 Sound pressure level field (dB) at 4000Hz produced by single 6.35mm cylinder at center of duct (large black circle) for different real nondimensional volumetric damping ( $Q_{nd}$ ) values. Small circles represent microphone positions in our experimental setup. From top to bottom: No damping,  $Q_{nd} = 3, 5$  and 10.

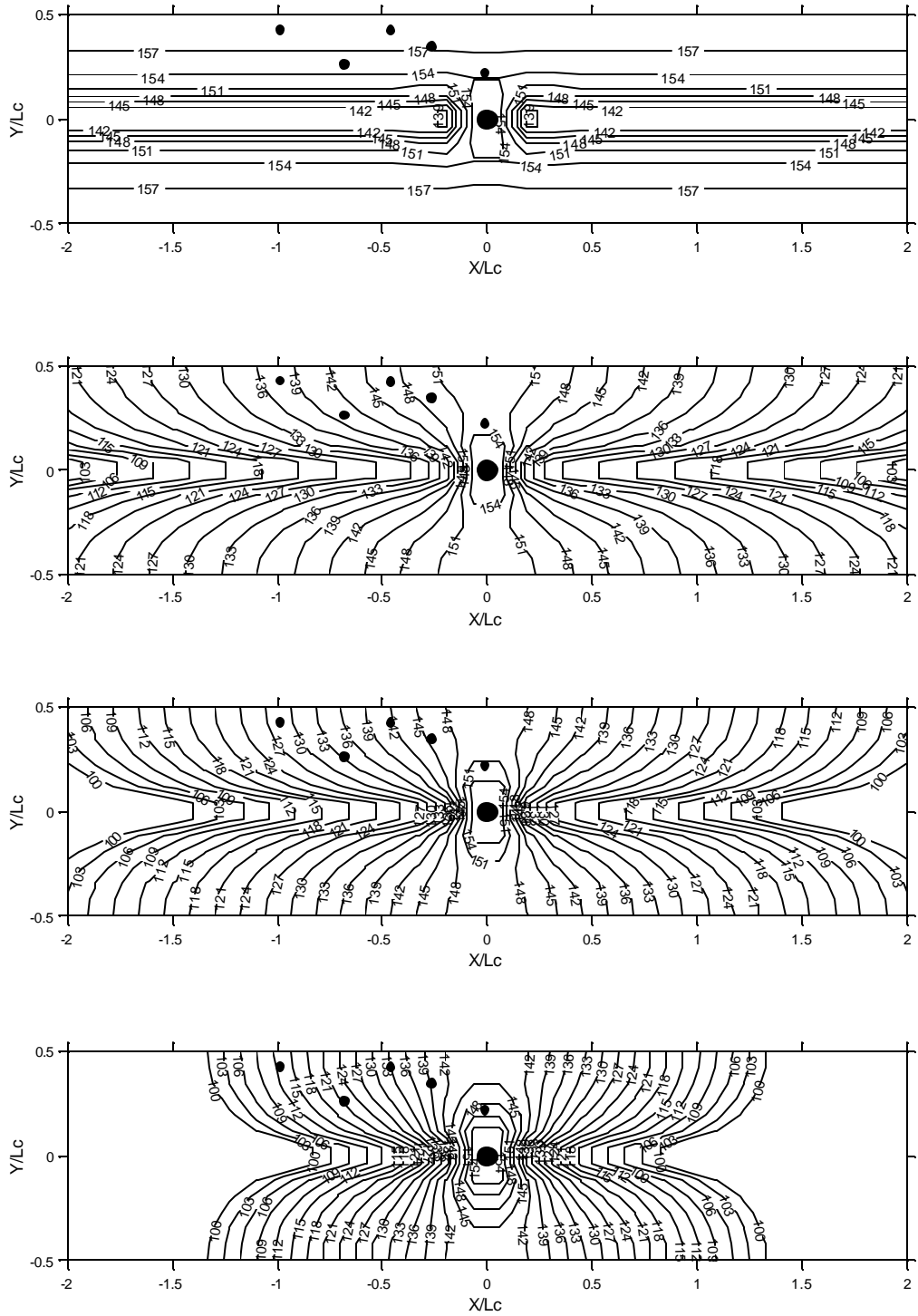


Figure J.2 Sound pressure level field (dB) at 5000Hz produced by single 6.35mm cylinder at center of duct (large black circle) for different real nondimensional volumetric damping ( $Q_{nd}$ ) values. Small circles represent microphone positions in our experimental setup. From top to bottom: No damping,  $Q_{nd} = 3, 5$  and 10.

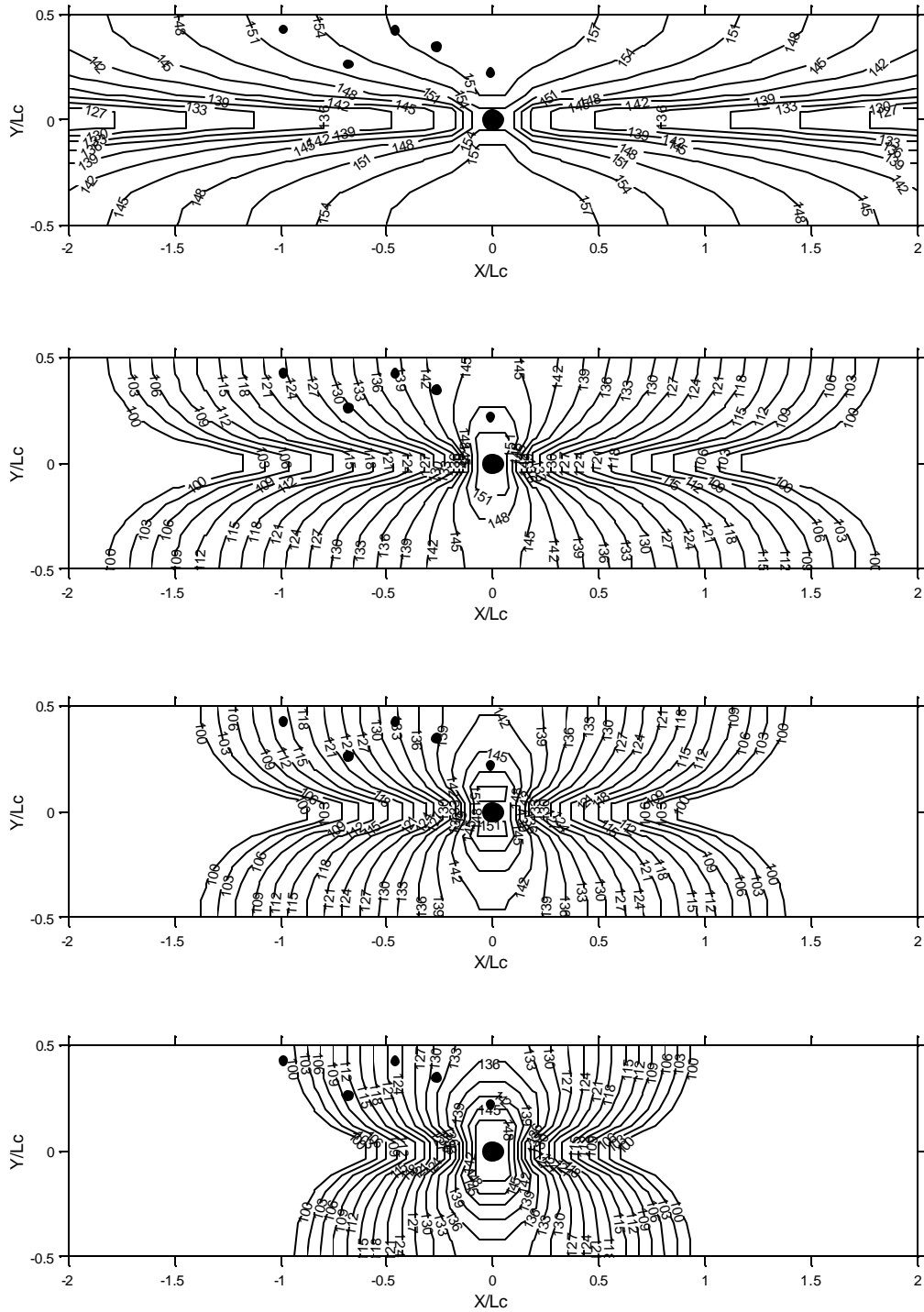


Figure J.3 Sound pressure level field (dB) at 4000Hz produced by single 6.35mm cylinder at center of duct (large black circle) for different imaginary nondimensional volumetric damping ( $Q_{nd}$ ) values. Small circles represent microphone positions in our experimental setup. From top to bottom: No damping,  $Q_{nd} = 3i$ ,  $5i$  and  $10i$ .



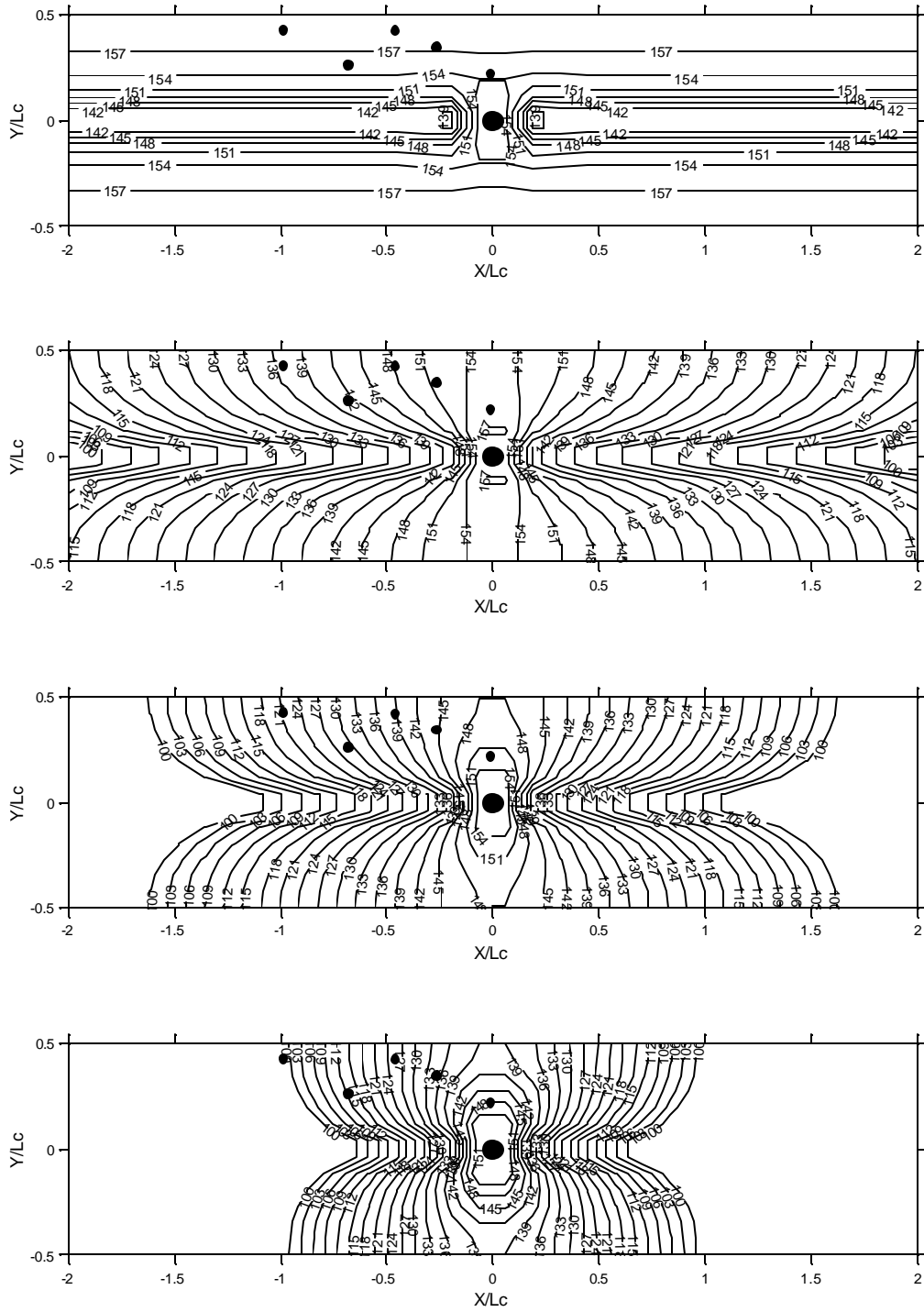


Figure J.4 Sound pressure level field (dB) at 5000Hz produced by single 6.35mm cylinder at center of duct (large black circle) for different imaginary nondimensional volumetric damping ( $Q_{nd}$ ) values. Small circles represent microphone positions in our experimental setup. From top to bottom: No damping,  $Q_{nd} = 3i$ ,  $5i$  and  $10i$ .

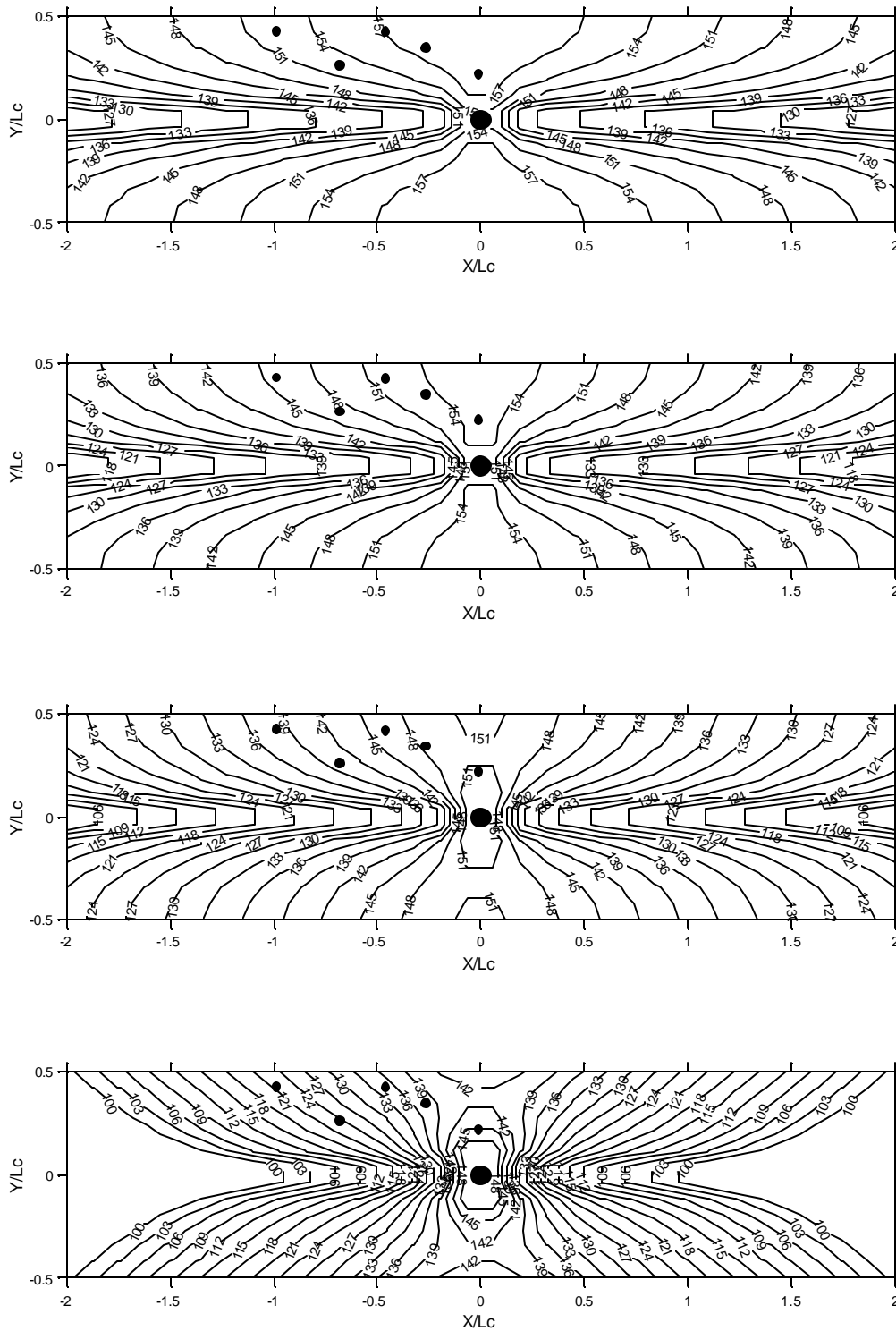


Figure J.5 Sound pressure level field (dB) at 4000Hz produced by single 6.35mm cylinder at center of duct (large black circle) for different real y-walls specific acoustic impedances ( $z_y$ ). Small circles represent microphone positions in our experimental setup. From top to bottom: No damping,  $z_y = 5$ , 2 and 0.5.

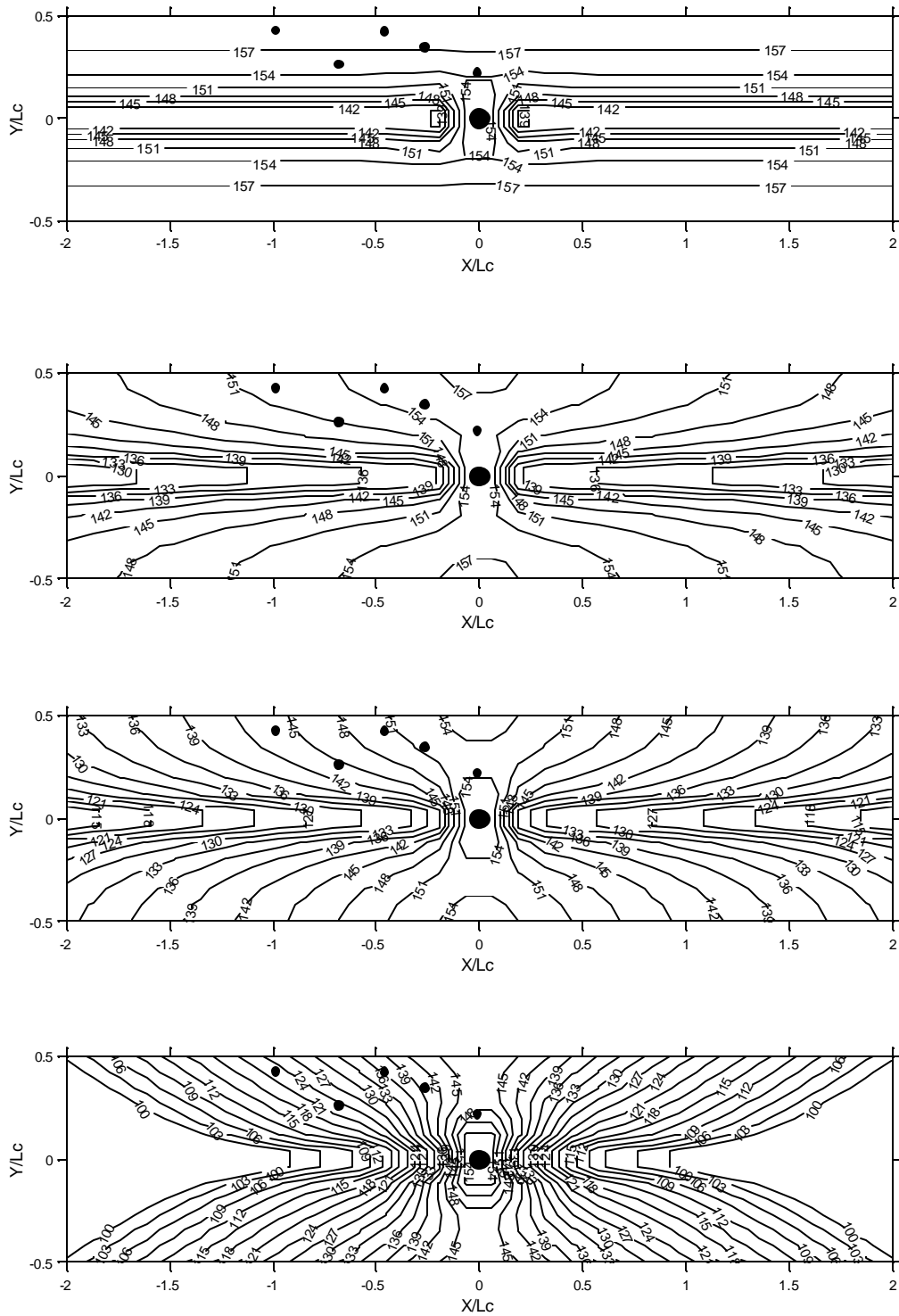


Figure J.6 Sound pressure level field (dB) at 5000Hz produced by single 6.35mm cylinder at center of duct (large black circle) for different real y-walls specific acoustic impedances ( $z_y$ ). Small circles represent microphone positions in our experimental setup. From top to bottom: No damping,  $z_y = 5$ , 2 and 0.5.

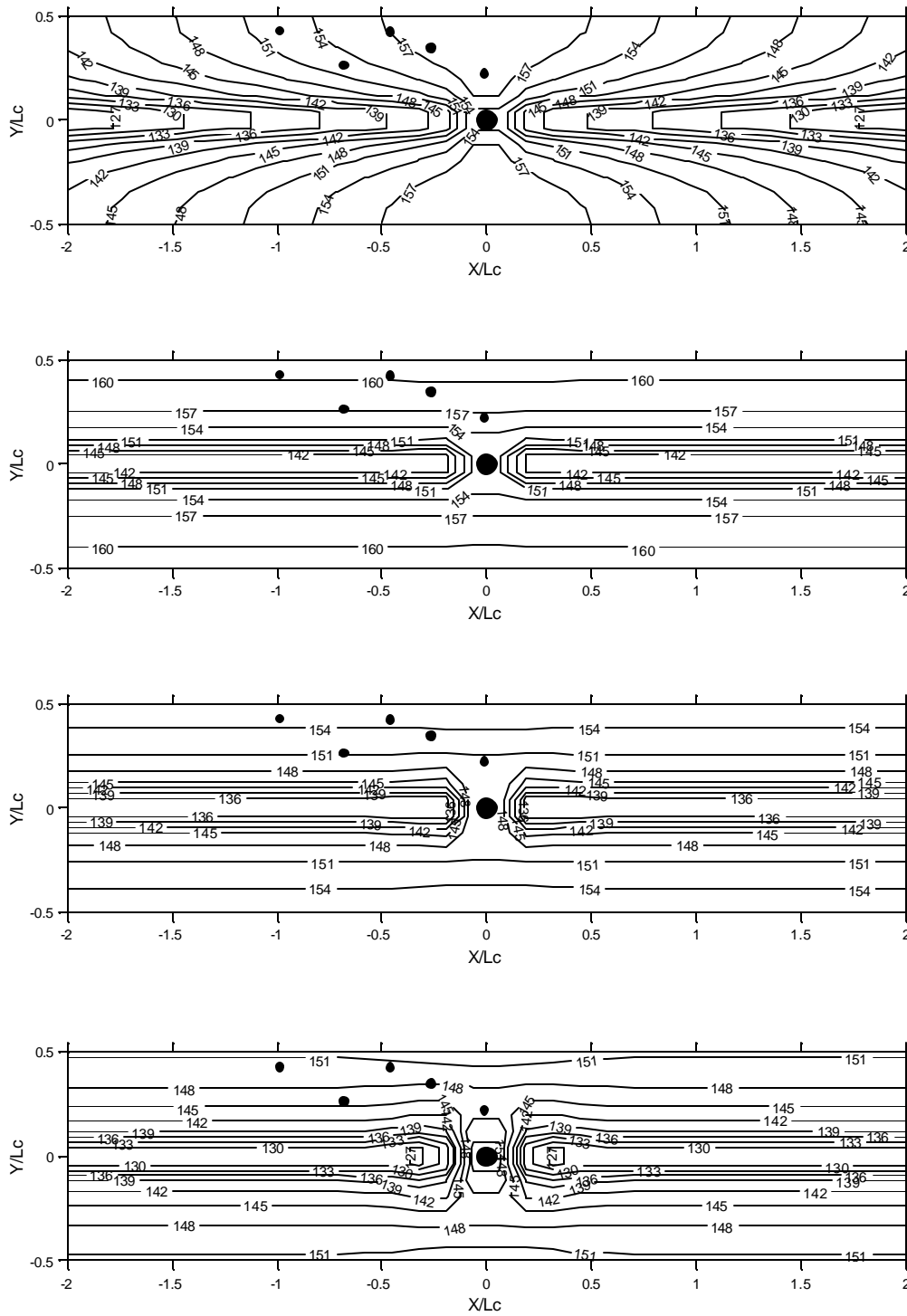


Figure J.7 Sound pressure level field (dB) at 4000Hz produced by single 6.35mm cylinder at center of duct (large black circle) for different imaginary y-walls specific acoustic impedances ( $z_y$ ). Small circles represent microphone positions in our experimental setup. From top to bottom: No damping,  $z_y = 5i$ ,  $2i$  and  $0.5i$ .

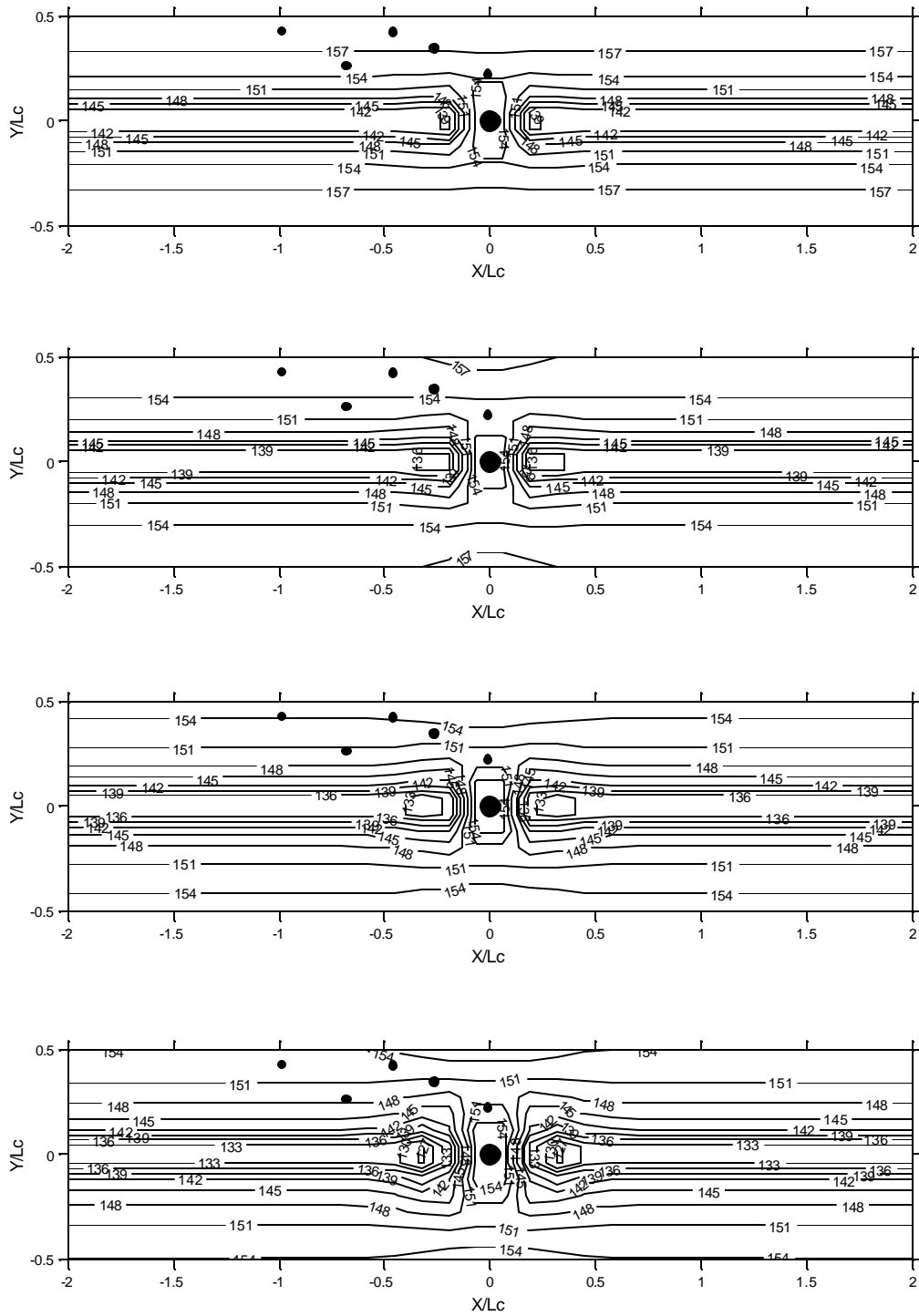


Figure J.8 Sound pressure level field (dB) at 5000Hz produced by single 6.35mm cylinder at center of duct (large black circle) for different imaginary y-walls specific acoustic impedances ( $z_y$ ). Small circles represent microphone positions in our experimental setup. From top to bottom: No damping,  $z_y = 5i$ ,  $2i$  and  $0.5i$ .

## Bibliography

- Abd-Rabbo A., Weaver D.S., 1986, "A flow visualization study of flow development in a staggered tube array", *Journal of Sound and Vibration* 106, 241-256.
- Achenbach E., 1971, "Influence of surface roughness on the cross-flow around a circular cylinder", *Journal of Fluid Mechanics*, 46, 321-335.
- Achenbach E., Heinecke E., 1981, "On vortex shedding from smooth and rough cylinders in the range of Reynolds numbers 6,000 to 5,000,000", *Journal of Fluid Mechanics*, 109, 239-251.
- Alemdaroglu N., Rebillat J.C., Goethals R., 1980, "An aeroacoustic coherence function method applied to circular cylinder flows", *Journal of Sound and Vibration*, 69, 427-439.
- Arie M., Kiya M., Tamura H., Mori H., 1983, "Pressure fluctuations in two circular cylinders in tandem", *ASME Journal of Fluids Engineering*, 105, 161-167.
- ASTM Standard E 1050-90 "Standard Test Method for Impedance and Absorption of Acoustical Materials Using a Tube, Two Microphones, and a Digital Frequency Analysis System"
- Baird R.C., 1954, "Pulsation-Induced Vibration in Utility Steam Generation Units", *Combustion*, 25, 38-44.
- Barrington E.A., 1973, "Acoustic vibrations in tubular exchangers", *Chemical Engineering Progress*, 69, 62-68.
- Baumeister K.J., Kreider K.L., 1996, "Finite difference time marching in the frequency domain: A parabolic formulation for the convective wave equation", *Journal of Vibration and Acoustics, Transactions of the ASME*, 118, 622-629
- Baylac G., Bai D., Gregoire J.P., 1973, "Study of flow and acoustic phenomena in a tube-bank", *Proceedings of Symposium on Vibration Problems in Industry, Keswick England*, paper 219.
- Bishop R.E.D., Hassan A.Y., 1963a, "The lift and drag forces on a circular cylinder in a flowing fluid", *Proceedings of the Royal Society of London, Series A*, 277, 32-50.
- Bishop R.E.D., Hassan A.Y., 1963b, "The lift and drag forces on a circular cylinder oscillating in a flowing fluid", *Proceedings of the Royal Society of London, Series A*, 277, 51-75.
- Blackburn H.M., 1994, "Effect of blockage on spanwise correlation in a circular cylinder", *Experiments in Fluids*, 18, 134-136.
- Blackburn H.M., Melbourne W.H., 1996, "The effect of free-stream turbulence on sectional lift forces on a circular cylinder", *Journal of Fluid Mechanics*, 306, 267-292.
- Blake W.K., 1986, *Mechanics of flow-induced sound and vibration, Vol. I*, Academic Press Inc.
- Blevins R.D. and Bressler M.M., 1993, "Experiments on acoustic resonance in heat exchanger tube bundles", *Journal of Sound and Vibration*, 164, 503-533.
- Blevins R.D., 1985, "The effect of sound on vortex shedding from cylinders" *Journal of Fluid Mechanics* 161, 217-237.
- Blevins R.D., 1986, "Acoustic modes of heat exchanger tube bundles", *Journal of Sound and Vibration* 109, 19-31.
- Blevins R.D., Bressler M.M., 1987b, "Acoustic Resonance in Heat Exchanger Tube Bundles- part II: Prediction and Suppression of Resonance", *Journal of Pressure Vessel Technology, Transactions of the ASME*, 109, 282-288.
- Blevins R.D., Bressler M.M., 1987a, "Acoustic resonance in heat exchanger tube bundles- part I: physical nature of the phenomenon", *Journal of Pressure Vessel Technology, Transactions of the ASME*, 109, 275-281.
- Blevins R.D., 1994, *Flow Induced Vibration*, Second edition, Krieger publishing company.
- Brayton, R.K., S.W. Director, G.D. Hachtel, and L. Vidigal, 1979, "A New Algorithm for Statistical Circuit Design Based on Quasi-Newton Methods and Function Splitting", *IEEE Trans. Circuits and Systems*, Vol. CAS-26, 784-794.

- Bruun H.H., Davies P.O.A.L., 1975, "An experimental investigation of the unsteady pressure forces on a circular cylinder in a turbulent cross flow", *Journal of Sound and Vibration*, 40, 535-559.
- Bull M.K., 1968, *Noise and acoustic fatigue in aeronautics, Chapter 8*, Editors E.J. Richards and D.J. Mead, John Wiley and Sons Ltd. Great Britain.
- Bull M.K., 1996, "Wall-pressure fluctuations beneath turbulent boundary layers: Some reflections on forty years of research", *Journal of Sound and Vibration*, 190, 299-315.
- Buresti G., 1981, "The effect of surface roughness on the flow regime around circular cylinders", *Journal of Wind Engineering and Industrial Aerodynamics*, 8, 105-114.
- Chen S.S., 1987, *Flow-induced vibration of circular cylindrical structures*, Hemisphere Publishing Corporation.
- Chen Y.N., 1968, "Flow-induced vibration and noise in tube-bank heat exchangers due to von Karman streets", *Journal of Engineering for Industry*, 90, 134-146.
- Chen Y.N., 1972a, "Fluctuating lift forces of the Karman vortex streets on single circular cylinders and in tube bundles. Part 2- Lift forces of single cylinders", *Journal of Engineering for Industry*, 94, 613-622.
- Chen Y.N., 1972b, "Fluctuating lift forces of the Karman vortex streets on single circular cylinders and in tube bundles Part 3- Lift forces in tube bundles", *Journal of Engineering for Industry*, 94, 623-628.
- Chen Y.N., 1984, "Flow-induced vibrations of in-line tube banks", *Proceedings ASME Symposium on Flow-Induced Vibrations*, Editors: M.P. Paidoussis, J.N. Chenoweth and J.M. Bernstein, Vol 3., 163-170, New York, ASME
- Chung J.Y., Blaser D. A., 1980a, "Transfer function method of measuring in-duct acoustic properties. I. Theory", *Journal of the Acoustical Society of America*, 68, 907-913.
- Chung J.Y., Blaser D. A., 1980b, "Transfer function method of measuring in-duct acoustic properties. II. Experiment", *Journal of the Acoustical Society of America*, 68, 914-921.
- Collinson A.E., Robinson R.G.J., 1991, "Cross-flow Strouhal numbers in square and triangular pitch tube arrays at Reynolds numbers from 80000–350000", *Proceedings I. Mech.E. International Conference on Flow Induced Vibrations, I. Mech. E. Vol. 6*, 217-230.
- Corcus G.M., 1964, "The structure of the turbulent pressure field in boundary layer flows", *Journal of Fluid Mechanics*, 18, 353-379.
- Cox J.S., Brentner K.S., Rumsey C.L., 1998, "Computation of vortex shedding and radiated sound for a circular cylinder: subcritical to transcritical Reynolds numbers", *Theoretical and Computational Fluid Dynamics*, 12, 233-253.
- Cox J.S., Rumsey C.L., Brentner K.S., Younis B.A., 1997, "Computation of vortex shedding and radiated sound for a circular cylinder", *4th International Symposium on Fluids-Structures Interactions, Aeroelasticity, Flow-Induced Vibration and Noise, Vol. 1*, 447-454.
- Cumpsty N.A., Whitehead D.S., 1971, "The excitation of acoustic resonances by vortex shedding", *Journal of Sound and Vibrations* 18, 353-369.
- Curle N., 1955, "The influence of solid boundaries upon aerodynamic sound", *Proceedings of the Royal Society of London, Series A*, 231, 505-514.
- Curle N., 1968, *Noise and acoustic fatigue in aeronautics, Chapter 5*, Editors E.J. Richards and D.J. Mead, John Wiley and Sons Ltd. Great Britain.
- Duarte-Ribeiro J.L., 1992, "Fluctuating lift and its spanwise correlation on a circular cylinder in a smooth and in a turbulent flow: a critical review", *Journal of Wind Engineering and Industrial Aerodynamics*, 40, 179-198.
- Eisinger F.L., 1998, "Acoustic vibration in steam generator and heat exchanger tube banks: An Overview", *Symposium on Flow-Induced Vibration in Shell-and-Tube Heat Exchangers*, Houston, USA, Heat Transfer Research Inc.

- Eisinger F.L., Francis J.T., Sullivan R.E., 1996, "Prediction of acoustic vibration in steam generator and heat exchanger tube banks", *Journal of Pressure Vessel Technology*, 118, 221-236.
- Eisinger F.L., Sullivan R.E., 1996, "Experience with unusual acoustic vibration in heat exchanger and steam generator tube banks", *Journal of Fluids and Structures* 10, 99–107.
- Etkin B., Korbacher G.K., Keefe R.T., 1957, "Acoustic radiation from a stationary cylinder in a fluid stream (Aeolian tones)", *Journal of the Acoustical Society of America*, 29, 30-36.
- Eversman W., Baumeister K.J., 1984, "Modelling of wind tunnel wall effects on the radiation characteristics of acoustic sources", AIAA-84-2364, AIAA-NASA 9th Aeroacoustics Conference October 15-17, Williamsburg Virginia.
- Eversman W., Steck J.E., 1984, "Finite element modelling of acoustic singularities with application to near and far field propeller noise", AIAA-84-2286, AIAA-NASA 9th Aeroacoustics Conference, October 15-17, Williamsburg, Virginia.
- Farassat F., 1992, *The acoustic analogy as a tool of computational aeroacoustics in Computational Aeroacoustics*, Ed. J.C. Hardin and M.Y. Hussaini, Springer Verlag, 133-155.
- Ffowcs-Williams J.E., Hawkings D.L., 1969, "Sound generation by turbulence and surfaces in arbitrary motion", *Philosophical Transactions of the Royal Society of London, Series A*, 264, 321-342.
- Ffowcs-Williams J.E., Zhao B.C., 1989, "The active control of vortex shedding", *Journal of Fluids and Structures* 3, 115-122.
- Fitz-Hugh J.S., 1973, "Flow induced vibration in heat exchangers", UKAEA/NPL International Symposium on Vibration Problems in Industry, Keswick, England paper no. 427.
- Fitzpatrick J.A., 1985, "The prediction of flow-induced noise in heat exchanger tube arrays", *Journal of Sound and Vibration* 99, 425-435.
- Fitzpatrick J.A., 1986, "A design guide proposal for avoidance of acoustic resonances in in-line heat exchangers", *Journal of Vibrations, Acoustics, Stress and Reliability in Design*, 108, 296-300.
- Fitzpatrick J.A., Donaldson I.S., 1977, "A preliminary study of flow and acoustic phenomena in tube banks", *Journal of Fluids Engineering, Transactions of the ASME*, 99, 681-686.
- Fitzpatrick J.A., Donaldson I.S., 1980, "Row depth effects on turbulence spectra and acoustic vibrations in tube banks", *Journal of Sound and Vibration*, 73, 225-237.
- Fitzpatrick J.A., Donaldson I.S., 1984, "Effects of scale on parameters associated with flow induced noise in tube arrays", *Proceedings of Symposium on Flow-Induced Vibrations, Vol 2. Vibrations of Arrays of Cylinders in Cross Flow* Editors M.P. Paidousiss, M.K. Au-Yang and S.S. Chen, 243-250.
- Fitzpatrick J.A., Donaldson I.S., McKnight W., 1988, "Strouhal numbers for flows in deep tube array models", *Journal of Fluids and Structures*, 2, 145-160.
- Gerrard J.H., 1955, "Measurements of the sound from circular cylinders in an airstream", *Proceedings of the Physical Society London, Series B*, 68, 453-461.
- Gerrard J.H., 1961, "An experimental investigation of the oscillating lift and drag of a circular cylinder shedding turbulent vortices", *Journal of Fluid Mechanics*, 11, 244-256.
- Goldstein M.E., 1976, *Aeroacoustics*, McGraw Hill.
- Grosche F.R., 1985, "Wind tunnel investigation of aeolian tones from rough surface cylinders", *Aero- and Hydro-Acoustics IUTAM Symposium*, Editors G. Compte-Bellot and J.E. Ffowcs-Williams, Lyon, France.
- Grotz B.J., Arnold F.R., 1956, "Flow-induced vibrations in heat exchangers", Technical Report Number 31, Department of Mechanical Engineering, Stanford University.
- Holle W., 1938, "Frequenz- und schallstarkemessungen an hiebtone", *Akust. Z.* 3, 321-331.



- Holtz M., 1998, "Treatment of flow-induced vibration in heat exchangers in the 8<sup>th</sup> edition of the TEMA (Tubular Exchanger Manufacturers Association) standards", Symposium on Flow-Induced Vibration in Shell-and-Tube Heat Exchangers, Houston, USA. Heat Transfer Research Inc.
- Howe M.S., 1998, *Acoustics of fluid-structure interactions*, Cambridge University Press.
- Hrnjak P., Miller N.R. and Rodarte E., 1997, "Acoustic Resonance in Plate Evaporators", Air Conditioning and Refrigeration Center, Mechanical and Industrial Engineering Department, University of Illinois at Urbana-Champaign, Contract Report ACRC CR-10.
- Hussain A.K.M.F., Reynolds W.C., 1975, "Measurements in fully developed turbulent channel flow" *Journal of Fluids Engineering*, Transactions of the ASME, 97, 568-580.
- Johnson C.O., Loehrke R.I., 1984, "An experimental investigation of wake edge tones", *AIAA Journal*, 22, 1249-1253.
- Keefe R.T., 1961, "An investigation of the fluctuating forces acting on a stationary circular cylinder in a subsonic stream and of the associated sound field", Institute of Aerophysics, University of Toronto, Report 76.
- Keefe R.T., 1962, "Investigation of the fluctuating forces acting on a stationary circular cylinder in a subsonic stream and of the associated sound field", *Journal of the Acoustical Society of America*, 34, 1711-1714.
- Klein S.A., Alvarado F.L. 2001, "Engineering equation solver", Version 6.026, F-Chart Software, www.fChart.com
- Koopman G.H., 1969, *Wind induced vibration and its associated sound fields*, Ph.D. Thesis, Catholic University, Washington D.C.
- Kouba J., 1986, "Vortex shedding and acoustic emission in finned tube banks exposed to cross flow", ASME Symposium on Flow-Induced Vibrations, Editors Chen S.S., Simonis J.C., Shin Y.S., PVP-Vol. 104, 213-217.
- Kubo Y., Miyazaki M., Kato K., 1989, "Effects of end plates and blockage of structural members on drag forces", *Journal of Wind Engineering and Industrial Aerodynamics*, 32, 329-342.
- Laufer J., 1950, "Investigation of turbulent flow in a two-dimensional channel", NACA Technical Report 2123.
- Leehey P., Hanson C.E., 1971, "Aeolian tones associated with resonant vibration", *Journal of Sound and Vibration*, 13, 465-483.
- Levine H., 1983, "On the radiation impedance of a rectangular piston", *Journal of Sound and Vibration*, 89, 447-455.
- Lighthill M.J., 1952, "On sound generated aerodynamically I. General theory", *Proceedings of the Royal Society of London, Series A*, 211, 564-587.
- Lighthill M.J., 1954, "On sound generated aerodynamically II. Turbulence as a source of sound", *Proceedings of the Royal Society of London, Series A*, 222, 1-33.
- Mair W.A., Jones P.D.F., Palmer R.K.W., 1975, "Vortex shedding from finned tubes", *Journal of Sound and Vibration*, 39, 293-296.
- Mechel F.P., 1988, "Notes on the radiation impedance, especially of piston-like radiators", *Journal of Sound and Vibration*, 123, 537-572.
- Miller N.R., Hrnjak P., Rodarte E. 1998, "Continued research on plate evaporator noise emissions", Air Conditioning and Refrigeration Center, Mechanical and Industrial Engineering Department, University of Illinois at Urbana-Champaign, Contract Report ACRC CR-31.
- Miller R.W., 1996, *Flow measurement engineering handbook*, McGraw-Hill.
- Morse P.M., Ingard K.U. 1968, *Theoretical Acoustics*, McGraw-Hill.
- Mosher M., 1986a, "Effect of a wind tunnel on the acoustic field from various aeroacoustic sources", AIAA 10th Aeroacoustics conference, July, Seattle WA, Paper AIAA 86-1897-CP.
- Mosher M., 1986b, *The influence of wind tunnel walls on discrete frequency noise*, Ph.D. Thesis, Stanford University.

- Murray B.G., Rae G.J., Bryce W.B., 1982, "Strouhal numbers in tube arrays", Proceedings of 3<sup>rd</sup> Vibration in Nuclear Plants Conference, Keswick, England.
- Nemoto A., Yamada M., 1992, "Flow-induced acoustic resonance caused by fin-tube bundles", Symposium on Flow-Induced Vibration and Noise, PVP-Vol. 243, Vol. 4, ASME, 137-153.
- Niederschulte M.A., 1989, *Turbulent flow through a rectangular channel*, Ph.D. Thesis, University of Illinois at Urbana-Champaign.
- Norberg C., Sunden B., 1987, "Turbulence and Reynolds number effects on the flow and fluid forces on a single cylinder in cross flow", *Journal of Fluids and Structures*, 1, 337-357.
- Norton M.P., 1989, *Fundamentals of noise and vibration analysis for engineers*, Cambridge University Press.
- Oengören A., Ziada S., 1992, "Vorticity shedding and acoustic resonance in an in-line tube bundle part II: acoustic resonance", *Journal of Fluids and Structures* 6, 293-309.
- Oengören A., Ziada S., 1998, "An in depth study of vortex shedding, acoustic resonance and turbulent forces in normal triangle tube arrays", *Journal of Fluids and Structures*, 12, 717-758.
- Owen P.R., 1965, "Buffeting excitation of boiler tube vibration", *Journal of Mechanical Engineering Science*, 7, 431-439.
- Paidoussis M.P., 1982, "A review of flow-induced vibrations in reactors and reactor components", *Nuclear Engineering and Design*, 74, 31-60.
- Parker R., 1978, "Acoustic resonances in passages containing banks of heat exchanger tubes", *Journal of Sound and Vibration*, 57, 245-260.
- Parker R., Welsh M.C. 1983, "Effects of sound on flow separation from blunt flat plates", *International Journal of Heat and Fluid Flow*, 4, 113-127.
- Parker R., Welsh M.C., 1982, "The effect of sound on flow over bluff bodies", Proceedings of 3<sup>rd</sup> Vibration in Nuclear Plants Conference, Keswick, England.
- Patel V.C., Head M.R., 1969, "Some observations on skin friction and velocity profiles in fully developed pipe and channel flows", *Journal of Fluid Mechanics*, 38, 181-201.
- Pedersen R.C., Norton M.P., 1997, "Quantification of acoustic and hydrodynamic fields in flow duct systems", *Applied Acoustics*, 50, 205-230.
- Peterka J.A., Richardson P.D., 1969, "Effects of sound on separated flows", *Journal of Fluid Mechanics*, 37, 265-287.
- Phillips O.M., 1956, "The intensity of aeolian tones", *Journal of Fluid Mechanics*, 1, 607-624.
- Pierce A.D., 1994, *Acoustics: An introduction to its physical principles and applications*, Acoustical Society of America.
- Polak D.R., Weaver D.S., 1995, "Vortex shedding in normal triangular tube arrays", *Journal of Fluids and Structures*, 9, 1-17.
- Price S.J., Paidoussis M.P., Mark B., 1995, "Flow visualization of the interstitial cross-flow through parallel triangular and rotated square arrays of cylinders", *Journal of Sound and Vibrations*, 181, 85-98.
- Putman A.A., 1959, "Flow-Induced Noise in Heat Exchangers", *Journal of Engineering for Power*, 81, 417-422.
- Rae G.J., Wharmby J.S., 1987, "Strouhal numbers for in-line tube arrays", International Conference on Flow-Induced Vibrations, Ed. Roger King, Bowness-on-Windermere, England, May 12-14.
- Rayleigh Lord, 1896, *Theory of Sound, Volume II*, 2<sup>nd</sup> Edition Dover.
- Rayleigh, J.W.S., 1915, "Aeolian tones", *Philosophical Magazine*, Vol. XXIX, 433-444, also in *Scientific Papers*, Vol. VI, 315-325, Dover, New York 1964.
- Ribner H.S., 1964, "The generation of sound by turbulent jets", *Advances in Applied Mechanics*, 8, 103-132.

- Richardson E.G., 1923, "Aeolian tones", Proceedings of the Physical Society London, Series B, 36, 153-167.
- Richardson E.G., 1958, "The flow and sound field near a cylinder towed through water", Applied Scientific Research, Vol. 7, Section A, 341-350.
- Richter A., Naudascher E., 1976, "Fluctuating forces on a rigid circular cylinder in confined flow" Journal of Fluid Mechanics, 78, 561-576.
- Rodarte E., Miller N.R., 2000, "Flow-induced acoustic resonance in plate heat exchangers: comparisons to large heat exchangers", Proceedings of 7<sup>th</sup> International Conference on Flow-Induced Vibrations, Editors S. Ziada and T. Staubli, Lucerne, Switzerland, June 19-23. 637-644.
- Rodarte E., Miller N.R., Hrnjak P., 1998a, "Acoustic resonance of plate heat exchangers", International Journal of Refrigeration, 21, 626-638.
- Rodarte E., Miller N.R., Hrnjak P., 1998b, "Use of stereolithography as a design tool for developing quiet plate mobile air conditioning evaporators", SAE International Congress and Exposition, Detroit USA, Feb. 23-26 Paper No. 980287.
- Rodarte E., Singh G., Miller N., Hrnjak P., 1999a, "Refrigerant expansion noise propagation through downstream tube walls", SAE International Congress and Exposition, Detroit USA, March 1-4. Paper number 1999-01-1197. Also selected for publication in Journal of Passenger Cars, SAE Transactions Vol. 108, Section 6, 2224-2234.
- Rodarte E., Singh G., Miller N., Hrnjak P., 1999b, "Noise generation from expansion devices in refrigerant", SAE International Congress and Exposition, Detroit USA, March 1-4. Paper number 1999-01-0866.
- Rodarte E., Singh G., Miller N.R., and Hrnjak P., 2000, "Sound attenuation in tubes due to visco-thermal effects", Journal of Sound and Vibration, 231, 1221-1242.
- Rogers J.D., Penterson C.A., 1977, "Predicting sonic vibration in cross flow heat exchangers- experimental and model testing", ASME paper 77-WA/DE-28.
- Savkar S.D., 1984, "Buffeting of cylindrical arrays in cross flow", Symposium on flow-Induced Vibrations, Vol. 2, Vibrations of arrays of cylinders in cross flow, Ed. M.P Paidoussis, M.K. Au-Yang, S.S. Chen.
- Schewe G., 1983, "On the force fluctuations acting on a circular cylinder in crossflow from subcritical up to transcritical Reynolds numbers", Journal of Fluid Mechanics, 133, 265-285.
- So R.M.C., Savkar S.D., 1981, "Buffeting forces on rigid circular cylinders in cross flows", Journal of Fluid Mechanics, 105, 397-425.
- Stansby P.K., 1974, "The effects of end plates on the base pressure coefficient of a circular cylinder", Aeronautical Journal, 78, 36-37.
- Stoneman, S.A.T., Hourigan, K., Stokes, A.N. & Welsh, M.C., 1988, "Resonant sound caused by flow past two plates in tandem in a duct", Journal of Fluid Mechanics, 192, 455-484.
- Stowell E.Z., Deming A.F., 1935, "Vortex noise from rotating cylindrical rods", NACA Technical Note No. 519.
- Stowell E.Z., Deming A.F., 1936, "Vortex noise from rotating cylindrical rods", Journal of the Acoustical Society of America, 7, 190-98.
- Stratton J.A., 1941, *Electromagnetic Theory*, New York, McGraw-Hill.
- Strouhal V., 1878, "Ueber eine besondere art der tonenegung", Annalen der Physik und Chemie (Leipzig), Series 5, 5, 216-251.
- Szepessy S., 1993, "On the control of circular cylinder flow by end plates", European Journal of Mechanics B/ Fluids, 12, 217-244.
- Szepessy S., 1994, "On the spanwise correlation of vortex shedding from a circular cylinder at high subcritical Reynolds number", Physics of Fluids, 6, 2406-2416.
- Szepessy S., Bearman P.W., 1992, "Aspect ratio and end plate effects on vortex shedding from a circular cylinder", Journal of Fluid Mechanics, 234, 191-217.

- Taylor B.N. and Kuyatt, C.E., 1994, "Guidelines for evaluating and expressing the uncertainty of NIST measurement results", National Institute of Standards and Technology Technical Note 1297.
- Taylor J.R., 1997, "An introduction to error analysis, the study of uncertainties in physical measurements", Second Edition, University Science Books. ISBN 0-935702-75-X
- Weaver D.S., 1993, "Vortex shedding and acoustic resonance in heat exchanger tube arrays", Technology for the 90's, Chapter 6, Edited by Au-Yang M.K., ASME
- Weaver D.S., Abd-Rabbo A., 1985, "A flow visualization study of a square array of tubes in water crossflow", Journal of Fluids Engineering, 107, 354-363.
- Weaver D.S., Fitzpatrick J.A., 1988, "A review of cross-flow induced vibrations in heat exchanger tube arrays", Journal of Fluids and Structures, 2, 73-93.
- Weaver D.S., Fitzpatrick J.A., ElKashlan M., 1987, "Strouhal numbers for heat exchanger tube arrays in cross flow", Journal of Pressure Vessel Technology 109, 219-223.
- Welsh M.C., Hourigan K., Welch L.W., Downie R.J. Thompson M.C., Stokes A.N., 1990, "Acoustics and experimental methods: the influence of sound on flow and heat transfer", Experimental Thermal and Fluid Science, 3, 138-152.
- West G.S., Apelt C.J., 1993, "Measurements of fluctuating pressures and forces on a circular cylinder in the Reynolds number range  $10^4$  to  $2.5 \times 10^5$ ", Journal of Fluids and Structures, 7, 227-244.
- Weston P.G., Dunn W.E. Miller N.R., 1996, "Design and construction of a mobile air conditioning test facility for transient studies", University of Illinois, Air Conditioning and Refrigeration Center Technical Report 97, ACRC TR-97.
- White F.M., 1979, *Fluid Mechanics*, McGraw-Hill. 318-345.
- Wylie C.J., Barret L.C., 1985, *Advanced engineering mathematics*, fifth edition, McGraw-Hill International Editions.
- Xia Y., 1986, "Acoustic resonances induced by vortex shedding with a single tube in a duct", Flow induced vibrations, Ed. Chen S.S., Simonis J.C., Shin Y.S., ASME, PVP-Vol. 243, Vol. 104, 201-205.
- Zdravkovich M.M., 1987, "The effects of interference between circular cylinders in cross flow", Journal of Fluids and Structures, 1, 239-261.
- Zdravkovich M.M., 1990, "Conceptual overview of laminar and turbulent flows past smooth and rough circular cylinders", Journal of Wind Engineering and Industrial Aerodynamics, 33, 53-62.
- Zdravkovich M.M., 1997, *Flow around circular cylinders- Vol. 1 Fundamentals*, Oxford University Press.
- Ziada S., 1998, "Strouhal Numbers of Vortex Shedding and Acoustic Resonance of Heat Exchanger Tube Bundles", Symposium on Flow-Induced Vibration in Shell-and-Tube Heat Exchangers, Feb. 16, Houston, USA. Heat Transfer Research Inc.
- Ziada S., Bolleter U., Chen Y.N., 1984, "Vortex shedding and acoustic resonance in staggered yawed array of tubes", ASME Symposium on Flow-Induced Vibrations, Vol. 2, Vibrations of Arrays of Cylinders in Cross Flow, Editors M.P. Paidoussis, M.K. Au-Yang, S.S. Chen, 227-241.
- Ziada S., Oengören A., 1992, "Vorticity shedding and acoustic resonance in an in-line tube bundle part I: Vorticity shedding", Journal of Fluids and Structures, 6, 271-292.
- Ziada S., Oengören A., 1993, "Vortex shedding in an in-line tube bundle with large tube spacings", Journal of Fluids and Structures, 7, 661-687.
- Ziada S., Oengören A., Bühlmann E.T., 1989a, "On acoustical resonance in tube arrays, Part I: Experiments ", Journal of Fluids and Structures, 3, 293-314.
- Ziada S., Oengören A., Bühlmann E.T., 1989b, "On acoustical resonance in tube arrays, Part II Damping criteria ", Journal of Fluids and Structures, 3, 315-324.

Zukauskas A., Katinas V, 1980, "Flow induced vibration in heat exchanger tube banks", IUTAM-IAHT Symposium on Practical Experiences with Flow-Induced Vibrations, Editors Naudascher E. and Rockwell D., Berlin, Germany, Springer-Verlag, 188-196.